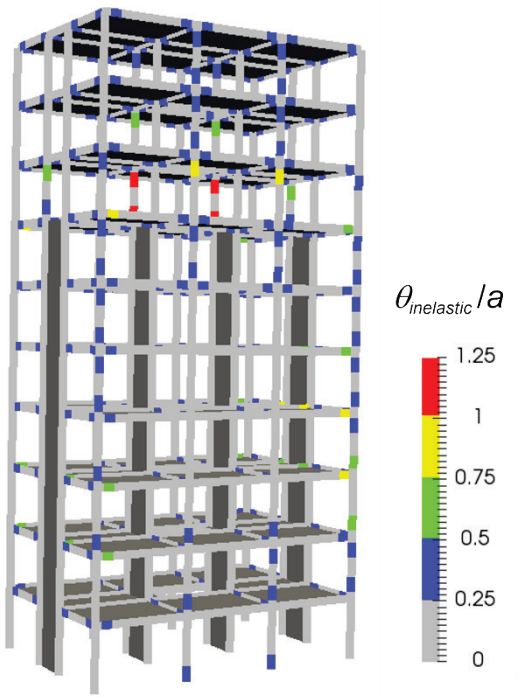
NIST GCR 22-917-50



Benchmarking Evaluation Methodologies for Existing Reinforced Concrete Buildings

Applied Technology Council

This publication is available free of charge from:
https://doi.org/10.6028/NIST.GCR.22-917-50

March 2022

nehrp

NIST
National Institute of Standards and Technology
U.S. Department of Commerce

AUTHENTICATED
U.S. GOVERNMENT
INFORMATION
GPO

Disclaimer

This report was prepared for the Engineering Laboratory of the National Institute of Standards and Technology (NIST) under Contract SB1341-13-CQ-0009, Task Order 16-476 and 1333ND19PNB730832. The contents of this publication do not necessarily reflect the views and policies of NIST or the U.S. Government.

This report was produced by the Applied Technology Council (ATC). While endeavoring to provide practical and accurate information, the Applied Technology Council, the authors, and the reviewers assume no liability for, nor express or imply any warranty with regard to, the information contained herein. Users of information contained in this report assume all liability arising from such use.

Unless otherwise noted, photos, figures, and data presented in this report have been developed or provided by ATC staff or consultants engaged under contract to provide information as works for hire. Any similarity with other published information is coincidental. Photos and figures cited from outside sources have been reproduced in this report with permission. Any other use requires additional permission from the copyright holders.

Certain commercial software, equipment, instruments, or materials may have been used in the preparation of information contributing to this report. Identification in this report is not intended to imply recommendation or endorsement by NIST, nor is it intended to imply that such software, equipment, instruments, or materials are necessarily the best available for the purpose.

NIST policy is to use the International System of Units (metric units) in all its publications. In this report, however, information is presented in U.S. Customary Units (inch-pound), as this is the preferred system of units in the U.S. engineering industry.

NIST GCR 22-917-50

Benchmarking Evaluation Methodologies for Existing Reinforced Concrete Buildings

Prepared for
U.S. Department of Commerce
Engineering Laboratory
National Institute of Standards and Technology
Gaithersburg, MD 20899-8600

By
Applied Technology Council
201 Redwood Shores Parkway, Suite 240
Redwood City, CA 94065

This publication is available free of charge from:
https://doi.org/10.6028/NIST.GCR.22-917-50

March 2022

U.S. Department of Commerce
Gina M. Raimondo, Secretary

National Institute of Standards and Technology
James K. Olthoff, Performing the Non-Exclusive Functions and Duties of the Under Secretary of Commerce for Standards and Technology & Director

Participants

National Institute of Standards and Technology

Siamak Sattar, Acting Group Leader, Earthquake Engineering Group
Dustin Cook, NRC Post-doctoral Fellow, Earthquake Engineering Group
Steven L. McCabe, Associate Division Chief for Statutory Programs, Materials and Structural Systems Division
Engineering Laboratory
www.NEHRP.gov

Applied Technology Council

201 Redwood Shores Parkway, Suite 240
Redwood City, California 94065
www.ATCouncil.org

Program Management

Jon A. Heintz (Program Manager)
Ayse Hortacsu (Associate Program Manager)

Program Committee on Seismic Engineering

Jon A. Heintz (Chair)
Michael Cochran
James R. Harris
James Jirsa
Roberto Leon
Stephen Mahin
James O. Malley
Donald Scott
Andrew Whittaker

Project Technical Committee

Russell Berkowitz (Project Director)
Wassim Ghannoum
Insung Kim
Dawn Lehman
Abbie Liel
Laura Lowes
Adolfo Matamoros
Farzad Naeim
Rob Smith
John Wallace

Working Group Members

Saman A. Abdullah
Tarbin Basnet
Travis Chrupalo
Alex Chu
Dustin Cook
Ariel Creagh
John A. Egan
Hamid Khodadadi
Kristijan Kolozvari
Ali Roufegarinejad
Andrew Sen

Project Review Panel

Brian Kehoe
Santiago Pujol
Peter Somers
Daniel Zepeda

This publication is available free of charge from: https://doi.org/10.6028/NIST.GCR.22-917-50

Preface

In 2016, the Applied Technology Council (ATC), with funding from National Institute of Standards and Technology (NIST) under Contract SB1341-13-CQ-0009 Task Order 16-476, commenced the ATC-134 project to benchmark evaluation procedures in ASCE/SEI 41 with respect to data recorded for six reinforced concrete structures subjected to actual earthquakes or tested on a shake table. A secondary objective of the effort was to compare the evaluation results predicted by ASCE 41 with other evaluation standards. In 2019, ATC was awarded NIST Contract No. 1333ND19PNB730832 to extend the project to include evaluation of two additional buildings under the ATC-134-1 project. The need for benchmarking ASCE 41 methodologies was identified as a top priority by a workshop conducted in 2008 (NIST, 2009).

This report presents summary findings from studies of eight reinforced concrete structures and recommendations for improvements to the next edition of ASCE 41, as well as opportunities for future work.

ATC is indebted to members of the ATC-134 and ATC-134-1 Project Teams for their efforts in conducting the studies presented in this report. The Project Technical Committee, consisting of Russell Berkowitz (Chair), Wassim Ghannoum, Insung Kim, Dawn Lehman, Abbie Liel, Laura Lowes, Adolfo Matamoros, Farzad Naeim, Rob Smith, and John Wallace, managed the technical development efforts and served as primary authors of this report. Saman Abdullah, Tarbin Basnet, Travis Chrupalo, Alex Chu, Dustin Cook, Ariel Creagh, John Egan, Hamid Khodadadi, Kristijan Kolozvari, Ali Roufegarinejad, and Andrew Sen conducted focused studies as members of the Project Working Group. The Project Review Panel, consisting of Brian Kehoe, Santiago Pujol, Peter Somers, and Daniel Zepeda provided technical review and advice at key stages of the work. The names and affiliations of all who contributed to this report are provided in the list of Project Participants.

ATC also gratefully acknowledges Siamak Sattar, Dustin Cook, and Steve McCabe at NIST for their input and guidance in the preparation of this document. ATC staff members Ginevra Rojahn and Carrie Perna provided report production services.

Ayse Hortacsu
ATC Director of Projects

Jon A. Heintz
ATC Executive Director

Table of Contents

This publication is available free of charge from: https://doi.org/10.6028/NIST.GCR.22-917-50

Preface ..... **iii**

List of Figures ..... **xiii**

List of Tables ..... **xxxv**

1. Introduction **1-1**
- 1.1 Background and Motivation 1-1
- 1.2 Project Overview 1-2
- 1.3 Seismic Evaluation Methodologies 1-2
  - 1.3.1 ASCE/SEI 41, *Seismic Evaluation and Retrofit of Existing Buildings* 1-3
  - 1.3.2 Other Seismic Building Evaluation Methodologies 1-3
- 1.4 Selection of Buildings for Study 1-4
- 1.5 Report Organization 1-7

2. Project Approach **2-1**
- 2.1 Overview 2-1
- 2.2 Seismic Evaluation per ASCE 41 2-1
  - 2.2.1 Analysis Model 2-1
  - 2.2.2 Acceptance Criteria and Performance Objectives 2-2
- 2.3 Comparison of Analytical Results to Observed Performance 2-5
  - 2.3.1 Use of Test Data in Literature 2-6
  - 2.3.2 Use of FEMA P-58 Fragility Database 2-7
- 2.4 Fragility Assessment 2-9
  - 2.4.1 Approach 2-9
  - 2.4.2 Interpretation of Fragility Assessments 2-10
- 2.5 Comparison to Other Evaluation Methods 2-11
  - 2.5.1 FEMA P-2018 2-11
  - 2.5.2 Eurocode 2-12
  - 2.5.3 NZSEE Guidelines 2-12

3. Three-story Test Frame **3-1**
- 3.1 Overview 3-1
- 3.2 Building Description and Observed Performance 3-2
  - 3.2.1 Building Description 3-2
  - 3.2.2 Building Instrumentation 3-4
  - 3.2.3 Ground Motion 3-4
  - 3.2.4 Observed Performance 3-6
- 3.3 Nonlinear Dynamic Procedure using Perform3D 3-8
  - 3.3.1 Modeling Approach 3-8
  - 3.3.2 Global Performance: Model vs. Observation 3-8

3.3.3 Component Performance: Model vs. Observation 3-12
3.4 Nonlinear Dynamic Procedure using OpenSees 3-17
3.4.1 Modeling Approach 3-17
3.4.2 Global Performance: Model vs. Observation 3-18
3.4.3 Component Performance: Model vs. Observation 3-19
3.5 Linear Procedures 3-20
3.5.1 Modeling Approach 3-20
3.5.2 Ground Motion Demands for Linear Static and Linear Response Spectrum Analyses 3-20
3.5.3 Global Performance: Model vs. Observation 3-21
3.5.4 Component Performance: Model vs. Observation 3-25
3.6 Fragility Assessment 3-28
3.7 FEMA P-2018 Evaluation 3-28
3.7.1 Evaluation Approach 3-28
3.7.2 Global Performance: Evaluation Procedure vs. Observation 3-28
3.8 Summary 3-29
3.8.1 Global Performance 3-29
3.8.2 Component Performance 3-31
3.8.3 Fragility Assessment and FEMA P-2018 Evaluation 3-31
3.8.4 Analytical Study Takeaways 3-32
3.8.5 Study Limitations 3-32

4. Four-story Frame and Wall Test Structure 4-1
4.1 Overview 4-1
4.2 Building Description and Observed Performance 4-2
4.2.1 Building Description 4-2
4.2.2 Ground Motion 4-5
4.2.3 Observed Performance 4-7
4.3 Nonlinear Dynamic Procedure using OpenSees 4-10
4.3.1 Modeling Approach 4-10
4.3.2 Global Performance: OpenSees LP NJ Model vs. Observation 4-16
4.3.3 Global Performance: OpenSees LP Models vs. Observation 4-22
4.3.4 Global Performance: OpenSees Fiber Models vs. Observation 4-24
4.3.5 Component Performance: OpenSees LP NJ Model vs. Observation 4-31
4.3.6 Summary Findings 4-36
4.4 Nonlinear Dynamic Procedure using Perform3D 4-36
4.4.1 Modeling Approach 4-37
4.4.2 Global Performance: Perform3D EJ Model vs. Observation 4-38
4.4.3 Global Performance: Perform3D NJ Model vs. Observation 4-43
4.4.4 Component Performance: Perform3D NJ Model vs. Observation 4-44
4.4.5 Summary Findings 4-48
4.5 Comparison of Perform3D and OpenSees LP Models 4-49
4.5.1 Global Performance Comparison 4-49

This publication is available free of charge from: https://doi.org/10.6028/NIST.GCR.22-917-50

4.6 Linear Dynamic Procedure 4-51
4.6.1 Modeling Approach 4-51
4.6.2 Global Performance: Model vs. Observation 4-52
4.6.3 Component Performance: Model vs. Observation 4-53
4.6.4 Summary Findings 4-53
4.7 Fragility Assessment 4-44
4.8 Eurocode Evaluation 4-58
4.9 New Zealand Assessment Guidelines 4-59
4.9.1 Beam and Column Assessment 4-60
4.9.2 Beam-Column Joint Assessment 4-65
4.9.3 Wall Assessment 4-68
4.9.4 Evaluation of the Hierarchy of Strength and Sequence of Events for a Beam-Column Joint Sub-Assembly 4-71
4.9.5 Global Capacity of Moment Resisting Frame 4-73
4.9.6 Dual Capacity of Wall-Frame 4-76
4.10 FEMA P-2018 Evaluation 4-84
4.10.1 Evaluation Approach 4-84
4.10.2 Global Performance: Evaluation Procedure vs. Observation 4-84
4.11 Summary 4-86
4.11.1 Global Performance 4-86
4.11.2 Component Performance 4-90
4.11.3 Analytical Study Takeaways 4-90
4.11.4 Fragility Analysis 4-91
4.11.5 Study Limitations 4-91

5. Ten-story Frame and Wall Test Structure 5-1
5.1 Overview 5-1
5.2 Building Description and Observed Performance 5-2
5.2.1 Building Description 5-2
5.2.2 Ground Motion 5-6
5.2.3 Instrumentation 5-8
5.2.4 Observed Performance 5-8
5.2.5 Response Quantities 5-10
5.3 Nonlinear Dynamic Procedure using OpenSees 5-11
5.3.1 Modeling Approach 5-11
5.3.2 Building Performance: OpenSees NJ vs. Observation 5-18
5.3.3 Building Performance: OpenSees EJ vs. Observation 5-35
5.3.4 Building Performance: Sequential Application of Ground Motions 5-38
5.4 Nonlinear Dynamic Procedure using Perform3D 5-40
5.4.1 Modeling Approach 5-40
5.4.2 Building Performance: Perform3D EJ vs. Observation 5-43
5.4.3 Building Performance: Perform3D EJ vs. Perform3D NJ 5-50
5.4.4 Building Performance: Sequential Application of Ground Motions 5-53
5.5 Comparison of Perform3D and OpenSees Models 5-56
5.6 Fragility Assessment 5-58
5.7 Summary 5-61
5.7.1 Global Performance 5-61

This publication is available free of charge from: https://doi.org/10.6028/NIST.GCR.22-917-50

5.7.2 Component Performance 5-63
5.7.3 Analytical Study Takeaways 5-63
5.7.4 Study Limitations 5-64

6. Six-Story Frame and Wall Building in California 6-1
6.1 Overview 6-1
6.2 Building Description and Observed Performance 6-1
6.2.1 Building Description 6-2
6.2.2 Building Instrumentation 6-4
6.2.3 Ground Motion 6-5
6.2.4 Observed Performance 6-5
6.3 Nonlinear Dynamic Procedure 6-6
6.3.1 Modeling Approach 6-6
6.3.2 Global Performance: Model vs. Observation 6-7
6.3.3 Component Performance: Model vs. Observation 6-10
6.3.4 Column Performance: Model vs. Observation vs. Test Data 6-13
6.4 Nonlinear Dynamic Procedure with Vertical Ground Motion 6-15
6.4.1 Modeling Approach 6-15
6.4.2 Results and Comparison to Observed Performance 6-15
6.5 Nonlinear Dynamic Procedure with Soil-Structure Interaction 6-15
6.5.1 Modeling Approach 6-15
6.5.2 Global Performance: Model vs. Observation 6-16
6.5.3 Component performance: Model vs. Observation 6-17
6.6 Linear Dynamic Procedure 6-17
6.6.1 Modeling Approach 6-17
6.6.2 Global Performance: Model vs. Observation 6-17
6.6.3 Component Performance: Model vs. Observation 6-19
6.7 FEMA P-58 Assessment 6-21
6.8 Fragility Assessment 6-23
6.9 Eurocode Evaluation 6-27
6.10 Summary 6-28
6.10.1 Global Performance 6-28
6.10.2 Component Performance 6-28
6.10.3 Analytical Study Takeaways 6-29
6.10.4 Study Limitations 6-29

7. Seven-story Frame Building in California 7-1
7.1 Overview 7-1
7.2 Building Description and Observed Performance 7-2
7.2.1 Building Description 7-2
7.2.2 Building Instrumentation 7-5
7.2.3 Ground Motion 7-6
7.2.4 Observed Performance 7-9
7.3 Nonlinear Dynamic Procedure 7-12
7.3.1 Modeling Approach 7-12
7.3.2 Global Performance: Model vs. Observation 7-17
7.3.3 Component Performance: Model vs. Observation 7-26
7.4 Linear Dynamic Procedure 7-32
7.4.1 Modeling Approach 7-33
7.4.2 Global Performance: Model vs. Observation 7-34

This publication is available free of charge from: https://doi.org/10.6028/NIST.GCR.22-917-50

7.4.3 Component Performance: Model vs. Observation 7-36
7.5 Fragility Assessment 7-38
7.6 Summary 7-51
7.6.1 Global Performance 7-51
7.6.2 Component Performance 7-53
7.6.3 Analytical Study Takeaways 7-54
7.6.4 Fragility Analysis 7-54
7.6.5 Study Limitations 7-55

8. Five-story Wall Building in New Zealand 8-1
8.1 Overview 8-1
8.2 Building Description and Seismic Performance 8-2
8.2.1 Building Description 8-2
8.2.2 Building Instrumentation 8-5
8.2.3 Ground Motion 8-5
8.2.4 Observed Performance 8-8
8.3 Nonlinear Dynamic Procedure 8-11
8.3.1 Modeling Approach 8-11
8.3.2 Global Performance: Model vs. Observation 8-14
8.3.3 Component Response: Model vs. Observation 8-17
8.4 Linear Dynamic Procedure 8-25
8.4.1 Modeling Approach 8-25
8.4.2 Global Performance: Model vs. Observation 8-25
8.4.3 Component Performance: Model vs. Observation 8-26
8.4.4 Comparison to Linear Response History Method 8-27
8.5 FEMA P-2018 Evaluation 8-29
8.5.1 Evaluation Approach 8-29
8.5.2 Global Performance: Evaluation Procedure vs. Observation 8-29
8.6 New Zealand Assessment Guidelines 8-31
8.7 Summary 8-31
8.7.1 Global Performance 8-31
8.7.2 Component Performance 8-32
8.7.3 Analytical Study Takeaways 8-33
8.7.4 Study Limitations 8-34

9. Three-story Frame with Masonry Infill Building in Taiwan 9-1
9.1 Overview 9-1
9.2 Building Description and Observed Performance 9-2
9.2.1 Building Description 9-2
9.2.2 Ground Motion 9-5
9.2.3 Observed Performance 9-8
9.3 Nonlinear Dynamic Procedure 9-10
9.3.1 Modeling Approach 9-10
9.3.2 Global Performance: Model vs. Observation 9-12
9.3.3 Component Performance: Model vs. Observation 9-15
9.4 Linear Dynamic Procedure 9-21
9.4.1 Modeling Approach 9-21
9.4.2 Global Performance: Model vs. Observation 9-24
9.4.3 Component Performance: Model vs. Observation 9-25
9.5 FEMA P-58 Damage Assessment 9-28

This publication is available free of charge from: https://doi.org/10.6028/NIST.GCR.22-917-50

9.6 Fragility Assessment 9-29
9.7 FEMA P-2018 Evaluation 9-30
9.8 Summary 9-33
9.8.1 Global Response 9-34
9.8.2 Component Response 9-34
9.8.3 Analytical Study Takeaways 9-35
9.8.4 Study Limitations 9-36

10. Seven-Story Moment Frame and Wall Building in Mexico City 10-1
10.1 Overview 10-1
10.2 Building Description and Observed Performance 10-2
10.2.1 Building Description 10-2
10.2.2 Building Instrumentation 10-9
10.2.3 Ground Motion 10-9
10.2.4 Observed Performance 10-11
10.3 Nonlinear Dynamic Procedure 10-17
10.3.1 Modeling Approach 10-17
10.3.2 Global Performance: Model vs. Observation 10-28
10.3.3 Component Performance: Model vs. Observation 10-39
10.4 Summary 10-48
10.4.1 Global Performance 10-48
10.4.2 Component Performance 10-49
10.4.3 Analytical Study Takeaways 10-50
10.4.4 Study Limitations 10-51

11. Summary Results 11-1
11.1 Overview 11-1
11.2 Results from ASCE 41 Studies 11-2
11.2.1 Global Response 11-6
11.2.2 Component Based Response 11-9
11.2.3 Component Based Response Acceptance Criteria Assessment 11-12
11.2.4 Global Acceptance Criteria Assessment 11-12
11.3 Comparison of Global Fragility Curves 11-13
11.4 Results from Additional Studies 11-14
11.4.1 FEMA P-2018 Evaluations 11-14
11.4.2 Eurocode Evaluations 11-15
11.4.3 NZSEE Assessments 11-16
11.4.4 FEMA P-58 Damage Assessments 11-16

12. Findings and Recommendations 12-1
12.1 Overview 12-1
12.2 Key Takeaways from the ASCE 41 Studies 12-2
12.2.1 Simulated Performance Estimates with Good Correlation to Observed Performance 12-2
12.2.2 Simulated Performance Estimates with Mixed or Poor Correlation to Observed Performance 12-2
12.3 Recommendations for Improving ASCE 41 12-3
12.3.1 Consideration of Uncertainty of Element Strength and Deformation Capacities Related to Hierarchy of Mechanism Formation 12-3

This publication is available free of charge from: https://doi.org/10.6028/NIST.GCR.22-917-50

12.3.2 General Element Modeling 12-4
12.3.3 Acceptance Criteria for Collapse Prevention 12-5
12.3.4 Use of Limit-State and Mechanism Analysis to Augment Linear Evaluation Methods 12-5
12.4 Opportunities for Future Work 12-5

Appendix A: Modeling of Elements per ASCE 41 ..... A-1
A.1 Material Properties and Component Strengths A-1
A.1.1 Expected Material Properties A-1
A.1.2 Lower Bound Material Properties A-2
A.1.3 Concrete Material Nonlinear Properties A-2
A.1.4 Reinforcement Material Nonlinear Properties A-4
A.2 Modeling of Beam Elements A-4
A.2.1 Linear Analysis A-4
A.2.2 Nonlinear Analysis A-5
A.3 Modeling of Column Elements A-10
A.3.1 Linear Analysis A-10
A.3.2 Nonlinear Analysis A-12
A.4 Modeling of Joint Elements A-14
A.4.1 Linear Analysis A-14
A.4.2 Nonlinear Analysis A-16
A.5 Modeling of Wall Elements A-16
A.5.1 Wall Elements A-16

References B-1

Project Participants C-1

This publication is available free of charge from: https://doi.org/10.6028/NIST.GCR.22-917-50

List of Figures

Figure 2-1 Generalized force-deformation relation 2-3

Figure 2-2 Description of overall building damage and performance levels.... 2-4

Figure 2-3 Description of structural performance levels and illustrative damage for concrete frames and walls 2-5

Figure 2-4 Illustration of FEMA P-58-based damage assessment procedure for each component, including fragility classification, structural response from ASCE 41 models, and damage assessment 2-8

Figure 3-1 Photo of two-dimensional reinforced concrete frame on shake table..... 3-1

Figure 3-2 Reinforcement details. 3-3

Figure 3-3 Acceleration history of Dynamic Test 1 ground motion as measured on the shake table. 3-5

Figure 3-4 Response spectra for Dynamic Test 1 ground motion with 3% damping. 3-5

Figure 3-5 Maximum interstory drift distribution at each story. 3-6

Figure 3-6 Schematic distribution of observed experimental damage; red circles represent severe damage in the member, yellow circles represent moderate damage, and green circles represent limited damage. 3-6

Figure 3-7 Column D1 and Column C1 after Dynamic Test 1 at base..... 3-7

Figure 3-8 Column B1 and Column A1 after Dynamic Test 1 at base..... 3-7

Figure 3-9 NDP Perform3D: Comparison of story drift response history..... 3-9

Figure 3-10 NDP Perform3D: Comparison of maximum story drift..... 3-10

Figure 3-11 NDP Perform3D: Comparison of maximum story displacement. 3-10

Figure 3-12 NDP Perform3D: Comparison of story displacement response history. 3-11

Figure 3-13 NDP Perform3D: Comparison of the maximum floor acceleration. 3-12

Figure 3-14 NDP Perform3D: Acceptance criteria range results for modeled nonlinear hinges. Shown for Immediate Occupancy, Life Safety, and Collapse Prevention. 3-13

This publication is available free of charge from: https://doi.org/10.6028/NIST.GCR.22-917-50

Figure 3-15 NDP Perform3D: Comparison of (a) simulated response, (b) observed damage, and (c) similar lab specimen for Column A1 at base....3-14

Figure 3-16 NDP Perform3D: Comparison of (a) simulated response, (b) observed damage, and (c) similar lab specimen for Column B1 at base....3-14

Figure 3-17 NDP Perform3D: Comparison of (a) simulated response, (b) observed damage, and (c) similar lab specimen for Column D1 at base....3-15

Figure 3-18 NDP Perform3D: Comparison of (a) simulated response, (b) observed damage, and (c) similar lab specimen for Column C1 at base....3-15

Figure 3-19 Column D1 and column C1 observations after Dynamic Test 1 at Level 1....3-16

Figure 3-20 Column B1 and column A1 observations after Dynamic Test 1 at Level 1....3-16

Figure 3-21 NDP Perform3D: Simulated beam plastic hinge rotation at beam between columns A1 and B1 on Story 1....3-17

Figure 3-22 NDP OpenSees: Comparison of normalized base shear history. ..3-19

Figure 3-23 NDP Opensees: Comparison of column lateral drift ratio versus bottom moment for Column D1 and Column C1....3-19

Figure 3-24 NDP OpenSees: Comparison of column lateral drift ratio versus bottom moment for Column B1 and Column A1....3-20

Figure 3-25 Calculation of modified smoothed demand spectrum: 3% average spectrum....3-21

Figure 3-26 All: Comparison of maximum story drift....3-22

Figure 3-27 All: Comparison of maximum floor displacement....3-22

Figure 3-28 All: Comparison of maximum floor acceleration....3-23

Figure 3-29 Linear Response History: Acceptance criteria range without consideration of limit state. 3-24

Figure 3-30 Linear Response History: Acceptance criteria range including limit state consideration for beams and joints. 3-24

Figure 3-31 Collapse fragility curve showing collapse based on exceeding 6% drift and collapse based on exceeding the range of acceptable response....3-25

Figure 3-32 Collapse fragility curve showing simulated fragility with 6% drift and effect of adjustments from FEMA P-695 for the spectral shape factor and uncertainty 3-26

This publication is available free of charge from: https://doi.org/10.6028/NIST.GCR.22-917-50

Figure 3-33 Collapse fragility curve showing simulated fragility using Unacceptable Response and effect of adjustments from FEMA P-695 for the spectral shape factor and uncertainty 3-26

Figure 3-34 Fragility curves showing probability of exceedance for various limit states. 3-27

Figure 3-35 Comparison of adjusted FEMA P-695 fragility curves and FEMA P-2018 ratings. 3-28

Figure 4-1 Two structures tested at E-Defense shake table, study structure is on the left side of the photo. 4-1

Figure 4-2 Typical floor plan and member nomenclature 4-3

Figure 4-3 Elevations and member nomenclature 4-3

Figure 4-4 Reinforcement details 4-4

Figure 4-5 Ground motion records for 100% JMA-Kobe 4-6

Figure 4-6 Response spectra for 100% JMA-Kobe 4-6

Figure 4-7 Maximum interstory drift distribution over the height of the building 4-7

Figure 4-8 Schematic distributions of observed damage in the frame at Gridline 1 and couple wall at Gridline C based on the observed experimental damage 4-8

Figure 4-9 Observed damage in first story of shear walls 4-8

Figure 4-10 Observed damage in moment frame at Gridline 2 4-9

Figure 4-11 Observed joint damage at the second floor level 4-9

Figure 4-12 OpenSees LP model with material model listed for the nonlinear zero-length springs 4-11

Figure 4-13 Element topology for fiber section and lumped plasticity models 4-11

Figure 4-14 Stress-strain relationship for concrete 4-12

Figure 4-15 Regularized stress-strain relationships for concrete in compression 4-12

Figure 4-16 Calculated stress-strain relationship for steel 4-13

Figure 4-17 Moment-rotation relationships for fiber section models of columns 4-14

Figure 4-18 Calculated moment-rotation relationships for fiber section models of walls with steel strain limits of 0.08 and 0.10 4-14

This publication is available free of charge from: https://doi.org/10.6028/NIST.GCR.22-917-50

Figure 4-19 Calculated force-deformation relationships for Column C-1 simulated with a fiber section in the lumped-plasticity model and envelope curve with ASCE 41 modeling parameters 4-15

Figure 4-20 NDP OpenSees LP NJ: Schematic damage distribution in frame at Gridline 1 and wall at Gridline C based on deformation criteria $\theta_{inelastic}/a$ 4-17

Figure 4-21 NDP OpenSees LP NJ: Maximum drift ratio comparison over the height of the building for 100% JMA-Kobe in frame direction and wall direction 4-17

Figure 4-22 NDP OpenSees LP NJ: Roof drift ratio history comparison for 100% JMA-Kobe, in frame direction, and wall direction 4-18

Figure 4-23 NDP OpenSees LP NJ: First-story drift ratio history comparison for 100% JMA-Kobe, in frame direction, and wall direction 4-18

Figure 4-24 NDP OpenSees LP NJ: Normalized base shear history for 100% JMA-Kobe, in frame direction, and wall direction 4-21

Figure 4-25 NDP OpenSees LP NJ: Maximum floor accelerations over the height of the building for 100% JMA-Kobe, in frame direction, and wall direction 4-22

Figure 4-26 NDP OpenSees LP NJ: Roof acceleration time histories for 100% JMA-Kobe, in frame direction, and wall direction 4-22

Figure 4-27 NDP OpenSees LP EJ: Schematic damage distribution in the frame at Gridline 1 and the frame at Gridline C based on deformation criteria $\theta_{inelastic}/a$ for the model with elastic joints 4-23

Figure 4-28 NDP OpenSees LP: Maximum drift ratio comparison for OpenSees LP NJ and EJ models over the height of the building for 100% JMA-Kobe 4-24

Figure 4-29 NDP OpenSees Fiber: Schematic damage distribution from OpenSees Fiber EJ and OpenSees Fiber NJ models in frame at Gridline 1 and wall at Gridline C based on deformation criteria $\theta_{inelastic}/a$ 4-25

Figure 4-30 NDP OpenSees: Maximum drift ratio comparison over the height of the building after 100% JMA-Kobe, in frame direction and wall direction 4-26

Figure 4-31 NDP OpenSees: Roof drift ratio history comparison for 100% JMA-Kobe, in frame direction, and wall direction 4-26

Figure 4-32 NDP OpenSees: First-story drift ratio history comparison for 100% JMA-Kobe, in frame direction, and wall direction 4-27

Figure 4-33 NDP OpenSees Fiber NJ: Normalized base shear history for 100% JMA-Kobe, in frame direction, and wall direction 4-29

This publication is available free of charge from: https://doi.org/10.6028/NIST.GCR.22-917-50

Figure 4-34 NDP OpenSees: Maximum floor accelerations over the height of the building for 100% JMA-Kobe, in frame direction, and wall direction 4-30

Figure 4-35 NDP OpenSees Fiber: Roof acceleration histories for 100% JMA-Kobe, in frame direction, and wall direction 4-30

Figure 4-36 NDP OpenSees LP NJ: Computed moment vs rotation behavior of hinges in the frame at Gridline 2 for the 100% JMA-Kobe motion 4-31

Figure 4-37 NDP OpenSees LP NJ: Computed moment vs rotation plots for the beam-column joint hinges of exterior joints and interior joints at Gridline 1 4-32

Figure 4-38 NDP OpenSees LP NJ: Computed moment vs rotation plots for the shear wall hinges at wall base at Gridline C and Gridline A . 4-33

Figure 4-39 Column deformation criteria: $\theta_{inelastic}/a$, $\theta_{inelastic}/b$ 4-34

Figure 4-40 Wall deformation criteria: $\theta_{inelastic}/a$, $\theta_{inelastic}/b$ 4-34

Figure 4-41 Beam deformation criteria: $\theta_{inelastic}/a$..... 4-35

Figure 4-42 Joint deformation criteria: $\theta_{inelastic}/a$ and $\theta_{inelastic}/b$..... 4-36

Figure 4-43 Nonlinear analysis model in Perform3D..... 4-37

Figure 4-44 NDP Perform3D: Schematic damage distribution in frame at Gridline 1 and wall at Gridline C based on deformation criteria $\theta_{inelastic}/a$..... 4-39

Figure 4-45 NDP Perform3D: Maximum drift ratio comparison over the height of the building for 100% JMA-Kobe, in frame direction and wall direction..... 4-40

Figure 4-46 NDP Perform3D: Roof drift ratio history comparison for 100% JMA-Kobe, in frame direction and wall direction 4-40

Figure 4-47 NDP Perform3D: Normalized base shear history compared to maximum from 100% JMA-Kobe, in frame direction and wall direction 4-41

Figure 4-48 NDP Perform3D: Maximum absolute floor accelerations over the height of the building for 100% JMA-Kobe from Sensor A2, in frame direction and wall direction..... 4-42

Figure 4-49 NDP Perform3D EJ: Roof acceleration histories for 100% JMA-Kobe from Sensor A2, in frame direction and wall direction 4-42

Figure 4-50 NDP Perform3D: Maximum drift ratio comparison between linear and nonlinear joint models..... 4-43

Figure 4-51 NDP Perform3D: Schematic damage distribution in frame at Gridline 1 based on deformation criteria $\theta_{inelastic}/a$..... 4-44

This publication is available free of charge from: https://doi.org/10.6028/NIST.GCR.22-917-50

Figure 4-52 NDP Perform3D: Column deformation criteria: $\theta_{inelastic}/a$ (top), $\theta_{inelastic}/b$ (bottom) 4-45
Figure 4-53 NDP Perform3D: Bi-directional hinge rotation orbit plot 4-45
Figure 4-54 NDP Perform3D: Wall deformation criteria: $\theta_{inelastic}/a$, $\theta_{inelastic}/b$ 4-46
Figure 4-55 NDP Perform3D: Deformation criteria $\theta_{inelastic}/a$ 4-46
Figure 4-56 NDP Perform3D: Deformation criteria $\theta_{inelastic}/b$ 4-47
Figure 4-57 NDP Perform3D: Beam deformation criteria: $\theta_{inelastic}/b$ 4-47
Figure 4-58 NDP Perform3D NJ: Location of predicted joint damage 4-48
Figure 4-59 NDP Perform3D: Hysteresis at Level 2 joint at Gridline B 4-48
Figure 4-60 Maximum interstory drift comparison in frame direction and wall direction 4-50
Figure 4-61 Maximum floor acceleration comparison over the height of the building in frame direction (left) and wall direction (right) 4-51
Figure 4-62 LDP: Story drift in the wall direction 4-52
Figure 4-63 LDP: Story drift in the frame direction 4-53
Figure 4-64 LDP: Collapse Prevention DCR/*m* for all columns 4-54
Figure 4-65 LDP: Collapse Prevention DCR/*m* at first story 4-54
Figure 4-66 Fragility curves for ASCE 41-17 modeling parameters and collapse 4-57
Figure 4-67 Fragility curves for ASCE 41-17 acceptance criteria and collapse 4-58
Figure 4-68 Fragility curves for Eurocode acceptance criteria and collapse 4-59
Figure 4-69 Moment-rotation relationships for beam and column elements according to ASCE 41-17 and NZSEE *Guidelines* 4-65
Figure 4-70 Moment-shear deformation relationship for exterior beam column joint in the first story of Frame 1 calculated according to ASCE 41-17 and NZSEE *Guidelines* 4-68
Figure 4-71 Moment-curvature relationship for wall on Gridline C 4-69
Figure 4-72 Moment-rotation relationship for walls calculated according to the ASCE 41-17 and NZSEE *Guidelines* 4-70
Figure 4-73 Beam and column span definitions in Equation 4-36 4-71
Figure 4-74 Internal forces in beam-column external and internal joints 4-72
Figure 4-75 Controlling modes of failure for Frame 1 4-73
Figure 4-76 Force distribution for the calculation of base shear strength 4-75

This publication is available free of charge from: https://doi.org/10.6028/NIST.GCR.22-917-50

Figure 4-77 Force distribution for the calculation of base shear strength 4-75
Figure 4-78 Capacity curve for Frame 1..... 4-76
Figure 4-79 Controlling modes of failure for Frame C 4-81
Figure 4-80 Capacity curve for Frame C..... 4-82
Figure 4-81 Capacity of dual system in Gridline C..... 4-83
Figure 4-82 FEMA P-2018 rating and spectral acceleration relationship 4-86
Figure 5-1 10-story structure tested at E-Defense shake table in 2015. 5-1
Figure 5-2 Plan dimensions for typical floors. 5-3
Figure 5-3 Building elevation views. 5-4
Figure 5-4 Components of the target ground motion record and the associated spectra 5-7
Figure 5-5 Measured periods after each applied excitation. 5-9
Figure 5-6 Photos of observed damage. 5-10
Figure 5-7 Observed cracking in the 50% Kobe record for the (a) sliding base test and (b) fixed base test at the 1st and 4th floors. 5-10
Figure 5-8 Maximum floor acceleration and story drift angles. 5-11
Figure 5-9 General element modeling approaches. 5-12
Figure 5-10 Calibrated material relations for: (a) reinforcement and (b) concrete in compression. 5-12
Figure 5-11 Representative moment-rotation responses for calibrated section of structural elements. 5-13
Figure 5-12 Moment frame element modeling approaches. 5-14
Figure 5-13 Modeling of beam-column joints in OpenSees NJ model. 5-16
Figure 5-14 Detail of beam-column joints tested by Shiohara et al. (2013)..... 5-16
Figure 5-15 Nonlinear joint modeling approach. 5-17
Figure 5-16 Comparison of mass distribution for test and model. 5-18
Figure 5-17 OpenSees mode shapes, periods, and mass participation factors for modes 1 to 3. 5-19
Figure 5-18 Comparison of model and test periods: (a) frame direction (nonlinear joint model), and (b) wall direction. 5-20
Figure 5-19 Pushovers analysis results compared to experimental base shear versus lateral displacement relations. 5-21

This publication is available free of charge from: https://doi.org/10.6028/NIST.GCR.22-917-50

Figure 5-20 Ground motion applied in frame direction: (a) test structure, and (b) computational model. 5-21

Figure 5-21 NDP OpenSees NJ: Option 1 model results showing schematic damage distribution in (a) frame joints, and (b) beams/columns based on estimated plastic rotation $\theta_{inelastic}$. 5-23

Figure 5-22 NDP OpenSees NJ: Option 2 model showing schematic damage distribution in (a) frame joints and (b) beams/columns based on estimated plastic rotation $\theta_{inelastic}$. 5-23

Figure 5-23 NDP OpenSees NJ: Schematic damage distribution with (a) Option 1 and (b) Option 2 showing frame joints and beams/columns compared to ASCE 41-17 plastic rotation parameter *a*. 5-25

Figure 5-24 Schematic damage distribution with (a) Option 1 and (b) Option 2 showing frame joints and beams/columns compared to ASCE 41-17 plastic rotation parameter *b*. 5-26

Figure 5-25 Observed joint damage. 5-27

Figure 5-26 NDP OpenSees NJ: Schematic damage distribution showing (a) Option 1 and (b) Option 2 in frame joints and beams/columns compared to ASCE 41-17 performance levels. 5-28

Figure 5-27 NDP OpenSees NJ: Schematic damage distribution within wall, compared to ASCE 41-17 plastic rotation parameter *a* and rotation parameter b and performance levels. 5-29

Figure 5-28 Observed wall damage. 5-29

Figure 5-29 NDP OpenSees NJ: Roof drift versus base shear histories for (a) Option 1 and (b) Option 2 in wall direction and frame direction for 100% JMA-Kobe. 5-30

Figure 5-30 NDP OpenSees NJ: Roof drift histories for (a) Option 1 and (b) Option 2 in wall direction and frame direction for 100% JMA-Kobe. 5-31

Figure 5-31 NDP OpenSees NJ: Base shear histories for (a) Option 1 and (b) Option 2 in wall direction and frame direction for 100% JMA-Kobe. 5-32

Figure 5-32 NDP OpenSees NJ: Peak story drift ratios for (a) Option 1 and (b) Option 2 in wall direction and frame direction for 100% JMA-Kobe. 5-33

Figure 5-33 NDP OpenSees NJ: Peak floor acceleration for (a) Option 1 and (b) Option 2 in wall direction and frame direction for 100% JMA-Kobe. 5-34

Figure 5-34 NDP OpenSees NJ: Peak residual story drifts for (a) Option 1 and (b) Option 2 in wall direction and frame direction for 100% JMA-Kobe. 5-35

This publication is available free of charge from: https://doi.org/10.6028/NIST.GCR.22-917-50

Figure 5-35 NDP OpenSees: Schematic damage distribution in columns for (a) OpenSees NJ model Option 1 and (b) OpenSees EJ columns for 100% JMA-Kobe. 5-36

Figure 5-36 NDP OpenSees: Maximum floor acceleration comparison for (a) OpenSees NJ Option 1 and (b) OpenSees EJ models throughout the height of the building for 100% JMA-Kobe..... 5-37

Figure 5-37 NDP OpenSees: Maximum story drift comparison for (a) OpenSees NJ Option 1 and (b) OpenSees EJ models throughout the height of the building for 100% JMA-Kobe..... 5-37

Figure 5-38 NDP OpenSees NJ Option1: Comparison of peak story drift ratios and peak floor acceleration for wall direction and for 100% JMA-Kobe and 50% JMA-Kobe and 100% JMA-Kobe.. 5-38

Figure 5-39 NDP OpenSees NJ Option1: Peak story drift ratios for frame direction for (a) 100% JMA-Kobe and (b) 50% JMA-Kobe and 100% JMA-Kobe. 5-39

Figure 5-40 NDP OpenSees NJ Option1: Peak floor acceleration for frame direction for (a) 100% JMA-Kobe and (b) 50% JMA-Kobe and 100% JMA-Kobe. 5-39

Figure 5-41 Nonlinear analysis model in Perform3D..... 5-40

Figure 5-42 Modeling approaches used for the beam-column joints. 5-42

Figure 5-43 Floor tributary area used to calculate gravity loads for each element..... 5-43

Figure 5-44 NDP Perform3D EJ: Roof drift versus base shear histories for (a) frame direction, and (b) wall direction for 100% JMA-Kobe. 5-44

Figure 5-45 NDP Perform3D EJ: Roof drift and base shear histories for 100% JMA-Kobe. 5-45

Figure 5-46 NDP Perform3D EJ: Peak story drift ratios for (a) frame direction, and (b) wall direction for 100% JMA-Kobe..... 5-46

Figure 5-47 NDP Perform3D EJ: Peak floor acceleration for (a) frame direction, and (b) wall direction for 100% JMA-Kobe..... 5-46

Figure 5-48 NDP Perform3D EJ: Schematic damage distribution in the beams and columns compared to ASCE 41-17 plastic rotation parameter *a*. 5-48

Figure 5-49 NDP Perform3D EJ: Schematic damage distribution in the beams and columns compared to ASCE 41-17 plastic rotation parameter *b*. 5-48

Figure 5-50 NDP Perform3D EJ: Schematic distribution of the plastic rotation demands in the beams and columns for 100% JMA-Kobe compared to ASCE 41-17 acceptance criteria. 5-49

This publication is available free of charge from: https://doi.org/10.6028/NIST.GCR.22-917-50

Figure 5-51 NDP Perform3D EJ: Wall maximum strains at the extreme fibers over structure height for 100% JMA-Kobe. 5-49

Figure 5-52 NDP Perform3D EJ: Wall rotation over structure height for 100% JMA-Kobe compared with ASCE 41-23 modeling parameters. 5-50

Figure 5-53 NDP Perform3D NJ: Typical hysteretic behavior of the beam-column joints at the 1st, 2nd, and 3rd stories of the building for 100% JMA-Kobe..... 5-51

Figure 5-54 NDP Perform3D: Schematic damage distribution in (a) Perform3D NJ and (b) Perform3D EJ models compared to ASCE 41-17 plastic rotation parameter *a*..... 5-51

Figure 5-55 NDP Perform3D: Schematic damage distribution in the Perform3D NJ and Perform3D EJ models compared to ASCE 41-17 plastic rotation parameter *b*..... 5-52

Figure 5-56 NDP Perform3D: Peak floor acceleration for (a) Perform3D NJ and (b) Perform3D NJ models over the height of the building for 100% JMA-Kobe..... 5-52

Figure 5-57 NDP Perform3D: Peak story drift ratio comparison for (a) Perform3D NJ and (b) Perform3D EJ models over the height of the building for 100% JMA-Kobe. 5-53

Figure 5-58 NDP Perform3D NJ: Comparison of peak floor acceleration and peak story drifts due to sequential application of 50% and 100% JMA-Kobe. 5-54

Figure 5-59 NDP Perform3D NJ: Schematic damage distribution in comparison to ASCE 41-17 plastic rotation parameter a far (a) 100% JMA-Kobe and (b) 50% JMA-Kobe and 100% JMA-Kobe. 5-55

Figure 5-60 NDP Perform3D NJ: Schematic damage distribution in comparison to ASCE 41-17 plastic rotation parameter b far (a) 100% JMA-Kobe and (b) 50% JMA-Kobe and 100% JMA-Kobe. 5-55

Figure 5-61 Fragility curve corresponding to a first element exceeding ASCE 41-17 modeling parameters and acceptance criteria. 5-59

Figure 5-62 Fragility curve for ASCE 41-17 modeling parameters and acceptance criteria for beam-column joints..... 5-59

Figure 5-63 Fragility curve for ASCE 41-17 modeling parameters and acceptance criteria for beams. 5-60

Figure 5-64 Fragility curve for ASCE 41-17 modeling parameters and acceptance criteria for columns. 5-60

Figure 5-65 Fragility curve for ASCE 41-17 modeling parameters and acceptance criteria for walls. 5-61

This publication is available free of charge from: https://doi.org/10.6028/NIST.GCR.22-917-50

Figure 6-1 Photograph of Imperial County Services Building in Imperial County, California 6-1

Figure 6-2 Schematic illustration of study building 6-2

Figure 6-3 Plan view of study building, showing location of first-story walls. 6-3

Figure 6-4 Details of typical first-story column base connections into the pile cap 6-3

Figure 6-5 Diagram of instrumentation of study building 6-4

Figure 6-6 Recorded response spectra, calculated with 5% of critical damping: (a) at the foundation and (b) in the free field 6-5

Figure 6-7 Damage to building 6-6

Figure 6-8 Elevation view of damage to building 6-6

Figure 6-9 NDP: Comparison of recorded and simulated peak acceleration and displacement profiles. 6-8

Figure 6-10 NDP: Comparison of recorded and simulated acceleration time histories at the roof. 6-8

Figure 6-11 NDP: Plan review of response of first-story column bases showing (a) peak rotation demand, θ, normalized by b; (b) maximum compressive axial load on columns from the analysis; and (c) peak torsional response of the model 6-10

Figure 6-12 Damage photos of column G-2, with model backbones and hysteretic response in the recorded ground motion 6-11

Figure 6-13 NDP: Assessment of column and beam response relative to ASCE 41-17 nonlinear acceptance criteria. Immediate Occupancy, Life Safety, and Collapse Prevention 6-12

Figure 6-14 NDP: Model backbone and hysteretic response of a beam at the second floor 6-12

Figure 6-15 Comparison of observed and experimental damage for column G1 in the first story 6-14

Figure 6-16 Comparison of observed and experimental damage for column G2 in the first story 6-14

Figure 6-17 NDP with SSI: Comparison of recorded and simulated peak displacement profiles for the model with soil-structure-interaction 6-16

Figure 6-18 NDP with SSI: Comparison of roof acceleration spectra from models with and without soil-structure-interaction 6-17

Figure 6-19 LDP: Comparison of recorded and simulated peak acceleration and displacement profiles 6-18

This publication is available free of charge from: https://doi.org/10.6028/NIST.GCR.22-917-50

Figure 6-20 LDP: Comparison of recorded and simulated acceleration time histories at the roof 6-19

Figure 6-21 LDP: Comparison of recorded and simulated peak torsion response 6-19

Figure 6-22 Linear Collapse Prevention Demand-Capacity Ratios modified by *m*-factors at base of first-story columns for: (a) flexure; (b) shear; and (c) axial 6-20

Figure 6-23 Assessment of column and beam response relative to ASCE 41-17 acceptance criteria 6-21

Figure 6-24 FEMA P-58 assessment of damage to base of Column G2, comparing ASCE 41-17 backbone to FEMA P-58 fragilities 6-22

Figure 6-25 FEMA P-58 assessment at base of Column G1, comparing ASCE 41 backbone to FEMA P-58 fragilities 6-23

Figure 6-26 Collapse fragility and unacceptable response limit state curves with respect to spectral accelerations at the fundamental period of the building in the east-west direction 6-24

Figure 6-27 Comparison of *b* values at bottom and top of first-story columns 6-25

Figure 6-28 Fragility curves showing probability of percent of components in collapse mechanism exceeding the Collapse Prevention acceptance criteria 6-26

Figure 6-29 Probability of resulting in a “near-collapse” Collapse Margin for (a) component-based CP limit states, and for (b) drift-based limit states 6-27

Figure 6-30 Fragility curves obtained from Eurocode Near Collapse limit state, as compared to ASCE 41-17 Collapse Prevention limit state, showing probability the limit state is exceeded in (a) one column hinge, and (b) 50% of the column hinges 6-28

Figure 7-1 Photograph of reinforced concrete moment frame building in Van Nuys. 7-1

Figure 7-2 Photograph of south-west elevation 7-3

Figure 7-3 Typical floor plan 7-3

Figure 7-4 Elevation of study building 7-4

Figure 7-5 Building instrumentation plan 7-6

Figure 7-6 Acceleration record for 1994 Northridge Earthquake at the ground level, north-south component. 7-7

Figure 7-7 Acceleration record for 1994 Northridge Earthquake at the ground level, east-west component. 7-8

Figure 7-8 1994 Northridge earthquake acceleration spectra for 5% damping. 7-8

This publication is available free of charge from: https://doi.org/10.6028/NIST.GCR.22-917-50

Figure 7-9 1994 Northridge earthquake displacement spectra for 5% damping. 7-9

Figure 7-10 Structural damage to south perimeter frame after 1994 Northridge Earthquake 7-10

Figure 7-11 Structural damage to north perimeter frame after 1994 Northridge Earthquake 7-11

Figure 7-12 Structural damage to columns of south exterior frame after 1994 Northridge Earthquake..... 7-11

Figure 7-13 Structural damage to fifth floor columns of south exterior frame after 1994 Northridge Earthquake 7-12

Figure 7-14 Representative east-west frame of OpenSees lumped-plasticity model with nonlinear zero-length rotational springs. 7-13

Figure 7-15 Modeling parameters of Ibarra-Krawinkler-Medina model..... 7-13

Figure 7-16 Shear distress in beam-column joint 7-16

Figure 7-17 Shear distress in Column A5, fifth floor. 7-16

Figure 7-18 NDP: Maximum accelerations at each floor level in the north-south direction. 7-17

Figure 7-19 NDP: Maximum accelerations at each floor level in the east-west direction. 7-18

Figure 7-20 NDP: Acceleration time history for instrument 3, north-south direction at the roof. 7-19

Figure 7-21 NDP: Acceleration time history for instrument 9, east-west direction at the roof. 7-19

Figure 7-22 NDP: Acceleration time history for instrument 5, north-south direction at the third floor. 7-20

Figure 7-23 NDP: Acceleration time history for instrument 11, east-west direction at the third floor. 7-20

Figure 7-24 NDP: Acceleration time history for instrument 12, east-west direction at the second floor..... 7-21

Figure 7-25 NDP: Displacement time history for instrument 2, north-south direction at the roof. 7-22

Figure 7-26 NDP: Displacement time history for instrument 2, north-south direction at the roof. 7-22

Figure 7-27 NDP: Maximum drift ratio at each story, north-south direction... 7-23

Figure 7-28 NDP: Maximum drift ratio at each story, east-west direction. 7-23

Figure 7-29 NDP: Base shear history in the north-south direction..... 7-24

This publication is available free of charge from: https://doi.org/10.6028/NIST.GCR.22-917-50

Figure 7-30 NDP: Base shear history in the east-west direction. 7-24
Figure 7-31 NDP: Calculated performance level for rotational springs in north-south frames for Northridge Earthquake. 7-27
Figure 7-32 NDP: Calculated performance level for rotational springs in east-west frames for Northridge Earthquake. 7-27
Figure 7-33 NDP: Ratio of maximum beam and column rotation to ASCE 41 parameter *a* for exterior frame oriented in the north-south direction 7-28
Figure 7-34 NDP: Ratio of maximum beam and column rotation to ASCE 41 parameter *a* for the interior frame oriented in the north-south direction 7-29
Figure 7-35 NDP: Ratio of maximum beam and column rotation to ASCE 41 parameter *a* for the exterior frame oriented in the east-west direction 7-29
Figure 7-36 NDP: Ratio of maximum beam and column rotation to ASCE 41 parameter *a* for the interior frame oriented in the east-west direction 7-30
Figure 7-37 Columns (a) A5 at the fifth floor of the south frame, and (b) Specimen 3CLH18 tested by Lynn (1999). 7-31
Figure 7-38 NDP: Calculated moment-rotation relationship for rotational spring at the top of Column A5. 7-32
Figure 7-39 ETABS Linear 3D Model. 7-33
Figure 7-40 LDP: Seismic drift at center of mass (a) north-south direction, and (b) east-west direction. 7-35
Figure 7-41 LDP: Seismic floor displacement at the southeast corner of the building in the (a) north-south direction and (b) east-west direction 7-36
Figure 7-42 Collapse prevention demand capacity ratio for each story 7-37
Figure 7-43 Fragility curve for ASCE 41-17 modeling parameters 7-39
Figure 7-44 Fragility curve for ASCE 41-17 acceptance criteria. 7-39
Figure 7-45 Fragility curve for different percentages of critical springs exceeding the yield rotation. 7-45
Figure 7-46 Fragility curve for different percentages of critical springs exceeding the rotation corresponding to loss of flexural strength. 7-46
Figure 7-47 Fragility curve for different percentages of critical springs exceeding the rotation corresponding to loss of gravity load carrying capacity. 7-46

This publication is available free of charge from: https://doi.org/10.6028/NIST.GCR.22-917-50

Figure 7-48 Fragility curve for different percentages of critical springs exceeding the IO performance level. 7-47
Figure 7-49 Fragility curve for different percentages of critical springs exceeding LS performance level..... 7-47
Figure 7-50 Fragility curve for different percentages of critical springs exceeding CP performance level. 7-48
Figure 8-1 Photograph of Pyne Gould Corporation Building prior to collapse 8-1
Figure 8-2 Building plan showing (a) first story and (b) upper stories 8-3
Figure 8-3 Building drawing showing column and wall dimensions and reinforcement details..... 8-4
Figure 8-4 Acceleration time history at REHS site for two earthquakes..... 8-6
Figure 8-5 Horizontal acceleration response spectra with 3% damping at REHS site for two earthquakes 8-7
Figure 8-6 Horizontal velocity response spectra with 3% damping at REHS site for two earthquakes 8-7
Figure 8-7 Horizontal displacement response spectra with 3% damping at REHS site for two earthquakes 8-7
Figure 8-8 Damage observed after 2010 Darfield Earthquake 8-8
Figure 8-9 Photo showing collapsed building viewed from south 8-9
Figure 8-10 Photo of damaged beam-column joints..... 8-10
Figure 8-11 Photo showing overview of collapsed building from north..... 8-10
Figure 8-12 Photo of fractured slab reinforcement at slab-wall interface 8-11
Figure 8-13 Wall segments in nonlinear analysis model..... 8-12
Figure 8-14 First mode shape 8-13
Figure 8-15 NDP: Comparison of story drift response histories in east-west direction 8-14
Figure 8-16 NDP: Comparison of story drift response histories in north-south direction 8-15
Figure 8-17 NDP: Heatmap of second-story column and wall plastic rotation DCRs relative to modeling parameter a in the east-west direction 8-19
Figure 8-18 NDP: Heatmap of second-story column and wall plastic rotation DCRs relative to modeling parameter b in east-west direction 8-20
Figure 8-19 NDP: Heatmap of second-story column and wall plastic rotation acceptance criteria in east-west direction 8-21

This publication is available free of charge from: https://doi.org/10.6028/NIST.GCR.22-917-50

Figure 8-20 Measured hysteretic response and damage for Specimen 2 8-22
Figure 8-21 Wall moment-rotation response at base of second story in elastic wall shear response model..... 8-23
Figure 8-22 Wall shear-story drift response at base of second story in nonlinear wall shear response model..... 8-24
Figure 8-23 Measured hysteretic response and toe damage at end of each test for Specimens C1, C2, and C3..... 8-24
Figure 8-24 Linear: 3D model developed with ETABS 8-25
Figure 8-25 Linear: Maximum story drift at two different locations..... 8-26
Figure 8-26 Linear: Demand-capacity ratios for Collapse Prevention 8-27
Figure 8-27 Linear: Comparison of modal and direct integration methods for linear response history method..... 8-28
Figure 8-28 Relationship of FEMA P-2018 rating and spectral acceleration... 8-30
Figure 9-1 Photograph of building from the south..... 9-1
Figure 9-2 Plan dimensions of building..... 9-2
Figure 9-3 Elevations: (a) frame at Gridline A, (b) frame at Gridline E (c) frame at Gridline G..... 9-4
Figure 9-4 Ground motion recording stations site, and epicenter..... 9-5
Figure 9-5 USGS intensity map for 2016 Meinong Earthquake..... 9-6
Figure 9-6 PGV intensity map with location of study building relative to epicenter. 9-7
Figure 9-7 Measured records for recording Station A730. 9-7
Figure 9-8 Station A730 (a) acceleration orbital with building axes in gray, (b) building-oriented acceleration response spectra, (c) building-oriented velocity response spectra, and (d) building-oriented displacement spectra. 9-8
Figure 9-9 Damage to column and interior walls..... 9-9
Figure 9-10 Illustration of column and full-height masonry wall damage at first story. 9-10
Figure 9-11 Column modeling approaches with lumped plasticity using (a) conventional moment-rotation springs and (b) fiber-limit state hinge..... 9-11
Figure 9-12 First mode shapes; diagonal struts for masonry infill 9-12
Figure 9-13 NDP: Story drift response histories in east-west direction..... 9-13
Figure 9-14 NDP: Story drift response histories in north-south direction. 9-14

This publication is available free of charge from: https://doi.org/10.6028/NIST.GCR.22-917-50

Figure 9-15 NDP: Story drift vertical distribution at maximum first-story drift 9-14

Figure 9-16 NDP: Heatmap of first-story column shear DCR in east-west direction 9-15

Figure 9-17 NDP: Heatmap of first-story column plastic rotation DCR relative to parameter a in east-west direction 9-16

Figure 9-18 NDP: Heatmap of first-story column plastic rotation DCR relative to parameter b in east-west direction. 9-16

Figure 9-19 NDP: Heatmap of first-story column acceptance criteria in east-west direction 9-17

Figure 9-20 ND: Heatmap of first-story column acceptance criteria in north-south direction..... 9-17

Figure 9-21 NDP: Moment-rotation spring model column hysteretic response in east-west direction. 9-18

Figure 9-22 NDP: Fiber-based limit-state hinge model column hysteretic response. 9-18

Figure 9-23 Comparison of observed column damage in building to Specimen SC3 9-20

Figure 9-24 Hysteretic response of similar experimental specimens. 9-20

Figure 9-25 Comparison of observed column damage in building to Specimen 40.033 9-21

Figure 9-26 Linear model variations. 9-23

Figure 9-27 LDP: Heatmap of first-story flexural and shear DCR/m values. .. 9-27

Figure 9-28 LDP: Spatial comparison of predicted versus observed damage based on flexure and shear limit states 9-28

Figure 9-29 Heatmap of first-story column probabilities of exceedance of damage states in east-west direction based on FEMA P-58 evaluation..... 9-29

Figure 9-30 Incremental dynamic analysis curves. 9-29

Figure 9-31 Fragility curves for column collapse prevention acceptance criteria 9-30

Figure 9-32 SRSS 5%-damped acceleration response spectrum for best-estimate ground motion (A730) and UHS for Tainan..... 9-31

Figure 10-1 Photograph of west façade of reinforced concrete moment frame and structural wall building in Canal de Miramontes, Colonia Girasoles, Mexico City following the 2017 Puebla Earthquake... 10-1

Figure 10-2 Photo showing building plan view from the top. 10-2

This publication is available free of charge from: https://doi.org/10.6028/NIST.GCR.22-917-50

Figure 10-3 Original structural drawing showing typical floor plan. 10-3
Figure 10-4 Simplified typical floor plan used in this study..... 10-4
Figure 10-5 Elevation in the north-south direction. 10-5
Figure 10-6 Schematic of raft foundation shown in original drawings..... 10-6
Figure 10-7 Roof area housing mechanical systems..... 10-8
Figure 10-8 Acceleration record for 2017 Puebla Earthquake at Jardín de Niños Luz García Campillo station, in the north-south direction. .. 10-10
Figure 10-9 Acceleration record for 2017 Puebla Earthquake at Jardín de Niños Luz García Campillo station, in the east-west direction. .. 10-10
Figure 10-10 Acceleration spectra for 2017 Puebla Earthquake at Jardín de Niños Luz García Campillo station, 5% damping ratio. 10-10
Figure 10-11 Displacement spectra for 2017 Puebla Earthquake at Jardín de Niños Luz García Campillo station, 5% damping ratio. 10-11
Figure 10-12 Structural damage observed in the building after the 2017 Puebla Earthquake..... 10-12
Figure 10-13 Inclined cracks observed in first story column..... 10-13
Figure 10-14 Damage at the edge of first story structural wall..... 10-13
Figure 10-15 Damage to west façade masonry walls..... 10-15
Figure 10-16 Damage to façade masonry walls in north illumination shaft. 10-15
Figure 10-17 Damage to first story masonry walls in north building boundary..... 10-16
Figure 10-18 Photograph showing damage to first story masonry walls and close proximity of adjacent building in south boundary 10-16
Figure 10-19 Damage to interior masonry walls in apartment unit 10-17
Figure 10-20 Damage to interior masonry walls in apartment unit 10-17
Figure 10-21 Column tributary areas shown for the northwest corner of the symmetric plan 10-19
Figure 10-22 Drop panel reinforcement details 10-20
Figure 10-23 Schematic of OpenSees lumped-plasticity model with nonlinear zero-length rotational springs shown as green dots..... 10-20
Figure 10-24 Dimensions and reinforcement configuration of a typical beam element 10-21
Figure 10-25 Modeling parameters of Ibarra-Krawinkler-Medina model. 10-21

This publication is available free of charge from: https://doi.org/10.6028/NIST.GCR.22-917-50

Figure 10-26 Moment-rotation relationship for rotational spring of column element controlled by shear. 10-23

Figure 10-27 Moment-rotation relationship for rotational spring of wall element. 10-24

Figure 10-28 Masonry wall and infill wall locations for an apartment unit of a typical floor. 10-24

Figure 10-29 Masonry wall, infill wall, and elastic masonry beam element location and designation for an apartment unit of a typical floor. .. 10-25

Figure 10-30 Hysteretic behavior of masonry infill strut element..... 10-26

Figure 10-31 Hysteretic behavior for masonry partition frame element $C3_m$... 10-26

Figure 10-32 Masonry spring designation and location. 10-27

Figure 10-33 Masonry frame system used to model the façade. 10-27

Figure 10-34 Masonry frame system used to model partition walls..... 10-28

Figure 10-35 Pushover analysis results in (a) frame direction and (b) wall direction. 10-30

Figure 10-36 Acceleration profiles calculated with nonlinear model including masonry walls and infills for the 2017 Puebla Earthquake (a) frame direction, and (b) wall direction. 10-31

Figure 10-37 Drift ratio profiles calculated with nonlinear model including masonry walls and infills for the 2017 Puebla Earthquake (a) frame direction, and (b) wall direction. 10-31

Figure 10-38 Hysteretic response of (a) first story masonry infill and (b) façade masonry element for the 2017 Puebla Earthquake. ... 10-32

Figure 10-39 Base shear history in the frame direction..... 10-32

Figure 10-40 Base shear history in the wall direction. 10-32

Figure 10-41 Acceleration profiles for (a) frame and (b) wall direction calculated with nonlinear model including masonry walls and infills for the 2017 Puebla Earthquake scaled to the MCE uniform hazard spectrum. 10-35

Figure 10-42 Drift ratio profiles for (a) frame and (b) wall direction calculated with nonlinear model including masonry walls and infills for the 2017 Puebla Earthquake scaled to the MCE uniform hazard spectrum..... 10-35

Figure 10-43 Drift ratio histories for (a) frame and (b) wall direction calculated with nonlinear model including masonry walls and infills for the 2017 Puebla Earthquake scaled to the MCE uniform hazard spectrum..... 10-36

This publication is available free of charge from: https://doi.org/10.6028/NIST.GCR.22-917-50

Figure 10-44 Hysteretic response of first story beam springs in the (a) frame and (b) wall directions for the 2017 Puebla Earthquake scaled to the MCE uniform hazard spectrum. 10-37

Figure 10-45 Hysteretic response of first story column springs in the (a) frame and (b) wall directions for the 2017 Puebla Earthquake scaled to the MCE uniform hazard spectrum. 10-37

Figure 10-46 Hysteretic response of first story wall springs in the (a) frame and (b) wall directions for the 2017 Puebla Earthquake scaled to the MCE uniform hazard spectrum. 10-38

Figure 10-47 Base shear in the frame direction for the 2017 Puebla Earthquake scaled to the MCE uniform hazard spectrum. 10-38

Figure 10-48 Base shear in the wall direction for the 2017 Puebla Earthquake scaled to the MCE uniform hazard spectrum. 10-39

Figure 10-49 Sketch showing frames for which element performance is presented: (a) Gridline 10 in the frame direction, and (b) Gridline O in the wall direction. 10-40

Figure 10-50 Element performance levels for the 2017 Puebla Earthquake: (a) Gridline 10 in the frame direction, and (b) Gridline O in the wall direction..... 10-40

Figure 10-51 Element performance levels for the 2017 Puebla Earthquake scaled to the MCE hazard level: (a) Gridline 10 in the frame direction, and (b) Gridline O in the wall direction 10-41

Figure 10-52 Ratio of inelastic rotation to modeling parameter *a* for the 2017 Puebla Earthquake, Gridline 10 in the frame direction. 10-42

Figure 10-53 Ratio of inelastic rotation to modeling parameter *a* for the 2017 Puebla Earthquake, Gridline O in the wall direction..... 10-43

Figure 10-54 Ratio of inelastic rotation to modeling parameter *a* for the 2017 Puebla Earthquake scaled to the MCE hazard level, Gridline 10 in the frame direction 10-43

Figure 10-55 Ratio of inelastic rotation to modeling parameter *a* for the 2017 Puebla Earthquake scaled to the MCE hazard level, Gridline O in the wall direction..... 10-44

Figure 10-56 Comparison of observed damage and hysteretic response for masonry elements in building façade for unscaled and scaled ground motion. 10-46

Figure 10-57 Comparison of observed damage and hysteretic response for masonry infills in the frame direction for unscaled and scaled ground motion 10-47

Figure A-1 Nonlinear cyclic concrete model, which employs the monotonic Modified Kent-Park model..... A-3

This publication is available free of charge from: https://doi.org/10.6028/NIST.GCR.22-917-50

Figure A-2 Example of nonlinear reinforcing steel model for 60 ksi steel. A-3

Figure A-3 Generalized force-deformation relation for concrete elements or components A-7

Figure A-4 Idealizations of models used for simulating the nonlinear response of reinforced concrete components using concentrated plasticity or distributed plasticity approaches A-9

Figure A-5 Illustration of ASCE 41-17 Section 10.3.3 P-M interaction requirements..... A-10

Figure A-6 Beam-column joint modeling A-15

Figure A-7 Calibration of stress-strain relationship of the fiber elements to simulate the nonlinear moment-rotation relationships..... A-17

Figure A-9 Plastic hinge rotation in shear wall where flexure dominates inelastic response A-18

Figure A-10 Story drift in structural wall where shear dominates inelastic response A-19

Figure A-10 Chord rotation for structural wall coupling beams A-20

This publication is available free of charge from: https://doi.org/10.6028/NIST.GCR.22-917-50

List of Tables

Table 1-1 Summary of Study Structures 1-7

Table 3-1 Yield and Ultimate Values of Steel 3-4

Table 3-2 Building Weight by Floor Level 3-4

Table 3-3 Fragility Assessment Results 3-27

Table 3-4 Summary of Key Evaluation Parameters and Results 3-29

Table 3-5 Summary of First Mode Period and Maximum Base Shear Normalized by Building Weight 3-29

Table 3-6 Summary of Maximum Absolute Story Drift Ratio and Residual Drift Ratio 3-30

Table 3-7 Summary of Maximum Absolute Floor Acceleration 3-30

Table 4-1 Average Material Properties 4-4

Table 4-2 Building Weight by Floor Level 4-5

Table 4-3 Period Comparison after 50% JMA-Kobe and 100% JMA-Kobe Ground Motion 4-20

Table 4-4 Period Comparison for Different OpenSees Models 4-28

Table 4-5 First Mode Period Comparison in Each Direction 4-49

Table 4-6 Maximum Base Shear Normalized by Building Weight 4-51

Table 4-7 Calculated Strength and Deformation Capacities for Beams 4-62

Table 4-8 Governing Strength and Deformation Capacities for Beams 4-63

Table 4-9 Calculated Strength and Deformation Capacities for Columns 4-63

Table 4-10 Governing Strength and Deformation Capacities for Columns 4-64

Table 4-11 Calculated Strength and Deformation Capacities for Beam-Column Joints for Minimum Axial Load 4-66

Table 4-12 Calculated Strength and Deformation Capacities for Beam-Column Joints for Maximum Axial Load 4-67

Table 4-13 Calculated Equivalent Column Moments for Axis 1C 4-72

Table 4-14 Calculated Equivalent Column Moments for Axis 1B 4-73

This publication is available free of charge from: https://doi.org/10.6028/NIST.GCR.22-917-50

Table 4-15 Calculated Equivalent Column Moments for Axis 1A....4-73
Table 4-16 Calculated Strength and Deformation Capacities for Beams in Wall Direction....4-77
Table 4-17 Governing Strength and Deformation Capacities for Beams in Wall Direction....4-77
Table 4-18 Calculated Strength and Deformation Capacities for Columns in Wall Direction, Maximum Axial Load....4-78
Table 4-19 Calculated Strength and Deformation Capacities for Columns in Wall Direction, Minimum Axial Load....4-78
Table 4-20 Governing Strength and Deformation Capacities for Columns in Wall Direction, Maximum Axial Load....4-79
Table 4-21 Governing Strength and Deformation Capacities for Columns in Wall Direction, Minimum Axial Load....4-79
Table 4-22 Calculated Strength and Deformation Capacities for Beam-Column Joints in Wall Direction, Maximum Axial Load....4-80
Table 4-23 Calculated Strength and Deformation Capacities for Beam-Column Joints in Wall Direction, Minimum Axial Load....4-80
Table 4-24 Calculated Equivalent Column Moments for Location C-1....4-81
Table 4-25 Calculated Equivalent Column Moments for Location C-2....4-81
Table 4-26 Summary of Key Evaluation Parameters and Results....4-84
Table 4-27 Story Ratings....4-84
Table 4-28 Summary of Periods and Maximum Base Shear Normalized by Building Weight....4-86
Table 4-29 Summary of Maximum Absolute Story Drift Ratios and Residual Drift Ratios....4-87
Table 4-30 Summary of Maximum Absolute Floor Accelerations....4-88
Table 5-1 Concrete Material Properties as Specified....5-4
Table 5-2 Reinforcing Bar Material Properties as Specified....5-5
Table 5-3 Concrete Material Properties Based on Test Results....5-5
Table 5-4 Longitudinal Reinforcing Bar Material Properties Based on Test Results....5-5
Table 5-5 Transverse Reinforcing Bar Material Properties Based on Test Results....5-6
Table 5-6 Building and Floor Weights....5-6
Table 5-7 Testing Protocol....5-7

This publication is available free of charge from: https://doi.org/10.6028/NIST.GCR.22-917-50

Table 5-8 Natural Periods and Maximum Story Drift Angles 5-9
Table 5-9 Gravity Load and Masses..... 5-18
Table 5-10 Test and Model Periods 5-19
Table 5-11 Maximum Base Shear Normalized by Building Weight with Errors between Models and Experiment..... 5-58
Table 6-1 Comparison of Column G1 and G2 Properties to Selected Columns in the Experimental Database..... 6-13
Table 6-2 FEMA P-695 Assessment of the Fixed Base Model..... 6-25
Table 7-1 Average Material Properties 7-5
Table 7-2 Building Weight by Floor Level..... 7-5
Table 7-3 Properties for Column A5 and Test Specimen..... 7-31
Table 7-4 Location of Collapse Mechanism and Percentage of Beam and Slab-Column Connection Spring Elements Exceeding Collapse Prevention Performance Level..... 7-43
Table 7-5 Location of Collapse Mechanism and Percentage of Column Springs Exceeding Collapse Prevention Performance Level..... 7-44
Table 7-6 Summary of Calculated Building Response Parameters..... 7-52
Table 8-1 Overview of Column and Wall Properties at Second Story..... 8-5
Table 8-2 Mode Shapes..... 8-13
Table 8-3 Comparison of Simulated Response to Observed Damage 8-17
Table 8-4 Comparison of Predicted Local Response to Observed Damage.. 8-18
Table 8-5 Summary of Key Evaluation Parameters and Results 8-29
Table 8-6 Story Ratings..... 8-29
Table 9-1 Vertical Distribution of Building Weight 9-3
Table 9-2 Salient Material Properties..... 9-4
Table 9-3 Modes of Vibration for Nonlinear Models 9-12
Table 9-4 Comparison of Predicted Global Response to Observed Damage 9-14
Table 9-5 Comparison of Predicted to Observed Damage at Critical Story . 9-15
Table 9-6 Building and Similar Experimental Column Properties 9-19
Table 9-7 Dead and Live Loads 9-22
Table 9-8 Modes of Vibration for Linear Models..... 9-24
Table 9-9 Comparison of Predicted Global Response to Observed Damage 9-25

This publication is available free of charge from: https://doi.org/10.6028/NIST.GCR.22-917-50

Table 9-10 Comparison of Predicted Local Response to Observed Damage..9-26
Table 9-11 Summary of Key Evaluation Parameters and Results Using SRSS Response Spectrum....9-32
Table 9-12 Summary of Key Evaluation Parameters and Results Using 5%/50-Year UHS....9-32
Table 9-13 Story Ratings....9-32
Table 10-1 Column Dimensions....10-6
Table 10-2 Average Material Properties....10-8
Table 10-3 Building Weight by Floor Level....10-9
Table 10-4 Calculated Periods for Models with and without Masonry Elements....10-29
Table 11-1 Summary of Study Structures....11-1
Table 11-2 Global Response for Nonlinear Models....11-4
Table 11-3 Global Response for Linear Models....11-5
Table 11-4 Component-Based Response for Nonlinear Models....11-7
Table 11-5 Component-Based Acceptance Criteria at Critical Location for Nonlinear Models....11-10
Table 11-6 Component-Based Acceptance Criteria at Critical Location for Linear Models....11-10
Table 11-7 Nonlinear Global Acceptance Criteria....11-12
Table 11-8 Linear Global Acceptance Criteria....11-12
Table A-1 Factors to Translate Lower-Bound Material Properties to Expected Strength Material Properties....A-2

This publication is available free of charge from: https://doi.org/10.6028/NIST.GCR.22-917-50

Chapter 1
Introduction

This publication is available free of charge from: https://doi.org/10.6028/NIST.GCR.22-917-50

The primary objective of this report is to benchmark evaluation methodologies for existing reinforced concrete buildings and present recommendations for improvement of the seismic evaluation procedures of ASCE/SEI 41-17, *Seismic Evaluation and Retrofit of Existing Buildings* (ASCE, 2017b). For this purpose, calculated results from implementing evaluation procedures described in applicable methodologies are compared to data available for eight reinforced concrete structures subjected to ground motion shaking.

1.1 Background and Motivation

The objective of the seismic evaluation provisions described in ASCE 41 is to evaluate deficiencies in a building that prevent the building from achieving a selected Performance Objective. A workshop conducted in 2008 by the National Earthquake Hazards Reduction Program (NEHRP) for leading practitioners and researchers from around the United States found that ASCE 41 procedures are perceived to be overly conservative, and existing performance based seismic design methods are not accepted by practitioners as providing a uniform level of confidence (NIST, 2009). As a result, "benchmarking current performance-based design methodologies found in the American Society of Civil Engineers (ASCE)/Structural Engineering Institute (SEI) report ASCE/SEI 41" was identified as the highest priority need by the workshop participants.

Previous work assessed new reinforced concrete buildings designed according to ASCE/SEI 7, *Minimum Design Loads for Buildings and Other Structures*, using ASCE 41 and identified relative inconsistencies between the two standards; specifically, structures designed in accordance with ASCE 7 may not "pass" the linear and nonlinear static evaluations of ASCE 41 (Sattar, 2018). However, the structures were shown to comply with ASCE 41 nonlinear dynamic procedures (Sattar, 2018; Buniya et al., 2020). These findings are limited to the study of code-compliant buildings that typically would be considered "benchmark" buildings and deemed to comply with ASCE 41 due to their incorporation of prescriptive ductile detailing and minimum strength requirements.

There is a need to systematically benchmark the primary outcomes of the evaluation process and determine how well ASCE 41 represents actual damage that could occur under strong shaking. This is particularly relevant with the structural engineering

profession moving towards risk assessment of buildings that relies on accurate estimation of damage across a wide range of shaking intensities. Seismically retrofitting existing non-ductile concrete structures tends to require measures that have a significant environmental impact due to the carbon-intensive nature of the new structural elements. In order to minimize these impacts, accurate damage assessment methodologies are required to ensure that only the buildings requiring retrofit are identified and that the retrofit scope is highly efficient.

1.2 Project Overview

The primary intended audience for this document is the ASCE/SEI Standards Committee on Seismic Rehabilitation and ACI 369 Seismic Repair and Rehabilitation Committee. It may also be useful for practitioners and researchers in seismic evaluation, as well as individuals engaged in development of structural analysis and design standards and guidelines including ASCE 7.

In this study, analytical models for eight reinforced concrete structures were created following ASCE 41-17 provisions. Analyses were conducted in accordance with the Linear Dynamic and Nonlinear Dynamic Procedures described in ASCE 41-17 using a variety of software tools when subjected to an excitation equivalent to that recorded at the site or located as close as possible. The following software tools were used: OpenSees (McKenna et al., 2000), Perform3D, ETABS, and SAP2000 (Computers and Structures, Inc.). Analytical results were compared to observed performance of the structure through component and global response and damage.

In addition, collapse sensitivity of models was evaluated through incremental dynamic analysis resulting in a set of fragility functions for the structure that define the probability of collapse and probability of exceeding acceptance criteria. Results from additional evaluation methodologies were also studied to benchmark the procedures to observed performance and ASCE 41-17.

As a result of the studies, recommended improvements to the currently published procedures are presented for consideration by the ASCE Standards Committee on Seismic Rehabilitation in future editions of the ASCE 41 standard. It is noted that throughout the duration of this project, coordination and communication with the ASCE and ACI Committees took place on a regular basis, and some of the recommended improvements are already under consideration.

1.3 Seismic Evaluation Methodologies

The following is a brief overview of performance-based design building evaluation methodologies and standards studied in this project.

This publication is available free of charge from: https://doi.org/10.6028/NIST.GCR.22-917-50

1.3.1 ASCE/SEI 41, Seismic Evaluation and Retrofit of Existing Buildings

In 2014, the ASCE/SEI Standards Committee on Seismic Rehabilitation combined ASCE/SEI 31-03, *Seismic Evaluation of Existing Buildings* (ASCE, 2003) and ASCE/SEI 41-06, *Seismic Rehabilitation of Existing Buildings* (including Supplement No. 1) (ASCE, 2007). These two preceding standards are based on methodologies set forth in a series of documents. ASCE 31-03 was an updated version of FEMA 310, *Handbook for Seismic Evaluation of Buildings - A Prestandard* (FEMA, 1998), which in turn was an update of the original FEMA 178 report, *NEHRP Handbook for the Seismic Evaluation of Existing Buildings* (BSSC, 1992), which was based on ATC-14, *Evaluating the Seismic Resistance of Existing Buildings* (ATC, 1987). ASCE/SEI 41-06, *Seismic Rehabilitation of Existing Buildings* (ASCE, 2007), was published in 2007 as an updated version of FEMA 356, *Prestandard and Commentary for the Seismic Rehabilitation of Buildings* (FEMA, 2000), which was in turn an update of FEMA 273, *NEHRP Guidelines for the Seismic Rehabilitation of Buildings* (FEMA, 1997a), and FEMA 274, *NEHRP Commentary on the Guidelines for the Seismic Rehabilitation of Buildings* (FEMA, 1997b). The current version of the Standard was published in 2017, and an updated version is under development, expected to be published in 2023.

ASCE 41-17 includes provisions for linear and nonlinear analysis, both of which capture the effect of ductility and yielding through individual modifiers rather than global ones. In both linear and nonlinear analyses, global seismic demands applied to the analysis model are unreduced from the elastic level. Linear analysis accounts for the ductility of individual components by applying component-specific *m*-factors, which allow the calculated elastic seismic demands on individual elements to reach several times the elements' expected capacities. In nonlinear analysis, component ductility is modeled directly through component-specific nonlinear yielding curves, so that ductile elements can deform and soften when overloaded.

FEMA P-2006, *Example Application Guide for ASCE/SEI 41-13 Seismic Evaluation and Retrofit of Existing Buildings with Additional Commentary for ASCE/SEI 41-17*, (FEMA, 2018a) provides helpful guidance on the interpretation and the use of ASCE 41-13 through a set of examples and commentary that address key selected topics, as well as discussion of revisions to the Standard made in the 2017 publication.

1.3.2 Other Seismic Building Evaluation Methodologies

The following methodologies are implemented on selected buildings in this project to aid with benchmarking ASCE 41 models and results:

- **FEMA P-2018, *Seismic Evaluation of Older Concrete Buildings for Collapse Potential* (FEMA, 2018b).** This evaluation methodology is intended for use in

This publication is available free of charge from: https://doi.org/10.6028/NIST.GCR.22-917-50

identifying the most collapse-prone buildings among an inventory of older concrete buildings. This is accomplished through the development of a building rating, which represents the probability of collapse under the seismic demand level of interest. The collapse risk assessments are relative and intended for comparison between buildings evaluated following the FEMA P-2018 methodology.

- **FEMA P-58, *Seismic Performance Assessment of Buildings* (FEMA, 2018c).** This methodology describes a loss estimation methodology that can be used to predict damage levels for a specific earthquake demand. The estimates are based on an extensive library of fragility specifications provided with FEMA P-58. FEMA P-58 measures performance in terms of casualties (death and serious injuries), cost of repair, and downtime associated with either a given level of earthquake hazard, or in terms of annual value of such losses (expected values and dispersions) for a time-based evaluation.
- **Eurocode 8, *Design of Structures for Earthquake Resistance – Part 3: Assessment and Retrofitting of Buildings* (EN 1998-3:2005).** This methodology is focused on the assessment of existing structures and design of seismic upgrades. The document allows a number of different analysis methods, and can be used to predict performance of buildings to different levels of earthquakes. The methodology to calculate deformation capacities is suitable for comparing results from a nonlinear analysis, and little guidance is given on how to apply these capacities to results from a linear analysis. The focus of the document is on quantitative analysis rather than identifying common deficiencies in buildings.
- ***The Seismic Assessment of Existing Buildings* (NZSEE et al., 2017).** This methodology quantifies capacity of existing buildings as a percentage of "New Building Standard," which refers to code-based design demands intended to achieve a minimum level of life safety performance. The nonlinear pushover procedure within the NZSEE *Guidelines* is most relevant to this study and compares the pushover capacity of the structure to an acceleration-displacement response spectrum (ADRS, ordinarily the design spectrum). As such, the procedure focuses on global performance evaluation.

1.4 Selection of Buildings for Study

The project was initiated in 2016 with a first phase of work that studied six structures. In 2020, two additional structures were added. All study buildings present the following characteristics:

- Reinforced concrete structure
- Availability of building drawings to enable accurate modeling

This publication is available free of charge from: https://doi.org/10.6028/NIST.GCR.22-917-50

- Availability of documentation of damage due to ground shaking, e.g., photos, reports in literature, strain gage measurements for shaketable specimens
- Availability of documentation of ground motion at or near the site
- Moderate to high level of damage

The following is a list of the buildings studied and brief information about each building. Chapters 3 through 10 of this report present detailed information about the geometry and construction of each building and observed performance.

- **Three-story Test Frame:** This reinforced concrete frame was tested at the University of California, Berkeley in 2008 and subjected to a series of ground motions with increasing amplitudes. Design drawings, testing instrumentation, ground motion information, and weight documentation are available in literature. Accelerometers were attached at all floor levels, and drifts of all joints were recorded. Primary failure mode was shear and axial failure at columns.
- **Four-story Frame and Wall Test Structure:** This four-story reinforced concrete frame building was tested on the E-Defense shake table in Japan in 2010. The structure was subjected to a series of ground motions with increasing amplitudes. Design drawings, testing instrumentation, ground motion information, and weight documentation are available in literature. Floor displacement data are taken from the wire type displacement transducers in the building. Primary failure was observed at the joints.
- **Ten-story Frame and Wall Test Structure:** This 10-story reinforced concrete structure was tested on the E-Defense shake table in Japan in 2015. The structure was subjected to a series of ground motions with increasing amplitudes. Design drawings, testing instrumentation, shake table motion information, and weight documentation are available in literature. Data from the displacement transducers were processed to determine relative story displacements and story drift ratios calculated as the maximum displacement in that story divided by the story height. Primary failure was observed at the joints.
- **Six-story Frame and Wall Building in California:** This six-story reinforced concrete frame and shear wall structure was located in Southern California and served as the Imperial County Services Building. It was constructed in 1971, damaged in the 1979 Imperial County Earthquake, and subsequently demolished. The building was instrumented by the California Strong Motion Instrumentation Program with a 13-channel array of accelerometers at various locations throughout the structure and in the free field. Documentation of damage is available in literature. Primary failure mode was column bending and axial interaction impacted by bidirectional effects.

This publication is available free of charge from: https://doi.org/10.6028/NIST.GCR.22-917-50

- **Seven-story Frame Building in California:** This seven-story reinforced concrete moment frame building located in Van Nuys, California was constructed in 1966 and served as a hotel. The building was instrumented and the strongest earthquakes for which digitized records are available are the 1971 San Fernando, the 1987 Whittier Narrows, and the 1994 Northridge earthquakes. Observed damage records are available from the 1971 and 1994 earthquakes. In the 1994 Northridge Earthquake, severe structural damage was concentrated in the 4th and 5th levels where several columns sustained shear failure.
- **Five-story Wall Building in New Zealand:** This five-story reinforced-concrete shear wall building located in Christchurch, New Zealand was constructed circa 1966 and served as the Pyne Gould Corporation building. The building collapsed in the 2010-2011 Canterbury Earthquake Sequence. Ground motions were measured nearby, and damage was documented in photographs.
- **Three-story Frame with Masonry Infill Building in Taiwan:** This three-story reinforced concrete building located in Nanhua, Taiwan was designed and built in 1967 and served as the Nanhua District Office. The building was damaged in the 2016 Meinong Earthquake, and ground motion was recorded at nearby sites. The damage was primarily in one bay of the first story and diagonal cracking in columns was observed.
- **Seven-story Frame and Wall Building in Mexico:** This seven-story reinforced concrete residential building is located in Mexico City, Mexico. The building construction was initiated in 1981, and it is a representative example of non-ductile reinforced concrete construction in Mexico City designed in accordance with the 1976 Mexico City Building Code, which had detailing requirements similar to ACI 318-71. The building was damaged in the 2017 Puebla Earthquake, and ground motion was recorded at nearby sites. The damage documented shows inclined cracks in columns and significant cracking of unreinforced masonry infill and partitions.

Table 1-1 summarizes the structural system, geometry, and observed performance for study buildings.

This publication is available free of charge from: https://doi.org/10.6028/NIST.GCR.22-917-50

Table 1-1 Summary of Study Structures

Chapter No.	Structural System (Name, Location)	Earthquake Event	Data Availability	Observed Performance
3	3-story test frame (UC Berkeley 2008)	Shaketable: 4.06 × Llolleo recording of 1985 Valparaiso (Chile)	Measured	Column diagonal (shear) and axial failure
4	4-story test frame and wall (E-Defense 2010)	Shaketable: 100% of JMA recording of 1995 Kobe (Japan)	Measured	Beam-column joint failure and wall boundary element failure
5	10-story test frame and wall (E-Defense 2015)	Shaketable: 100% of JMA recording of 1995 Kobe (Japan)	Measured	Damage to joints, minor spalling of wall boundary zones and minor cracking and spalling at base of columns
6	6-story frame and wall building (Imperial County Services Building, California)	1979 Imperial County	Accelerometer	Column diagonal (shear) and axial failure, amplified by torsion
7	7-story frame building (Hotel in Van Nuys, California)	1994 Northridge	Accelerometer	Column diagonal (shear) failure
8	5-story wall building (Pyne Gould Corporation Building, New Zealand)	2010-2011 Canterbury Sequence (New Zealand)	Photographs and observations	Collapse
9	3-story frame with masonry infill building (Nanhua District Office Building, Taiwan)	2016 Meinong (Taiwan)	Photographs and observations	Column diagonal cracking
10	7-story frame and wall with masonry infill building (Residential building in Mexico)	2017 Puebla (Mexico)	Photographs and observations	Damage to masonry infill panels and perimeter masonry spandrel frames

1.5 Report Organization

Chapter 2 describes the application of the seismic evaluation methodologies, approach for comparison of analytical results to observed performance and other evaluation methods, and the methodology for fragility assessment.

Chapters 3 through 10 present available information, analytical results, and findings for each study building as follows:

- Chapter 3 describes the following studies of the three-story test frame: Application of ASCE 41-17 nonlinear dynamic procedure using Perfom3D and OpenSees and ASCE 41-17 linear procedures using ETABS, fragility assessment, and FEMA P-2018 evaluation. In addition, an OpenSees model was developed using ASCE 41-13 provisions to investigate the effects of updated modeling parameters and acceptance criteria for columns in ASCE 41-17.

This publication is available free of charge from: https://doi.org/10.6028/NIST.GCR.22-917-50

- Chapter 4 describes the following studies of the four-story test frame and wall structure: Application of ASCE 41-17 nonlinear dynamic procedure using Perfom3D and OpenSees and ASCE 41-17 linear procedure using ETABS, fragility assessment, and evaluation with Eurocode, NZSEE *Guidelines*, and FEMA P-2018.
- Chapter 5 describes the following studies of the 10-story test frame and wall structure: Application of ASCE 41-17 nonlinear dynamic procedure using Perfom3D and OpenSees, and fragility assessment.
- Chapter 6 describes the following studies of the six-story frame and wall building in California: Application of ASCE 41-17 nonlinear dynamic procedure using OpenSees with a fixed base, vertical ground motion, and soil-structure interaction, and ASCE 41-17 linear procedure using OpenSees; damage assessment using FEMA P-58; fragility assessment; and Eurocode evaluation.
- Chapter 7 describes the following studies of the seven-story frame building in California: Application of ASCE 41-17 nonlinear dynamic procedure using OpenSees and ASCE 41-17 linear dynamic procedure using OpenSees, and fragility assessment.
- Chapter 8 describes the following studies of the five-story wall building in New Zealand: Application of ASCE 41-17 nonlinear dynamic procedure using OpenSees and ASCE 41-17 linear procedure using ETABS, and FEMA P-2018 evaluation. A brief summary of evaluation with NZSEE *Guidelines* by others is also included.
- Chapter 9 describes the following studies of the three-story frame with masonry building in Taiwan: Application of ASCE 41-17 nonlinear dynamic procedure using OpenSees and ASCE 41-17 linear dynamic procedure using SAP2000, damage assessment using FEMA P-58, fragility assessment, and FEMA P-2018 evaluation.
- Chapter 10 describes the following studies of the seven-story frame and wall building with masonry infill in Mexico City: Application of ASCE 41-17 nonlinear dynamic procedure using OpenSees.

Chapter 11 presents generalized findings from the studies and Chapter 12 lists key take aways and recommendations for improvements to the next edition of ASCE 41, as well as opportunities for future work.

Appendix A describes the modeling approaches that form the basis for all studies. List of references and project participants are provided at the end of the report.

This publication is available free of charge from: https://doi.org/10.6028/NIST.GCR.22-917-50

Chapter 2
Project Approach

2.1 Overview

During the conduct of this project, it was important to establish a consistent approach to be applied to the eight reinforced concrete structures. This chapter presents the agreed upon project approach for developing analysis models in accordance with ASCE 41-17 provisions and for comparing results of analytical models to observed or measured damage. In the case of instrumented structures, the responses from the model and the actual building can be directly compared. In other cases, the representation of damage to the model is compared to photos of damage from reconnaissance reports. Exceedance of ASCE 41-17 acceptance criteria is reported for the simulations and estimated based on the level of damage for observed structures. Further, to benchmark ASCE 41-17 models at other levels of excitation, building models are subjected to a suite of ground motions, resulting in a set of fragility curves for the building. These curves define the probability of collapse and probability of exceeding acceptance criteria in varying fractions of components.

Benchmarking with respect to other evaluation methods is also discussed.

2.2 Seismic Evaluation per ASCE 41

2.2.1 Analysis Model

Analytical models of each study building are created following the requirements of ASCE 41-17 for linear dynamic procedure (LDP) and nonlinear dynamic procedure (NDP). All models comply with ASCE 41-17 modeling guidelines, but represent different decisions about software, types of element models, and other model characteristics. For selected buildings, additional nonlinear models are developed to investigate modeling assumptions regarding member nonlinear behavior.

For nonlinear procedures, analytical models are developed in the open-source software OpenSees (McKenna et al., 2000) and Perform3D (Computers & Structures, Inc.); for linear procedures, OpenSees, ETABS (Computers & Structures, Inc.), or SAP2000 (Computers & Structures, Inc.) were used to develop the models. For three buildings (3-story test frame, 4-story test frame and wall, and 10-story test frame and wall, presented in Chapters 3, 4, and 5, respectively), nonlinear models were developed in both OpenSees and Perform3D to study the difference in simulated response. Details about the modeling decisions are provided in each building-

This publication is available free of charge from: https://doi.org/10.6028/NIST.GCR.22-917-50

specific chapter. In addition, Appendix A presents the underlying assumptions for modeling of elements per ASCE 41-17 provisions for this project.

ASCE 41 is based on a deterministic approach that uses expected values from test data and the provisions do not require the analyst to consider material and modeling uncertainties in the assessment process. Because the goal of this study is to compare simulated outcomes following ASCE 41 guidelines against recorded building performance, the analytical models do not explicitly consider uncertainty in material properties, nonlinear component modeling parameters, element stiffness, or damping. In addition, uncertainty in observed damage and measured response are not considered in this study, and only best estimates and available data are used for comparison.

Ground motion selection and scaling procedures described in ASCE 41-17 are not followed. Rather, the model is subjected to the best estimate of the ground motion at the building site during the selected earthquake event, i.e., recorded ground motions at the building site when available and recorded ground motions nearest to the site where necessary. For structures constructed for shake table testing, the recorded table motion is used.

NIST GCR 12-917-21, *Soil Structure Interaction for Building Structures*, (NIST, 2012) presents recommendations for when consideration of soil-structure interaction (SSI) may be important related to foundation flexibility. The recommendations are based on the structure-to-soil stiffness ratio, $h/(V_s T)$. Where this ratio exceeds 0.1, SSI can significantly lengthen the building period and the distribution of force and deformation demands within the structure. This check was performed for all of the study buildings (excluding those tested on shake tables), and where it was found that the ratio exceeded the 0.1 limit and sufficient soil property information was available, SSI effects were investigated. This applies for only one building (6-story frame and wall building in Chapter 6). The effects of foundation flexibility were studied and are documented in Chapter 6. The remaining study building models do not include consideration of soil-structure interaction effects as defined in ASCE 41-17 Section 8.5 due to either ratios below 0.1 or insufficient availability of soil information. Rather, per ASCE 41-17 Section 7.2.3.4, foundations are modeled assuming either a rigid or flexible base condition when soil-structure interaction per ASCE 41-17 Section 8.5 is not considered. For most of the buildings the foundations are assumed to be rigid.

2.2.2 Acceptance Criteria and Performance Objectives

Acceptance criteria, sometimes also called capacities, are limiting values of strength and/or deformation demands, as predicted by analysis, that are used to determine either the probable performance of a structure or its conformance with design

This publication is available free of charge from: https://doi.org/10.6028/NIST.GCR.22-917-50

requirements. The acceptance criteria in ASCE 41-17 are derived from the hysteretic backbone curve and is presented graphically in Figure 2-1.

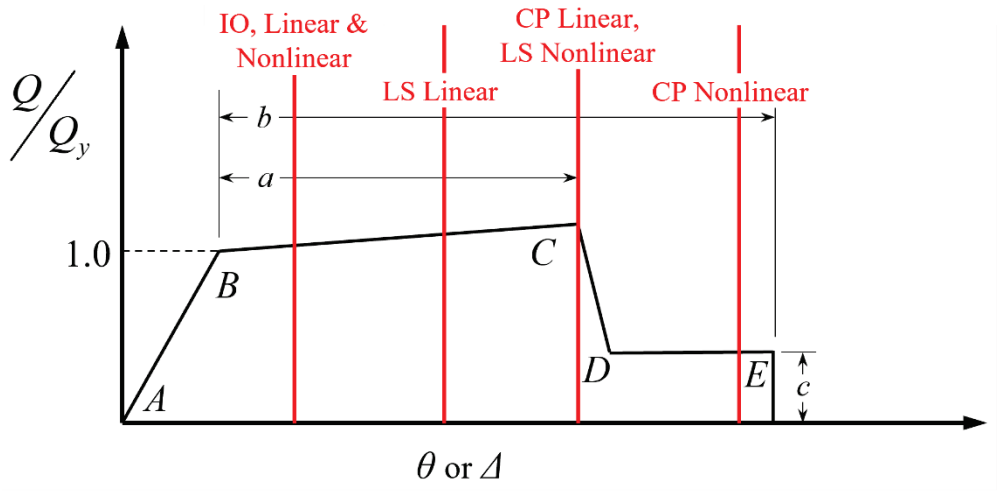


Figure 2-1 Generalized force-deformation relation (adapted from ASCE 41-17 Figure 10-1a).

Per ASCE 41-17 Section 10.3.1.2.2, the generalized load-deformation relation shown in Figure 2-1 shall be described by linear response from point A to an effective yield at point B, then a linear response at reduced stiffness from point B to point C, then sudden reduction in force resistance to point D, then response at reduced resistance to point E and loss of strength beyond that point.

In ASCE 41-17, performance-based design concepts are implemented through a selection of one or more targeted building Performance Objectives consisting of pairings of *Building Performance Levels* and *Seismic Hazard Levels*. A *Building Performance Level* is a combination of the performance of both the structural and nonstructural components and is expressed as a discrete damage state: Immediate Occupancy (IO), Damage Control, Life Safety (LS), Limited Safety, and Collapse Prevention (CP) for *Structural Performance Level*s.

For nonlinear procedures, Collapse Prevention performance is deemed to occur at the deformation associated with point E in Figure 2-1, which is assumed to include loss of some reserve deformation capacity, before true failure occurs. Some acceptance criteria use deformations slightly below point E to include some measure of conservatism. Life Safety performance for deformation-controlled actions is generally taken as approximately 75% of the acceptance criteria for Collapse Prevention, and Immediate Occupancy is taken as the deformation at which permanent, visible damage occurs but not greater than (0.67 × 0.75) times the deformation at point C. Slightly different acceptance criteria are used for column elements based on ratios of plastic deformation as compared to the modeling

This publication is available free of charge from: https://doi.org/10.6028/NIST.GCR.22-917-50

parameter *b*. For columns, Collapse Prevention is taken as 0.7 × *b*, Life Safety is taken as 0.5 × *b*, and Immediate Occupancy is taken as 0.15 × *b*

For linear procedures, the deformations used as the basis for computing *m*-factors are as follows: Collapse Prevention performance is taken as point C, but not greater than 0.75 times the deformation at point E; Life Safety is taken as 0.75 times the deformation at point C; and Immediate Occupancy performance for deformation-controlled actions is deemed to occur when deformation at which permanent, visible damage has occurred but does not exceed 67% of the Life Safety acceptance criteria.

ASCE 41-17 Chapter 10 presents modeling parameters for nonlinear procedures as tabulated values for *a*, *b*, and *c*, as illustrated in Figure 2-1 with additional parameters for shear-controlled walls as shown in ASCE 41-17 Figure 10-1c.

Observed damage for global performance, specifically for concrete frames and walls, are estimated based on the qualitative descriptions of structural performance levels provided in ASCE 41-17 Tables C2-3 and C2-4, presented below as Figures 2-2 and 2-3.

Table C2-3. Damage Control and Building Performance Levels

	Target Building Performance Levels			
	Collapse Prevention Level (5-D)	**Life Safety Level (3-C)**	**Immediate Occupancy Level (1-B)**	**Operational Level (1-A)**
Overall damage	**Severe**	**Moderate**	**Light**	**Very light**
Structural components	Little residual stiffness and strength to resist lateral loads, but gravity load-bearing columns and walls function. Large permanent drifts. Some exits blocked. Building is near collapse in aftershocks and should not continue to be occupied.	Some residual strength and stiffness left in all stories. Gravity-load-bearing elements function. No out-of-plane failure of walls. Some permanent drift. Damage to partitions. Continued occupancy might not be likely before repair. Building might not be economical to repair.	No permanent drift. Structure substantially retains original strength and stiffness. Continued occupancy likely.	No permanent drift. Structure substantially retains original strength and stiffness. Minor cracking of facades, partitions, and ceilings as well as structural elements. All systems important to normal operation are functional. Continued occupancy and use highly likely.
Nonstructural components	Extensive damage. Infills and unbraced parapets failed or at incipient failure.	Falling hazards, such as parapets, mitigated, but many architectural, mechanical, and electrical systems are damaged.	Equipment and contents are generally secure but might not operate due to mechanical failure or lack of utilities. Some cracking of facades, partitions, and ceilings as well as structural elements. Elevators can be restarted. Fire protection operable.	Negligible damage occurs. GPower and other utilities are available, possibly from standby sources.
Comparison with performance intended for typical buildings designed to codes or standards for new buildings, for the design earthquake	Significantly more damage and greater life-safety risk.	Somewhat more damage and slightly higher life-safety risk.	Less damage and low life-safety risk.	Much less damage and very low life-safety risk.

Figure 2-2 Description of overall building damage and performance levels (reproduced from ASCE 41-17 Table C2-3). Printed with permission from ASCE.

NIST GCR 17-917-45, *Recommended Modeling Parameters and Acceptance Criteria for Nonlinear Analysis in Support of Seismic Evaluation, Retrofit, and Design* (NIST, 2017), presents a comprehensive discussion on existing ASCE 41 acceptance criteria, and presents recommendations for improved hysteretic relationships for use in nonlinear seismic analysis in support of performance-based seismic design and evaluation.

This publication is available free of charge from: https://doi.org/10.6028/NIST.GCR.22-917-50

Seismic-Force-Resisting System	Type	Structural Performance Levels		
		Collapse Prevention (S-5)	Life Safety (S-3)	Immediate Occupancy (S-1)
Concrete frames	Primary elements	Extensive cracking and hinge formation in ductile elements. Limited cracking or splice failure in some nonductile columns. Severe damage in short columns.	Extensive damage to beams. Spalling of cover and shear cracking in ductile columns. Minor spalling in nonductile columns. Joint cracks.	Minor cracking. Limited yielding possible at a few locations. Minor spalling of concrete cover.
	Secondary elements	Extensive spalling in columns and beams. Limited column shortening. Severe joint damage. Some reinforcing buckled.	Major cracking and hinge formation in ductile elements. Limited cracking or splice failure in some nonductile columns. Severe damage in short columns.	Minor spalling in a few places in ductile columns and beams. Flexural cracking in beams and columns. Shear cracking in joints.
	Drift	Transient drift sufficient to cause extensive nonstructural damage. Extensive permanent drift.	Transient drift sufficient to cause nonstructural damage. Noticeable permanent drift.	Transient drift that causes minor or no nonstructural damage. Negligible permanent drift.
Concrete walls	Primary elements	Major flexural or shear cracks and voids. Sliding at joints. Extensive crushing and buckling of reinforcement. Severe boundary element damage. Coupling beams shattered and virtually disintegrated.	Some boundary element cracking and spalling and limited buckling of reinforcement. Some sliding at joints. Damage around openings. Some crushing and flexural cracking. Coupling beams: extensive shear and flexural cracks; some crushing, but concrete generally remains in place.	Minor diagonal cracking of walls. Coupling beams experience diagonal cracking.
	Secondary elements	Panels shattered and virtually disintegrated.	Major flexural and shear cracks. Sliding at construction joints. Extensive crushing. Severe boundary element damage. Coupling beams shattered and virtually disintegrated.	Minor cracking of walls. Some evidence of sliding at construction joints. Coupling beams experience x-cracks. Minor spalling.
	Drift	Transient drift sufficient to cause extensive nonstructural damage. Extensive permanent drift.	Transient drift sufficient to cause nonstructural damage. Noticeable permanent drift.	Transient drift that causes minor or no nonstructural damage. Negligible permanent drift.

Figure 2-3 Description of structural performance levels and illustrative damage for concrete frames and walls (reproduced from ASCE 41-17 Table C2-4, edited to show concrete frames and walls only). Printed with permission from ASCE.

2.3 Comparison of Analytical Results to Observed Performance

The primary objective of this project is to compare analytical results obtained from models developed in accordance with ASCE 41-17 provisions to observed performance of buildings. The comparison examines both component and global response and damage. In the case of instrumented structures, the responses from model and the actual building can be directly compared. In other cases, the representation of damage to the model is compared to photos of damage from reconnaissance reports. Exceedance of ASCE 41-17 acceptance criteria is also recorded.

At the global level, the comparison examines the following questions:

- **Did the model predict the correct story mechanism and location within the building?** This comparison applies to all study buildings.
- **Did the model accurately predict the value of the drift at critical story?** Computed drifts are compared to the observed or measured drifts at the expected critical story. Accuracy of drifts is judged to be a match if the difference between the modeled and measured value is within 20%. For non-measured buildings, the comparison is based on deformations in comparable test specimens as described in Section 2.3.1.
- **Did the model predict the value of the drift at stories other than critical?** Computed drifts are compared to the observed or measured drifts elsewhere within the structure. Accuracy of drifts is judged to be a match if the difference

This publication is available free of charge from: https://doi.org/10.6028/NIST.GCR.22-917-50

between the modeled and measured value is within 20%. For non-measured buildings, the comparison is based on deformations in comparable test specimens as described in Section 2.3.1.

- **Did the model predict the floor and roof accelerations?** This comparison only applies to measured buildings. Accuracy of peak floor accelerations is judged to be a match if the difference between the modeled and measured value is within 20%.
- **Did the model predict the value of residual drift at roof?** This comparison only applies to measured buildings. Accuracy of residual drift is judged to be a match if the difference between the modeled and measured value is within 20%.

At the component level, the comparison examines the following questions for each element type (columns, beams, joints, walls):

- **Did the model predict the correct failure mechanism (shear, flexure, shear-flexure, axial, splice)?** This comparison applies to all study buildings.
- **Did the model predict the correct ASCE 41 acceptance criteria range for the components?** This comparison to applies to all study buildings. Observed damage to deformation-controlled elements is compared to structural performance level damage descriptions presented in Figure 2-2. The following distinctions are made for this report:
    - "Limited" damage occurs if the damage description is less than Immediate Occupancy in Figure 2-2
    - "Moderate" damage occurs if the damage description is more than Immediate Occupancy but less than Collapse Prevention in Figure 2-2
    - "Severe" damage occurs if the damage description exceeds Collapse Prevention in Figure 2-2

At the component level, two other types of comparisons are also used: (1) component response is compared to similar test data found in literature; and (2) component damage is interpreted through fragility data provided in FEMA P-58 (FEMA, 2018c). These comparisons are useful to map model response observations (primarily drifts) to damage of the type represented by photos and reconnaissance observations of damaged buildings.

2.3.1 Use of Test Data in Literature

In most buildings studied, direct measurement of story drift and associated component deformation demands are not available. In such cases, it is not possible to directly assess whether a computational model is delivering the correct story drift demands that occurred at the building during the considered earthquake. The only

This publication is available free of charge from: https://doi.org/10.6028/NIST.GCR.22-917-50

avenue of direct comparison for these buildings is through damage observed in components during the event and those predicted by the computational models. However, computational models only indicate the range of behavior (limited, moderate, or severe damage) to which a component was pushed (as documented on the resulting backbone curve in relation to performance points on Figure 2-1), i.e., before strength degradation occurs (capping point on the backbone force-deformation curve, point C in Figure 2-1 corresponding to a plastic deformation of *a*), after strength degradation initiates but before loss of lateral strength is reached, (between points C and E in Figure 2-1) and after loss of lateral strength is reached (beyond point E in Figure 2-1 corresponding to a plastic deformation of *b*).

In cases where ASCE 41-17 presents explicit descriptions of the mode of failure, the type of damage that a component sustains can be postulated from the computational model (e.g., shear damage or splice damage).

To benchmark ASCE 41-17 modeling parameters and damage mode classification in non-measured buildings, the following steps are followed:

- A literature review is conducted to identify experiments with components of similar material properties and reinforcement detailing as the damaged components in the study buildings.
- Photos of test components at the drift or deformation levels estimated in the computational models are identified.
- Test specimen photos are compared to the damage observed in the building components.

This approach allows comparison of damage mode classification and level of damage. A satisfactory match is achieved when the test specimen exhibits a similar damage type and level to that observed visually or estimated based on the backbone behavior relation for the element. A match indicates that the model captures the correct level of lateral drift and that the modeling parameters represent well the damage type and level at that deformation state. Outcomes can vary with one or more of these measures not matching, which could indicate that certain scenarios, such as the drift level delivered by the model, are not correct, or that the modeling parameters in ASCE 41 are not accurately capturing the type or level of damage.

2.3.2 Use of FEMA P-58 Fragility Database

FEMA P-58 presents a methodology for estimating seismic performance, in terms of economic losses, downtime, casualties, or other metrics of interest to decision makers, and provides an extensive fragility database compiled from test results and expert judgment. This study adopts one part of the FEMA P-58 assessment methodology to link engineering demand parameters from nonlinear simulation

This publication is available free of charge from: https://doi.org/10.6028/NIST.GCR.22-917-50

models to damage in components. The goal of this effort is to map simulation results to damage descriptors that can be used to compare model output to observed damage.

Figure 2-4 illustrates implementation of the FEMA P-58 methodology: First, each component of the selected study building is classified to match the FEMA P-58 fragility database. For example, beam-column subassemblies are classified based on their detailing (e.g., non-conforming), relative strength of columns, beams, and joints, and expected demands (e.g., axial and shear demands). For each classification, the FEMA P-58 fragility database identifies the expected failure mechanism and presents a suite of fragility curves that define the probability of being in one of several damage states of interest as a function of the demand parameter (typically, story drift).

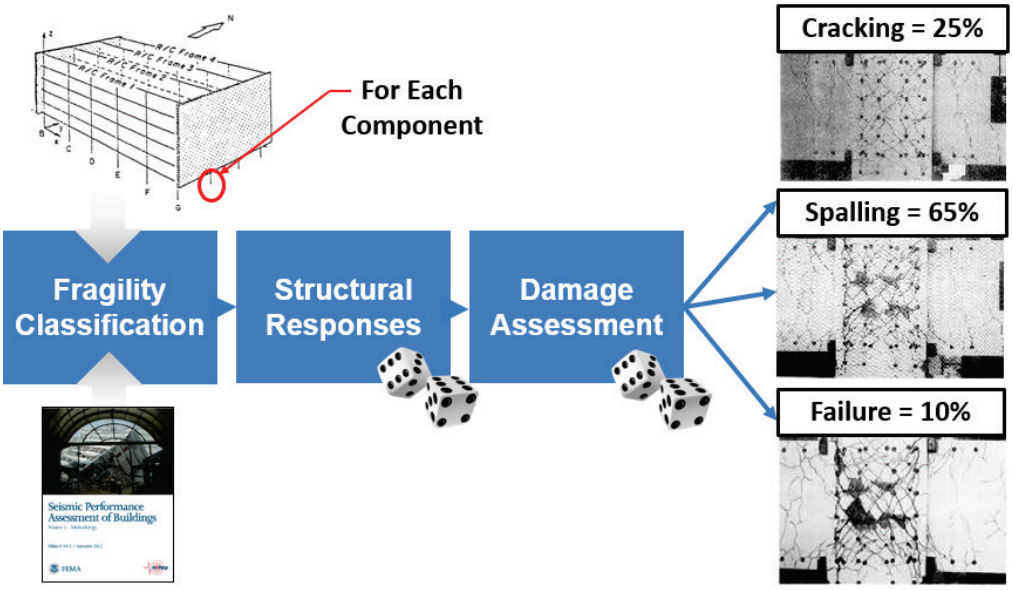


Figure 2-4 Illustration of FEMA P-58-based damage assessment procedure for each component, including fragility classification, structural response from ASCE 41 models, and damage assessment.

Next, the structural response of the selected component from the ASCE 41 model, such as story drift, is calculated. The fragility curve for the given structural response parameter is used to determine the probability that a particular component is in each damage state.

Although structural responses from the ASCE 41 models are deterministic, to be consistent with the FEMA P-58 methodology, modeling uncertainty is applied to the peak responses from ASCE 41 models (corresponding to a logarithmic standard deviation of 0.15 around the median value obtained from the analysis model, applicable to models of superior quality). This uncertainty is propagated through the damage assessment of each component using Monte Carlo simulation with 2,000

This publication is available free of charge from: https://doi.org/10.6028/NIST.GCR.22-917-50

randomly generated structural responses, which are compared to 2,000 randomly generated damage state thresholds defined by the fragility curve.

The outcome of this process, for each component of interest, is a probabilistic description of the likelihood of each component being in a particular damage state, together with qualitative descriptions of those damage states from FEMA P-58 that can be compared to damage photos and observations.

The FEMA P-58 component fragility curves can also be compared directly with the ASCE 41 backbone curves. However, to make a likewise comparison, fragility curves need to be converted from story drift ratios to hinge rotation. The conversion is performed by multiplying the fragility damage state story drift thresholds by the ratio of the maximum total rotation of each component to the maximum story drift ratio from the nonlinear dynamic analysis.

2.4 Fragility Assessment

2.4.1 Approach

In order to examine the collapse sensitivity of study buildings, the models are also subjected to shaking intensities beyond the intensity of the record of shaking experienced in the damaging earthquake. Accordingly, each building model is evaluated through incremental dynamic analysis (IDA; Vamvatsikos and Cornell, 2002) with variable ground motion input, by scaling selected ground motions to increased intensities until collapse limit state is reached.

The implementation of IDA adopted here follows the FEMA P-695 procedures (FEMA, 2009). Each building is subjected to each record in the FEMA P-695 far field record set consisting of 22 pairs of records. For most models, ground motions are applied twice to each model (changing the orientation of the records relative to the model); however, in some cases, due to computational expense, each pair of ground motion is applied only once, with the orientation of the ground motion relative to the building chosen at random.

Ground motion intensity is defined as the maximum direction spectral acceleration at the period of the building model (Huang et al., 2008) and intensity is defined as the mean of the maximum direction spectral acceleration of all the records at a given scale level. For buildings with two different periods in the two orthogonal directions, a single period is chosen (either corresponding to the period in one of the directions, or an intermediate period).

Each building model is simulated for each motion and intensity level of interest, with the following limit states of interest:

This publication is available free of charge from: https://doi.org/10.6028/NIST.GCR.22-917-50

- **Collapse.** The Collapse limit state represents the best estimate of the collapse resistance of the ASCE 41 building model. Here, Collapse is defined as story drifts exceeding 6% transient drift in any story. Although collapse mechanisms of nonductile reinforced concrete buildings can be complex, many of the phenomena, including shear and axial failure, are represented in rotational hinge backbones that produce (in the model) a sidesway mechanism that can be identified by these drift limits. The 6% transient drift limit was selected based on discussions by the ASCE 41 committee that may consider a global limit state based on a drift limit in the next cycle. The 6% transient drift limit is also used by ASCE 7-22 as a measure of unacceptable response for structures up to a height of 100 feet. Generally, not all elements or failure modes are directly modeled in the simulations. The 6% drift limit is intended to indicate when non-modeled elements begin to lose strength and initiate collapse. In addition, the 6% limit is used because mathematical solvers in the available software may not adequately simulate nonlinear behavior beyond 6%.
- **Unacceptable Response.** The limit state is considered Unacceptable Response if the response of any element plastic deformation exceeds 1.5 times ASCE 41-17 modeling parameter *b* (Figure 2-1), or the model fails to converge to a solution. This limit is meant to be an estimate of the valid range of modeling being considered by the ASCE 41 and ASCE 7 committees as unacceptable response.
- **Collapse Prevention.** ASCE 41 provides Collapse Prevention acceptance criteria for each component in the structure. Currently, ASCE 41-17 defines Collapse Prevention as when any element exceeds that acceptance criteria. This study employs several Collapse Prevention-based limit states that span the range between component and system behavior. To study the fragility associated with current ASCE 41 acceptance criteria, fragilities are developed to identify when the first component reaches its Collapse Prevention acceptance criterion. In addition, fragilities are computed for the case where a certain percentage of components exceed the acceptance criteria. The percentiles considered and the components of interest (columns, beams, joints, or walls) depend on the characteristics and failure mechanisms of the building. These fragilities are developed to assess whether the ASCE 41 individual component acceptance criteria may be an overly conservative indicator of overall building performance.

2.4.2 Interpretation of Fragility Assessments

Each limit state is quantified through a fragility curve, which shows the probability of being in or exceeding the limit state of interest, as a function of ground motion intensity.

The collapse curve provides a benchmark for comparing the response of these building models to the targeted collapse risk of modern code-conforming buildings in

This publication is available free of charge from: https://doi.org/10.6028/NIST.GCR.22-917-50

ASCE 7, which targets a less than 1% probability of collapse in 50 years, corresponding to less than 10% probability of collapse under the MCE_R shaking (FEMA, 2009), in areas where the MCE_R hazard is controlled by the 2% in 50 years probabilistic hazard definition. In areas where deterministic caps control the MCE_R hazard definition, the probability of collapse will be higher than 1%.

For study buildings located in the United States for which MCE_R shaking intensity is well defined, the comparison is carried out as follows. First, the MCE_R value is obtained from the 2014 USGS Seismic Design Maps referenced in ASCE 7-16. Next, the collapse fragility curve is adjusted as per FEMA P-695 methodology. These adjustments account for the expected spectral shape of ground motions, which may differ from those used in the analysis. In this study, spectral shape factors are taken directly from FEMA P-695 based on the period and ductility capacity of the building model. An adjustment is made for three-dimensional building models and to increase the uncertainty in the collapse fragility curve to incorporate model, design, and test data uncertainty. In all cases, the uncertainty is taken as 0.60. Once these adjustments are undertaken, collapse probabilities can be compared to the 10% benchmark probability of collapse for modern buildings.

The component-based Collapse Prevention fragility curves are developed to compare global measures of performance (e.g., sidesway collapse, or drift limits) to component-based acceptance criteria and are presented in each building-specific chapter.

2.5 Comparison to Other Evaluation Methods

2.5.1 FEMA P-2018

Four study buildings are evaluated with the methodology described in FEMA P-2018, *Seismic Evaluation of Older Concrete Buildings for Collapse Potential* (FEMA, 2018), and results are presented in Chapters 3, 4, 8, and 9. This methodology uses simplified estimates of drift demand to identify collapse prone buildings. The approach does not require a nonlinear model and instead relies on mechanism analysis, analytical drift relations, and structural reliability theory. The outcome of the FEMA P-2018 methodology is a building rating and risk classification that provides a measure of collapse risk.

At the level of ground shaking producing the observed damage, the building rating can be compared to the observed performance and to ASCE 41 model results. In addition, intermediate outputs from FEMA P-2018, such as building strength, drift demands, fundamental periods, and critical story and direction can be compared to ASCE 41 model results.

This publication is available free of charge from: https://doi.org/10.6028/NIST.GCR.22-917-50

2.5.2 Eurocode

Results from ASCE 41 building models for two buildings were evaluated with acceptance criteria of *Eurocode 8 Design of structures for earthquake resistance – Part 3: assessment and retrofitting of buildings* (EN 1998-3:2005) and documented in Chapters 4 and 6. In this standard, Near Collapse acceptance criteria for components including columns, beam, walls, and joints are reported where Near Collapse defines a structure that is heavily damaged, with low residual lateral strength and stiffness, and most nonstructural components collapsed. For columns under flexure, these acceptance criteria are provided in Equations A.1 and A.3 in Annex A of that document. These equations take as input transverse and longitudinal reinforcement, axial load and shear span length, and produce element plastic rotation capacities at which the limit state is exceeded. These acceptance criteria are used to develop Near Collapse fragility curves that can be compared to ASCE 41 Collapse Prevention curves. The same model that is used for the assessment of ASCE 41 acceptance criteria is used to assess Eurocode acceptance criteria, so this comparison addresses only acceptance criteria differences.

2.5.3 NZSEE Guidelines

The ASCE 41-17 model developed for one structure was used for comparison of the modeling and acceptance criteria definitions of *The Seismic Assessment of Existing Buildings* (NZSEE et al., 2017) Part C, Detailed Seismic Assessment with those of ASCE 41-17. The nonlinear strength and backbone modeling parameters used by the NZSEE *Guidelines* for beam, column, beam-column joints, and wall elements were computed for various elements and presented for comparison with the modeling parameters defined by ASCE 41-17. The overall lateral strength of the building based on pushover analysis based on computations and element modeling criteria of each of the two standards was compared to examine the effect on estimation of building lateral capacity.

This publication is available free of charge from: https://doi.org/10.6028/NIST.GCR.22-917-50

Chapter 3

Three-story Test Frame

3.1 Overview

This chapter presents benchmarking studies for a two-dimensional reinforced concrete frame tested at the University of California Berkeley shake table, shown in Figure 3-1. The frame was a three-story, one-third scale structure with no slab, and the frame was braced from moving in the out-of-plane direction by steel frames. Ground motion records and response parameters are available since the structure was tested on a shake table. In this chapter, analysis results are compared with experimentally derived values.

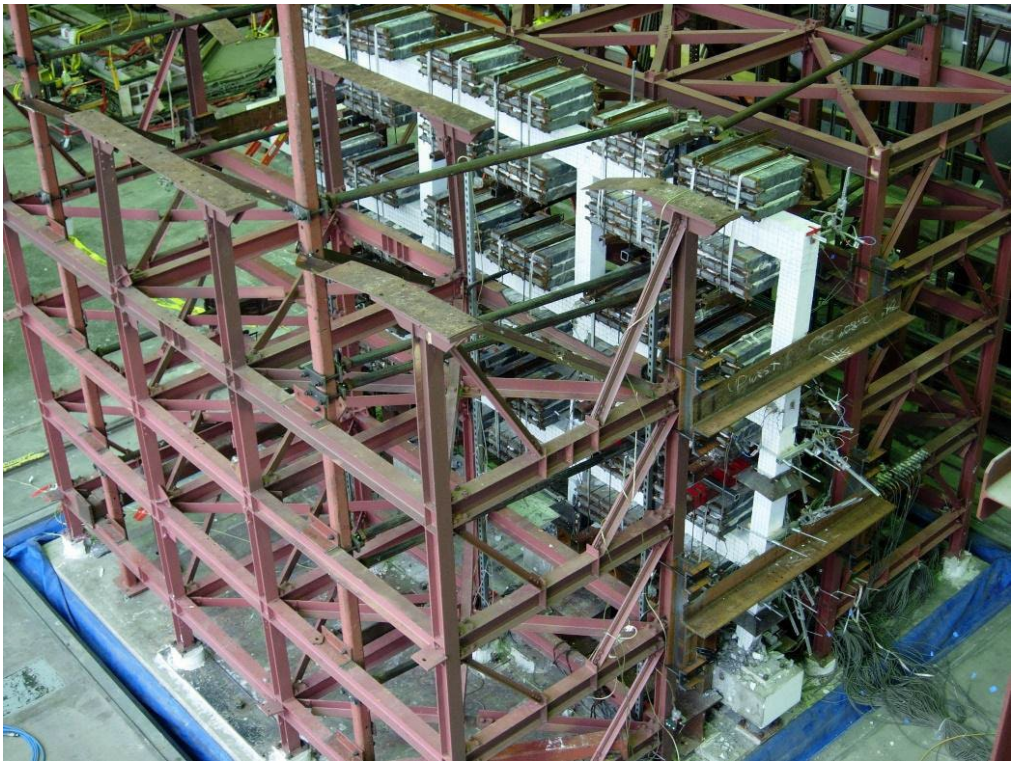


Figure 3-1 Photo of two-dimensional reinforced concrete frame on shake table.

The frame was evaluated in accordance with the linear and nonlinear dynamic procedures of ASCE 41-17. The nonlinear dynamic procedure (NDP) of ASCE 41-13 is also explored as the column provisions changed substantially from the 2013 and 2017 versions of the standard. Nonlinear models were developed using Opensees, with the primary model utilizing lumped-plasticity elements for all frame members, as well as Perform3D that utilizes lumped-plasticity hinges with P-M-M interaction

This publication is available free of charge from: https://doi.org/10.6028/NIST.GCR.22-917-50

for columns. The models were constructed per details presented in Appendix A, unless otherwise noted. The structure was evaluated using the linear procedures of ASCE 41-17, linear static, response spectrum analysis, and response history analysis.

This chapter also provides results of a fragility analysis showing the collapse potential of the model, as compared to the likelihood of exceeding ASCE 41-17 acceptance criteria. Results from a FEMA P-2018, *Seismic Evaluation of Older Concrete Buildings for Collapse Potential*, (FEMA, 2018b) evaluation are also presented.

3.2 Building Description and Observed Performance

3.2.1 Building Description

The experimental program for this frame is detailed in Ghannoum and Moehle (2012) and Ghannoum (2008), which document design drawings and weight documentation.

The two-dimensional reinforced concrete frame was designed as a one-third scale prototype of a full-scale frame building. Bays are regular, and columns are spaced 5 ft.-10 in. apart. Floor heights are 4 ft., columns are 6 in. square, and beams are 6 in. wide by 9 in. deep.

The frame was designed to have two non-ductile column lines at Gridlines A and B and two ductile column lines at Gridlines C and D (Figure 3-2). The columns at Gridlines A and B were designed to sustain flexural yielding prior to shear and axial degradation (flexure-shear critical columns). Observed damage consisted of severe shear damage in first story non-ductile columns. The first story column at Gridline B (Column B1) shortened axially during this test, shedding axial load to adjacent columns. Beam-column joints, beams, and columns at Gridlines C and D sustained moderate levels of cracking and damage.

Longitudinal bars were continuous in all members, so no lap slices were used. Transverse reinforcement was well detailed with 135° hooks in all members except columns at Gridlines A and B where ties have 90° hooks and were spaced relatively wide at 4 in.

Material Properties

Measured material strengths from testing are used for all elements in this study: Measured concrete compressive strength was 3.57 ksi and measured properties for steel reinforcing bars are summarized in Table 3-1.

This publication is available free of charge from: https://doi.org/10.6028/NIST.GCR.22-917-50

This publication is available free of charge from: https://doi.org/10.6028/NIST.GCR.22-917-50

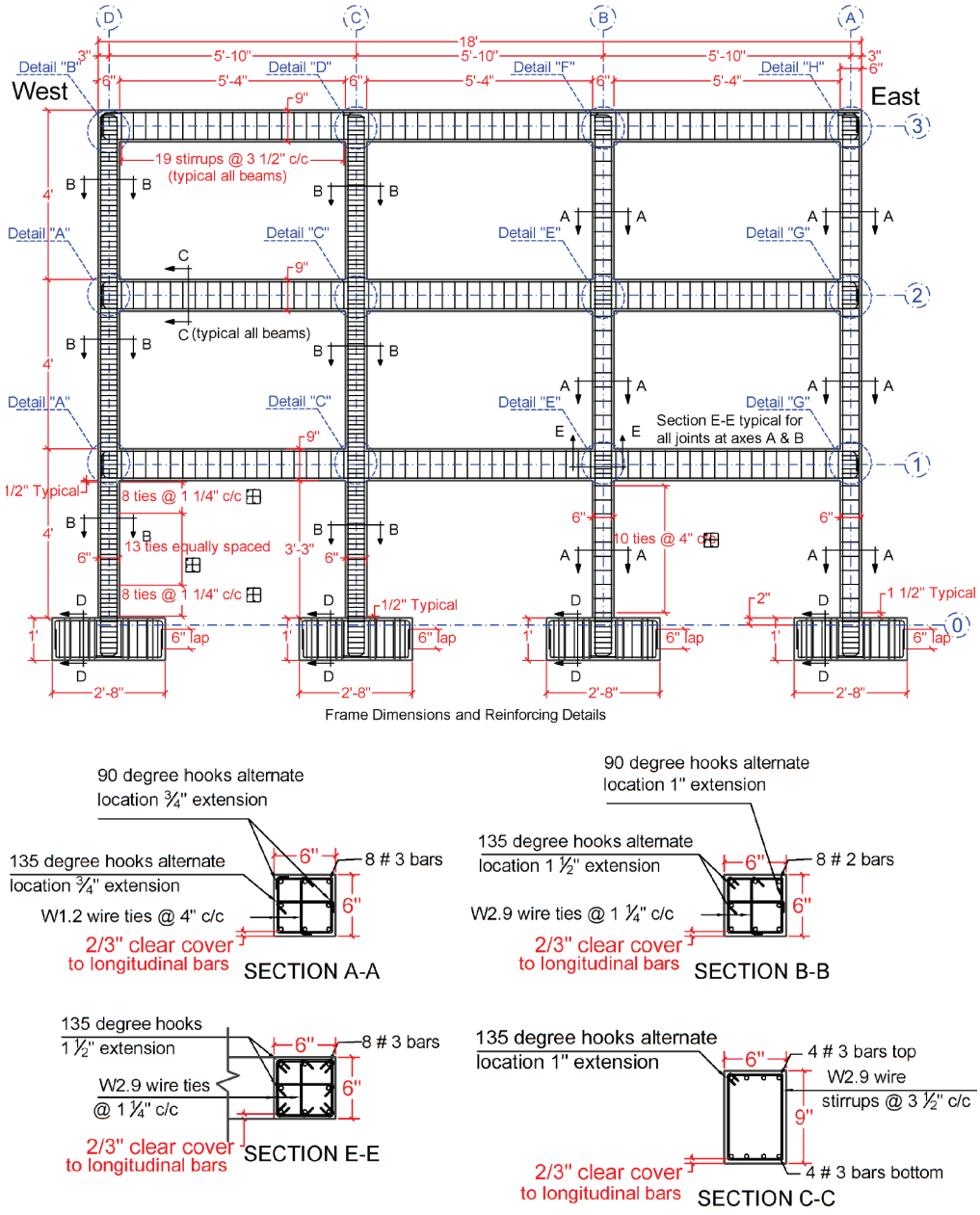


Figure 3-2 Reinforcement details.

Table 3-1 Yield and Ultimate Values of Steel

Parameters	#3 Bars[1]	#2 Bars[2]	3/16 in. Wire[3]	2/16 in. Wire[4]
Specified reinforcement yield strength (ksi)	60.00	60.00	60.00	60.00
Measured reinforcement yield strength (ksi)	64.00	70.00	80.71	95.00
Measured reinforcement tensile strength (ksi)	84.70	90.40	80.70	98.70

[1] Longitudinal bars in all beams and columns at Gridlines C and D.
[2] Longitudinal bars in columns at Gridlines A and B.
[3] Hoops in all beams, joints, and columns at Gridlines C and D.
[4] Hoops in columns at Gridlines A and B.

Building Weight

Building weight including the weight of attached lead weights are summarized in Table 3-2 by floor level. The lead weights were connected to each beam at four discrete locations using neoprene pads and steel plates.

Table 3-2 Building Weight by Floor Level

Floor Level	Dead Load (kips)
3rd floor	19.3
2nd floor	19.6
1st floor	19.6
Total	58.5

3.2.2 Building Instrumentation

Notably, all columns were set on load cells that allowed the recording of axial load, shear forces, and moments in the columns at the first story. Accelerometers were attached at all floor levels and drifts of all joints were recorded. The experimental program is detailed in Ghannoum and Moehle (2012) and Ghannoum (2008), which document testing instrumentation.

3.2.3 Ground Motion

Comprehensive ground motion records are available because the frame was tested on a shake table. The frame was tested under Component 100 of the ground motion recorded at the Llolleo station (coordinates: 32.6350, -71.6300) during the 1985 Valparaiso, Chile earthquake that was applied with increasing amplitude until partial collapse occurred.

For this study, Dynamic Test 1 during which the ground motion was scaled by a factor of 4.06 is considered. This was the first motion that produced severe damage; the highest intensity motion prior to Dynamic Test 1 only generated moderate

This publication is available free of charge from: https://doi.org/10.6028/NIST.GCR.22-917-50

$\sqrt{3}$ to satisfy similitude requirements. Models in this study were only subjected to the Dynamic Test 1 without being subjected to the prior motions applied to the test frame in the experimental program both because prior motions did not produce residual deformations and only resulted in moderate yielding of some member, and because ASCE 41 evaluation procedures do not require subjecting buildings to prior earthquake motions.

The acceleration history of the Dynamic Test 1 ground motion as recorded on the shake table is plotted in Figure 3-3. Figure 3-4 presents the response spectra with 3% damping for this ground motion. The damping ratio was measured from the experimental program. Although bare structures tend to have a damping ratio around 2%, the higher damping ratio for this frame may be attributed to the attached lead weights that contacted the frame using neoprene pads.

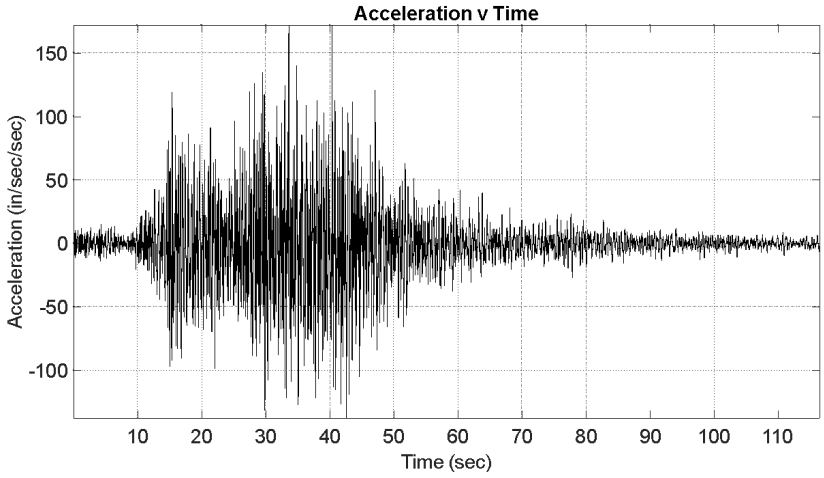


Figure 3-3 Acceleration history of Dynamic Test 1 ground motion as measured on the shake table.

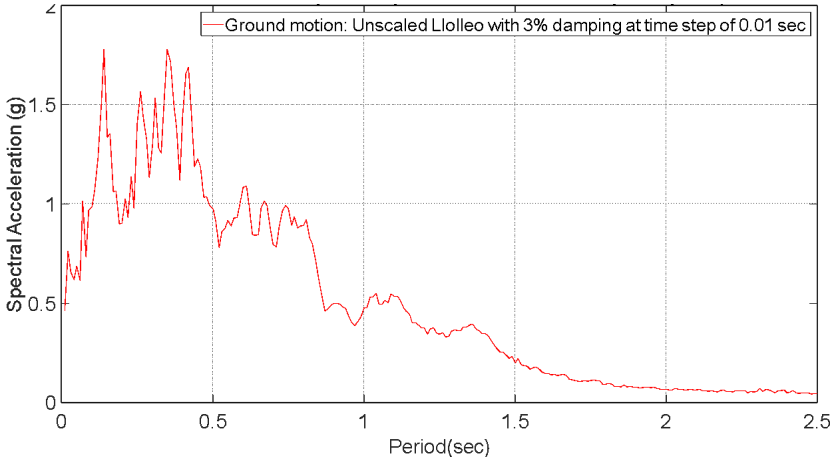


Figure 3-4 Response spectra for Dynamic Test 1 ground motion with 3% damping.

This publication is available free of charge from: https://doi.org/10.6028/NIST.GCR.22-917-50

This publication is available free of charge from: https://doi.org/10.6028/NIST.GCR.22-917-50

3.2.4 Observed Performance

Response Quantities

Floor displacement data were taken from wire type displacement transducers. A maximum story drift ratio is calculated as the maximum displacement in that story divided by the story height (48 in.). The drift ratio is maximum in the first story (5.18%). The distributions of the maximum drift ratios are shown in Figure 3-5 and indicate that the frame was pushed to relatively large drift demands.

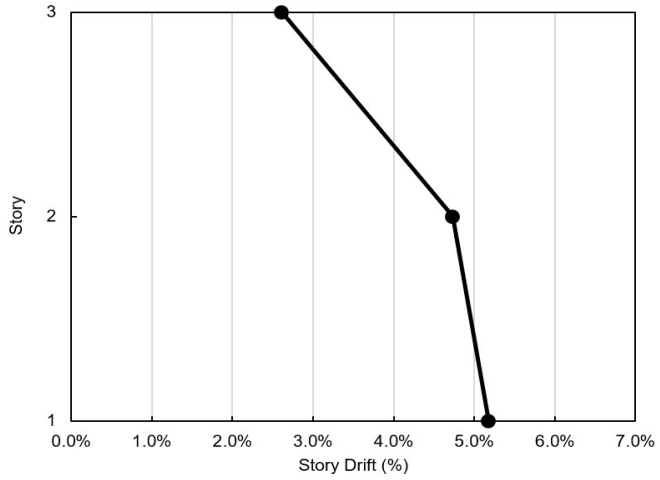


Figure 3-5 Maximum interstory drift distribution at each story.

The natural first mode period of the frame was measured as 0.30 sec. prior to any shaking being applied to it, and 0.34 sec. just prior to being subjected to the first high intensity motion during Dynamic Test 1.

Damage Observed during Dynamic Test 1 The distribution of damage in frame members observed after Dynamic Test 1 is schematically represented in Figure 3-6.

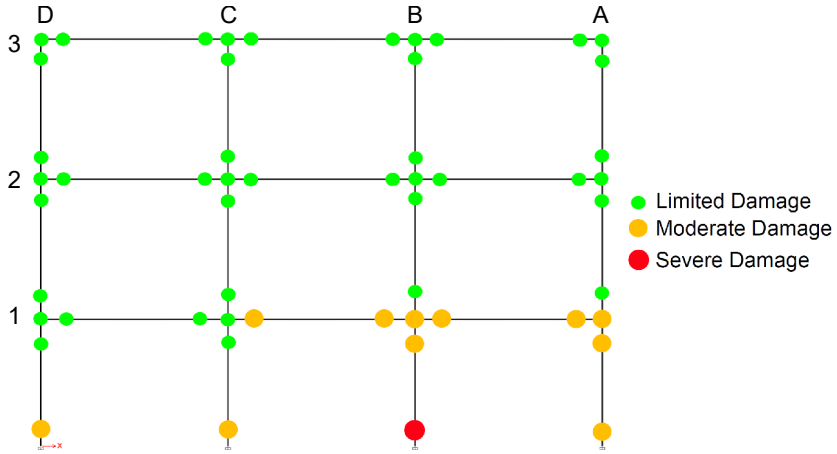


Figure 3-6 Schematic distribution of observed experimental damage; red circles represent severe damage in the member, yellow circles represent moderate damage, and green circles represent limited damage.

The frame sustained limited to moderate flexural cracking in columns at Gridlines D and C (Figure 3-7). The column at Gridline B at the first story (Column B1) sustained severe shear damage and partial axial shortening at its base (Figure 3-8). Despite being nominally identical to Column B1, the column at Gridline A at the first story (Column A1) only sustained moderate diagonal cracking damage (Figure 3-8). Due to the axial shortening of Column B1, beams spanning to Columns A1 and C1 at the first floor sustained moderate levels of damage and diagonal cracking as they transferred axial loads to those columns away from Column B1. Beam-column joints sustained limited to moderate levels of diagonal cracking and spalling but maintained integrity (Figure 3-8).



Figure 3-7 Column D1 (left) and Column C1 (right) after Dynamic Test 1 at base.

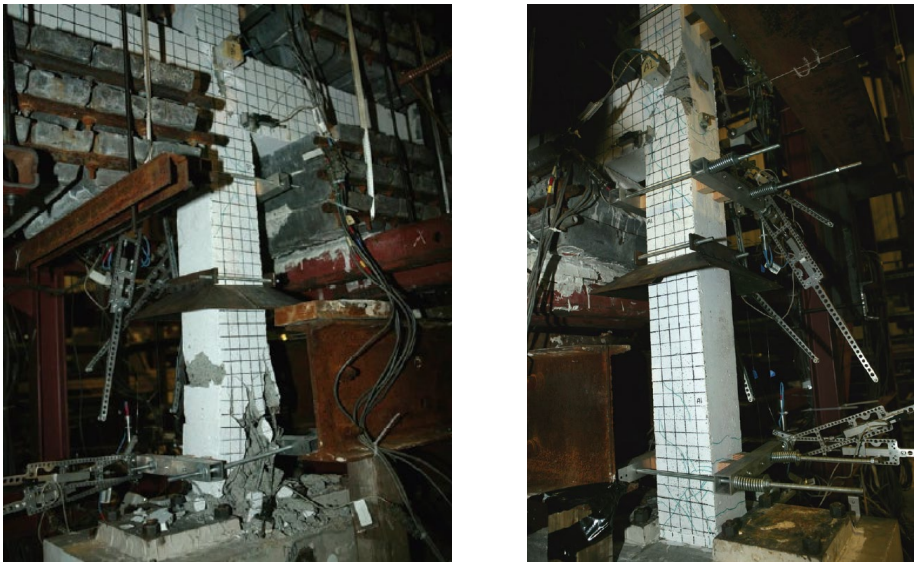


Figure 3-8 Column B1 (left) and Column A1 (right) after Dynamic Test 1 at base.

This publication is available free of charge from: https://doi.org/10.6028/NIST.GCR.22-917-50

3.3 Nonlinear Dynamic Procedure using Perform3D

3.3.1 Modeling Approach

A two-dimensional numerical model of the structure was created in Perform3D with columns fixed at the base. Columns were modeled using P-M-M hinges at each end with properties defined by ASCE 41 (as described in Appendix A this report). Axial loads used in calculating model parameters were obtained as the maximum axial demands developed in each element from the nonlinear response history analysis. The axial loads were determined by iterating twice while adjusting modeling parameters with each subsequent iteration. Shear strength of all columns exceed the shear associated with flexural strength of the columns, with V_{yE}/V_{col} ranging from 0.2 to 0.88. Therefore, column hinge capacities were based on the flexural-axial interaction strength of the member. Beams were modeled with lumped plasticity flexural hinges at each end of the member. Hinge properties were modeled according to ASCE 41 modeling criteria. The beam-column joints were modeled with nonlinear panel zone elements according to the ASCE 41 modeling criteria. The analysis employed 3% modal damping, which corresponds to the damping level derived experimentally. The analysis employed a combination of 2.5% modal damping and 0.5% Rayleigh damping. P-delta effects are included in the analysis.

3.3.2 Global Performance: Model vs. Observation

The simulated and measured performance of the frame is compared for drift, displacement, acceleration, natural periods, and base shear.

Figures 3-9 and 3-10 compare the drift profile and response history records between the measured values and the simulated response. The overall drift profile from the simulated response shows general agreement with the measured response, with relative differences of 17%, 17%, and 27% at Story 1, 2, and 3, respectively. Tables comparing key metrics for this and other models, as well as experimental values, are provided in Section 3.8. Figure 3-9 displays significant differences in response between the simulated and measured response. The simulated response predicts large permanent drift at all three levels, while the measured response shows only minor permanent drift.

This publication is available free of charge from: https://doi.org/10.6028/NIST.GCR.22-917-50

This publication is available free of charge from: https://doi.org/10.6028/NIST.GCR.22-917-50

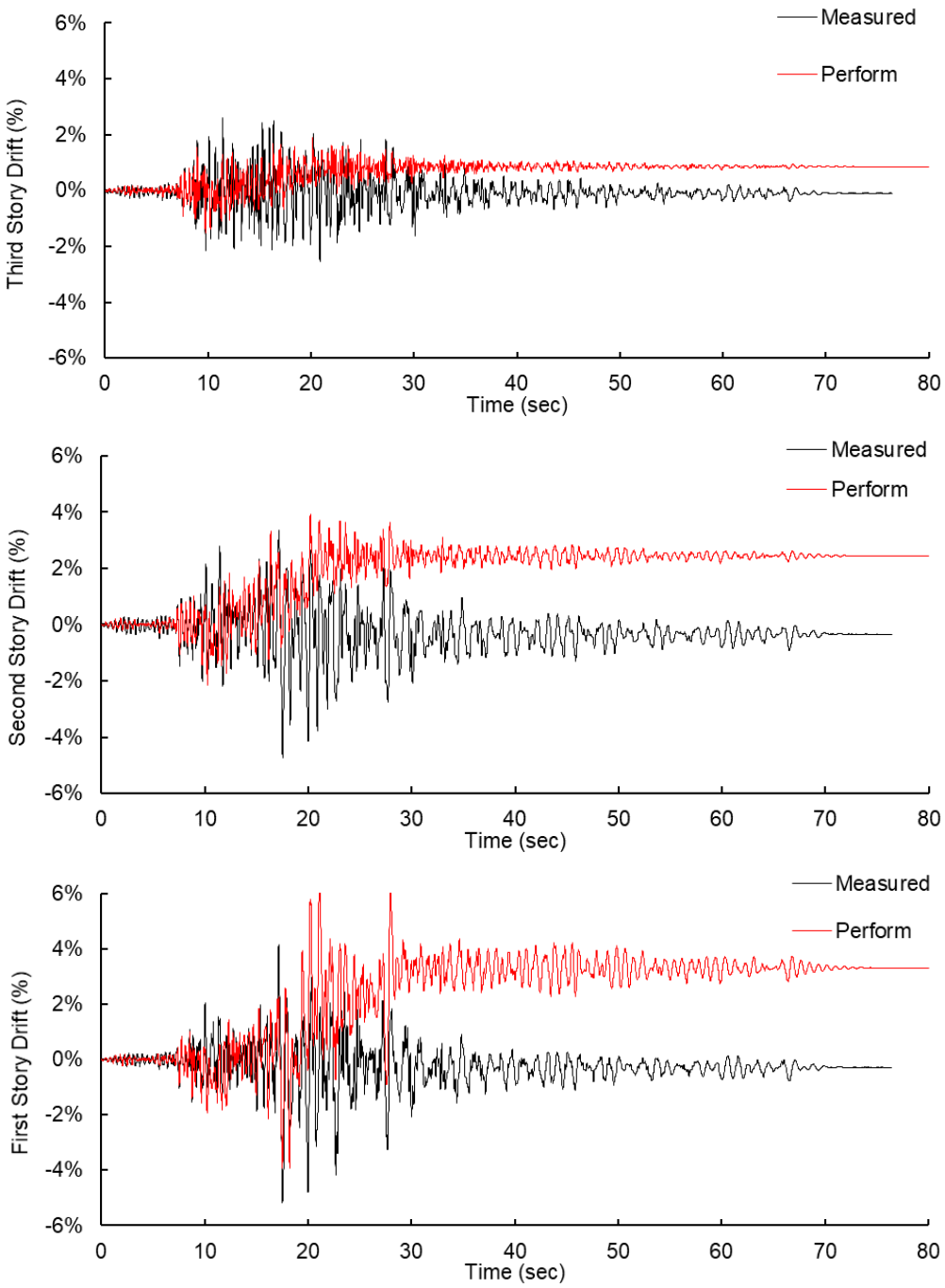


Figure 3-9 NDP Perform3D: Comparison of story drift response history.

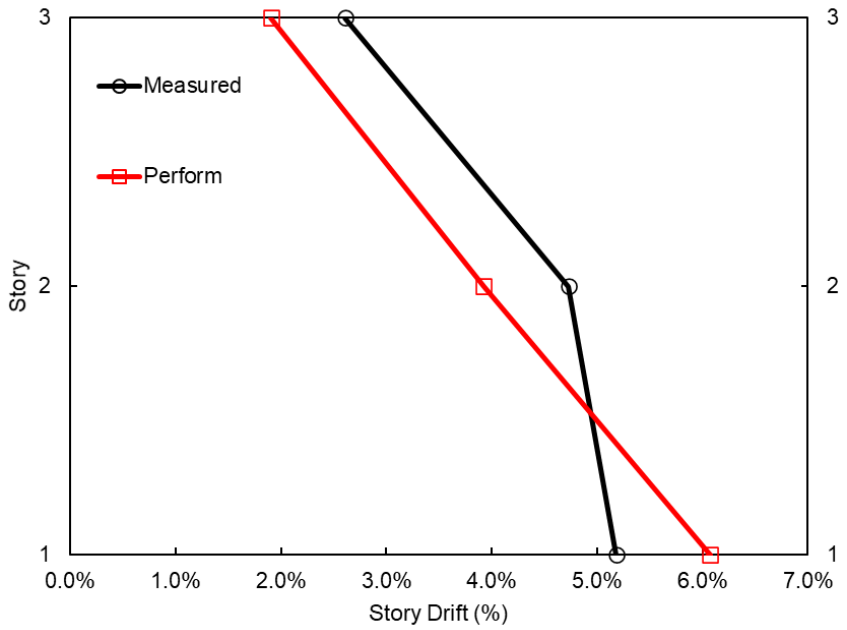


Figure 3-10 NDP Perform3D: Comparison of maximum story drift.

Figures 3-11 and 3-12 compare the displacement profile and response history records between the measured recordings and the simulated response. The maximum displacement profile in Figure 3-11 presents good agreement at the upper two levels (less than 4% difference), but the maximum displacement predicted by analysis at Story 1 is 28% larger than the measured displacement. Figure 3-12 displays significant differences in response between the simulated and measured response. The simulated response predicts large permanent displacement at all three levels, while the measured response shows only minor permanent displacements.

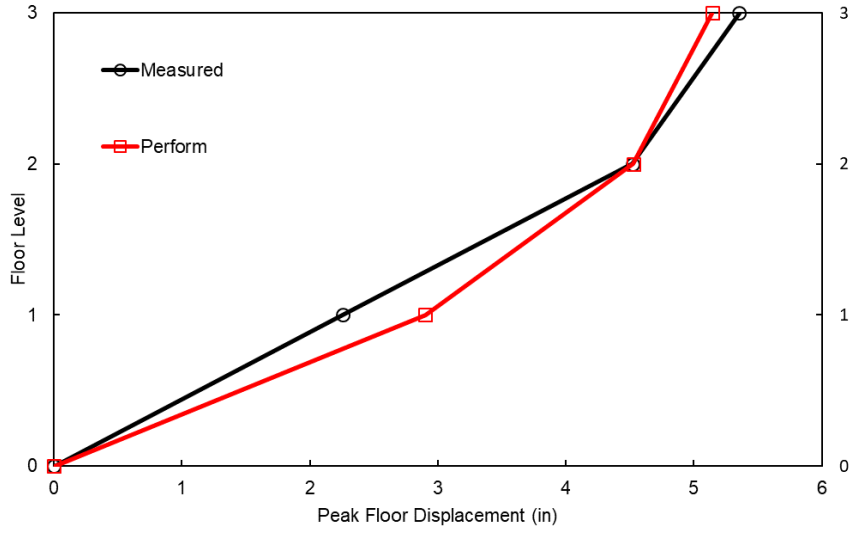


Figure 3-11 NDP Perform3D: Comparison of maximum story displacement.

This publication is available free of charge from: https://doi.org/10.6028/NIST.GCR.22-917-50

This publication is available free of charge from: https://doi.org/10.6028/NIST.GCR.22-917-50

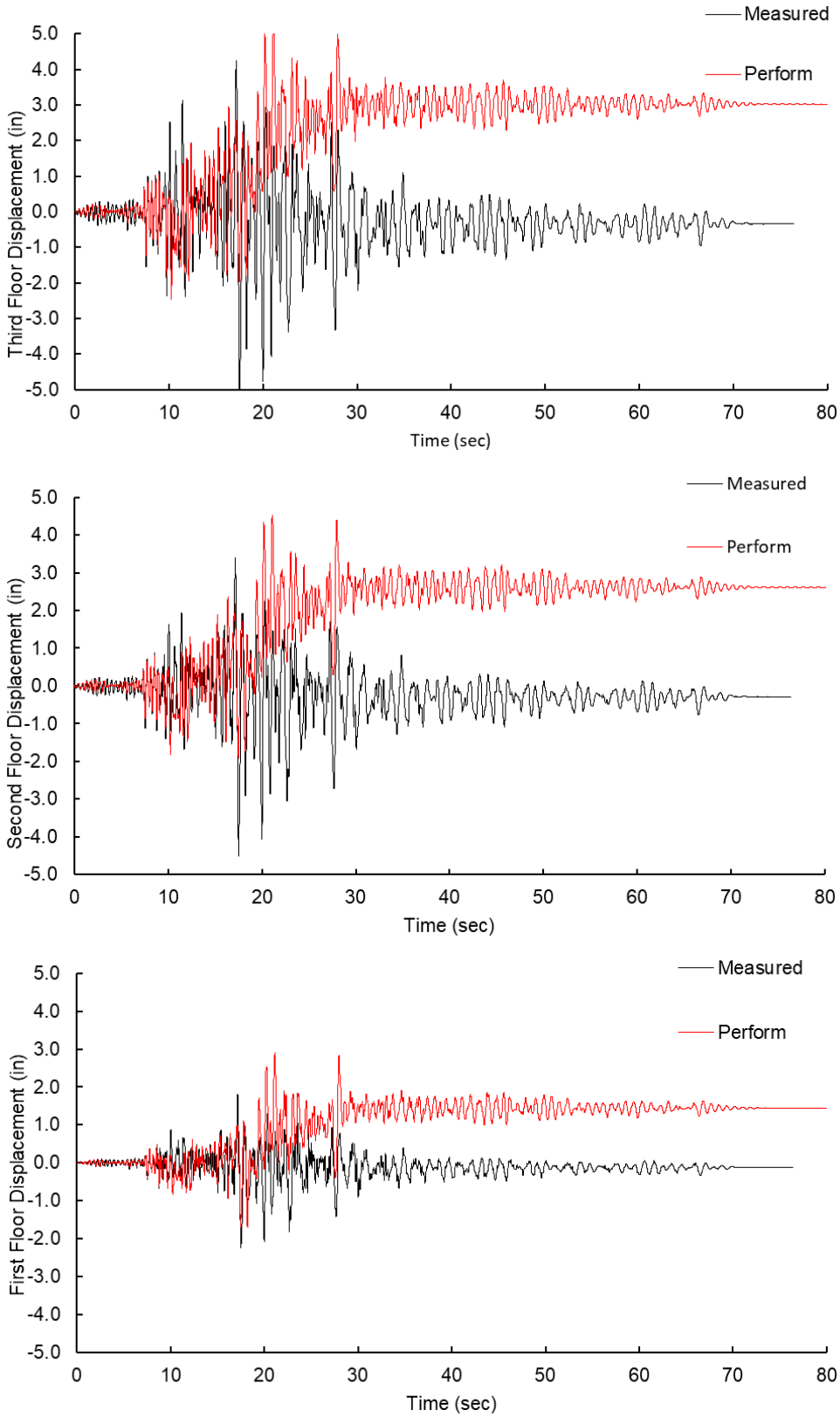


Figure 3-12 NDP Perform3D: Comparison of story displacement response history.

Figure 3-13 compares the acceleration profile of the measured recordings and simulated response. The simulated accelerations overestimate the response significantly compared to the measured accelerations at Story 2 and 3 (38% and 55%, respectively), while providing relatively good agreement at the roof (9%).

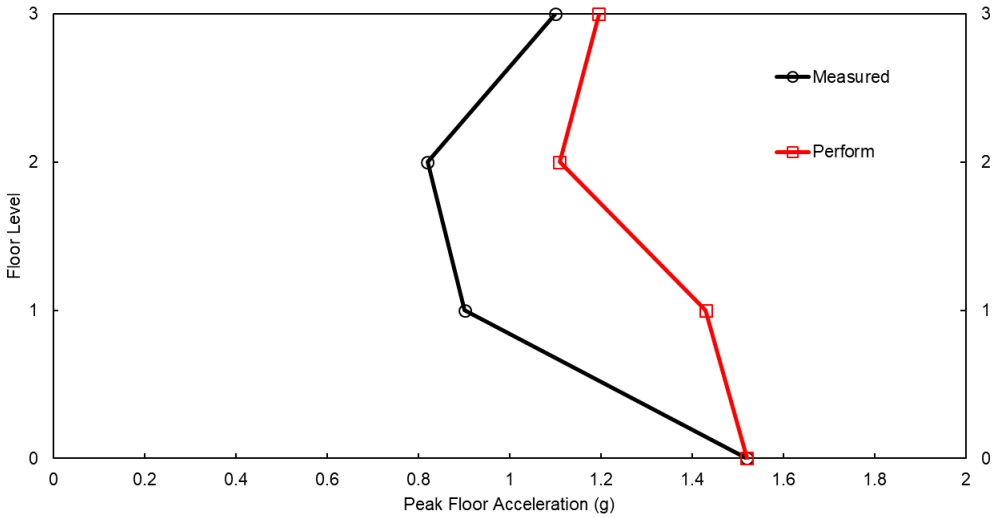


Figure 3-13 NDP Perform3D: Comparison of the maximum floor acceleration.

Natural periods of the simulated and measured frame are also compared. The measured first mode period of the frame at the beginning of Dynamic Test 1 was recorded as 0.34 sec. The models predicted a first mode period of 0.48 sec. prior to being subjected to the high-intensity ground motion. All the first story columns reached flexural yielding during the motion prior to Dynamic Test 1, while other members reached lower loads and cracking levels likely below the yield point (Ghannoum and Moehle, 2012). ASCE 41 specifies member stiffness values corresponding to a secant stiffness at yield. Since concrete members soften gradually as their load increases to yield, the softer predicted response of the frame could be attributed to this difference in assumed cracking level in the various members prior to the application of the Dynamic Test 1.

The maximum base shear values of the model show good agreement with the measured values (29.8 kips measured with 27.9 kips simulated, less than 7% difference).

3.3.3 Component Performance: Model vs. Observation

Simulated response of column, beam, and joint hinges are summarized in Figures 3-14 through 3-16. Figure 3-14 shows the range outcomes from the assessment for each of the nonlinear hinges in the model in terms of ASCE 41 acceptance criteria Immediate Occupancy (IO), Life Safety (LS), and Collapse Prevention (CP). The majority of nonlinear behavior occurs in the columns, with only one beam showing significant strength degradation. Two of the beam-column joints exceed the IO

This publication is available free of charge from: https://doi.org/10.6028/NIST.GCR.22-917-50

acceptance criteria. Three of the four columns at the lowest level exceed the CP acceptance criteria, with only the two flexure-shear critical columns modeling parameter *b* on the ASCE 41 backbone curve (Figure 2-1).

The model correctly identifies flexure-shear and ductile flexure yielding in the lower level columns as the overall mechanism, with higher levels of damage in the flexure-shear critical columns compared to the flexure-critical columns. However, the model predicts damage in the second story columns that was not observed in the frame. In Dynamic Test 1, Column B1 sustained axial degradation and shortened while other columns in the first story, including Column A1, did not. Although the model cannot directly capture axial failure of the columns or their load redistribution, the model response does show that flexure-shear critical columns have exceeded modeling parameter *b* on the backbone curve, which represents loss of vertical load bearing capacity.

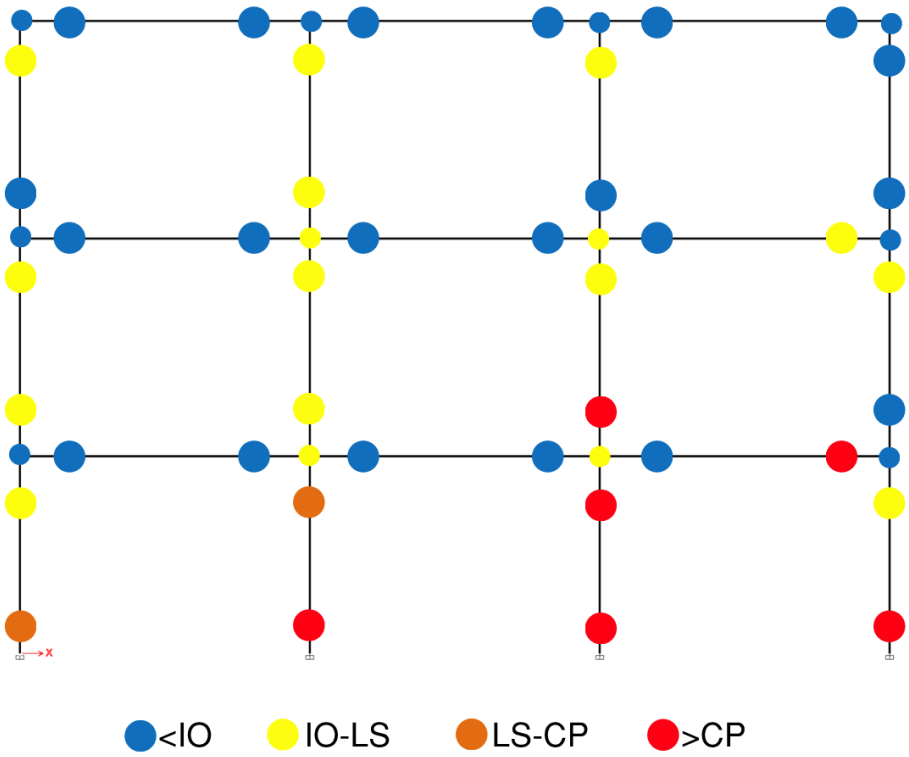


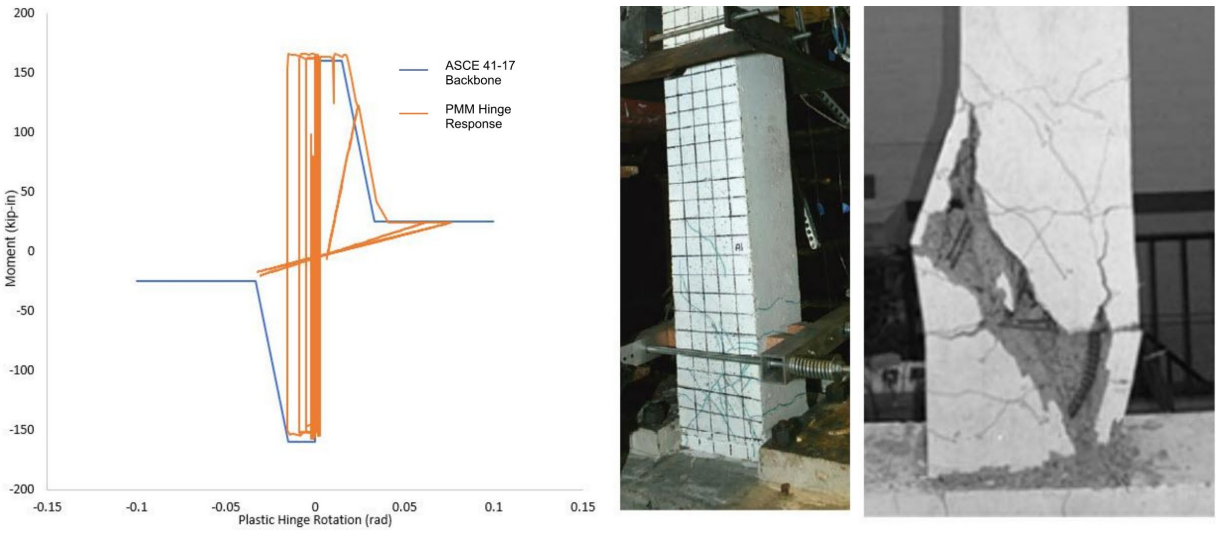
Figure 3-14 NDP Perform3D: Acceptance criteria range results for modeled nonlinear hinges. Shown for Immediate Occupancy (IO), Life Safety (LS), and Collapse Prevention (CP).

3.3.3.1 Column Performance: Model vs. Observation vs. Test Data

It would be expected that the damage observed to components at a known drift level would be similar to the damage observed during testing of similar components in the laboratory. Comparisons of the observed damage to the columns of the tested frame to the damage inferred from the simulated demands and testing of a similar column in

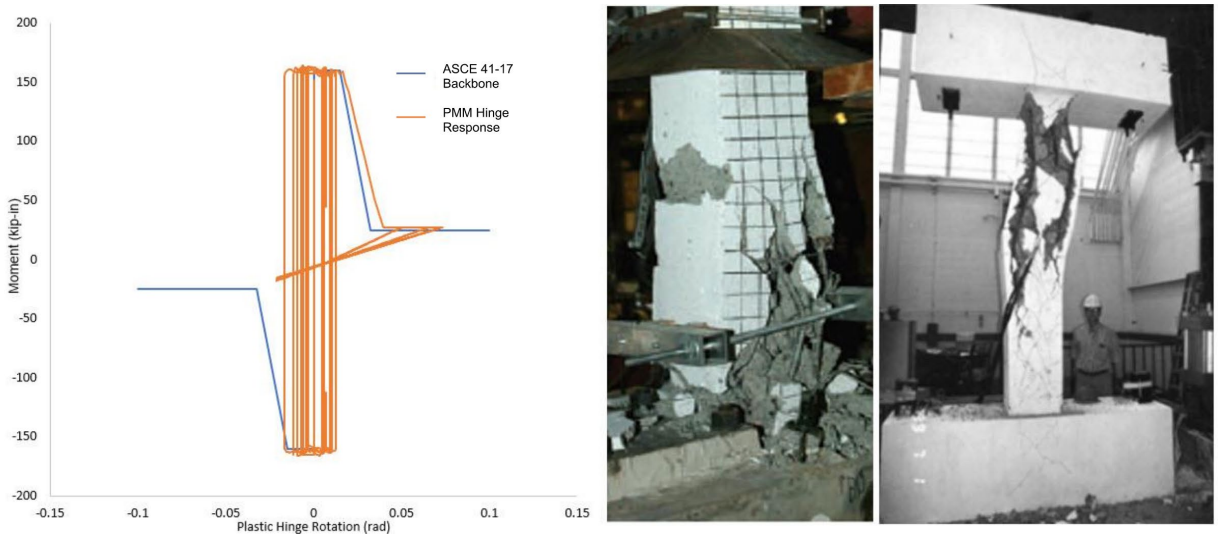
This publication is available free of charge from: https://doi.org/10.6028/NIST.GCR.22-917-50

a laboratory are shown in Figures 3-15 through 3-18. These figures show comparisons of plastic hinge demands from simulated response, observed damage from the tested frame, and laboratory test specimens with similar detailing, axial loads, and drift demands. The observed damage for the flexure-shear critical Column A1 is far less than what would be expected based on the plastic rotation from the simulated response and the similar test specimen. The flexure-shear critical Column B1 and the ductile, flexure-controlled Column D1 and Column C1 show general agreement between the simulated and observed damage.



(a) (b) (c)

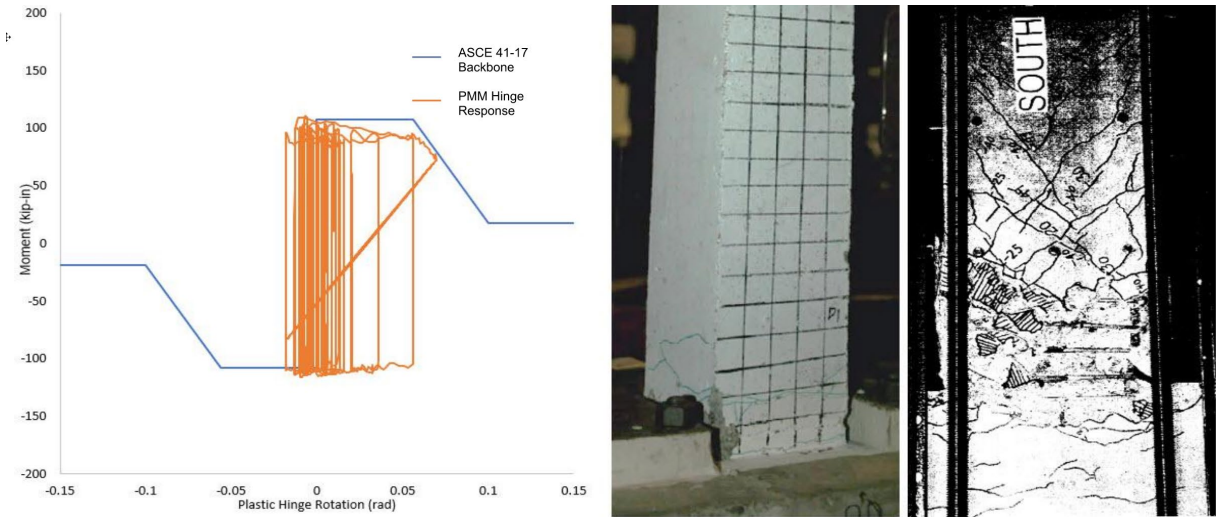
Figure 3-15 NDP Perform3D: Comparison of (a) simulated response, (b) observed damage, and (c) similar lab specimen (specimen at 5.5% drift, from Sezen and Moehle (2006)) for Column A1 at base.



(a) (b) (c)

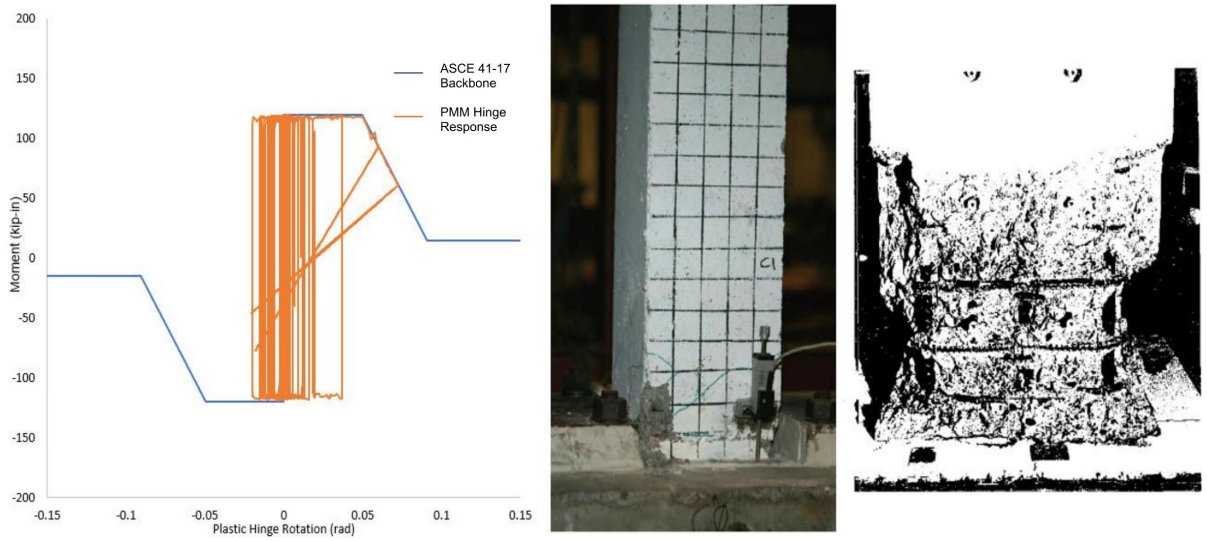
Figure 3-16 NDP Perform3D: Comparison of (a) simulated response, (b) observed damage, and (c) similar lab specimen (specimen at 5.5% drift, from Sezen and Moehle (2006)) for Column B1 at base.

This publication is available free of charge from: https://doi.org/10.6028/NIST.GCR.22-917-50



(a) (b) (c)

Figure 3-17 NDP Perform3D: Comparison of (a) simulated response, (b) observed damage, and (c) similar lab specimen (specimen at 5% drift, from Pujol (2002)) for Column D1 at base.



(a) (b) (c)

Figure 3-18 NDP Perform3D: Comparison of (a) simulated response, (b) observed damage, and (c) similar lab specimen (specimen at 7.5% drift, from Tanaka (1990)) for Column C1 at base.

The simulated response at the top of Column D1 and C1 indicated damage in the IO-LS and LS-CP ranges, respectively. The observed damage shown in Figure 3-19 for these two columns suggest damage below the predicted level. The simulated response at the top of Column B1 indicated damage beyond CP. The observed damage shown in Figure 3-20 (left) for this column suggests damage below the predicted level. The simulated response at the top of Column A1 indicated damage in the IO-LS range. The observed damage shown in Figure 3-20 (right) for this column appears consistent with the simulated damage.

This publication is available free of charge from: https://doi.org/10.6028/NIST.GCR.22-917-50

This publication is available free of charge from: https://doi.org/10.6028/NIST.GCR.22-917-50



Figure 3-19 Column D1 (left) and column C1 (right) observations after Dynamic Test 1 at Level 1.



Figure 3-20 Column B1 (left) and column A1 (right) observations after Dynamic Test 1 at Level 1.

3.3.3.2 Beam Performance: Model vs. Observation

Figure 3-21 shows a plot of simulated moment versus plastic rotation at the ends of the beam framing between Columns A1 and B1. As the axial loads carried by Column B were transferred to Column A, the beam between the two columns is required to transfer the column axial load through beam shear and flexure. The observed damage shown in Figure 3-20 is consistent with moderate levels of damage. The simulated response predicts severe damage adjacent to the Column A, and moderate yielding adjacent to Column B. The observed and simulated damage is consistent at Column B. However, the observed beam damage at Column A is much less than is indicated by the simulated response. This could be due to the fact that the simulated response is not able to accurately capture the axial shortening of Column B that could have an impact on the distribution of demands to the beam elements.

This publication is available free of charge from: https://doi.org/10.6028/NIST.GCR.22-917-50

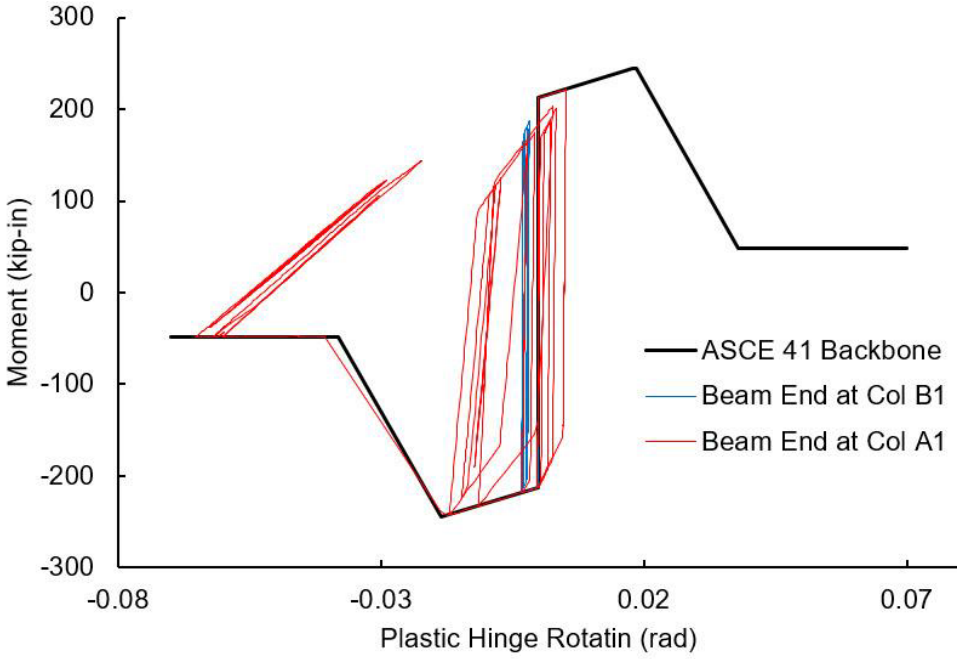


Figure 3-21 NDP Perform3D: Simulated beam plastic hinge rotation at beam between columns A1 and B1 on Story 1.

3.3.3.3 Joint Performance: Model vs. Observation

In general, both the simulated response and observations showed that the joints remained nearly elastic, with only moderate yielding at selected locations. However, the joint at Level 1 at Column A underwent moderate spalling that was not consistent with the damage predicted by the simulated behavior. The observed damage was likely a result of high joint shear demands imposed as the beam transferred loads through the joint when Column B1 began to lose axial capacity. The simulated response cannot accurately capture the dynamic effect of the sudden loss of axial stiffness, which may tend to lessen the transfer of loads through the joint.

3.4 Nonlinear Dynamic Procedure using OpenSees

3.4.1 Modeling Approach

Two numerical models of the structure were created in OpenSees: one in accordance with ASCE 41-13 and a second one in accordance with ASCE 41-17. The objective was to investigate the effects of updated modeling parameters and acceptance criteria for columns in ASCE 41-17.

The nonlinear OpenSees models were two-dimensional and constructed per details presented in Appendix A, unless otherwise noted in this section. The frame was modeled with fixed base with zero-length hinge elements at member ends where inelastic deformations were anticipated. Hinge properties for all members were defined using the ASCE 41-17 or ASCE 41-13 modeling parameters and standard

backbone shape. Axial loads used in calculating modeling parameters were obtained as the maximum axial demands developed in each element from a pushover analysis of the frame out to initiation of loss of lateral load carrying capacity.

Maximum axial load ratio was less than 15% of the column gross sectional capacity throughout the height of the frame. Columns at Gridlines C and D were flexure dominated as they had relatively high levels of confinement, such that their shear strength exceeded by a significant margin the shear demand associated with flexural hinging. Columns at Gridlines A and B had shear strengths that were just slightly higher than the shear demands based on flexural hinging and were expected to sustain shear failure after flexural yielding and eventually axial collapse. All beams were flexure-controlled.

Beam-column joints were classified as conforming per ASCE 41-17 and not expected to reach their shear strength. As such they were modeled linearly through elastic elements extending from the beams and columns and connecting at the center of the joint. Joint elastic stiffness was modeled implicitly according to ASCE 41-17 Section 10.4.2.2.1.

The analysis employed 3% modal damping, which corresponds to the damping level derived experimentally. The analysis accounted for large geometry effects using the P-delta transformation.

3.4.2 Global Performance: Model vs. Observation

The simulated and measured performance of the frame is compared for roof drift ratio, natural periods, and base shear.

Both OpenSees models resulted in a sidesway collapse mechanism, which did not occur in the test. Tables comparing key metrics for these models to measured values are provided in Section 3.8.

The measured first mode period of the frame at the beginning of Dynamic Test 1 was recorded as 0.34 sec. The models delivered a first mode period of 0.54 sec. prior to being subjected to the high-intensity ground motion.

Prior to sidesway collapse, Figure 3-22 indicates reasonably good agreement in the maximum base shear values but not in the base shear history between the ASCE 41-17 OpenSees model and experimental results.

This publication is available free of charge from: https://doi.org/10.6028/NIST.GCR.22-917-50

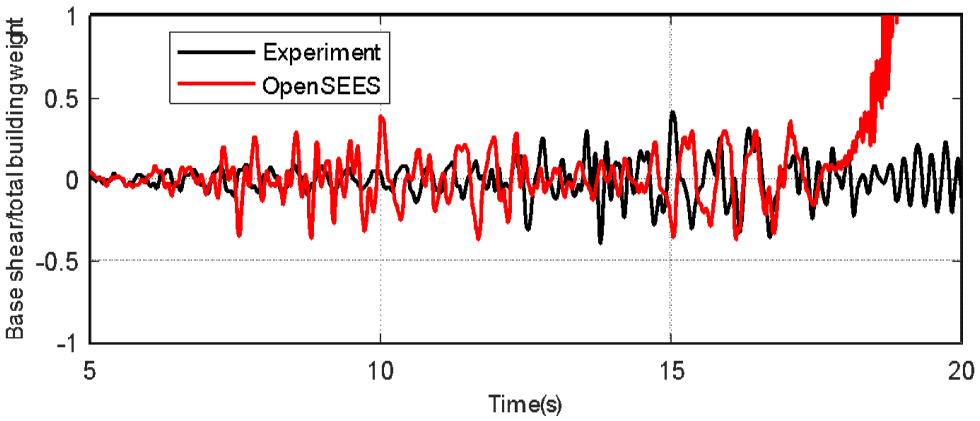


Figure 3-22 NDP OpenSees: Comparison of normalized base shear history.

3.4.3 Component Performance: Model vs. Observation

It is not possible to make component-level comparisons that are based on the damage states of the members because the models resulted in a sidesway collapse mechanism. Instead, Figures 3-23 and 3-24 show a comparison of the hysteretic column behavior as lateral drift ratio to moment at the base of column recorded for the first-story columns. The column hinges used for this model use peak-oriented hysteretic hinges. This could potentially lead to higher damage and drift demands as compared to the use of adaptive P-M-M hinges. As can be seen in Figure 3-24, Columns A1 and B1 are estimated to sustain complete loss of lateral strength by both ASCE 41-13 and ASCE 41-17 models, with the columns modeled using the larger deformation capacities of ASCE 41-17 providing a closer match to the drift capacities recorded. The strengths of Columns A1 and B1 are underestimated by both versions of ASCE 41. Figure 3-23 shows that the behavior of Columns C1 and D1 are captured well by the models both in terms of strength and cyclic behavior.

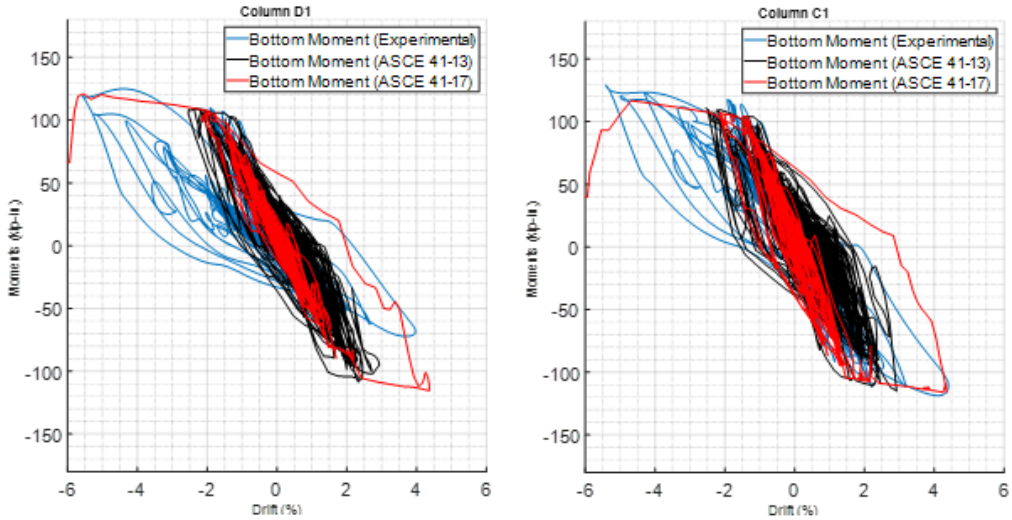


Figure 3-23 NDP Opensees: Comparison of column lateral drift ratio versus bottom moment for Column D1 (left) and Column C1 (right).

This publication is available free of charge from: https://doi.org/10.6028/NIST.GCR.22-917-50

This publication is available free of charge from: https://doi.org/10.6028/NIST.GCR.22-917-50

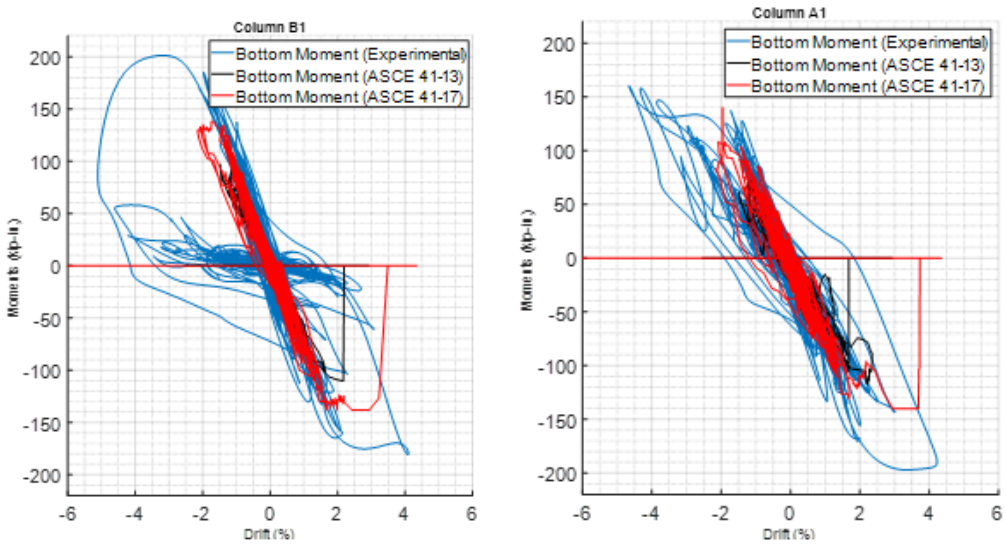


Figure 3-24 NDP OpenSees: Comparison of column lateral drift ratio versus bottom moment for Column B1 (left) and Column A1 (right).

3.5 Linear Procedures

3.5.1 Modeling Approach

A two-dimensional model of the structure was created in ETABS v18 and evaluated using the linear static procedure (LSP, ASCE 41-17 Section 7.4.1), response spectrum method for linear dynamic procedure (ASCE 41-17 Section 7.4.2.2.3), and the linear response history method (ASCE 41-17 Section 7.4.2.2.4). Stiffness for beams and columns were based on ASCE 41-17 (0.3 for beams and 0.3-0.36 for columns, based on axial load), joints were modeled directly using panel zone elements, and columns were assumed fixed at the base. The linear model used 3% modal damping for all analysis methods. This damping is higher than the values recommend per ASCE 41-17 Section 7.2.3.6; however, the damping value is consistent with the measured damping.

As modeled, the frame has a period of 0.50 sec. The model is substantially more flexible than indicated by the ambient period of 0.34 sec. measured at the end of the Half-Yield Test, and shorter than the ambient period of 0.87 sec. measured at the end of the full Dynamic Test 1.

3.5.2 Ground Motion Demands for Linear Static and Linear Response Spectrum Analyses

The linear static and linear response spectrum analysis procedures implemented in this study use a modified smoothed demand spectrum to lower the spectral demand variability at close period ranges. The spectrum was modified using the following process:

1. Spectra are calculated from the recorded motions for damping ratios of 2%, 3%, 5%, 7%, 10%, 15%, and 20%.
2. Resulting spectra were modified to a 5% equivalent spectrum using the B_1 factors per ASCE 41-17 Section 2.4.1.7.1 (ASCE 41-17 Equation 2-3).
3. Spectra are then scaled from 5% to 3% using the ratio of the B_1 factors.
4. Average of the spectra after modification in Step 3 is taken as the 3% demand spectrum. See Figure 3-25.
5. For LSP, spectral acceleration, S_a, is taken from the 3% average spectrum at the first fundamental period. For this frame, S_a at the simulated fundamental period, T_1 is 1.8.
6. For the response spectrum LDP method, the 3% average spectrum is used.

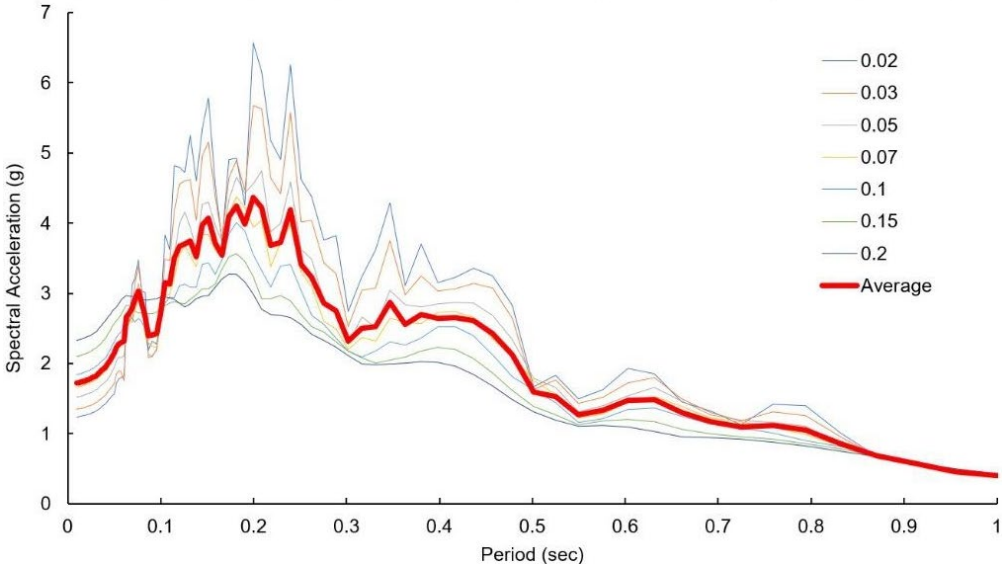


Figure 3-25 Calculation of modified smoothed demand spectrum: 3% average spectrum.

3.5.3 Global Performance: Model vs. Observation

Figures 3-26 through 3-28 compare the maximum story drift, displacement, and acceleration, respectively, of the measured recordings, to the simulated response from the three linear methods, as well as the Perform3D nonlinear model.

Linear methods show story drift profiles that do not accurately capture the pattern exhibited by the test frame: the linear methods underestimate drifts at the lower story, while overestimating drifts at the upper stories (relative differences of approximately 10% to 30% at the lower levels, and 25% to 87% at the top level), see Figure 3-26. These linear drift profiles could potentially identify the second story as the critical story, rather than the lower story, as shown in the test. The higher drift values in the upper stories predicted by the linear methods are likely due to the underestimation of

This publication is available free of charge from: https://doi.org/10.6028/NIST.GCR.22-917-50

the flexural stiffness of the members in the upper floors and the overestimation of demands since yielding of the lower levels is not captured in the model.

Figure 3-27 shows good agreement at the lower two levels (5% to 16% difference) with fair agreement at the top level (15% to 24%) for magnitude of maximum floor displacement values. This would suggest that the linear methods are generally able to capture overall peak roof drift but the distribution of story drift over the height of the building is less accurate.

Figure 3-28 shows poor agreement of maximum acceleration values as the linear methods do not account for yielding of the frame.

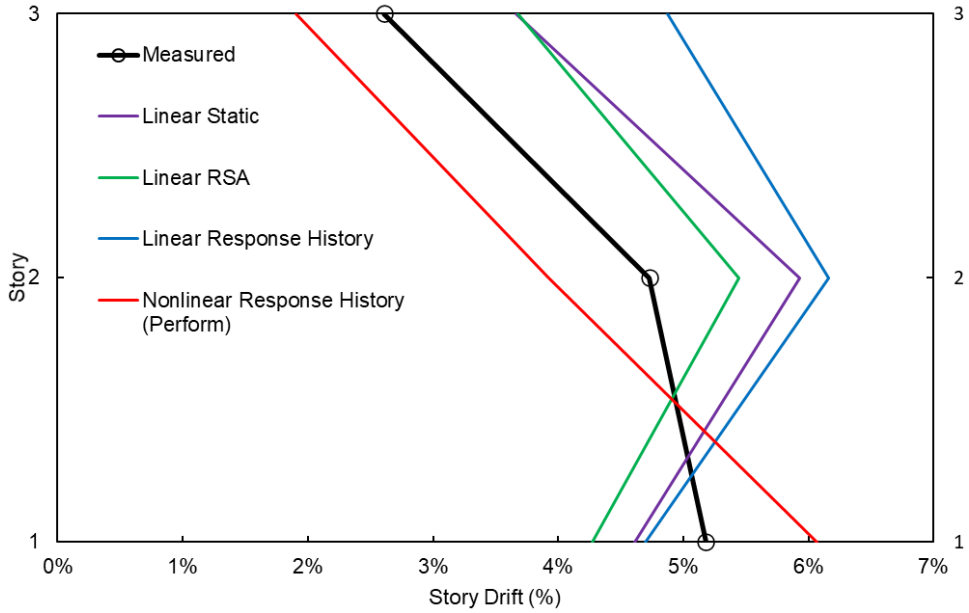


Figure 3-26 All: Comparison of maximum story drift.

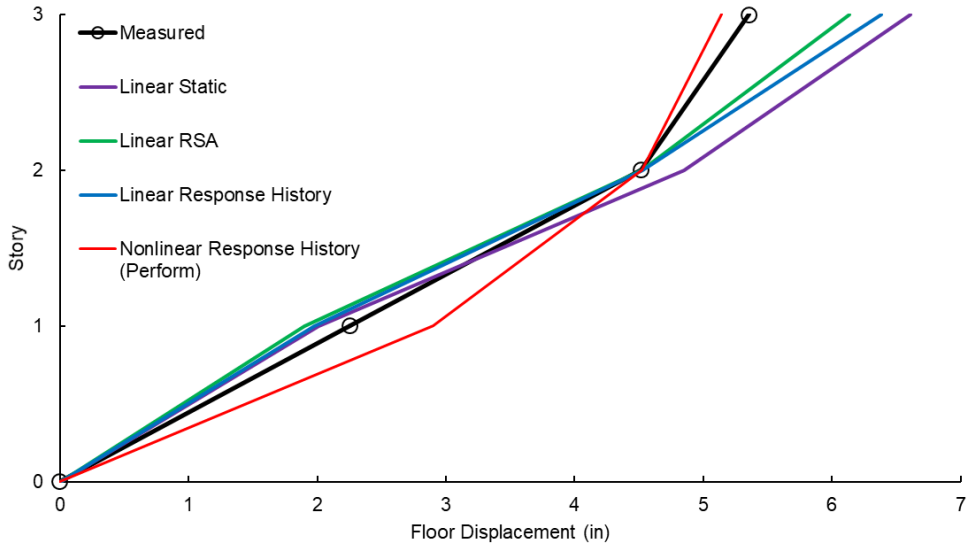


Figure 3-27 All: Comparison of maximum floor displacement.

This publication is available free of charge from: https://doi.org/10.6028/NIST.GCR.22-917-50

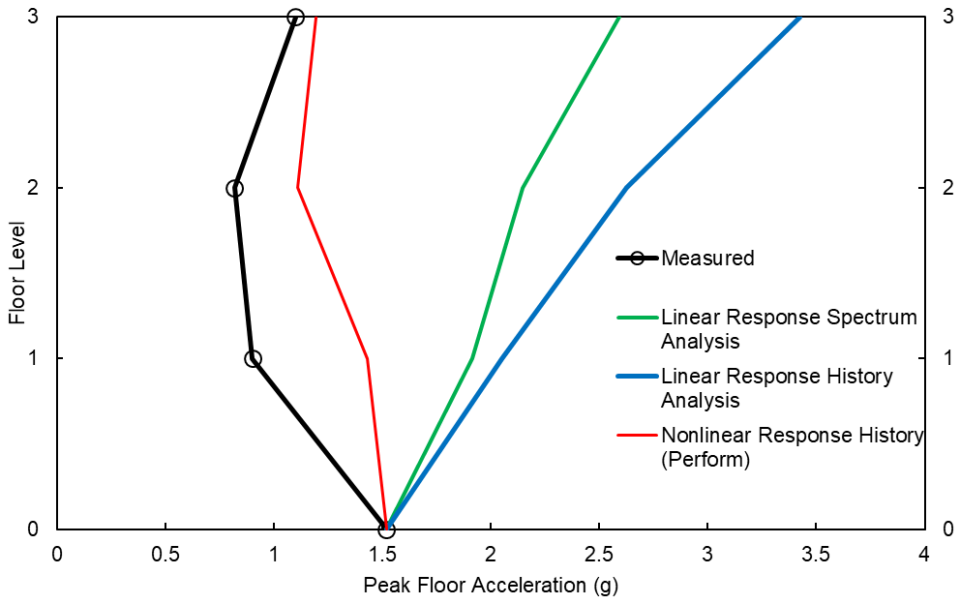


Figure 3-28 All: Comparison of maximum floor acceleration.

3.5.4 Component Performance: Model vs. Observation

Figures 3-29 and 3-30 show comparisons of DCR values for column, beam, and joints elements for the linear response history analysis evaluation. The force demands for all components are taken directly from the linear response history analysis evaluation, without consideration of possible mechanisms.

Figure 3-29 shows the predicted simulated acceptance criteria. Despite the significant differences between simulated and recorded engineering demand parameters, the model predicts that the frame will fail CP, which is consistent with the observed damage to the frame. However, because limit states are not considered in the evaluation, many elements that are shown to exceed CP in the simulated response showed little to no damage in the test (such as the joints, beams, and columns at the upper two levels).

As an alternative to using the forces directly from the simulation, a limit-state approach was considered to estimate element demands. For this case, the beam and joint demands are determined based on yielding of the column elements while the column demands are taken directly from the linear response history analysis evaluation. Figure 3-30 shows simulated acceptance criteria using this approach. The columns exceed the CP acceptance criteria at nearly all locations with only two joints exceeding the IO acceptance criteria. This approach shows much closer agreement with the observed performance. The model correctly identifies flexural yielding in the lower level columns as the overall mechanism, with higher levels of damage in the less ductile flexure-shear critical columns compared to the ductile flexure-critical columns. However, the damage predicted is higher than the observed

This publication is available free of charge from: https://doi.org/10.6028/NIST.GCR.22-917-50

performance since it does not account for reduced demands at the upper levels resulting from a story mechanism at the lower level.

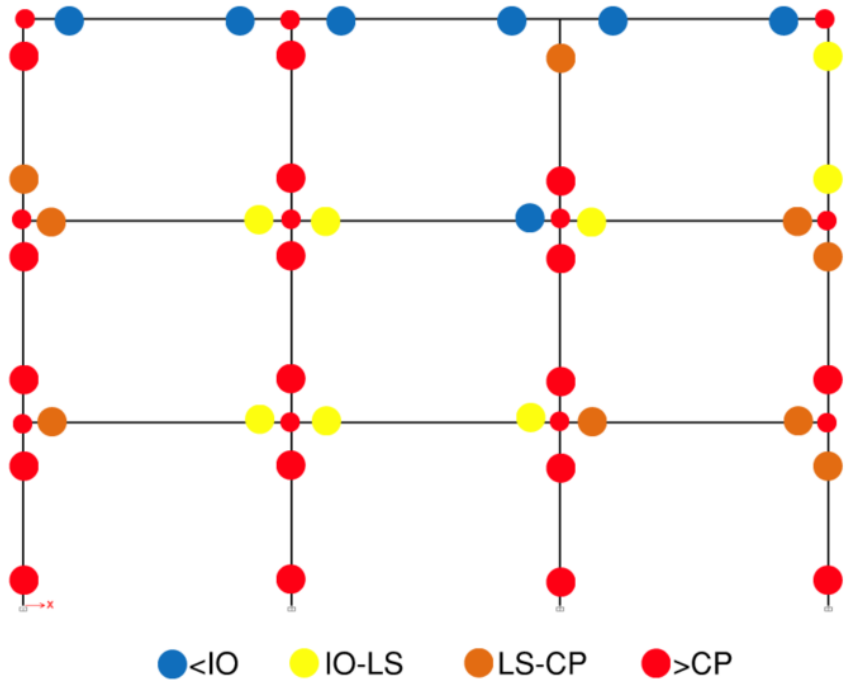


Figure 3-29 Linear Response History: Acceptance criteria range without consideration of limit state. Shown for Immediate Occupancy (IO), Life Safety (LS), and Collapse Prevention (CP).

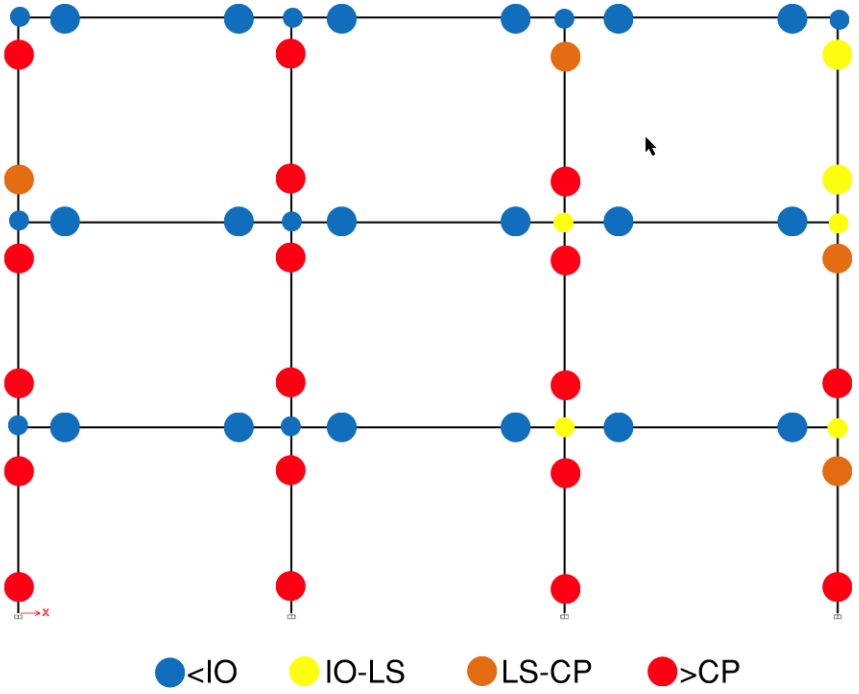


Figure 3-30 Linear Response History: Acceptance criteria range including limit state consideration for beams and joints. Shown for Immediate Occupancy (IO), Life Safety (LS), and Collapse Prevention (CP).

This publication is available free of charge from: https://doi.org/10.6028/NIST.GCR.22-917-50

3.6 Fragility Assessment

Fragility curves for Unacceptable Response and Collapse are developed for the frame are shown in Figure 3-31. Collapse is defined as exceeding 6% drift, and the model consistently converged out to that point. Figure 3-31 shows that the frame exceeds the range of Unacceptable Response (defined as any element, including all beams, columns, and joints, exceeding 1.5 times the ASCE 41-17 modeling parameter *b*, see Figure 2-1) before it reaches collapse criteria as defined above. The simulated frame response is able remain stable beyond the 6% drift due to the ability of the two ductile flexural columns to resist lateral loads at large deformation capacities. However, loss of gravity load carrying capacity of the flexure-shear controlled columns is not explicitly simulated.

The fragility curves can be compared to the demands on the frame during the shake table test. The spectral acceleration from the shake table test is taken as 1.8g (corresponding to the acceleration at the fundamental period from the Perform3D model), from the 3% average spectrum shown in Figure 3-32.

The simulated fragility curve is adjusted in accordance with the procedures of FEMA P-695 Section 7.2 to account for the effects of spectral shape of the ground motion set as shown in Figures 3-32 and 3-33. At the recorded spectral acceleration at T_1 value, the adjusted curve produces a 52% probability of collapse and a 67% probability of unacceptable response (see also Table 3-3).

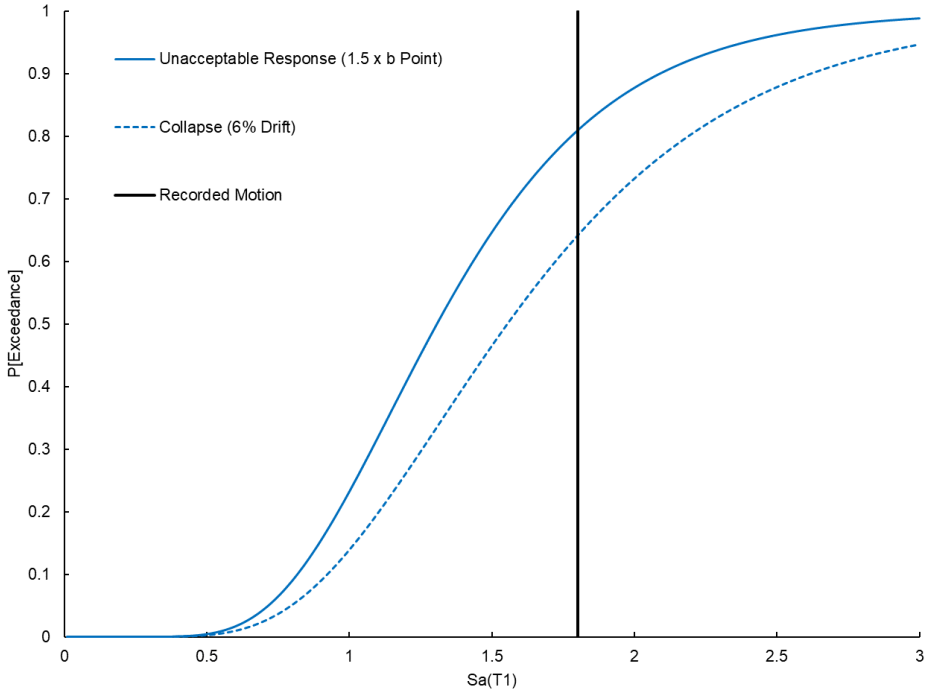


Figure 3-31 Collapse fragility curve showing collapse based on exceeding 6% drift and collapse based on exceeding the range of acceptable response.

This publication is available free of charge from: https://doi.org/10.6028/NIST.GCR.22-917-50

This publication is available free of charge from: https://doi.org/10.6028/NIST.GCR.22-917-50

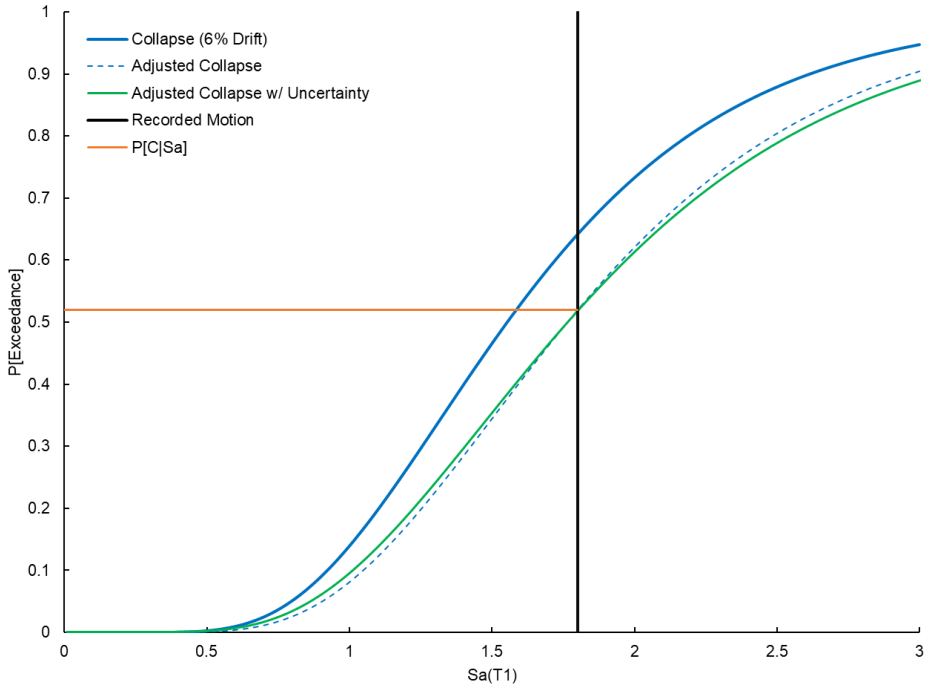


Figure 3-32 Collapse fragility curve showing simulated fragility with 6% drift and effect of adjustments from FEMA P-695 for the spectral shape factor and uncertainty.

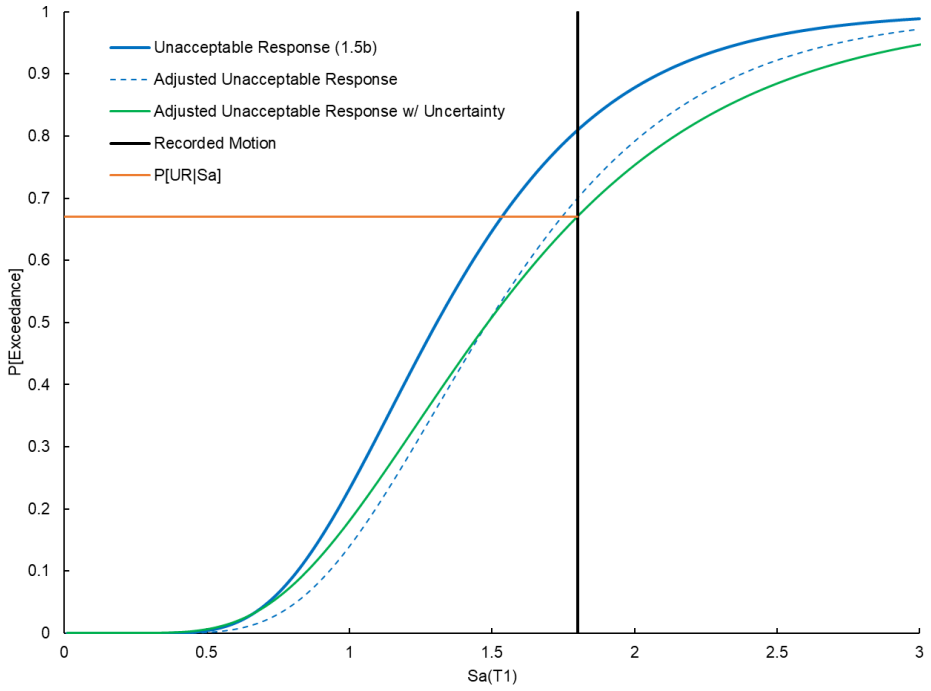


Figure 3-33 Collapse fragility curve showing simulated fragility using Unacceptable Response (1.5 × *b*) and effect of adjustments from FEMA P-695 for the spectral shape factor and uncertainty.

Table 3-3 Fragility Assessment Results

Case	Median S_a (g)	CMR[1]	SSF[2]	3D Factor[3]	ACMR	Adjusted P["C"|1.8g]
Collapse	1.55	0.86	1.12	1.0	0.96	52%
Unacceptable Response	1.31	0.73			0.82	67%

[1] CMR is ratio of the median S_a to the recorded S_a at T_1 value.

[2] *SSF* is spectral shape factor as defined in FEMA P-695 and Chapter 2.

[3] 3D factor of 1.0 was used here, based on the 2-D analysis.

Figure 3-34 compares fragility curves for additional limit states including ASCE 41-17 acceptance criteria and modeling parameter *b* to the collapse and unacceptable response limit states. The fragilities are based on the first element passing the associated limit state; accordingly, no FEMA P-695 adjustments are applied to the curves. Results show that the first element exceeds the Collapse Prevention rotation limits (CP value) at a median intensity of $S_a(T_1 = 0.5\text{sec.})$ of 1.09g, Unacceptable Response (1.5 × modeling parameter *b*) at a median intensity of $S_a(T_1 = 0.5\text{sec.})$ of 1.31g and Collapse (6% drift) at $S_a(T_1 = 0.5\text{sec.})$ of 1.55g. Taken together, these results indicate potentially substantial conservatism in using element acceptance criteria to indicate collapse. However, since the column models are unable to accurately capture shortening in the elements, this could impact the collapse assessment.

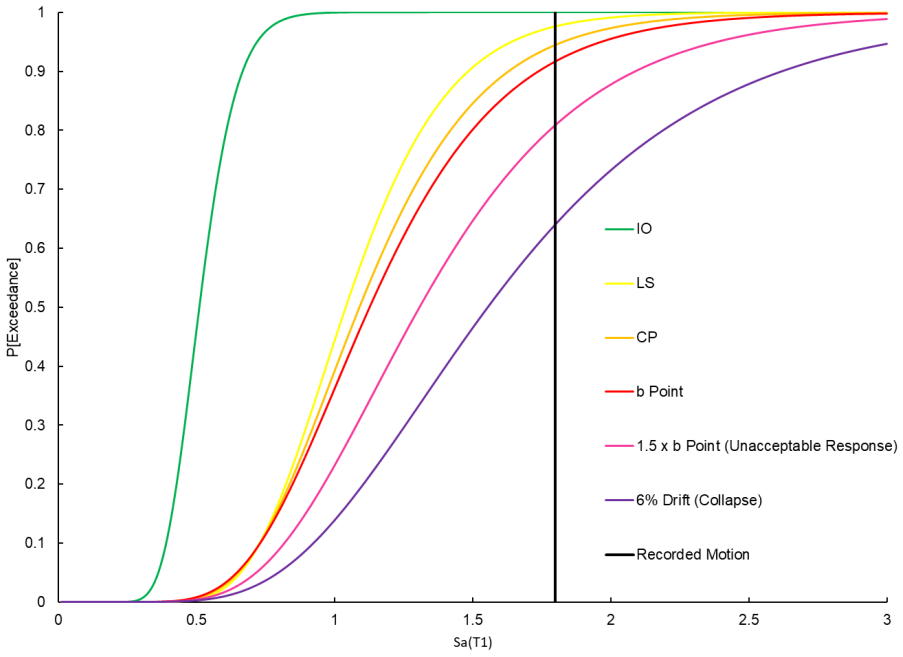


Figure 3-34 Fragility curves showing probability of exceedance for various limit states.

This publication is available free of charge from: https://doi.org/10.6028/NIST.GCR.22-917-50

Figure 3-35 presents adjusted FEMA P-695 fragility curves compared to FEMA P-2018 ratings. The FEMA P-2018 ratings were determined using multiple values of S_a at T_1 so that a complete FEMA P-2018 assessment could be made for a range of intensities. These results indicate that FEMA P-2018 building rating is generally more conservative than any of the other measures for this frame example at lower levels of intensity, but the match improves at higher levels of intensity.

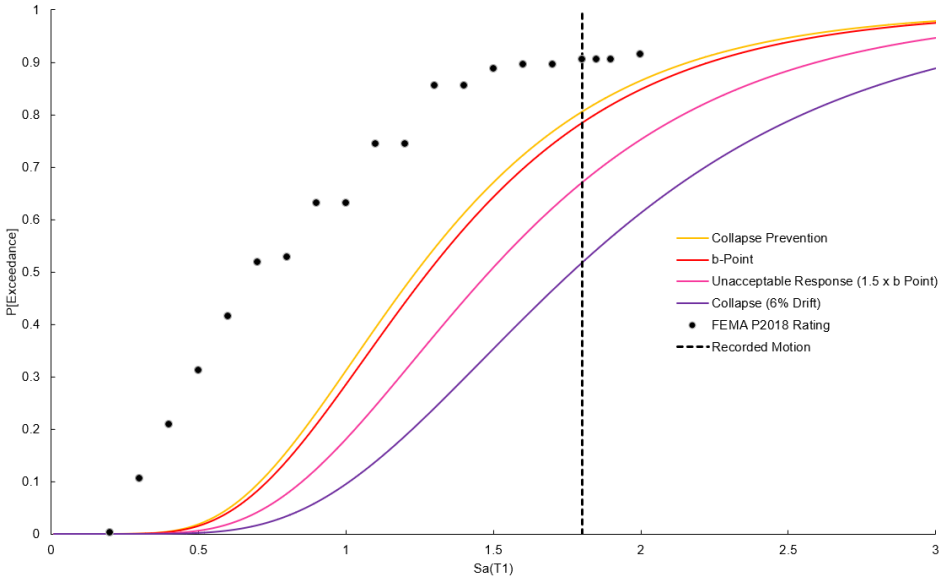


Figure 3-35 Comparison of adjusted FEMA P-695 fragility curves and FEMA P-2018 ratings.

3.7 FEMA P-2018 Evaluation

3.7.1 Evaluation Approach

The frame was evaluated using the procedure outlined in FEMA P-2018, *Seismic Evaluation of Older Concrete Buildings for Collapse Potential* (FEMA, 2018b). The frame is classified as a "frame system" and accordingly evaluated per Chapter 6 of FEMA P-2018. The spectral acceleration for the recorded motion was taken from a response spectrum generated as described in Section 3.5.2 for a 3% damping assumption (Figure 3-25).

3.7.2 Global Performance: Evaluation Procedure vs. Observation

Table 3-4 provides a summary of the key evaluation parameters and results. The frame was found to be governed by a column-yielding mechanism at the first story. The drift capacity at the lowest level for the flexure-shear controlled columns is 1.26 inches, and 5.6 inches for the ductile columns. The column ratings are based on this drift capacity, and the story rating is based on the average of the column ratings. The story rating for this story was calculated to be 0.91. In accordance with FEMA

This publication is available free of charge from: https://doi.org/10.6028/NIST.GCR.22-917-50

P-2018 Section 10.3.1, the frame was deemed an "exceptionally high seismic risk building," because the building rating exceeded 0.7.

The results of this FEMA P-2018 evaluation generally appear to be consistent with the observed response of the frame. The flexure-shear column at Gridline B suffered severe damage and appeared to be at the onset of axial failure.

Table 3-4 Summary of Key Evaluation Parameters and Results

Parameter	X-Direction	Units	Description
W	58.2	kips	Total frame weight
T_e	0.50	sec	Effective fundamental period
S_a @ T_e	1.80	g	Spectral acceleration at T_e
V_y	23.3	kips	Base shear yield strength
Mechanism	1	-	Governing plastic mechanism
Critical Story	1	-	Critical story
$\mu_{strength}$	4.1	-	Global DCR
δ_{eff}	5.4	in	Global equivalent SDOF drift
$\delta_{eff,story\ 1}$	4.8	in	Story 1 drift
$\delta_{eff,story\ 1\ P\Delta}$	6.3	in	Story 1 drift with P delta
Δ_D	5.3	in	Story 1 drift demand on critical components
Story/Building Rating	0.91	-	Story rating at story 1

3.8 Summary

3.8.1 Global Performance

Tables 3-5 through 3-7 present comparisons of key global performance metrics for all ASCE 41 models studied and measured values.

Table 3-5 Summary of First Mode Period and Maximum Base Shear Normalized by Building Weight

Metric	Measured Value	OpenSees ASCE 41-13		OpenSees ASCE 41-17		Perform3D		Lin. Response History	
		Value	*Err.*	*Value*	*Error*	*Value*	*Err.*	*Value*	*Err.*
First Mode Period (s)	0.34	0.54	59%	0.54	59%	0.48	41%	0.50	47%
Max. Normalized Base Shear	0.51	N/A	N/A	N/A	N/A	0.48	5.9%	1.50	194%

This publication is available free of charge from: https://doi.org/10.6028/NIST.GCR.22-917-50

Table 3-6 Summary of Maximum Absolute Story Drift Ratio and Residual Drift Ratio

Metric	Measured Value	OpenSees ASCE 41-13		OpenSees ASCE 41-17		Perform3D		Lin. Response History	
		Value	*Err.*	*Value*	*Error*	*Value*	*Err.*	*Value*	*Err.*
1st Story Max Absolute Drift Ratio (%)	5.18	N/A	N/A	N/A	N/A	6.07	17%	4.70	9.0%
2nd Story Max Absolute Drift Ratio (%)	4.7	N/A	N/A	N/A	N/A	3.92	17%	6.16%	30%
3rd Story Max Absolute Drift Ratio (%)	2.61	N/A	N/A	N/A	N/A	1.91	27%	4.87%	9.0%
1st Story Absolute Residual Drift Ratio (%)	0.30	N/A	N/A	N/A	N/A	3.0	900%	N/A	N/A
Roof Absolute Residual Drift Ratio (%)	0.24	N/A	N/A	N/A	N/A	1.9	690%	N/A	N/A

Table 3-7 Summary of Maximum Absolute Floor Acceleration

Metric	Measured Value	OpenSees ASCE 41-13		OpenSees ASCE 41-17		Perform3D		Lin. Response History	
		Value	*Err.*	*Value*	*Error*	*Value*	*Err.*	*Value*	*Err.*
1st Floor Max Absolute Acceleration (g)	5.18	N/A	N/A	N/A	N/A	1.43	58.5%	2.05	127%
2nd Floor Max Absolute Acceleration (g)	4.7	N/A	N/A	N/A	N/A	1.11	35.3%	2.63	221%
Roof Max Absolute Acceleration (g)	2.61	N/A	N/A	N/A	N/A	1.20	8.7%	3.42	211%

Nonlinear simulations using OpenSees produced a sidesway collapse mechanism and therefore overpredicted structural responses and damage levels. Thus, more detailed comparisons between OpenSees analyses and experimental results are not possible.

Both the linear and Perform3D nonlinear evaluations identified the first-story column deficiencies as the likely failure mechanism. The maximum floor displacement estimates from both the linear and nonlinear simulations are fairly close to the measured values. However, the drift profile from the linear methods incorrectly showed higher drifts at the second story compared to the first story. The drift profile from the Perform3D nonlinear evaluation is in general agreement with the measured values and correctly predicts the first story having the largest drift demands. However, this model resulted in significant permanent displacements at all levels that were not observed in the test.

Both the linear and Perform3D nonlinear methods significantly overestimated the floor accelerations. Although this would be expected from the linear methods since yielding of the frame is not captured, it was expected that the accelerations at the first

This publication is available free of charge from: https://doi.org/10.6028/NIST.GCR.22-917-50

level predicted by the nonlinear model would be closer to the measured values given that base shears of the nonlinear analysis and measured values were a close match.

The Perform3D nonlinear model utilizes P-M-M hinges in columns, which account for variations in axial loads on moment strength. The P-M-M hinges also use cyclic properties with higher energy dissipation potential (Figures 3-19 to 3-22) than the peak-oriented hysteretic hinges used in the OpenSees models (Figures 3-29 and 3-29). The more severe damage and drift demands generated by the nonlinear OpenSees models may be attributed, at least partially, to these differences in modeling approaches.

3.8.2 Component Performance

In general, both the Perform3D nonlinear and linear models show element deformation demands higher than what would be implied by the observed performance.

The Perform3D nonlinear model correctly identified the vulnerability of the lower story columns, but also predicted deformations beyond modeling parameter *b* for one column in the second story and at the top of the first story columns that were not observed in the test. The two flexure-shear controlled columns were predicted to go beyond modeling parameter *b*, which would imply loss of vertical load carrying capacity. The column at Gridline B in the test was observed to near the point of losing vertical capacity, and the measured axial load showed that this column did shed some load to the neighboring columns. However, the column at Gridline A did not show damage consistent with the onset of axial failure. The predicted deformations in the lower level beam near Gridline A appear to be higher than the actual demands seen in the test. This may be due to the way the loads from Column B are redistributed to adjacent elements after initiation of column strength loss in the model.

The linear model correctly identified the vulnerability of the lower story columns, but predicted significantly more deformation demands in the upper level columns, all beams, and all joints than those observed in the test. The higher DCR values at the lower level columns are correlated with the reduction of acceptance criteria values associated with the higher axial column loads at the lower story. When the demands on the beams and joints were calculated on a limit-state analysis, the demands appear to be consistent with the damage observed in the test.

3.8.3 Fragility Assessment and FEMA P-2018 Evaluation

The fragility assessment of the Perform3D nonlinear model shows that component-based acceptance criteria for Collapse Prevention are similar to a fragility defined by modeling parameter *b* of a single element. However, the model is not expected to

This publication is available free of charge from: https://doi.org/10.6028/NIST.GCR.22-917-50

undergo sidesway collapse until much larger demands (much larger median capacity), which indicates that there is still significant residual capacity in the frame after the failure of the first component-based trigger. This difference is in part due to the inability of the model to capture load redistribution. However, the simulations point to the potential conservatism of a component-based procedure, as well as the importance of continuing to refine models at higher demands (i.e., pushing the limits of what is meant by unacceptable response).

The FEMA P-2018 evaluation predicted a building rating of 0.91, which is in fairly close agreement with the probability of exceedance for the Collapse Prevention and modeling parameter *b* fragilities (approximately 8% difference in probability of exceedance), but appear conservative when compared to the assumed collapse (taken as 6% drift) and 1.5 × modeling parameter *b*. The nonlinear model was able to remain stable at high deformation levels, however the column models do not accurately capture loss of axial load capacity, which may overestimate the collapse fragility.

3.8.4 Analytical Study Takeaways

In general, the results show that as the model becomes more complex, estimates of response and damage generally become less conservative and closer to observed performance. For example, the nonlinear global and component results are less conservative than the linear results and better match the observed response. The shortcomings of linear methods are attributed to the lack of yielding of the model that does not capture the associated change in behavior and redistribution of forces. Overall element demands and floor accelerations are overestimated for capacity-protected elements where limit-state analysis is not utilized. However, even the simplest approach identifies the critical first story column mechanism.

The hinges of the column elements in the nonlinear model show deformations well beyond modeling parameter *b*, which would indicate loss of vertical load-carrying capacity. The nonlinear elements used cannot accurately capture this behavior, which could lead to unreliable prediction of overall behavior. Further, the backbone models in ASCE 41 that are based on cyclic testing appear to overestimate the observed damage. This may be due to the actual response being closer to monotonic behavior rather than cyclically degraded behavior. This may also be partly responsible for the nonlinear model showing significantly more permanent story drifts, even though the predicted maximum story drifts were in general agreement with the measured drifts.

3.8.5 Study Limitations

A potential limitation of the study is related to the scale-model nature of the test frame. It is unclear whether the applicability of the ASCE 41-17 modeling and acceptance criteria to the smaller tested elements could lead to bias in the results.

This publication is available free of charge from: https://doi.org/10.6028/NIST.GCR.22-917-50

Chapter 4

Four-story Frame and Wall Test Structure

This publication is available free of charge from: https://doi.org/10.6028/NIST.GCR.22-917-50

4.1 Overview

This chapters presents benchmarking studies for a 4-story reinforced concrete structure tested on the E-Defense shake table in Japan in 2010, shown in Figure 4-1. Ground motion records and response parameters are available since the structure was tested on a shake table. In this chapter, computed responses for analytical models and predicted damage are compared with measured responses and observed damage for strong motion records from Southern Hyogo Prefecture Earthquake of January 17, 1995.



Figure 4-1 Two structures tested at E-Defense shake table, study structure is on the left side of the photo. (Nagae et al., 2015).

The structure was evaluated in accordance with the nonlinear and linear dynamic procedures of ASCE 41-17. Nonlinear models were developed using OpenSees and Perform3D software with nonlinear and linear elastic joint elements. Linear models were developed using ETABS software. The models were constructed per details presented in Appendix A, unless otherwise noted.

This chapter also provides results of a fragility analysis showing the collapse potential of the model, as compared to the likelihood of exceeding ASCE 41-17 acceptance criteria. In addition, the structure was evaluated according to Eurocode 8 (European Committee for Standardisation, 2005) column acceptance criteria, New Zealand Guidelines, *The Seismic Assessment of Existing Buildings* (NZSEE et al., 2017), and FEMA P-2018, *Seismic Evaluation of Older Concrete Buildings for Collapse Potential*, (FEMA, 2018b).

4.2 Building Description and Observed Performance

4.2.1 Building Description

The study structure was one of two structures tested simultaneously that were nearly identical in dimensions but differed in construction technique and reinforcing design. The objective of the testing program was to compare the seismic performance of traditional concrete construction with that of newly developed post-tensioned (PT) systems. The structure evaluated in this chapter was cast-in-place concrete with mild reinforcing and is the leftmost structure shown in Figure 4-1. The second structure shown on the right side was composed of precast concrete members with mild and post-tensioned reinforcing.

The testing program for both buildings is documented extensively in PEER Report 2011/104 (2011). The report contains design drawings, testing instrumentation, ground motion information, and weight documentation. A typical floor plan, elevations, and reinforcement detailing are presented in Figure 4-2 to 4-4.

The study structure has two lines of moment frames in the longitudinal direction and two shear walls in the transverse direction. The building was structurally regular and has major gridlines spaced 7.2m (23.62ft) apart. It was designed to conform to the seismic design provisions of the Architectural Institute of Japan (AIJ, 1999) and meet most of the ACI 318-11 provisions for special moment frame and wall systems as detailed in Nagae et al., 2015. Floor heights were 3000mm (118.1 inch). The slab system is a pan joist system with a 130mm (5.12 inch) slab thickness at all levels. The two walls were 250mm (9.84 inch) thick by 2500mm (98.4 inch) long. The columns were 500mm (19.69 inch) square. Beams in the frame direction were 300mm (11.81 inch) wide by 600mm (23.62 inch) deep, while those coupling the walls to the corner columns were 300mm (11.81 inch) wide and deep.

Lap splice failure was precluded from the study since all splices in the beams, columns, and walls were welded. Additionally, transverse reinforcement was well detailed with 135° hooks. The ratio of column to beam moment strengths at interior joints in the frame direction were close to 1.0 at the lower three floors (Nagae et al., 2015), which is lower than the ACI 318-19 requirement for Special Moment Frames for the ratio not to be smaller than 6/5.

This publication is available free of charge from: https://doi.org/10.6028/NIST.GCR.22-917-50

This publication is available free of charge from: https://doi.org/10.6028/NIST.GCR.22-917-50

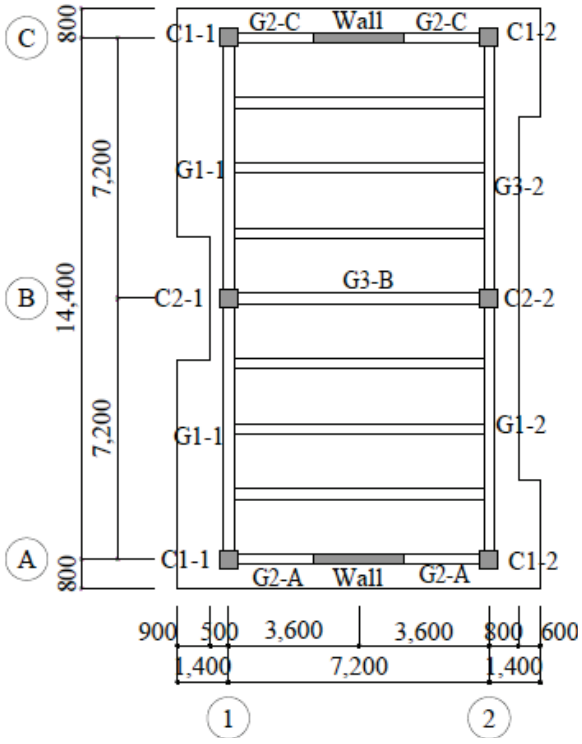


Figure 4-2 Typical floor plan and member nomenclature (measurements shown in mm) from Nagae et al. (2015).

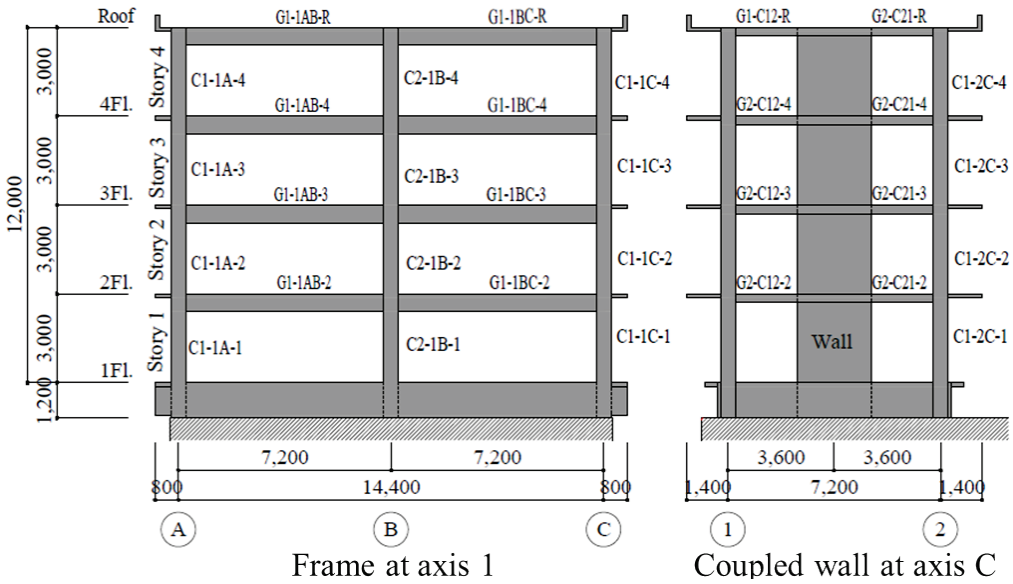


Figure 4-3 Elevations and member nomenclature (measurements shown in mm) from Nagae et al. (2015).

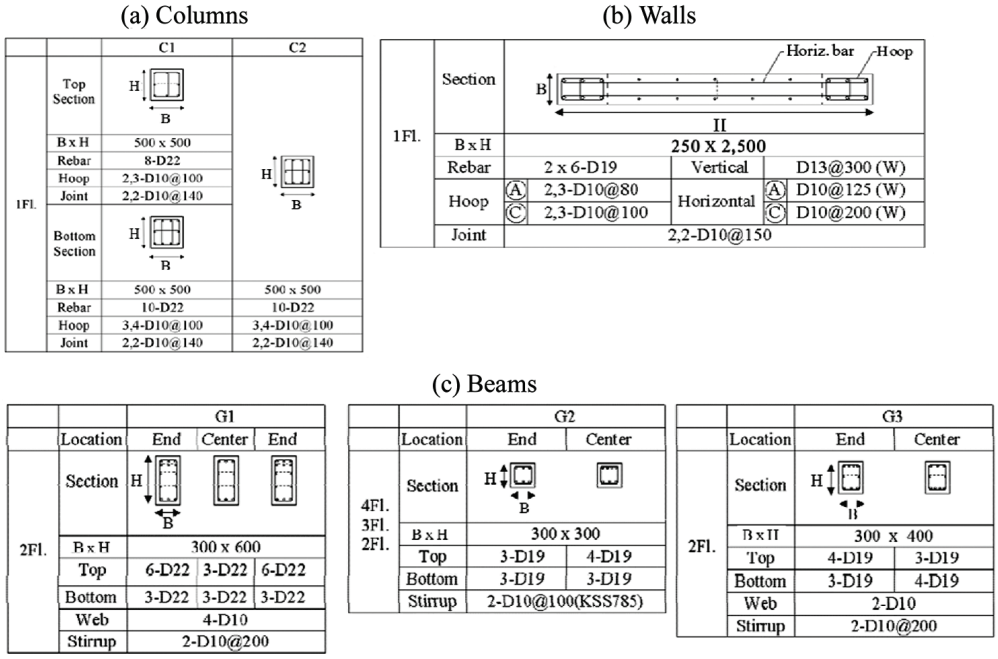


Figure 4-4 Reinforcement details (adapted from Nagae et al., 2015).

Material Properties

The design values and testing results can be found in PEER (2011). For the purposes of this evaluation, the measured material strengths from testing were used for all elements. These values are summarized in Table 4-1.

Table 4-1 Average Material Properties

		Based on Test Results	
Component	Property	Lower-Bound (Specified)	Measured (Expected)
Reinforcing bars	Yield Stress, f_y	350 MPa (50 ksi)	372 MPa (54 ksi)
Concrete	Peak Strength, f_c'	27 MPa (4 ksi)	30.2 to 41 MPa (4.4 to 6.0 ksi)

Building Weight

The weight of the building, including testing instrumentation, is known. See Table 4-2 for a summary of measured building weight by story. Weight was assumed to be evenly distributed across the slab.

This publication is available free of charge from: https://doi.org/10.6028/NIST.GCR.22-917-50

Table 4-2 Building Weight by Floor Level

Floor Level	Dead Load kN (kips)
RFl	934 (210)
4Fl	867 (195)
3Fl	872 (196)
2Fl	867 (195)
Total	3540 (796)

4.2.2 Ground Motion

The structure was tested with two series of increasing ground motion intensities starting with 25%, 50%, and 100% JMA-Kobe followed by 40% and 60% JR-Takatori. The building was subjected to all three components of a ground motion simultaneously (including the vertical component). For the purposes of this study, the 100% JMA-Kobe record (Japan Meteorological Agency, Kobe Marine Meteorological Observatory station recording during the Southern Hyogo Prefecture Earthquake on January 17, 1995) was used to evaluate members and for comparison to observed performance because it was the first ground motion record during which severe damage and significant nonlinear response was recorded. Only minor yielding was recorded during the 50% JMA-Kobe motion that did not result in any appreciable permanent deformations leading into the 100% JMA-Kobe motion (Nagae et al., 2015). The acceleration histories of the two horizontal components of the ground motion are shown in Figure 4-5. Figure 4-6 presents the response spectra with 5% damping for these ground motions. The period measured before the 100% JMA-Kobe event is shown in the plot.

This publication is available free of charge from: https://doi.org/10.6028/NIST.GCR.22-917-50

This publication is available free of charge from: https://doi.org/10.6028/NIST.GCR.22-917-50

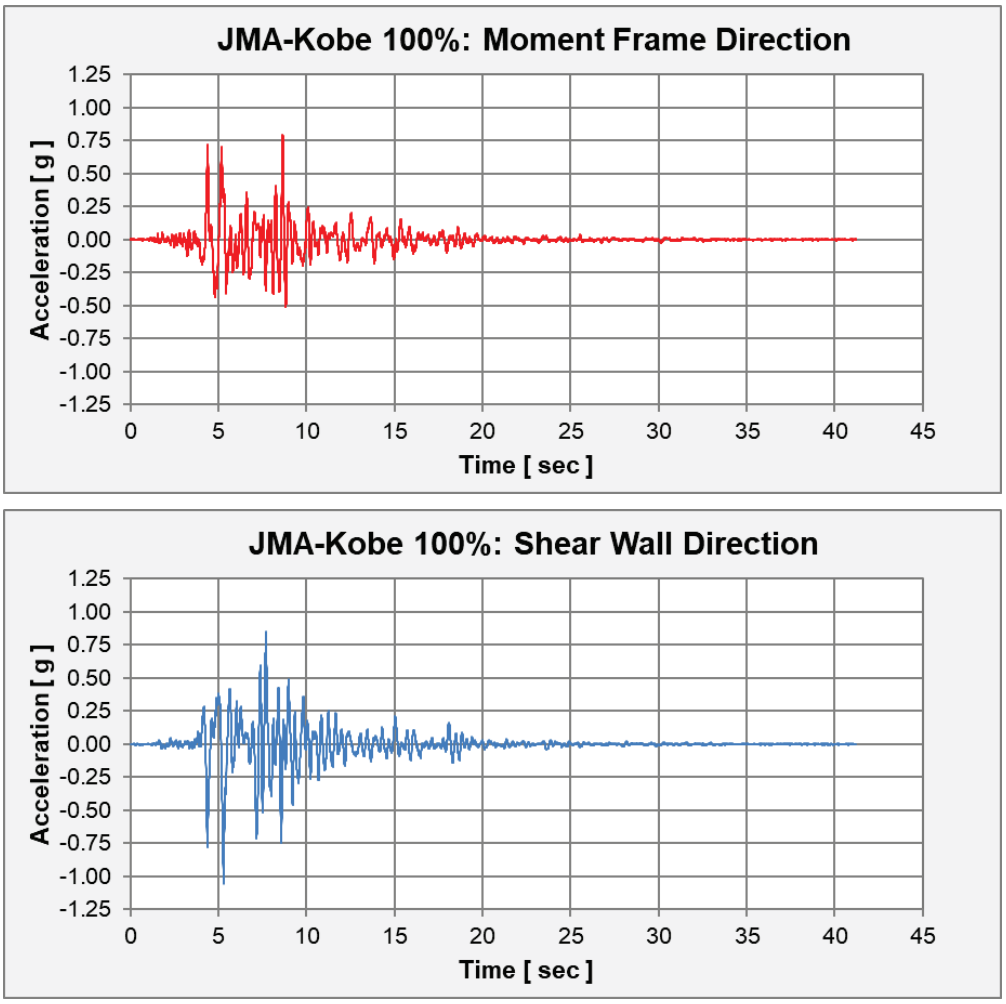


Figure 4-5 Ground motion records for 100% JMA-Kobe (first 10 seconds are truncated).

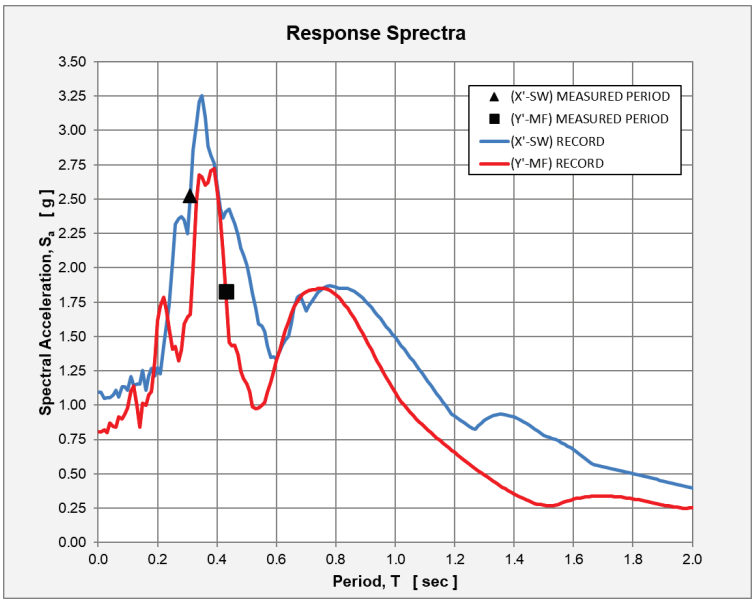


Figure 4-6 Response spectra for 100% JMA-Kobe (5% damping).

4.2.3 Observed Performance

Observed damage from the 100% Kobe motion consisted of severe shear damage in first floor beam-column joints, limited cracking and spalling of beam and column ends, and cracking and crushing of the shear walls at their base. The boundary elements of the wall sustained considerable crushing damage, and sliding was observed at the base of the walls.

Response Quantities

Floor displacement data were taken from the wire type displacement transducers in the building. A maximum story drift ratio is calculated as the maximum displacement in that story divided by the story height (3 m; 118.1 in.). The drift ratio was maximum in the first story for both the frame (3.36%) and wall (3.33%) directions. The distributions of the maximum drift ratio are shown in Figure 4-7 and indicate that the building was pushed to relatively large drift demands.

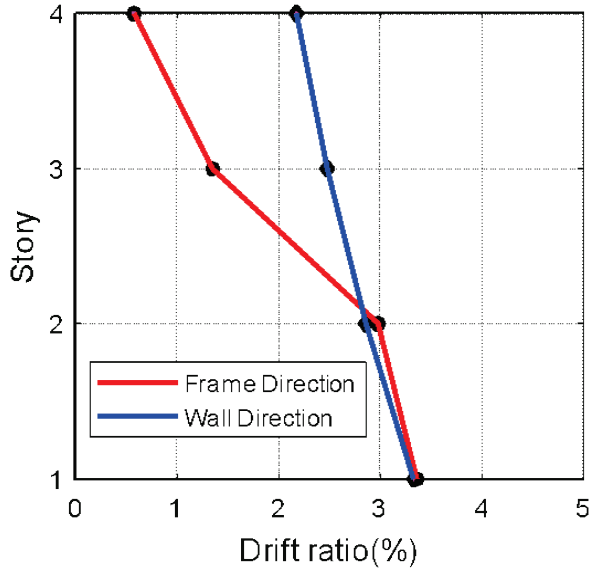


Figure 4-7 Maximum interstory drift distribution over the height of the building.

The building had a measured natural first mode period in the frame direction of 0.43 sec. and in the wall direction of 0.31 sec. prior to the application of the 100% JMA-Kobe motion.

The distribution of damage in frame and wall members observed after the high intensity test are schematically represented in Figure 4-8.

This publication is available free of charge from: https://doi.org/10.6028/NIST.GCR.22-917-50

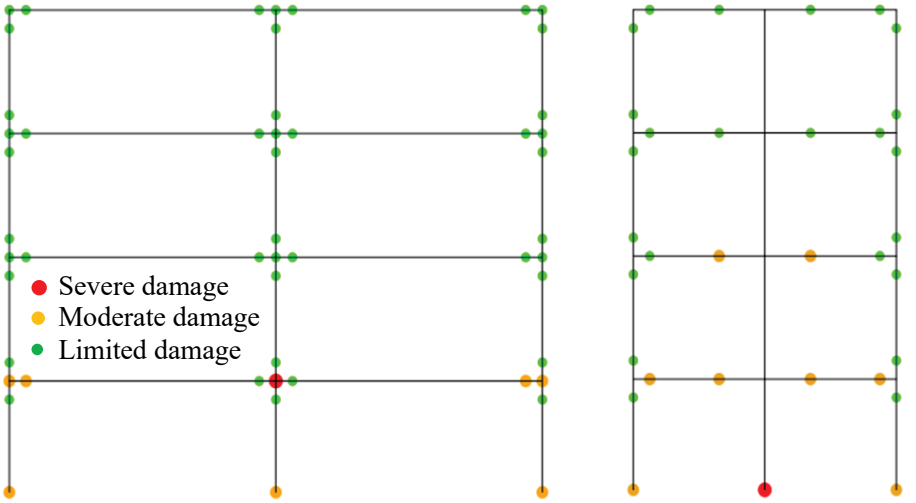


Figure 4-8 Schematic distributions of observed damage in the frame at Gridline 1 (left) and couple wall at Gridline C (right) based on the observed experimental damage.

Damage Observed in Shear Wall Direction

According to Nagae et al. (2015), cracking was observed in all stories of the shear walls with concentrated damage in the first story. Limited cracking damage was present at the end of the 50% JMA-Kobe test and the walls were severely damaged during the 100% JMA-Kobe test. Severe spalling was concentrated in the boundary element regions of both shear walls at the interface with the foundation, which is shown in Figure 4-9. Some longitudinal bars fractured in the damaged regions of the walls. Sliding at the foundation interface was also recorded for both walls.



Figure 4-9 Observed damage in first story of shear walls (adapted from Nagae et al., 2015). Top left photos: base of wall at Gridline C closer to Gridline 2 (left) and Gridline 1 (right); Bottom left photo wall base at Gridline A; Photo on the right shows wall at Gridline C.

This publication is available free of charge from: https://doi.org/10.6028/NIST.GCR.22-917-50

The beams and columns in line with the walls sustained moderate damage at their ends, with the greatest damage occurring at the lower levels (Figure 4-8).

Damage Observed in Moment Frame Direction

Flexural yielding was recorded in beams and columns up to the third story. Various levels of cracking were observed at the ends of beams and at the base of columns in the first level. Minor concrete spalling also occurred at the base of the columns in the first story as highlighted in Figure 4-10. The beam-column joints suffered shear damage at the second floor, with the interior joints sustaining the most severe damage (Figure 4-10 and Figure 4-11). Damage was anticipated in the joints since they did not satisfy the confinement requirements of ACI 318-14 for Special Moment Frames.

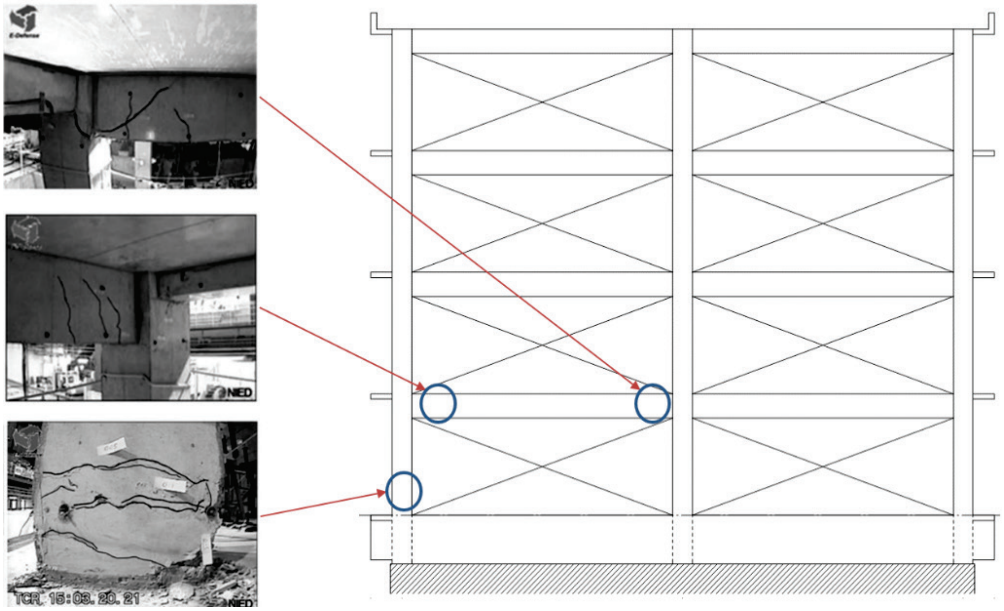


Figure 4-10 Observed damage in moment frame at Gridline 2 (Nagae et al., 2015).

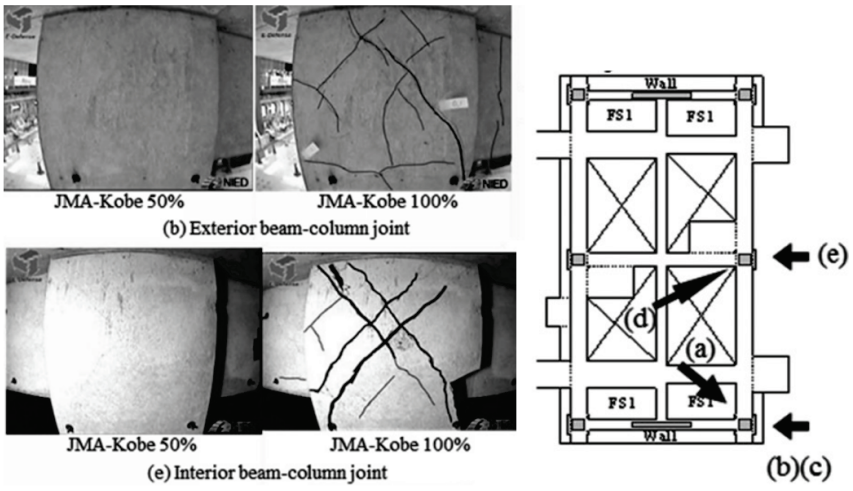


Figure 4-11 Observed joint damage at the second floor level (adapted from Nagae et al., 2015).

This publication is available free of charge from: https://doi.org/10.6028/NIST.GCR.22-917-50

4.3 Nonlinear Dynamic Procedure using OpenSees

OpenSees models were developed per ASCE 41-17 as discussed in Appendix A. The models were built using lumped-plasticity (LP) or fiber section (Fiber) approaches and two different beam-column joint elements: (1) one accounting for nonlinear joint (NJ) behavior, and (2) one treating joints through linear elastic elements (EJ). Four models were developed accordingly: OpenSees LP NJ, OpenSees LP EJ, OpenSees Fiber NJ, and Opensees Fiber EJ. The lumped-plasticity models utilized lumped-plasticity elements for all frame and wall members and the fiber section models utilized fiber section elements for columns and walls and lumped-plasticity elements for beams.

This section primarily presents results from the Opensees LP NJ model and compares them to test data both at the global structural level, as well as the component level. Results from the other three models are compared with those from the OpenSees LP NJ model at the global structural level to highlight differences in analysis outcomes that arise from various modeling choices.

4.3.1 Modeling Approach

Three-dimensional numerical models of the structure were created in OpenSees with fixed base and a rigid diaphragm.

For the lumped-plasticity approach, beams, columns and walls were modeled with zero-length hinge elements at member ends where inelastic deformations were anticipated (Figures 4-12 and 4-13). For the fiber section models, columns and walls were discretized using force-based fiber section elements with 5 integration points and Gauss Lobatto integration, while beams were modeled with zero-length hinge elements at member ends where inelastic deformations were anticipated (Figure 4-13). Fiber section elements had a zero-length rotational spring at each end to account for bar slip (Figure 4-12). Hinge properties for all frame and wall members were defined using the ASCE 41-17 modeling parameters and standard backbone shape.

This publication is available free of charge from: https://doi.org/10.6028/NIST.GCR.22-917-50

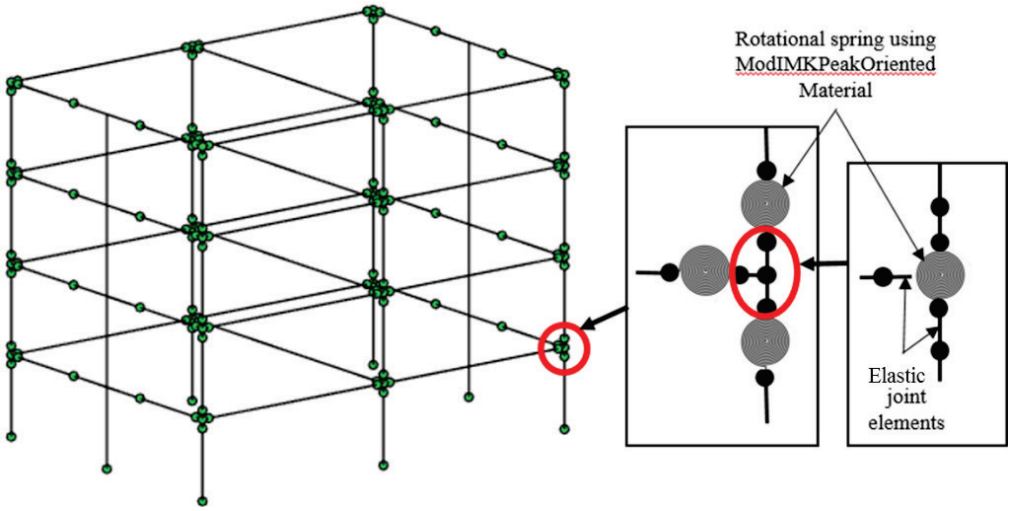


Figure 4-12 OpenSees LP model with material model listed for the nonlinear zero-length springs.

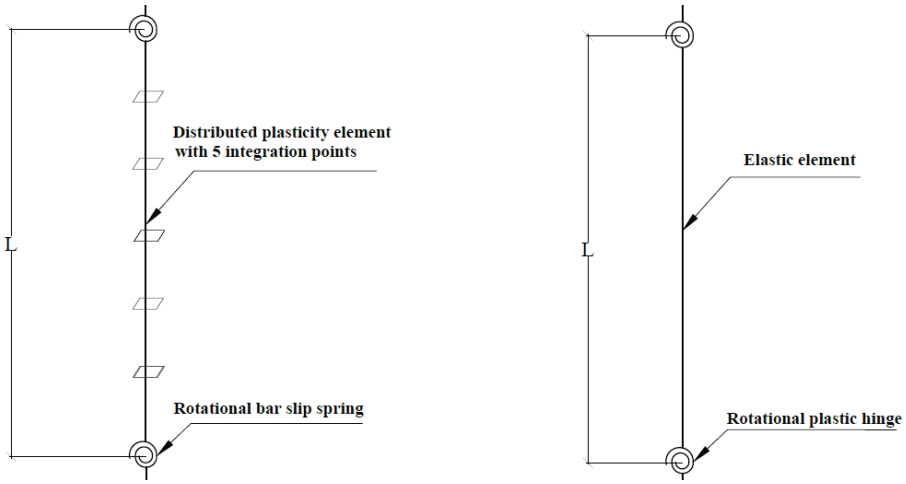


Figure 4-13 Element topology for fiber section (left) and lumped plasticity (right) models.

For the fiber section elements, sections were discretized and assigned material models Concrete02 for unconfined concrete in the column and wall cover and wall web, Concrete04 for confined concrete in the column core and wall boundary elements, and Steel 02 for reinforcing bars. Basic parameters of the stress-strain curve for concrete in compression were calculated using the model by Mander et al. (1988a). The stress-strain relationship (Figure 4-15) was regularized to prevent localized deformations after concrete entered the descending branch of the stress-strain curve. Strain at 20% of the peak stress was calculated using the relationship proposed by Coleman and Spacone (2001) for constant fracture energy:

$$\varepsilon_{20} = \frac{G_f^c}{0.6 f_c' L_p} - \frac{0.8 f_c'}{E_c} + \varepsilon_0 \qquad \text{Eq. 4-1}$$

This publication is available free of charge from: https://doi.org/10.6028/NIST.GCR.22-917-50

In Equation 4-1 L_p is the plastic hinge length defined as the weight of the first integration point times the length of the element. For five integration points using the Gauss-Lobatto integration scheme, the weight for the first integration point is 0.05 L. The term G_f^c is the constant fracture energy. Based on a sensitivity analyses of column tests a fracture energy G_f^c = 0.342 kip/in. = 59893.36 N/m was used. The values of ε_{20} (Equation 4-1, Figure 4-14) for the first and second through fourth story columns were -0.02041 and -0.02061, respectively. Regularized stress-strain relationships for cover and core concrete are presented in Figure 4-15.

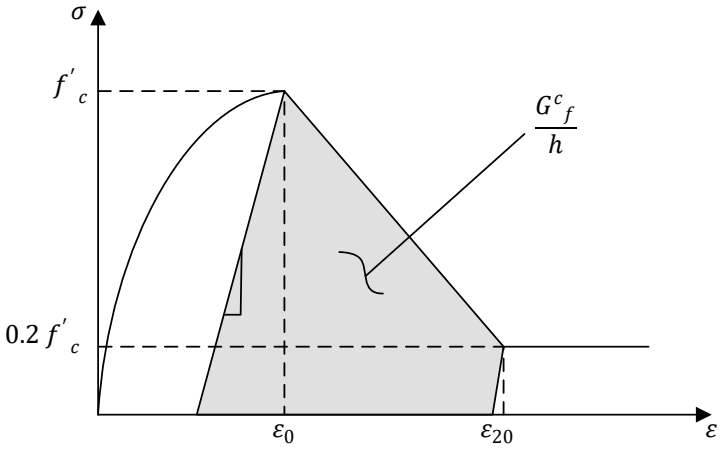


Figure 4-14 Stress-strain relationship for concrete.

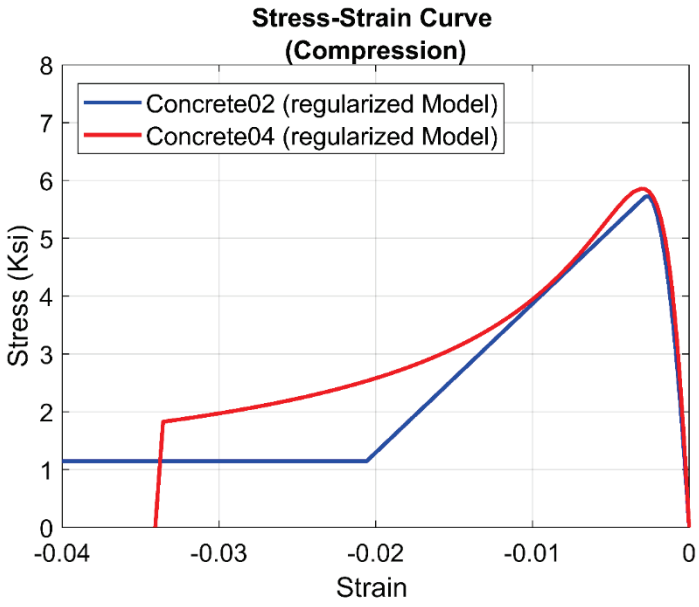


Figure 4-15 Regularized stress-strain relationships for concrete in compression.

Concrete compressive strength was defined using measured strength values. Tensile strength of concrete was taken as 10% of compressive strength for unconfined concrete and 7% for confined concrete. The tangent stiffness of concrete material at

This publication is available free of charge from: https://doi.org/10.6028/NIST.GCR.22-917-50

f_c'/ε_0 and the degrading slope E_t was defined as 10% of the tangent stiffness of concrete material at zero load.

The stress-strain relationship for steel was simulated using the Steel02 material model in combination with a MinMax material object in OpenSees. A stress-strain relationship simulated by the Steel02 material model is presented in Figure 4-16, with a stress-strain relationship calculated with the reinforcing bar model by Mander and Matamoros (2019) is shown for reference.

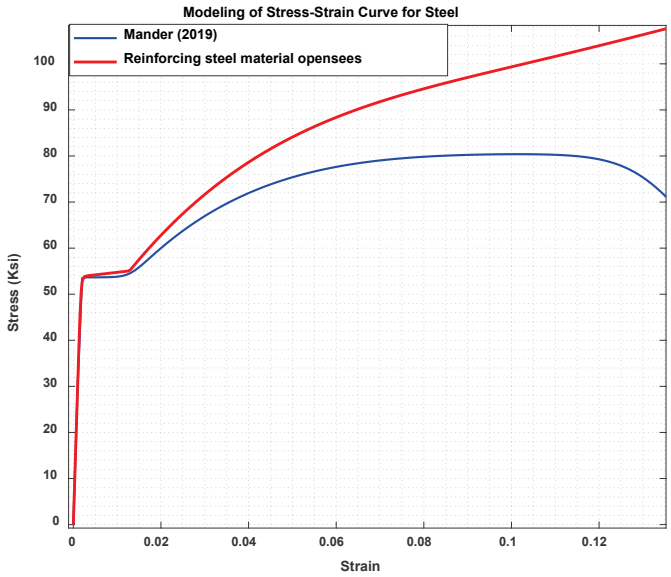


Figure 4-16 Calculated stress-strain relationship for steel.

The MinMax material object used the stress-strain behavior provided by Steel02 material model while strains remain within the minimum and maximum limiting values. After a limiting value is exceeded the MinMax object assumes that the material has failed and both stiffness and stress become zero. Minimum and maximum strain limits were calibrated to cause loss of lateral load capacity at a rotation similar to the backbone curve in ASCE 41. Calibrated strain limits for steel were 0.13 for all columns and 0.11 for walls. This concept is illustrated in Figure 4-17, which shows the calculated backbone curves for the fiber section column elements and the corresponding backbone curve calculated with the provisions of ASCE 41-17. The method adopted was effective in producing a plastic rotation similar to that specified by ASCE 41-17, although not succesful in producing a residual capacity because the MinMax object reduced the strength to zero after the limiting strain was exceeded. This limitation was of greater significance for the wall elements than the column elements, because residual capacity of the wall according to the ASCE 41-17 modeling parameters is substantially high, and the drop in lateral load capacity achieved through damage of the concrete was not large enough to mimic the ASCE 41-17 backbone curve. As a result, the MinMax strain limit was

This publication is available free of charge from: https://doi.org/10.6028/NIST.GCR.22-917-50

chosen giving more importance to accurately matching modeling parameter *b* than modeling parameter *a* (Figure 2-1), so the envelop would represent loss of gravity load instead of loss of lateral load capacity, as shown Figure 4-18.

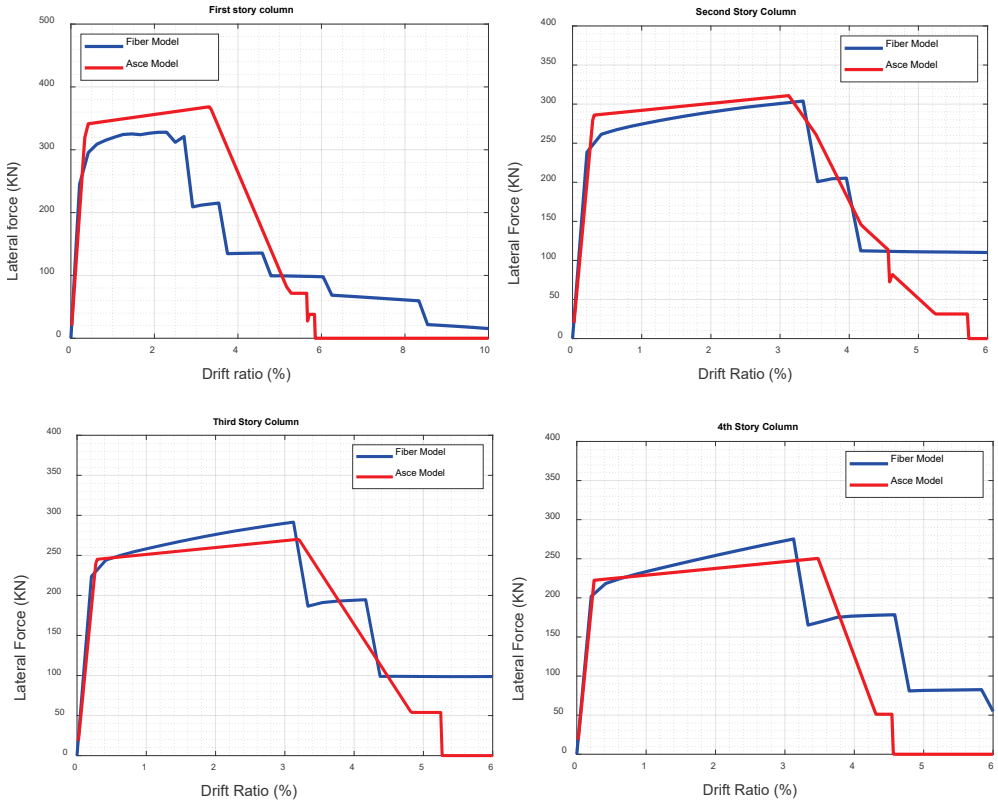


Figure 4-17 Moment-rotation relationships for fiber section models of columns.

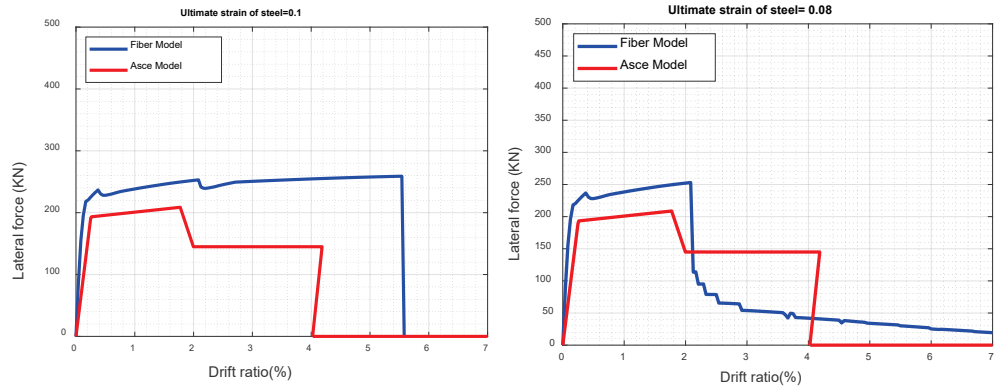


Figure 4-18 Calculated moment-rotation relationships for fiber section models of walls with steel strain limits of 0.08 and 0.10.

To test the validity of the model, Column C-1 in the lumped-plasticity model was replaced with a fiber section model in all four stories, modeling all the remaining columns with the lumped-plasticity approach. The force-deformation relationships in the wall and frame directions calculated with the 100% JMA-Kobe record are shown in Figure 4-19. The blue curve shows the force-deformation relationships for the first

This publication is available free of charge from: https://doi.org/10.6028/NIST.GCR.22-917-50

story of Column C-1 calculated with fiber section, while the red curves show the load-deformation relationships of Column C-1 calculated with a model in which all elements were simulated using lumped plasticity. Calculated forces with the two models were similar, and forces calculated with the fiber-section model were consistently lower due to the effects of biaxial bending.

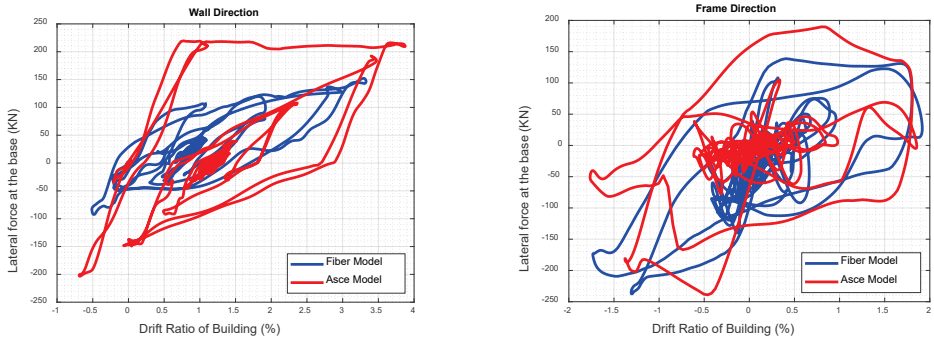


Figure 4-19 Calculated force-deformation relationships for Column C-1 simulated with a fiber section in the lumped-plasticity model and envelope curve with ASCE 41 modeling parameters. All remaining columns were modeled using lumped plasticity.

Axial loads used in calculating modeling parameters were obtained as the maximum compressive axial demands developed in each element from a pushover analysis of the building out to initiation of loss of lateral load carrying capacity. Slab out-of-plane bending was not modeled explicitly, but was rather accounted for through effective flange widths assigned to the beams. The joists supporting the slab were not included in the model.

The maximum compressive axial load ratio was less than 10% of the column gross sectional capacity over the height of the building. All columns were expected to respond primarily in a flexure mode as they had relatively high levels of confinement, such that their shear strength exceeded by a significant margin the shear demand associated with flexural hinging. Gross elastic shear stiffness was used for frame members.

All beams were likewise expected to respond primarily in a flexure mode. Beam moment strength was estimated including an effective flange width that was determined based on ASCE 41-17 provisions.

Beam-column joints were classified as conforming per ASCE 41-17 despite the relatively wide hoop spacing (140 mm, 5.5 in.). Beam-column joints were determined to exceed their shear strength in the lower levels in the frame direction but not in the wall direction using ACI 318-19 methodology using a static mechanism analysis. In the OpenSees EJ (Elastic Joint) model, beam-column joints were modeled through elastic elements extending from the beams and columns and connecting at the center of the joint directly. Joint elastic stiffness was modeled

This publication is available free of charge from: https://doi.org/10.6028/NIST.GCR.22-917-50

implicitly according to ASCE 41-17 Section 10.4.2.2.1. Joints were modeled in the same manner in the lumped plasticy and fiber section OpenSees NJ (Nonlinear Joint) models. In both models, joint elastic elements extending from beams and columns remained but rotational springs were introduced in the frame direction, to generate a scissor motion in the joint as described in Celik and Ellingwood (2008). The nonlinear behavior of the rotational springs was calibrated to properties defined in ASCE 41-17 Section 10.4.2.

The walls were determined to respond primarily in a flexure mode based on their long height-to-length aspect ratio and high shear strength to shear demand ratio. Modeling parameters for wall hinges at the foundation interface corresponded to values specified in ASCE 41-17 for walls controlled by flexure.

Because the building did not contain any nonstructural elements, the analysis employed 2% Rayleigh damping defined at the fundamental first and third mode periods of the building. The analysis accounted for nonlinear geometry effects using the P-delta transformation.

Nonlinear models were only subjected to all three components of the 100% JMA-Kobe motion without being subjected to the prior motions applied to the building in the experimental program.

4.3.2 Global Performance: OpenSees LP NJ Model vs. Observation

Global Mechanism and Damage Distribution

Damage distribution data are compared in order to assess the extent to which the OpenSees Lumped Plasticity NJ computational model was able to capture the overall building deformation mechanisms and damage distribution. To this end, Figure 4-20 was produced using model results, in a similar layout to Figure 4-8, which illustrates the level and distribution of experimental damage. The level of damage from analysis was obtained by comparing the inelastic rotations at element ends, $\theta_{inelastic}$, with the ASCE 41-17 modeling parameter *a* that indicates the beginning of lateral strength loss. If a rotation exceeded its *a* value, then that member is considered to have sustained moderate to severe damage per the analysis, otherwise, it is classified as only having light to moderate damage. The computational rotations presented here were taken from the springs in each direction of loading separately and were not combined for bi-directional effects. Bi-directional combination of rotation results are discussed in Section 4.3.3 for column demands, where the peak rotation demands at a column end from each direction are combined using the square-root of sum of squares method (SRSS).

This publication is available free of charge from: https://doi.org/10.6028/NIST.GCR.22-917-50

This publication is available free of charge from: https://doi.org/10.6028/NIST.GCR.22-917-50

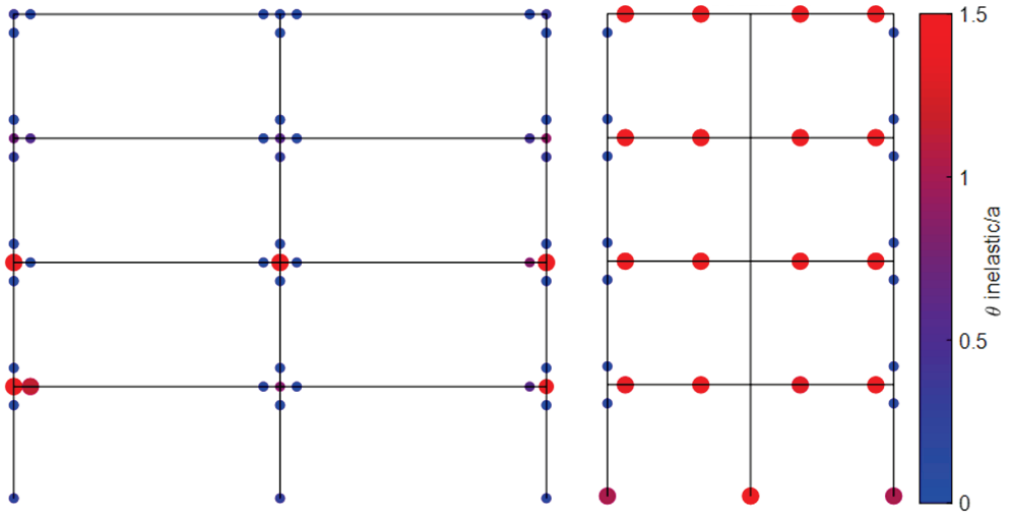


Figure 4-20 NDP OpenSees LP NJ: Schematic damage distribution in frame at Gridline 1 (left) and wall at Gridline C (right) based on deformation criteria $\theta_{inelastic}/a$.

Figures 4-21 through 23 compare OpenSees LP NJ model results to measurements from the experiment: distribution of maximum story drifts over the building heights in Figure 4-21, roof drift ratio histories in Figure 4-22, and first story drift ratio histories in Figure 4-23. The roof drift ratio is defined as the roof lateral drift with respect to the foundation divided by the total building height of 12 m (39.37 ft.).

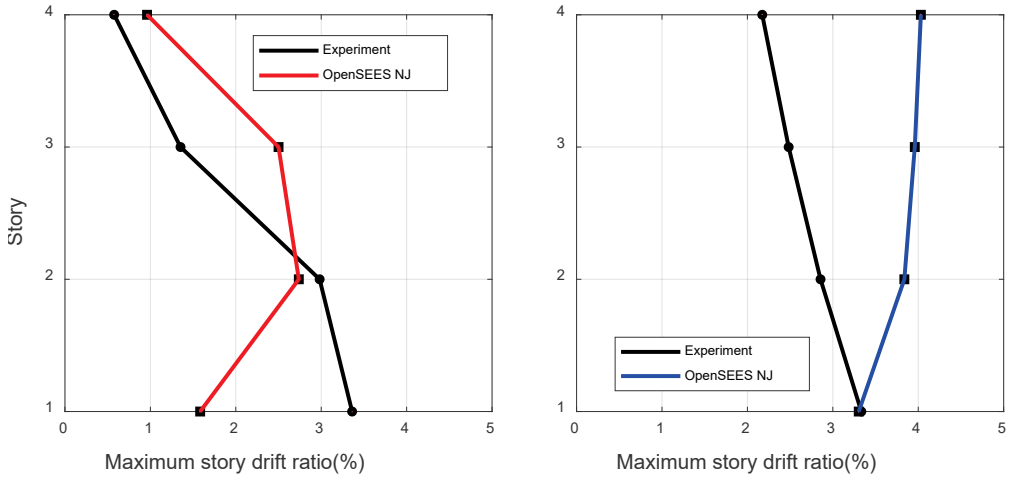


Figure 4-21 NDP OpenSees LP NJ: Maximum drift ratio comparison over the height of the building for 100% JMA-Kobe in frame direction (left) and wall direction (right).

This publication is available free of charge from: https://doi.org/10.6028/NIST.GCR.22-917-50

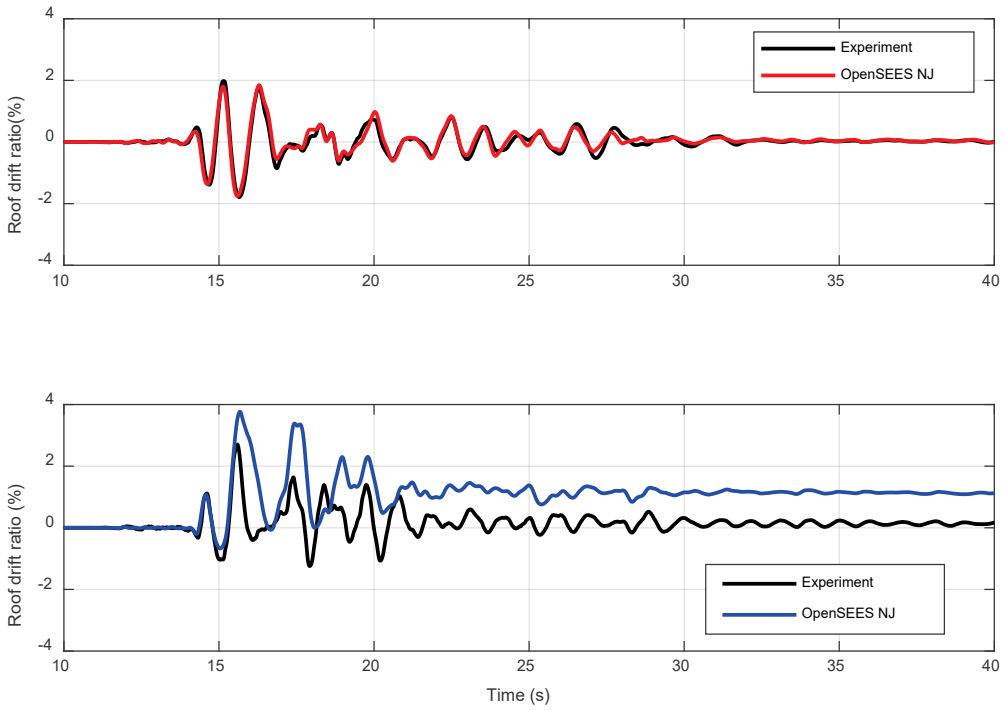


Figure 4-22 NDP OpenSees LP NJ: Roof drift ratio history comparison for 100% JMA-Kobe, in frame direction (top), and wall direction (bottom).

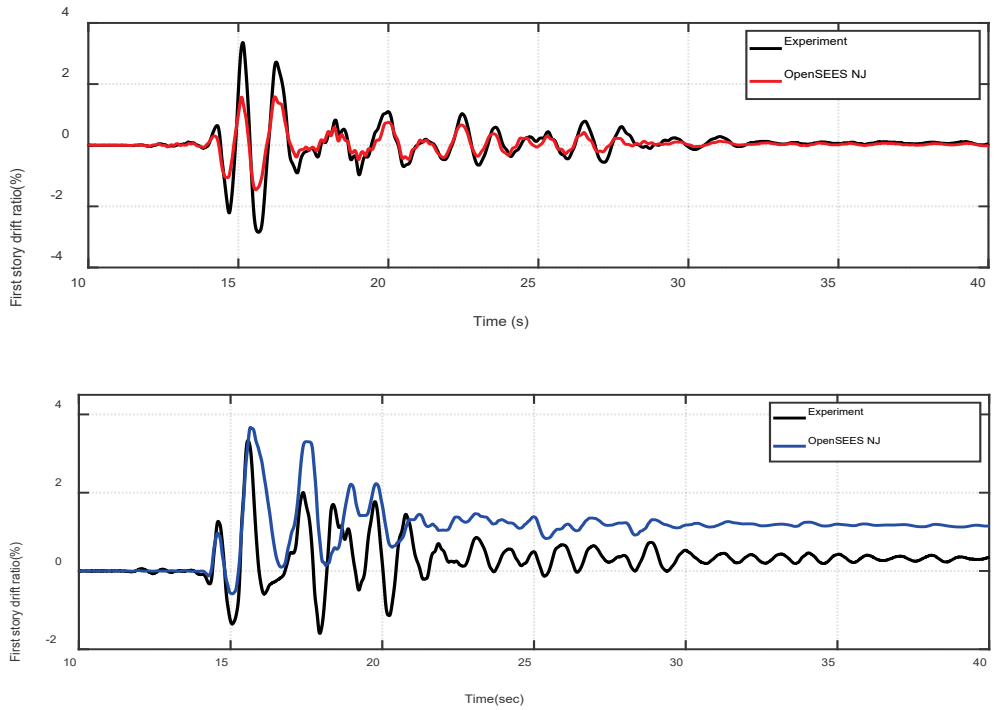


Figure 4-23 NDP OpenSees LP NJ: First-story drift ratio history comparison for 100% JMA-Kobe, in frame direction (top), and wall direction (bottom).

Frame Direction

In the frame direction, the computational model concentrates inelastic deformations and associated damage in the beam-column joints of the first two floors and particularly the exterior joints (Figure 4-21). In contrast, the experiment only showed severe joint damage in the second floor and mainly in the interior joints (Figure 4-9).

The discrepancy in the first story maximum drift ratio between model and experiment is significant (Figure 4-22). The maximum first story drift ratio is 3.36% experimentally and 1.60% computationally (a difference of 52%). This observation is attributed mainly to bi-directional effects on the columns in the first story and is discussed in Section 4.4.4 where Perform3D model results are presented that accounted for bi-directional effects. On the other hand, the maximum drift ratios in the upper stories are similar for the experiment and model in the frame direction. The roof drift ratios from the model are also in good agreement with the experimental drift ratios in the frame direction, as shown in Figure 4-22.

Wall Direction

In the wall direction, Figure 4-21 indicates that the model predicts a damage distribution that is significantly different from the experimental one (Figure 4-9), particularly in the beams. Figure 4-23 on the other hand indicates that the maximum drift ratios in the first story of the wall direction are in good agreement between model and experiment (a difference of 2%), but the profiles along building height of the maximum story drift ratio differ significantly. The profile of the experimental drifts indicates a coupled wall behavior whereby story drifts reduce with building height. This is contrary to the drift profile obtained from the model, which indicates more of a cantilever wall behavior with increasing drifts at higher stories. The maximum roof drift ratio estimated in the wall direction was 37% larger than the experimental value.

The model captures the damage levels at the base of the shear walls and first-story columns. However, the model predicts severe strength loss in beams framing into the walls at all floor levels, whereas the experiment showed moderate damage at the second floor and limited damage at higher floors in those beams (Figure 4-9). This indicates that beams may have lost strength prematurely in the model, decoupling the frames from the walls and altering the behavior from a coupled wall behavior to more of a cantilever behavior. Results therefore indicate that beam modeling parameters in ASCE 41-17 may be too conservative, resulting in beams losing strength prematurely. Moreover, sliding of the walls at their base in the experiment altered the drift profile over the height of the building. The model does not capture wall sliding at the base, a mechanism not treated in ASCE 41-17.

This publication is available free of charge from: https://doi.org/10.6028/NIST.GCR.22-917-50

This publication is available free of charge from: https://doi.org/10.6028/NIST.GCR.22-917-50

Natural Periods

The building first mode periods at the beginning and end of the 100% JMA-Kobe motion are compared in Table 4-3. The computational model produces larger periods in both directions than measured experimentally prior to the 100% JMA-Kobe motion. Almost all first story columns sustained limited flexural yielding during the 50% JMA-Kobe motion in the building, while other members reached lower loads and cracking levels (Nagae et al., 2015; Kwon and Ghannoum, 2016). ASCE 41-17 specifies member stiffness values corresponding to a secant stiffness at yield. Since concrete members soften gradually as their load increases to yield (Elwood and Eberhard, 2009; Kwon and Ghannoum, 2016), the softer predicted response of the building in both directions could be attributed to this difference in assumed cracking level in the various members prior to the application of the 100% JMA-Kobe motion. It is noted that all columns were under low axial loads such that their simulated flexural rigidities were around the lower bound value in ASCE 41-17 of $0.3E_{cE}I_{g}$.

The model softens the response in the frame direction due to 100% JMA-Kobe motion by a similar amount as recorded experimentally (Table 4-3), which indicates the model and experiment sustained similar levels of member softening. In the wall direction, however, the model does not soften the first mode period as much as recorded in the experiment. This implies that the model predicts lower level of member softening, which may have been caused by inaccuracies in the modeling of the degrading behaviors of members or the different simulated damage mechanism than the base sliding mechanism observed in the experiment.

Table 4-3 Period Comparison after 50% JMA-Kobe and 100% JMA-Kobe Ground Motion

	Experiment		OpenSees LP NJ Model	
	Frame Direction	*Wall Direction*	*Frame Direction*	*Wall Direction*
First mode period at the beginning of 100% JMA-Kobe (sec.)	0.43	0.31	0.64	0.40
First mode period at the end of 100% JMA-Kobe (sec.)	0.99	0.88	1.33	0.63

Base Shear

Figure 4-24 indicates reasonably good agreement in the base shear history between the OpenSees LP NJ model and experimental results, albeit underestimating peak demand. The maximum base shear predicted by the model was 12% lower in the frame direction and 20% lower in the wall direction compared with experimental values.

This publication is available free of charge from: https://doi.org/10.6028/NIST.GCR.22-917-50

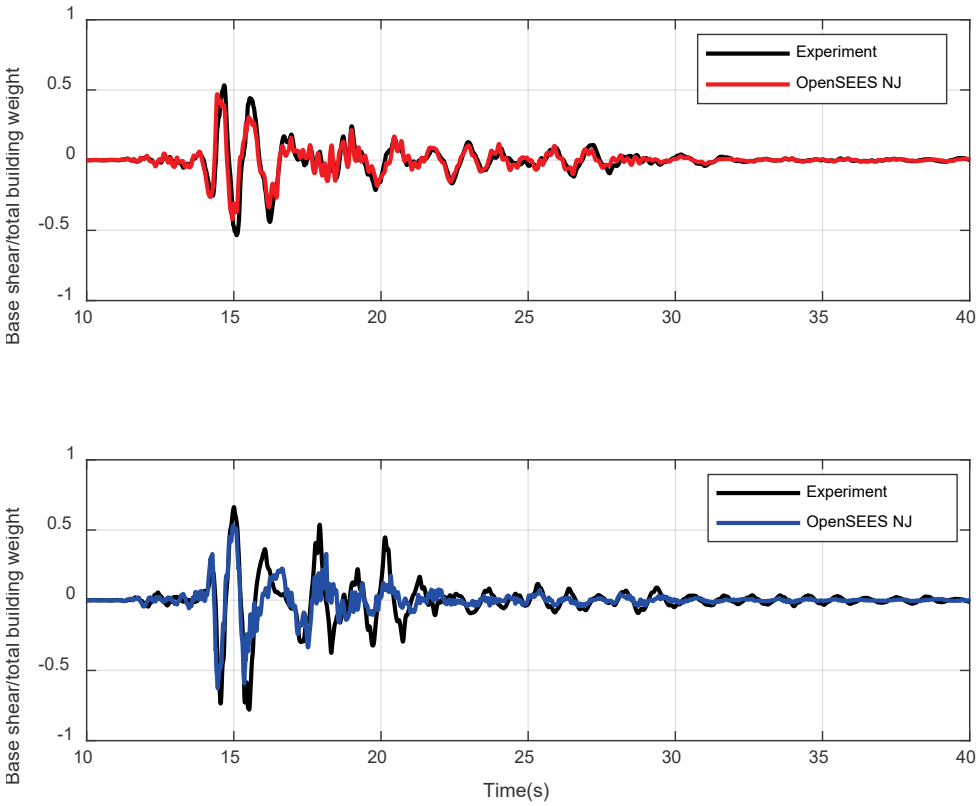


Figure 4-24 NDP OpenSees LP NJ: Normalized base shear history for 100% JMA-Kobe, in frame direction (top), and wall direction (bottom).

Floor Accelerations

Figure 4-25 compares the maximum floor accelerations from the NJ model and experiment. The figure indicates general agreement in the acceleration profile at the lower levels but not at the higher floor levels. In the wall direction, the acceleration profiles differ greatly, with the maximum floor accelerations in the second floor being about 60% lower in the model than in the experiments. One possible explanation for this disconnect is that the walls slid at their base in the experiment while they did not in the model. Sliding is a mechanism that tends to produce acceleration spikes when the sliding reverses direction. The roof accelerations in both directions, however, are in good agreement between model and experiment (Figure 4-26).

This publication is available free of charge from: https://doi.org/10.6028/NIST.GCR.22-917-50

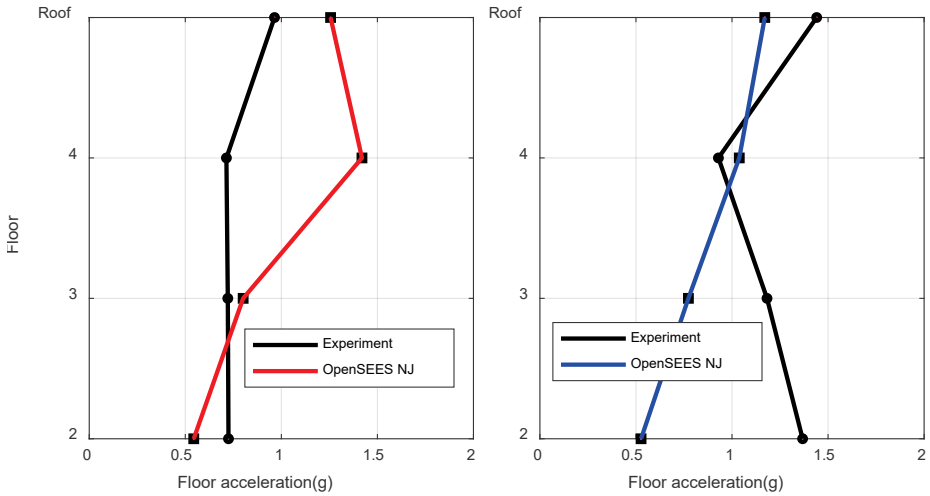


Figure 4-25 NDP OpenSees LP NJ: Maximum floor accelerations over the height of the building for 100% JMA-Kobe, in frame direction (left), and wall direction (right).

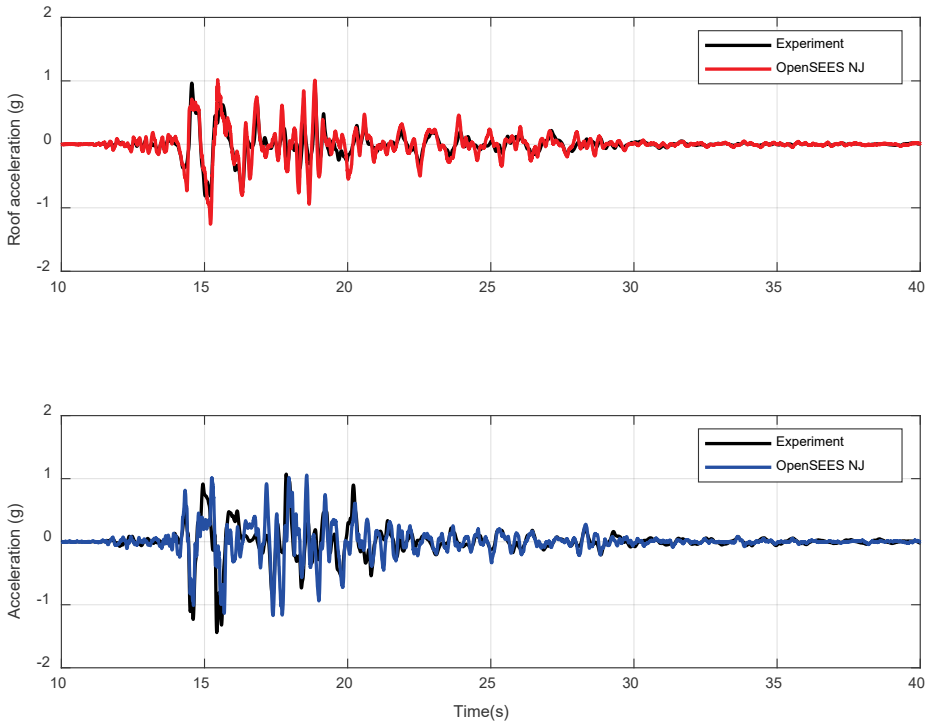


Figure 4-26 NDP OpenSees LP NJ: Roof acceleration time histories for 100% JMA-Kobe, in frame direction (top), and wall direction (bottom).

4.3.3 Global Performance: OpenSees LP Models vs. Observation

The OpenSees LP NJ model was modified to have elastic joint elements, which are not allowed to yield or lose strength (OpenSees LP EJ model). In light of the noted premature joint strength loss that occurred in the OpenSees LP NJ model, this

OpenSees LP EJ model is considered to investigate the effects of preventing joint failures on demands in adjacent members.

The damage distribution derived from the computational OpenSees LP EJ model in the same method as for Figure 4-20 is presented in Figure 4-27. The wall direction damage distribution is almost identical for this model as for the OpenSees LP NJ model as joints remained elastic in both cases in that direction. In the frame direction, the second and third floor beams are more severely damaged in the model with elastic joints than in the OpenSees LP NJ model or in the experiment. In addition, an increased, yet still moderate damage level is observed in the second and third story interior columns in the model with elastic joints compared to the OpenSees LP NJ model. When nonlinear joints are used, the damage concentrated in the joints which unloads the beams and columns as seen in the OpenSees LP NJ model. When joints are prevented from losing strength, the damage concentrates more in the beams than the columns, which was evident in models with elastic joints.

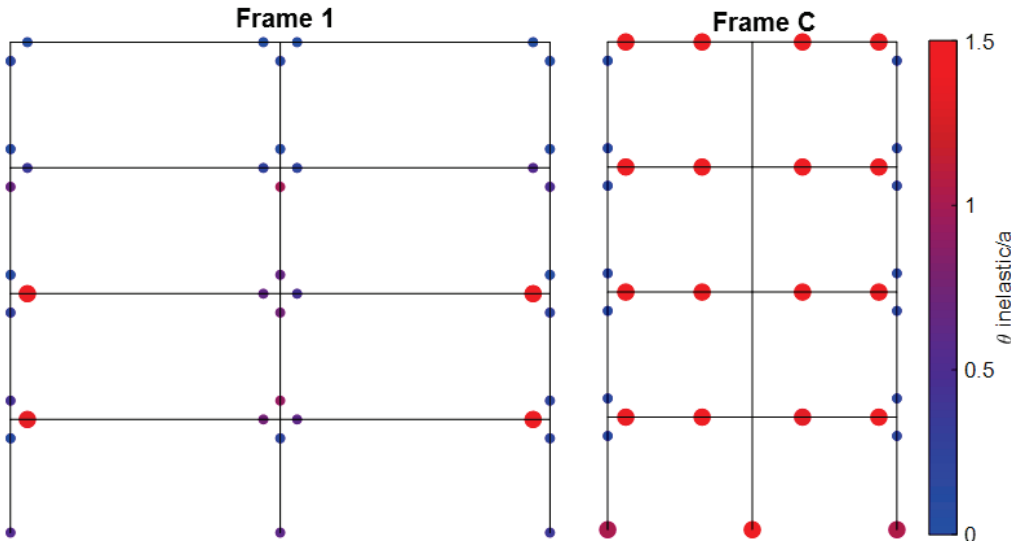


Figure 4-27 NDP OpenSees LP EJ: Schematic damage distribution in the frame at Gridline 1 (left) and the frame at Gridline C (right) based on deformation criteria $\theta_{inelastic}/a$ for the model with elastic joints.

Figure 4-28 presents a comparison of OpenSees LP model results and the experiment for distribution of maximum story drifts over the building height, showing that joint modeling did not alter the wall direction drift results measurably. However, in the frame direction, modeling joints elastically resulted in significant increases in maximum story drift demands (in excess of 30% in the second story) from those of the model with nonlinear joints. Since the beams sustained severe damage when adjacent joints were prevented from losing strength, this increase in story drift demand may be attributed to the more rapid strength degradation that beams sustained compared to joints based on current ASCE 41-17 modeling parameters.

This publication is available free of charge from: https://doi.org/10.6028/NIST.GCR.22-917-50

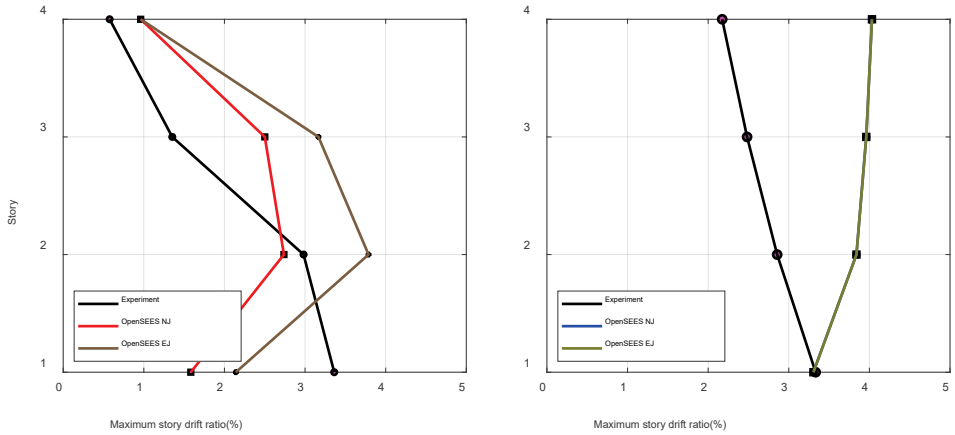


Figure 4-28 NDP OpenSees LP: Maximum drift ratio comparison for OpenSees LP NJ and EJ models over the height of the building for 100% JMA-Kobe, in frame direction (left) and wall direction (right).

Findings from comparing the OpenSees LP NJ and EJ models highlight the importance of using accurate unbiased modeling parameters in nonlinear analysis to avoid skewing building demands, component demands, and damage distributions.

4.3.4 Global Performance: OpenSees Fiber Models vs. Observation

Global Mechanism and Damage Distribution

Damage distribution data are compared in order to assess the extent to which the OpenSees fiber section models with elastic (EJ) and nonlinear joints (NJ) were able to capture the overall building deformation mechanisms and damage distribution. To this end, Figure 4-29 presents model results, in a layout similar to Figure 4-27, and illustrates the level and distribution of experimental damage. In both models damage was severe in beam elements in the wall direction. The nonlinear joint model showed significant damage in exterior beam-column joints that reduced the severity of the beam element damage. In neither model did the columns or the walls experience severe damage.

This publication is available free of charge from: https://doi.org/10.6028/NIST.GCR.22-917-50

This publication is available free of charge from: https://doi.org/10.6028/NIST.GCR.22-917-50

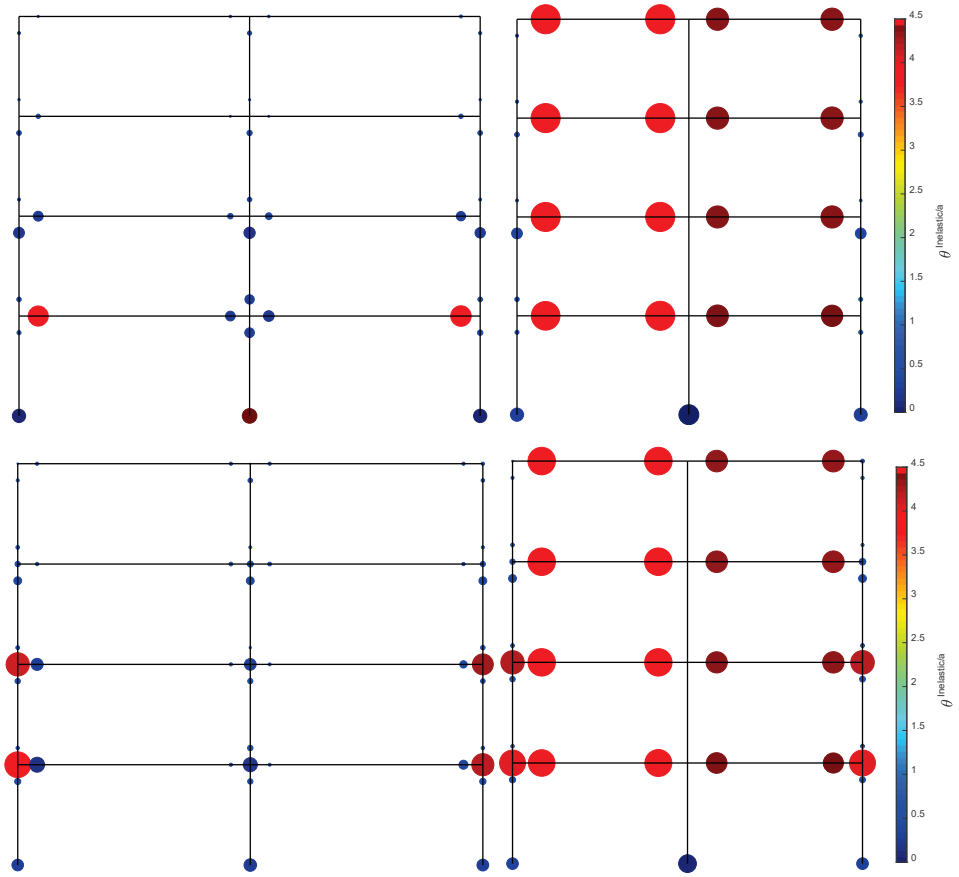


Figure 4-29 NDP OpenSees Fiber: Schematic damage distribution from OpenSees Fiber EJ (top row) and OpenSees Fiber NJ (bottom row) models in frame at Gridline 1 (left) and wall at Gridline C (right) based on deformation criteria $\theta_{inelastic}/a$.

Distribution of maximum story drifts over the building heights are compared between the OpenSees Fiber NJ model and experiment in Figure 4-30, roof drift ratio histories are compared in Figure 4-31, and the first story drift ratio histories in Figure 4-32.

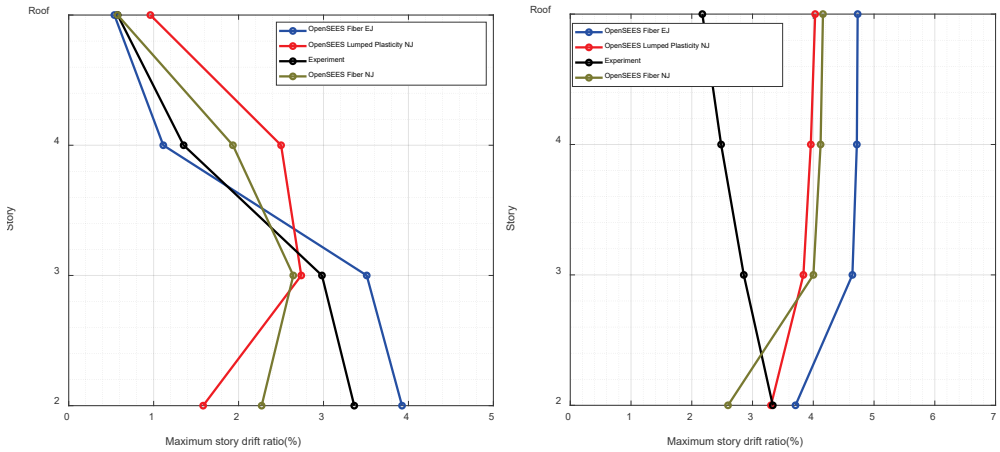


Figure 4-30 NDP OpenSees: Maximum drift ratio comparison over the height of the building after 100% JMA-Kobe, in frame direction (left) and wall direction (right).

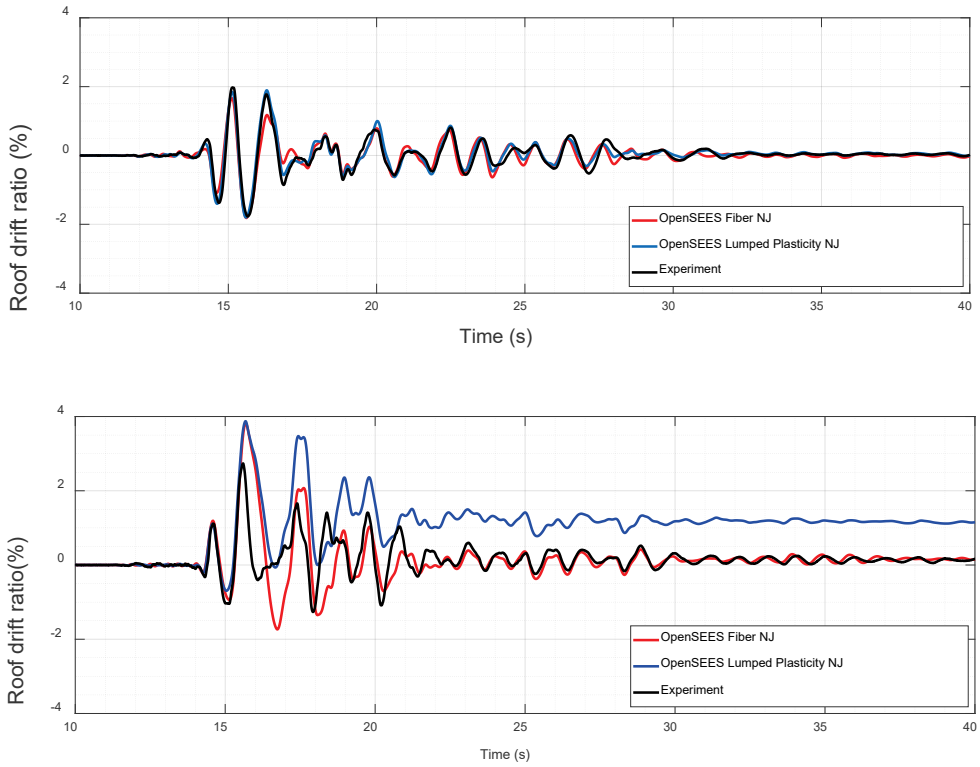


Figure 4-31 NDP OpenSees: Roof drift ratio history comparison for 100% JMA-Kobe, in frame direction (top), and wall direction (bottom).

This publication is available free of charge from: https://doi.org/10.6028/NIST.GCR.22-917-50

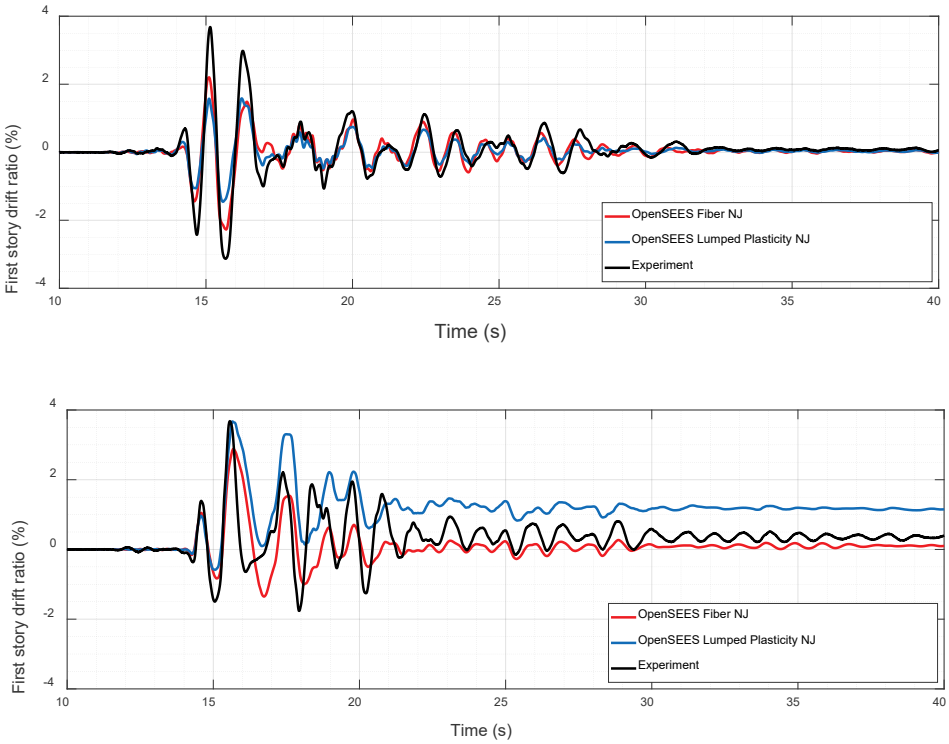


Figure 4-32 NDP OpenSees: First-story drift ratio history comparison for 100% JMA-Kobe, in frame direction (top), and wall direction (bottom).

Frame Direction

In the frame direction, the model that provided the closest match to the maximum drift ratio profile was the fiber section model with elastic joints. Drift ratio profiles for the lumped plascity and fiber section models with nonlinear joints were similar. Both of them underestimate the drift ratio in the first story and overestimate the drift ratio in the upper two stories. While the computational model concentrates inelastic deformations and associated damage in the beam-column joints of the first two floors, and particularly the exterior joints (Figure 4-30), the experiment only showed severe joint damage in the second floor and mainly in the interior joints (Figure 4-9). In that respect the fiber section model with elastic joints was a more accurate representation of the behavior of the building

Maximum drift ratios at the roof level were similar for the experiment and all models in the frame direction (Figure 4-30 and 4-31), and the two fiber section models were more accurate than the lumped-plasticity model.

Wall Direction

In the wall direction, Figure 4-30 indicates that similar to the lumped plascity model, the fiber models produced a damage distribution different from the experiment (Figure 4-9). Figures 4-30 and 4-32 show that the most accurate estimate of

This publication is available free of charge from: https://doi.org/10.6028/NIST.GCR.22-917-50

maximum drift ratios in the first story of the wall direction was obtained with the lumped-plasticity model. The fiber section model with inelastic joints underestimated the drift ratio in the first story (Figures 4-30 and 4-31) and the fiber section model with elastic joints overestimated the drift ratio (Figure 4-30). Maximum story drift ratios over the building height for all three OpenSees models differed significantly with the measured results. The shape of the profile was similar for the three models and was indicative of cantilever wall behavior with increasing drifts at higher stories. The nature of the discrepancy and the consistency between OpenSees models lend creadance to the hypothesis that beams may have lost strength prematurely in the model, decoupling the frames from the walls and altering the behavior from a coupled wall behavior to more of a cantilever behavior. Also, none of the OpenSees models simulated sliding of the wall at the base, which was observed during the test.

Natural Periods

Building fundamental periods at the beginning of the 100% JMA-Kobe motion are presented in Table 4-4 and compared with calculated periods from the lumped-plasticity and fiber section models. The lumped-plasticity model produced the largest periods in both directions, which was expected due to effective stiffness factors used in the lumped-plasticity model. Periods calculated with the fiber section models were slightly lower than those calculated with the lumped-plasticity model and generally higher than those measured experimentally. As previously stated, almost all first story columns sustained limited flexural yielding during the 50% JMA-Kobe motion in the building, while other members reached lower loads and cracking levels (Nagae et al., 2015; Kwon and Ghannoum, 2016).

Table 4-4 Period Comparison for Different OpenSees Models

Period	Frame Direction	Wall Direction
Experiment - First mode period at the beginning of 100% JMA-Kobe	0.43 sec.	0.31 sec.
OpenSees LP NJ Model	0.64 sec.	0.40 sec.
OpenSees Fiber EJ and NJ Models	0.56 sec.	0.30 sec.

This publication is available free of charge from: https://doi.org/10.6028/NIST.GCR.22-917-50

This publication is available free of charge from: https://doi.org/10.6028/NIST.GCR.22-917-50

Base Shear

Figure 4-33 indicates reasonably good agreement in the base shear history between the OpenSees Fiber NJ model and experimental results, with greater accuracy in the range of strongest shaking (15 sec. to 22 sec.) for the frame direction. The maximum base shear calculated with the model was approximately 20% lower in both directions compared with experimental values. Possibly, strain rate effects may have caused increased strengths in the building as discussed by Kwon (2016). The retraining effects of the slab system on beams with associated axial forces in the beams may also contribute to higher than expected strength.

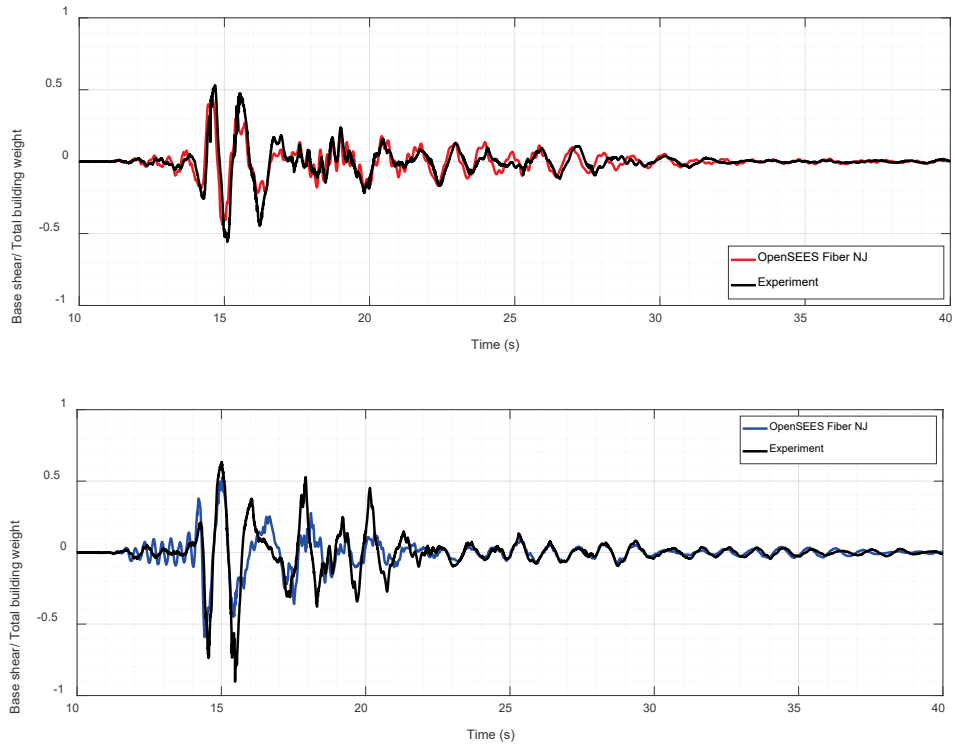


Figure 4-33 NDP OpenSees Fiber NJ: Normalized base shear history for 100% JMA-Kobe, in frame direction (top), and wall direction (bottom).

Floor Accelerations

Figure 4-34 compares the maximum floor accelerations from the OpenSees LP NJ, Fiber NJ, and Fiber EJ models with the peak values measured during the experiment. In the frame direction, both fiber section models had higher acceleration in the lower two stories than the lumped-plasticity model, lower than the lumped plasticiy model in the top two stories. The shape of the profiles from the fiber section models was similar to the shape of the experimental profile, although both fiber models had higher accelerations over the height of the building. Among the two fiber section models, the model with elastic joints had the closest match in terms of magnitude, with the most accurate estimates of peak acceleration calculated in the second story and the roof. The shape of the profile from OpenSees Fiber NJ model was the closest

to the experimental profile, but resulted in accelerations approximately 25% higher than the measured values in all stories. In the wall direction, the OpenSees Fiber EJ model provided very accurate estimates of peak acceleration in all stories. The acceleration profile from OpenSees Fiber NJ was very similar with the acceleration profile from OpenSees LP NJ. Both models were in close agreement with measured accelerations for the upper two stories and significantly underestimated the peak acceleration in the lower two stories. Maximum floor accelerations in the first floor wall direction were approximately 47% lower in OpenSees Fiber NJ than in the experiment, and 62% lower in OpenSees LP NJ. Roof accelerations in both directions, were in good agreement between model and experiment (Figures 4-34 and 4-35).

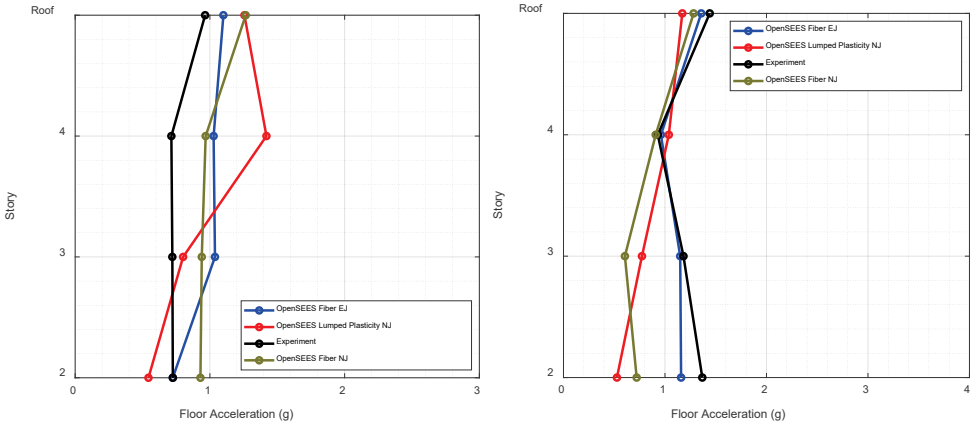


Figure 4-34 NDP OpenSees: Maximum floor accelerations over the height of the building for 100% JMA-Kobe, in frame direction (left), and wall direction (right).

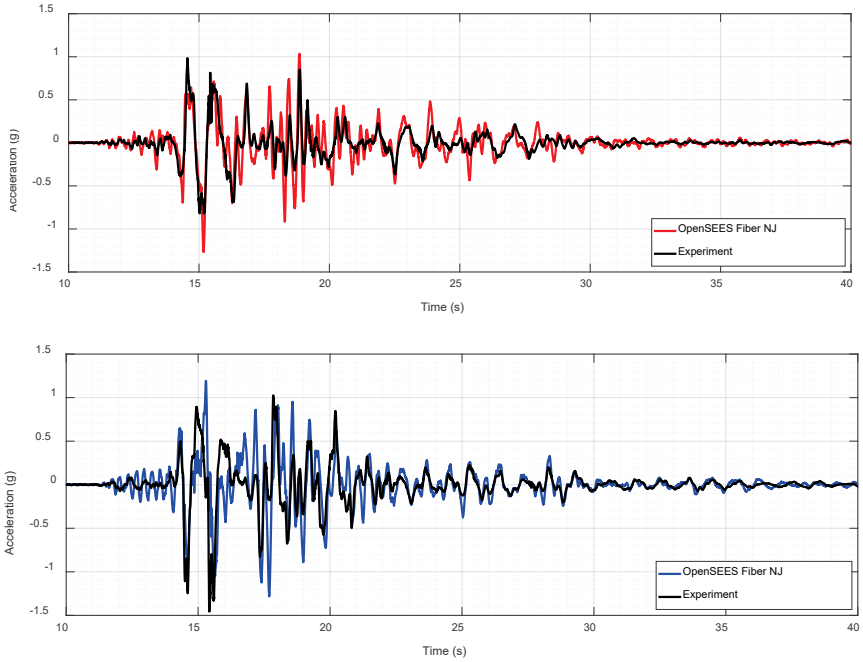


Figure 4-35 NDP OpenSees Fiber: Roof acceleration histories for 100% JMA-Kobe, in frame direction (top), and wall direction (bottom).

This publication is available free of charge from: https://doi.org/10.6028/NIST.GCR.22-917-50

4.3.5 *Component Performance: OpenSees LP NJ Model vs. Observation*

The component level comparisons are based on the damage states of the members at the end of the 100% JMA-Kobe motion. Figure 4-36 illustrates the moment-rotation behavior of frame components at the frame at Gridline C illustrating the degree of inelastic action and strength degradation of the Opensees LP NJ model. Similarly, Figure 4-37 illustrates the moment-rotation behavior of beam-column joints in the frame direction at the second floor and Figure 4-38 illustrates the response of the shear walls at their base.

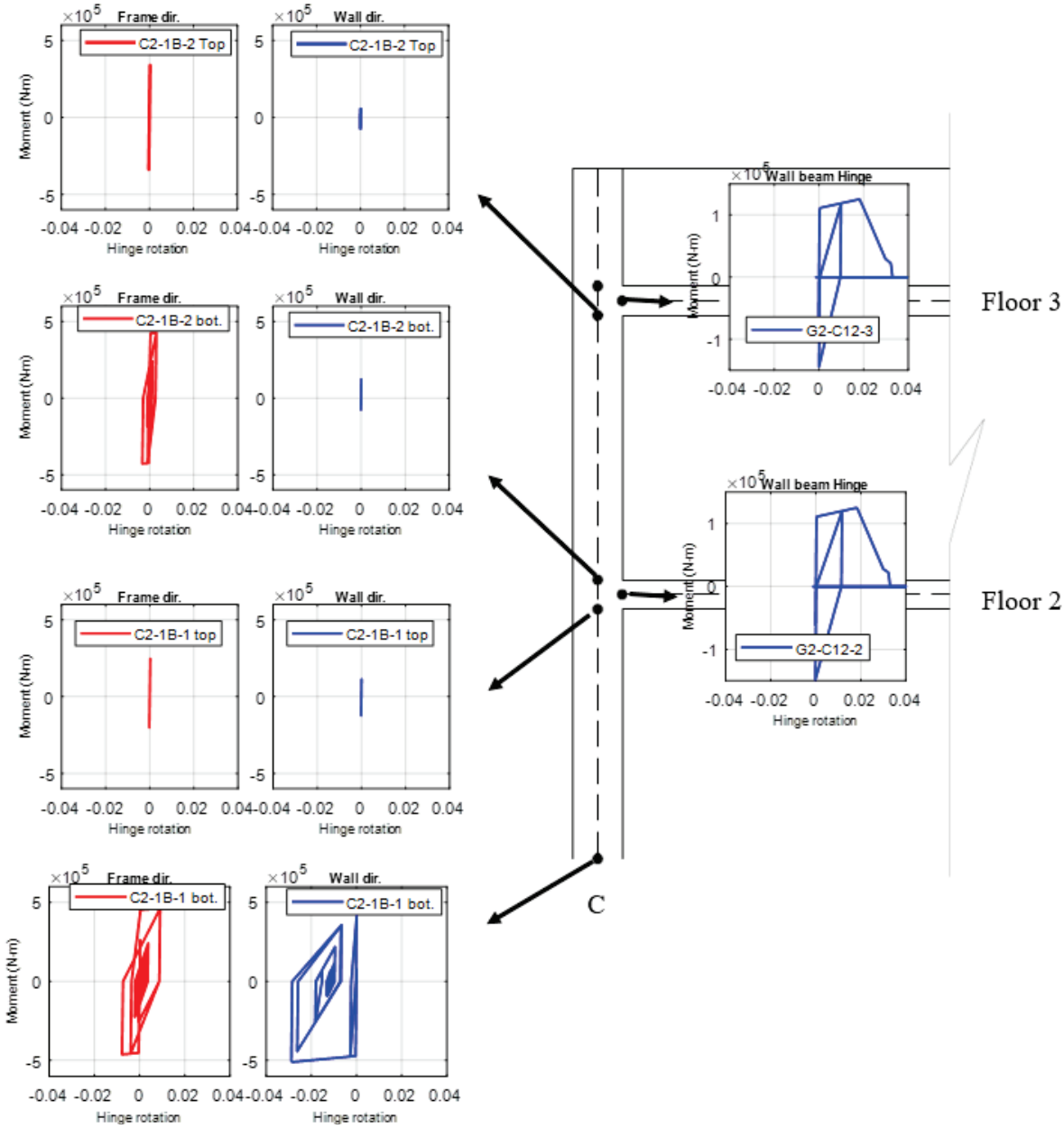


Figure 4-36 NDP OpenSees LP NJ: Computed moment vs rotation behavior of hinges in the frame at Gridline 2 for the 100% JMA-Kobe motion.

This publication is available free of charge from: https://doi.org/10.6028/NIST.GCR.22-917-50

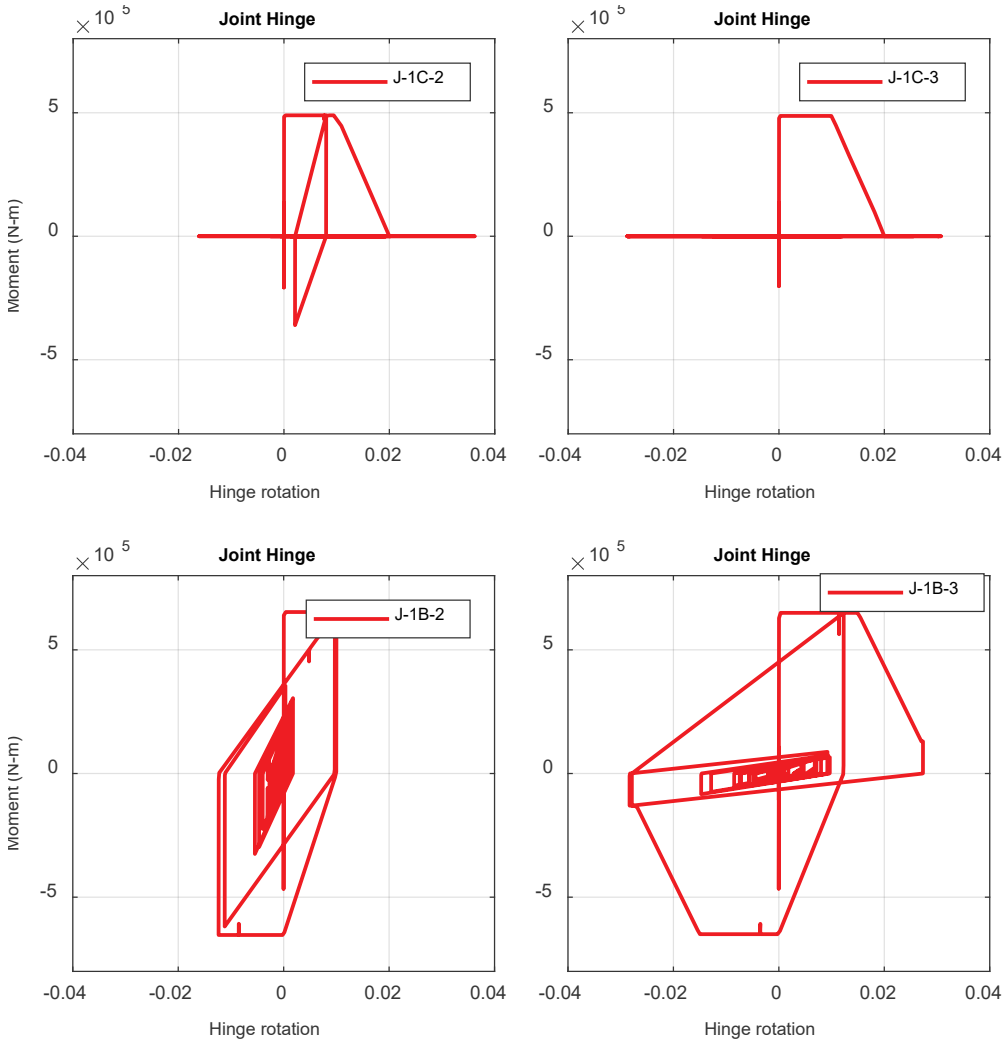


Figure 4-37 NDP OpenSees LP NJ: Computed moment vs rotation plots for the beam-column joint hinges of exterior joints (top) and interior joints (bottom) at Gridline 1.

In the following sections, component maximum inelastic rotations in the hinges at the end of the analysis are normalized by their modeling parameters *a* and *b* from ASCE 41-17 to categorize their damage level and compared with the Immediate Occupancy (IO), Life Safety (LS), and Collapse Prevention (CP) acceptance criteria from ASCE 41-17. The total rotation of the member was obtained by summing the spring rotation at the end of the dynamic analysis and yield rotation due to linear elastic element.

This publication is available free of charge from: https://doi.org/10.6028/NIST.GCR.22-917-50

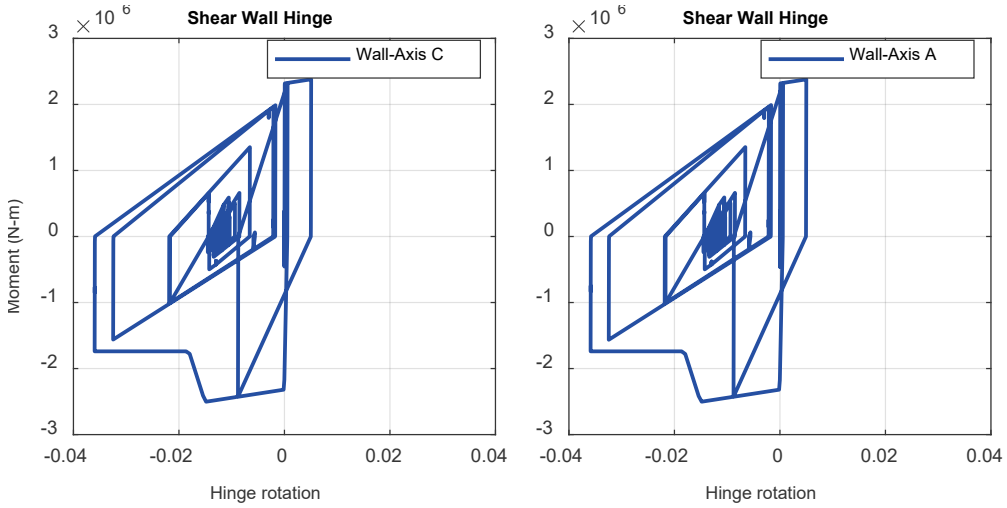


Figure 4-38 NDP OpenSees LP NJ: Computed moment vs rotation plots for the shear wall hinges at wall base at Gridline C (left) and Gridline A (right).

Columns

To better assess the demand on the columns, bi-directional effects were considered by applying the SRSS method to the maximum inelastic rotations, $\theta_{inelastic}$, of each direction spring at a given column end. Figure 4-39 plots the maximum SRSS-combined inelastic rotations between top and bottom for columns in the first story normalized by each element's modeling parameters. The figure also indicates the acceptance criteria from ASCE 41-17. As can be seen in the figure, moderate to severe damage is predicted for the first story columns, with inelastic rotations exceeding the *a* parameter for all columns and reaching deformation levels that place them in between a LS and CP performance objective. Observed damage is consistent with model predictions. It is noted here that without combining the maximum rotational demands from both directions, the first story column demands in the model are relatively low in the frame direction compared with experimental observations (Figure 4-8, Figure 4-13). This observation indicates that accounting for bi-directional effects is simulation is useful for this building.

This publication is available free of charge from: https://doi.org/10.6028/NIST.GCR.22-917-50

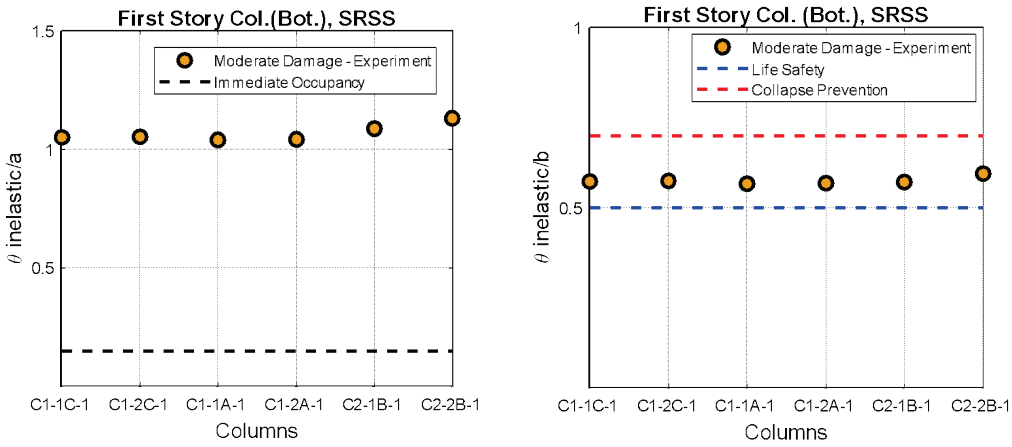


Figure 4-39 Column deformation criteria: $\theta_{inelastic}/a$ (left), $\theta_{inelastic}/b$ (right).

Shear Walls

The damage at the base of the structural walls was severe from both experimental and computational results (Figure 4-40). The walls experienced sliding after severe boundary damage and crushing in the experiment (Nagae et al., 2015). Therefore, ASCE 41-17 provisions identified the correct initial mode of degradation but not the second one; since wall sliding is not treated in the standard.

Results from ASCE 41-17 analyses indicate that the walls substantially exceeded their *b*-values and CP acceptance criteria at their base, and therefore should be at risk of loosing axial capacity (Figure 4-30). ASCE 41-17 would therefore have triggered retrofit for the walls at the CP performance objective. In the experiment on the other hand, even though the walls sustained severe damage, they maintained sufficient reserve strength to withstand two additional high-intenstity ground motions without collapse, likely placing them between the LS and CP performance objectives per ASCE 41-17 definition of the acceptance criteria. The findings therefore indicate that ASCE 41-17 wall provisions for flexure-controlled walls may be conservative.

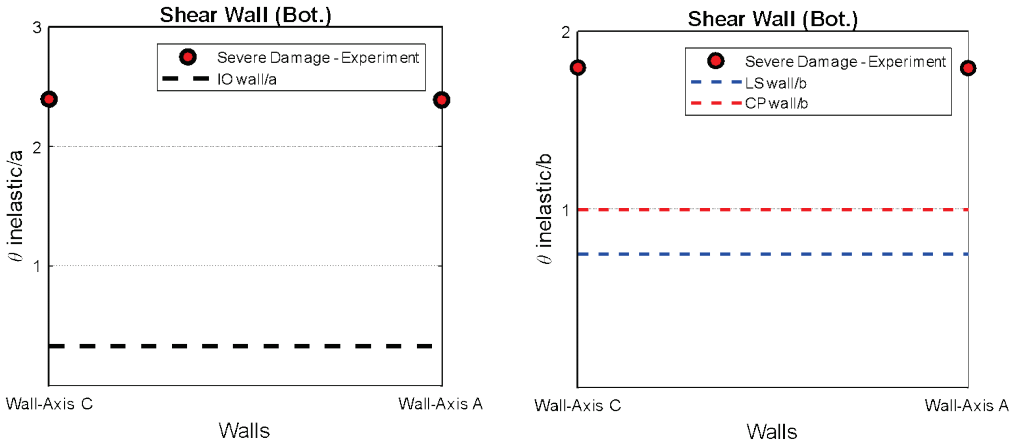


Figure 4-40 Wall deformation criteria: $\theta_{inelastic}/a$ (left), $\theta_{inelastic}/b$ (right).

This publication is available free of charge from: https://doi.org/10.6028/NIST.GCR.22-917-50

Beams

The OpenSees NJ model predicts severe damage in half of the beam hinges on the second floor in the frame direction. This is contradictory with the experimental evidence that indicated moderate beam damage on the second floor (Figure 4-41). For all the beams connected to the walls and throughout all the floors, the OpenSees NJ model predicts severe damage, which contradicts the observed moderate damage in the second and third floor beams and limited damage for the higher floors. The observed discrepancies indicate that the beam modeling parameters and acceptance criteria may be too low for the beams of this building.

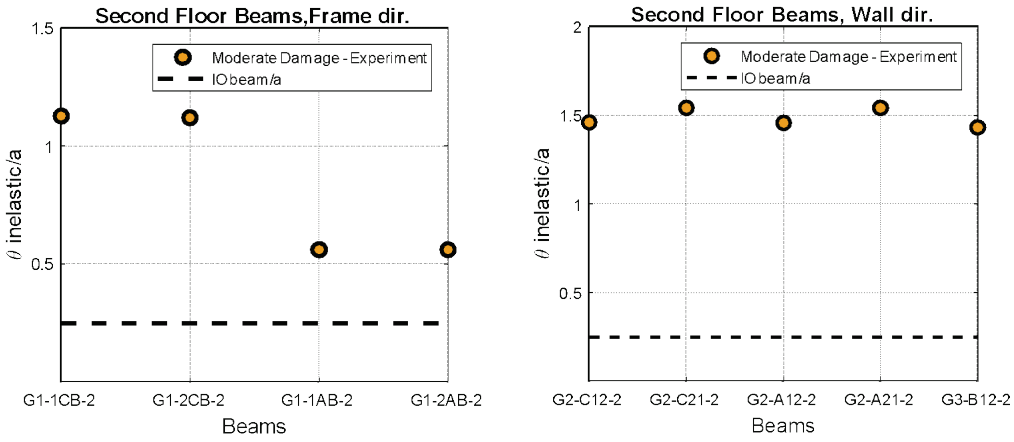


Figure 4-41 Beam deformation criteria: $\theta_{inelastic}/a$.

Beam-Column Joints

The OpenSees NJ model indicates severe damage in the exterior beam-column joints of the second floor and moderate damage for interior joints on the second floor. This is at odds with the observed moderate damage in the exterior joints and severe damage in the interior joints (Figure 4-42). Exterior joints in the second floor lost strength substantially, which effectively pinned the joint connection, thereby curtailing moment transmission to the first story columns. The findings highlight that more conservative modeling parameters (i.e., those that cause elements to fail prematurely) can lead to unconservative lowered demands on other members. Joint shear strength and nonlinear modeling parameters may benefit from updates to ASCE 41-17 based on these findings.

This publication is available free of charge from: https://doi.org/10.6028/NIST.GCR.22-917-50

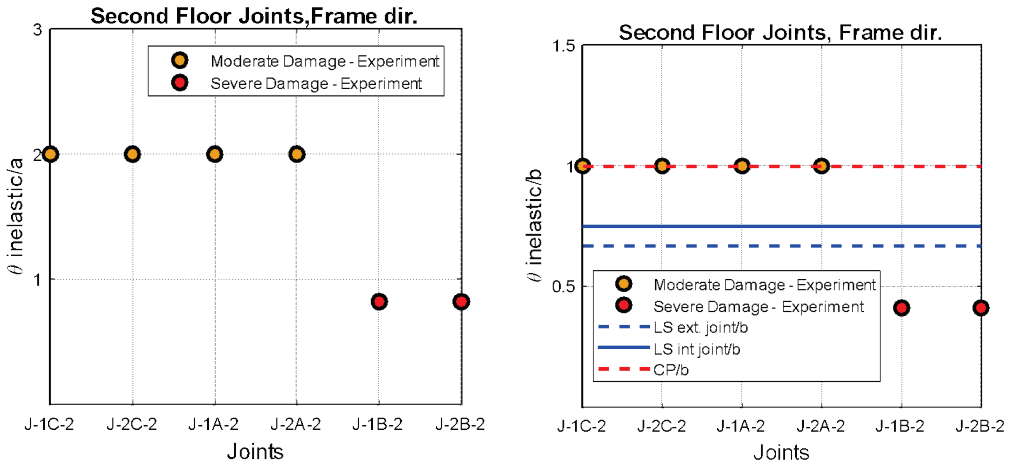


Figure 4-42 Joint deformation criteria: $\theta_{inelastic}/a$ (left) and $\theta_{inelastic}/b$ (right).

4.3.6 Summary Findings

Overall, the models with nonlinear joints matched experimental data and damage distribution more closely than models with linear joints. Where joints were modeled linearly, nonlinear deformations concentrated in the adjacent second floor beams, causing larger damage estimates than was observed experimentally. In the experiment, joint degradation concentrated deformations in the joints at the second floor easing demands on adjacent members.

In the frame direction, both lumped-plasticity and fiber section NJ models under-estimated drifts in first story and damage in the first story columns. On the other hand, corner column damage was overestimated in the LP model in the wall direction first story, but matched experimental observations for the fiber section model. Bi-directional effects were very pronounced on the corner columns in the experiments, which may have lead to the lumped-plasticity model not capturing corner column behavior as well as the fiber section model.

In all models, damage was overestimated in many beams, particularly the one in the wall direction. This indicates that modeling parameters and acceptance criteria for beams may be too conservative in ASCE 41-17.

Wall sliding was not captured by any model as it is not currently treated in ASCE 41-17. Not capturing this mechanism altered the drift profile over building height in the models compared with the experiment.

4.4 Nonlinear Dynamic Procedure using Perform3D

Perform3D models were developed per ASCE 41-17 as discussed in Appendix A. Two models were developed on this platform. The models were identical except for the beam-column joint elements: one with nonlinear joint elements (Perform3D NJ) and one with linear elastic joint elements (Perform3D EJ).

This publication is available free of charge from: https://doi.org/10.6028/NIST.GCR.22-917-50

Perform3D models utilized lumped-plasticity hinges with P-M-M interaction for columns and fiber elements for the walls.

4.4.1 Modeling Approach

Figure 4-43 shows the three-dimensional Perform3D model used for the dynamic analysis. Gravity loads were defined with distributed line loads on beam elements and mass was divided based on tributary area at each floor level. Modal damping of 1.8 % and Rayleigh damping of 0.2%, for a total of 2% were introduced in the model. ASCE 41-17 limits the damping to 3% but 2% is selected since the structure did not have any partition walls or cladding.

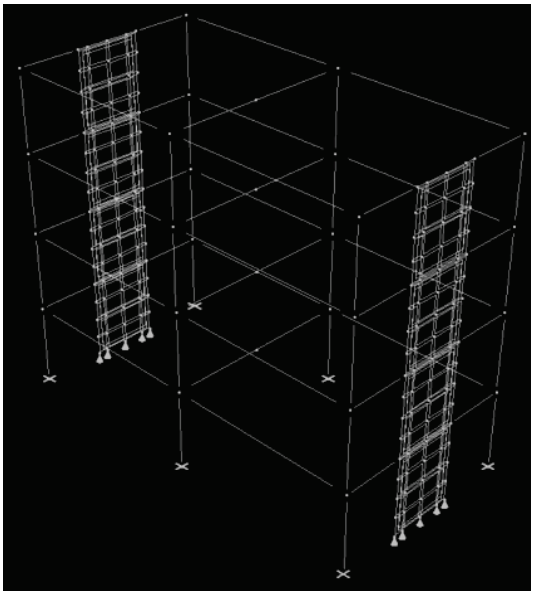


Figure 4-43 Nonlinear analysis model in Perform3D.

The model was developed as follows:

- Walls were modeled with Shear Wall Element in Perform3D at all stories. Each shear wall element mesh included distributed nonlinear vertical fibers and a nonlinear shear material. The nonlinear stress-strain relationships of the fibers and shear material were calibrated to simulate the rotation or drift responses presented by the nonlinear modeling parameters in ASCE 41-17. Out-of-plane behavior was modeled linearly.
- Frame beams were modeled in Perform3D with "compound frame elements" consisting of an elastic frame segment along the beam clear span followed by an inelastic moment rotation hinge and a rigid end-zone at each end as applicable.
- Columns were modeled with compound frame elements consisting of an elastic frame segment along the column clear span, an inelastic P-M-M hinge at each end, and rigid end-zones at the beam joint as applicable.

This publication is available free of charge from: https://doi.org/10.6028/NIST.GCR.22-917-50

- Beam-column joints were modeled with elastic linear frame elements (EJ) or a nonlinear rotational spring at the panel zone node when joint nonlinearity is considered (NJ).
- Base conditions were taken as a fixed-restraint at the columns (translationally and rotationally restrained) and a pinned-restraint at the base of wall shell nodes (translationally restrained only).
- Diaphragm was modeled with nodes serving secondary to a rigid diaphragm definition. Shell elements representing the slabs are not modeled.
- Gravity beams (supported by girders) were not modeled.
- Gravity loads were defined with distributed line loads on beam elements.
- Mass was divided based on tributary area amongst nine points at each floor level.

The lumped-plasticity hinges in the columns consider P-M-M interaction. The axial load from the nonlinear analysis did not exceed the 10% minimum axial compressive load, so the minimum load governed for determination of the hinge modeling parameters at all stories.

The nonlinear model was only subjected to all three components of the 100% JMAKobe motion without being subjected to the prior motions applied to the building in the experimental program.

4.4.2 Global Performance: Perform3D EJ Model vs. Observation

Damage distribution data are compared in order to assess the extent to which the Perform3D EJ computational model was able to capture the overall building deformation mechanisms and damage distribution. Figure 4-44 identifies the ratio of plastic rotation to modeling parameter *a*. Damage distribution results from the model are in good agreement with the observed damage except for beams for which damage is overestimated. See Figure 4-8 for observed damage.

This publication is available free of charge from: https://doi.org/10.6028/NIST.GCR.22-917-50

This publication is available free of charge from: https://doi.org/10.6028/NIST.GCR.22-917-50

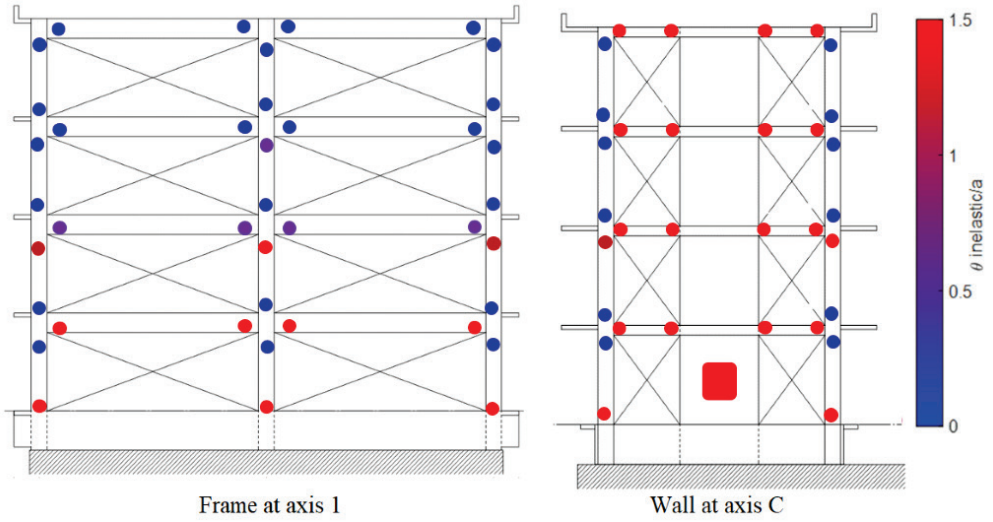


Figure 4-44 NDP Perform3D: Schematic damage distribution in frame at Gridline 1 (left) and wall at Gridline C (right) based on deformation criteria $\theta_{inelastic}/a$.

Story Drift

The distribution of maximum story drifts over the building height is compared between the Perform3D EJ model results and the experiment in Figure 4-45. Similarly, Figure 4-46 compares roof drift ratio histories where roof drift ratio is defined as the roof lateral drift with respect to the foundation divided by the total building height of 12m (39.37 ft.).

Maximum story drift in the moment frame direction from the analysis matches closely with the recorded drift results. Maximum story drift in the shear wall direction was overestimated in the analysis at all except the first story. If the drift due to base sliding is subtracted from the first story drift (dashed line in Figure 4-45) the general shape of the experimental drift profile better matches that from analysis.

In both directions, the residual drift was overestimated possibly because the hysteretic shapes of the hinges and fibers were selected to have more pinching than those observed from experimental studies for a conservative estimation of energy dissipation capacity of the structural components.

This publication is available free of charge from: https://doi.org/10.6028/NIST.GCR.22-917-50

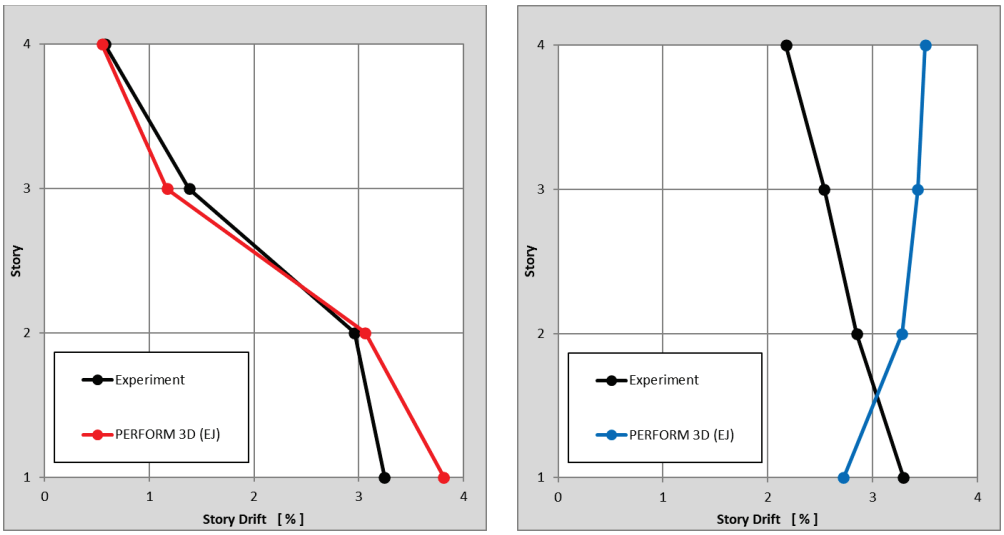


Figure 4-45 NDP Perform3D: Maximum drift ratio comparison over the height of the building for 100% JMA-Kobe, in frame direction (left), and wall direction (right).

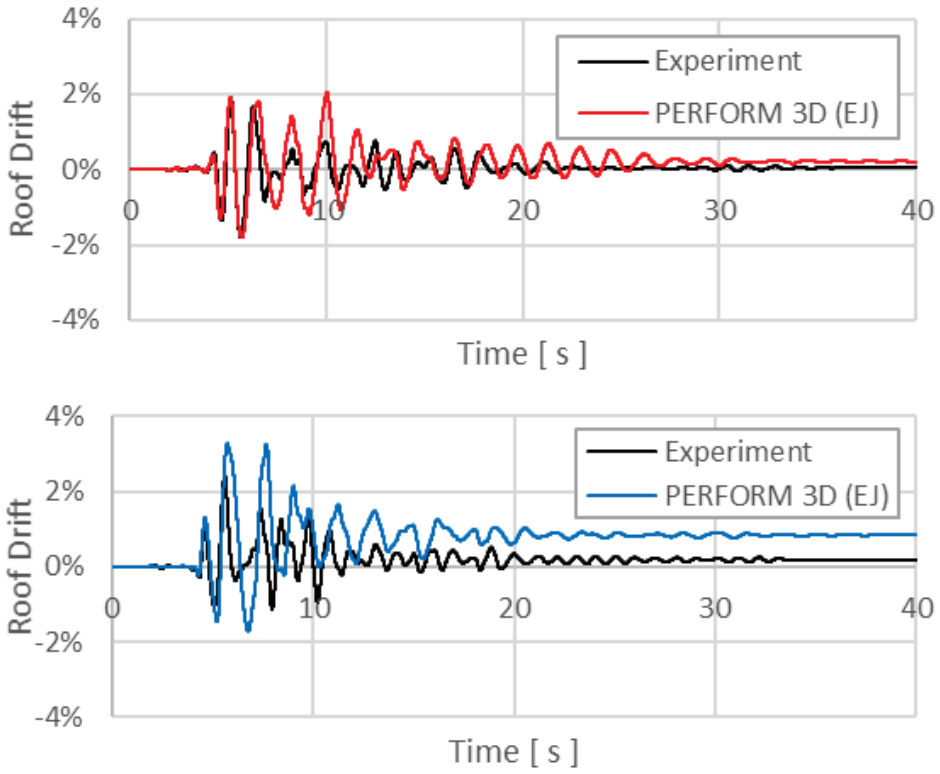


Figure 4-46 NDP Perform3D: Roof drift ratio history comparison for 100% JMA-Kobe, in frame direction (top), and wall direction (bottom).

Base Shear

As shown in Figure 4-47, the maximum base shear in the frame direction matches the base shear from the recorded test results. However, the maximum base shear in the shear wall direction is underpredicted by approximately 50%.

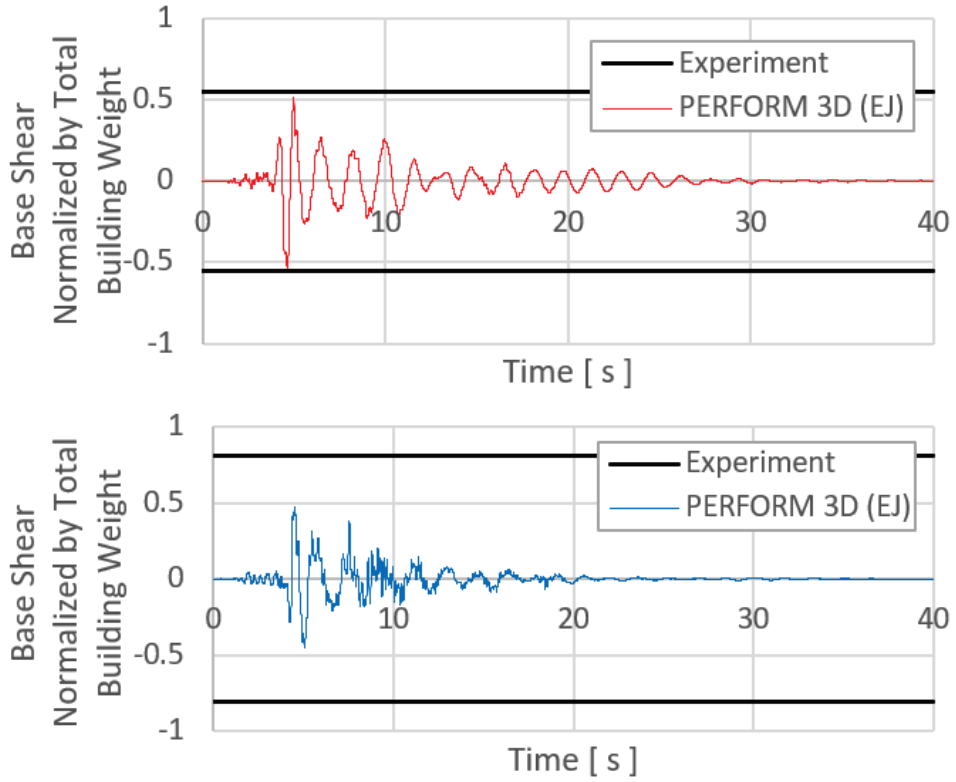


Figure 4-47 NDP Perform3D: Normalized base shear history compared to maximum from 100% JMA-Kobe, in frame direction (left), and wall direction (right).

Floor Accelerations

The center of mass maximum floor absolute accelerations from the Perform3D EJ analysis are shown along with the experimental results from Sensor A2 in Figure 4-48. The frame direction matches the experimental results well while the wall direction underestimates the floor acceleration at all floors.

The roof acceleration response histories are shown in Figure 4-49. The frame direction matches well; the wall direction results are mixed.

This publication is available free of charge from: https://doi.org/10.6028/NIST.GCR.22-917-50

This publication is available free of charge from: https://doi.org/10.6028/NIST.GCR.22-917-50

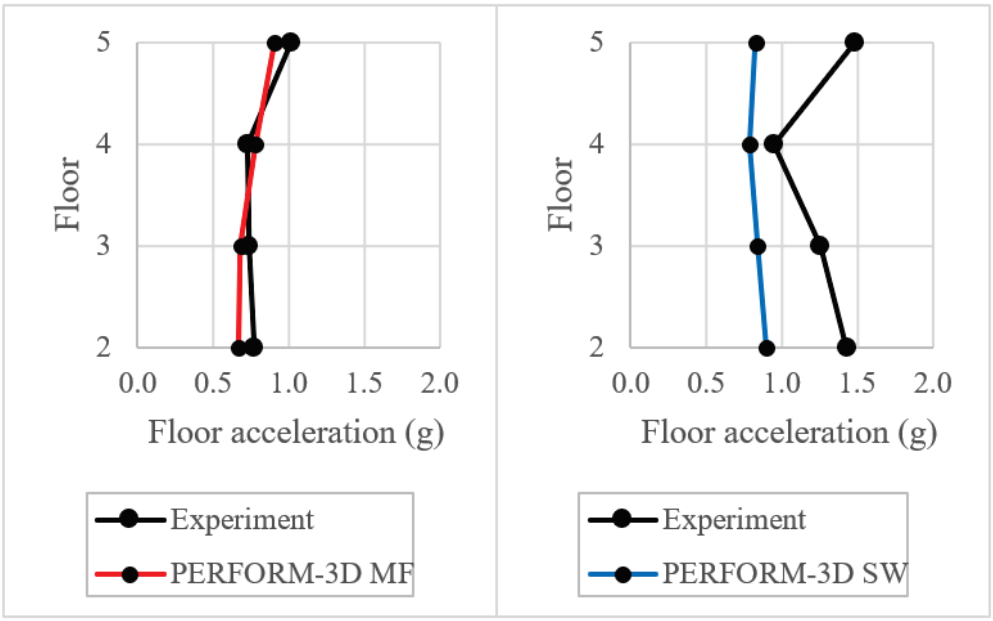


Figure 4-48 NDP Perform3D: Maximum absolute floor accelerations over the height of the building for 100% JMA-Kobe from Sensor A2, in frame direction (left) and wall direction (right).

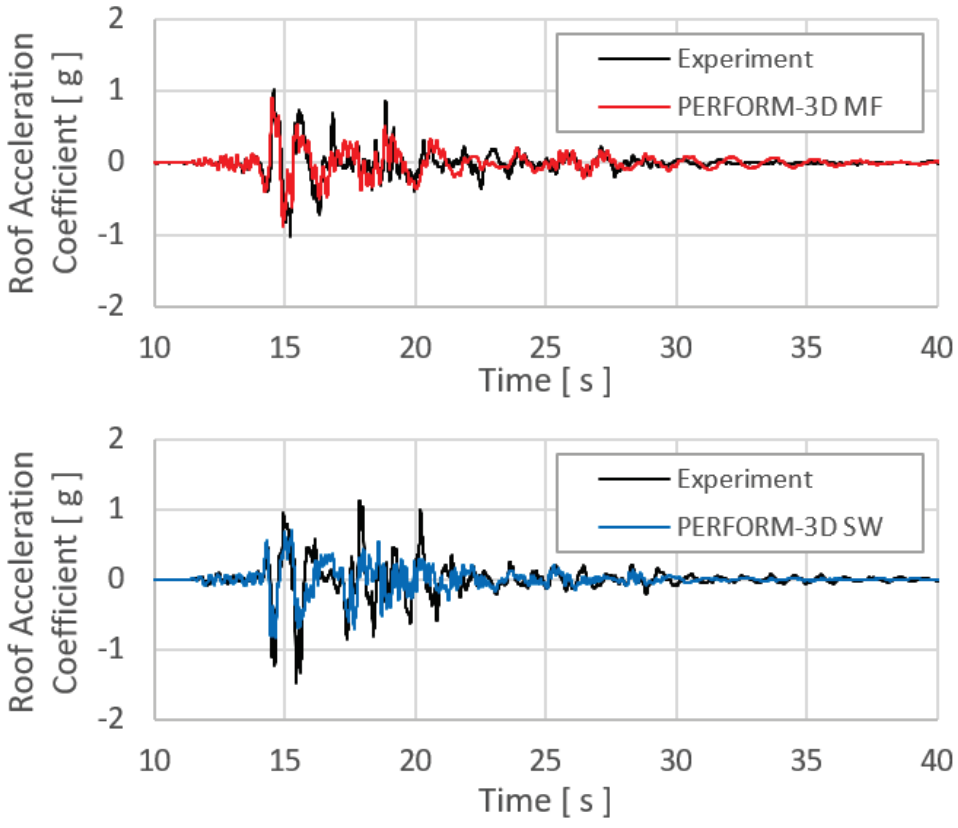


Figure 4-49 NDP Perform3D EJ: Roof acceleration histories for 100% JMA-Kobe from Sensor A2, in frame direction (top) and wall direction (bottom).

4.4.3 *Global Performance: Perform3D NJ Model vs. Observation*

An additional study of the model was conducted with inclusion of joint nonlinearity (Perform3D NJ). Due to limitations of the program, joint nonlinearity can only be modeled in one plane for a given joint. Therefore, joint nonlinearity was modeled in the plane of the frame, not the plane of the shear walls. As such, inclusion of joint nonlinearity in the frame direction did not affect the wall direction results measurably. Frame direction results are summarized below.

The drift distribution in the nonlinear joint model was more closely matched than that of the elastic joint model to the measured drift in the frame direction, as shown in Figure 4-50. The model identified the second level interior joint as the critical joint, which is in agreement with the observed damage. However, the analysis results did not predict damage in any other joints, which is not in agreement with observed damage in the exterior joints (Figure 4-8). See Figure 4-51 for the damage distribution from the model in the frame direction.

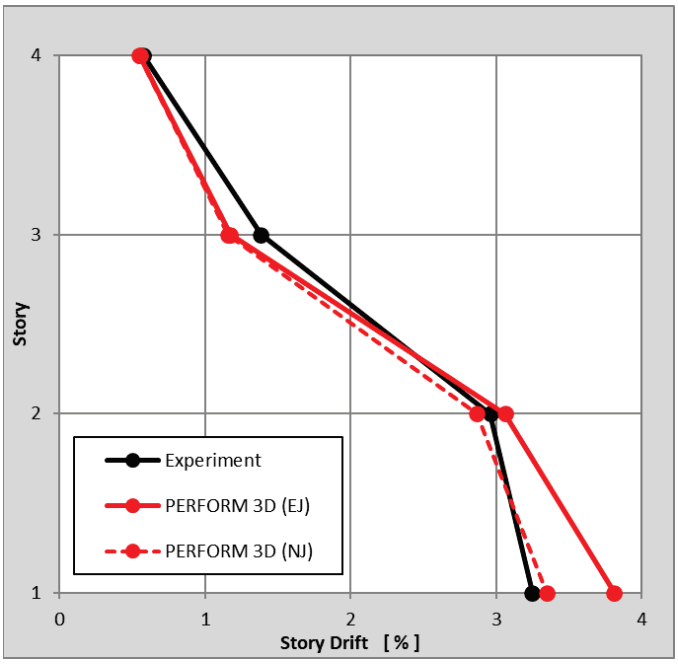


Figure 4-50 NDP Perform3D: Maximum drift ratio comparison between linear and nonlinear joint models.

This publication is available free of charge from: https://doi.org/10.6028/NIST.GCR.22-917-50

This publication is available free of charge from: https://doi.org/10.6028/NIST.GCR.22-917-50

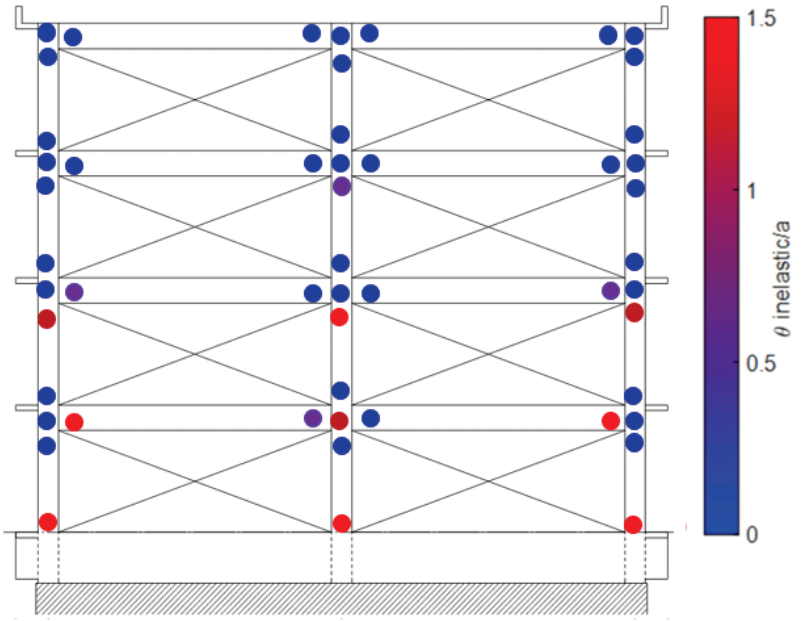


Figure 4-51 NDP Perform3D: Schematic damage distribution in frame at Gridline 1 based on deformation criteria $\theta_{inelastic}/a$.

4.4.4 Component Performance: Perform3D NJ Model vs. Observation

Component level comparisons in this section are based on the damage states of the members at the end of the 100% JMA-Kobe motion. Component maximum inelastic rotations in the hinges at the end of the analysis are normalized by their modeling parameters *a* and *b* from ASCE 41-17 to categorize their damage level. Results are shown for both single directional and bi-directional analyses. The "X-dir" results correspond to when the ground motions parallel to the shear wall direction only are applied. The "Y-dir" results correspond to when the ground motions parallel to the moment frame direction only are applied. The "X&Y-dir" results correspond to the SRSS of the results from when ground motions from both directions are applied simultaneously.

Columns

The first story moment frame columns exceeded both LS and CP acceptance criteria despite performing reasonably well during testing. The analysis did not form a collapse mechanism at the 100% JMA-Kobe motion. The locations of exceedance were at the base of the first story columns and both ends of the moment frame beams at the second floor level. The nonlinear hinge rotations relative to deformation parameters are shown in Figure 4-52 below. Hinge locations identified with a red X above the acceptance criteria threshold have exceeded the specified limit state.

The plots in the two right columns in Figure 4-52 present the ratio of the demand to the deformation limit in each direction. The third column presents the SRSS of the ratio from each direction. Since columns were loaded in both directions simultaneously, the bi-directional response should be considered in the analysis. The bi-directional response of an example column and deformation limits are presented in Figure 4-53.

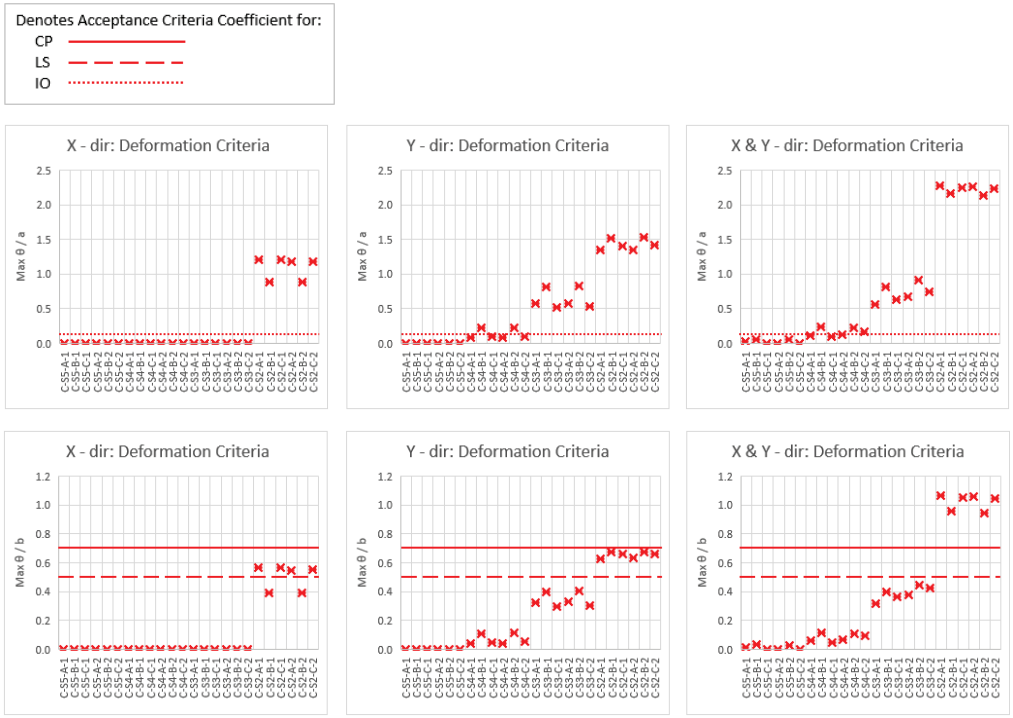


Figure 4-52 NDP Perform3D: Column deformation criteria: $\theta_{inelastic}/a$ (top), $\theta_{inelastic}/b$ (bottom).

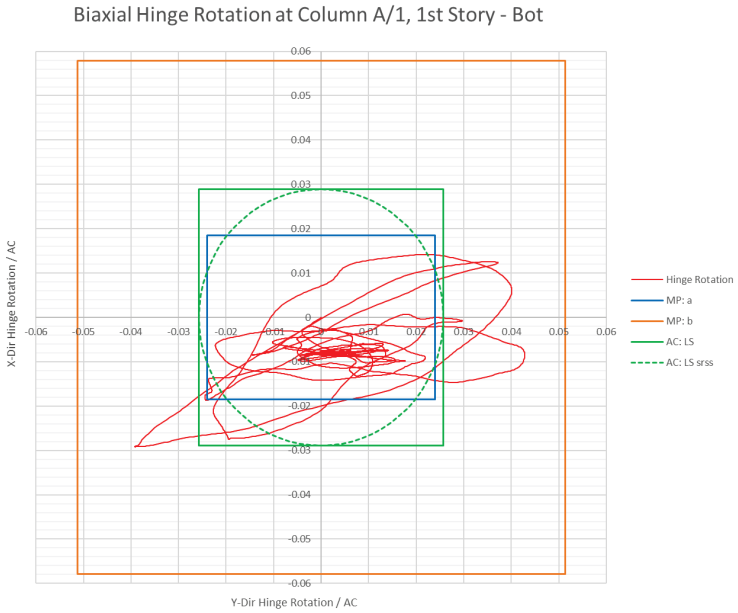


Figure 4-53 NDP Perform3D: Bi-directional hinge rotation orbit plot.

This publication is available free of charge from: https://doi.org/10.6028/NIST.GCR.22-917-50

This publication is available free of charge from: https://doi.org/10.6028/NIST.GCR.22-917-50

Shear Walls

The damage of the structural walls at their base was severe in both experimental and computational results (Figure 4-54). ASCE 41-17 provisions therefore adequately predicted wall damage level. Even if the sliding mode of damage is not predicted by the model, having captured the severity of damage in the walls, ASCE 41-17 would have triggered retrofit for the walls. The acceptance criteria only considers in-plane action since out-of-plane nonlinear behavior was not considered.

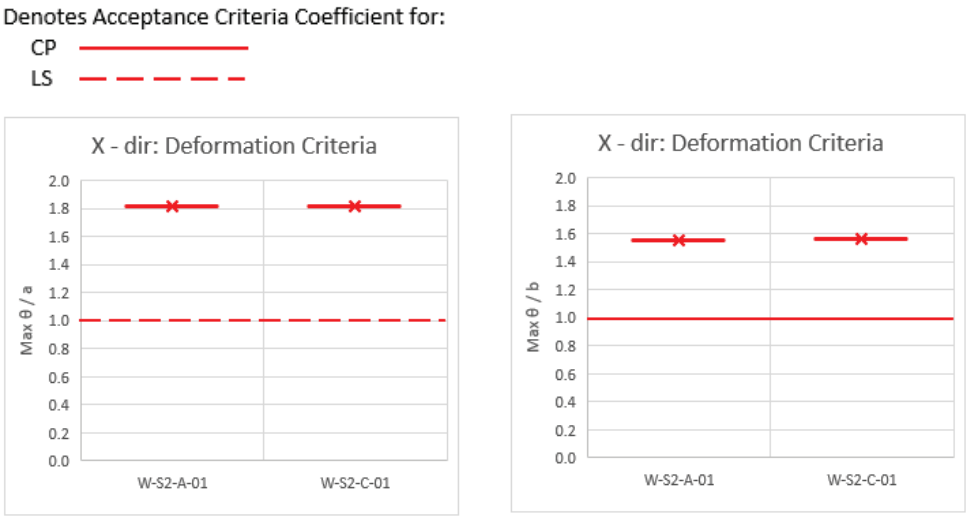


Figure 4-54 NDP Perform3D: Wall deformation criteria: $\theta_{inelastic}/a$ (left), $\theta_{inelastic}/b$ (right).

First Story Columns and Shear Walls

Figure 4-55 and 4-56 show the damage distribution within the first story vertical elements. The interaction effects at the corner columns are significant. For example, the deformation demands in the wall direction tax the column columns nearly as much as deformation demands in the frame direction. Applying seismic excitation in both directions simultaneously further increases deformation demands.

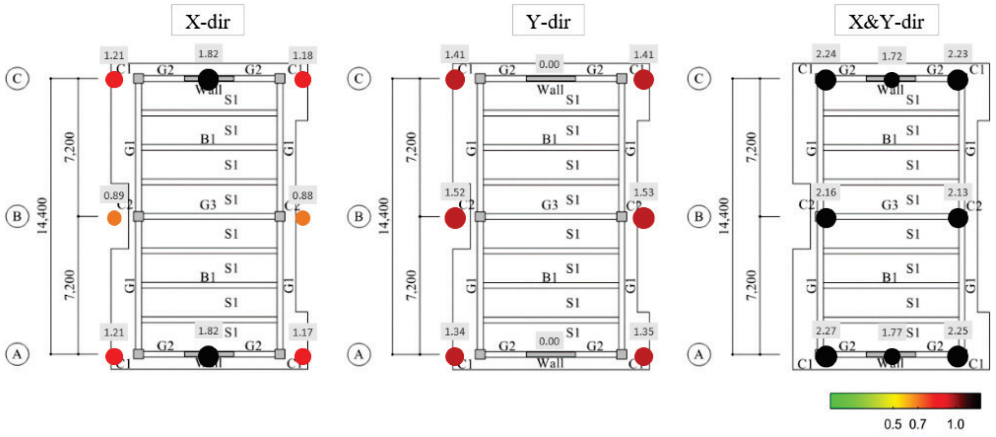


Figure 4-55 NDP Perform3D: Deformation criteria $\theta_{inelastic}/a$.

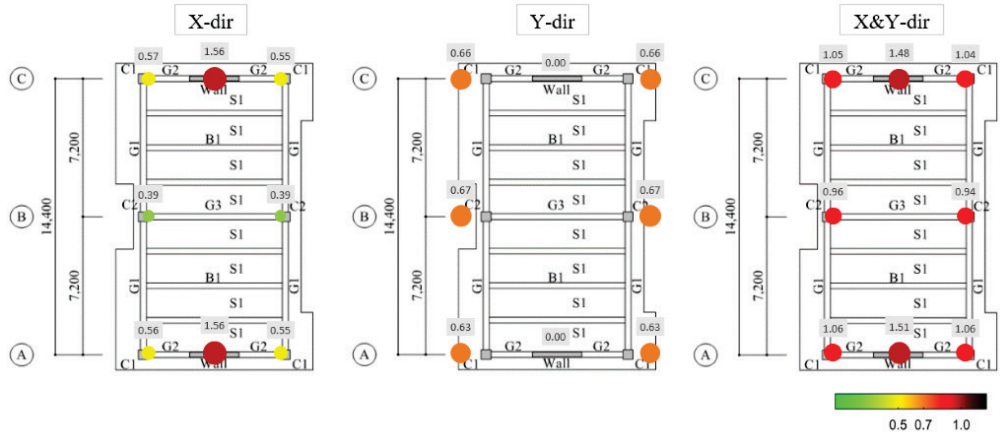


Figure 4-56 NDP Perform3D: Deformation criteria $\theta_{inelastic}/b$.

Beams

The second level moment frame beams exceeded both the LS and CP acceptance criteria despite performing reasonably well during testing. The locations of exceedance were limited to the first story in the frame direction and was uniform at all levels in the wall direction. The nonlinear hinge rotations relative to deformation parameters are shown in Figure 4-57. Hinge locations identified with a red X above the acceptance criteria threshold have exceeded the specified limit state. The results overpredict beam damage.

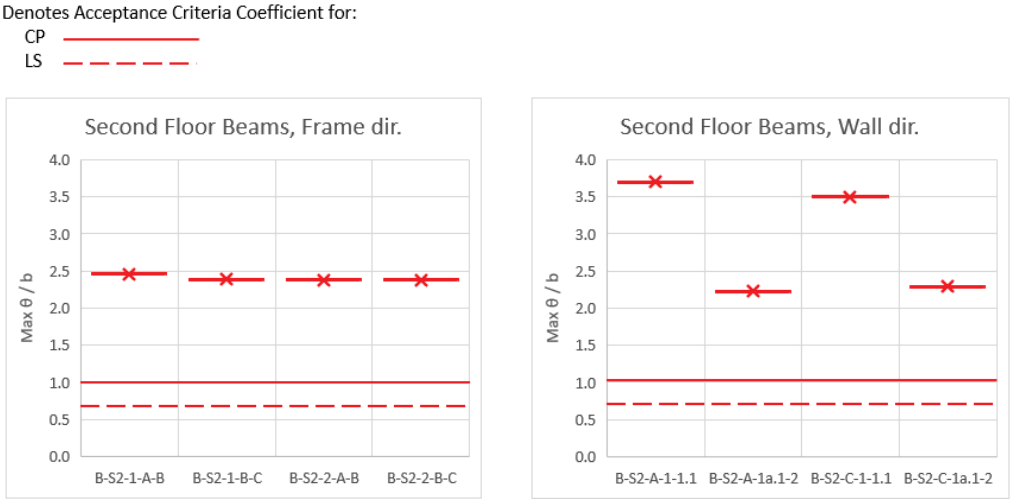


Figure 4-57 NDP Perform3D: Beam deformation criteria: $\theta_{inelastic}/b$.

Beam-Column Joints

Joint damage was underpredicted in the analytical results in all cases except for the critical joint at the second floor, the center joint. Damage at this joint matched the observed damage and predicted slight exceedance of CP. See Figure 4-58 for location of critical joint where damage was predicted by analysis. It was the only

This publication is available free of charge from: https://doi.org/10.6028/NIST.GCR.22-917-50

joint to reach the CP limit. Response history hysteresis results can be seen in Figure 4-59.

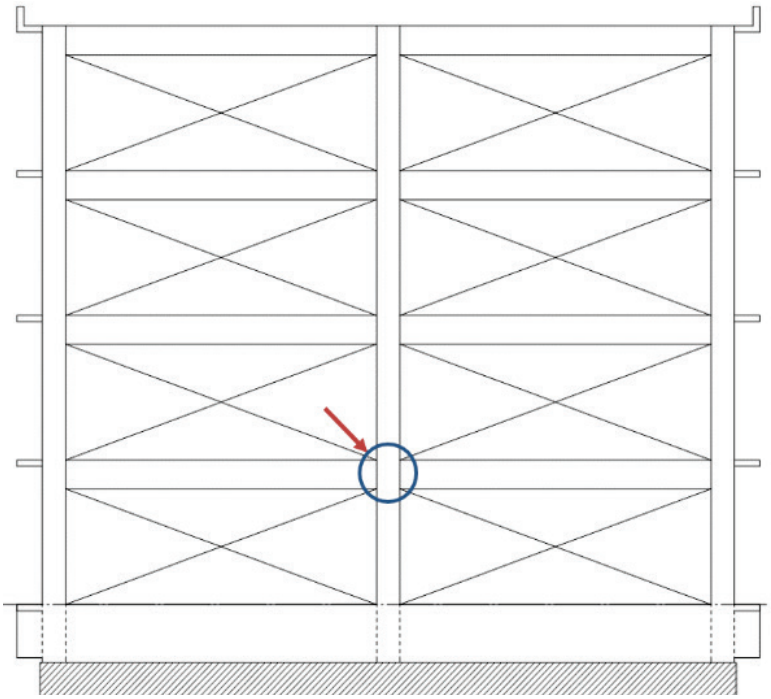


Figure 4-58 NDP Perform3D NJ: Location of predicted joint damage.

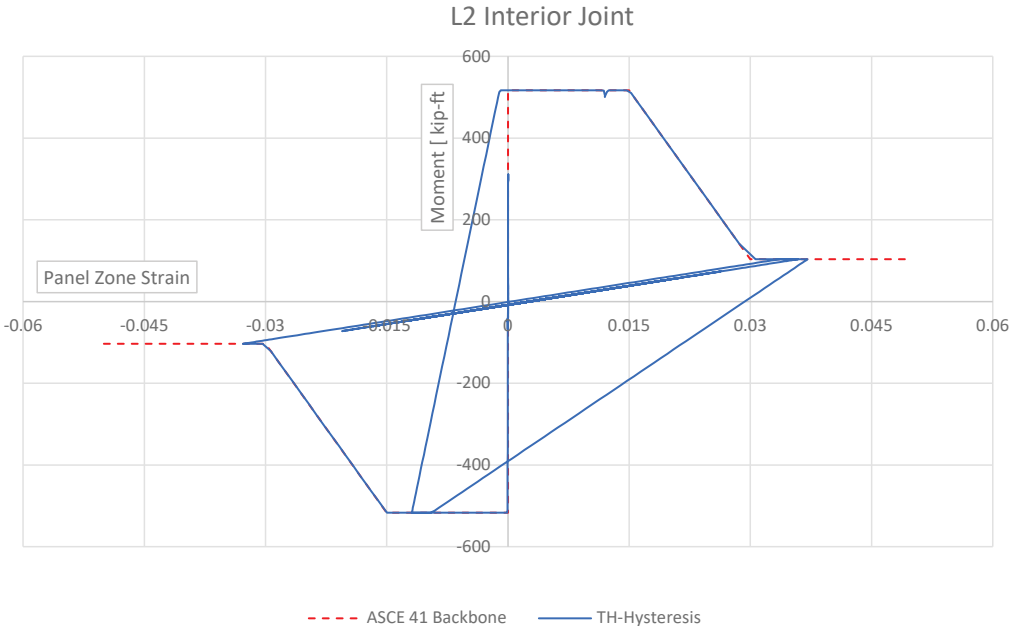


Figure 4-59 NDP Perform3D: Hysteresis at Level 2 joint at Gridline B.

4.4.5 Summary Findings

In the wall direction, story drifts were overestimated, but not significantly at the first story where the maximum drift occurred in the experiment. Due to the sliding of the

This publication is available free of charge from: https://doi.org/10.6028/NIST.GCR.22-917-50

base of the wall, the drift distribution from analysis over building height was not consistent with the measured drifts. The shear wall component evaluation results matched the observed damage level.

In the moment frame direction, the model with nonlinear joints matched experimental data better than the one with linear joints. Story drifts were matched closely by the NJ analysis over all stories. The column, beam, and joint components evaluation results also matched well the observed damage.

Additional general observations are summarized below:

- Single directional analysis underpredicted response. It is recommended that bi-directional interaction be considered.
- Wall-frame interaction for columns closely located near walls has a sizeable effect on force and drift distribution.
- Sliding of the base of the walls should be explicitly considered.

4.5 Comparison of Perform3D and OpenSees LP Models

ASCE 41-17 allows modeling concrete members using lumped plasticity or fiber section distributed plasticity elements. Furthermore, different software provide different material and element formulations that may alter seismic assessment results. Comparisons in this section are limited to OpenSees LP and Perform3D models, which have primarily lumped-plasticity elements (except for the walls).

4.5.1 Global Performance Comparison

The first mode periods from both OpenSees and Perform3D models are presented in Table 4-5.

Table 4-5 First Mode Period Comparison in Each Direction

	Frame Dir.	Wall Dir.
Experiment	0.43 sec.	0.31 sec.
OpenSees LP Models	0.64 sec.	0.40 sec.
Perform3D Models	0.68 sec.	0.32 sec.

The maximum story drift profiles from all models are presented in Figure 4-60. In the frame direction, the Perform3D NJ model provided the best match to the experimental maximum drift levels at all stories among the four models, as well as the general drift profile recorded experimentally. The maximum drift in the first story is only 0.35% lower in the Perform3D NJ model than the experimental value. On the other hand, both OpenSees models produced a drift profile that concentrated deformation and damage more in the second and third stories than in the first story. Premature failures of the joints in the OpenSees LP NJ model or the beams in the

This publication is available free of charge from: https://doi.org/10.6028/NIST.GCR.22-917-50

OpenSees LP EJ model may have played a role in generating such profiles. Additionally, drift demands on the first story columns were significant and in some cases larger in the wall direction than in the frame direction. The Perform3D P-M-M column hinges account for bi-directional interaction and therefore captured some of the effects of damage incurred due to wall-direction demands on the response of the corner columns in the frame direction. The OpenSees models do not have bi-directional coupling and therefore maintained higher capacities in the first story columns in the frame direction than in the Perform3D model. These discrepancies may have caused lower first story demands in the OpenSees models compared to those recorded experimentally and in the Perform3D model.

The maximum story drift profiles in the wall direction were consistent for all four nonlinear models and indicated cantilever-wall behavior. However, all of the models did not accurately capture the recorded drift profile, likely due to the observed wall sliding that was not captured in the models.

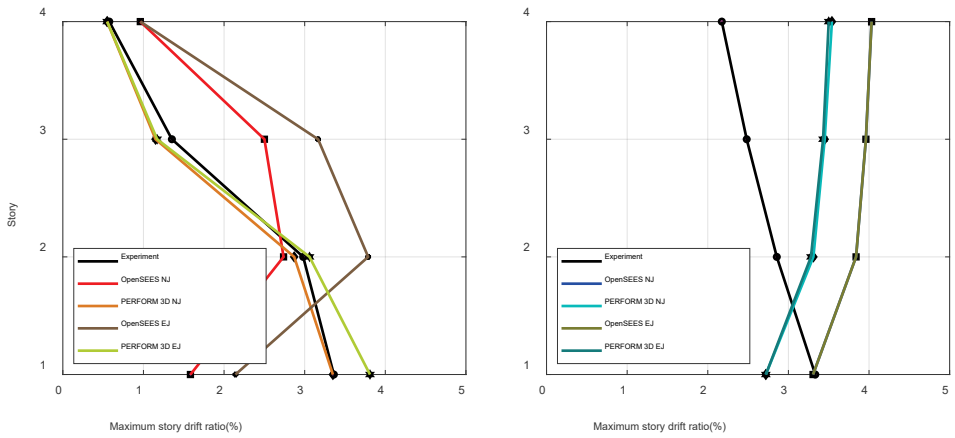


Figure 4-60 Maximum interstory drift comparison in frame direction (left) and wall direction (right).

In the frame direction, maximum floor acceleration profiles from the Perform3D models matched reasonably well with the experimental values (Figure 4-61). The OpenSees LP models provided less accuracy in estimating floor acceleration in the frame direction, particularly at floor level 4. All models showed discrepancies with experimental maximum floor accelerations in the wall direction. The discrepancies in the wall direction are at least partially attributable to the wall sliding behavior that occurred experimentally but was not captured in the models.

This publication is available free of charge from: https://doi.org/10.6028/NIST.GCR.22-917-50

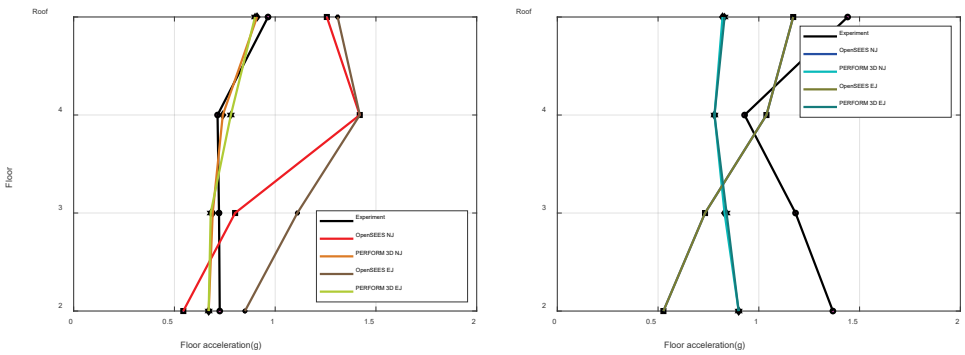


Figure 4-61 Maximum floor acceleration comparison over the height of the building in frame direction (left) and wall direction (right).

Comparison of the maximum base shears between the experiment and all nonlinear models are presented in Table 4-6. In the frame direction, OpenSees LP EJ and NJ model strengths bracketed the experimental maximum base shear value. When joints were prevented from failing, the base shear in the OpenSees model increased substantially, from 12% lower to 21% higher than in the experiment. Perform3D captured the maximum base shear with reasonable accuracy in the frame direction. In the wall direction, all models underestimated base shear, by 20% to 39%.

Table 4-6 Maximum Base Shear Normalized by Building Weight

	Frame Dir. (error%*)	Wall Dir.(error%*)
Experiment	0.534	0.780
OpenSees LP NJ	0.470 (-12%)	0.627 (-20%)
OpenSees LP EJ	0.644 (+21%)	0.627 (-20%)
Perform3D NJ	0.538 (+1%)	0.472 (-39%)
Perform3D EJ	0.551 (+3%)	0.472 (-39%)

* Error between model result and experiment

4.6 Linear Dynamic Procedure

4.6.1 Modeling Approach

Three-dimensional numerical model of the structure was created in ETABS to perform a modal response spectrum analysis. The corresponding internal forces and system displacements were determined using linear elastic, dynamic analysis in accordance with ASCE 41-17 Section 7.4.2 and compared against the acceptance criteria of ASCE 41-17 Section 7.5.2. All elements are modeled as linear elastic.

In order to account for the reduced effective stiffness of an element during seismic loading, the stiffness of elements in a linear analysis model are modified per ASCE

This publication is available free of charge from: https://doi.org/10.6028/NIST.GCR.22-917-50

41-17 Table 10-5 for concrete elements. The element stiffness values used in the analysis are as follows::

- Wall in-plane stiffness: $0.35E_{cE}I_g$
- Column flexural stiffness: $0.3E_{cE}I_g$ (for lightly loaded columns)
- Beam flexural stiffness: $0.6E_{cE}I_g$ (This number is increased by a factor of two in order to account for stiffness effect of monolithic slab T-beam)

The joint offsets in the linear analysis model were either fully or partially rigid in accordance with ASCE 41-17.

4.6.2 Global Performance: Model vs. Observation

The primary modes had periods of 0.68 sec. in the frame direction and 0.38 sec. in the wall direction. Spectral accelerations associated with the primary orthogonal directions are 2.8g in the wall direction and 1.75g in the frame direction according to the recorded response spectra.

Analysis results for story drift in the wall direction varied significantly from the experimental drift response of the building. These results are shown in Figure 4-62. It can be seen from the results that the linear analysis substantially underestimated the drift. Story drift was better matched in the frame direction, see Figure 4-63; however, the results were mixed. Story drift in the upper stories was overestimated while story drift in the first story was underestimated. The second story drift matches the recorded results.

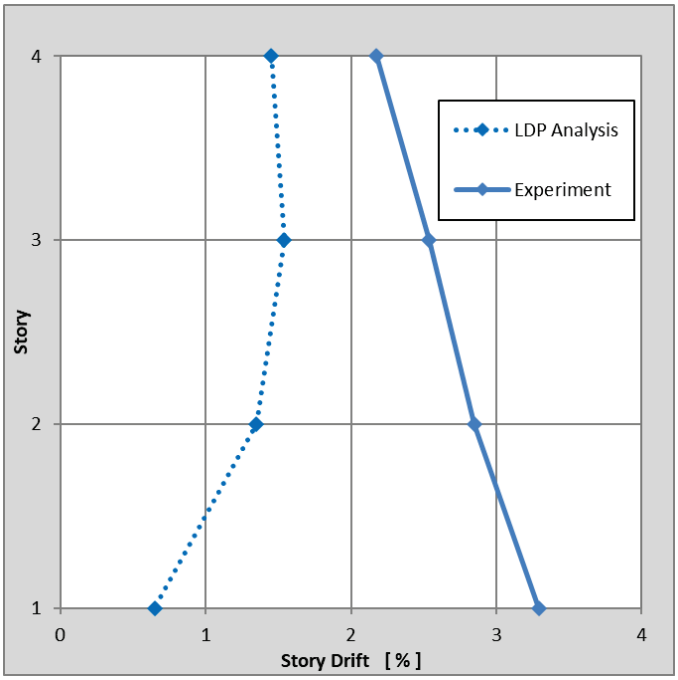


Figure 4-62 LDP: Story drift in the wall direction.

This publication is available free of charge from: https://doi.org/10.6028/NIST.GCR.22-917-50

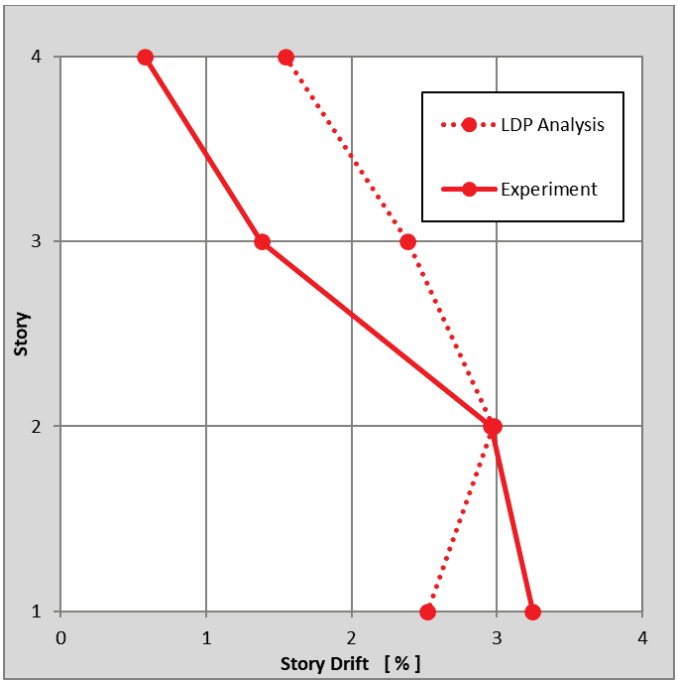


Figure 4-63 LDP: Story drift in the frame direction.

4.6.3 Component Performance: Model vs. Observation

The linear analysis results for the first and second story are shown in Figures 4-64 and 4-65. The shear and flexure demand-capacity-ratios (DCRs) modified by the *m*-factors are presented in the results. Those components with DCR/*m* values greater than 1.0 indicate failure to meet the CP acceptance criteria. The results show that both the columns and walls exceed the CP criteria in the first story. Large differences in DCR/*m* values can be observed in the corner columns, which are caused by tension on sections with only 20% difference in reinforcing ratios.

4.6.4 Summary Findings

In the wall direction, story drifts were significantly underpredicted. The wall component evaluation results matched the observed damage relatively well. It should be noted that the DCR/*m* in linear analysis was lower than the DCR from the nonlinear Perform3D NJ analysis. In other words, the nonlinear analysis was more conservative than the linear analysis for the wall acceptance criteria evaluation.

In the frame direction, story drifts from the simulation provided an approximate match to those observed, but did not identify the appropriate story mechanism. The column and beam component evaluation results predicted more severe damage than the observed damage. Axial tension caused by wall-frame interaction effects was the primary cause of the overprediction of the damage in the columns. As indicated from nonlinear analysis results, beam modeling parameters and acceptance criteria may be overly conservative in ASCE 41-17.

This publication is available free of charge from: https://doi.org/10.6028/NIST.GCR.22-917-50

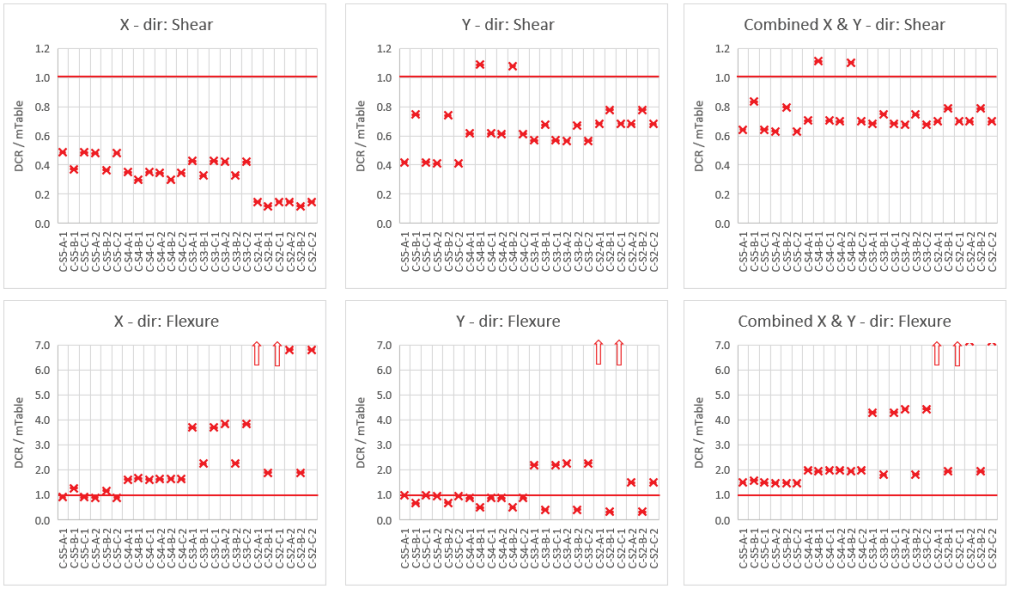
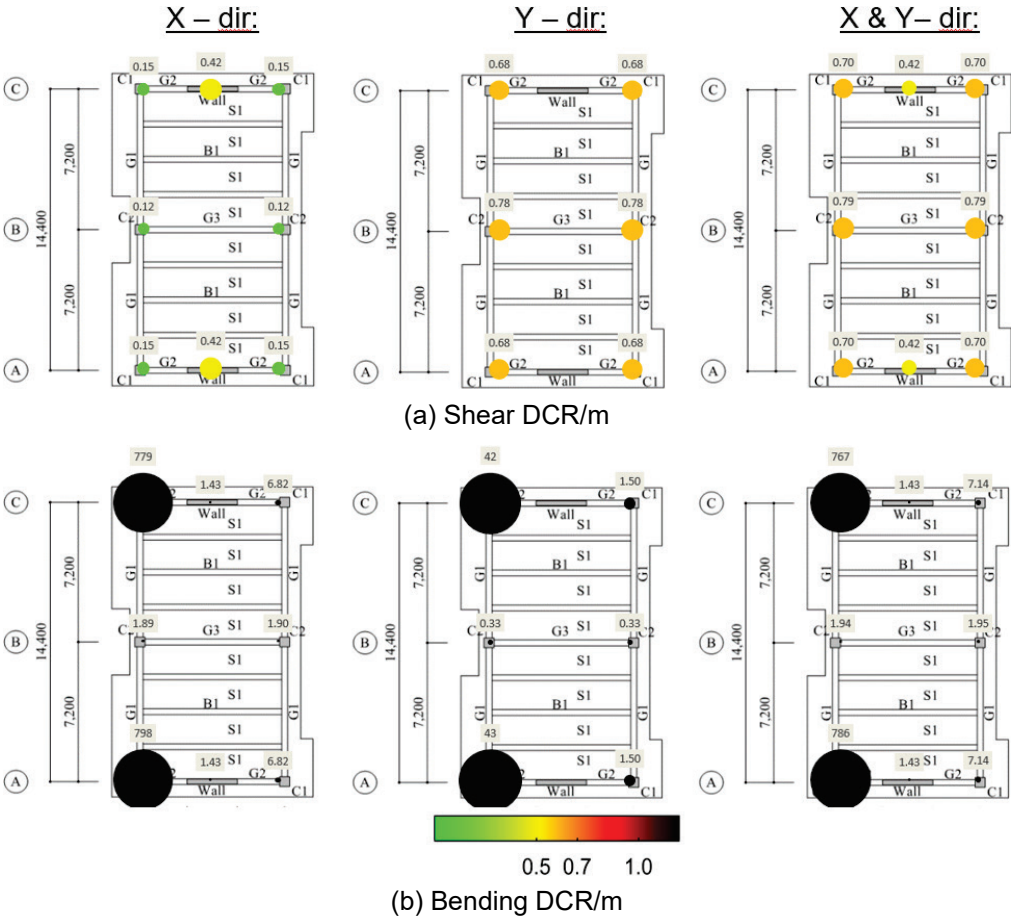


Figure 4-64 LDP: Collapse Prevention DCR/*m* for all columns.



(a) Shear DCR/m

(b) Bending DCR/m

Figure 4-65 LDP: Collapse Prevention DCR/*m* at first story.

This publication is available free of charge from: https://doi.org/10.6028/NIST.GCR.22-917-50

4.7 Fragility Assessment

Fragility curves calculated using the OpenSees LP NJ model with ASCE 41-17 modeling parameters, acceptance criteria, and building collapse indicators are provided in Figures 4-66 and 4-67. The fragility curves were calculated based on incremental dynamic analyses using the 22 earthquake records included in the FEMA P-695 far-field set. All analyses were performed with the two components of the earthquake record applied in the wall and frame directions of the building. Collapse was defined as the intensity measure at which an interstory drift ratio of 6% was exceeded at any of the stories, or the highest intensity measure at which the model reached numerical convergence. A second metric, used as an indicator of unacceptable response, was the intensity measure corresponding to the first element to exceed an inelastic rotation of 1.5 times modeling parameter *b*. For the study building, the unnaceptable response indicator occurred at smaller spectral accelerations than the 6% collapse indicator, which shows that sidesway collapse in the IDA occurred after very large deformations were achieved in some elements. A likely reason for this trend is that modeling parameters for some elements are more conservative than others, which introduces modeling bias and causes inelastic deformation demads to be larger at elements with conservative modeling parameters. The fact that inelastic models overestimated deformation demands on beams, and that observed damage in joints was less than estimated by the nonlinear models (Figures 4-20 and 4-29) is consistent with trend. Even though the inelastic rotation corresponding to parameter *b* in ASCE 41 was exceeded in some elements of the lumped-plasticity nonlinear model for the 100% JMA-Kobe ground motion, all elements in the building maintained their ability to carry gravity loads during the test and no instance of local collapse was observed (Figures 4-66 and 4-67). Another justification for this trend is that exceeding modeling parameter *b* does not have the same consequences for all elements. Nonlinear analyses with the 100% JMA-Kobe ground motion showed that beams framing into structural walls experienced some of the largest inelastic deformation demands. Unacceptable response of beam elements is not as dangerous as unacceptable response of column or wall elements because beams are capable of transferring gravity loads through catenary action and redistribution through the floor system.

Fragility curves presented in Figures 4-66 and 4-67 correspond to the intensity measure at which the first element in the model exceeded a modeling parameter in ASCE 41. The curves were scaled to the spectral acceleration at the effective fundamental period of the structure. Because the fundamental periods were significantly different in the wall and frame directions, scaling was performed using the spectral acceleration at the largest period in the direction each limit state was exceeded. In most instances the frame direction controlled. The only instance in

This publication is available free of charge from: https://doi.org/10.6028/NIST.GCR.22-917-50

which the wall direction controlled was for the yield modeling parameter, due to the large stiffness of the wall.

Vertical lines in Figures 4-66 and 4-67 show spectral accelerations at which the first element exceeded the corresponding modeling parameter or acceptance criterion for an IDA with the 100% JMA-Kobe record. Spectral accelerations for the vertical lines in Figures 4-66 and 4-67 were calculated as the product of the scale factor extracted from the IDA and the acceleration at the fundamental effective period of the building obtained from the response spectrum of the 100% JMA-Kobe ground motion. The yellow dashed line shows the spectral acceleration at the effective fundamental period of the model for the 100% JMA-Kobe response spectrum, in the frame direction and is an indicator of intensity of shaking during the test.

Results from the IDA indicate that the intensity of shaking for the 100% JMA-Kobe ground motion was strong enough to cause a large number of elements in the wall and frame direction to deform beyond 1.5×*b*, but not enough to reach a drift ratio of 6%. Close examination of the results from the IDA showed that at an intensity measure of 0.7 there were 12 beam springs in the wall direction exceeding parameter *a*, and 2 beam springs in the frame direction near parameter *a*. Column and wall springs at this intensity measure had very small rotation demands and none exceeded LS performance level. At an intensity measure of 0.8, results from the IDA showed that most beams in the wall direction, some beams in the frame direction, and some columns in both directions had inelastic rotations that exceeded 1.5 × *b*. The progression of damage suggests that loss of beam stiffness triggered a very sudden change in the behavior of the building, causing the walls and columns to become uncoupled and act as cantilever elements. Although this beam-induced damage mechanism caused a large increase in lateral deflections, it was not sufficient to cause collapse due to excessive drift demand.

Vertical lines corresponding to capping (loss of flexural strength), ultimate (loss of lateral load capacity), inelastic rotation of 1.5×*b*, and 6% drift ratio for the JMA-KOBE ground motion corresponded to relatively low probabilities of exceedance in the FEMA P-695 fragility curves. The probability of exceedance of the capping point was approximately 15%, and the probability of exceedance of the ultimate point (same line as 1.5 × *b*) was approximately 23%. To that effect, both Figures 4-66 and 4-67 show that spectral accelerations corresponding to a probability of exceedance of 50% of modeling parameter and acceptance criteria in FEMA P-695 far fault set fragilities were significantly higher than spectral accelerations for the 100% JMA-Kobe record, except for yield modeling parameter and IO acceptance criterion.

The low probabilities of exceedance in Figures 4-66 and 4-67 were caused in part by the difference between the effective period of the structure in the frame and wall directions. For the frame direction, the spectral acceleration at the fundamental

This publication is available free of charge from: https://doi.org/10.6028/NIST.GCR.22-917-50

This publication is available free of charge from: https://doi.org/10.6028/NIST.GCR.22-917-50

period of the average FEMA P-695 spectrum was 0.65g, while the spectral acceleration for the 100% JMA-Kobe spectrum was 1.3g. For the wall direction, the two accelerations were 0.84g and 2.75g, respectively. If fragilities and vertical lines were to be scaled by the spectral accelerations corresponding to the wall direction instead, vertical lines would shift to the right by a factor of 2.75/1.3 = 2.11, and fragility curves would shift to the right by a factor of 0.84/0.65 = 1.29, causing probabilies of exceedance to increase significantly. This discrepancy highlights the challenges inherent to scaling fragilities when the shape of the two spectra are significantly different and the building has significantly different periods in the two principal directions.

Trends shown in Figure 4-67 for acceptance criteria are similar to those observed in Figure 4-66 for modeling parameters. Spectral accelerations extracted from the IDA with the 100% JMA-Kobe ground motion corresponded to relatively low probabilities of exceedance for LS and CP performance levels in the FEMA P-695 fragility curves. The spectral acceleration of the 100% JMA-Kobe ground motion at the fundamental period in the frame direction corresponded to a probability of exceedance of approximately 45% for CP and 50% for LS performance levels, which is significant and consistent with the level of damage observed in the test. Fragility curves in Figures 4-66 and 4-67 were derived for one element exceeding the stated modeling parameter or acceptance criteria and Figure 4-8 shows instances of severe damage in at least one joint in the frame direction and at the base of the structural wall after the 100% JMA-Kobe test.

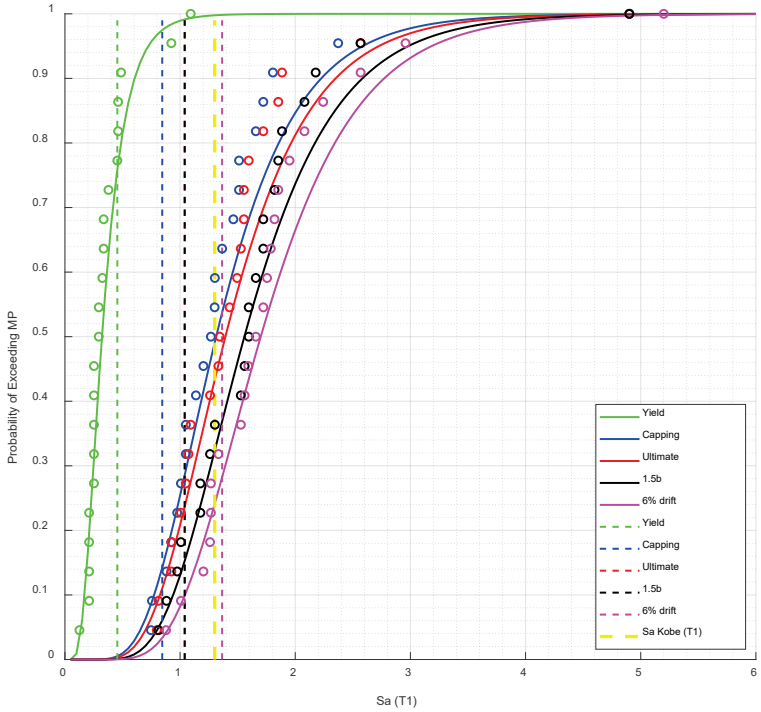


Figure 4-66 Fragility curves for ASCE 41-17 modeling parameters and collapse.

This publication is available free of charge from: https://doi.org/10.6028/NIST.GCR.22-917-50

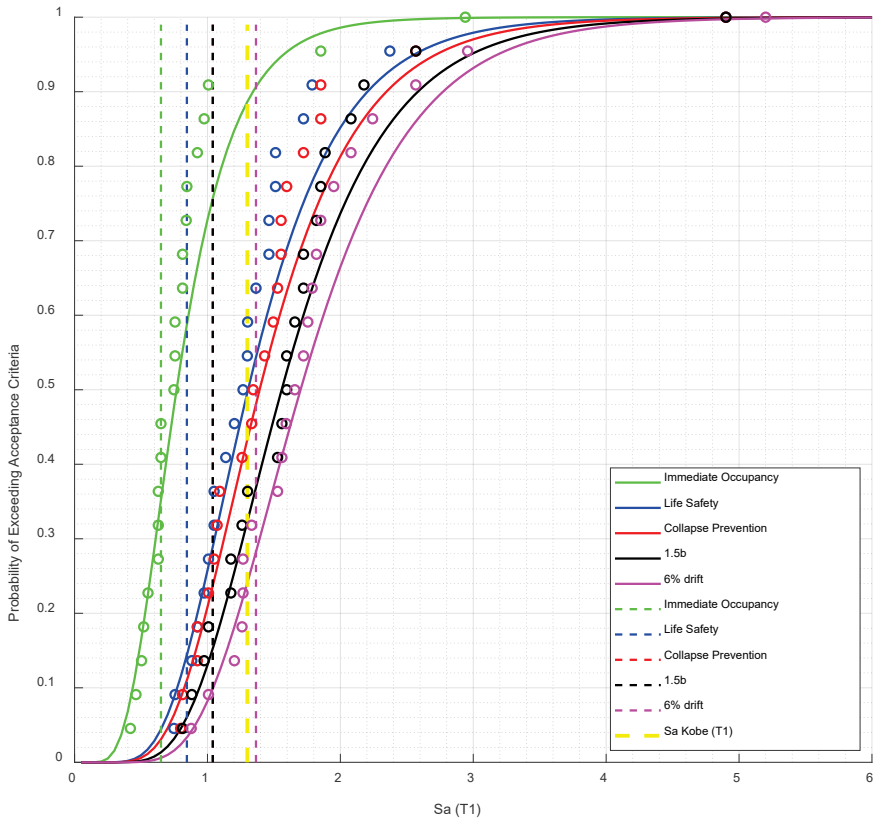


Figure 4-67 Fragility curves for ASCE 41-17 acceptance criteria and collapse.

4.8 Eurocode Evaluation

This building was also assessed using acceptance criteria of Eurocode 8 (2005) for columns for the Near Collapse limit state (Section 2.4.2) using the OpenSees LP NJ model, with results shown in Figure 4-68. The figure shows fragility curves for the study building for the Eurocode acceptance criteria and building collapse. Acceptance criteria for the Eurocode are very similar to those in ASCE 41-17 so the fragility curves and behavioral trends in Figure 4-68 are very similar to those in Figure 4-67. The spectral acceleration of the 100% JMA-Kobe ground motion at the fundamental period in the frame direction corresponded to a probability of exceedance of approximately 45% for Near Collapse (NC) performance level and approximately 62% for the Significant Damage (SD) performance level, which is consistent with the level of damage observed in the test.

This publication is available free of charge from: https://doi.org/10.6028/NIST.GCR.22-917-50

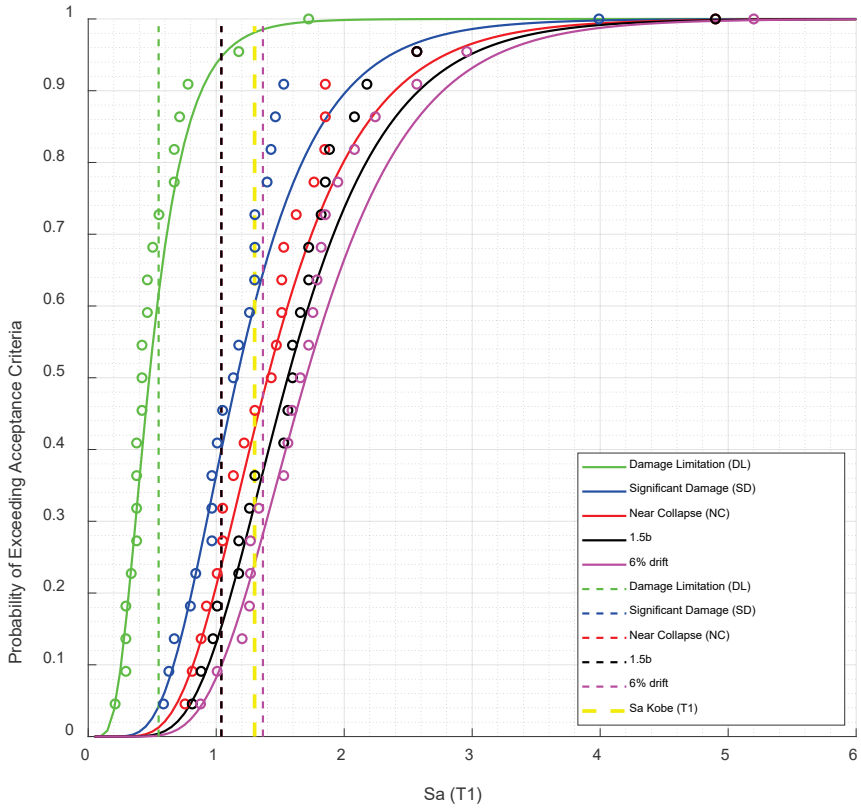


Figure 4-68 Fragility curves for Eurocode acceptance criteria and collapse.

4.9 New Zealand Assessment Guidelines

This section describes an assessment of the building according to *The Seismic Assessment of Existing Buildings* (NZSEE et al., 2017) Part C, Detailed Seismic Assessment. The methodology in the NZSEE *Guidelines* enables calculation of probable capacities for all building elements followed by an evaluation of the hierarchy of the strength and deformation capacity of members to determine the global capacity of the structure. The last part of the evaluation process is to calculate seismic demands using prescribed seismic hazards to establish a ratio of existing building element capacities to new building demands designated as percentage of the New Building Standard (%NBS). Because this building was designed to be tested in an earthquake simulator instead of a prescribed seismic hazard, this last step is omitted from the assessment.

Evaluation of beam, column, and wall elements requires calculating element strength and deformation capacities for limit states related to flexure, shear, development length, and buckling of the reinforcement. According to the guidelines, probable strength capacities may be taken as nominal capacities using probable material strengths, so all calculations were based on expected material strengths which in the case of this building were taken as measured values. The following sections present equations from NZSEE *Guidelines* and indicate equation numbers where available.

4.9.1 Beam and Column Assessment

Parameters needed for beams beams and columns include the probable flexural strength, probable yield curvature, and probable curvature capacity. For rectangular-section beams and columns, the probable yield curvature, ϕ_y, is defined as:

$$\phi_y = \frac{2.0\varepsilon_y}{h} \qquad \text{Eq. 4-2 (NZSEE C5.2)}$$

and for T-section beams

$$\phi_y = \frac{1.7\varepsilon_y}{h} \qquad \text{Eq. 4-3 (NZSEE C5.4)}$$

Probable curvature capacity is taken as the lesser of:

$$\phi_{cap} = \frac{\varepsilon_{c,max}}{c_{prob}} \qquad \text{Eq. 4-4 (NZSEE C5.7)}$$

and

$$\phi_{cap} = \frac{\varepsilon_{s,max}}{d - c_{prob}} \qquad \text{Eq. 4-5 (NZSEE C5.8)}$$

where c_{prob} is the neutral axis depth at probable capacity. Maximum concrete compressive strain at the extreme fiber $\varepsilon_{c,max}$ is defined in NZSEE *Guidelines* Table C5.6 as $\varepsilon_{c,max} = 0.004$ for unconfined concrete. For confined concrete, the maximum compressive strain is defined as:

$$\varepsilon_{c,max} = 0.004 + \frac{1.4\rho_{st} f_{yh} \varepsilon_{ten}}{f'_{cc}} \leq 0.0015$$

Eq. 4-6 (NZSEE Table C5.6)

where ε_{ten} is the available strain at tensile strength of the steel and f'_{cc} is the compression strength of the confined concrete.

The maximum accepted strain of the reinforcement steel in tension is defined also in NZSEE *Guidelines* Table C5.6 as

$$\varepsilon_{s,max} = 0.06 \leq 0.06\varepsilon_{ten}6 \qquad \text{Eq. 4-7 (NZSEE Table C5.6)}$$

The probable rotation capacity in flexure is defined as the sum of the yield rotation and the plastic rotation.

$$\theta_p = \theta_y + \theta_p \qquad \text{Eq. 4-8 (NZSEE C5.12)}$$

where

$$\theta_y = \phi_p(H/3) \qquad \text{Eq. 4-9 (NZSEE C5.13)}$$

and

This publication is available free of charge from: https://doi.org/10.6028/NIST.GCR.22-917-50

$$\theta_p = (\phi_{cap} - \phi_y)L_pH \qquad \text{Eq. 4-10 (NZSEE C5.14)}$$

The equivalent plastic hinge length, L_p, is approximated as

$$L_p = kL_c + L_{sp} \qquad \text{Eq. 4-11 (NZSEE C5.19)}$$

where

$$k = 0.2(f_u/f_y - 1) \le 0.08 \qquad \text{Eq. 4-12 (NZSEE C5.20)}$$

In Equation 4-12 the term kL_c represents the spread of plasticity, L_c is the distance from the critical section to the point of contraflexure, and L_{sp} is the strain penetration defined as $0.022\, f_y\, d_b$.

The probable rotation capacity in flexure must be compared with limit states associated with bar buckling and flexure shear to identify the governing mode of failure. The deformation limit associated with bar buckling for beams and columns is defined based on the equation proposed by Berry and Eberhard (2005):

$$\theta_{bb} = 0.0325\left(1 + k_{e_bb}\rho_{eff}\frac{d_b}{D}\right)\left(1 - \frac{N}{A_g f_c'}\right)\left(1 + \frac{L_c}{20D}\right)$$

Eq. 4-13 (NZSEE C5.11)

where k_{e_bb} is the transverse reinforcement coefficient, L_c is the distance from the critical section to the point of contraflexure, ρ_{eff} is the effective confinement ratio and D is the section effective depth.

The deformation capacity due to flexure shear failure mechanism is defined as

$$\theta_s = 0.03 + 4\rho_s - 0.024\frac{v}{\sqrt{f_c'}} - 0.025\frac{N}{A_g f_c'} \ge 0.01$$

Eq. 4-14 (NZSEE C5.36)

The probable rotation capacity of the member is the lowest obtained from Equations 4-8, 4-13, and 4-14.

Probable shear capacity of beams and columns is defined as:

$$V_{prob} = 0.85(V_c + V_s + V_n) \qquad \text{Eq. 4-15 (NZSEE C5.24)}$$

where V_c, V_s, and V_n are contributions to shear strength related to concrete, reinforcement, and axial compressive load. The contribution from the concrete, V_c, is defined as:

$$V_c = \alpha\beta\gamma\sqrt{f_c'}\left(0.8A_g\right) \qquad \text{Eq. 4-16 (NZSEE C5.25)}$$

where

$$1 \le \alpha = 3 - \frac{M}{VD} \le 1.5 \qquad \text{Eq. 4-17}$$

$$\beta = 0.5 + 20\rho_l \le 1 \qquad \text{Eq. 4-18}$$

This publication is available free of charge from: https://doi.org/10.6028/NIST.GCR.22-917-50

The term γ is a shear strength degradation factor that varies between 0.05 and 0.29 as a function of curvature ductility. The contribution of the reinforcement to shear strength in beams is defined as:

$$V_s = \frac{A_v f_{yt} d}{s} \qquad \text{Eq. 4-19 (NZSEE C5.29)}$$

The contribution of the reinforcement to shear strength in columns is defined as:

$$V_s = \frac{A_v f_{yt} d}{s} \cot 30° \qquad \text{Eq. 4-20 (NZSEE C5.28)}$$

The contribution of axial compressive force to shear strength is given by

$$V_n = N \tan\alpha \qquad \text{Eq. 4-21 (NZSEE C5.33)}$$

For columns subjected to double curvature, α, is the angle between the longitudinal axis of the column and a straight line between the centroids of the compressive forces in sections at the top and bottom of a column.

Calculated probable strengths and rotation capacities for beams are summarized in Tables 4-7 and 4-8. The results indicate that the probable rotation capacity of beams in the study building was controlled by buckling of the reinforcement in the positive moment direction and by flexure-shear in the negative moment direction.

Table 4-7 Calculated Strength and Deformation Capacities for Beams

Bay	Level	Bending Direction	M_y (KNm)	θ_y	M_u (KNm)	Flexure θ_f	Buckling θ_{bb}	Shear θ_s
AB	2G1	+	302	0.0056	343.12	0.0641	0.0506	
		-	740	0.0056	840.75	0.0641	0.0506	0.015
	3G1	+	297	0.0056	338.00	0.0644	0.0506	
		-	678	0.0056	775.37	0.0644	0.0506	0.017
BC	4G1	+	284	0.0056	323.77	0.0722	0.0506	
		-	605	0.0056	691.90	0.0722	0.0506	0.018
	RG1	+	254	0.0056	288.20	0.0633	0.0506	
		-	610	0.0056	699.80	0.0633	0.0506	0.019

This publication is available free of charge from: https://doi.org/10.6028/NIST.GCR.22-917-50

Table 4-8 Governing Strength and Deformation Capacities for Beams

Bay	Level	Bending Direction	$M_{vp,min}$ (KNm)	Governing Mode of Failure	Governing Rotation at Failure θ_u
AB	2G1	+	596.39	buckling	0.0506
		-	596.39	shear	0.0150
	3G1	+	595.79	buckling	0.0506
		-	595.79	shear	0.0170
BC	4G1	+	581.16	buckling	0.0506
		-	581.16	shear	0.0180
	RG1	+	598.50	buckling	0.0506
		-	598.50	shear	0.0190

Calculated probable strengths and rotation capacities of columns from the study building are presented in Tables 4-9 and 4-10. The flexure shear rotation capacity is omitted from Table 4-9 because it did not control in any case. The results summarized in Tables 4-9 and 4-10 show that the probable rotation capacity of columns in the building was controlled by buckling of the reinforcement.

Table 4-9 Calculated Strength and Deformation Capacities for Columns

Column	Level	M_y (KNm)	θ_y	M_u (KNm)	Flexure θ_f	Buckling θ_{bb}
Exterior 1C	1	351	0.0030	354	0.0631	0.0449
	2	228	0.0030	329	0.0649	0.0456
	3	298	0.0030	301	0.0637	0.0478
	4	273	0.0030	272	0.0700	0.0467
Interior 1B	1	286	0.0030	507	0.0385	0.0432
	2	286	0.0030	445	0.0503	0.0450
	3	285	0.0030	389	0.0514	0.0464
	4	285	0.0030	353	0.0665	0.0460
Exterior 1A	1	404	0.0030	426	0.0447	0.0431
	2	369	0.0030	379	0.0558	0.0444
	3	316	0.0030	329	0.0568	0.0469
	4	286	0.0030	285	0.0690	0.0464

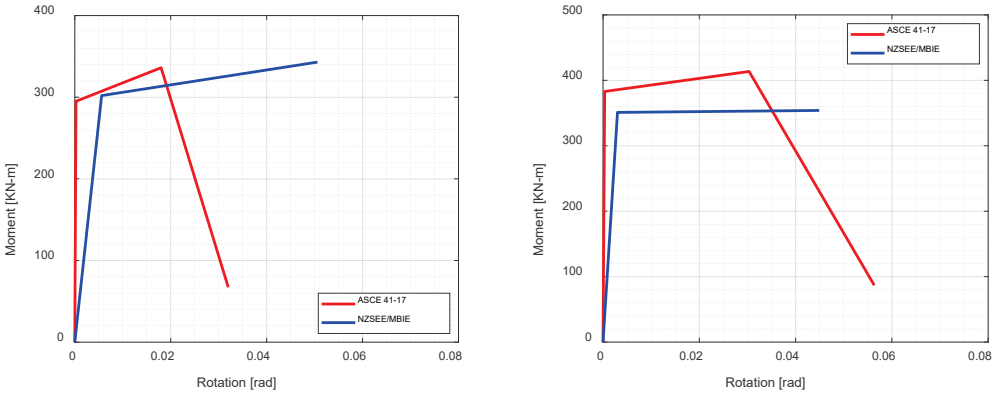
This publication is available free of charge from: https://doi.org/10.6028/NIST.GCR.22-917-50

Table 4-10 Governing Strength and Deformation Capacities for Columns

Column	Level	M (V_{pmin})	Governing Mode of Failure	Governing Rotation at Failure θ_u
Exterior 1C	1	769	Buckling	0.0449
	2	754	Buckling	0.0456
	3	728	Buckling	0.0478
	4	721	Buckling	0.0467
Interior 1B	1	773	Flex	0.0385
	2	776	Buckling	0.0450
	3	735	Buckling	0.0464
	4	743	Buckling	0.0460
Exterior 1A	1	953	Buckling	0.0431
	2	910	Buckling	0.0444
	3	864	Buckling	0.0469
	4	830	Buckling	0.0464

A comparison of backbone curves calculated with ASCE 41-17 and NZSEE *Guidelines* for a beam and column element are presented in Figure 4-69. The beam is located in the first floor, span BC, of Frame 1 (Figures 4-2 and 4-3), and the moment-rotation relationship shown corresponds to the positive moment direction. The column is the first story column on Gridline C of Frame 1 (Figures 4-2 and 4-3). Beam rotations corresponding to loss of lateral load capacity were significantly higher for NZSEE *Guidelines*, which illustrates the conservative nature of the ASCE 41 modeling parameters for beams. In the negative moment direction, where the NZSEE *Guidelines* rotation at loss of lateral load capacity is controlled by flexure shear, the inelastic rotation capacity was similar for both methods, and in both cases limiting rotations for beams, controlled by flexure shear under negative moment in the case of NZSEE *Guidelines*, were significantly lower than limiting column rotations, controlled by flexure in the case of the NZSEE *Guidelines*.

This publication is available free of charge from: https://doi.org/10.6028/NIST.GCR.22-917-50



Beam F1-BC: First floor Column 1C: First floor

Figure 4-69 Moment-rotation relationships for beam and column elements according to ASCE 41-17 and NZSEE *Guidelines*.

4.9.2 Beam-Column Joint Assessment

For interior and exterior beam-column joints, the probable horizontal joint shear force, V_{pjh}, that can be resisted is given by

$$V_{pjh} = 0.85\, v_{prob,h} b_j h \qquad \text{Eq. 4-22 (NZSEE C5.37)}$$

for exterior joints with some shear reinforcement, joint capacity is controlled by tensile cracking, and the strength is given by *NZ Guidelines* Eq. C5.39:

$$v_{pjh} = 0.85k\sqrt{f_c'}\sqrt{1 + k\sqrt{f_c'}\left(f_v + f_h\right) + f_v f_h}$$

Eq. 4-23 (NZSEE C5.39)

where

$$f_v = N/A_g \qquad \text{Eq. 4-24}$$

and

$$f_h = \frac{A_{st} f_{sy}}{b_j h_b} \qquad \text{Eq. 4-25}$$

For interior beam-column joints, joint capacity is controlled by crushing of the concrete and the probable horizontal joint shear force V_{pjh} that can be resisted for joints with some shear reinforcement is given by *NZ Guidelines* Eq. C5.40:

$$v_{pjh} = 0.85kf_c'\sqrt{1 + kf_c'\left(f_v + f_h\right) + f_v f_h} \qquad \text{Eq. 4-26 (NZSEE C5.40)}$$

NZSEE *Guidelines* provide the following values for k_j depending on reinforcement detailing:

- for interior joints, $k = 0.8$ (compression failure rather than tensile failure would govern in an interior beam-column joint)

This publication is available free of charge from: https://doi.org/10.6028/NIST.GCR.22-917-50

- for exterior joints with beam longitudinal (deformed) bars anchored by bending the hooks into the joint core, $k = 0.4$
- for exterior joints with beam longitudinal (deformed) bars anchored by bending the hooks away from the joint core (into the columns above and below), $k = 0.4$ at failure and 0.3 at first cracking

Calcuted joint capacities for minimum and maximum axial loads computed for the building are presented in Tables 4-11 and 4-12. Calculated strengths correspond to cracking and ultimate. Axial load demands due to overturning moment were calculated using a simplified procedure where only exterior columns are affected by varying axial load, and it was assumed that the seismic effect was equal to the shear demand in the beams associated with yielding of the flexural reinforcement.

Table 4-11 Calculated Strength and Deformation Capacities for Beam-Column Joints for Minimum Axial Load

Location	Level	V_{pjh,f_c} [KN]	θ_{crack} [Rad]	$V_{pjh,max}$ [KN]	θ_{peak} [Rad]	θ_u [Rad]
Exterior 1C	1	513.84	0.0002	648.21	0.005	0.010
	2	485.29	0.0002	619.74	0.005	0.010
	3	421.06	0.0002	539.99	0.005	0.010
	4	478.52	0.0002	616.58	0.005	0.010
Interior 1B	1	678.90	0.0003	1352.29	0.0075	0.015
	2	658.16	0.0003	1326.67	0.0075	0.015
	3	557.26	0.0003	1141.72	0.0075	0.015
	4	568.30	0.0003	1248.71	0.0075	0.015
Exterior 1A	1	0.00	0.0002	255.58	0.005	0.010
	2	218.98	0.0002	391.00	0.005	0.010
	3	291.59	0.0002	422.75	0.005	0.010
	4	438.35	0.0002	578.54	0.005	0.010

This publication is available free of charge from: https://doi.org/10.6028/NIST.GCR.22-917-50

Table 4-12 Calculated Strength and Deformation Capacities for Beam-Column Joints for Maximum Axial Load

Location	Level	V_{pjh,f_c} [KN]	θ_{crack} [Rad]	$V_{pjh,max}$ [KN]	θ_{peak} [Rad]	θ_u [Rad]
Exterior 1C	1	703.15	0.0002	839.20	0.005	0.010
	2	657.87	0.0002	792.00	0.005	0.010
	3	564.22	0.0002	681.28	0.005	0.010
	4	550.93	0.0002	687.15	0.005	0.010
Interior 1B	1	881.90	0.0003	1585.80	0.0075	0.015
	2	778.46	0.0003	1460.81	0.0075	0.015
	3	642.57	0.0003	1232.96	0.0075	0.015
	4	616.47	0.0003	1297.38	0.0075	0.015
Exterior 1A	1	825.28	0.0002	966.66	0.005	0.010
	2	744.64	0.0002	881.64	0.005	0.010
	3	615.31	0.0002	733.39	0.005	0.010
	4	578.27	0.0002	714.33	0.005	0.010

A comparison on joint moment-shear deformation relationships calculated according to NZSEE *Guidelines* and ASCE 41-17 for an exterior joint in the first floor is shown in Figure 4-70. Joint shears were converted to equivalent column moments using Equation 4-37. The figure shows a significant difference between shear strengths and deformation capacities, with the NZSEE *Guidelines* being more conservative for both parameters. The difference is caused in part because the NZSEE *Guidelines* provisions recognize the effect of axial load on joint strength, and uplift forces due to overturning were included in the calculations. Also, the difference between joint coefficients for interior and exterior joints was a factor. In ASCE-41 joint coefficients for exterior joints are on the order of 20 to 25% lower than joint coefficients for interior joints, while in the NZSEE *Guidelines* that difference is on the order of 50%. This compounds with the fact that joint shear coefficients for conforming joints in ASCE 41 are overall higher than those in NZSEE *Guidelines*. Another factor that causes the difference is how the two code provisions address the effect of joint reinforcement on strength. In Equations 4-23 and 4-26 strength increases proportional to the amount of reinforcement. In the study building the joint hoop spacing was relatively large, and the additional strength afforded by Equations 4-23 and 4-26 was not very large. A much larger amount of reinforcement in the joint would produce strengths similar to those calculated with ASCE 41-17 for conforming joints. ASCE 41-17 provisions set a low bar for classifying joints as conforming, which was met in the case of the joints in this building. The significant discrepancies between modeling parameters in the NZSEE *Guidelines* and ASCE 41, and the fact that joint damage was overestimated using both provisions suggest that

This publication is available free of charge from: https://doi.org/10.6028/NIST.GCR.22-917-50

joint classification criteria as well as modeling parameters in ASCE 41 should be scrutinized. The difference in joint modeling parameters calculated with the two standards may be partially caused by the data sets used to calibrate each standard and the probabilities of exceedance that equations in each standard were calibrated to achieve. For example, values of parameter k_j in NZSEE *Guidelines* Equation C5.37 are based on tests from Hakuto et al. (1999 and 2000) and Pampanim et al. (2002 and 2003), and the latter mostly included joints with plain round bars.

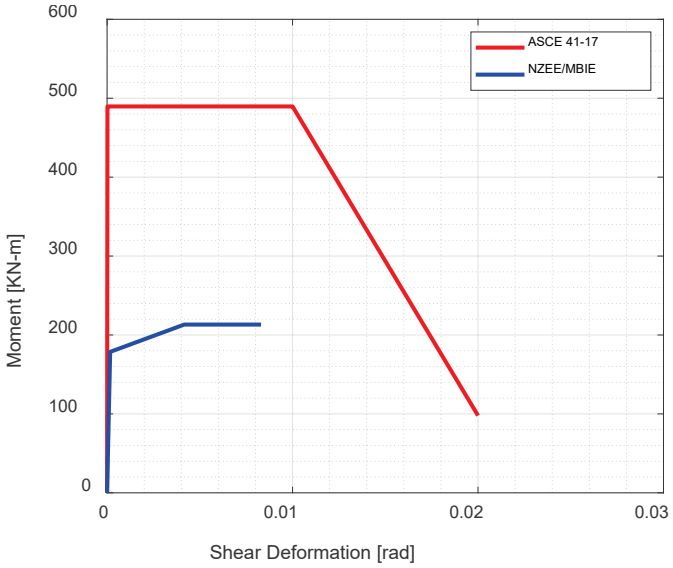


Figure 4-70 Moment-shear deformation relationship for exterior beam column joint in the first story of Frame 1 calculated according to ASCE 41-17 and NZSEE *Guidelines*.

4.9.3 Wall Assessment

Provisions for the assessment of joints are similar to those for beams and columns with a few differences. For rectangular section walls, the probable yield curvature ϕ_y is defined as:

$$\phi_y = \frac{2.0\varepsilon_y}{l_w} \qquad \text{Eq. 4-27 (NZSEE C5.5)}$$

Probable curvature capacity of walls where vertical reinforcement spacing is greater than 6 × d_b may controlled by buckling of the reinforcement. In those instances, the curvature capacity is a function of the plastic strain in the reinforcement ε_p^* and is calculated as:

$$\phi_{cap} = \frac{\varepsilon_p^*}{\gamma l_w} \qquad \text{Eq. 4-28 (NZSEE C5.9)}$$

where

This publication is available free of charge from: https://doi.org/10.6028/NIST.GCR.22-917-50

$$\varepsilon_p^* = \frac{11 - 5s/4d_b}{100} \qquad \text{Eq. 4-29 (NZSEE C5.10)}$$

Boundary elements in the walls of the E-Defense building had hoop spacing smaller than $6 \times d_b$ so it was assumed that buckling of the reinforcement would not limit the flexural deformation capacity of the walls.

The curvature capacity of the wall (Figure 4-71) in flexure is calculated based on maximum strains in the concrete $\varepsilon_{c,max}$ and steel $\varepsilon_{s,max}$ dictated by the NZSEE *Guidelines* as the lesser of

$$\phi_u = \frac{\varepsilon_{c,max}}{c} \text{ and } \phi_u = \frac{\varepsilon_{s,max}}{d-c} \qquad \text{(NZSEE C5.7 and C5.8)}$$

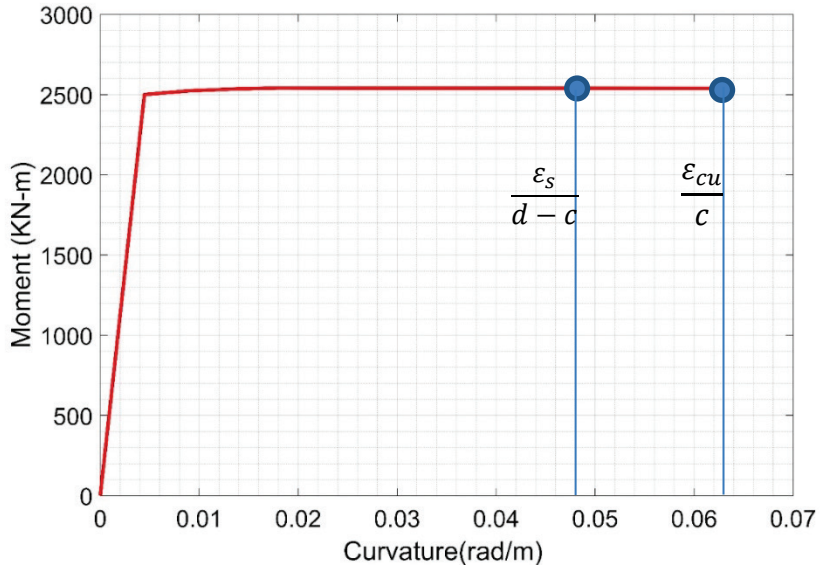


Figure 4-71 Moment-curvature relationship for wall on Gridline C.

The equation for plastic hinge length of walls includes an additional term that is a function of wall length l_w:

$$L_p = kL_c + L_{sp} + 0.1l_w \qquad \text{Eq. 4-30 (NZSEE C5.21)}$$

Shear strength of walls is calculated using Equations 4-15 through 4-17. The shear strength degradation factor γ also varies between 0.05 and 0.29, but does so as a function of displacement ductility. For walls, the contribution of the reinforcement to shear strength is defined as:

$$V_s = \frac{A_v f_{yh} h_{cr}}{s} \qquad \text{Eq. 4-31 (NZSEE C5.29)}$$

where

$$h_{cr} = \frac{l'}{\tan\theta_{cr}} \le h_w \qquad \text{Eq. 4-32 (NZSEE C5.30)}$$

This publication is available free of charge from: https://doi.org/10.6028/NIST.GCR.22-917-50

$$l' = l_w - c - c_0 \qquad \text{Eq. 4-33 (NZSEE C5.31)}$$

$$\theta_{cr} = 45° - 7.5\frac{M}{Vl_w} \geq 30° \qquad \text{Eq. 4-34 (NZSEE C5.32)}$$

In Equation 4-33 c is the depth of the compression zone and c_0 is the cover to the longitudinal bars. Shear strength contribution from the axial compressive load, N, on the wall is given by:

$$V_n = N\frac{(l_w - c)}{2h_w} \qquad \text{Eq. 4-35 (NZSEE C5.34)}$$

Wall pameters M_y and M_u (flexural strength) are computed using the cross-section analysis including the axial load at the base. In this case, the product of the probable shear capacity of the wall and the wall height, $V_{p,\,min} \times L_c$, is greater than M_u (864.5 kN × 12 m = 10,370 kNm > M_u = 2,539 kNm) so the wall is controlled by flexure and shear failure does not limit wall drift capacity.

A comparison between moment-rotation relationships of the walls in the study building calculated with the NZSEE *Guidelines* and ASCE 41-17 methods is presented in Figure 4-72. Modeling parameters in ASCE 41-17 were significantly more conservative given that the relatively close spacing of the hoops in the boundary elements precluded bar buckling from limiting the rotation capacity calculated with NZSEE *Guidelines*. As previously stated, structural walls in the building slid after severe boundary damage and crushing (Figure 4-9, Nagae et al., 2015). In the context of this comparison, it appears that concrete crushing was the limiting mode of failure, which is contrary to the assessment in Figure 4-71. Modeling parameters in ASCE 41-17 provided a more accurate representation of wall behavior than NZSEE *Guidelines* provisions for structural walls.

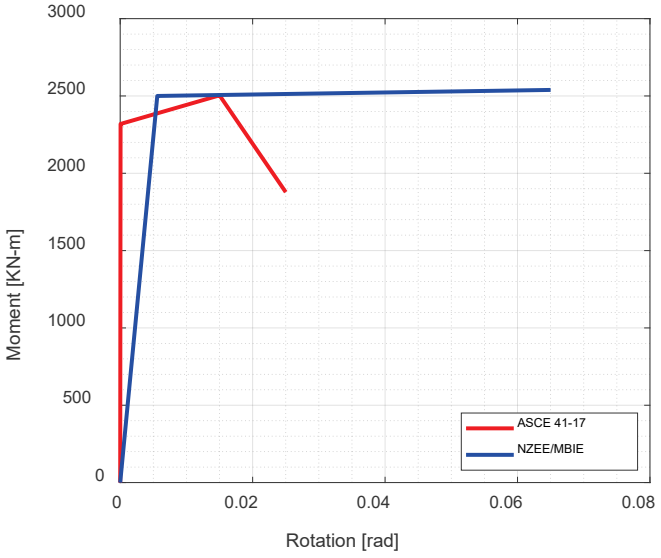


Figure 4-72 Moment-rotation relationship for walls calculated according to ASCE 41-17 and NZSEE *Guidelines*.

This publication is available free of charge from: https://doi.org/10.6028/NIST.GCR.22-917-50

4.9.4 *Evaluation of the Hierarchy of Strength and Sequence of Events for a Beam-Column Joint Sub-Assembly*

After probable strengths and deformation capacities are evaluated, the expected sequence of failure events within beam-column joints is established by comparing capacity and demands of the elements framing into the joint and the joint itself in terms of a common parameter, the equivalent column moment. To that effect, capacities of beams and beam-column joints are transformed into equivalent column moments that would cause those demands based on equilibrium. The failure mechanism associated with the lowest equivalent column moment is considered to govern the strength hierarchy. The effect of changes in axial load demand due to overturning moment must be considered in this analysis because it may change the sequence in which the three members fail and lead to an ineffective retrofit strategy.

Based on joint equilibrium, the equivalent column moment for exterior joint beams is given by:

$$M_c = M_b \frac{l_b l_c'}{l_b' l_c} \qquad \text{Eq. 4-36}$$

where beam and column spans are shown in Figure 4-73 for an exterior and interior joints. In exterior joints M_b was evaluated separately for the positive and negative moment directions, and in the case of the study building the positive moment capacity provided the lower of the two. For interior joints, M_b in Equation 4-35 is the sum of the positive and negative moment capacities. The equilibrium equation can be easily adjusted for beams controlled by shear capacity, but that was not the case for this building. For Frame 1, the scale factor to convert the external beam moments to equivalent column moment was equal to 0.43 ($M_c = 0.43 \times M_b$).

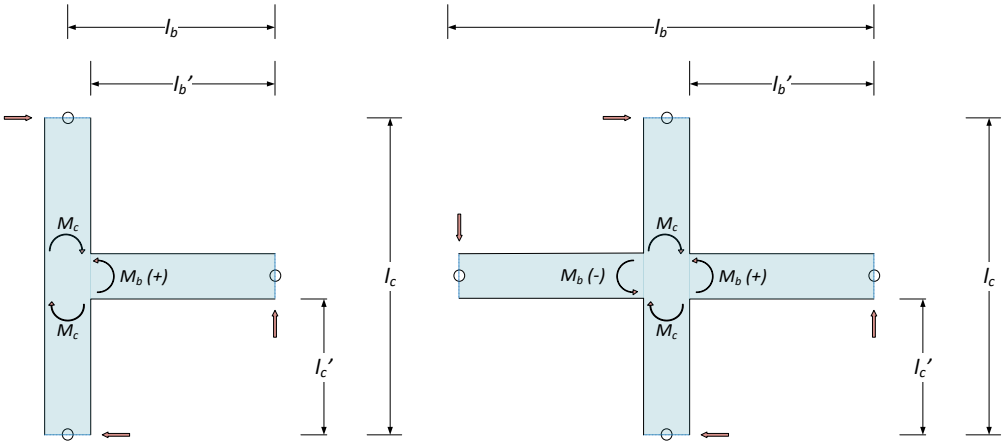


Figure 4-73 Beam and column span definitions in Equation 4-36.

This publication is available free of charge from: https://doi.org/10.6028/NIST.GCR.22-917-50

Similarly, joint capacity can be converted into an equivalent column moment. Equilibrium of internal forces in the horizontal direction (Figure 4-74), is used to establish a relationship between beam shear V_b, column shear, V_c, and joint shear, V_j.

$$V_c = T_b - V_j = M_b/(jd) - V_j \qquad \text{Eq. 4-37}$$

substituting the relationship between the column moment and beam moment in Equation 4-36 and rearranging terms, the following expression is obtained for the equivalent column moment associated with joint capacity:

$$M_c = V_{jh}\frac{jdl_b l_c'}{l_b' l_c - jdl_b} \qquad \text{Eq. 4-38}$$

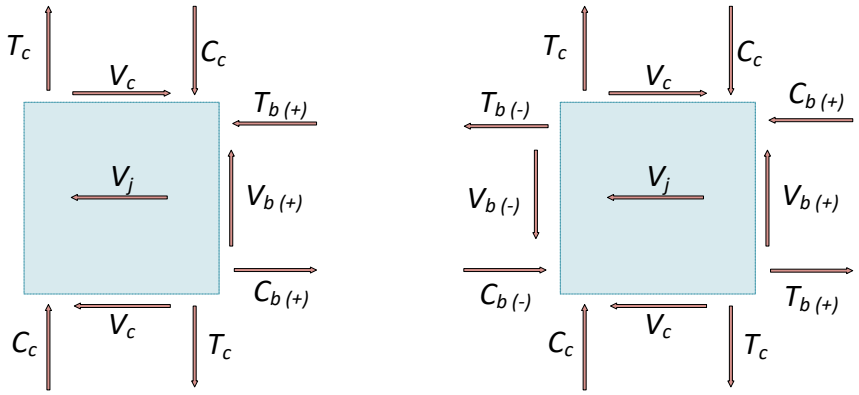


Figure 4-74 Internal forces in beam-column external and internal joints.

Calculated equivalent column moments and the controlling mode of failure for each level and each axis of Frame 1 are summarized in Tables 4-13 through 4-15 and Figure 4-75. The analysis showed that in most cases the controlling mode of failure was joint shear. This is consistent with the results from the Opensees LP NJ model (Figure 4-20) and Opensees Fiber NJ (Figure 4-29) models, which estimated damage to the joins, much more severe in the latter than the former. Figures 4-10 and 4-11 show that there was shear damage in interior and exterior joints, with the most severe damage occurring in the interior joints. This is in direct contradiction to the findings from both provisions, which estimated that the most severe damage would occur in exterior joints.

Table 4-13 Calculated Equivalent Column Moments for Axis 1C (Calculated with P_{max})

	Equivalent Column Moment [KNm]				
Level	*Beam Hinge*	*Column Hinge*	*Joint Cracking*	*Joint Failure*	*Failure*
1	318	354	178	213	JF
2	291	329	167	201	JF
3	260	301	143	173	JF
4	262	272	140	174	JF

This publication is available free of charge from: https://doi.org/10.6028/NIST.GCR.22-917-50

Table 4-14 Calculated Equivalent Column Moments for Axis 1B (Calculated with $P_{gravity}$)

	Equivalent Column Moment [KNm]				
Level	*Beam Hinge*	*Column Hinge*	*Joint Cracking*	*Joint Failure*	*Failure*
1	521	445	188	354	JF
2	487	410	174	337	JF
3	444	369	147	289	JF
4	432	343	144	309	JF

Table 4-15 Calculated Equivalent Column Moments for Axis 1A (Calculated with P_{min})

	Equivalent Column Moment [KNm]				
Level	*Beam Hinge*	*Column Hinge*	*Joint Cracking*	*Joint Failure*	*Failure*
1	129.8	135	0.0	64.9	JF
2	127.7	167	55.6	99.3	JF
3	122.1	199	74.1	107.4	JF
4	109.2	226	111.4	147.0	BH

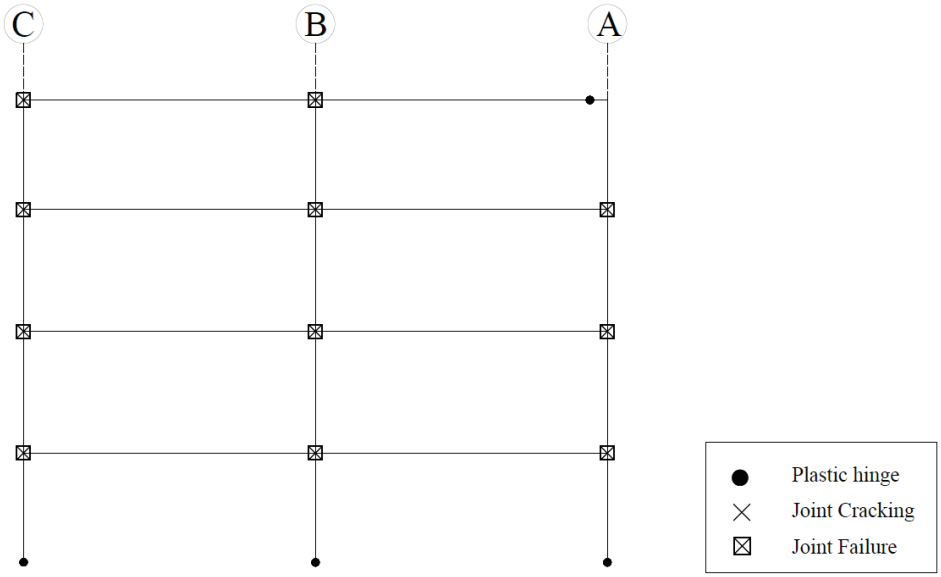


Figure 4-75 Controlling modes of failure for Frame 1.

4.9.5 Global Capacity of Moment Resisting Frame

The base shear capacity and force-displacement curve of the building was calculated through plastic analysis. The NZSEE *Guidelines* state that the upper bound capacity corresponds to a soft-story mechanism, the lower bound capacity to a beam-sway mechanism, and in-between capacities to mixed sidesway mechanism. In general, base shear capacity, V_B, is calculated as (Figure 4-76):

This publication is available free of charge from: https://doi.org/10.6028/NIST.GCR.22-917-50

$$V_B = \frac{1}{H_{eff}}\left[\left(\sum_i M_{col,i}\right) + \left(\sum_n M_{end\ beam,n}\right) L\right] \quad \text{Eq. 4-39}$$

where beam shear, $V_{end,beam}$, is computed in terms of the beam positive and negative moment capacities and the span length as $(M_b^+ + M_b^-)/L_{span}$. The effective height, H_{eff}, can be computed using displacement profiles suggested by NZSEE *Guidelines* for frames ranging between 4 and 20 stories. For beam sidesway frame mechanisms:

$$H_{eff} = [0.64 - 0.0125(n - 4)]H_{tot} \quad \text{Eq. 4-40}$$

where n is the number of sories and H_{tot} is the total height of the frame. For column sidesway frame mechanisms:

$$H_{eff} = 0.5H_{tot} \quad \text{Eq. 4-41}$$

For mixed sidesway frame mechanisms:

$$H_{eff} = 0.67H_{tot} \quad \text{Eq. 4-42}$$

In this section, calculations are presented for a mixed sidesway mechanism, but can be easily adjusted for beam and column sidesway mechanisms by substituting H_{eff} calculated with Equations 4-40 and 4-41. Equivalent beam moments used in the calculations are presented in Figure 4-77.

From Equation 4-40, H_{eff} is calculated as 0.67 × 12000 mm = 8040 mm. The base shear strength is:

$$V_b \times H_{eff} = (354 + 445 + 135) + (271 \times 14.4) = 4833 \text{ kNm}$$

$$V_b = 4833 \text{ kNm} / 8.04 \text{ m} = 601 \text{ kN}$$

In this case, the joint drift ratio at the peak strength is used to compute the frame displacement at failure because the hierarchy of strength outlined that joint shear failure governs frame response. The base shear-lateral deformation relationship for the frame is shown in Figure 4-78.

As shown in Table 4-6, in the frame direction, the base shear measured in the experiment was approximately 1890 kN, compared to 1202 kN (601 kN per frame × 2 frames) for the NZSEE *Guidelines*. ASCE 41-17 models summarized in Table 4-6 had base shear strengths in the frame direction ranging between 1664 kN and 2280 kN. One of the reasons for this difference is that element moment-rotation relationships for NZSEE *Guidelines* in this section were assumed to be elastic-perfectly-plastic while ASCE 41-17 models included a reduced post-yield stiffness. This is also attributed to the nature of the hierarchy method, which is intended to identify strength in terms of the element with the lowest capacity. This is in contrast with nonlinear analyses, which allow increasing the load in other elements while the first element deforms in the inelastic range if all elements maintain their flexural capacity. Mean drift ratio at joint failure for NZSEE *Guidelines* in Figure 4-78 was

This publication is available free of charge from: https://doi.org/10.6028/NIST.GCR.22-917-50

approximately 1%, compared with mean drift ratios at the third floor exceeding 2% recorded in the experiment and calculated with the NLDP.

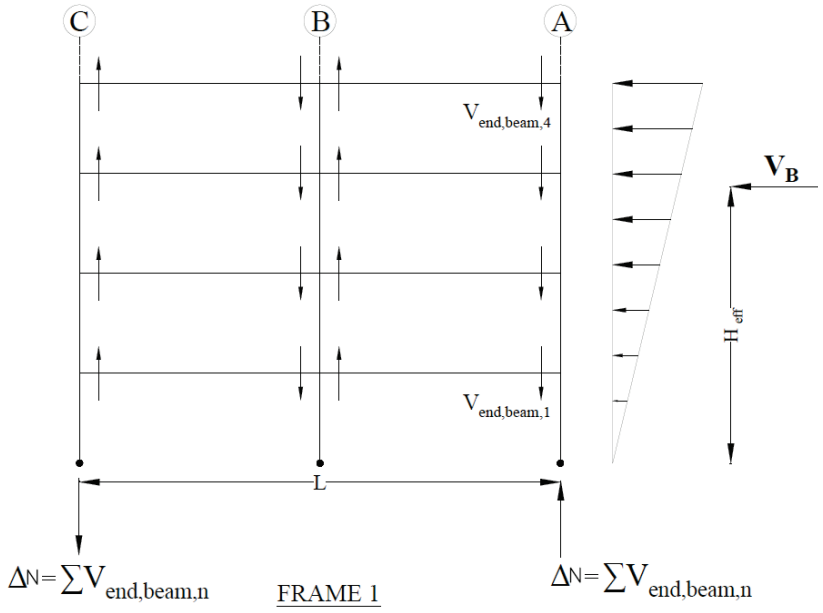


Figure 4-76 Force distribution for the calculation of base shear strength.

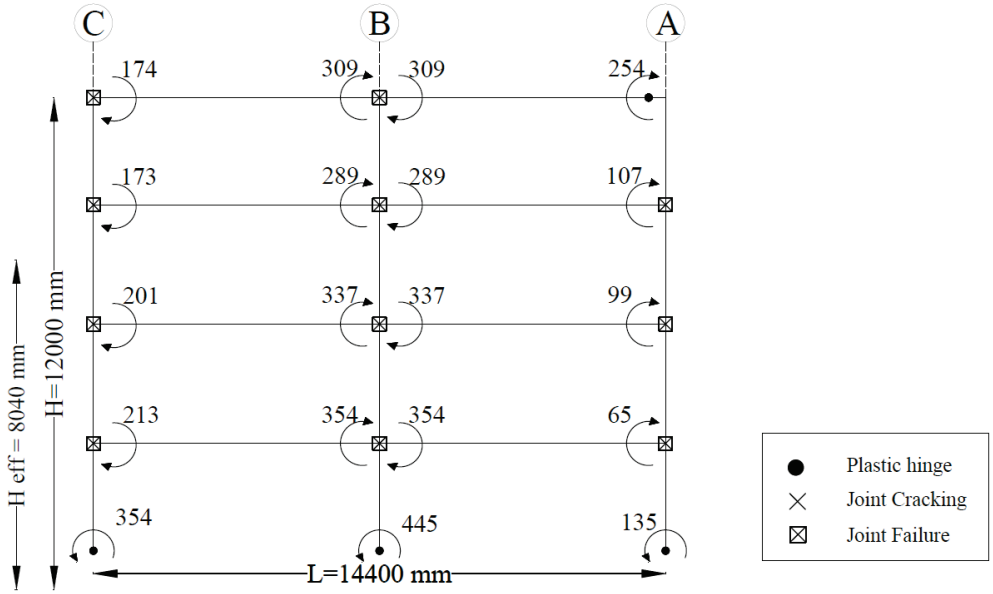


Figure 4-77 Force distribution for the calculation of base shear strength.

This publication is available free of charge from: https://doi.org/10.6028/NIST.GCR.22-917-50

This publication is available free of charge from: https://doi.org/10.6028/NIST.GCR.22-917-50

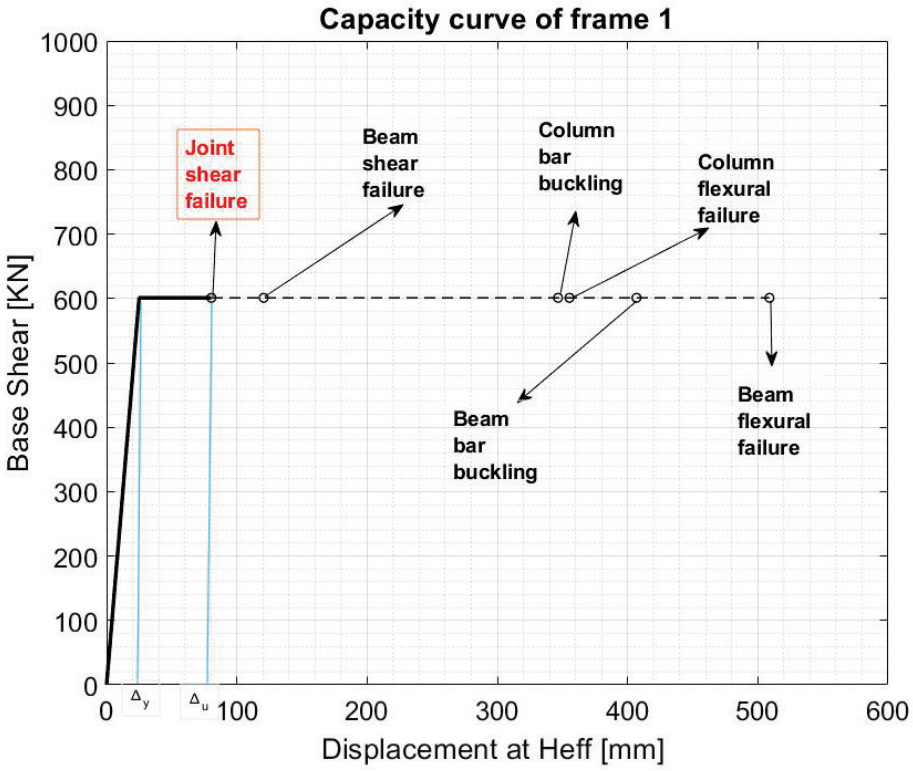


Figure 4-78 Capacity curve for Frame 1.

4.9.6 Capacity of Dual Wall-Frame

Frames A and C of the building (Figures 4-2 and 4-3) are considered to be dual systems because there is a wall between two column lines connected with beams. The methodology in the NZEE *Guidelines* relies on calculating the capacity of frame and wall elements, and using the combined strength hierarchy to calculate the load-deformation relationship for the dual frame. The procedure for frame component assessment is the same performed for the exterior joints of Frame 1. Assessment results for beams, columns, and beam-column joints are summarized in Tables 4-16 to 4-23.

Table 4-16 Calculated Strength and Deformation Capacities for Beams in Wall Direction

Bay	Level	Bending Direction	M_y (KNm)	θ_y	M_u (KNm)	Flexure θ_f	Buckling θ_{bb}	Flexure Shear θ_s
	2G2	+	111	0.0032	125.32	0.0723	0.0511	
		–	151	0.0032	171.12	0.0723	0.0511	0.014
1A1	3G2	+	111	0.0032	125.28	0.0722	0.0512	
		–	150	0.0032	171.42	0.0722	0.0512	0.015
1A2	4G2	+	106	0.0032	117.94	0.0702	0.0537	
		–	145	0.0032	163.85	0.0702	0.0537	0.015
	RG2	+	96	0.0032	102.32	0.0723	0.0509	
		–	151	0.0032	170.60	0.0723	0.0509	0.014

Table 4-17 Governing Strength and Deformation Capacities for Beams in Wall Direction

Bay	Level	Bending Direction	$M_{vp,min}$ (kNm)	Governing Mode of Failure	Governing Rotation at Failure θ_u
	2G2	+	136.11	buckling	0.0511
		–	136.11	flexure-shear	0.014
1A1	3G2	+	136.02	buckling	0.0512
		–	136.02	flexure-shear	0.015
1A2	4G2	+	133.85	buckling	0.0537
		–	133.85	flexure-shear	0.015
	RG2	+	134.95	buckling	0.0509
		–	134.95	flexure-shear	0.014

This publication is available free of charge from: https://doi.org/10.6028/NIST.GCR.22-917-50

Table 4-18 Calculated Strength and Deformation Capacities for Columns in Wall Direction, Maximum Axial Load

Column	Level	M_y (KNm)	θ_y	M_u (KNm)	Flexure θ_f	Buckling θ_{bb}
Exterior 1C	1	351	0.0034	354	0.0661	0.0460
	2	228	0.0034	329	0.0679	0.0467
	3	298	0.0034	301	0.0667	0.0489
	4	273	0.0034	272	0.0733	0.0478
Exterior 2C	1	445	0.0034	477	0.0379	0.0427
	2	399	0.0034	421	0.0476	0.0443
	3	333	0.0034	353	0.0504	0.0471
	4	299	0.0034	299	0.0711	0.0472

Table 4-19 Calculated Strength and Deformation Capacities for Columns in Wall Direction, Minimum Axial Load

Column	Level	M_y (KNm)	θ_y	M_u (KNm)	Flexure θ_f	Buckling θ_{bb}
Exterior 1C	1	260	0.0034	260	0.0739	0.0484
	2	248	0.0034	248	0.0747	0.0487
	3	243	0.0034	243	0.0722	0.0511
	4	242	0.0034	242	0.0758	0.0485
Exterior 2C	1	139	0.0034	144	0.0896	0.0512
	2	175	0.0034	178	0.0806	0.0504
	3	195	0.0034	195	0.0759	0.0525
	4	226	0.0034	226	0.0771	0.0489

This publication is available free of charge from: https://doi.org/10.6028/NIST.GCR.22-917-50

Table 4-20 Governing Strength and Deformation Capacities for Columns in Wall Direction, Maximum Axial Load

Column	Level	M ($V_{p,min}$)	Governing Mode of Failure	Governing Rotation at Failure θ_u
Exterior 1C	1	865.49	Buckling	0.0460
	2	848.72	Buckling	0.0467
	3	819.46	Buckling	0.0489
	4	811.31	Buckling	0.0478
Exterior 2C	1	861.60	Flexure	0.0379
	2	866.56	Buckling	0.0443
	3	819.78	Buckling	0.0471
	4	829.52	Buckling	0.0472

Table 4-21 Governing Strength and Deformation Capacities for Columns in Wall Direction, Minimum Axial Load

Column	Level	M ($V_{p,min}$)	Governing Mode of Failure	Governing Rotation at Failure θ_u
Exterior 1C	1	800.23	Buckling	0.0484
	2	791.90	Buckling	0.0487
	3	775.91	Buckling	0.0511
	4	789.56	Buckling	0.0485
Exterior 2C	1	721.05	Buckling	0.0512
	2	740.82	Buckling	0.0504
	3	745.51	Buckling	0.0525
	4	778.29	Buckling	0.0489

This publication is available free of charge from: https://doi.org/10.6028/NIST.GCR.22-917-50

Table 4-22 Calculated Strength and Deformation Capacities for Beam-Column Joints in Wall Direction, Maximum Axial Load

Location	Level	V_{pjh,f_c} [KN]	θ_{crack} [Rad]	$V_{pjh,max}$ [KN]	θ_{peak} [Rad]	θ_u [Rad]
Exterior 1C	1	703.15	0.0002	839.20	0.005	0.010
	2	657.87	0.0002	792.00	0.005	0.010
	3	564.22	0.0002	681.28	0.005	0.010
	4	550.93	0.0002	687.15	0.005	0.010
Exterior 2C	1	908.86	0.0002	1055.06	0.005	0.010
	2	814.07	0.0002	954.31	0.005	0.010
	3	661.50	0.0002	781.03	0.005	0.010
	4	605.95	0.0002	742.11	0.005	0.010

Table 4-23 Calculated Strength and Deformation Capacities for Beam-Column Joints in Wall Direction, Minimum Axial Load

Location	Level	V_{pjh,f_c} [KN]	θ_{crack} [Rad]	$V_{pjh,max}$ [KN]	θ_{peak} [Rad]	θ_u [Rad]
Exterior 1C	1	513.84	0.0002	648.21	0.005	0.010
	2	485.29	0.0002	619.74	0.005	0.010
	3	421.06	0.0002	539.99	0.005	0.010
	4	478.52	0.0002	616.58	0.005	0.010
Exterior 2C	1	0	0.0002	277.28	0.005	0.010
	2	259.16	0.0002	420.19	0.005	0.010
	3	288.18	0.0002	419.88	0.005	0.010
	4	436.98	0.0002	577.26	0.005	0.010

Calculated equivalent column moments and the controlling mode of failure for each level at location C-1 (intersection of axis C in the wall direction and axis 1 in the frame direction) and location C-2 (intersection of axis C in the wall direction and axis 2 in the frame direction) are summarized in Tables 4-24 and 4-25 and Figure 4-79. The difference between the two locations is due to earthquake-induced axial loads, assumed to be compressive at location C-1 and tensile at location C-2. Analysis showed that at location C-1, beam flexural capacity (either due to longitudinal reinforcement buckling or shear failure after yield) was the controlling mode of failure. At location C-2, joint failure controlled in the first floor and beam capacity at all other floors.

This publication is available free of charge from: https://doi.org/10.6028/NIST.GCR.22-917-50

Table 4-24 Calculated Equivalent Column Moments for Location C-1 (Calculated with P_{max})

	Equivalent Column Moment [KNm]				
Level	*Beam*	*Column*	*Joint Cracking*	*Joint Failure*	*Failure*
1	74	351	104	124	BH
2	73	228	97	117	BH
3	71	298	84	101	BH
4	74	273	82	102	BH

Table 4-25 Calculated Equivalent Column Moments for Location C-2 (Calculated with P_{min})

	Equivalent Column Moment [KNm]				
Level	*Beam*	*Column*	*Joint Cracking*	*Joint Failure*	*Failure*
1	54	139	-	41.1	JF
2	54	175	38.4	62.2	JC-BH
3	52	195	42.7	62.2	JC-BH
4	47	226	64.7	85.5	BH

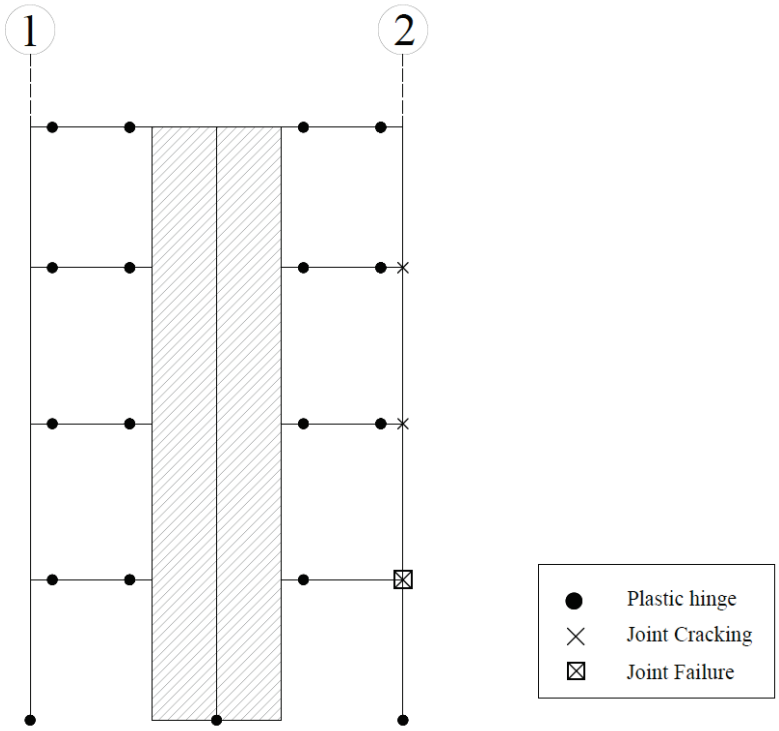


Figure 4-79 Controlling modes of failure for Frame C.

In this case, the beam displacement capacity is used to compute the frame displacement at the yielding and ultimate states. The strength hierarchy showed that beam plastic hinges are expected to have significant influence on the expected frame

This publication is available free of charge from: https://doi.org/10.6028/NIST.GCR.22-917-50

response, but that joint rotation capacity would limit the ultimate displacement. In this frame, the displacement at yield is controlled by beam yielding and the ultimate displacement capacity is controlled by the ultimate drift capacity of the first story joint. Displacements at yield and ultimate were calculated as

$$\Delta_y = \min(\theta_y(\text{beams})) \times H_{eff} = 0.0032 \times 8.04 = 0.025\text{m} = 25\text{mm}$$

$$\Delta_u = \min(\theta_u(\text{joints})) \times H_{eff} = 0.01 \times 8.04 = 0.08\text{m} = 80\text{mm}$$

Frame base shear was calculated assuming H_{eff} for a mixed sideway mechanism, and the base shear capacity of the frame was:

$$V_b \times H_{eff} = (351 + 139) + (452 \times 7.2) = 3744 \text{ kNm}$$

$$V_b = 3744 / 8.04 = 466 \text{ kN}$$

The base shear-lateral deformation relationship for Frame C is shown in Figure 4-80.

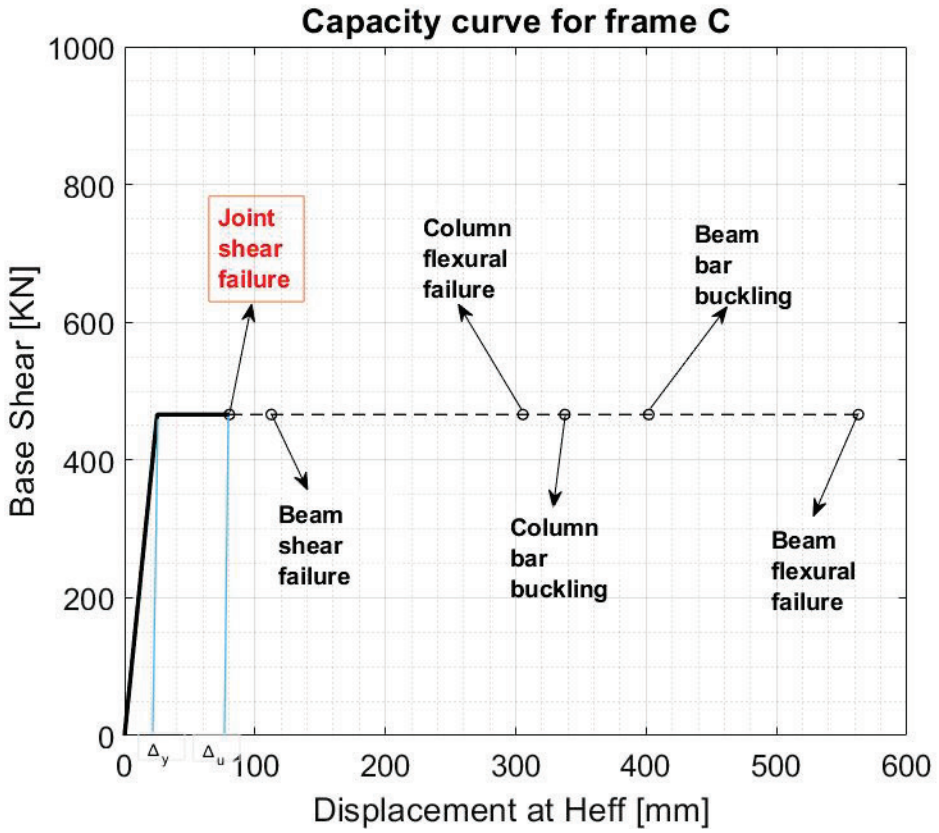


Figure 4-80 Capacity curve for Frame C.

In the wall assessment, it was found that flexural strength governed the behavior of the wall and that shear failure was not expected along the wall height. First mode behavior with $H_{eff} = 0.67H_{tot} = 0.67 \times 12$ m = 8.04 m was assumed to calculate the contribution of the wall to the base shear capacity of the dual system:

This publication is available free of charge from: https://doi.org/10.6028/NIST.GCR.22-917-50

$$V_{wall\ base} = \frac{M_{u,wall}}{H_{eff}} = \frac{2539}{8.04} = 316 \text{ kN} \qquad \text{Eq. 4-43}$$

Displacements at yield and at ultimate for the wall are calculated as:

$$\Delta_y = \theta_y \times H_{eff} = 0.0056 \times 8.04 \text{ m} = 0.045 \text{ m} = 45 \text{ mm}$$

The ultimate displacement computed with the ultimate rotation is:

$$\Delta_u = \theta_u \times H_{eff} = 0.065 \times 8.04 \text{ m} = 0.53 \text{ m} = 530 \text{ mm}$$

The load-deformation capacity of the dual system is calculated by adding the contribution to base shear capacity of the wall and the frame, and adopting the liming deformation capacity as shown in Figure 4-81. As shown in Figure 4-81, deformation capacity was controlled by frame components, specifically the exterior beam-column joint in the first floor.

As shown in Table 4-6, in the wall direction the base shear measured in the experiment was approximately 2760 kN, compared with 2030 kN ((466 kN per frame × 3 frames) + (316 kN per wall × 2 walls) for the NZSEE *Guidelines*. ASCE 41-17 models summarized in Table 4-6 had base shear strengths in the wall direction ranging between 1670 kN and 2220 kN. Mean drift ratio at joint failure for NZSEE *Guidelines* in Figure 4-78 was also approximately 1%, compared with mean drift ratios at the third floor of approximately 3% recorded in the experiment and calculated with the nonlinear dynamic procedures.

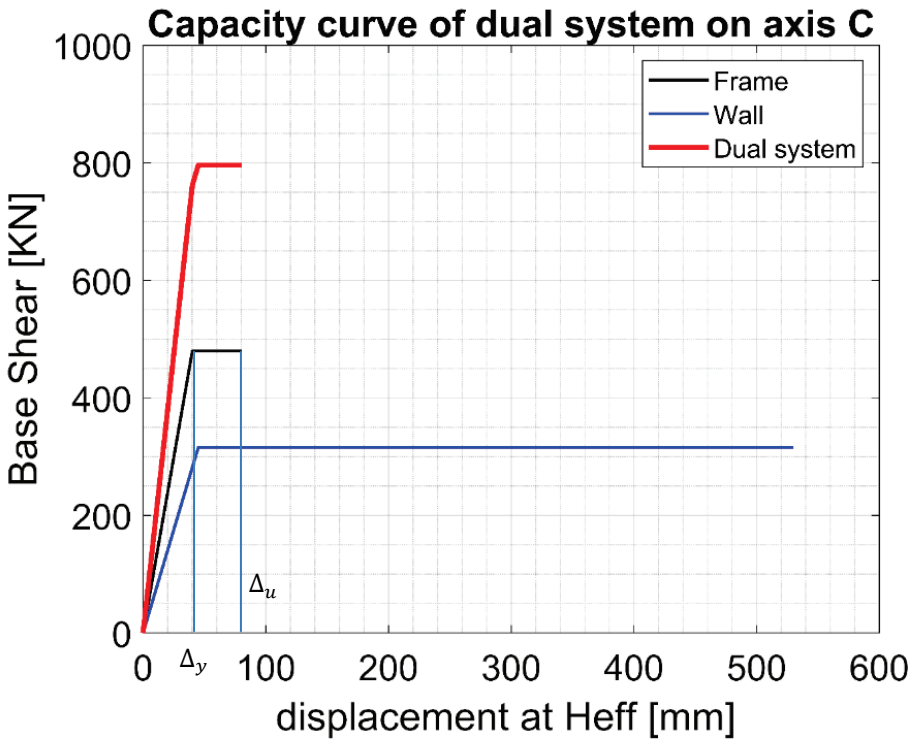


Figure 4-81 Capacity of dual system in Gridline C.

This publication is available free of charge from: https://doi.org/10.6028/NIST.GCR.22-917-50

4.10 FEMA P-2018 Evaluation

4.10.1 Evaluation Approach

The building was evaluated using the evaluation procedure outlined in FEMA P-2018, *Seismic Evaluation of Older Concrete Buildings for Collapse Potential* (FEMA, 2018b). The building was classified as a "Frame-Wall System" in the transverse direction and a "Frame System" in the longitudinal direction and accordingly evaluated per Chapter 7 and Chapter 6 of FEMA P-2018, respectively. The spectral accelerations utilized in the analysis were extracted from response spectra that were generated from the recorded ground motions.

4.10.2 Global Performance: Evaluation Procedure vs. Observation

Table 4-26 provides a summary of the key evaluation parameters and results in the wall-direction and frame-direction. Table 4-27 provides a summary of the corresponding story ratings calculated in each direction.

Table 4-26 Summary of Key Evaluation Parameters and Results

Parameter	X-Direction (SW)	Y-Direction (MF)	Units	Description
W	796	796	kips	Total Building Weight
T_e	0.42	0.71	sec	Effective Fundamental Period
S_a @ T_e	2.38	1.84	g	Spectral Acceleration at T_e
V_y	249	303	kips	Base Shear Yield Strength
Mechanism	2	1	-	Governing Plastic Mechanism
Critical Story	1	1	-	Critical Story
$\mu_{strength}$	6.1	4.4	-	Global DCR
δ_{eff}	7.1	10.1	in	Global Equivalent SDOF Drift
$\delta_{eff,roof}$	9.4	13.4	in	Global Roof Drift
$\delta_{eff,roof} / h_{roof}$	2.0%	2.8%	-	Global Roof Drift Ratio

Table 4-27 Story Ratings

Story	X-Direction (SW)	Y-Direction (MF)
1	0.10*	0.35*
2	0.11	0.10
3	0.11	0.10
4	0.15	0.10

* Indicates critical story

This publication is available free of charge from: https://doi.org/10.6028/NIST.GCR.22-917-50

In the X-direction, the building was found to be governed by yielding at the first story. The imited lateral strength at this critical story resulted in a large global demand-capacity ratio, $\mu_{strength}$, of 6.1, and global roof drift ratio, $\delta_{eff,roof} / h_{roof}$, of 2.0%. The story rating for this story was calculated to be 0.10, which we believe to be underpredicted due to the low percentage of gravity load in the walls. Since the story rating is calculated using a weighted average based on tributary gravity load in the vertical components, the possibility of the local collapse or the loss of lateral force resisting capacity may not be captured in the calculation of the story rating where the tributary gravity load on these components is small. The issue could be more significant where the limited number of vertical components resist most of the lateral load, and they resist relatively low gravity load.

In the Y-direction, the building was found to be governed by yielding at the first story, and the story rating was calculated to be 0.35. The building was found to have a higher base shear yield strength, and higher roof drift in the Y-direction than in the X-direction. However, the global demand-capacity ratio of the building was lower in the Y-direction. Even though the demand capacity ratio, e.g., ductility demand, was low in the Y-direction, the story rating was more than two times higher than the X-direction. One of the main reasons for this discrepancy was that the story rating calculation is based on the tributary gravity load distribution, as discussed previously.

The FEMA P-2018 building rating was taken as the larger of the critical story ratings in the X- and Y-directions. Since the Y-direction governed, the building rating was accordingly found to be 0.35. In accordance with FEMA P-2018 Section 10.3, the building was deemed a "high seismic risk building," since its building rating is greater than 0.3 but less than 0.7.

The building rating, 0.35, generally appeared to be consistent with the observed response of the building, but it was not consistent with the ASCE 41-17 CP performance estimate of the components. The ASCE 41 evaluation results indicated that the deformation demands in the moment frames and shear walls exceeded the Collapse Prevention acceptance criteria. However, the building rating was relatively low for the range of High Seismic Risk Buildings (between 0.3 and 0.7) per FEMA P-2018, and the relationship between the rating and the spectral acceleration shown in Figure 4-82 follows the trend of the fragility curve with the 6% drift criteria in Figure 4-67.

This publication is available free of charge from: https://doi.org/10.6028/NIST.GCR.22-917-50

This publication is available free of charge from: https://doi.org/10.6028/NIST.GCR.22-917-50

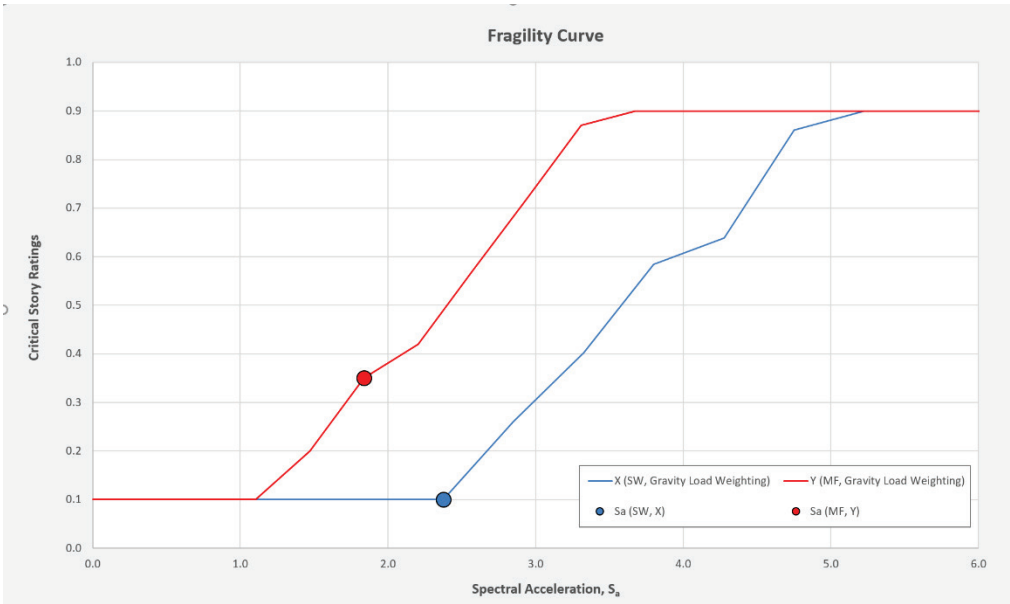


Figure 4-82 FEMA P-2018 rating and spectral acceleration relationship.

4.11 Summary

4.11.1 Global Performance

Tables 4-28 through 4-30 compare key global performance metrics for all ASCE 41-17 models with their respective experimental values.

Table 4-28 Summary of Periods and Maximum Base Shear Normalized by Building Weight

Metric	Experiment	OpenSees LP NJ (error%)	OpenSees LP EJ (error%)	Perform3D NJ (error%)	Perform3D EJ (error%)
		Frame Direction			
First Mode Period	0.43 sec.	0.64 sec. (+45%)	0.64 sec. (+45%)	0.68 sec. (+58%)	0.68 sec. (+58%)
Maximum Normalized Base Shear	0.534	0.470 (-12%)	0.644 (+21%)	0.538 (+1%)	0.551 (+3%)
		Wall Direction			
Second Mode Period (s)	0.31sec.	0.40 sec. (+29%)	0.40 sec. (+29%)	0.32 sec. (+0.0%)	0.32 sec. (+0.0%)
Maximum Normalized Base Shear	0.780	0.627 (-20%)	0.627 (-20%)	0.472 (-39%)	0.472 (-39%)

Table 4-29 Summary of Maximum Absolute Story Drift Ratios and Residual Drift Ratios

Metric	Experiment	OpenSees LP NJ (error%)	OpenSees LP EJ (error%)	Perform3D NJ (error%)	Perform3D EJ (error%)
		Frame Direction			
1st Story Max Absolute Drift (%)	3.36	1.58 (-53%)	2.14 (-36%)	3.35 (-0.3%)	3.81 (+13%)
2nd Story Max Absolute Drift (%)	2.98	2.73 (-8%)	3.78 (+27%)	2.87 (-4%)	3.06 (+3%)
3rd Story Max Absolute Drift (%)	1.35	2.50 (+85%)	3.16 (+134%)	1.15 (-15%)	1.17 (-13%)
4th Story Max Absolute Drift (%)	0.58	0.961 (+66%)	0.961 (+66%)	0.55 (-4%)	0.55 (-4%)
Roof Max Absolute Drift (%)	1.97	1.89 (-4%)	2.38 (+21%)	1.98 (+0.5%)	2.15 (+9%)
1st Story Residual Drift (%)	0.097	0.023 (-76%)	0.18 (+85%)	0.25 (+158%)	0.38 (+292%)
Roof Residual Drift (%)	0.05	0.038 (-24%)	0.026 (-48%)	0.11 (+120%)	0.19 (+280%)
		Wall Direction			
1st Story Max Absolute Drift (%)	3.33	3.30 (-1%)	3.30 (-1%)	2.72 (-18%)	2.72 (-18%)
2nd Story Max Absolute Drift (%)	2.85	3.83 (+34%)	3.83 (+34%)	3.31 (+16%)	3.28 (+15%)
3rd Story Max Absolute Drift (%)	2.48	3.96 (+60%)	3.96 (+60%)	3.45 (+39%)	3.43 (+38%)
4th Story Max Absolute Drift (%)	2.17	4.03 (+86%)	4.03 (+86%)	3.54 (+63%)	3.50 (+61%)
Roof Max Absolute Drift (%)	2.70	3.87 (+43%)	3.87 (+43%)	3.26 (+21%)	3.23 (+20%)
1st Story Residual Drift (%)	0.31	1.00 (+222%)	1.00 (+222%)	0.93 (+200%)	0.76 (+145%)
Roof Residual Drift (%)	0.19	1.11 (+484%)	1.11 (+484%)	1.03 (+442%)	0.84 (+342%)

This publication is available free of charge from: https://doi.org/10.6028/NIST.GCR.22-917-50

Table 4-30 Summary of Maximum Absolute Floor Accelerations

Metric	Experiment	OpenSees LP NJ (error%)	OpenSees LP EJ (error%)	Perform3D NJ (error%)	Perform3D EJ (error%)
		Frame Direction			
2nd Floor Max Absolute Accel. (g)	0.724	0.544 (-25%)	0.85 (+17%)	0.67 (-7%)	0.67 (-7%)
3rd Floor Max Absolute Accel. (g)	0.721	0.801 (+11%)	1.11 (+54%)	0.69 (-4%)	0.68 (-5%)
4th Floor Max Absolute Accel. (g)	0.714	1.42 (+98%)	1.42 (+98%)	0.74 (+3%)	0.78 (+9%)
Roof Max Absolute Accel. (g)	0.96	1.25 (+30%)	1.31 (+36%)	0.91 (-5%)	0.90 (-6%)
		Wall Direction			
2nd Floor Max Absolute Accel. (g)	1.36	0.52 (-61%)	0.52 (-61%)	0.90 (-34%)	0.90 (-34%)
3rd Floor Max Absolute Accel. (g)	1.18	0.73 (-38%)	0.73 (-38%)	0.83 (-29%)	0.84 (-29%)
4th Floor Max Absolute Accel. (g)	0.92	1.03 (+12%)	1.03 (+12%)	0.78 (-15%)	0.78 (-15%)
Roof Max Absolute Accel. (g)	1.44	1.17 (-19%)	1.17 (-19%)	0.82 (-43%)	0.83 (-42%)

For the frame direction, the ASCE 41-17 nonlinear dynamic evaluation procedures are able to successfully identify the damage distribution over building height and its extent. However, the procedures did not accurately capture damage distributions between various components in the frames in either software. When decoupled concentrated hinge models are used in each direction for columns (OpenSees), the discrepancy in drift demands and damage estimates were largest compared with experimental values. Accounting for bi-directional effects (Perform3D), namely strength degradation in both directions due to deformation demands in primarily one direction, resulted in relatively accurate drift and damage estimates over the height of the frames. ASCE 41-17 is not specific on when and how to treat bi-directional effects on member capacities. Adding such guidance would enhance the standard.

For the wall direction, the damage location and severity at the base of the walls were captured well by nonlinear models constructed to ASCE 41-17 specifications. However, because sliding at the wall base was not explicitly modeled due to lack of provisions on the subject in ASCE 41-17, the drift profile over the height of the building was not captured well by any of the models. Furthermore, beams degraded

This publication is available free of charge from: https://doi.org/10.6028/NIST.GCR.22-917-50

in strength prematurely in the wall direction, which also contributed to the discrepancies in the global mechanism in the wall direction.

This study highlights the effects of having modeling parameters with varying degrees of conservatism, or conversely accuracy, in ASCE 41-17. In the wall direction, the premature failure of beams in the computational models, decoupled the walls from the frames altering the dynamic response of the building substantially. In the frame direction, when joints sustained severe strength degradation in the models, they attracted large inelastic rotations and unloaded adjacent beams and columns, thereby protecting them from damage. When the joints were modeled linearly and prevented from failing, the adjacent beams sustained much more severe strength loss and damage, while columns saw increased demands. Each of these scenarios would therefore result in different retrofit outcomes for the building and highlight the importance to ensure that ASCE 41 nonlinear modeling parameters all target mean or median estimates from experimental data, such that building response is not artificially skewed, and the correct elements are targeted for retrofit.

All computational models produced softer periods by 22% to 46% from those measured experimentally. ASCE 41-17 stipulates that all the members in a building should be modeled using stiffness values corresponding to yield levels of cracking. In the experimental building, as is also expected in real buildings, not all members reach yield levels of cracking, particularly at higher floor levels, and therefore would tend to be stiffer than estimated. An investigation into the sensitivity of building response to the varying stiffness across building height based on expected level of cracking may be useful to guide updates to the ASCE 41-17 approach to component stiffness.

Figures 4-74 and 4-75 show that in the frame direction, the provisions in the NZSEE *Guidelines* identified joints, followed by beams, followed by columns as the most vulnerable elements. A comparison with Figures 4-8, 4-20, and 4-29 shows that the NZSEE *Guidelines* estimated joint damage in many more locations than ASCE 41-17 nonlinear models and than were observed in the test. According to the hierarchy used in the NZSEE *Guidelines* capacity was reached at most joints, limiting demands on beams and columns and preventing them from deforming in the nonlinear range. ASCE 41 nonlinear models estimated light and moderate damage to most beams, which was consistent with test results, and virtually no damage to columns, also consistent with the test.

In the wall direction, Figure 4-76 shows that provisions in the NZSEE *Guidelines* estimated yielding at most beams and at the base of the wall, forming a collapse mechanism. Capacity was limited by failure of an exterior beam-column joint at the first floor. The damage pattern obtained with the NZSEE *Guidelines* was very similar to the distribution of damage calculated with the OpenSees Fiber model

This publication is available free of charge from: https://doi.org/10.6028/NIST.GCR.22-917-50

(Figure 4-29), which also indicated severe distress in exterior joints of the first floor. A comparison with Figure 4-8 shows that in the wall direction, the NZSEE *Guidelines* and the ASCE 41 nonlinear models overstimated damage to joints and beams, and underestimated damage at the base of the structural wall.

4.11.2 Component Performance

Column modeling parameters were updated twice since FEMA 273 (FEMA, 1997; Elwood et al., 2007; Ghannoum and Matamoros, 2014; Ghannoum, 2017), and in the process were increased substantially to reach mean estimates of experimental data. Moreover, the beam modeling parameters and acceptance criteria remained unchanged since FEMA 273 and are substantially lower than column values given similar detailing. These differences in conservatism in modeling parameters generated skewed damage outcomes per ASCE 41-17, whereby more severe damage was predicted in beams than the columns. This is inconsistent with observed damage that was moderate to limited in the beams in the frame direction, as well as in the wall direction. Updates for the beam modeling parameters and acceptance criteria therefore may be in order for ASCE 41.

Beam-column joints modeled using ASCE 41-17 nonlinear dynamic procedures lost strength severely, particularly the exterior joints. This is contrary to experimental results in which the interior joints suffered the most damage and exterior joint only sustained moderate damage. A review and update of the joint shear strength and nonlinear modeling parameters and acceptance criteria in ASCE 41-17 may be justified for future study.

The damage at the base of the structural walls was severe in both the experiment and the nonlinear analyses conducted in accordance with ASCE 41-17. ASCE 41-17 analyses indicated that the walls failed the CP performance objective by a substantial margin, and therefore should be retrofitted. In the experiment however, the wall damage is more consistent with placing them between the LS and CP performance objectives since they maintained sufficient reserve strength to withstand two additional high-intensity ground motions without collapse. This indicates that the ASCE 41-17 wall provisions for flexure-controlled walls may be conservative.

In addition, the base sliding mode of damage is not captured in ASCE 41-17 and should be introduced in updates to the standard as that mode can significantly alter the structure global mechanism.

4.11.3 Analytical Study Takeaways

For this building, the analyses indicate important needs to improve modeling capabilities. These include modeling strategies to capture bi-directional moment-axial coupling and ensuring that all modeling parameters are set to their mean

This publication is available free of charge from: https://doi.org/10.6028/NIST.GCR.22-917-50

estimates based on experimental data such that model response and damage distributions are not artificially skewed.

4.11.4 Fragility Analysis

Spectral accelerations corresponding to modeling parameters and acceptance criteria obtained from an incremental dynamic analysis of the study building using the 100% JMA-Kobe record corresponded to relatively low probabilities of exceedance in the fragility curves generated with the FEMA P-695 far-field set. The low probabilities of exceedance are attributed in part to the difference between the effective period of the structure in the frame and wall directions, and the difference in shape between the P 695 far field set average response spectrum and the 100% JMA-Kobe spectrum. This discrepancy highlights the challenges inherent to scaling fragility curves and demands when the shape of the two spectra are significantly different and the building has significantly different periods in the two principal directions.

The spectral acceleration of the 100% JMA-Kobe ground motion at the fundamental period in the frame direction corresponded to a probability of exceedance of approximately 45% for CP performance level in FEMA P-695 fragility curves, which is consistent with the level of damage observed in the test.

Fragility analyses based on the Eurocode and ASCE 41 provided very similar results.

4.11.5 Study Limitations

These conclusions must be considered in the context of several limitations:

- Sliding effects are not captured in the ASCE 41-17 models presented.

This publication is available free of charge from: https://doi.org/10.6028/NIST.GCR.22-917-50

Chapter 5

Ten-story Frame and Wall Test Structure

This publication is available free of charge from: https://doi.org/10.6028/NIST.GCR.22-917-50

5.1 Overview

This chapter presents benchmarking studies for a 10-story reinforced concrete structure tested at the E-Defense shake table in Japan in 2015 (Nagae et al., 2015), shown in Figure 5-1. Ground motion records and response parameters are available since the structure was tested on a shake table. In this chapter, computed responses for nonlinear models of the building and predicted damage are compared with measured responses and observed damage for strong motion records from Southern Hyogo Prefecture Earthquake of January 17, 1995.



Figure 5-1 10-story structure tested at E-Defense shake table in 2015 (photo courtesy of J. Wallace).

The structure was evaluated in accordance with the nonlinear dynamic procedures of ASCE 41-17 and ACI 369.1-17, *Standard Requirements for Seismic Evaluation and Retrofit of Existing Concrete Buildings and Commentary* (ACI, 2017). For the evaluation of wall elements, proposed updates for the ASCE 41-23 wall modeling parameters have been included. Nonlinear models were developed using OpenSees and Perform3D software with nonlinear wall, beam, and column elements, and with nonlinear and linear elastic joint elements. The models were constructed per details presented in Appendix A, unless otherwise noted.

This chapter also provides results of a fragility analysis showing the collapse

potential of the model, as compared to the likelihood of exceeding ASCE 41-17 acceptance criteria.

5.2 Building Description and Observed Performance

5.2.1 Building Description

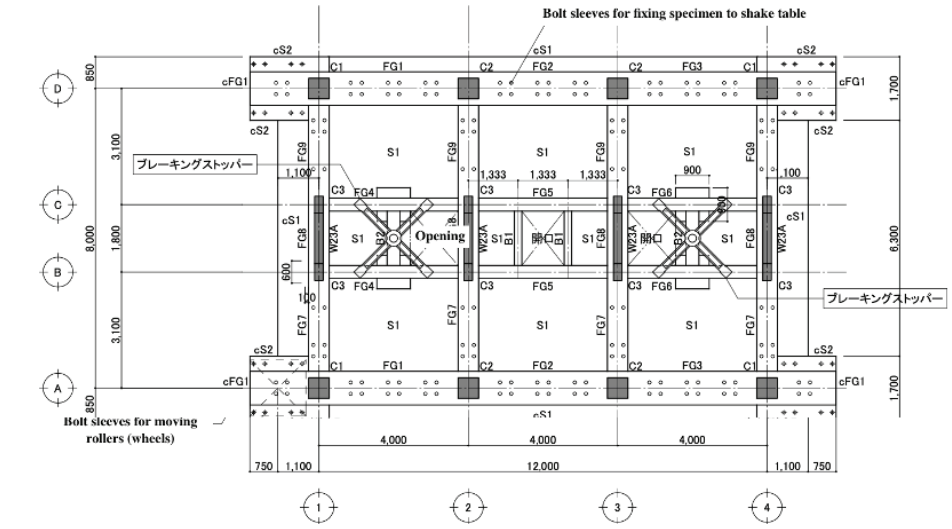
The structure was one of two similar 10-story buildings tested, the first in 2015 and the second in 2018/2019. The structure evaluated in this chapter was cast-in-place reinforced concrete with mild reinforcing. The objectives of the testing program included assessing the performance of mid-rise concrete moment frames and shear walls with both sliding and fixed foundation support conditions.

Typical plans and elevation dimensions for the building are shown in Figure 5-2 and Figure 5-3, respectively. The test specimen measured 27.4 m (89.9 ft.) tall, and plan dimensions were 9.7 m by 15.7 m (31.8 ft. by 51.5 ft.) at the first floor and 9.5 m by 13.5 m (31.2 ft. by 44.3 ft.) at other floors. The first story was 2.8 m (9.2 ft.) tall with the height reducing every three stories to 2.6 m (8.5 ft.), 2.55 m (8.4 ft.), and 2.5 m. (8.2 ft.). The lateral force-resisting system consisted of two lines of perimeter moment frames in the longitudinal (Y) direction and four shear walls in the transverse (X) direction that terminate at the top of the 8th floor (Figure 5-3). There also were two lines of interior beams (three beams per line) in the longitudinal (Y) direction that frame between the shear walls, and four lines of beams (two beams per line) in the transverse (X) direction that framed between the perimeter columns and the shear walls. The building was structurally regular and was designed to conform to the seismic design provisions of the Architectural Institute of Japan (AIJ, 1999) and meet most provisions for Special Moment Frame and Special Structural Wall systems of ACI 318-14, *Building Code Requirements for Structural Concrete and Commentary* (ACI, 2014), as detailed in Unal et al. (2020).

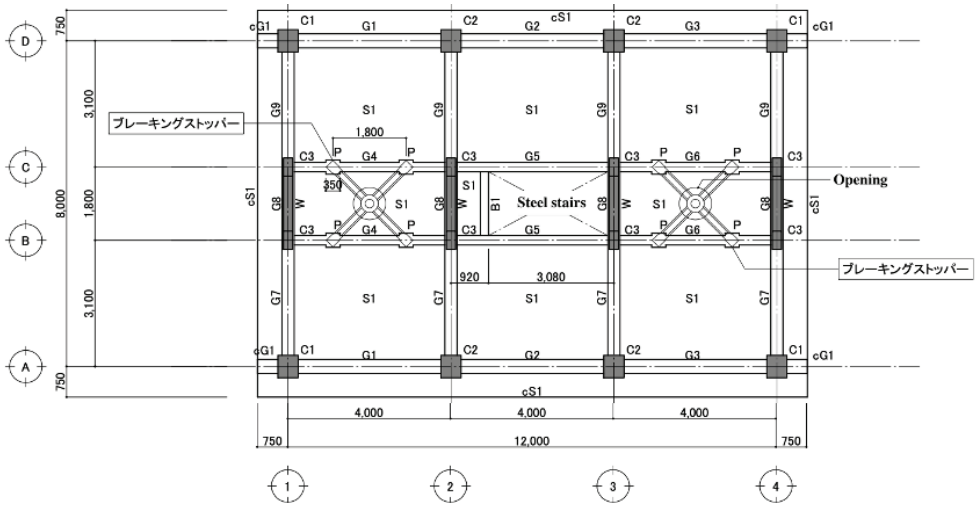
Geometry and reinforcement details for columns, beams, and shear walls can be found in Kajiwara et al. (2017). Typical moment frame column sections are 500mm by 500 mm (19.69 in. by 19.69 in.) and typical beam sections are 350 mm by 500 mm (13.77 in. by 19.69 in.); both columns and beams are well-confined at member ends. The webs of the shear walls were 150 mm (5.91 in.) thick at 1st through 7th levels and reduced to 120 mm (4.72 in.) at the 8th level and above. The transverse reinforcement of the beam-column joints consists of two overlapped hoops using D10 spaced at 150 mm (5.91 in.). Steel stairs extend through the center of the building to allow inspection of damage in the upper stories (Figure 5-2). The structure was built in two separately fabricated sections to allow transportation of the specimen inside the test facility - both sections are bolted together at the midpoint of columns and shear walls at the 6th story (Figure 5-3a and b); therefore, any comparisons between test and model results adjacent to this splice should be considered carefully.

This publication is available free of charge from: https://doi.org/10.6028/NIST.GCR.22-917-50

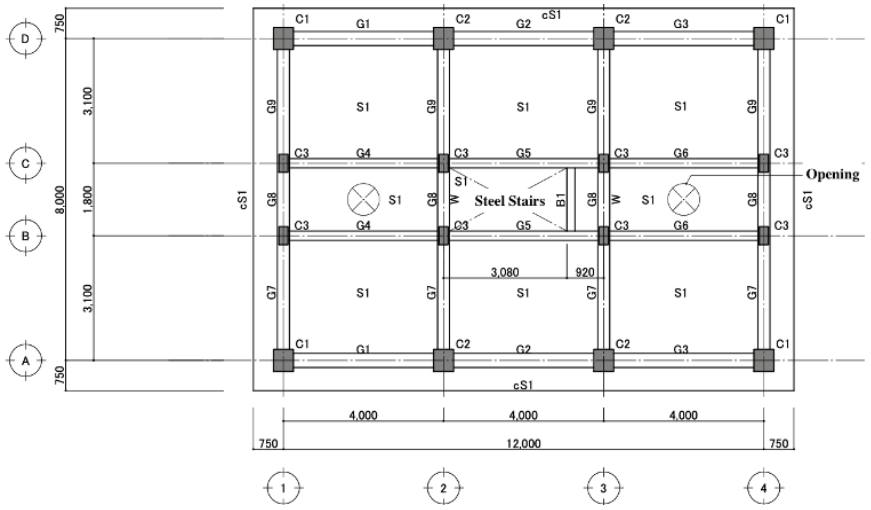
This publication is available free of charge from: https://doi.org/10.6028/NIST.GCR.22-917-50



(a) 1st Level



(b) Typical floor (5-8)



(c) Typical floor (9-Roof)

Figure 5-2 Plan dimensions for typical floors.

This publication is available free of charge from: https://doi.org/10.6028/NIST.GCR.22-917-50

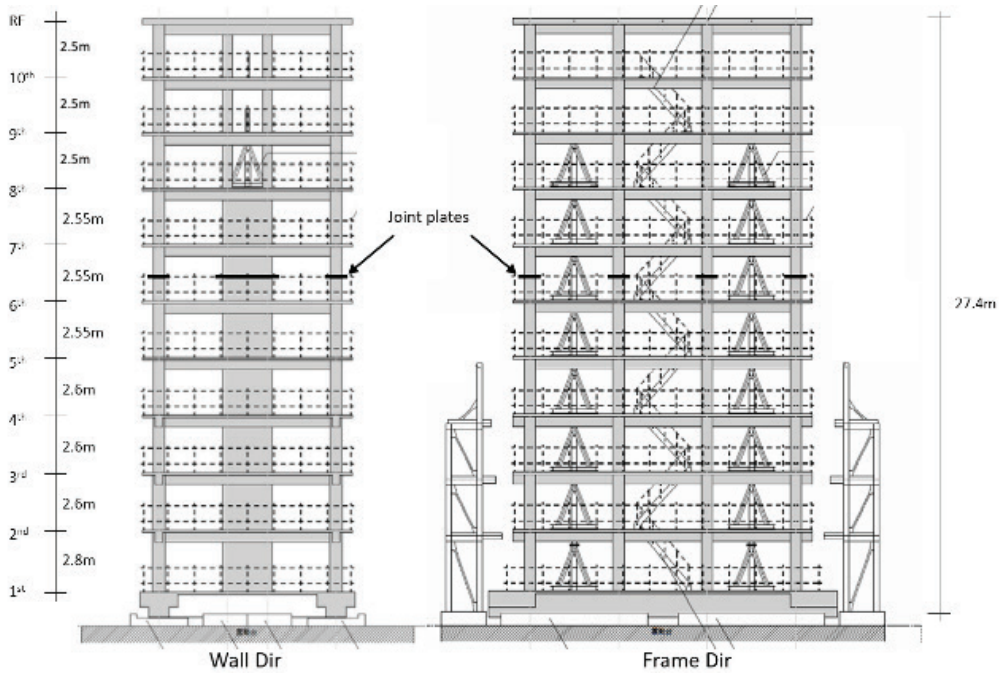


Figure 5-3 Building elevation views.

The test was carried out in two phases. In Phase 1, the building sat on eight flat-plate friction sliders allowing the building to dissipate energy, whereas in Phase 2, the building was bolted to the shake table to provide a fixed restraint support condition.

Material Properties

The material design values and testing results provided in Unal et al. (2020) are presented in Tables 5-1 through 5-5. For the purposes of this evaluation, the measured (representative or mean) material strengths from testing were used for all elements.

Table 5-1 Concrete Material Properties as Specified

Floor	f_c' (MPa)
1 - 2	42
3 - 5	33
6 - Roof	27

Table 5-2 Reinforcing Bar Material Properties as Specified

Bar Designation	*Grade (in MPa)*	*Bar Nominal Area (mm^2)*	*f_y (MPa)*	*f_u (MPa)*
D22	SD345	387	345	490
D19	SD345	287	345	490
D13	SD295A	127	295	440
D10	SD295A	71	295	440
S10	KSS785	71	785	930

Table 5-3 Concrete Material Properties Based on Test Results (Mean Values)

		f_c' (ksi)			
Floor	Height (ft)	*Wall*	*Beam*	*Column*	E_c (ksi)
R	-	-	3.92	-	-
10	8.20	3.92	3.92	3.92	4409
9	8.20	3.92	3.92	3.92	4706
8	8.20	3.92	3.92	3.92	4769
7	8.37	3.92	3.92	3.92	4730
6	8.37	3.92	4.79	3.92	5000
5	8.37	4.79	4.79	4.79	4366
4	8.53	4.79	4.79	4.79	4374
3	8.53	4.79	6.09	4.79	4896
2	8.53	6.09	6.09	6.09	5344
1	9.19	6.09	6.09	6.09	5096

Table 5-4 Longitudinal Reinforcing Bar Material Properties Based on Test Results (Mean Values)

Reinforcement		Mean	Median	Standard Deviation
D19	F_y (MPa)	388	392	11.5
	F_u (MPa)	582	585	10.7
	E_s (GPa)	190	190	5.6
D22	F_y	389	389	5.4
	F_u (MPa)	574	576	6.1
	E_s (GPa)	189	188	2.6

This publication is available free of charge from: https://doi.org/10.6028/NIST.GCR.22-917-50

Table 5-5 Transverse Reinforcing Bar Material Properties Based on Test Results (Mean Values)

Transverse Reinforcement	F_y (MPa)	F_u (MPa)	E_s (GPa)
D10	408	536	197
D13	361	498	197
Transverse Reinforcement	**$F_{y,0.2}$ (MPa)**	**F_u (MPa)**	**E_s (GPa)**
S10 (1)	900	1049	206
S10 (3)	962	1153	204

Building Weight

The building weighed 9,545 kN, which includes the dead load (structural elements) and attached fixtures, such as stairs, steel framing, and instrumentation, as shown in Table 5-6. Weight was assumed to be evenly distributed across the slab.

Table 5-6 Building and Floor Weights

Floor	Weight of Fixtures (kN)	Dead Load (kN)	Total Floor Weight (kN)
RF	0	579	579
10th	57	706	763
9th	28	639	667
8th	28	657	685
7th	29	721	750
6th	188	870	1058
5th	28	716	744
4th	28	732	760
3rd	28	750	778
2nd	57	848	905
1st	29	1827	1856
		Total Building Weight (kN)	9545

5.2.2 Ground Motion

The ground motions recorded at Japan Meteorological Agency (JMA) Kobe Marine Meteorological Observatory station during the Southern Hyogo Prefecture Earthquake on January 17, 1995 were used as the input excitation for the test building. The maximum acceleration for the north-south (NS), east-west (EW), and up-down (UD) directions are 8.18 m/s^2, 6.17 m/s^2, and 3.32 m/s^2, respectively. The NS component of the ground motion was applied in the frame direction and the EW component was applied in the wall direction. Table 5-7 presents the testing protocol that was used to apply ground motions scaled by 10%, 25%, 50%, and 100% and

This publication is available free of charge from: https://doi.org/10.6028/NIST.GCR.22-917-50

applied sequentially in the two phases of testing: sliding test (Phase 1) and fixed-base test (Phase 2). In Phase 1, four scaled versions of the JMA-Kobe ground motion were applied sequentially. In Phase 2, the foundation was bolted to the shake table to provide a fixed-base condition, and five scaled versions of the JMA-Kobe ground motion were applied sequentially. White noise excitation was applied before and after each individual ground motion to estimate the first mode period of the structure.

Table 5-7 Testing Protocol

No. of Test Run	Test Case	Input Wave	Magnification (Scale)
1	Sliding Base	JMA-Kobe	10%
2			25%
3			50%
4			100%
5	Fixed Base	JMA-Kobe	10%
6			25%
7			50%
8			100%
9			60%

The horizontal and vertical components of the target ground motion (100% JMA-Kobe) applied to the building are shown in Figure 5-4, along with the response spectra of the motion for 5% damping.

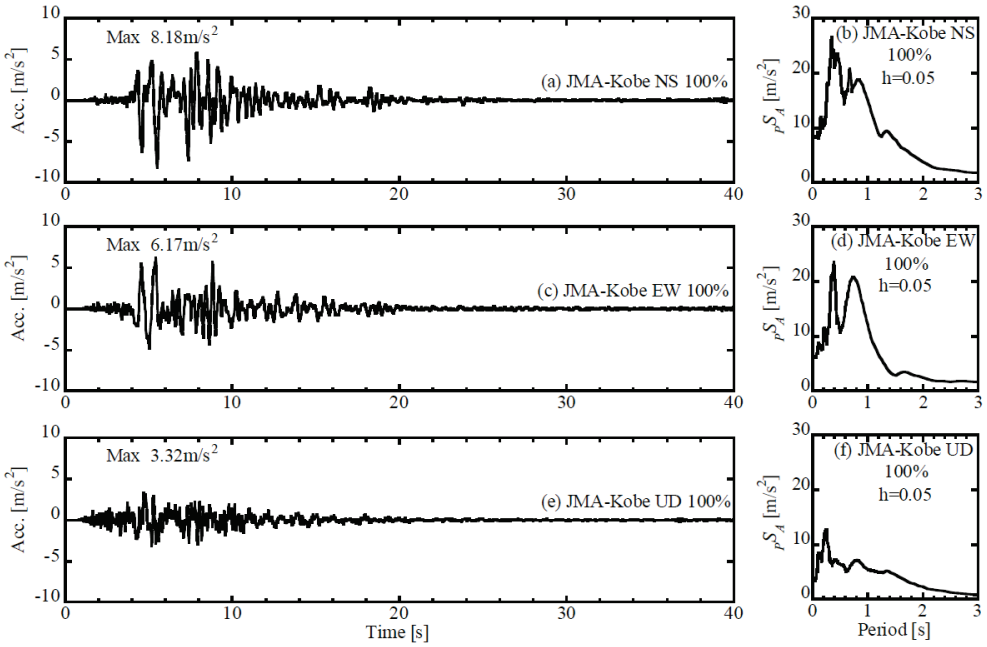


Figure 5-4 Components of the target ground motion record (100% JMA-Kobe) and the associated spectra (5% damping).

This publication is available free of charge from: https://doi.org/10.6028/NIST.GCR.22-917-50

This publication is available free of charge from: https://doi.org/10.6028/NIST.GCR.22-917-50

For the purposes of this study, the acceleration histories of the two horizontal components of the 100% JMA-Kobe record as measured at the base of the structure during the fixed-base test were used for the OpenSees and Perform3D models to assess the building performance. These records were used for comparison to observed performance because it was the first test during which severe damage and significant nonlinear response was recorded. Only minor yielding was recorded during the 50% JMA-Kobe fixed-base test, and the yielding did not result in any appreciable permanent deformations prior to the 100% JMA-Kobe motion (Nagae et al., 2015). The potential influence of the prior tests (50% and 100%) is addressed by conducting a limited sensitivity study.

5.2.3 Instrumentation

Instrumentation included 654 channels sampled at 1000 Hz to record responses that included story displacements, floor acceleration, joint deformations, beam and column end rotations, wall average shear strains, and wall average vertical strains (Sato et al., 2017). Floor acceleration was measured using two triaxial accelerometers attached to the floor slabs at north-east and south-west corners. Story displacements were measured using displacement transducers attached to steel frames at every floor level. Foundation slip and uplift during the sliding-base tests were measured using laser displacement sensors and Linear Variable Differential Transducers (LVDT) at locations around the perimeter of the foundation. Wall vertical strains were captured using LVDTs attached to wall boundaries over the first three stories. To capture member-end rotations, displacement transducers were installed along beam and column hinging regions.

5.2.4 Observed Performance

Natural periods and maximum story drift angles for the building after each excitation for both the frame and wall directions are shown in Table 5-8. The table shows that after initial softening in the sliding base tests, the natural periods for the frame and wall directions increased slightly in the 10% and 25% JMA-Kobe fixed base tests, modestly in the 50% JMA-Kobe fixed base test, and appreciably in the 100% JMA-Kobe fixed base test. Figure 5-5 illustrates the change in measured periods for Phase 1 and 2.

In terms of damage, under the 100% excitation for the fixed base test, observations included significant beam-column joint damage characterized by diagonal cracking (Figure 5-6a) at the 3rd, 4th and 5th floors, minor concrete cover spalling at the base of 1st floor corner columns (Figure 5-6b) and at the base shear wall (Figure 5-6c). Damage to the beam-column joints appeared to produce softening that led to fairly large story drift ratios (3.05%) in the frame direction for the 100% JMA-Kobe record (Table 5-8), whereas damage in the wall direction was fairly modest. More

information on the test procedure, specimen design, instrumentation, and experimental results for the 2015 tests can be found in Kajiwara et al. (2015), Sato et al. (2017), and Tosauchi et al. (2017). Figure 5-7 presents observed cracking for the 50% JMA-Kobe ground motion for reference, as a similar record for 100% JMA-Kobe ground motion was not found in literature.

Table 5-8 Natural Periods and Maximum Story Drift Angles (Tosauchi et al., 2017)

No	Input Wave	Test Case	Natural Period [s]		Maximum Story Drift Angle [rad]	
			Frame Direction	*Wall Direction*	*Frame Direction*	*Wall Direction*
-	Initial	Base slip	0.57	0.57	-	-
1	JMA-Kobe 10%		0.61	0.61	0.0011	0.0006
2	JMA-Kobe 25%		0.69	0.63	0.0026	0.0010
3	JMA-Kobe 50%		0.76	0.64	0.0041	0.0017
4	JMA-Kobe 100%		0.87	0.69	0.006	0.0030
-	Initial	Fixed base	0.85	0.58	-	-
5	JMA-Kobe 10%		0.87	0.58	0.0028	0.0008
6	JMA-Kobe 25%		0.94	0.60	0.0075	0.0022
7	JMA-Kobe 50%		1.24	0.74	0.0171	0.0065
8	JMA-Kobe 100%		2.43	1.13	0.0305	0.0150
9	JMA-Kobe 60%		2.62	1.19	0.0131	0.0122

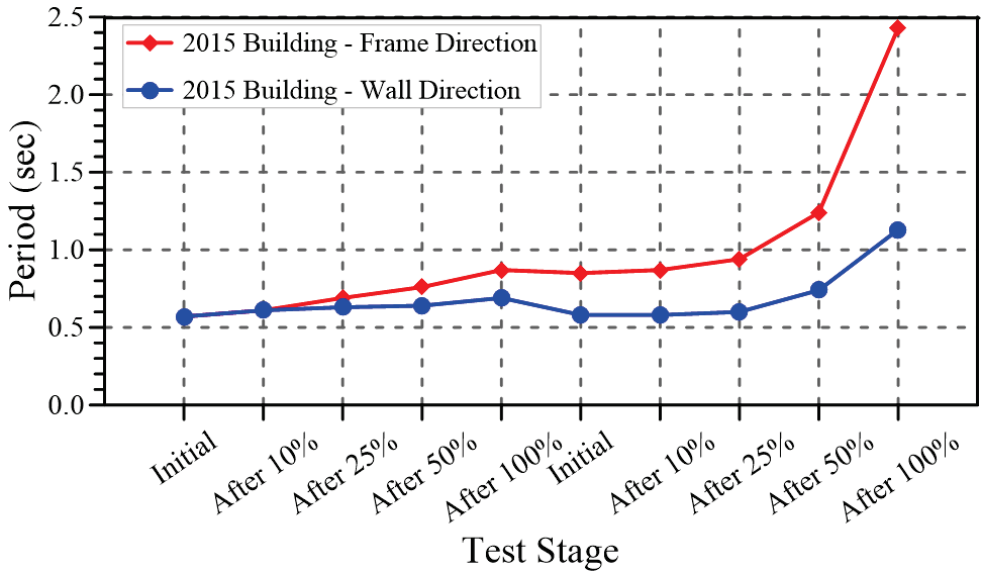


Figure 5-5 Measured periods after each applied excitation (Tosauchi et al., 2017).

This publication is available free of charge from: https://doi.org/10.6028/NIST.GCR.22-917-50



(a) 4th floor beam-column joint (b) 1st floor column base (c) 1st floor wall boundary element

Figure 5-6 Photos of observed damage (Tosauchi et al., 2017).

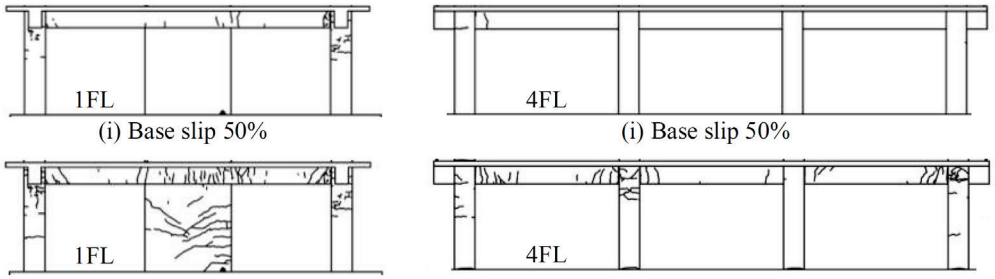


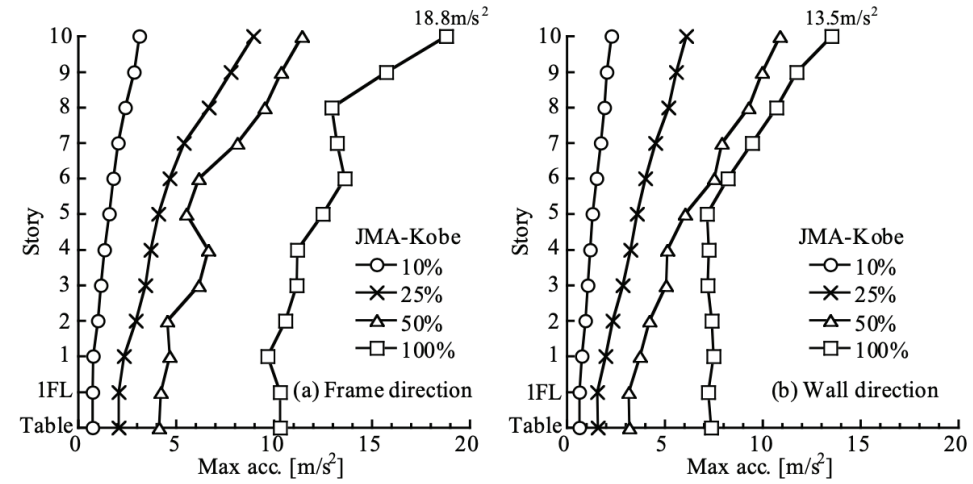
Figure 5-7 Observed cracking in the 50% Kobe record for the (a) sliding base test and (b) fixed base test (Tosauchi et al., 2017) at the 1st and 4th floors.

5.2.5 Response Quantities

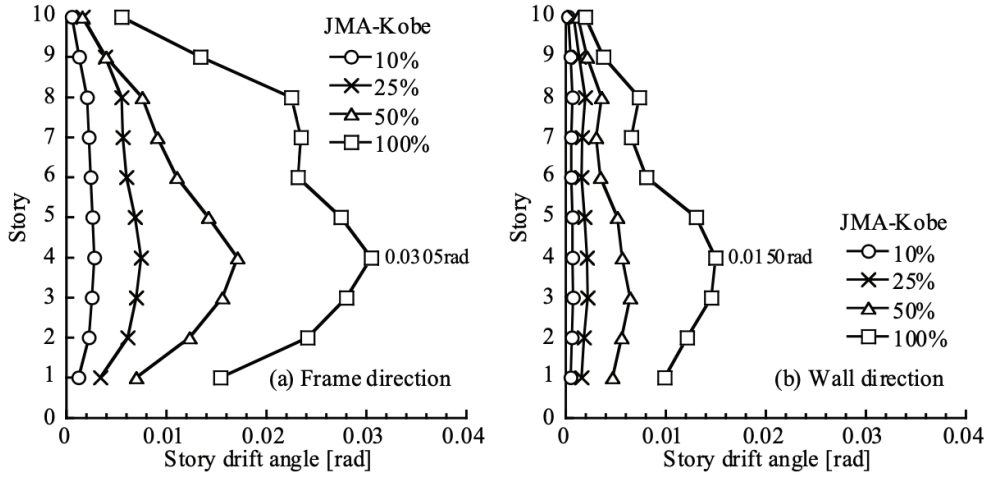
Data from the displacement transducers were processed to determine relative story displacements and story drift ratios calculated as the maximum displacement in that story divided by the story height (Figure 5-3, Table 5-8). For the fixed based test and the 100% JMA-Kobe motion the maximum story drift ratios of 3.05% and 1.50% were measured for the frame and wall directions, respectively. The distribution of the maximum floor acceleration and maximum story drift ratios are shown in Figure 5-8. The maximum story drift ratios are also reported in Table 5-8 and confirm that the building was pushed to relatively large drift demands in the frame direction and modest drift demands in the wall direction. Story drift ratios are largest for the frame direction between the 3rd and 4th story, where damage was concentrated, whereas story drift ratios for the wall direction increase only modestly above the 1st floor due to the rigid body rotation at the wall base due to the concentration of nonlinear curvature at the critical section (wall-foundation interface) and possible (minor) foundation rotation (Garcia Gomez, 2020).

This publication is available free of charge from: https://doi.org/10.6028/NIST.GCR.22-917-50

This publication is available free of charge from: https://doi.org/10.6028/NIST.GCR.22-917-50



(a) Maximum floor acceleration



(b) Maximum story drift

Figure 5-8 Maximum floor acceleration and story drift angles (Tosauchi et al., 2017).

5.3 Nonlinear Dynamic Procedure using OpenSees

Two models were developed using OpenSees software. They are identical for beams, columns, and walls that were modeled with nonlinear fiber sections. Two approaches were used to model the beam-column joints: one with elastic joints (OpenSees EJ) and the other with nonlinear joints (OpenSees NJ).

5.3.1 Modeling Approach

Three-dimensional numerical models of the structure were created in OpenSees with fixed base and a semi-rigid diaphragm using shell elements (Figure 5-9). For the fiber section models, columns and beams were discretized using several displacement-based fiber section elements along the length of the members, each element with three integration points and Legendre integration, whereas walls were

modeled with a three-dimensional multiple-vertical-line-element model (MVLEM-3D; Kolozvari et al., 2021) with nonlinear in-plane behavior and elastic out-of-plane behavior. Zero-length rotational springs were not added at each member-end to account for bar slip. Beam effective slab widths were based on ASCE 41-17 Section 10.3.1.3.

For the fiber section elements, sections were discretized and assigned material model Concrete02 for unconfined and confined concrete and wall boundary elements, and SteelMPF for reinforcing bars (Figure 5-9). Basic parameters of the stress-strain curve for unconfined and confined concrete in compression were calculated using the models proposed by Razvi and Saatcioglu (1999) and Mander et al. (1988a) based on cylinder test data and the amount of transverse reinforcement provided in the cross-section, while reinforcement stress-strain relations were based on coupon direct tension tests. Because local deformation demands for the beams, columns, and walls were generally less than those sufficient to produce strength loss, concrete stress-strain relations were not regularized. Calibrated material relations for concrete (unconfined and confined) and reinforcement are plotted with concrete cylinder and steel coupon test data in Figure 5-10.

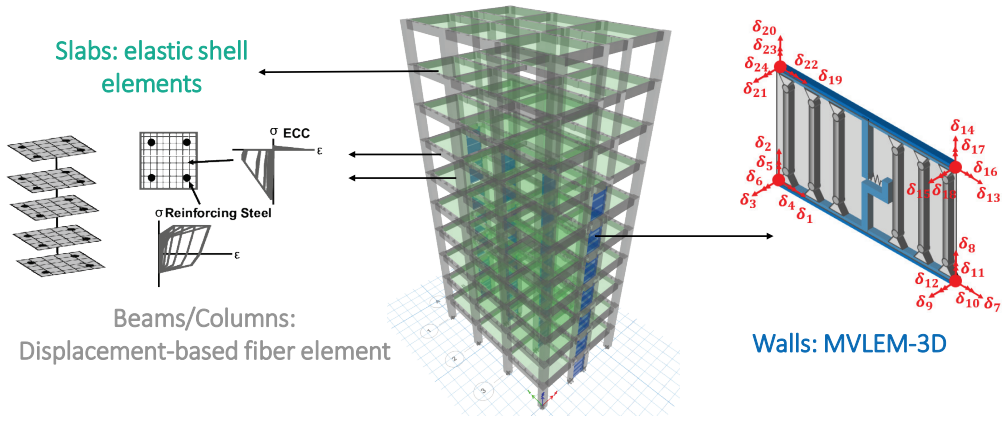


Figure 5-9 General element modeling approaches.

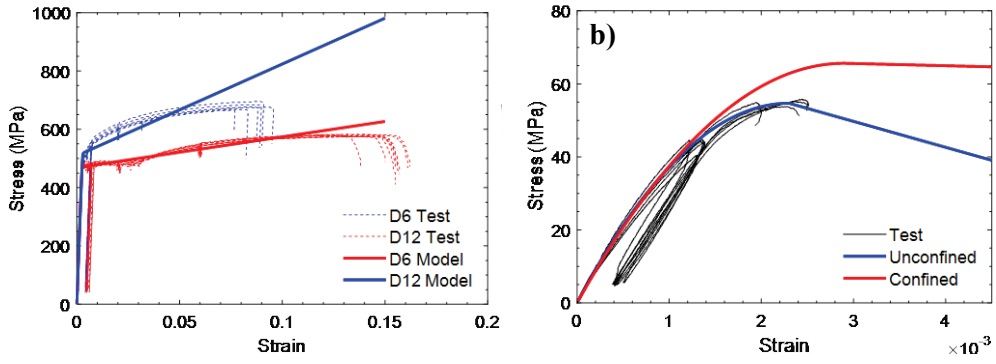
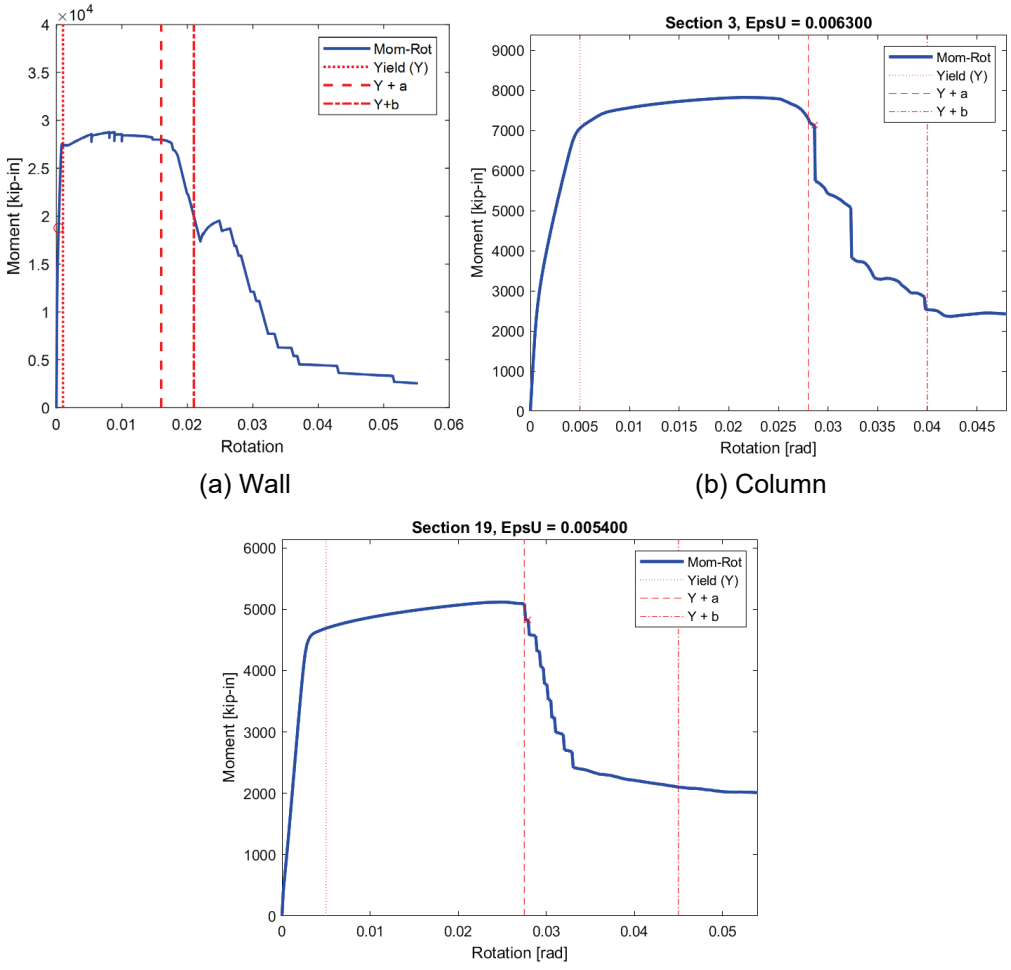


Figure 5-10 Calibrated material relations for: (a) reinforcement and (b) concrete in compression.

This publication is available free of charge from: https://doi.org/10.6028/NIST.GCR.22-917-50

Tensile strength of concrete was taken as $0.31\sqrt{f_c'}$ (MPa) based on Belarbi and Hsu (1994) constitutive model for concrete in tension. The tangent stiffness of concrete material at zero load was defined as $2\sqrt{f_c'}/\varepsilon_0$ and the degrading slope E_t was defined as 5% of the tangent stiffness of concrete material at zero load.

Material modes calibrated based on as-tested material properties were further modified in plastic hinge regions of walls, beams, and columns to capture strength degradation in these elements. It was assumed that steel reinforcement in compression loses its capacity at the strain where concrete reaches its residual capacity, EpsU. EpsU parameter was calibrated such that strength loss occurs at plastic rotation that corresponds to ASCE-41 modeling parameter *a* for walls, beams, and columns (Figure 2-1). Examples of calibrated moment-rotation relationships for a representative wall, beam, and column element are presented in Figure 5-11.



(a) Wall

(b) Column

(c) Beam

Figure 5-11 Representative moment-rotation responses for calibrated section of structural elements (walls, columns, beams).

This publication is available free of charge from: https://doi.org/10.6028/NIST.GCR.22-917-50

Axial loads used in calculating ASCE 41-17 modeling parameters for joints and acceptance criteria for all structural elements were obtained as the maximum compressive axial demands developed in each element from a pushover analysis of the building out to initiation of loss of lateral load carrying capacity using a first mode lateral load distribution. Slab out-of-plane bending was not modeled explicitly but was rather accounted for through effective flange widths assigned to the beams.

The maximum compressive axial load (due to gravity load and earthquake effects) did not exceed 16% of the column gross sectional capacity, $A_g f_c'$, throughout the height of the building. Typically, the moment frame columns in the bottom six stories had axial loads greater than $0.1 A_g f_c'$. It is noted the modeling parameters are computed for maximum compression axial load determined from pushover analysis using the first mode lateral load distribution, whereas column yielding generally occurred during the analysis at minimum axial load; therefore, the reported ratios for columns are likely on the conservative side. All columns were expected to respond primarily in flexure as they had relatively high levels of confinement, such that their shear strength exceeded the shear demand associated with flexural hinging by a significant margin. Therefore, gross elastic shear stiffness was used for frame members, as recommended by ASCE 41-17.

All beams were likewise expected to respond primarily in a flexure mode. Beam sections included an effective flange width determined based on ASCE 41-17 Section 10.3.1.3 (Figure 5-12). A biaxial mesh was used to model beams and columns, as shown in Figure 5-12.

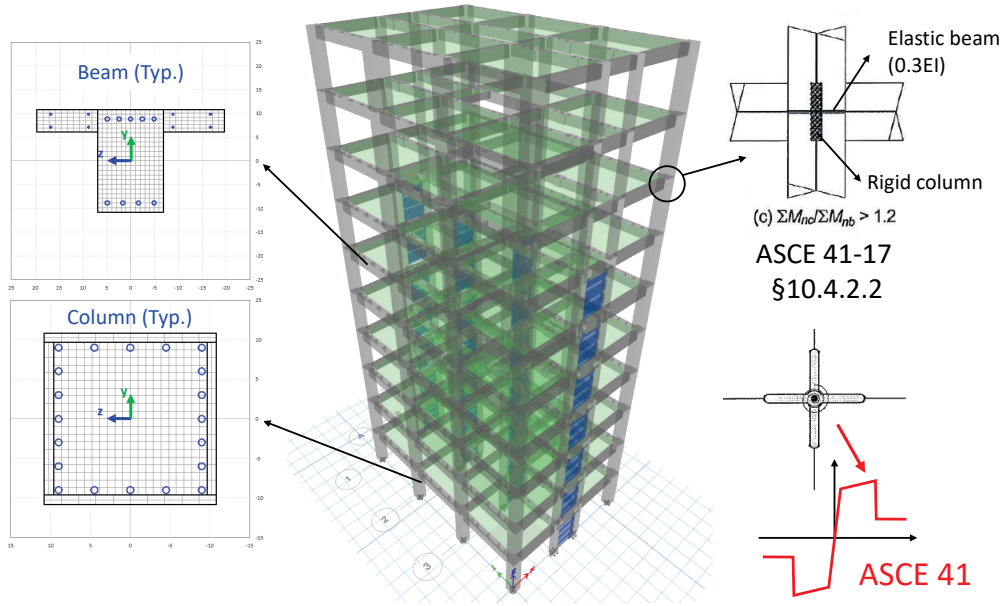


Figure 5-12 Moment frame element modeling approaches.

This publication is available free of charge from: https://doi.org/10.6028/NIST.GCR.22-917-50

Beam-column joints were classified as "conforming" per ASCE 41-17 despite the relatively wide hoop spacing (150 mm or 5.9 in.). Demand-to-capacity ratios, $V_u/\phi V_n$, for beam-column joints computed according to ACI 318-14 between Levels 2 and 7 were determined to range between 0.40 to 0.52 for exterior connections and 0.54 to 0.65, respectively (Unal et al., 2021).

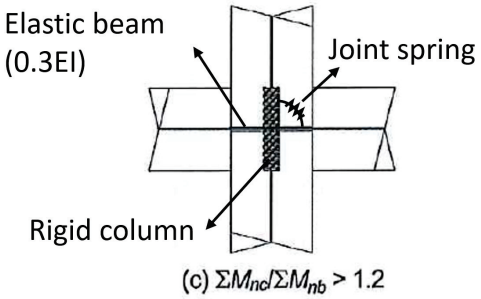
In the OpenSees EJ (Elastic Joint) model, beam-column joints were modeled using elastic elements extending from the beam-joint and column-joint interfaces and connecting at the center of the joint. Since the ratio of the summation of the column nominal moment capacities, $\sum M_{nc}$, to the summation of the beam nominal moment capacities, $\sum M_{nb}$, of each joint was greater than 1.2, joint elastic stiffness was modeled implicitly according to ASCE 41-17 Section 10.4.2.2 (option "c" from Figure 10-2 of ASCE 41-17 also shown in Figure 5-12) in the OpenSees EJ model.

In the OpenSees NJ (Nonlinear Joint) models (Figure 5-12), joints were modeled using the "scissor model" as described by Celik and Ellingwood (2008), where joint elastic elements extended from beams and columns, and rotational springs were introduced in the frame direction, to allow a scissor motion in the joint (Figure 5-12). The stiffness of the elastic elements and the nonlinear behavior of the rotational springs was calibrated using two options:

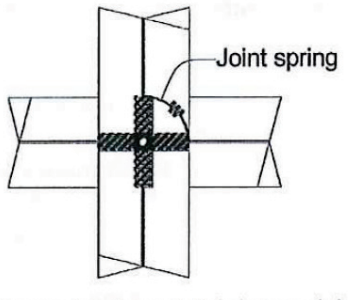
- Option 1, shown in Figures 5-13a and 5-13c: The stiffness of elastic beam/column elements framing into the joint was modeled according to ASCE 41-17 Section 10.4.2.2, and joint nonlinear behavior is as defined in ASCE 41-17 Section 10.4.2 and ASCE 41-17 Table 10-11. There is little to no variation in the modeling parameters and acceptance criteria as a function of axial load for joints with conforming transverse reinforcement. In ASCE 41-17, joint transverse reinforcement is classified as conforming if hoops within the joint are spaced at a distance equal, or less than, half the column depth. Otherwise, the transverse reinforcement is considered non-conforming. All the beam-column joints in this building fall into the conforming category and have ratios of joint shear demand-to-shear strength less than 1.2. For this option, results from pushover analysis indicated that including slip spring in the joint model had minor impact; therefore, slip springs are ignored.
- Option 2, shown in Figures 5-13b and 5-13d: The stiffness of elastic beam/column elements framing into the joint was assumed to be rigid per "explicit joint model" described in Figure 10-2(a) of ASCE 41-17, where the joint nonlinear behavior is calibrated using representative test results by Shiohara et al. (2013) (Figure 5-14). For both options, the hysteresis behavior was modeled using the Pinching4 hysteretic model in OpenSees (Figure 5-15).

This publication is available free of charge from: https://doi.org/10.6028/NIST.GCR.22-917-50

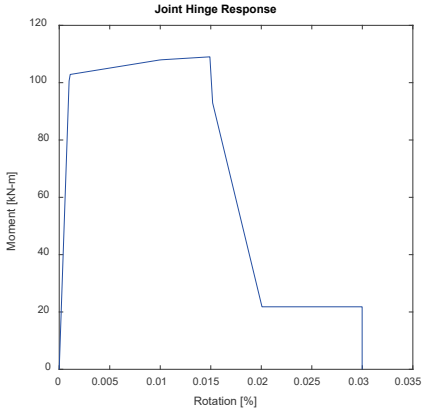
This publication is available free of charge from: https://doi.org/10.6028/NIST.GCR.22-917-50



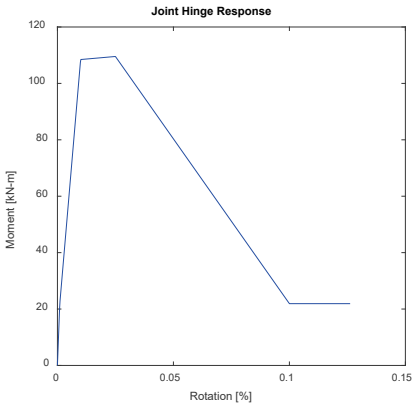
(a) Option 1: ASCE 41-17 joint model



(b) Option 2: Explicit joint model

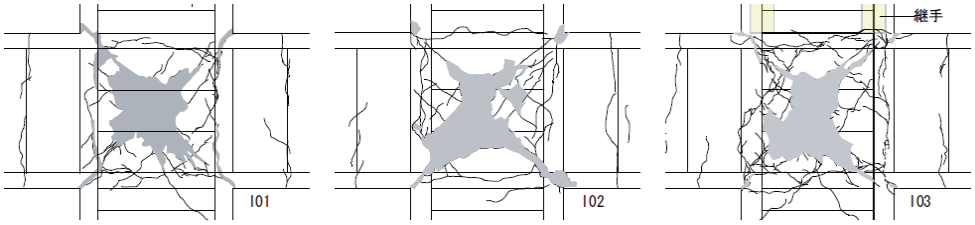


(c) Option 1: Joint response

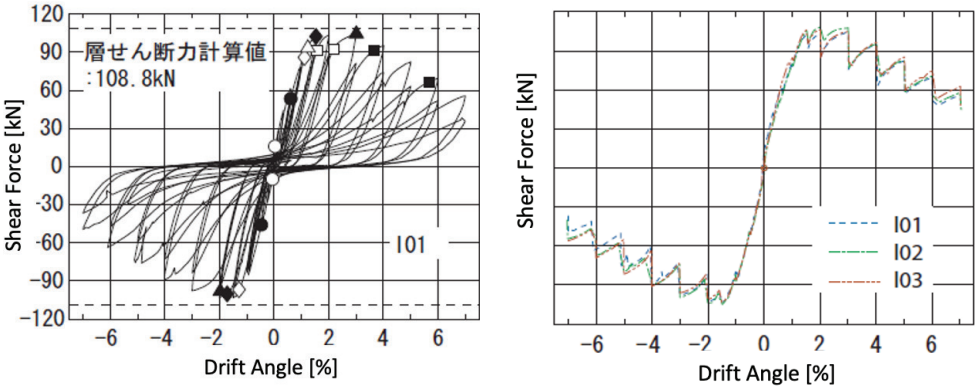


(d) Option 2: Joint response

Figure 5-13 Modeling of beam-column joints in OpenSees NJ model.

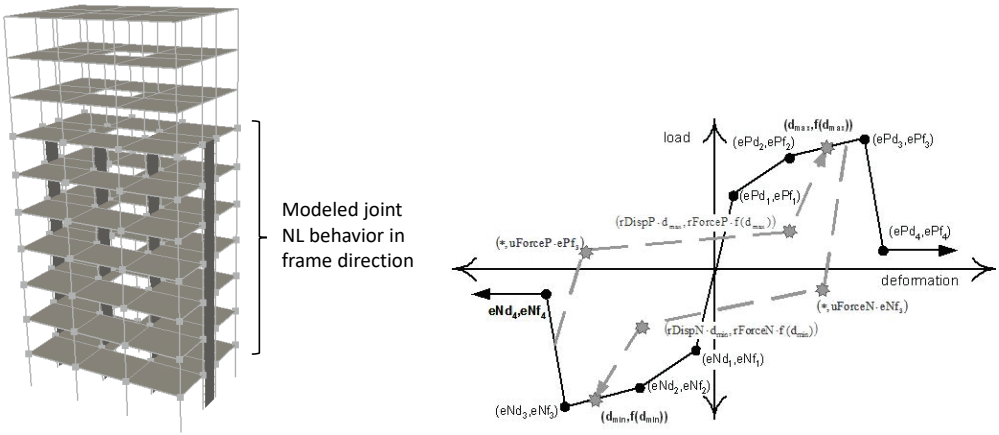


(a) Damage condition at 3% drift



(b) Force-drift and backbone relations

Figure 5-14 Detail of beam-column joints tested by Shiohara et al. (2013).



(a) Floors modeled with nonlinear joints (b) OpenSees Pinching4 model

Figure 5-15 Nonlinear joint modeling approach.

Nonlinear joint behavior was only modeled for perimeter frames over floors 1 to 7 because preliminary analyses indicated limited or no nonlinearity at levels 8 to 10 and results of a pushover analysis for a lateral load distribution based on a first mode shape indicated that the interior frames (beams connecting to wall boundary, versus perimeter frames) contributed only about 25% of the total lateral strength of the building (75% for perimeter frames).

The walls were determined to respond primarily in a flexure mode based on their long height-to-length aspect ratio and high shear strength to shear demand ratio (Unal et al., 2021). Therefore, shear behavior of the walls is modeled as essentially elastic using effective shear modulus of $0.2E_{cE}$, versus using a value of $0.4E_{cE}$, as recommended by ASCE 41-17. Since wall shear demands (and shear deformations) are low, this assumption has very little influence on the results presented later.

Because the building did not contain any nonstructural elements, the analysis employed 2% Rayleigh damping defined at $0.2T_1$ and $1.5T_1$. The analysis accounted for nonlinear geometry effects using the P-delta transformation.

Masses and gravity load at each level were based on values reported in Table 5-6 and are summarized in Table 5-9. For gravity load, self-weight (excluding the slab) was accounted for with a line load whereas the remaining gravity load was distributed on the slab. Masses were distributed to nodes at each floor level based on the distribution of gravity load. No load factors were applied to the gravity loads. A summary of gravity load and masses for the test is shown in Table 5-9, Figure 5-16 illustrates a comparison of mass distribution. The higher mass values at Floor 7 (Level 6) are due to the connection (splice) between the two portions of the building (constructed separately outside the lab, connected on the shake table).

This publication is available free of charge from: https://doi.org/10.6028/NIST.GCR.22-917-50

Table 5-9 Gravity Load and Masses

Floor	Height	Live Load (kN)	Dead Load (kN)	Sum (kN)
R	-	0	725	725
10	2.50	57	740	1522
9	2.50	28	694	2244
8	2.50	28	716	2988
7	2.55	188	949	4125
6	2.55	28	618	4771
5	2.55	28	780	5579
4	2.60	28	798	6405
3	2.60	28	817	7250
2	2.60	57	889	8196
1	2.80	-	-	-

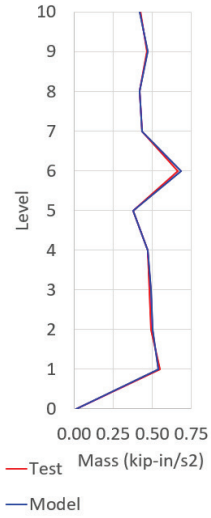


Figure 5-16 Comparison of mass distribution for test and model.

Nonlinear models were only subjected to the two horizontal components of the 100% JMA-Kobe motion (recorded on the shake table) without being subjected to the prior motions applied to the building in the experimental program. To consider the sensitivity of the model results to the loading history, the model was also subjected to the JMA-Kobe 50% and 100% motions sequentially; results of this study using Perform3D are presented in Section 5.4.4.

5.3.2 Building Performance: OpenSees NJ vs. Observation

Given significant nonlinearity in the joints that was observed in the test structure after 100% JMA-Kobe ground motion was applied, results in this section are presented for the OpenSees nonlinear joint (NJ) model.

This publication is available free of charge from: https://doi.org/10.6028/NIST.GCR.22-917-50

Natural Periods

The initial mode shapes, periods, and mass participation factors for modes 1 to 3 are shown in Figure 5-17 and periods are compared with values obtained from the test structure in Table 5-10 and Figure 5-18.

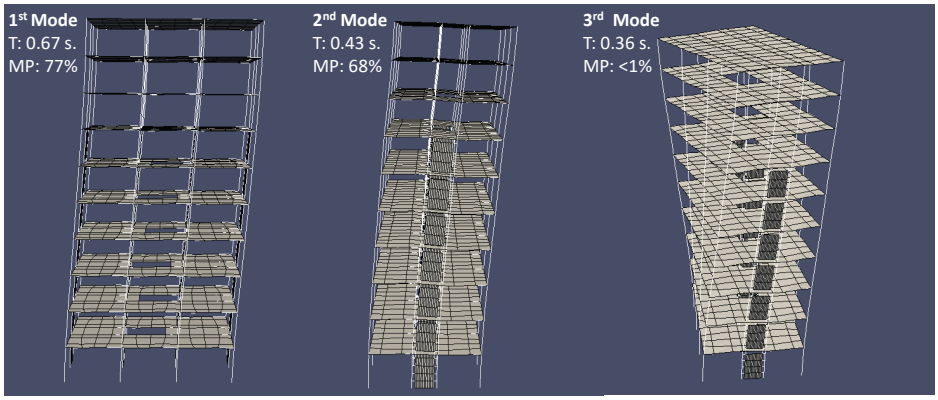


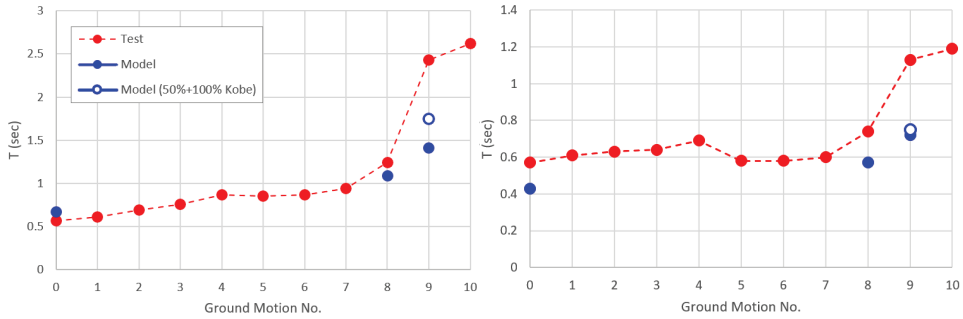
Figure 5-17 OpenSees mode shapes, periods, and mass participation factors for modes 1 to 3.

Table 5-10 Test and Model Periods

		Periods After Each Ground Motion			
		Test		OpenSees*	
	Ground Motion	*Frame Direction*	*Wall Direction*	*Frame Direction*	*Wall Direction*
Sliding Test	Initial	0.57	0.57	0.67	0.43
	10%	0.61	0.61	-	-
	25%	0.69	0.63	-	-
	50%	0.76	0.64	-	-
	100%	0.87	0.69	-	-
Fixed Test	Initial	0.85	0.58	-	-
	10%	0.87	0.58	-	-
	25%	0.94	0.60	-	-
	50%	1.24	0.74	1.09	0.57
	100%	2.43	1.13	1.41	0.72
	60%	2.62	1.19	-	-

* Ground motions are not applied consecutively

This publication is available free of charge from: https://doi.org/10.6028/NIST.GCR.22-917-50



(a) (b)

Figure 5-18 Comparison of model and test periods: (a) frame direction (nonlinear joint model), and (b) wall direction.

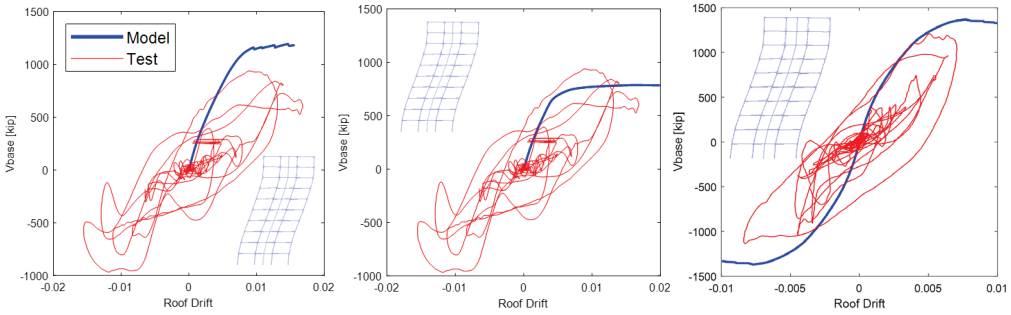
The building first mode periods at the beginning (initial) and end of the 50% and 100% JMA-Kobe motions are compared in Table 5-10. The computational model produces periods that are larger and smaller than the test structure for the frame and wall directions, respectively. The higher model period for the frame direction may be due to modeling of joint flexibility, which assumes zero rigid offset for the relatively short span beams. It is noted that Section 5.4.2 for the Perform3D model shows that even higher frame periods are estimated due to the use of effective stiffness values for beams and column elements (lumped plasticity modeling approach). In the wall direction, the lower model period may be due to the high initial stiffness values associated with the use of uniaxial stress-strain relations, whereas temperature and shrinkage cracking, especially at the foundation-wall interface, might be expected to lead to cracking and a reduction in stiffness for the test structure. Test periods elongate substantially in the 50% and especially the 100% JMA-Kobe tests for the frame direction likely due to joint damage, whereas elongation of model periods (for the elastic joint model) is less pronounced (Figure 5-18). Note that model periods obtained after application of a ground motion are obtained by conducting modal analysis after sufficient free vibration analysis time is applied. Therefore, calculated periods depend on tangent stiffness of each of the elements in the model and provide only an approximation of the building period after the application of the ground motions which might be sensitive to the element hysteresis rules used.

Pushover

Pushover results for a first mode lateral load distribution were compared with test results in Figure 5-19. The lateral load distribution was applied to the floor system along major gridlines based on tributary masses. The results shown in Figure 5-19 indicate that the pushover curve reasonably represents the measured base shear versus roof drift relation for both directions (a bit softer than the test structure in the frame direction). Comparison of analysis results obtained from OpeenSEES NJ (Figure 5-19a) and OpenSees EJ (Figure 5-19b) reveals considerable difference in the

This publication is available free of charge from: https://doi.org/10.6028/NIST.GCR.22-917-50

building capacity in the frame direction between the two cases, suggesting that the building strength was greatly influenced by strength of the joint beam-column joints.



(a) Frame direction-EJ (b) Frame direction-NJ (c) Wall direction

Figure 5-19 Pushovers analysis results compared to experimental base shear versus lateral displacement relations.

It should be noted that results of this analysis are also used to obtain column and wall axial load values for combined gravity and lateral loads that are used for determining ASCE 41-17 modeling parameters (backbone relations) for beam-column joints and acceptance criteria for all structural elements.

Ground Motions

The ground motions applied to the model were the recorded motions at the base of the test building (on the shake table). As shown in Figure 5-20, the base motion applied to the test structure in the frame direction (JMA-Kobe NS component) was scaled by various factors. For the analytical results presented below, only the 100% JMA-Kobe record is considered; however, later, as part of a sensitivity study, the influence of sequential motions on computed model responses is assessed.

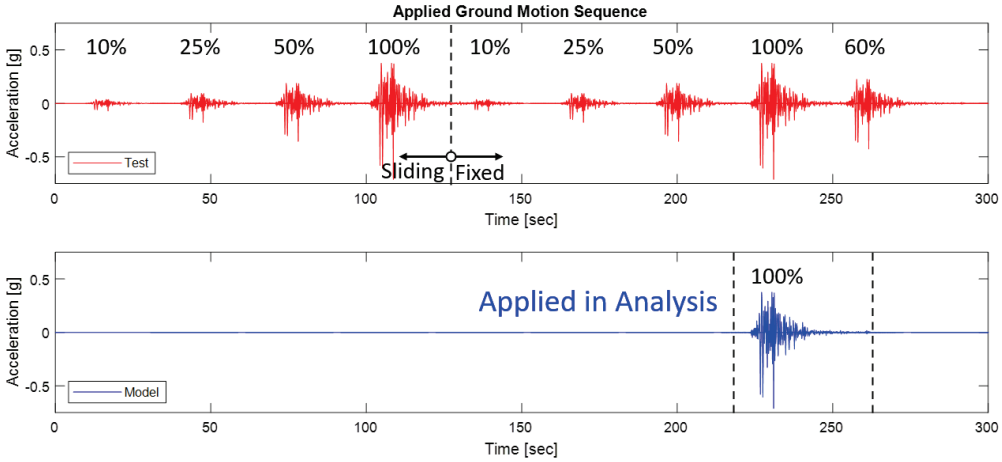


Figure 5-20 Ground motion applied in frame direction: (a) test structure, and (b) computational model.

This publication is available free of charge from: https://doi.org/10.6028/NIST.GCR.22-917-50

Global Mechanism and Damage Distribution

Damage distribution data are compared in order to assess the extent to which the OpenSees models were able to capture the overall building deformation mechanisms and damage distribution. Results are presented first for the frame direction and then for the wall direction.

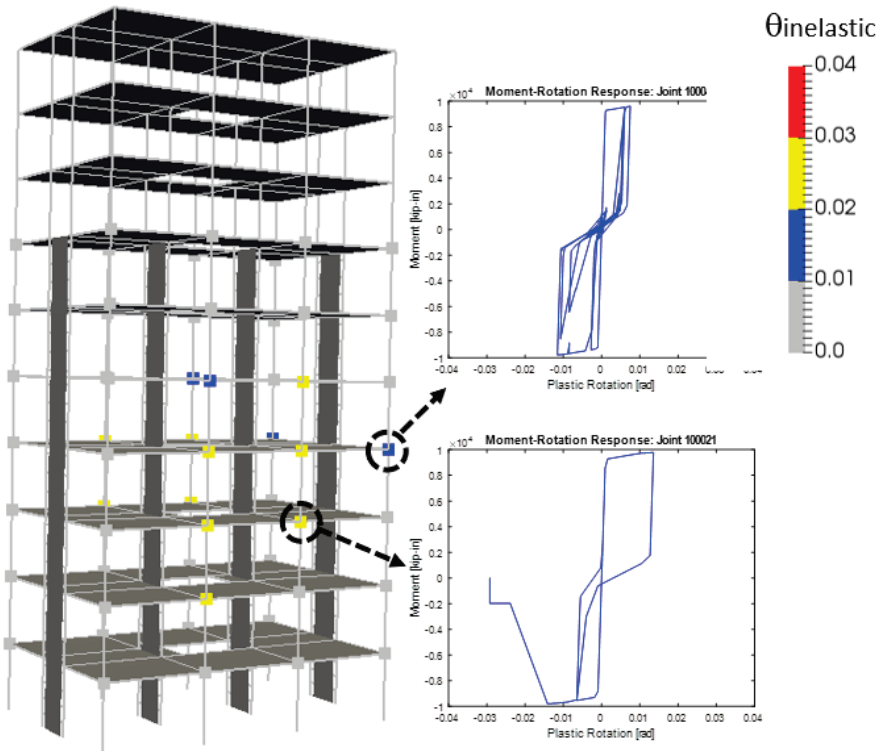
Estimated plastic rotations for the frame direction for the 100% JMA-Kobe record are presented in Figure 5-21, which also includes example joint and column hysteresis relations. The level of damage from analysis was obtained by comparing the inelastic rotations at element ends, $\theta_{inelastic}$, with the ASCE 41-17 modeling parameter *a* that indicates the beginning of lateral strength loss (Figure 5-22). If a rotation exceeded the *a* value, then that member was considered to have sustained severe damage per the analysis, otherwise, it was classified as only having moderate damage. For beams and columns, the computational rotations were obtained by integrating curvatures over the length (height) of the first element, generally set at one-member depth. The *a* and *b* values determined for the conforming joints from ASCE 41-17 Table 10-11 were 0.015 and 0.03 for the interior joints and 0.01 and 0.02 for the exterior joints, respectively. Results for the ASCE 41-17 backbone relations are presented as model Option 1. A refined model, with less drastic joint strength degradation to better match the test results for isolated beam-column-joint test by Shiohara et al. (2013), similar to the joints of the 10-story test structure, is referred to as model Option 2.

As expected, results for joint model Option 2 led to less concentration of inelastic deformations in the joints and in the columns, see Figures 5-21 through 5-23. For both joint modeling options, beams primarily remained elastic.

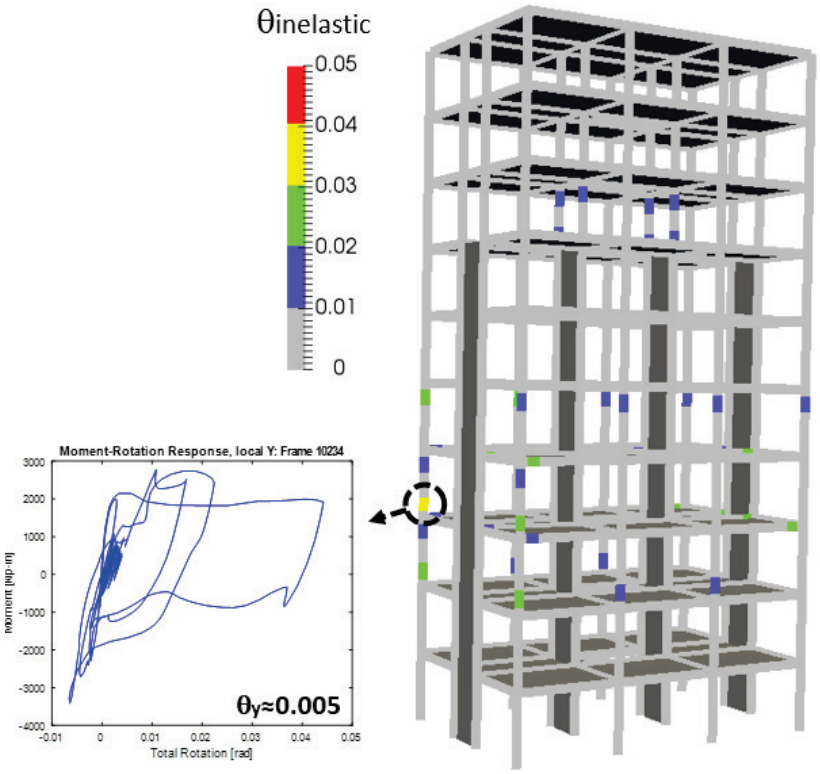
The ratios of plastic rotations to parameter *a* as shown in Figure 5-23a and to parameter *b* in Figure 5-24a indicate that most interior joints at floors 3 and 4 exceeded parameter *a* for joint model Option 1, with modestly lower ratios for joint model Option 2. This suggests that severe damage would occur at these joints; however, parameter *b* values were generally between 0.5 and 1.0, indicating a possibility of collapse for joint model Option 1 and less likelihood of collapse for joint model Option 2. The model results suggest no damage would be observed in the exterior joints. This is consistent with what was observed in the test (Figure 5-25) where severe damage was observed for interior joints at the 3rd and 4th floors and modest damage was observed for interior joints at the 2nd and 5th floors. Particularly for modeling Option 2, model results indicated the potential for damage in some interior columns at the 8th floor, above where the structural walls were terminated; modeling slip deformations at member ends might alleviate this concentration.

This publication is available free of charge from: https://doi.org/10.6028/NIST.GCR.22-917-50

This publication is available free of charge from: https://doi.org/10.6028/NIST.GCR.22-917-50



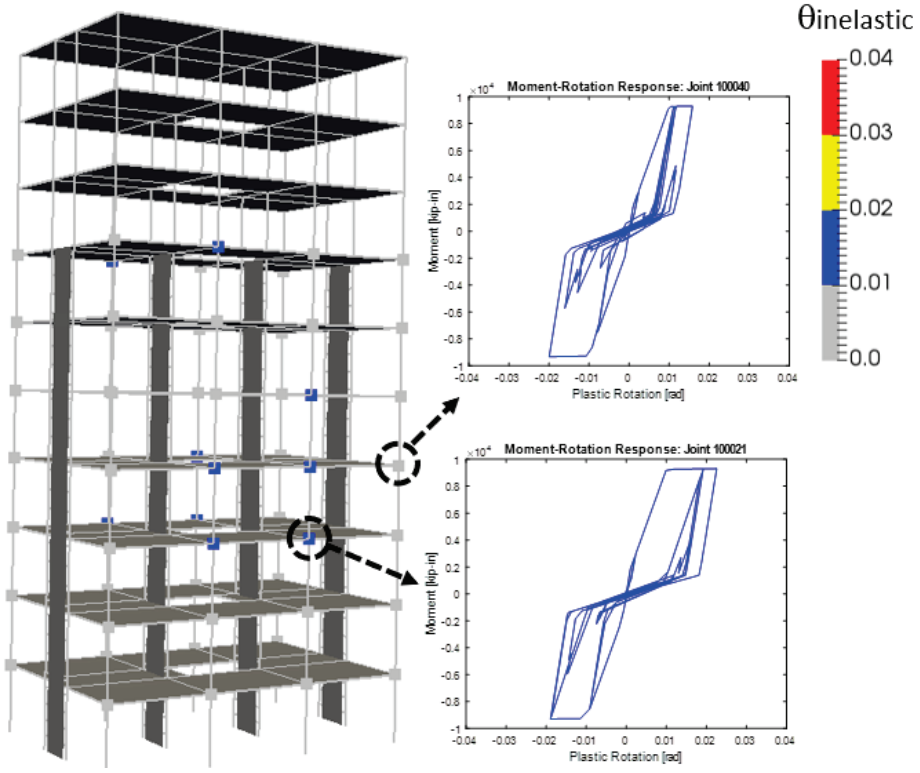
(a) Option 1 – Beam-column joints



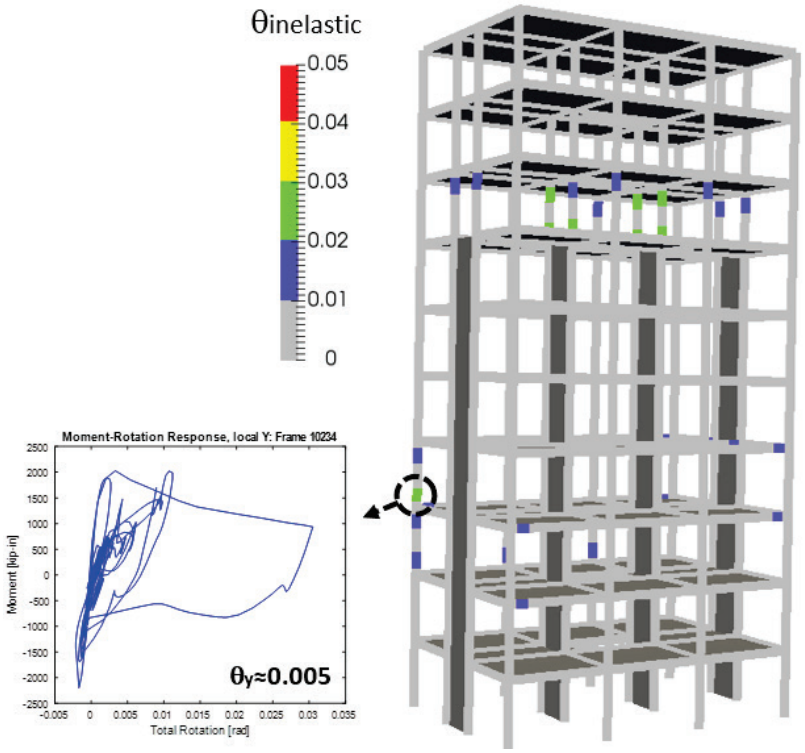
(b) Option 1 – Beams and columns

Figure 5-21 NDP OpenSees NJ: Option 1 model results showing schematic damage distribution in (a) frame joints, and (b) beams/columns based on estimated plastic rotation $\theta_{inelastic}$ (100% JMA-Kobe).

This publication is available free of charge from: https://doi.org/10.6028/NIST.GCR.22-917-50



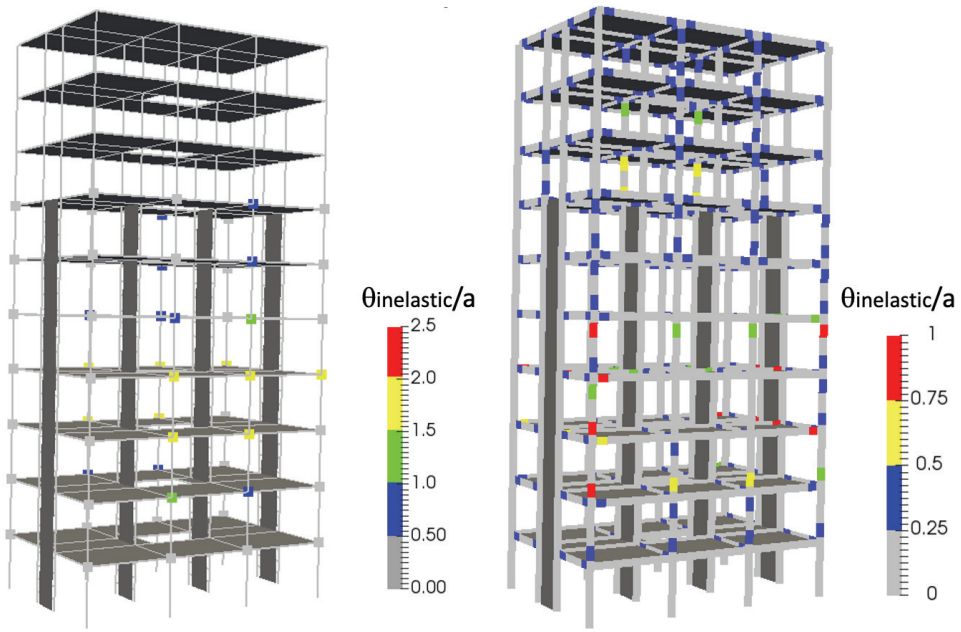
(a) Option 2 – Beam-column joints



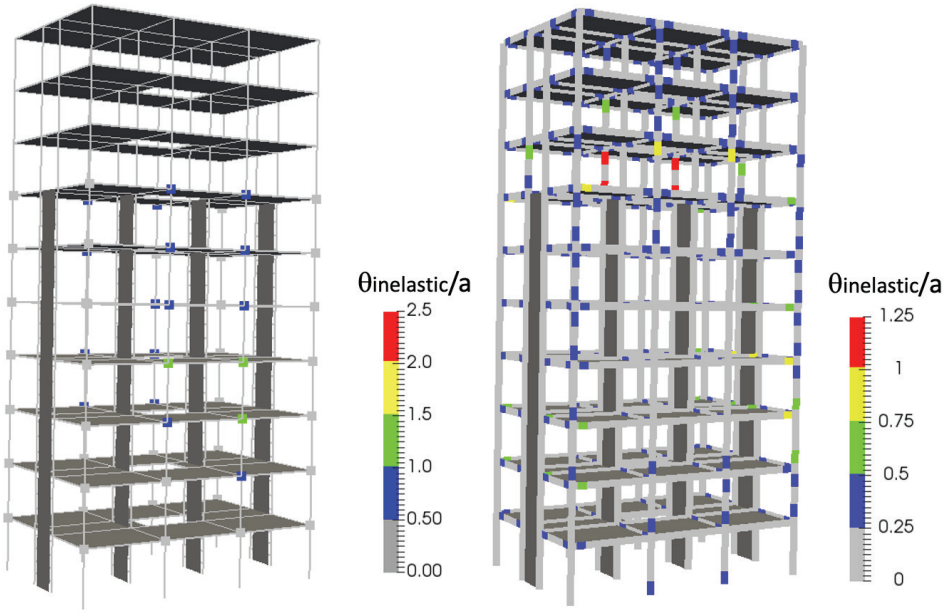
(b) Option 2 – Beams and columns

Figure 5-22 NDP OpenSees NJ: Option 2 model showing schematic damage distribution in (a) frame joints and (b) beams/columns based on estimated plastic rotation $\theta_{inelastic}$ (100% JMA-Kobe).

This publication is available free of charge from: https://doi.org/10.6028/NIST.GCR.22-917-50



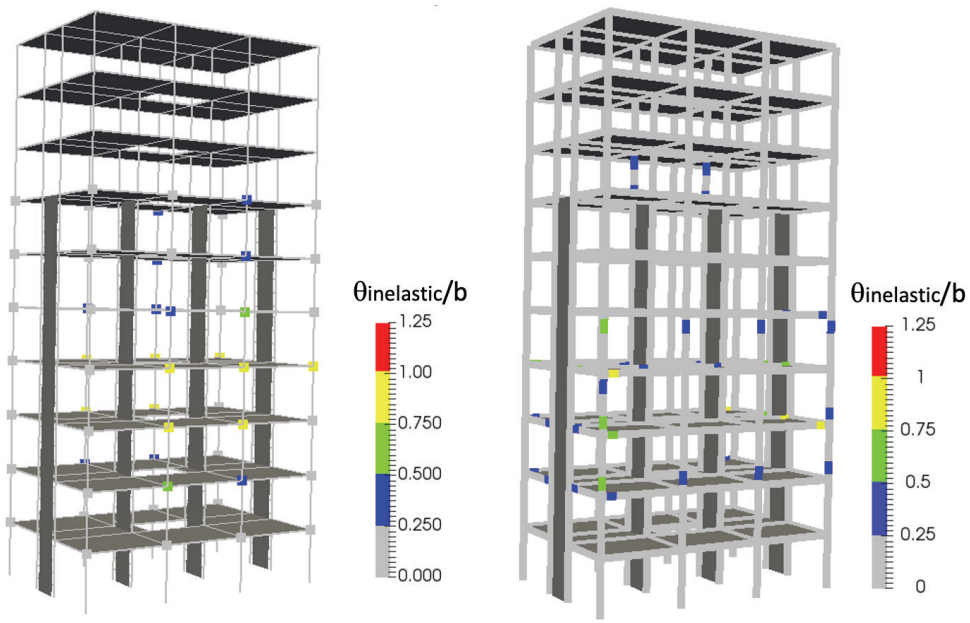
(a) Option 1



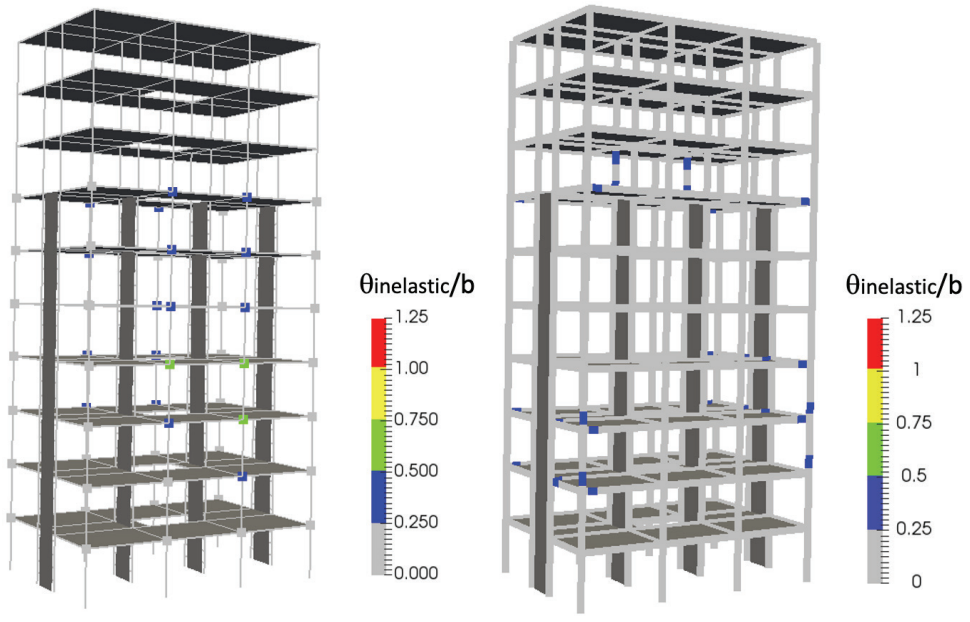
(b) Option 2

Figure 5-23 NDP OpenSees NJ: Schematic damage distribution with (a) Option 1 and (b) Option 2 showing frame joints (left) and beams/columns (right) compared to ASCE 41-17 plastic rotation parameter *a* (100% JMA-Kobe).

This publication is available free of charge from: https://doi.org/10.6028/NIST.GCR.22-917-50



(a) Option 1

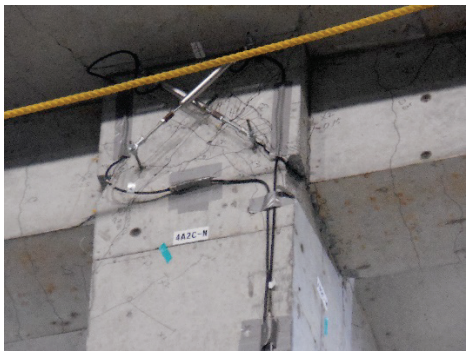


(b) Option 2

Figure 5-24 Schematic damage distribution with (a) Option 1 and (b) Option 2 showing frame joints (left) and beams/columns (right) compared to ASCE 41-17 plastic rotation parameter *b* (100% JMA-Kobe).



(a) 3rd Floor interior joint (South)



(b) 4th Floor interior joint (North)

Figure 5-25 Observed joint damage (100% JMA-Kobe).

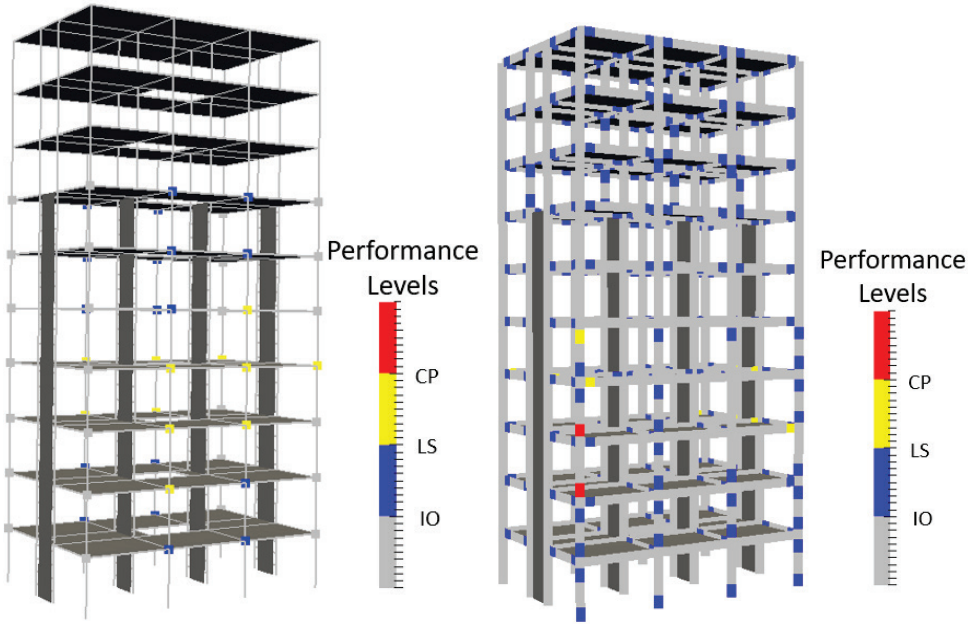
Peak column plastic rotation demands computed from the models were generally less than 1.0 times parameter *a*, with higher ratios for joint model Option 1 (particularly for exterior (corner) columns), as would be expected. As indicated in Figure 5-21, beam plastic rotations did not exceed 0.01 or 0.5 times parameter *a* for both joint model Options 1 and 2. Modeling parameters *a* and *b*, determined for columns for floors 3 through 5, averaged to 0.023 and 0.035, respectively, with a variation of only 0.001 for *a* and 0.002 for *b*). It is also noted the modeling parameters were computed for maximum compression axial load determined from the pushover analysis using the first mode lateral load distribution, whereas column yielding generally occurred during the analysis at minimum axial load; therefore, the reported ratios for columns are likely on the conservative side.

It also is noted that column yielding is observed in the model despite column-to-beam moment strength ratios exceeding the 1.2 value required by ACI 318-19, *Building Code Requirements for Structural Concrete and Commentary* (ACI, 2019), Section 18.7.3 (i.e., strong column requirement). Column yielding occurs because: (1) higher modes and nonlinear responses produce higher beam moment and shear demands than predicted by ASCE 7 (Moehle, 2014; NIST GCR 16-917-40 (NIST, 2016) Sections 3.1 and 5.5.3), and (2) the approach commonly used to determine column moments at a beam-to-column connection is approximate (e.g., see ACI PRC 352-02 (ACI, 2002); NIST GCR 16-917-40).

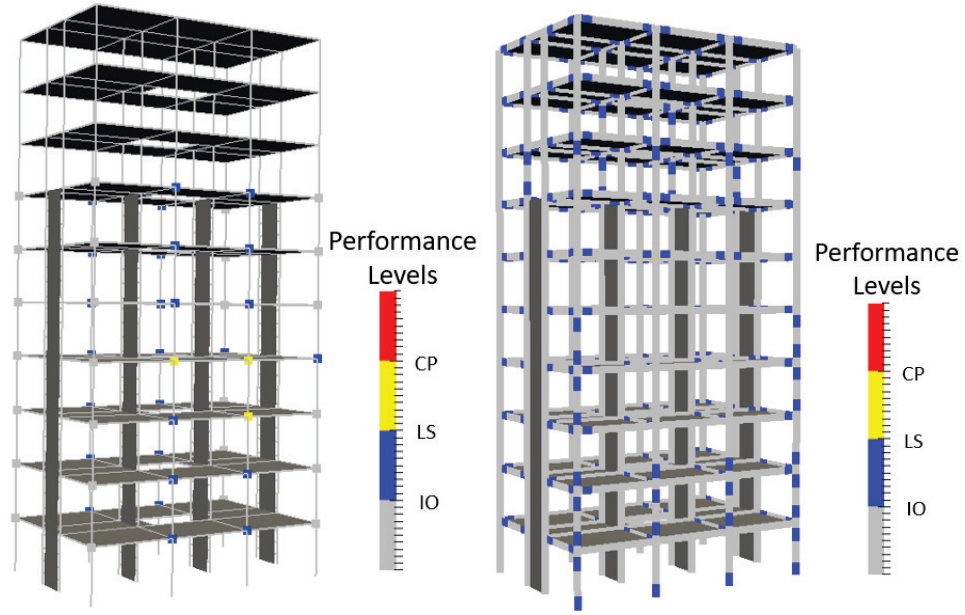
Figure 5-26 illustrates damage distribution in frame joints and beams and columns expressed in terms of ASCE 41-17 performance levels Immediate Occupancy (IO), Life Safety (LS), and Collapse Prevention (CP). Figure 5-26a shows damage distribution for OpenSees NJ model with Option 1 joint modeling parameters: about half of the joints exceed the IO or LS performance level, only two column sections experience plastic deformations that exceed CP, and the vast majority of the remaining beams and columns are within the LS performance level. Results in Figure 5-26b for OpenSees NJ model with Option 2 joint modeling parameters are similar, with smaller amount of nonlinearity in the joints, where only three interior

This publication is available free of charge from: https://doi.org/10.6028/NIST.GCR.22-917-50

joints exceed the LS performance level and all beams and columns are within the LS performance level.



(a) Option 1



(b) Option 2

Figure 5-26 NDP OpenSees NJ: Schematic damage distribution showing (a) Option 1 and (b) Option 2 in frame joints (left) and beams/columns (right) compared to ASCE 41-17 performance levels (IO, LS, CP) (100% JMA-Kobe).

Estimated plastic rotation demands for the wall direction are presented in Figure 5-27 and were determined to be less than 0.5*a* and 0.25*b* for ASCE 41-17, i.e., wall deformation demands are within IO performance level. The results indicate that

This publication is available free of charge from: https://doi.org/10.6028/NIST.GCR.22-917-50

limited yielding was expected at the base of the wall, which is consistent with observed wall damage that consisted of modest cracking and very limited spalling at the wall boundary (Figure 5-28).

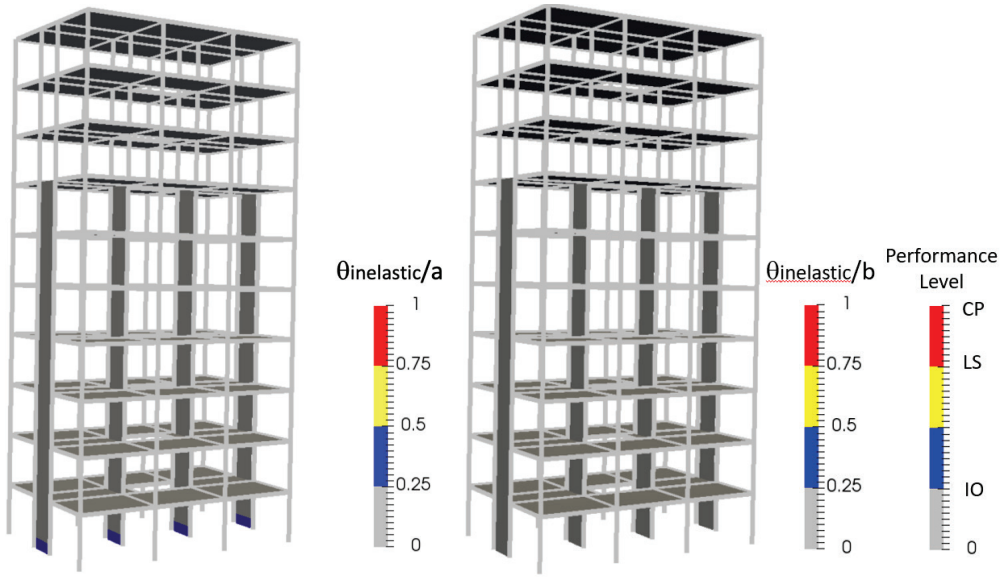


Figure 5-27 NDP OpenSees NJ: Schematic damage distribution within wall, compared to ASCE 41-17 plastic rotation parameter *a* (left) and rotation parameter *b* and performance levels (IO, LS, CP) (right) (100% JMA-Kobe).



(a) Wall damage at 1st Floor (b) Wall damage at 2nd Floor

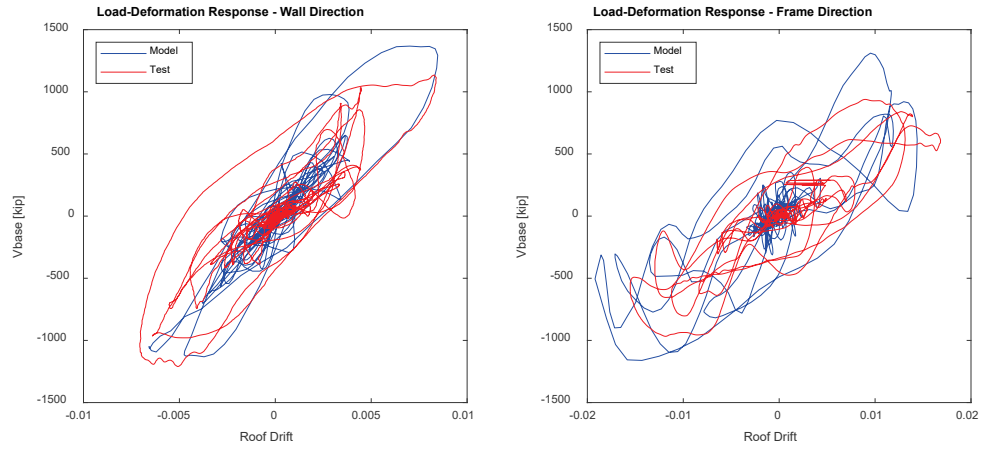
Figure 5-28 Observed wall damage (100% JMA-Kobe).

Base Shear and Roof Displacement (Drift)

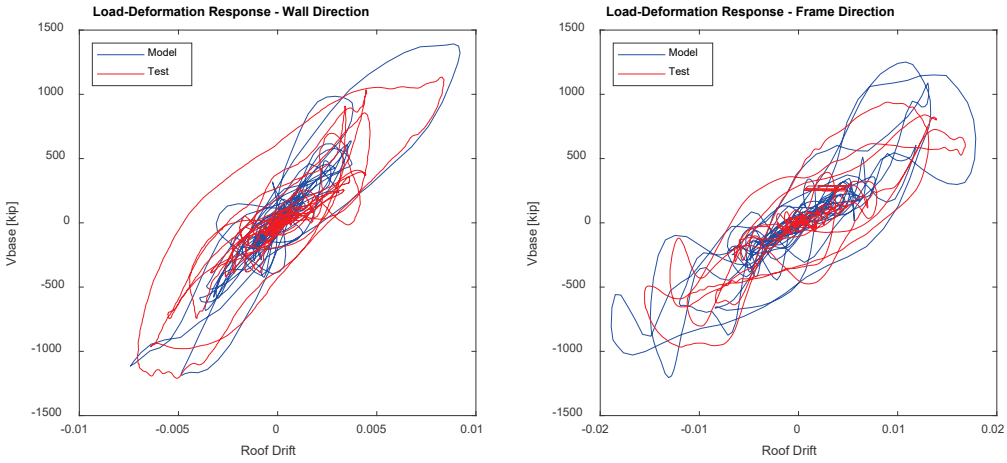
The history of the roof drift versus base shear for the test and model are shown in Figure 5-29 for the frame and wall directions for the 100% JMA-Kobe motion. Base

This publication is available free of charge from: https://doi.org/10.6028/NIST.GCR.22-917-50

shear was derived from the test results using acceleration computed at the center of mass of the test structure multiplied by the floor mass for each level, summed over the ten floors. In general, the test and model results match reasonably well for both joint model Options 1 and 2.



(a) Option 1



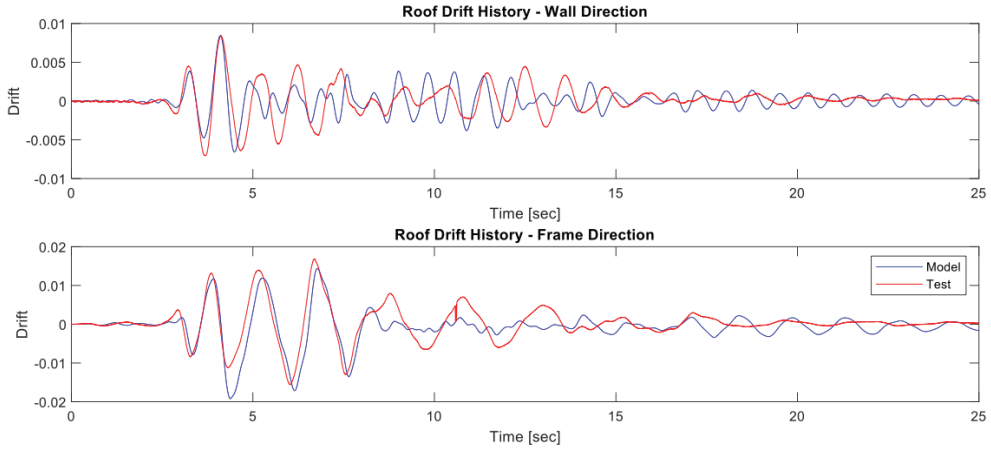
(b) Option 2

Figure 5-29 NDP OpenSees NJ: Roof drift versus base shear histories for (a) Option 1 and (b) Option 2 in wall direction (left) and frame direction (right) for 100% JMA-Kobe.

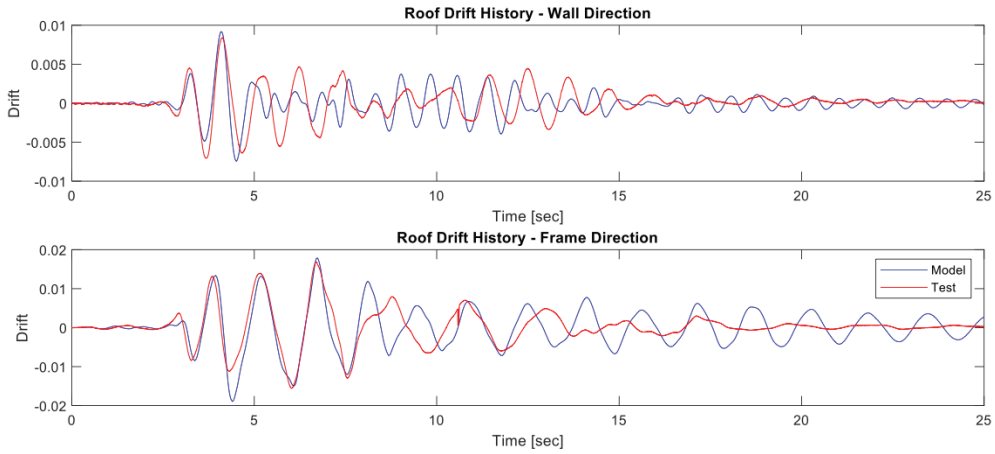
Roof drift histories derived for the building test data at center of mass (COM) and for the OpenSees model are plotted in Figure 5-30 for the 100% JMA-Kobe motion. Roof drift ratio is defined as the roof lateral displacement with respect to the foundation divided by the total building height (25.75 m, 84.48 ft.) from the base of the 1st story columns to the roof level. The results indicate that the histories, and especially the peak values, show similar tendencies, with slightly better match for joint model Option 2 later in the response history. The only notable discrepancy between the model and test results can be observed at about 4.5 seconds in the frame direction, where model overestimates the roof drift by approximately 80%.

This publication is available free of charge from: https://doi.org/10.6028/NIST.GCR.22-917-50

Fundamental periods for the model appear to be slightly low and high relative to the test building for the wall and frame directions, respectively. The model does appear to show higher peak drifts later in the history (especially for joint model Option 1), possibly due to contributions from higher models and variations in damping (e.g., foundation level damping); however, peak values are well captured by both joint model options.



(a) Option 1



(b) Option 2

Figure 5-30 NDP OpenSees NJ: Roof drift histories for (a) Option 1 and (b) Option 2 in wall direction (top) and frame direction (bottom) for 100% JMA-Kobe.

Base shear histories are plotted in Figure 5-31 for test and model results. Results comparison demonstrates that model predicts with very good accuracy history of base shear in the wall direction, while in the frame direction maximum base shear predicted by the model (around 4.5 seconds) is approximately 20% larger than the one obtained from test data.

This publication is available free of charge from: https://doi.org/10.6028/NIST.GCR.22-917-50

This publication is available free of charge from: https://doi.org/10.6028/NIST.GCR.22-917-50

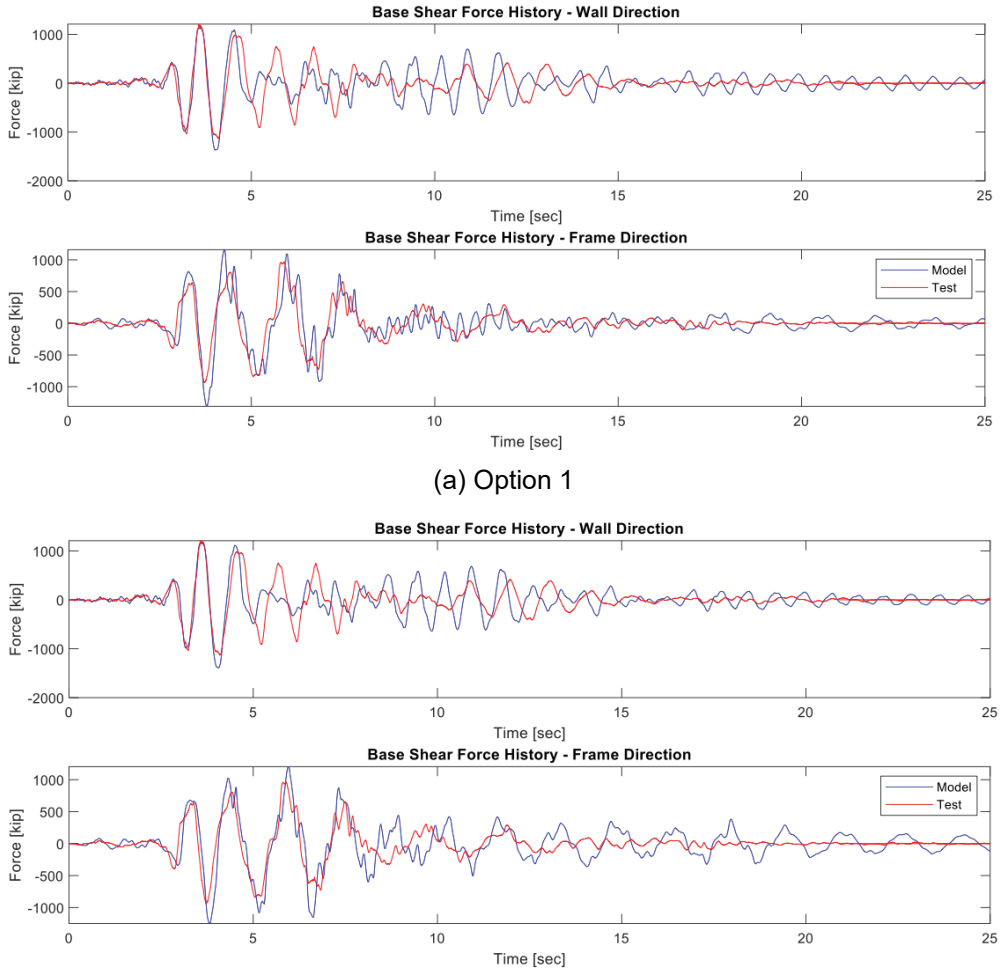
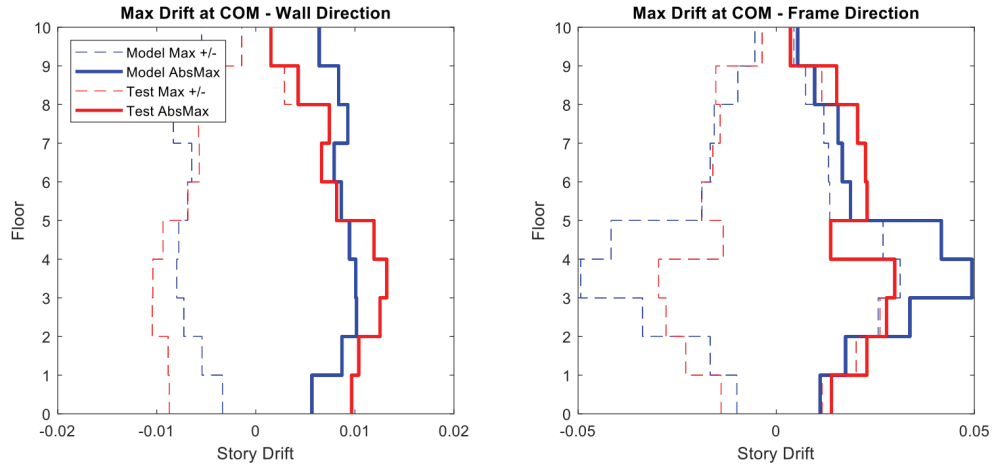


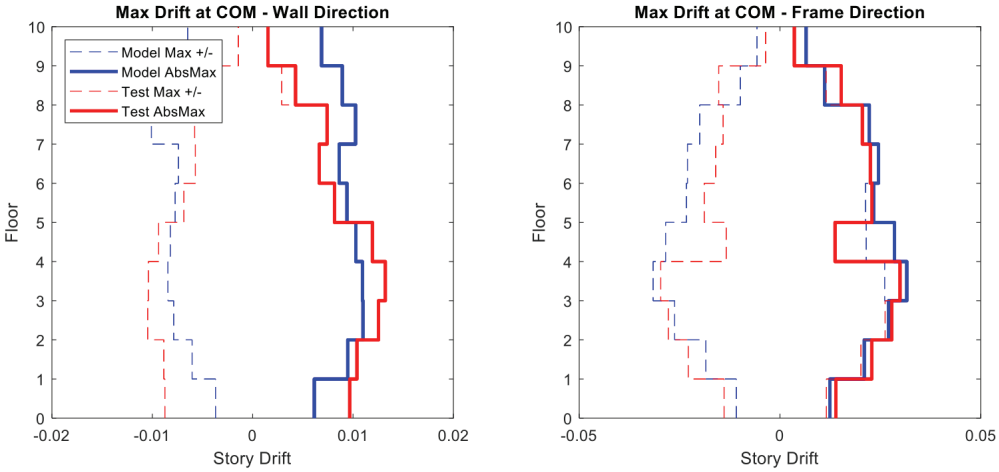
Figure 5-31 NDP OpenSees NJ: Base shear histories for (a) Option 1 and (b) Option 2 in wall direction (top) and frame direction (bottom) for 100% JMA-Kobe.

Peak Story Drift

Distribution of maximum story drifts over the building height are compared between the OpenSees NJ model and the test measurements in Figure 5-32. Results for the wall direction generally follow the overall distribution observed over the height of the structure, , although test values were approximately 10% higher (on the average) for the bottom 5 stories and 10% lower for the top 4 stories. Results for the frame direction show larger discrepancy between test and joint model Option 1, especially between the 2nd and 5th levels, where the model overestimates story drift by 80%. However, results for joint model Option 2 match the test results very well with mismatch between analytical and experimental results that is ±5%. The results imply that the strength degradation for the ASCE 41-17 joint backbone relations used in Option 1 are too abrupt.



(a) Option 1



(b) Option 2

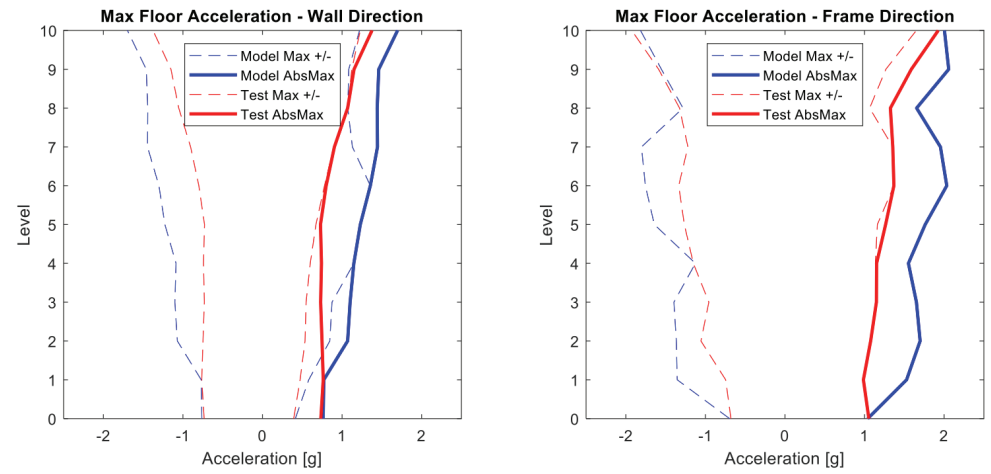
Figure 5-32 NDP OpenSees NJ: Peak story drift ratios for (a) Option 1 and (b) Option 2 in wall direction (left) and frame direction (right) for 100% JMA-Kobe.

Peak Floor Acceleration

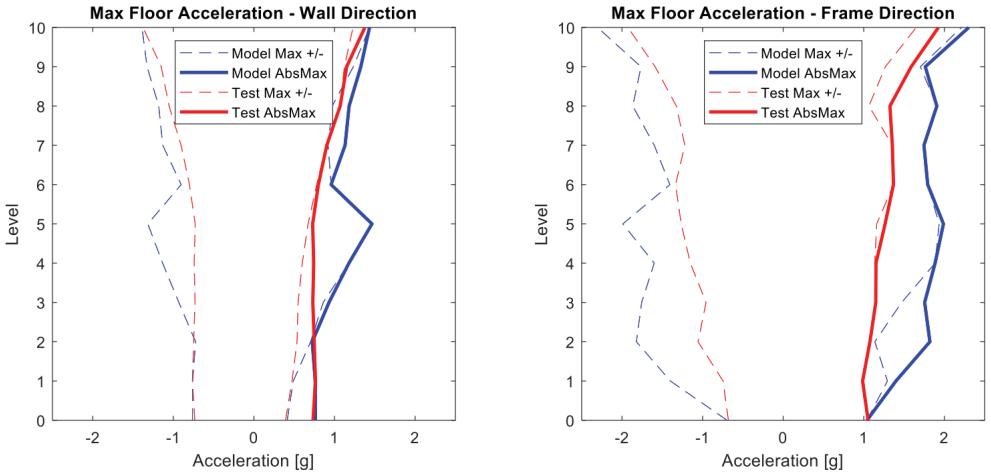
Figure 5-33 compares the peak floor acceleration from the OpenSees NJ model and measured in the experiment. The results presented in the figure indicate reasonable agreement in the acceleration profiles at all levels for both the wall and frame directions, although model results tend to systematically overestimate peak floor acceleration by approximately 1.5 to 2.0 times, especially in the frame direction. This may be related to damping assumptions used in the analysis.

This publication is available free of charge from: https://doi.org/10.6028/NIST.GCR.22-917-50

This publication is available free of charge from: https://doi.org/10.6028/NIST.GCR.22-917-50



(a) Option 1

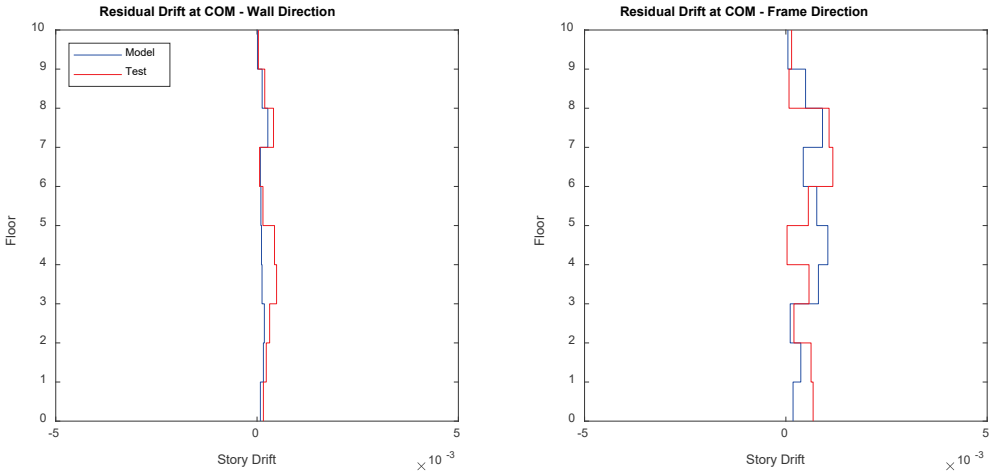


(b) Option 2

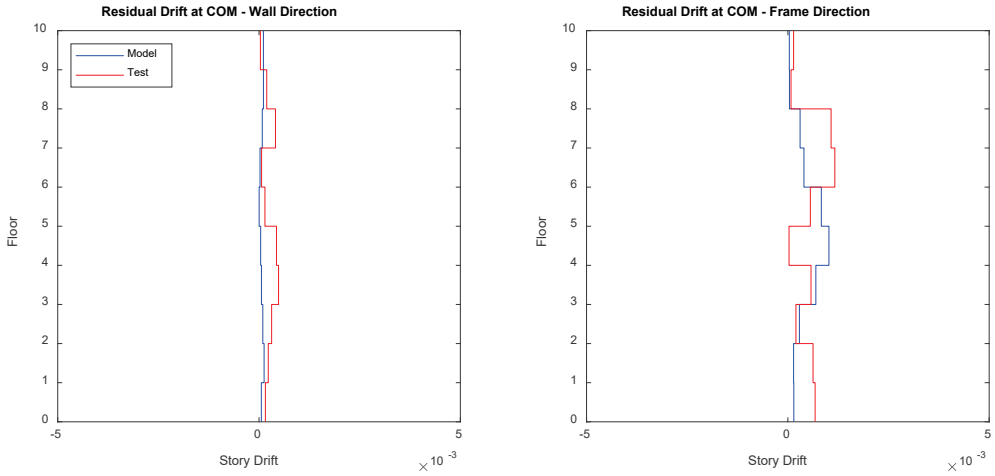
Figure 5-33 NDP OpenSees NJ: Peak floor acceleration for (a) Option 1 and (b) Option 2 in wall direction (left) and frame direction (right) for 100% JMA-Kobe.

Residual story drifts over the building height are plotted in Figure 5-34 for both the frame and wall directions for both joint model options. Residual drifts for both the model and the test building are relatively small, i.e., less than 0.001 for all stories.

This publication is available free of charge from: https://doi.org/10.6028/NIST.GCR.22-917-50



(a) Option 1



(b) Option 2

Figure 5-34 NDP OpenSees NJ: Peak residual story drifts for (a) Option 1 and (b) Option 2 in wall direction (left) and frame direction (right) for 100% JMA-Kobe.

5.3.3 Building Performance: OpenSees EJ vs. Observation

The OpenSees NJ model was modified to have elastic joint elements, which are not allowed to yield or lose strength (OpenSees EJ model). Considering the noted premature joint strength loss that occurred in the OpenSees NJ model Option 1 (ASCE 41-17 compliant model), the OpenSees EJ model is considered to investigate the effects of joint nonlinearity on demands in adjacent members and to compare test and model results.

Figure 5-35 shows the damage distribution derived from the OpenSees EJ model in the same format as used in Figure 5-21. The wall direction damage distribution is almost identical for this model as for the OpenSees NJ model. In the frame direction, the 3rd story columns are more severely damaged in the OpenSees EJ model than in

the OpenSees NJ model, that is, the peak column plastic rotation approximately doubles and exceeds parameter *b* for the 3rd story columns. When nonlinear joints are used, the damage concentrates in the joints which unloads the beams and columns as seen in the OpenSees NJ model. When joints are prevented from losing strength (i.e., modeled elastically), the damage concentrates more in the column than the beams.

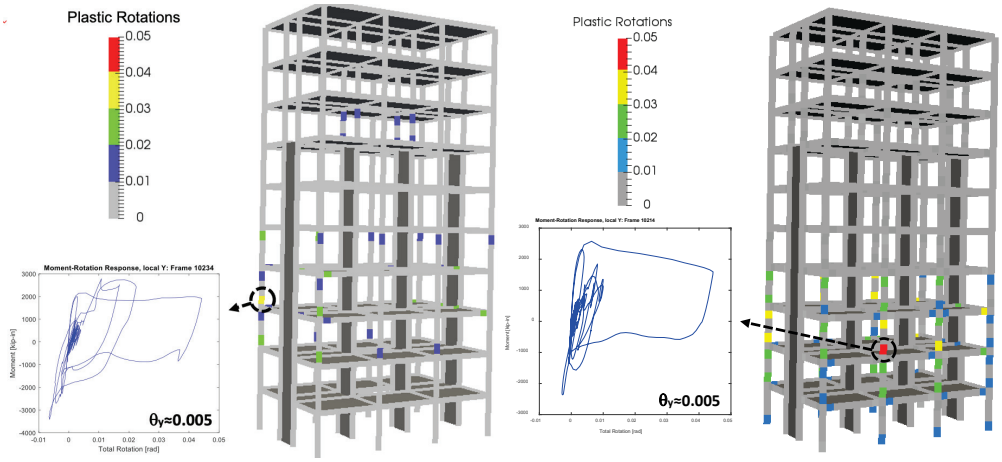
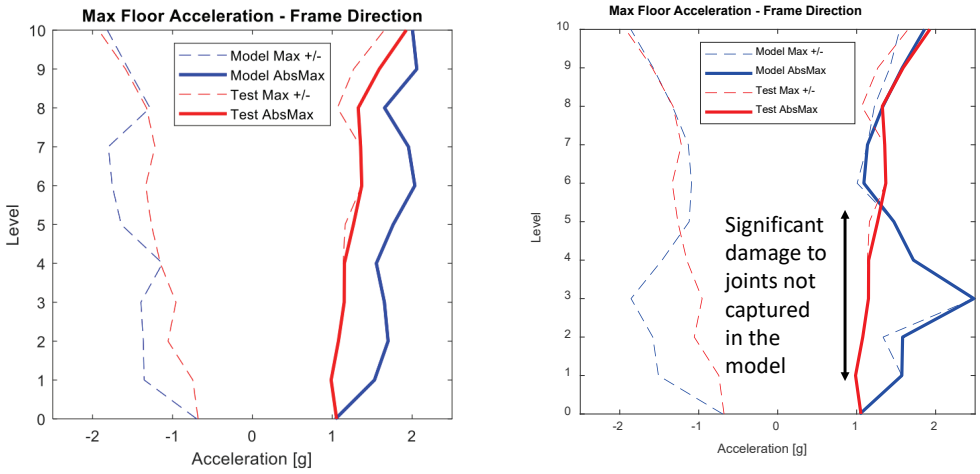


Figure 5-35 NDP OpenSees: Schematic damage distribution in columns for (a) OpenSees NJ model Option 1 and (b) OpenSees EJ columns for 100% JMA-Kobe.

Figure 5-36 shows the distribution of maximum floor acceleration over the building height for the OpenSees NJ and EJ models. The comparison reveals that joint yielding reduces the floor acceleration over the stories where joint damage was observed (3rd to 5th floors), and most notably, at the 3rd floor, to produce a much better match with measured floor acceleration at these levels. However, the OpenSees NJ models consistently overpredict peak floor acceleration at all floors.

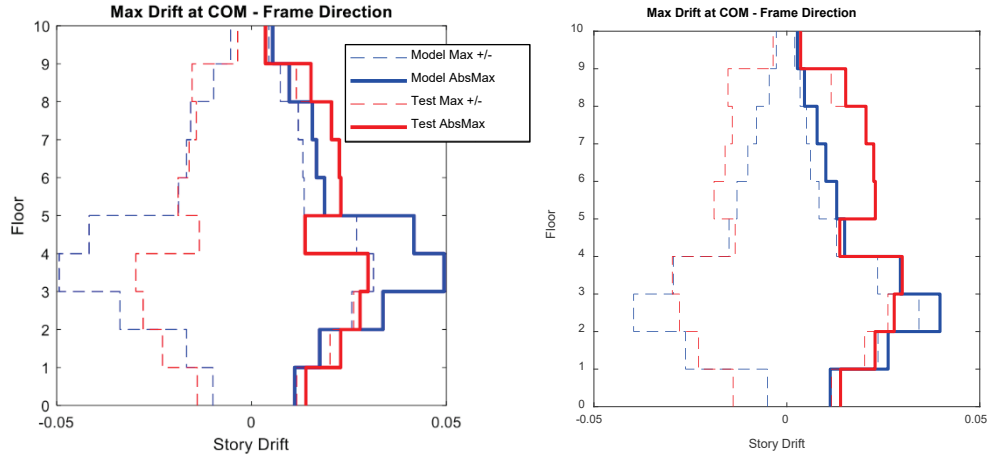
The distribution of maximum story drifts over the building height are compared between the OpenSees NJ Option 1 and OpenSees EJ models and test measurements in Figure 5-37. Joint modeling did not alter the wall direction drift results measurably, so they are not presented. For the frame direction, drifts predicted with the EJ model were significantly smaller in the 4th and 5th story and modestly smaller elsewhere, except the 2nd and 3rd, comparing to the results of NJ model; the reductions at levels 3 through 5 were likely because of damage concentration at these levels for both the OpenSees NJ model (in the joints) and OpenSees EJ model (in the columns).

This publication is available free of charge from: https://doi.org/10.6028/NIST.GCR.22-917-50



(a) (b)

Figure 5-36 NDP OpenSees: Maximum floor acceleration comparison for (a) OpenSees NJ Option 1 and (b) OpenSees EJ models throughout the height of the building for 100% JMA-Kobe.



(a) (b)

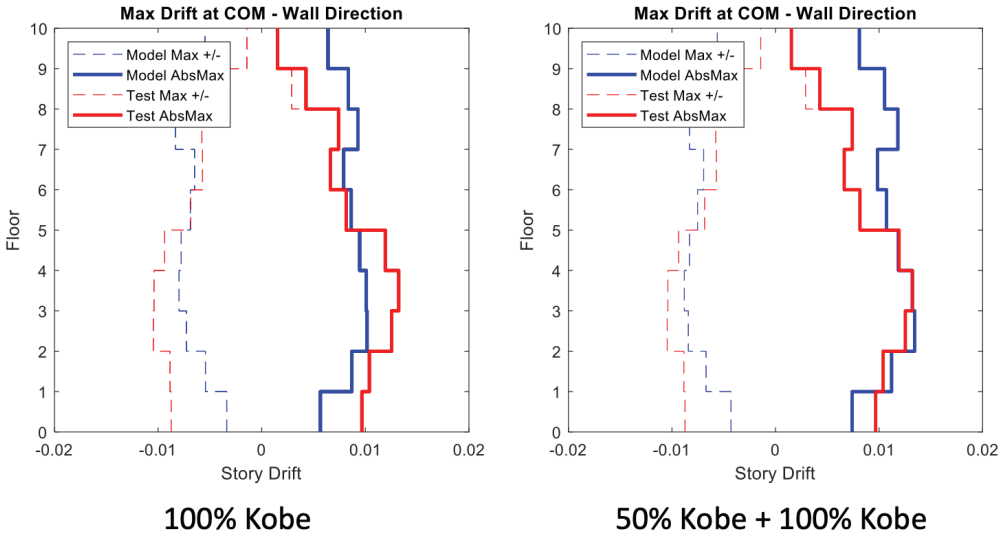
Figure 5-37 NDP OpenSees: Maximum story drift comparison for (a) OpenSees NJ Option 1 and (b) OpenSees EJ models throughout the height of the building for 100% JMA-Kobe.

Findings from comparing the OpenSees NJ and OpenSees EJ models highlight the importance of considering and modeling all sources of nonlinearity and also using accurate modeling parameters (e.g., rate of strength degradation) in nonlinear analysis to avoid skewing building demands, component demands, and damage distributions. The results also indicate that joint yielding may occur even if ASCE 41 mechanism analysis indicates joint shear strength is not exceeded because of differences in the assumptions used for the mechanism analysis and the demands from the nonlinear dynamic response history analysis.

This publication is available free of charge from: https://doi.org/10.6028/NIST.GCR.22-917-50

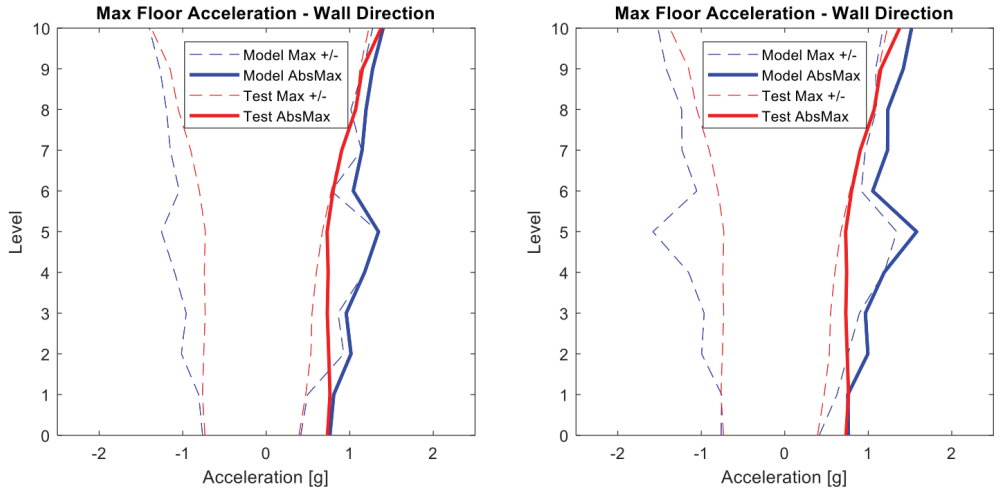
5.3.4 *Building Performance: Sequential Application of Ground Motions*

Ground motions for 50% and 100% JMA-Kobe were applied sequentially to the model to assess the potential influence of the repeated motions. Figures 5-38 through 5-40 present comparisons of model and test results for peak story drifts and peak floor acceleration. The influence of the sequential motions on periods was previously illustrated in Figure 5-18.



100% Kobe 50% Kobe + 100% Kobe

(a) Peak story drift ratios

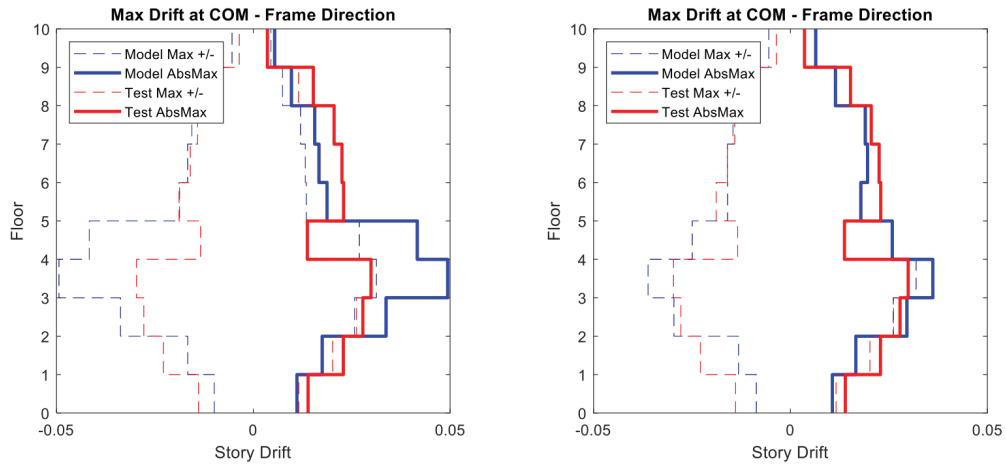


100% Kobe 50% Kobe + 100% Kobe

(b) Peak floor acceleration

Figure 5-38 NDP OpenSees NJ Option1: Comparison of peak story drift ratios and peak floor acceleration for wall direction and for 100% JMA-Kobe (left) and 50% JMA-Kobe and 100% JMA-Kobe (right).

This publication is available free of charge from: https://doi.org/10.6028/NIST.GCR.22-917-50



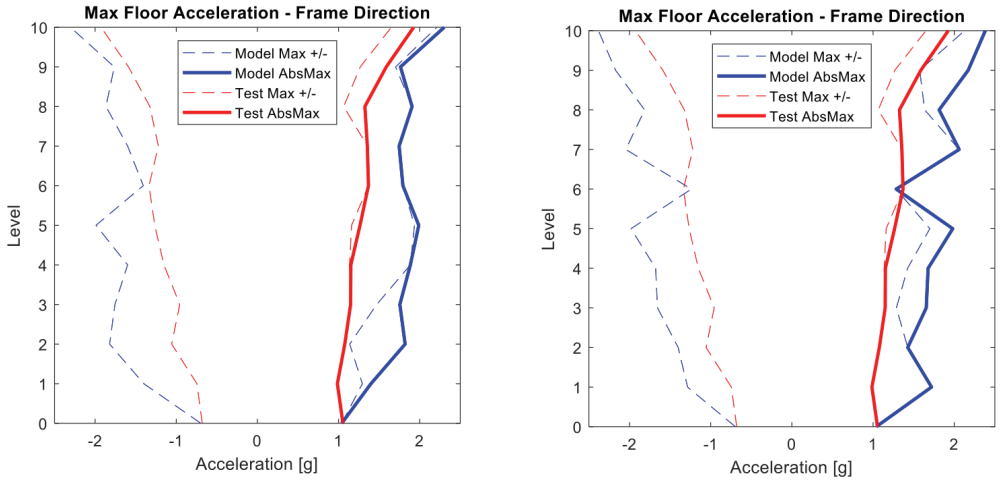
100% Kobe

(a)

50% Kobe + 100% Kobe

(b)

Figure 5-39 NDP OpenSees NJ Option1: Peak story drift ratios for frame direction for (a) 100% JMA-Kobe and (b) 50% JMA-Kobe and 100% JMA-Kobe.



100% Kobe

(a)

50% Kobe + 100% Kobe

(b)

Figure 5-40 NDP OpenSees NJ Option1: Peak floor acceleration for frame direction for (a) 100% JMA-Kobe and (b) 50% JMA-Kobe and 100% JMA-Kobe.

Results presented in Figures 5-38 to 5-40 indicate that maximum story drifts are modestly impacted and produce a better match between model and test results for the frame direction (all levels) and for the wall direction (at lower levels). Maximum floor accelerations do not change significantly. Note that analysis results for the frame direction (Figure 5-39) indicate that maximum drifts (stories 3-5) are smaller when sequential ground motions are applied, which might seem counter intuitive. However, detailed investigation of analysis results showed that 50% JMA-Kobe ground motion applied first to the model changed the dynamic properties of the

This publication is available free of charge from: https://doi.org/10.6028/NIST.GCR.22-917-50

building (the structure became softer) such that drifts in the model during subsequent 100% JMA-Kobe ground motion are smaller compared to drifts obtained from analysis conducted by applying only 100% JMA-Kobe ground motion. This observation is also a result of the spectral shape. This result was not observed for the wall direction, likely due to the limited nonlinear curvature demands at the wall base in the 50% JMA-Kobe test (essentially linear wall response).

5.4 Nonlinear Dynamic Procedure using Perform3D

Similar to Section 5.3, two models were developed using Perform3D software. They are identical for beams, columns, and walls that were modeled with nonlinear fiber sections. Two approaches were used to model the beam-column joints: one with elastic joints (Perform3D EJ) and the other with nonlinear joints (Perform3D NJ).

5.4.1 Modeling Approach

Three-dimensional numerical models of the structure were created in Perform3D, as shown in Figure 5-41. The nonlinear backbone of each element was defined using modeling parameters similar to those used for the OpenSees model.

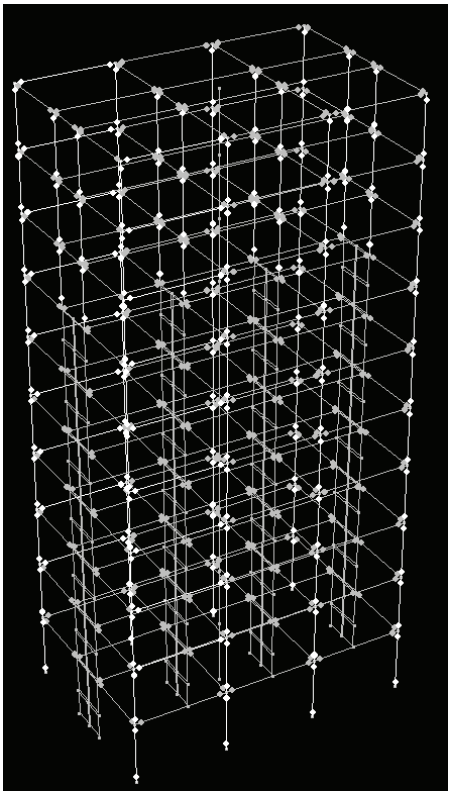


Figure 5-41 Nonlinear analysis model in Perform3D.

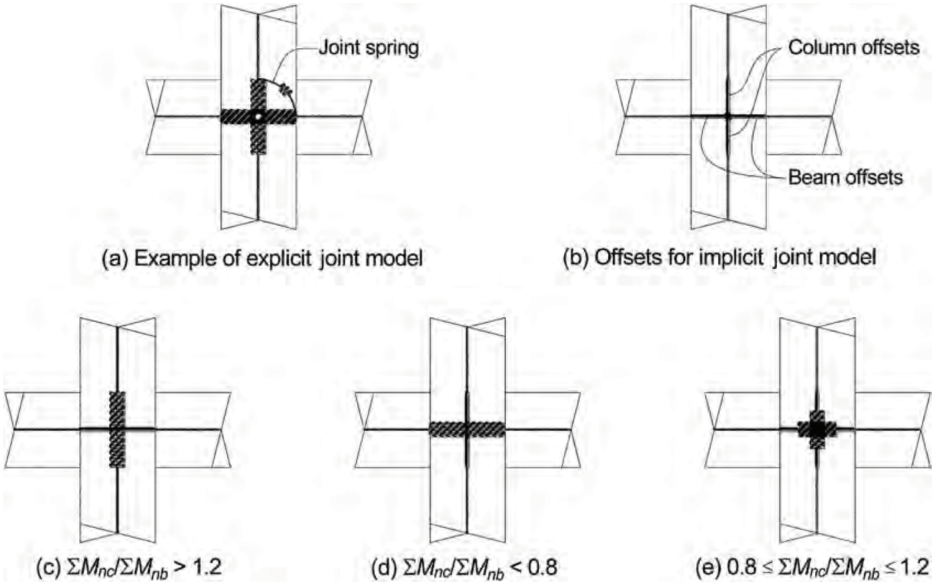
The following is a brief description of the Perform3D modeling approach:

This publication is available free of charge from: https://doi.org/10.6028/NIST.GCR.22-917-50

- Walls are modeled using Shear Wall Elements in Perform3D at all stories. Each Shear Wall Element mesh included distributed nonlinear vertical fibers and a linear shear material. More details on the properties of the fibers and material stress-strain relationships are given in Section 5.3.1. At each story, two elements were used over the story height (Figure 5-41). The shear behavior is modeled to remain elastic using effective shear modulus of $0.2E_{cE}$ (versus $0.4E_{cE}$ per ASCE 41) The out-of-plane behavior was modeled to behave elastically. As will be shown later, because the local deformation and drift demands for the walls were generally less than those sufficient to produce strength loss, material stress-strain relations were not regularized to capture strength loss.
- Frame beams are modeled with Compound Frame Elements in Perform3D, which consist of an elastic frame segment along the beam clear span followed by an inelastic Moment Rotation Hinge and an elastic end zone at the beam-column joints as applicable. The elastic flexural stiffness of $0.3E_{cE}I_g$ was used for all beams, except for beams embedded in the walls, which were modeled with an effective flexural stiffness of 20 times the stiffness of the beams connected to them. The effective slab width calculated per ASCE 41-17 was used in the calculation of the gross moment of inertia and moment capacity of the beams. The modeling parameters and acceptance criteria used to model the backbones of the beams are similar to those used for the OpenSees model. Cyclic degradation behavior of the beams was not modeled in this initial study and is not expected to significantly impact the results obtained given that the beam plastic rotation demands were smaller than parameter *a*.
- Columns are modeled with Compound Frame Elements in Perform3D, which consist of an elastic frame segment along the column clear span, an inelastic P-M-M rotation hinge at each end, and rigid end-zones at the beam-column joints as applicable. Since the gravity axial loads on the columns were smaller than $0.1A_g f'_{cE}$, an elastic flexural stiffness of $0.3E_{cE}I_g$ was used for the columns throughout the building. For the determination of the column nonlinear backbone modeling parameters, the axial load due to seismic effects was estimated as the maximum compression axial load obtained from pushover analysis based on first-mode lateral load distributions.
- Two modeling approaches were used for the beam-column joints: (1) elastic joint (EJ) with linear elastic frame elements for the beam portion in the joint and rigid end zones for the column portion in the joint (see Option c in Figure 5-42a), and (2) nonlinear joint (NJ) modeled using a nonlinear Connection Panel Zone element (Figure 5-42b) available in Perform3D, which was used for the perimeter moment frame joints in the frame direction to explicitly capture the joint nonlinearity. Since the ratio of the summation of the column nominal moment capacities, $\sum M_{nc}$, to the summation of the beam nominal moment capacities,

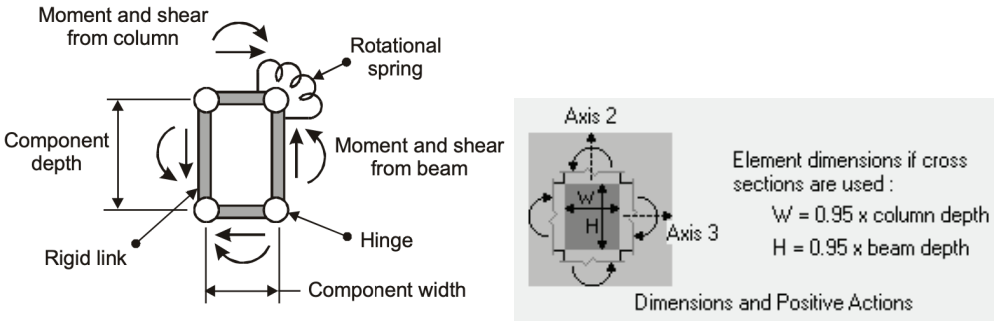
This publication is available free of charge from: https://doi.org/10.6028/NIST.GCR.22-917-50

$\sum M_{nb}$, of each joint was greater than 1.2, Option c in Figure 5-42a is applicable for modeling the joints per ASCE 41-17. The nonlinear modeling parameters and acceptance criteria for the Perform3D NJ model are similar to those used for the OpenSees model. Since moment strengths for the beams framing between the perimeter columns and the wall were considerably less than for beams framing between columns at the perimeter of the building, the joints in the wall direction were modeled as elastic. Additionally, the Connection Panel Zone element in Perform3D is only capable to model 2D joints.



Beam–Column Joint Modeling (Hatched Portions Indicate Rigid Element)

(a) Beam-column joint modeling approaches in ASCE 41-17



(b) Model for panel zone component in Perform3D

Figure 5-42 Modeling approaches used for the beam-column joints.

- Since this study evaluated the test with the fixed base, the base conditions are taken as a fixed restraint (translationally and rotationally restrained) at the columns and wall bases.
- Diaphragms are modeled using rigid diaphragm assumption, which is achieved by slaving nodes at the floor levels. Shell elements representing the slabs are not

This publication is available free of charge from: https://doi.org/10.6028/NIST.GCR.22-917-50

used. The influence of the slab on the stiffness and strength of the beams was considered based on the effective slab width determined per ASCE 41-17.

- The reported gravity loads (Table 5-9) are defined with distributed line loads on beam elements and point load on column per tributary area of each element, as shown in Figure 5-43. No load factors were applied to gravity loads.
- The reported mass of each floor (Table 5-9) is divided based on the tributary area among the 16 nodes at each floor level. Nodes at which masses are applied are located at beam-column and beam-wall boundary element connections.
- Modal damping of 1.5 % combined with Rayleigh damping of 0.75% at anchor points of $0.2T_1$ and $2.0T_1$, resulting in a total of approximately 2.0% damping, was used, where T_1 is the first fundamental period of the building. ASCE 41-17 Section 7.2.3.6 limits damping ratio for nonlinear analysis to 3%; however, 2% is selected since the structure did not include interior partition walls and exterior cladding. This approach is different than the OpenSees model but is consistent with common engineering practice and recommendations.
- The analysis accounted for nonlinear geometry effects (P-delta effects) using a leaning column located at the center of the building versus using the option to include directly for each element.

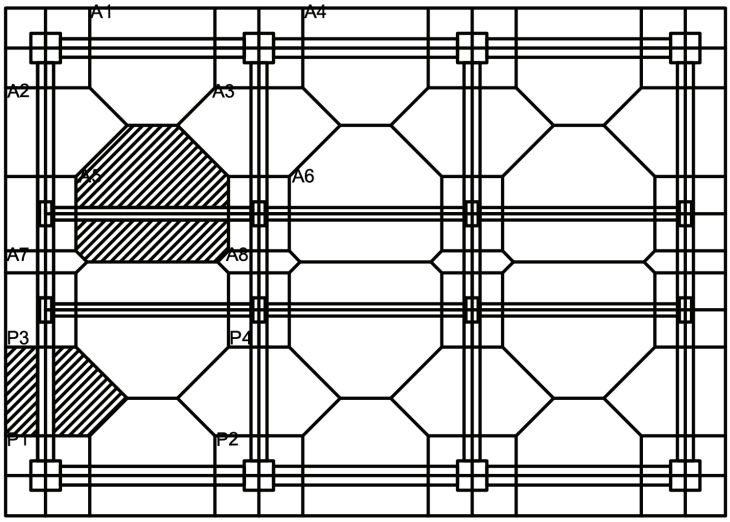


Figure 5-43 Floor tributary area used to calculate gravity loads for each element.

5.4.2 Building Performance: Perform3D EJ vs. Observation

Similar to the OpenSees models, the Perform3D models (model with elastic joints and nonlinear joints) were subjected to X- and Y-components of the 100% JMA-Kobe motion (Figure 5-20). The model periods of the building were 1.07 sec. and 0.82 sec. in the frame and wall directions, respectively, which are significantly larger than the test periods due to the use of effective secant stiffness values (to an

This publication is available free of charge from: https://doi.org/10.6028/NIST.GCR.22-917-50

effective yield point) in ASCE 41-17. As part of a sensitivity study, the effect of the damage from prior motion applied to the building in the experimental program was investigated by running the Perform3D NJ model subjected to X- and Y-components of the 50% and 100% JMA-Kobe motions sequentially (see Section 5.4.4). In the following subsections, the results obtained from the Perform3D model are discussed and compared with the experimental observations.

Base Shear and Roof Drift

The history of the roof drift versus base shear for the test and model with elastic joints (EJ) are shown in Figure 5-44 for the frame and wall directions for the 100% JMA-Kobe motion. Base shear was derived from the test results using acceleration computed at the center of mass of the test structure multiplied by the floor mass at each level, summed over the ten floors. The roof drift ratio is defined as the roof lateral displacement with respect to the foundation divided by the total building height (25.75 m, 84.48 ft.) from the base of the 1st story columns to the roof level. In general, the test and model results do not match well. The model significantly under-predicted the base shear, especially for the wall direction. This could partly be attributed to the low stiffness (0.3*EI*) of the beams framing into the walls in that direction.

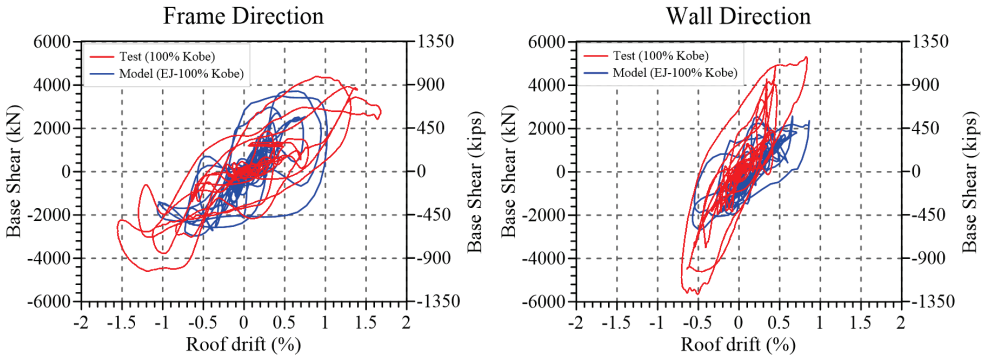
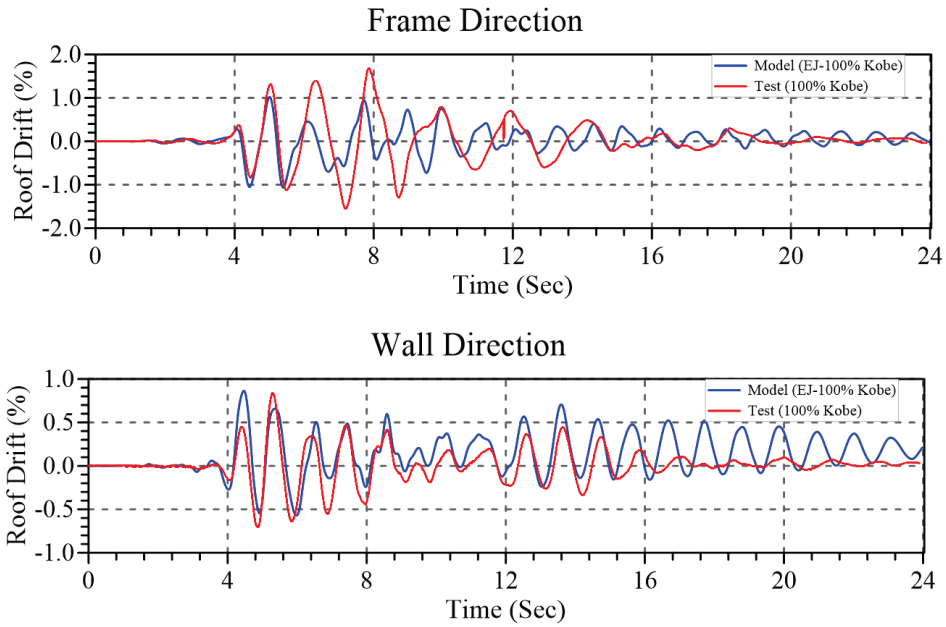


Figure 5-44 NDP Perform3D EJ: Roof drift versus base shear histories for (a) frame direction, and (b) wall direction for 100% JMA-Kobe.

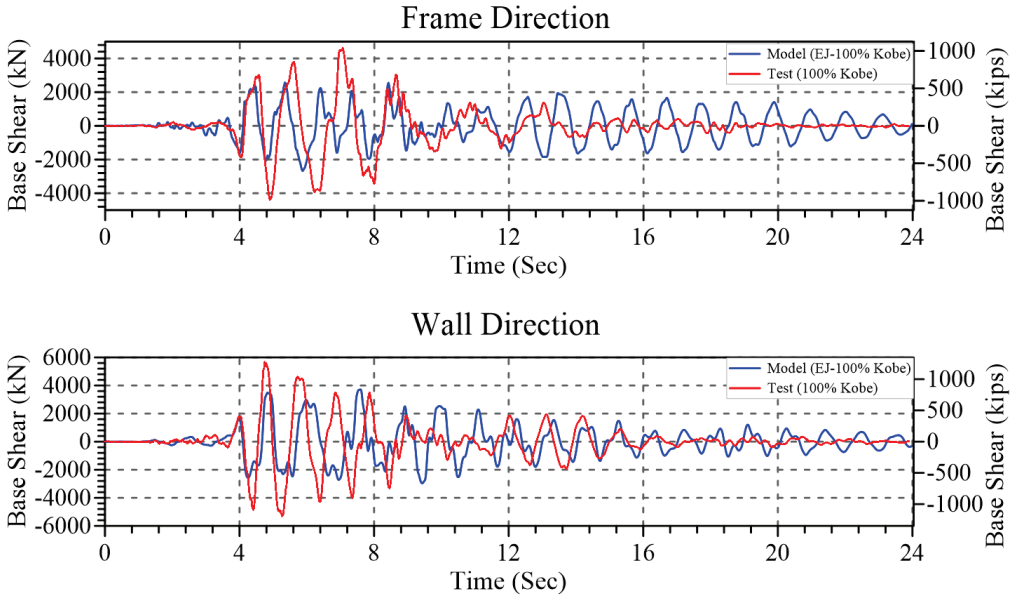
Roof drift and base shear histories are plotted in Figure 5-45 for test and model results. Figure 5-45a shows that the peak roof drift demands are significantly under-predicted for the frame direction, whereas the model results for peak roof drifts match relatively well with the experimental results for the wall direction. Figure 5-45a also indicates that the model shows greater higher mode contributions and higher peak drifts later in the history for the wall direction, possibly due to variations in damping (e.g., foundation level damping). Figure 5-45b shows that the peak base shear demands are significantly underpredicted.

This publication is available free of charge from: https://doi.org/10.6028/NIST.GCR.22-917-50

This publication is available free of charge from: https://doi.org/10.6028/NIST.GCR.22-917-50



(a) Roof drift histories for frame direction (top) and wall direction (bottom).



(b) Base shear histories for frame direction (top) wall direction (bottom).

Figure 5-45 NDP Perform3D EJ: Roof drift and base shear histories for 100% JMA-Kobe.

Peak Story Drift

Distribution of maximum story drifts over the building height are compared between the Perform3D EJ model and the test measurements in Figure 5-46. Results for the wall direction agree quite closely, although test values were slightly higher for the first story and slightly less for roof. Results for the frame direction show significant variation between test and model results. The model results for the frame direction

are generally smaller partly because the model does not capture the nonlinear joint rotations.

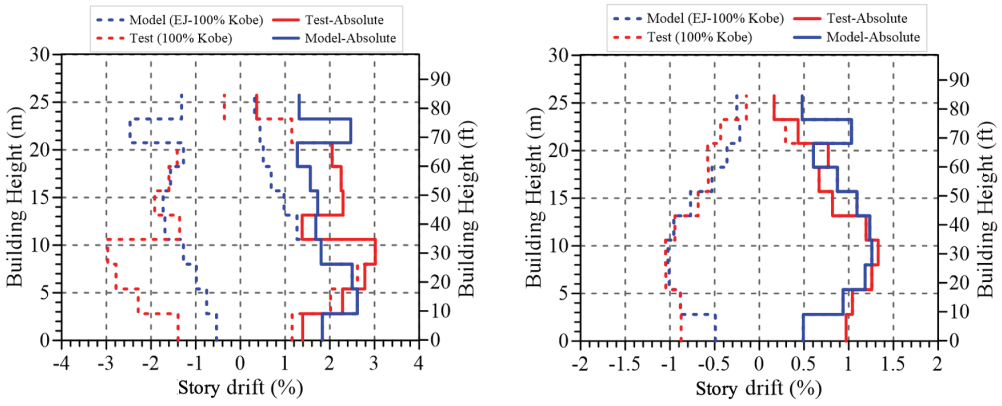


Figure 5-46 NDP Perform3D EJ: Peak story drift ratios for (a) frame direction, and (b) wall direction for 100% JMA-Kobe.

Peak Floor Acceleration

Figure 5-47 compares the peak floor acceleration from the Perform3D EJ model and those measured during the experiment. The results presented in the figure indicate very good agreement (within 5%) in the acceleration profiles for the wall direction up to the 7th story (where the walls are terminated), above which the model underpredicts floor acceleration partly due to significant yielding predicted by the model in the beams and columns at the top three stories, as will be discussed later. For the frame direction, the acceleration profiles of the test measurements and the model are in reasonable agreement for the positive direction, especially at the lower and high stories, whereas the model generally underpredicts acceleration for the negative direction.

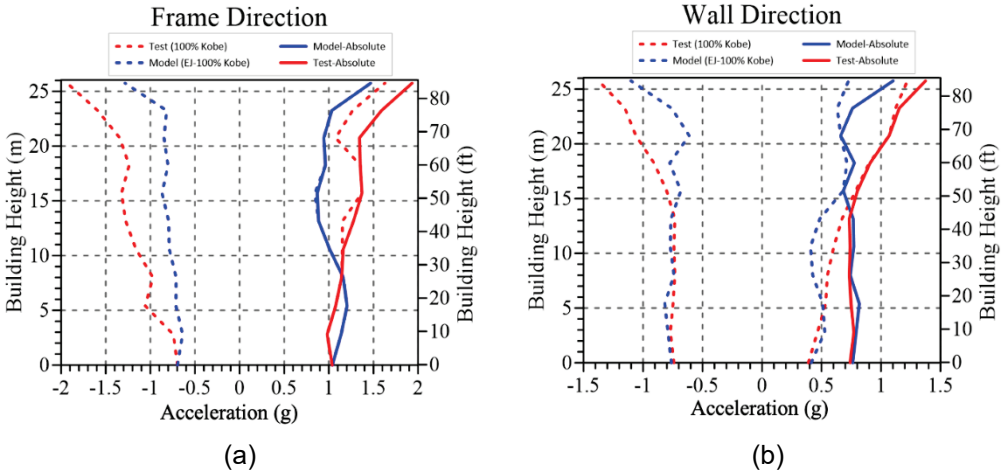


Figure 5-47 NDP Perform3D EJ: Peak floor acceleration for (a) frame direction, and (b) wall direction for 100% JMA-Kobe.

This publication is available free of charge from: https://doi.org/10.6028/NIST.GCR.22-917-50

Global Mechanism and Damage Distribution

Damage distribution data are compared to assess the extent to which the Perform3D EJ model was able to capture the overall building deformation mechanisms and damage distribution. The level of damage from analysis was obtained by comparing the inelastic rotations at ends of beams and columns, $\theta_{inelastic}$, with the ASCE 41-17 modeling parameter *a*, which indicates the beginning of lateral strength loss, and modeling parameter *b*, which indicates the beginning of axial failure. If the computed rotation for a component exceeds the value for parameter *a*, then that component is considered to have sustained severe damage per the analysis; otherwise, it is classified as only having a moderate level of damage.

The ratios of plastic rotations to parameter *a*, as shown in Figure 5-48, and to parameter *b*, as shown in Figure 5-49, indicate that plastic rotations of a number of beams and columns at the 2nd and 3rd floors and at floors where the walls are terminated exceeded parameter *a,* and in some cases parameter *b*, as well. This suggests that severe damage would occur at these locations (beam ends, column ends, or joints), and could lead to collapse. This is consistent with what was observed in the test (Figure 5-25) where severe damage was observed at the 3rd and 4th floors and modest damage was observed at the 2nd and 5th floors. For the Perform3D EJ model, since joints are modeled to remain elastic, the nonlinearity and damage occurs in the beams and columns, unlike the observed experimental damage (Figure 5-25). Unlike the OpenSees models and test results, the Perform3D model predicts damage in columns in the top three stories, which could partly be the relative stiffness values of the beams and columns used for the lumped-plasticity models. The same observations can be made from Figure 5-50, where the plastic rotation demands of the beams and columns are compared with ASCE 41-17 acceptance criteria.

Figure 5-51 shows the wall maximum strain demands at the extreme fibers over the height of the structure (up to 7th floor) for 100% JMA-Kobe for an exterior and interior wall and indicates that the largest tensile strains occur in the first element (half story height) at the base of the walls and are about four times the yield strain of the reinforcement. This figure also shows that the compression strain demands are smaller than yield strain of the reinforcement

This publication is available free of charge from: https://doi.org/10.6028/NIST.GCR.22-917-50

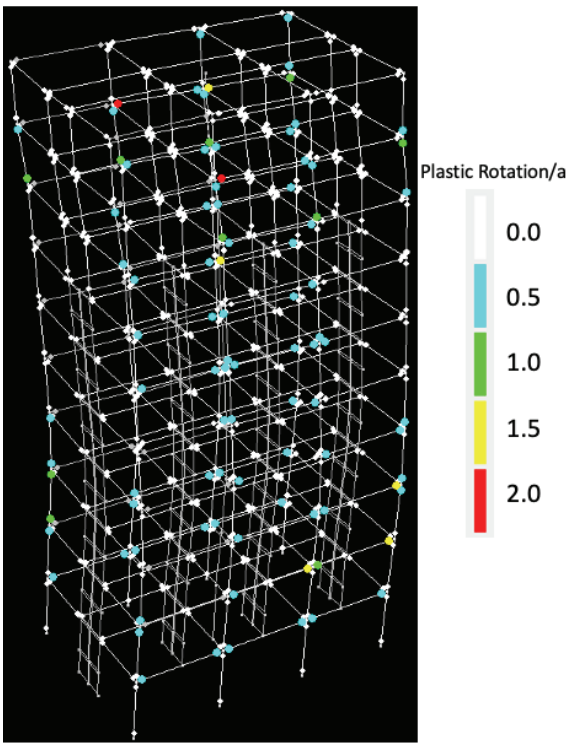


Figure 5-48 NDP Perform3D EJ: Schematic damage distribution in the beams and columns compared to ASCE 41-17 plastic rotation parameter *a* (100% JMA-Kobe).

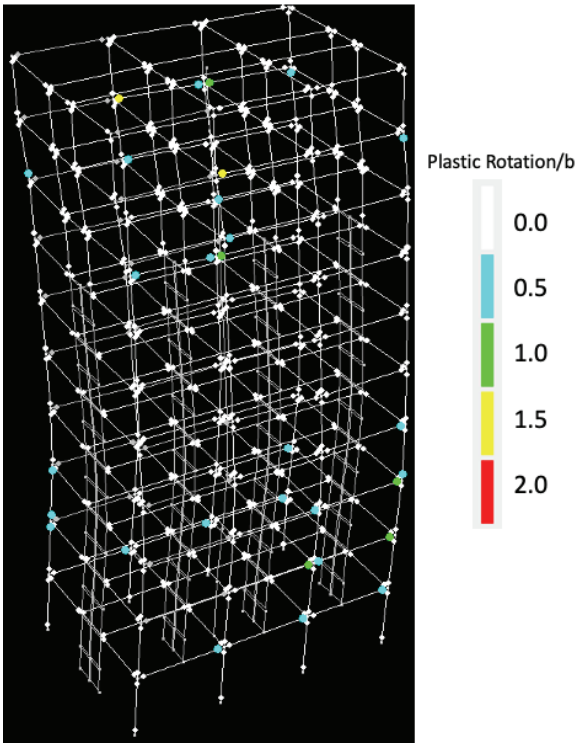
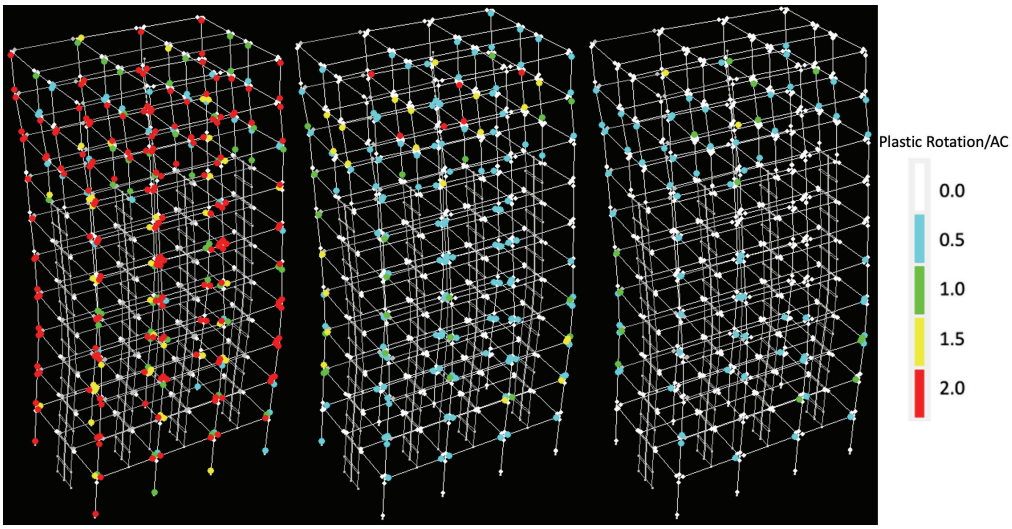


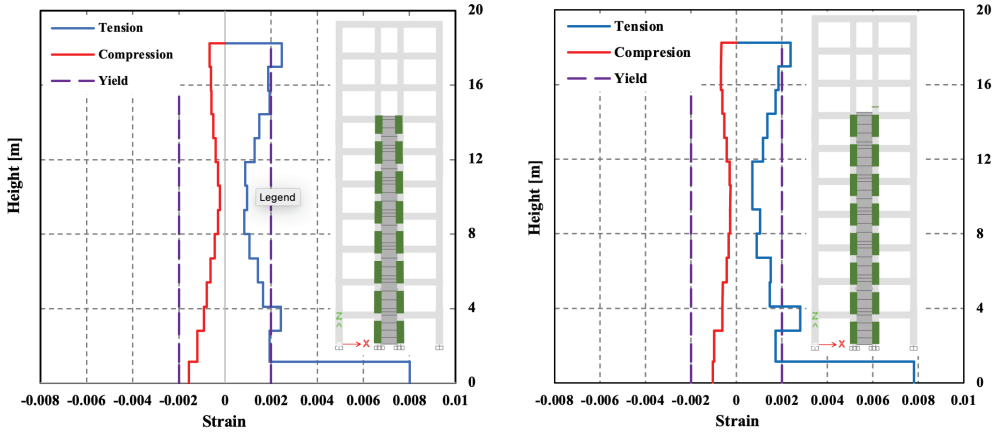
Figure 5-49 NDP Perform3D EJ: Schematic damage distribution in the beams and columns compared to ASCE 41-17 plastic rotation parameter *b* (100% JMA-Kobe).

This publication is available free of charge from: https://doi.org/10.6028/NIST.GCR.22-917-50



(a) Immediate Occupancy (b) Life Safety (c) Collapse Prevention

Figure 5-50 NDP Perform3D EJ: Schematic distribution of the plastic rotation demands in the beams and columns for 100% JMA-Kobe compared to ASCE 41-17 acceptance criteria.

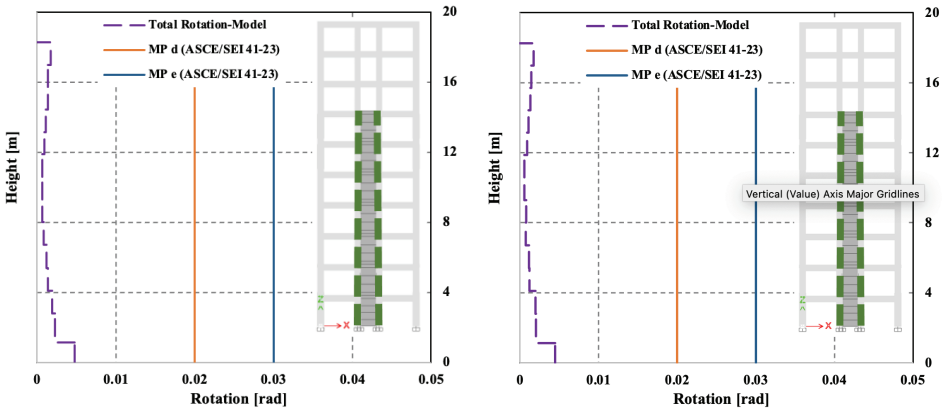


(a) Exterior wall (b) Interior wall

Figure 5-51 NDP Perform3D EJ: Wall maximum strains at the extreme fibers over structure height for 100% JMA-Kobe.

Figure 5-52 shows the total rotation demands of the walls over the height of the structure for 100% JMA-Kobe for an exterior and interior wall and the proposed modeling parameters *d* and *e* (total hinge rotations at lateral strength loss and axial failure, respectively) from ASCE 41-23. For convenience, proposed ASCE 41-23 modeling parameters are used because they are given in total hinge rotations, similar to the model results. This figure indicates that the rotation demands at the critical section of the walls (half story at the base) are only about 1/4 of the ASCE 41-23 modeling parameter at strength loss (parameter *d*). These results of limited strain and rotation demands are consistent with the observed wall damage, which consisted of modest cracking and very limited spalling at the wall boundaries at the base (Figure 5-27).

This publication is available free of charge from: https://doi.org/10.6028/NIST.GCR.22-917-50



(a) Exterior wall (b) Interior wall

Figure 5-52 NDP Perform3D EJ: Wall rotation over structure height for 100% JMA-Kobe compared with ASCE 41-23 modeling parameters.

5.4.3 Building Performance: Perform3D EJ vs. Perform3D NJ

The Perform3D model with elastic beam-column joints, which are not allowed to yield or lose strength (Perform3D EJ model, Figure 5-42a Option c, was modified to model the nonlinear behavior of the joints (Perform3D NJ model, Figure 5-42b). This model was considered to investigate the effects of joint nonlinearity on demands on adjacent members (beams and columns) and the ability of the model to capture the damage observed in the beam-column joints during the test. As noted in Section 5.4.1, only the joints in the frame direction were modeled. Nonlinear backbone of the joints were developed using parameters similar to those used for the OpenSees model.

For the frame direction, the results from the Perform3D NJ model showed limited nonlinearity in only a few interior joints in the 2nd and 3rd floors, as shown in Figure 5-53, unlike the test where significant joint yielding and damage was observed at these floors. All the exterior joints remained elastic. The OpenSees model results indicated more yielding of interior joints, likely due to the higher member stiffness values used compared to the Perform3D NJ model (which led to higher beam and column demands). The wall direction results were essentially identical for this model and for the Perform3D EJ model as joints remained elastic in both cases in that direction. The beam and column rotation demands and damage were almost identical between the two models (Figures 5-54 and 5-55), except for minor reductions at joints at 2nd and 3rd floors where limited joint nonlinearity occurred in the Perform3D NJ model. Since the joints did not significantly unload the beams and columns connecting to them, the results for maximum floor acceleration and drift demands are almost exactly identical between the Perform3D EJ and NJ models, as shown in Figures 5-56 and 5-57. The periods the building in both directions remained the same (1.07 sec. in the frame and 0.82 sec. wall directions).

This publication is available free of charge from: https://doi.org/10.6028/NIST.GCR.22-917-50

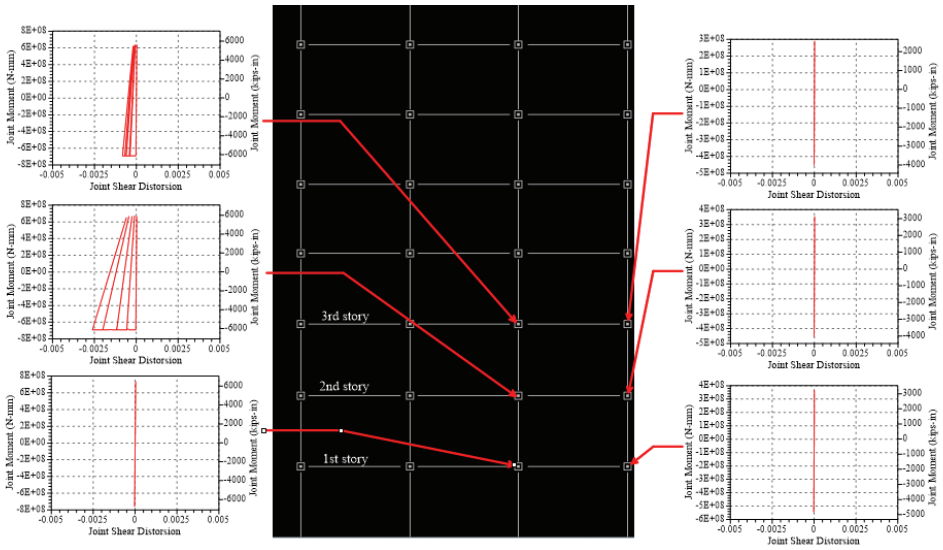
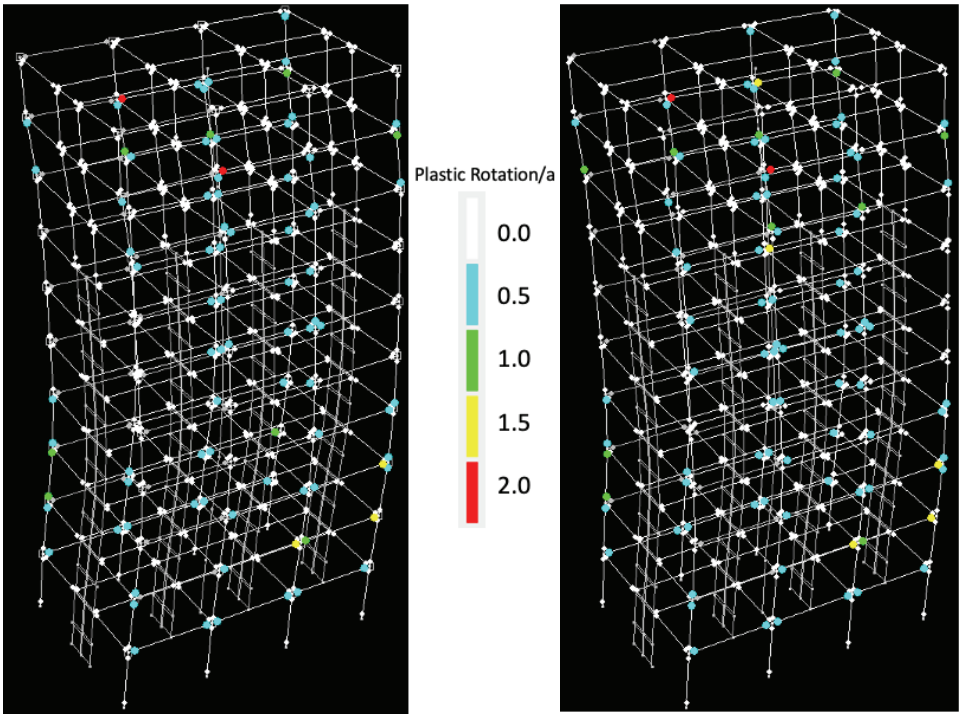


Figure 5-53 NDP Perform3D NJ: Typical hysteretic behavior of the beam-column joints at the 1st, 2nd, and 3rd stories of the building for 100% JMA-Kobe.

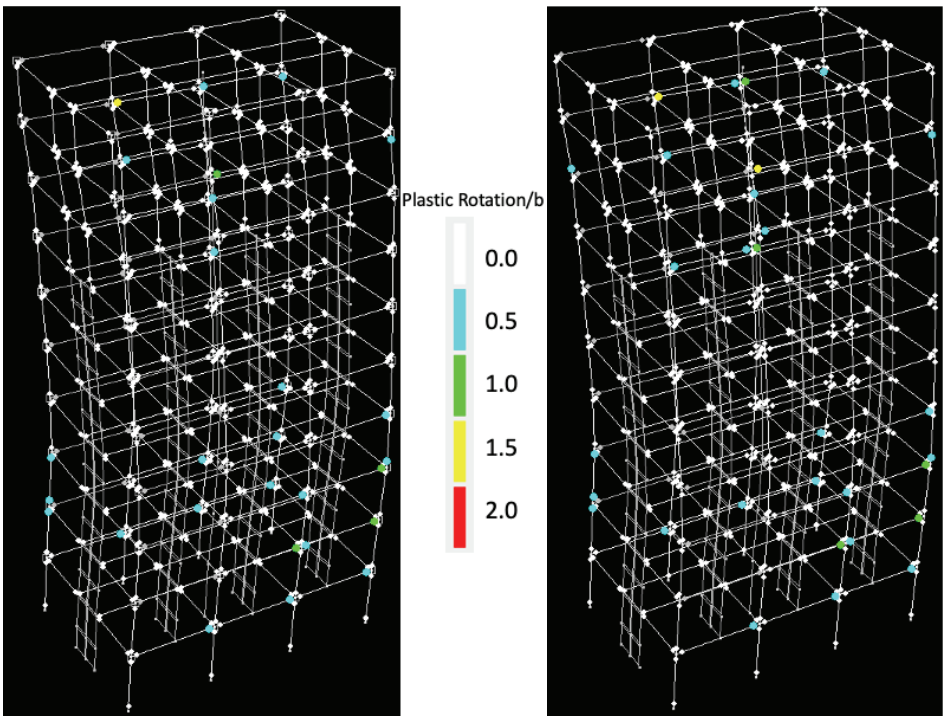


(a) (b)

Figure 5-54 NDP Perform3D: Schematic damage distribution in (a) Perform3D NJ and (b) Perform3D EJ models compared to ASCE 41-17 plastic rotation parameter *a* (100% JMA-Kobe). Note: no difference between the two plots.

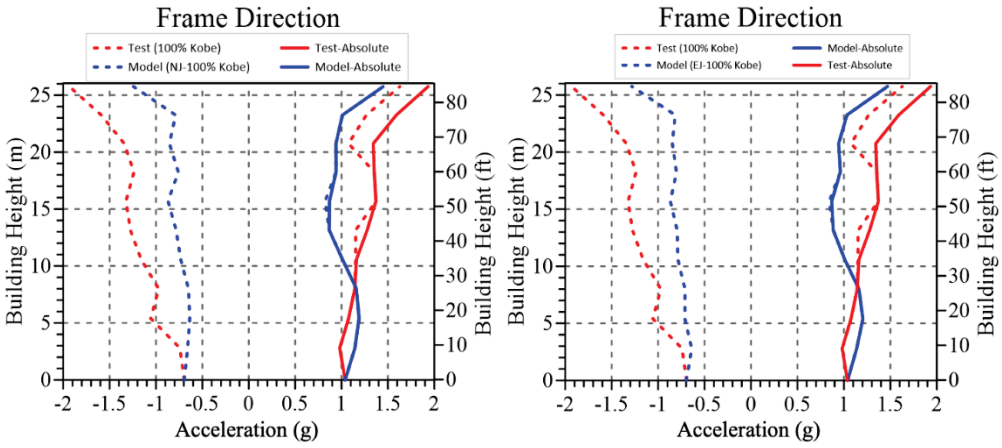
This publication is available free of charge from: https://doi.org/10.6028/NIST.GCR.22-917-50

This publication is available free of charge from: https://doi.org/10.6028/NIST.GCR.22-917-50



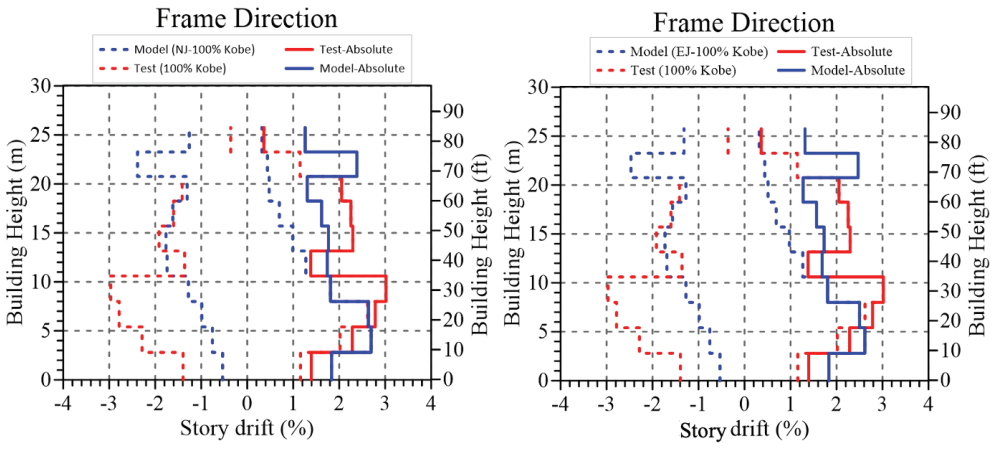
Perform3D Nonlinear Joint Perform3D Elastic Joint

Figure 5-55 NDP Perform3D: Schematic damage distribution in the Perform3D NJ (left) and Perform3D EJ (right) models compared to ASCE 41-17 plastic rotation parameter *b* (100% JMA-Kobe).



(a) (b)

Figure 5-56 NDP Perform3D: Peak floor acceleration for (a) Perform3D NJ and (b) Perform3D NJ models over the height of the building for 100% JMA-Kobe.



(a) (b)

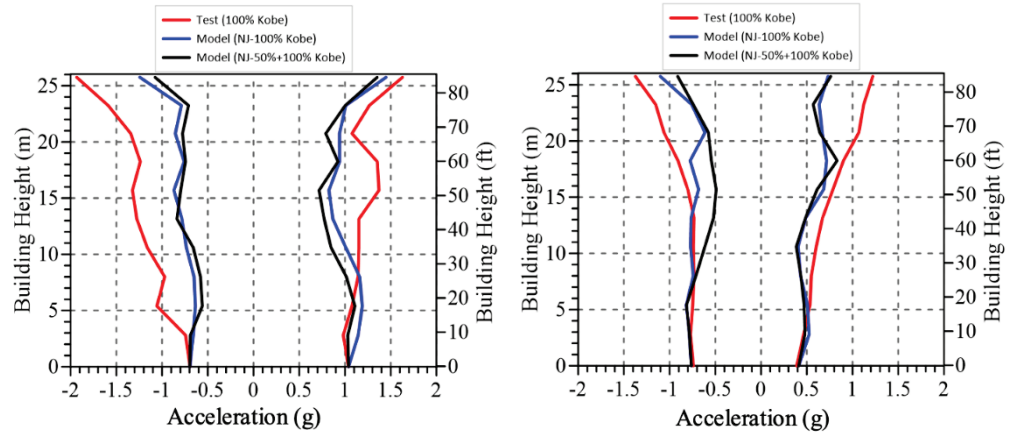
Figure 5-57 NDP Perform3D: Peak story drift ratio comparison for (a) Perform3D NJ and (b) Perform3D EJ models over the height of the building for 100% JMA-Kobe.

5.4.4 Building Performance: Sequential Application of Ground Motions

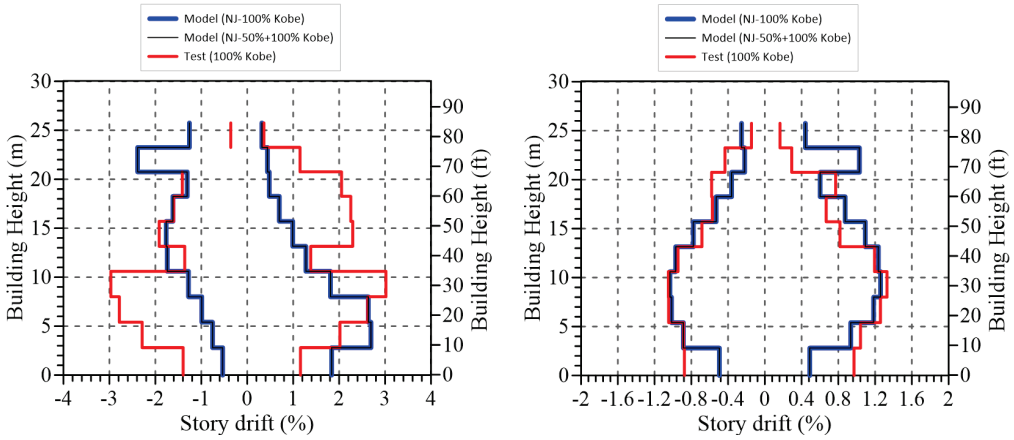
Ground motions for 50% and 100% JMA-Kobe were applied sequentially to the model to assess the potential influence of the repeated motions. Results presented in Figure 5-58a indicate that peak floor accelerations are modestly impacted, whereas Figure 5-58b indicates that peak story drifts are not impacted. Figures 5-59 and 5-60 indicate that the beams and columns of the model subjected to 50% and 100% JMA-Kobe sequentially present more nonlinearity and damage than beams and columns in the model subjected to 100% JMA-Kobe only.

This publication is available free of charge from: https://doi.org/10.6028/NIST.GCR.22-917-50

This publication is available free of charge from: https://doi.org/10.6028/NIST.GCR.22-917-50

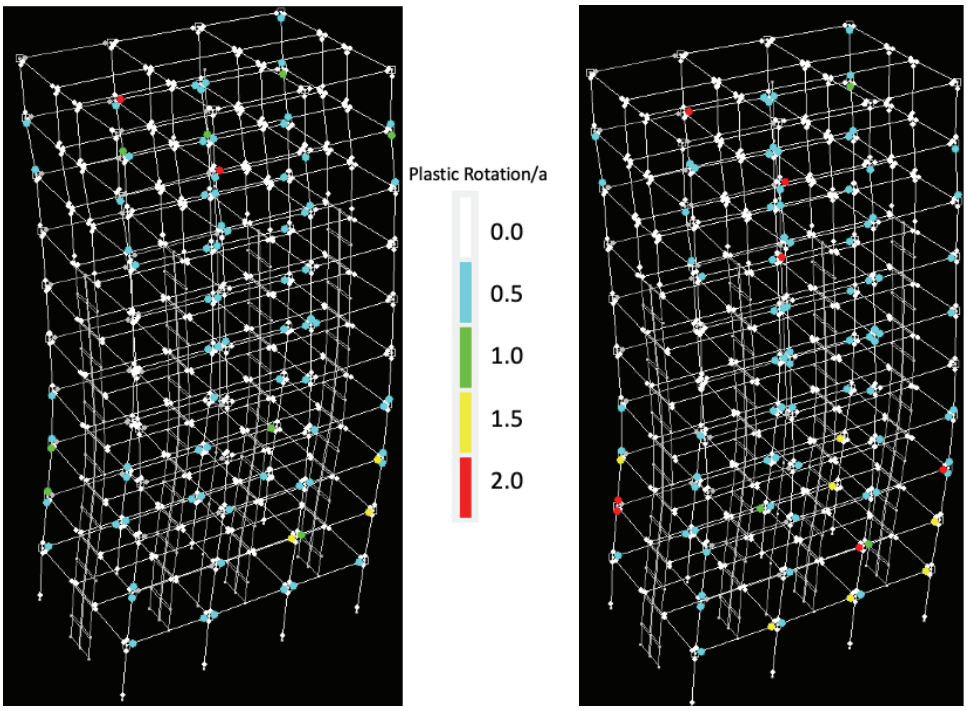


(a) Peak floor acceleration



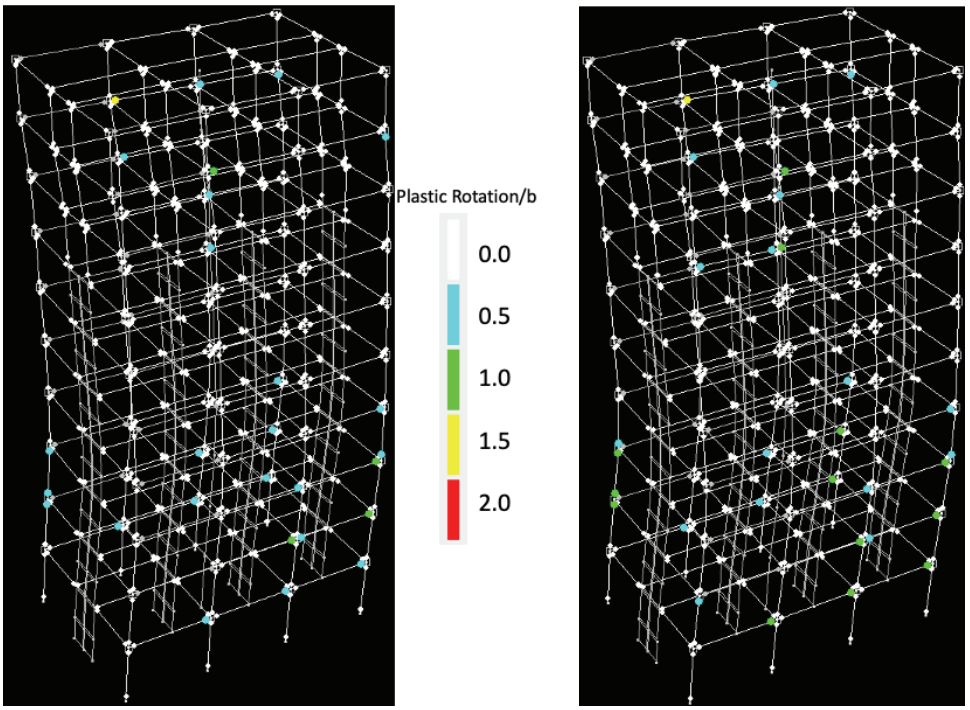
(b) Peak story drift

Figure 5-58 NDP Perform3D NJ: Comparison of peak floor acceleration and peak story drifts due to sequential application of 50% and 100% JMA-Kobe.



(a) 100% JMA-Kobe (b) JMA-Kobe 50%+100%

Figure 5-59 NDP Perform3D NJ: Schematic damage distribution in comparison to ASCE 41-17 plastic rotation parameter *a* far (a) 100% JMA-Kobe and (b) 50% JMA-Kobe and 100% JMA-Kobe.



(a)100% JMA-Kobe (b)JMA-Kobe 50%+100%

Figure 5-60 NDP Perform3D NJ: Schematic damage distribution in comparison to ASCE 41-17 plastic rotation parameter *b* far (a) 100% JMA-Kobe and (b) 50% JMA-Kobe and 100% JMA-Kobe.

This publication is available free of charge from: https://doi.org/10.6028/NIST.GCR.22-917-50

5.5 Comparison of Perform3D and OpenSees Models

ASCE 41-17 allows modeling concrete members using lumped-plasticity models or fiber-section (distributed plasticity elements) models. Furthermore, different software platforms and packages provide different material and element formulations that may influence the analysis results. The effect of such alternative modeling techniques was investigated using the OpenSees and the Perform3D models.

The building initial first mode periods at the beginning from both OpenSees models are 0.67 sec. in the frame direction and 0.43 sec. in the wall direction. Periods from Perform3D are considerably larger than those from OpenSees, with values of 1.07 sec. in the frame direction and 0.82 sec. in the wall direction. This difference is likely due to the reduced beam and column effective stiffness values used for the lumped-plasticity model used for Perform3D versus the fiber (material) modeling approach used for OpenSees and the exclusion of slip/extension springs at the beam-joint interface in the OpenSees model. A more detailed assessment of the beam and column effective stiffness values to determine if using $0.3E_cI_g$ underestimates the cracked stiffness was not conducted for this building, i.e., it is possible to use moment-curvature analysis to determine effective E_cI_{eff}.

Maximum story drift profiles were compared for OpenSees NJ Options 1 and 2 (Figure 5-31) and Perform3D NJ (Figure 5-45 and 5-56). In the frame direction, OpenSees NJ Option 2 provided a very good match of the experimental drift profile, whereas the OpenSees NJ Option 1 using ASCE 41-17 backbone parameters, i.e., with abrupt joint strength loss, matches the experimental drift profile quite well, except at the 2nd and 3rd levels, where drift concentrates due to the rapid strength loss. The OpenSees EJ model (Figure 5-36) predicts a slightly better match between model and measured drift profiles than the OpenSees NJ Option 1 because drift does not concentrate in the 2nd and 3rd levels. Results for the Perform3D EJ and NJ models were not significantly different and both models do not match the experimental profile over the building height well, except for peak story drifts near the base of the building in the frame direction that were reasonably predicted. The various joint models used for the frame direction for both OpenSees (NJ Option 1 and 2, EJ) and Perform3D (EJ, NJ) did not influence peak story drift profiles in the wall direction appreciably. OpenSees results for the frame direction generally matched the measured (test) results very well, slightly underestimating the peak story drifts at lower levels and slightly overestimating the peak story drifts at upper levels. Similar results were observed for the wall models, expect story drifts were overestimated at lower levels and underestimated at upper levels. Sequential application of the 50% and 100% JMA-Kobe motions led to improved predictions at the lower stories. Results from the Perform3D models or the wall direction produced a very good match in peak story drifts over most levels (and particularly levels 2 through 8). It is noted that 1st level story drift is not well predicted for the wall direction, possibly due

This publication is available free of charge from: https://doi.org/10.6028/NIST.GCR.22-917-50

to rotation of the foundation during the test (observed in videos, see Garcia Gomez, 2020), which was not explicitly modeled.

Maximum floor acceleration profiles for all models matched the experimental determined profiles reasonably well, although OpenSees model results (Figures 5-35 and 5-40) tended to overpredict and the Perform3D model results (Figure 5-55 and 5-57) tended to modestly underpredict peak floor accelerations, respectively, at all levels. The higher values for the OpenSees models are likely due to the higher member stiffness values (i.e., lower computed periods). Applying the sequential (50% and 100% JMA-Kobe) motions led to a modest improvement (Figure 5-38) for the OpenSees models but had little impact on the Perform3D model results (Figure 5-57), likely due to the stiffness assumptions. For the OpenSees EJ model, peak floor accelerations were significantly overpredicted at floors 3 and 4, indicating that modeling joint nonlinearity was required to produce improved comparisons.

Roof drift histories for OpenSees NJ Options 1 and 2 (Figure 5-29) and Perform3D (Figure 5-44) generally show that the OpenSees models do a much better job at predicting the experimental results. For both the frame and wall directions, OpenSees models capture the early responses (within the first 8 seconds) quite well, where peak responses occur, but significant differences between model and test results appear later in the response history (after 10 seconds).

Comparisons between test and model base shear response histories for OpenSees (Figure 5-30) indicate observations similar to those noted for roof drift, i.e., early responses and peak values correspond quite well, but results are not as good in the second half of the response history (after 10 seconds). For Perform3D (Figure 5-44), results for the frame model do not match well, with the peak experimental values about twice the model values. Results for the wall direction are slightly better, but still show significant difference.

The maximum base shear comparison from the experiment and all nonlinear models are presented in Table 5-11. In the frame direction, model strengths enveloped the experimental maximum base shear value, with Perform3D less than and OpenSees greater than the value derived from experimental results. When joints were prevented from yielding (EJ model), the base shear in the OpenSees model decreased modestly (0.652/0.679 = 96%), which is still roughly 23% higher than determined for the experiment. Perform3D captured the maximum base shear with reasonable accuracy in the frame direction; however, in the wall direction, the EJ and NJ models underestimated base shear by about 50%.

This publication is available free of charge from: https://doi.org/10.6028/NIST.GCR.22-917-50

Table 5-11 Maximum Base Shear Normalized by Building Weight with Errors between Models and Experiment

	Frame Direction		Wall Direction	
Experiment or Model	*Base Shear/ Building Weight*	*Error = (Exp-Model)/Exp (%)*	*Base Shear/ Building Weight*	*Error (%)*
Experiment	0.529	-	0.652	-
OpenSees NJ Opt. 1	0.679	28	0.760	17
OpenSees NJ Opt. 2	0.670	27	0.760	17
OpenSees EJ	0.652	23	0.706	8
Perform3D NJ	0.450	15	0.329	50
Perform3D EJ	0.452	15	0.326	50

5.6 Fragility Assessment

The section presents the assessment of fragility relationships for various ASCE 41-17 modeling parameters and acceptance criteria. Fragility curves for ASCE 41-17 modeling parameters, acceptance criteria, and building collapse developed for the building are shown in Figures 5-61 through 5-65. Results are obtained using OpenSees NJ Option 2. The curves are based on incremental dynamic analysis (IDA) using 22 earthquake records from the FEMA P-695 (FEMA, 2009) far-field set. Consistent with ASCE 41-17 requirements, all analyses were performed with the two components of the earthquake record applied in both directions of the building. Collapse was defined as the intensity measure in which a story drift ratio of 6% was exceeded at any of the floors, or at the highest intensity measure in which the model reached convergence. For all earthquake records, the building model achieved convergence when story drift ratios exceeded 6%. A second metric used as indicative of collapse was the intensity measure corresponding to the first element to reach an inelastic rotation of 1.5 times parameter *b*, which is assumed to a limit for the valid range of modeling.

Fragility curves that were developed presented in Figure 5-61, where the vertical line in the figure (as well as in Figures 5-62 to 5-65) shows the spectral acceleration at the fundamental period of the building model for the 100 % JMA-Kobe ground motion in relevant building direction ($S_a(T_1)$ Kobe). As it can be observed from Figure 5-61, the probability of exceeding collapse criteria based on local responses (any element exceeds 1.5*b*) or global responses (6.0% drift) is more than 95% at "$S_a(T_1)$ Kobe," where story drift of 6% is slightly liberal measure. Similar conclusions can be made by looking at fragilities for individual structural components (Figures 5-62 to 5-65). This is due to relatively high spectral acceleration at the fundamental period of the building model for the 100 % JMA-Kobe ground motion, which is approximately 1.8g and 2.0g for wall and wall directions, respectively. It should be noted that ground motion spectra for 100 % JMA-Kobe ground motion (Figure 5-4) is

This publication is available free of charge from: https://doi.org/10.6028/NIST.GCR.22-917-50

characterized with high variability around the building fundamental periods (Table 5-8), which could influence the results of the collapse assessment to some extent.

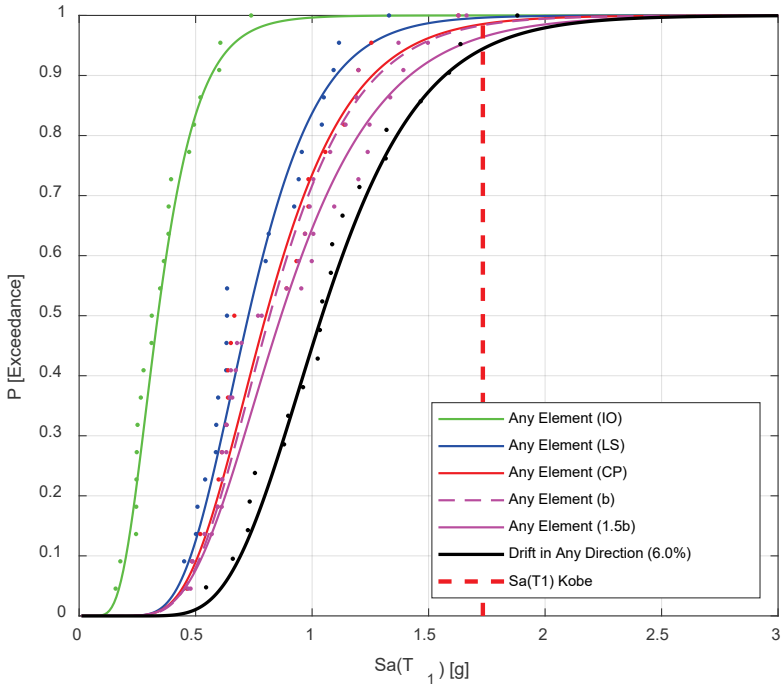


Figure 5-61 Fragility curve corresponding to a first element (any beam, column, beam-column joint, wall) exceeding ASCE 41-17 modeling parameters and acceptance criteria.

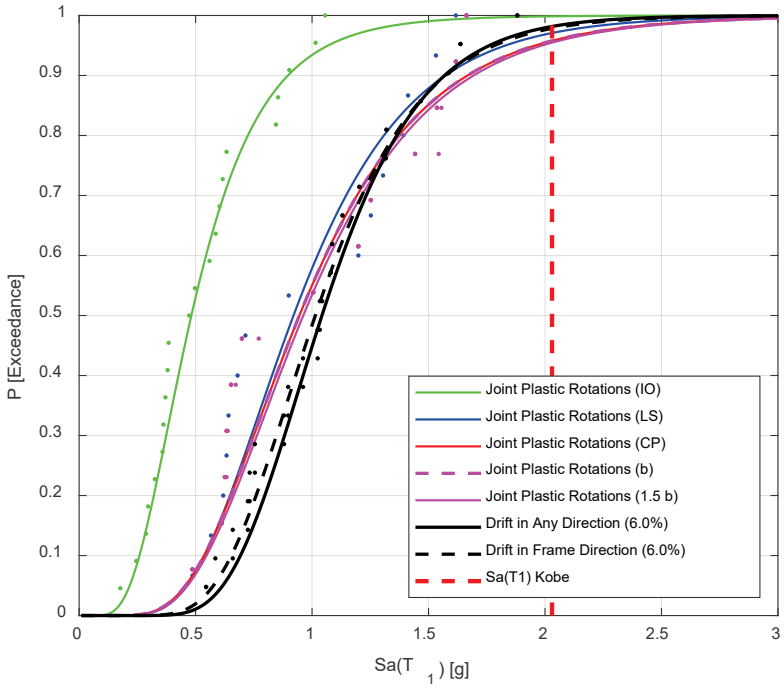


Figure 5-62 Fragility curve for ASCE 41-17 modeling parameters and acceptance criteria for beam-column joints.

This publication is available free of charge from: https://doi.org/10.6028/NIST.GCR.22-917-50

This publication is available free of charge from: https://doi.org/10.6028/NIST.GCR.22-917-50

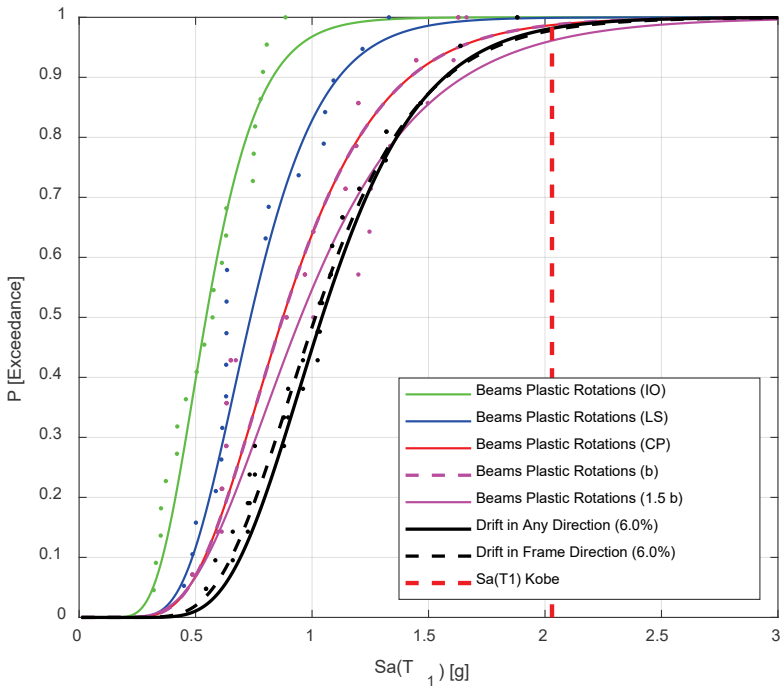


Figure 5-63 Fragility curve for ASCE 41-17 modeling parameters and acceptance criteria for beams.

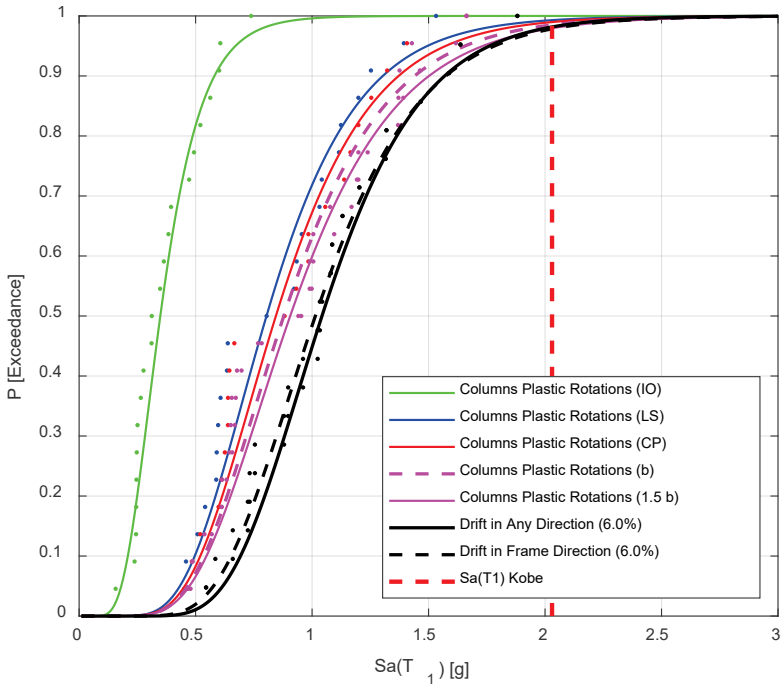


Figure 5-64 Fragility curve for ASCE 41-17 modeling parameters and acceptance criteria for columns.

This publication is available free of charge from: https://doi.org/10.6028/NIST.GCR.22-917-50

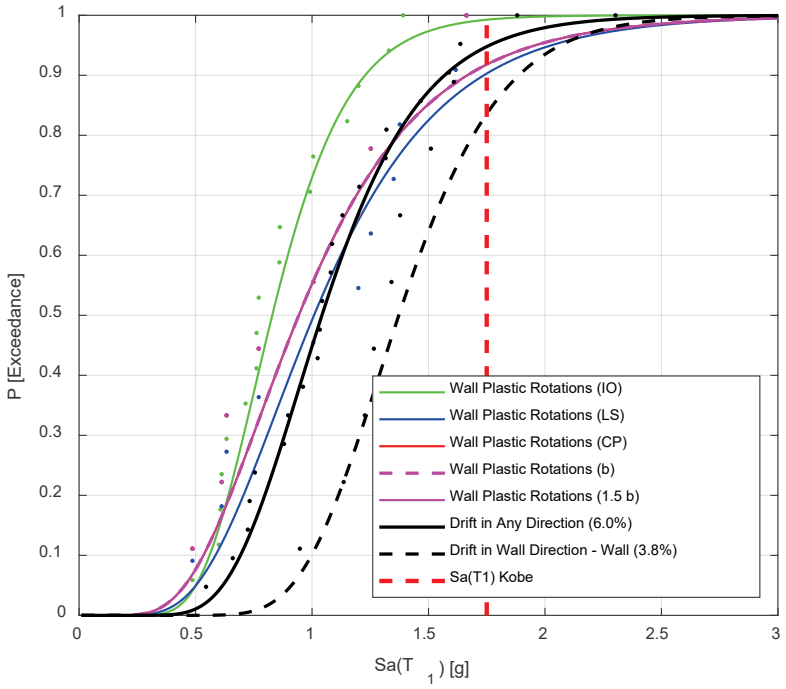


Figure 5-65 Fragility curve for ASCE 41-17 modeling parameters and acceptance criteria for walls.

5.7 Summary

5.7.1 Global Performance

Overall, the ASCE 41-17 nonlinear dynamic procedures were able to reasonably identify the general damage distribution and extent for the frame direction, with the more detailed model approach (OpenSees fiber models) generally providing improved predictions for roof drift and base shear in both the frame and wall directions. Good agreement was observed for roof drift histories (except later in the history) and for peak roof drift. Base shear was not as well predicted, possibly due to variations in the contributions of higher modes and the foundation flexibility.

The distribution of damage between various components in the frames (beams, columns, joints) varied significantly depending on the modeling approach, with better predictions obtained using the more detailed OpenSees models versus the Perform3D models. For OpenSees, modeling nonlinear joint behavior led to improved correlations, especially for joint model Option 2, with more gradual joint strength degradation. For the OpenSees NJ models, damage tended to concentrate within interior joints (more so for Option 1), which led to smaller nonlinear deformations in beams and columns. However, for the OpenSees EJ model, nonlinear deformations tended to concentrate in the columns. Due to various factors, e.g., higher modes, nonlinear responses, and analysis assumptions, joint yielding may occur in cases where a mechanism analysis indicates joint yielding is not expected.

For the wall direction, the damage location and severity at the base of the walls was captured well by nonlinear models constructed to ASCE 41-17 specifications. However, the plastic rotation demands imposed on the walls were fairly modest, only reaching from 25 to 50% of the ASCE 41-17 modeling parameter *a* (strength loss). Therefore, the light damage observed (very minor concrete spalling at extreme edge of wall) appears consistent with the computed demands.

This study highlights the effects of having modeling parameters with varying degrees of conservatism (or accuracy) in ASCE 41-17. In general, all models for the wall direction produced acceptable results for roof drift, story drifts, and floor acceleration, likely due to the simplicity of the structural system (lightly coupled, cantilever walls) and the limited nonlinear demands.

In the frame direction, modeling of nonlinear joint behavior was important to produce improved comparisons between test and model results, as nonlinear joint responses relieved deformation demands on the beams and columns. The EJ models prevented joints from yielding and degrading (stiffness and strength), resulting in higher demands (damage) on adjacent beams and columns. Each of these scenarios would therefore result in different retrofit outcomes for the building and highlight the importance to ensure that ASCE 41 nonlinear modeling parameters for all elements target consistent mean estimates from experimental data, such that building response is not artificially skewed.

Because the test structure was subjected to many different intensity runs, comparisons of test and model periods are somewhat complicated. For the OpenSees models, initial periods (initial tangent) are 0.67 sec. and 0.43 sec. for the frame and wall directions, respectively, whereas test structure periods were 0.57 s for both the frame and wall directions. However, prior to running the 100% JMA-Kobe motion test, test structure periods were determined from White Noise tests (low amplitude vibrations) to be 1.24 sec. and 0.74 sec., which are reasonably close to the Perform3D periods of 1.07 sec. and 0.82 sec. ASCE 41-17 stipulates that all the members in buildings should be modeled using stiffness values corresponding to secant to yield. In the test building, not all members reach yield level demands, particularly at higher floor levels and the test building was subjected to prior motions that induced cracking and stiffness reductions. Similar issues exist for real buildings. In this study, peak roof level and story drifts were reasonably well predicted with model results, although results for the more sophisticated OpenSees models generally produced closer predictions to the measured results, suggesting that using stiffness values that vary with demand level (i.e., fiber models) and with prior events is likely to yield more accurate comparisons. Additional studies that address this issue and whether the costs associated with the added model complexity and computer run time are worth these added costs might be useful.

This publication is available free of charge from: https://doi.org/10.6028/NIST.GCR.22-917-50

5.7.2 Component Performance

Columns modeling parameters have been updated twice since FEMA 273 (FEMA, 1997; Elwood et al., 2007; Ghannoum and Matamoros, 2014; Ghannoum, 2017), and in the process were modified to increase deformations for parameters *a* and *b* parameters substantially to reach mean estimates of experimental data. Beam modeling parameters and acceptance criteria have not undergone any significant change since FEMA 273 and are substantially lower than column values given similar detailing, although recent changes have been proposed to address this issue. These differences in conservatism in modeling parameters could skew the damage outcomes per ASCE 41-17, whereby more severe damage could be predicted in beams than the columns. This potential inconsistency was not observed in this study, except for the EJ models, because damage tended to be concentrated in joints.

Results for the NJ models highlighted the importance of modeling nonlinear joint behavior, with results for the OpenSees model for ASCE 41-17 indicating damage would concentrate within the interior joints as observed in the tests. However, results for the Perform3D model showed less concentration of damage, possibly due to the relative values used for effective stiffness values for beams and columns, again suggesting the importance of considering the importance of demand level on variation of stiffness modeling parameters. The results from the OpenSees models suggested that the beam-column joint modeling parameters in ASCE 41-17 for nonlinear dynamic procedures likely over-estimate the rate of strength loss with increasing demands. A review and update of the joint shear strength and nonlinear modeling parameters and acceptance criteria in ASCE 41-17 may be justified for future study.

The damage at the base of the walls during the experiment was relatively minor and was consistent with the analysis results from both OpenSees and Perform3D. As was noted for the frame direction, results for the more sophisticated models (OpenSees) were modestly better than obtained with the Perform3D model, likely due to the variation in stiffness modeling parameters with demand level for the walls and beams, and possibly to a less extent, for the columns.

5.7.3 Analytical Study Takeaways

For this building, the analyses indicate important needs to improve modeling capabilities. These include modeling strategies to capture joint behavior and the need to base modeling parameters for all elements to their mean estimates based on experimental data such that model response and damage distributions are not artificially skewed.

This publication is available free of charge from: https://doi.org/10.6028/NIST.GCR.22-917-50

5.7.4 Study Limitations

These conclusions must be considered in the context of several limitations:

- Model results were obtained for the 100% JMA-Kobe record, whereas the test building was subjected to a large number of runs, including base sliding tests, that induced various levels of cracking and slight damage (yielding) in some elements. A simple sensitivity study based on subjecting the model to the 50% and 100% JMA-Kobe records suggests that responses (drift, acceleration, rotation) were not overly sensitive to the prior demands. More detailed studies to further investigate this for test buildings and for instrumented buildings with responses measured in multiple events would be useful.
- Slip/extension springs were not included at the beam-joint and column-joint interfaces for the OpenSees models. Inclusion of these springs would reduce the frame stiffness slightly; however, overall findings are unlikely to be sensitive this modeling parameter.
- Cyclic modeling parameters for the beams for the Perform3D model did not include cyclic degradation. Since beam nonlinear demands were relatively modest, overall findings are unlikely to be sensitive to this assumption.
- The influence of bi-axial shear demands on column and joint modeling parameters was not considered. Any update of column and joint modeling parameters and acceptance criteria should include an assessment of bi-axial demands if sufficient data are available.
- The demands imposed on the wall direction of the test building were insufficient to study issues related to modeling strength loss. However, there have been other studies where wall strength loss has been observed (e.g., 4-story 2010 E-Defense tests).

This publication is available free of charge from: https://doi.org/10.6028/NIST.GCR.22-917-50

Chapter 6

Six-story Frame and Wall Building in California

This publication is available free of charge from: https://doi.org/10.6028/NIST.GCR.22-917-50

6.1 Overview

This chapter presents benchmarking studies for a 6-story reinforced concrete frame and wall building in Imperial County, California, shown in Figure 6-1. The building, was constructed in 1971 to serve as the Imperial County Services Building, damaged in the 1979 Imperial County Earthquake, and subsequently demolished. The building was instrumented with 13 accelerometers and calculated performance metrics are compared with observed damage for strong motion records from the 1979 Imperial County Earthquake.



Figure 6-1 Photograph of Imperial County Services Building in Imperial County, California (ATC, 1984).

The building was evaluated in accordance with the linear and nonlinear dynamic procedures of ASCE 41-17 using OpenSees software considering three cases: model with fixed-base structure with only the horizontal components of the ground motion, model with fixed-base structure with horizontal and vertical components of the ground motions, and model with springs representing pile foundation flexibility. The

models were constructed per details presented in Appendix A, unless otherwise noted.

This chapter also provides results of a fragility analysis showing the collapse potential of the as-modeled building, as compared to the likelihood of exceeding ASCE 41-17 acceptance criteria. Results from an evaluation in accordance with the acceptance criteria of Eurocode 8 (European Committee for Standardisation, 2005) are also presented.

6.2 Building Description and Observed Performance

6.2.1 Building Description

The study building was a six-story reinforced concrete frame and shear wall structure, shown in Figures 6-1 through 6-3. Shear walls are discontinuous and are present in the north-south direction on the exterior of the building at stories two and above, and in the interior of the building at the first story (see Figure 6-3). The layout of the shear walls at the first story is not symmetric in plan. The exterior upper level shear walls rest on cantilevered beams approximately 71 in. from the column line. First-story walls are 12 in. thick; upper-story walls are 7.5 in thick in the second story and 7 in. thick elsewhere. Typical wall reinforcement consists of two curtains of #4 bars spaced at 16 in. vertically and 12 in. horizontally on the first-story walls, and a single curtain of #4 bars spaced at 16 in. vertically and #5 bars spaced at 12 in. horizontally at upper levels.

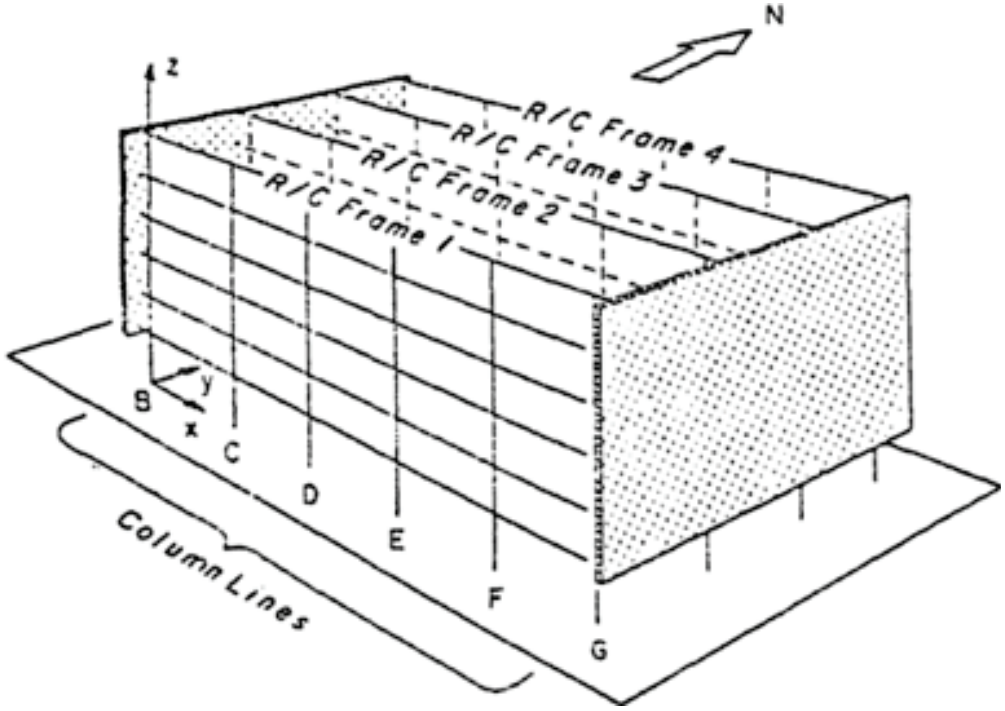


Figure 6-2 Schematic illustration of study building (Pardoen et al., 1979).

This publication is available free of charge from: https://doi.org/10.6028/NIST.GCR.22-917-50

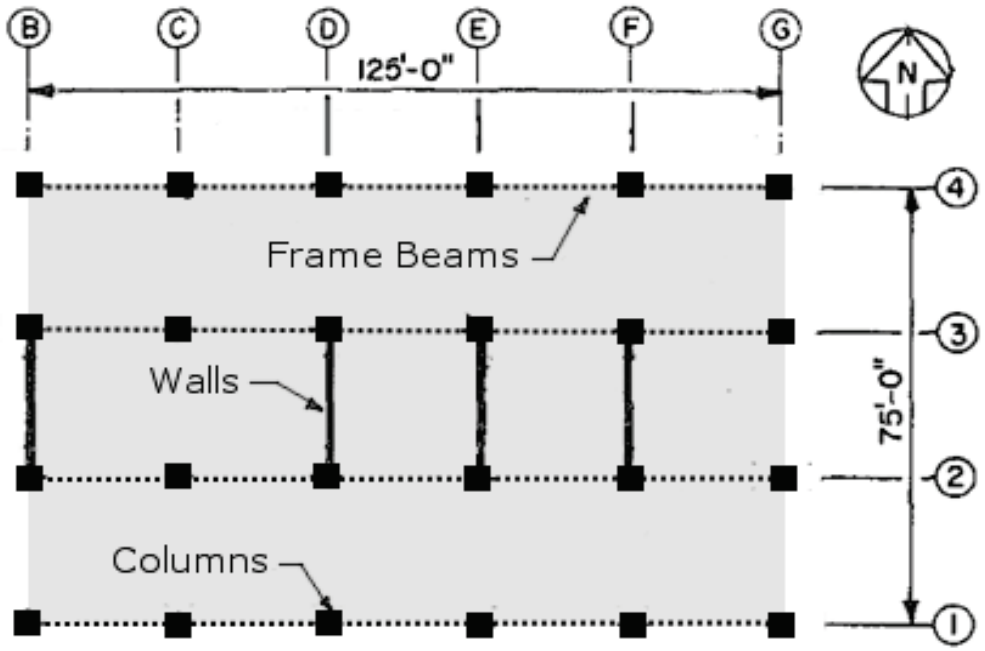


Figure 6-3 Plan view of study building, showing location of first-story walls (modified from Kreger and Sozen, 1990).

Columns generally have detailing similar to a modern intermediate moment frame, with transverse ties spaced at 2-3 inches in the hinge regions. However, at the base of the first-story columns, a slab-on-ground connects to the designed plastic hinge region; above this region, transverse reinforcement spacing is 12 inches (Figure 6-4).

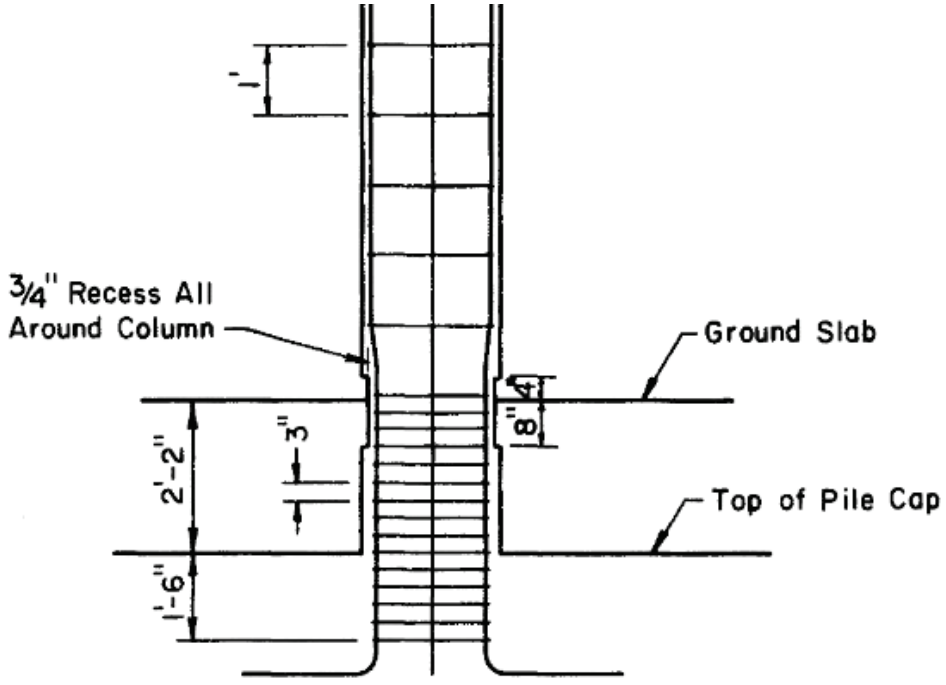


Figure 6-4 Details of typical first-story column base connections into the pile cap (Kreger and Sozen, 1990). First-story columns have 24 in. by 24 in cross-section.

This publication is available free of charge from: https://doi.org/10.6028/NIST.GCR.22-917-50

All first-story columns have 24 in. by 24 in. cross-sections except in the plastic hinge region at the base on the columns. The column cross-section is recessed by ¾ in. on all sides where the slab-on-ground meets the column. Above the first story, columns on east-west frame lines 1 and 4 reduce to 10 in. deep, with 54 in. wide tapered sections extruding orthogonal to the frame line to support a sunscreen system. Columns on the east-west frame lines 2 and 3 are 24 in. by 24 in. for the entire height of the building. Beams are present only in the east-west direction. The floor slab at a typical floor level has a depth of 3 inches supported by a pan-joist system in the north-south direction. The floor slab at the second floor is 5 inches thick to support the transfer of lateral loads from discontinuous walls. The foundations are pile caps on 45 ft. tapered piles connected by grade beams. Typical design concrete strengths are 3 ksi for foundations, 4 ksi for beams, 4 ksi for walls, and 5 ksi for columns. Steel reinforcement is 40 ksi everywhere.

6.2.2 Building Instrumentation

The building was instrumented by the California Strong Motion Instrumentation Program, with a 13-channel array of accelerometers at various locations throughout the structure, and in the free field. A diagram of instrumentation is provided in Figure 6-5. Displacement response is calculated from accelerometer response by double integration; this approach cannot capture any permanent displacements.

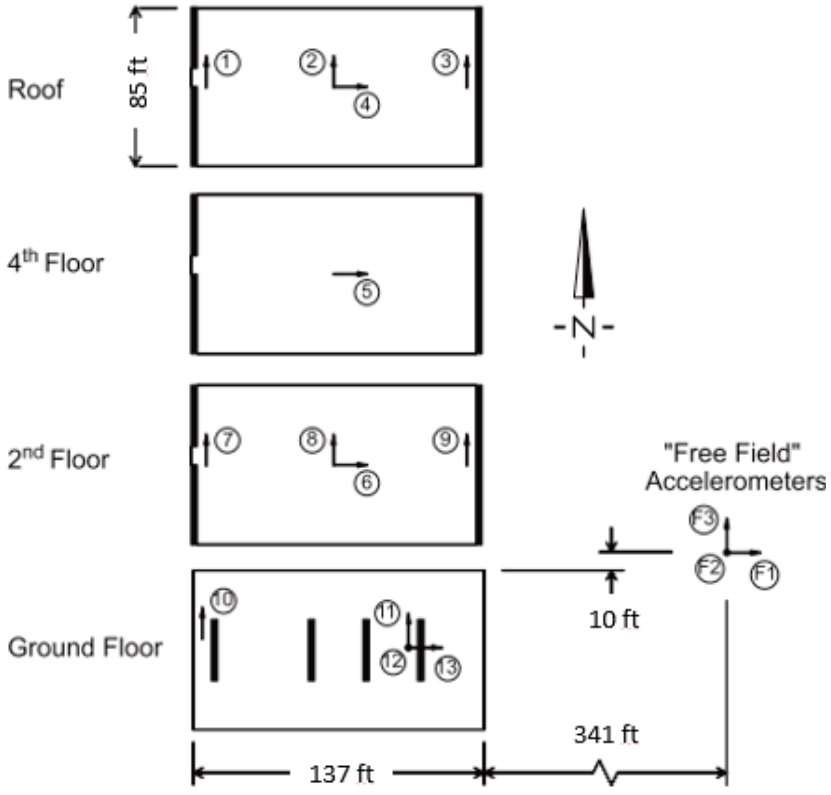


Figure 6-5 Diagram of instrumentation of study building (Todorovska and Trifunac, 2007).

This publication is available free of charge from: https://doi.org/10.6028/NIST.GCR.22-917-50

Based on this instrumentation, the ambient period of the building before the earthquake was estimated to be 0.67 seconds in the east-west frame direction, and 0.44 seconds in the north-south wall-frame direction (Pardoen and Shepherd, n.d.). The total weight of the building is 13,400 kips (ATC, 1984).

6.2.3 Ground Motion

The ground motion recorded at the foundation during the 1979 Imperial County Earthquake had a peak ground acceleration (PGA) of 0.33g in the east-west direction and 0.29g in the north-south direction. The response spectra in Figure 6-6 show significant energy in the range of 0.3 to 1.5 seconds. The vertical component of the ground motion has substantially smaller accelerations, except at periods smaller than 0.3 seconds. In the free field, the ground motion has PGA values of 0.24g and 0.21g in the east-west and north-south directions, respectively. The motion recorded at the foundation is used for all analyses, except in the model that considers foundation flexibility that uses free field recordings (Section 6.5).

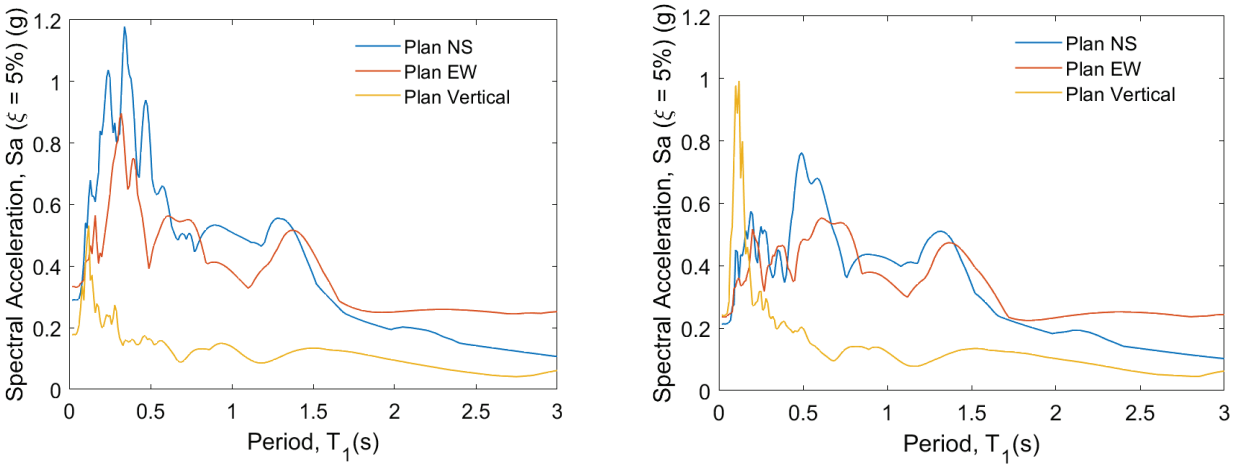


Figure 6-6 Recorded response spectra, calculated with 5% of critical damping: (a) at the foundation and (b) in the free field.

6.2.4 Observed Performance

A number of reports documented damage to this building (e.g., Pauschke, 1981; ATC, 1984; Kreger and Sozen, 1983). The building sustained significant damage to the first-story columns, especially on the eastern-most frame line, as shown in Figures 6-7 and 6-8. This eastern column line had shear failures followed by axial crushing above the ground slab where spacing transverse reinforcement was wider. Interior columns' damage in the first story consisted of shear cracks primarily associated with response in the east-west direction. First-story walls showed some shear (inclined) cracking. Damage concentration in the east column frame line was

This publication is available free of charge from: https://doi.org/10.6028/NIST.GCR.22-917-50

attributed to high axial loads from cantilevered walls above that level, as well as torsion due to asymmetric north-south wall layouts on the first story.

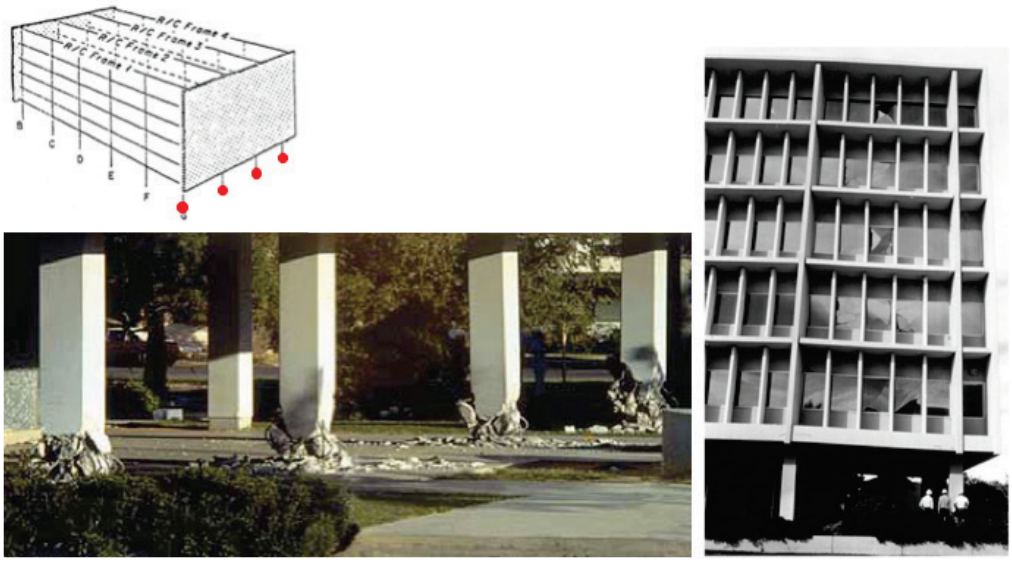


Figure 6-7 Damage to building (Faison et al., n.d.).

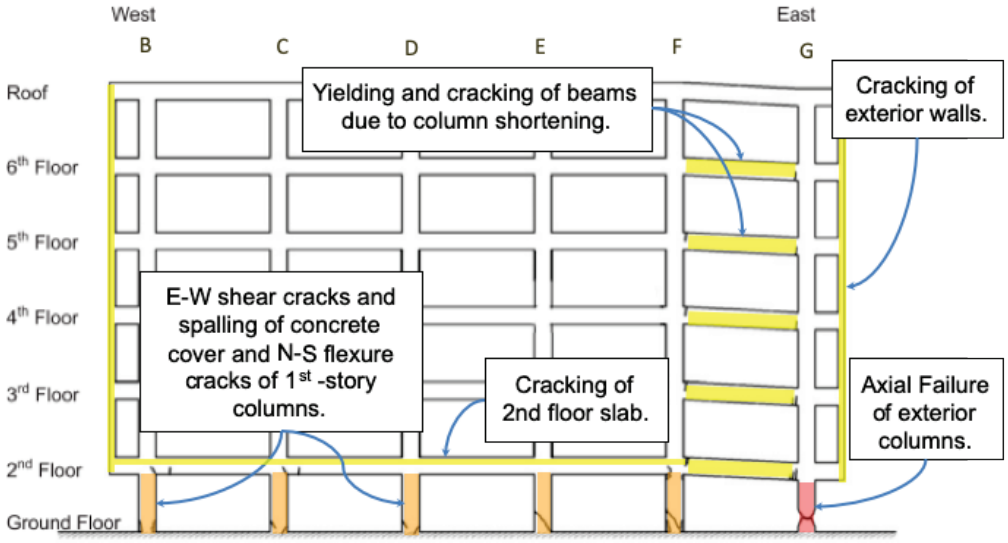


Figure 6-8 Elevation view of damage to building (annotation by authors; diagram from Todorovska and Trifunac, 2007).

6.3 Nonlinear Dynamic Procedure

6.3.1 Modeling Approach

A three-dimensional numerical model of the structure was created in OpenSees with fixed base. Concrete floor diaphragms (slab with pan joists) were modeled as rigid, justified by the static deformation check according to ASCE 41-17 Equation 7-21. Column models used rotational springs with properties defined by ASCE 41-17 and described in Section A2.2.1 in Appendix A. Axial loads used to calculate column

This publication is available free of charge from: https://doi.org/10.6028/NIST.GCR.22-917-50

and wall strength and nonlinear deformation capacities were obtained as the maximum axial demands developed in each element from a limit-state analysis (Section A3.2). Accordingly, the nonlinear model was pushed separately in each orthogonal direction to 1.5% roof drift. At this roof drift, the lateral strength in the east-west direction was 74% of peak capacity, and the lateral strength in the north-south direction was 2% of peak capacity. First-story columns were shear critical at their base and flexure controlled at the top; the rest of the columns in the building were flexure controlled. The hinge properties for the base of the first-story columns were based on reinforcement above the slab-on-ground.

In their in-plane (north-south) direction, walls were modeled as line elements with shear springs according to the ASCE 41-17 modeling criteria (Section A.5). Walls were also modeled nonlinearly in their out-of-plane (east-west) direction to account for the demands from large drifts in the first story. The nonlinear behavior of the moment frame joints was modeled using elastic beam column elements connected by a nonlinear rotational hinge (Section A.4).

Nonlinear joint properties were defined based on ASCE 41-17 Section 10.4.2. Joint stiffness was modeled implicitly according to ASCE 41-17 Section 10.4.2.2.1, which defines offsets and portions of the joint as rigid depending on the column to beam strength ratios at each joint. The analysis accounted for large geometry effects using the P-delta transformation.

As modeled, the structure has a period of 1.15 seconds in the east-west frame direction, and 0.29 seconds in the north-south wall-frame direction. In the east-west direction, the model is substantially more flexible than indicated by the ambient periods (Section 6.2), due to ASCE 41-17 stiffness assumptions. In the north-south direction, the stiffness is impacted by the foundation response, as explored in Section 6.5. The analysis employed 3% Rayleigh damping anchored at the fundamental periods of the building in the east-west and north-south directions.

6.3.2 Global Performance: Model vs. Observation

Figure 6-9 compares the acceleration and displacement profiles between the recordings and the simulation in both the east-west and north-south directions. In the east-west direction, accelerations show good agreement (difference less than 12 %) over the height of the building, except at the second floor where there is a 33% overestimation of the accelerations. Figure 6-10 demonstrates that the acceleration response history and frequency content at the roof also agree well. Displacement estimates for the first floor east-west (EW) direction show good agreement (difference less than 15 %), with the roof displacement slightly underestimated and the first story displacement slightly overestimated.

This publication is available free of charge from: https://doi.org/10.6028/NIST.GCR.22-917-50

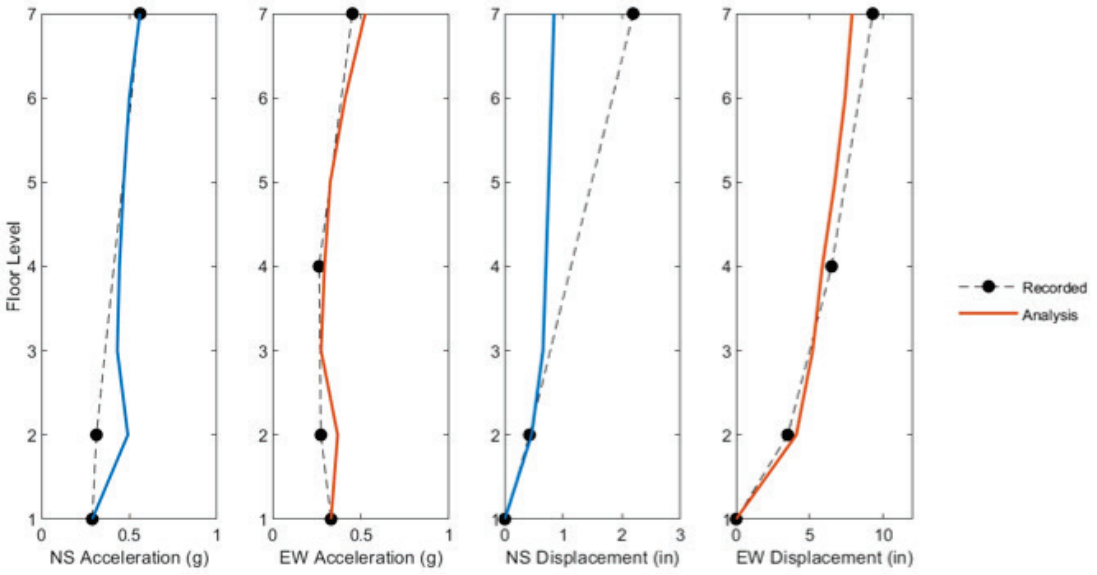


Figure 6-9 NDP: Comparison of recorded and simulated peak acceleration and displacement profiles. These displacements are measured at the center of building in plan in each direction.

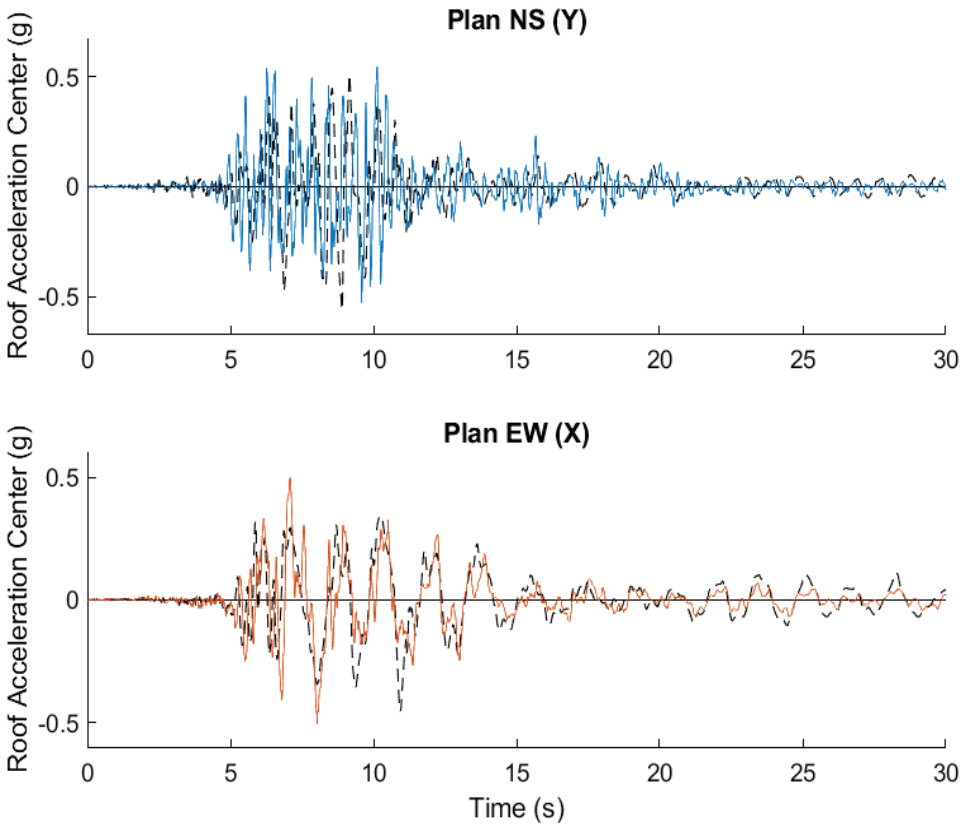


Figure 6-10 NDP: Comparison of recorded and simulated acceleration time histories at the roof.

This publication is available free of charge from: https://doi.org/10.6028/NIST.GCR.22-917-50

The underestimation of upper story drifts may be associated with three factors. First, models of the deep beams (54 inches deep) on the upper-story exterior frame lines only account for flexural deformations and shear deformations, which are estimated to be as high as 10% of the flexural deformations. In this study, the models neglect shear deformations as the shear deformation only represents a minor portion of the overall deformation and the deep beams only occur in the upper stories, which was the less critical portion of the building given its box-on-stilts architecture. Neglecting shear deformations is also the more common approach to modeling via ASCE 41. Secondly, joint stiffness is modeled using the implicit method outlined in ASCE 41-17 Section 10.4.2.2.1, which is based on the ratio of column to beam strength ratio of the joint. When this ratio is greater than 1.2, the "column offset" portion of the joint is assumed to be rigid, which can overestimate the stiffness of joints with deep beams. Lastly, the first-story column bases appear to fail prematurely in the model compared to the real building (see discussion below), leading to early concentration of damage in the first story of the model, effectively protecting the upper stories and reducing upper story displacements.

In the north-south direction, roof displacements are substantially underestimated (by 50%). Soil-structure interaction is more significant in that direction, the effects of which are discussed in Section 6.5. This interaction also contributes to the high accelerations at the second-floor level in Figure 6-9 in this direction.

The building underwent significant torsion due to an asymmetric wall layout, which was evident in recordings and in the model. However, the peak twist (corresponding to about 1.5 inches of additional displacement at the first-story eastern most column line) was underestimated by the model by about 50%, as shown in Figure 6-11c. Previous authors (Pauschke, 1981) estimated a torsion period of 0.35 sec. before the earthquake and 0.43 sec. after the earthquake. The torsional period of the model of 0.23 sec. is less than the ambient recordings, likely due to the fixed-base of the model, but could also be influenced by the rigid diaphragm assumption in the model.

This publication is available free of charge from: https://doi.org/10.6028/NIST.GCR.22-917-50

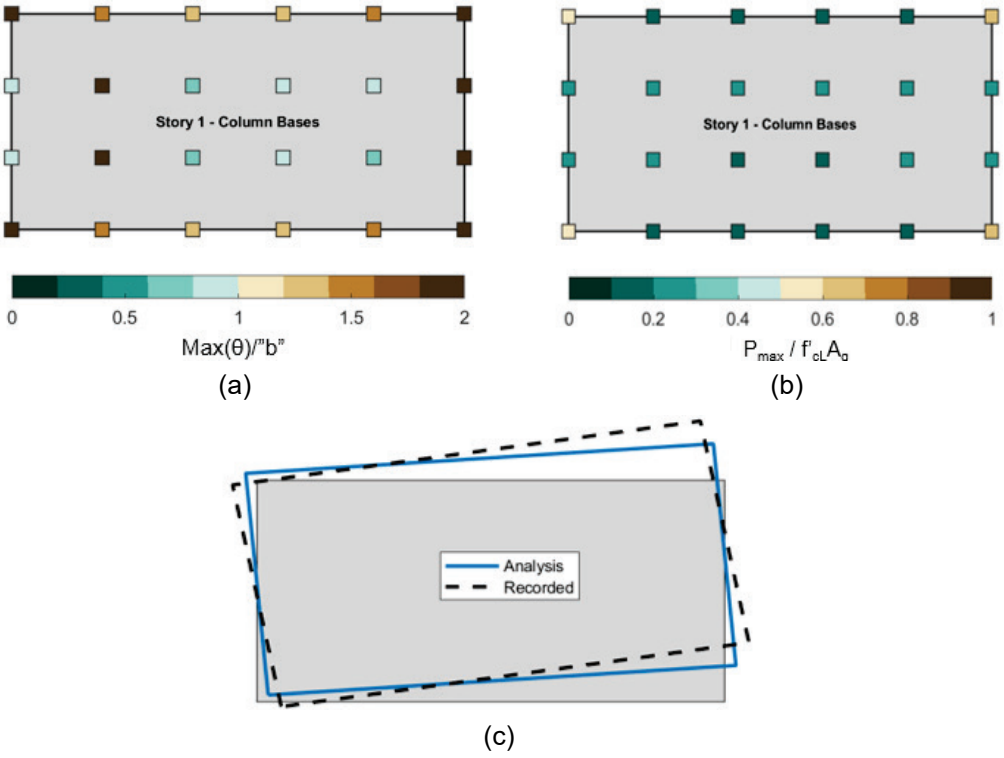


Figure 6-11 NDP: Plan review of response of first-story column bases showing (a) peak rotation demand, θ, normalized by b (in the east-west direction); (b) maximum compressive axial load on columns from the analysis; and (c) peak torsional response of the model (exaggerated by a factor of 100).

6.3.3 Component Performance: Model vs. Observation

The model of the building correctly indicates poor performance of the building in the first story, failing Collapse Prevention in most of the columns at the first-story level.

Responses of the column base hinges are summarized in Figure 6-12. All column hinges are shear critical in the model, which is consistent with the inclined cracking observed in the building. The model results predict that most of the column bases have substantially exceeded their modeling parameter value for b in the east-west direction. In the actual building, the eastern most column line had clearly begun to lose gravity load carrying capacity, consistent with rotations exceeding b. However, the other columns had also exceeded modeling parameter b in the model, but were clearly still carrying gravity load and had experienced only some shear cracking.

The response of the first-story columns is examined in more detail in Figure 6-12. These results show that, at the column base, the modeled column has lost practically all of its strength and stiffness, especially in the east-west direction. This creates essentially a pinned base. At the top of the column, however, where transverse reinforcement spacing is much narrower (2 in. to 3 in.), the columns have just reached their flexural capacity in the model in the east-west direction. These results

This publication is available free of charge from: https://doi.org/10.6028/NIST.GCR.22-917-50

seem qualitatively consistent with the damage photos provided in Figure 6-12, which show limited flexural cracking at the tops of the columns.

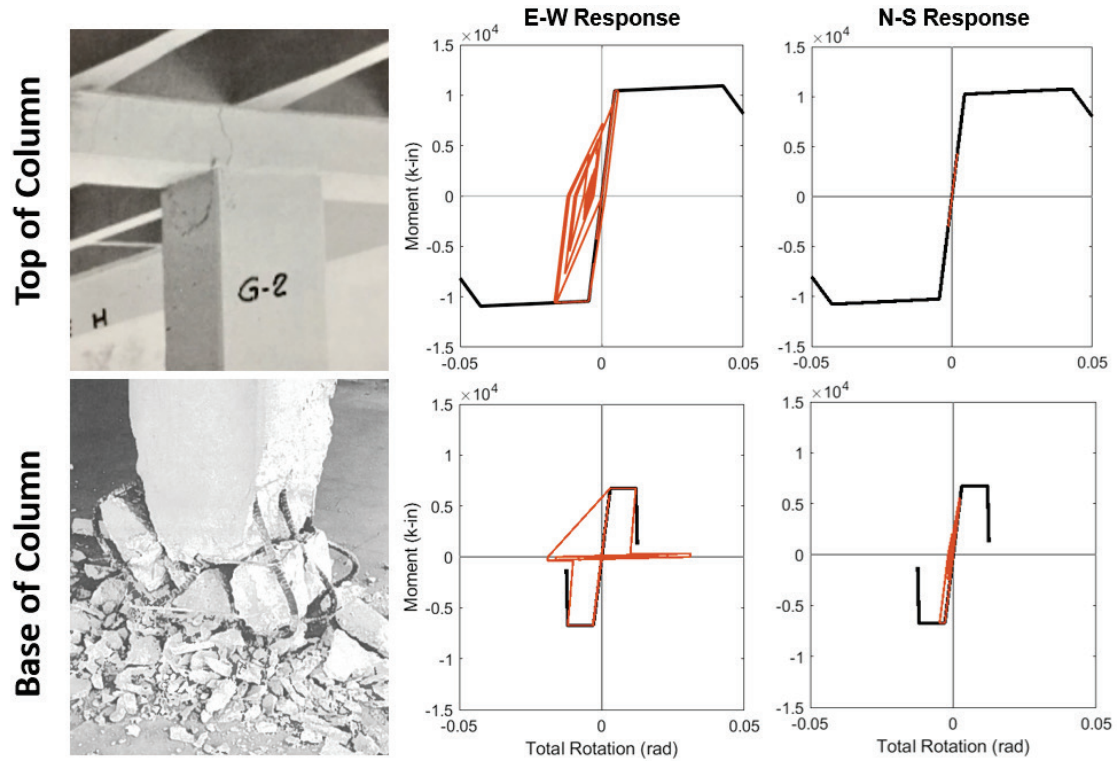


Figure 6-12 Damage photos (ATC, 1984) of column G-2 (see Figure 6-1 for column numbering), with model backbones and hysteretic response in the recorded ground motion. Total rotation of each hinge is defined as the sum of the elastic rotation of half of the column and the plastic rotation of the hinge.

The model predicts the least ductile behavior and response most exceeding *b* at the base of the columns on the eastern-most column line, due to the higher axial loads and torsional response of the east-side of the building, consistent with observations of damage. The model response also indicates that all columns have exceeded *b* and lost gravity-load bearing capacity, according to the definition of *b*. However, the observed damage would indicate that only the eastern most columns have lost gravity-load bearing.

Building torsion amplifies the response in the north-south direction on the east side, with responses in the north-south direction exceeding 0.5% interstory drift, compared to only 0.3% interstory drift on the west side. This torsional response resulted in several columns on the east side of the building reaching their shear capacity in the north-south direction, creating a potential bi-directional shear failure. The ASCE 41-17 model does not explicitly account for reductions in capacity or changes in nonlinear response due to the bi-directional shear behavior of these columns.

The distribution of damage over the height of the building is illustrated by comparison to ASCE 41-17 acceptance criteria in Figure 6-13. The model predicts

This publication is available free of charge from: https://doi.org/10.6028/NIST.GCR.22-917-50

that the columns fail Collapse Prevention (CP) at the base of the first-story columns, and Immediate Occupancy (IO) at the top of some of the first-story columns. Post-earthquake reconnaissance reported little to no damage in upper story columns, and the model response is consistent with these reports. The model predicts that most of the beams did not yield.

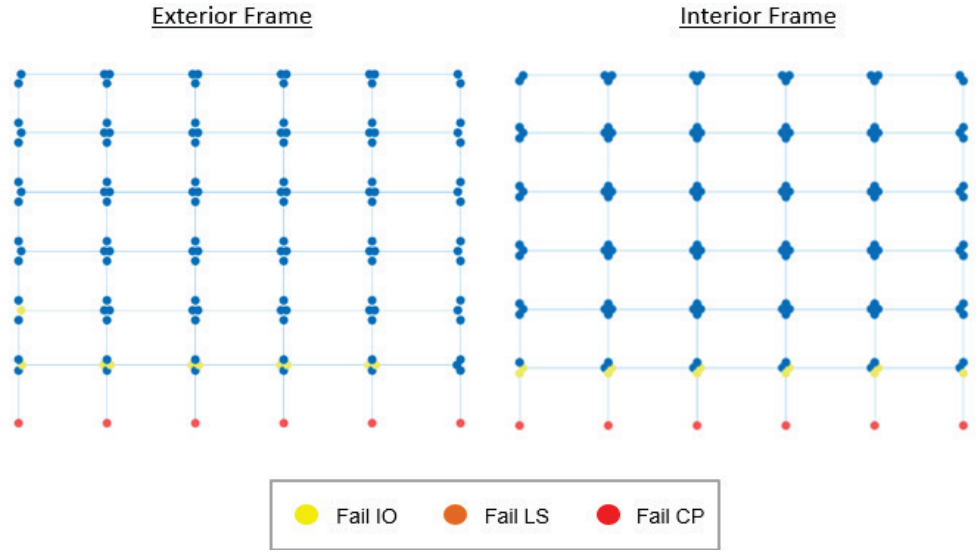


Figure 6-13 NDP: Assessment of column and beam response relative to ASCE 41-17 nonlinear acceptance criteria. Immediate Occupancy (IO), Life Safety (LS), and Collapse Prevention (CP).

The second-floor beams failed the Immediate Occupancy acceptance criteria, with hysteretic response illustrated in Figure 6-14. Damage surveys found only minor cracking in beams throughout the building. No damage was reported to joints in any of the available damage surveys, and no damage to joints was indicated by the analysis.

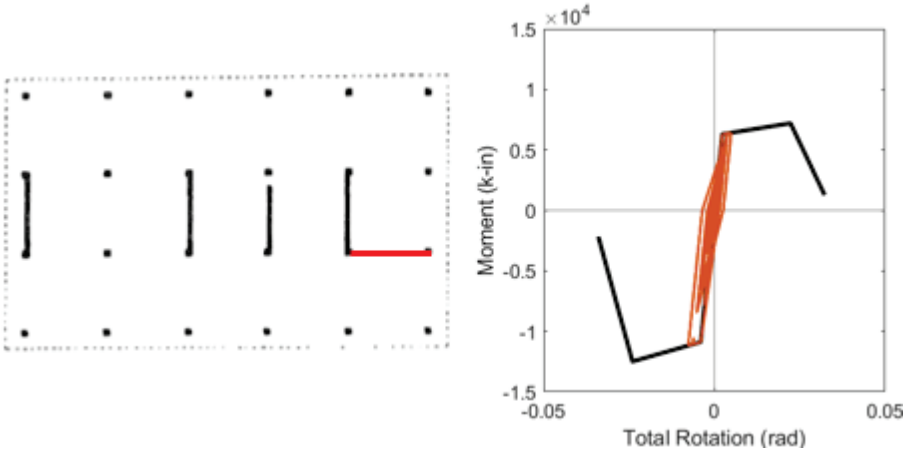


Figure 6-14 NDP: Model backbone and hysteretic response of a beam at the second floor. Total rotation of the hinge is defined as the sum of the elastic rotation of half of the column and the plastic rotation of the hinge.

This publication is available free of charge from: https://doi.org/10.6028/NIST.GCR.22-917-50

6.3.4 *Column Performance: Model vs. Observation vs. Test Data*

Responses from the ASCE 41 models were compared to test data for Columns G1 and G2 (See Figure 6-3) at the first story to further evaluate model prediction of component performance. Columns G1 and G2 are on the heavily-damaged eastern-most frame line. The test data selected are for columns similar to the columns in the building, but not identical. Key parameters informing the comparison are provided in Table 6-1. The selected test data are obtained from Sezen (2002) and Woods and Matamoros (2008).

Table 6-1 Comparison of Column G1 and G2 Properties to Selected Columns in the Experimental Database

Column ID	Column in Building	Column as Tested
G1		Sezen, 2002 – Specimen 3
	ρ_L = 2.7%	ρ_L = 2.5%
	ρ_t = 0.15%	ρ_t = 0.17%
	spacing = 12”	spacing = 12”
	a/d = 3	a/d = 3.75
	L/h = 6	L/h = 6.4
	Section Aspect Ratio = 1:1	Section Aspect Ratio = 1:1
	$N_{UD}/A_g f'_{cE}$ = 0.4	$N_{UD}/A_g f'_{cE}$ = 0.6
	b = 1.1% total rotation	
	Max chord rotation in analysis: 2.2%	Max chord rotation: 2.8%
G2		Woods and Matamoros, 2008 -Specimen 1
	ρ_L = 1.4%	ρ_L = 2.5%
	ρ_t = 0.11%	ρ_t = 0.07%
	spacing = 12”	spacing = 18”
	a/d = 3	a/d = 3.75
	L/h = 6	L/h = 6.5
	Aspect Ratio = 1:1	Aspect Ratio = 1:1
	$N_{UD}/A_g f'_{cE}$ = 0.2	$N_{UD}/A_g f'_{cE}$ = 0.3
	b = 1.0% total rotation	
	Max chord rotation in analysis: 2.2%	Max chord rotation: 1.1%

Photos of the observed damage at the base of corner Column G1, the element response from the analysis, and the damage to the experimental column are provided in Figure 6-15. The analysis results indicate that the column failed in shear and exceeded b (i.e., lost gravity-load carrying capacity) at 1.1% total rotation. The test column exhibited flexure and shear cracks, and lost axial load carrying capacity at 2.8% rotation, which is similar to the total rotation demand on the column in the simulation (3.1%). Damage pictures look similar, although the columns in the study building had more buckling of longitudinal rebar. The modeled column experienced

This publication is available free of charge from: https://doi.org/10.6028/NIST.GCR.22-917-50

more damage at lower drifts than the experimental column, even though the experimental column had a higher axial load, indicating that the *b* values calculated with ASCE 41-17 procedures may be conservative.

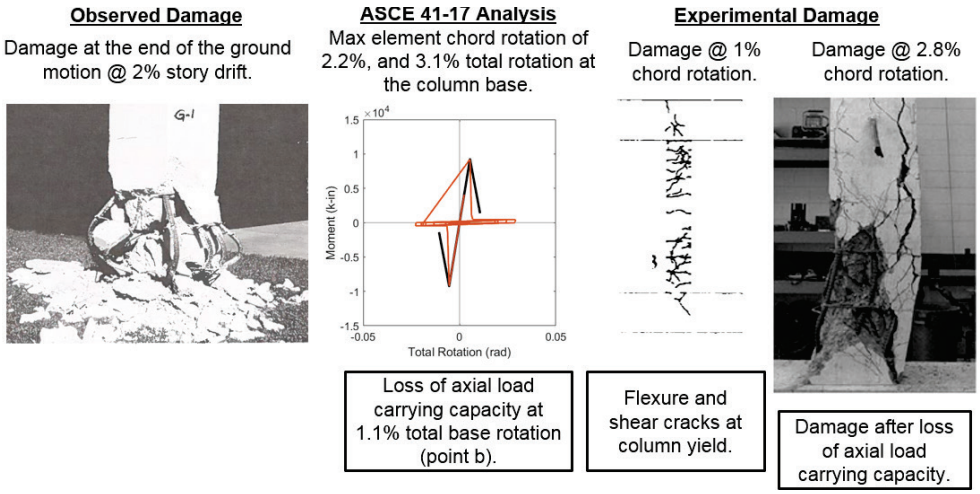


Figure 6-15 Comparison of observed and experimental damage for column G1 in the first story.

Photos of the observed damage at Column G2, the element response from the analysis, and the damage to the experimental column are provided in Figure 6-16. Figure 6-16 shows that the experimental column lost axial load capacity at around 1.1%, compared to the ASCE 41-17 *b* value of 1.0% (converted to total rotation). These results show reasonable agreement, although the experiment has wider spaced transverse reinforcement.

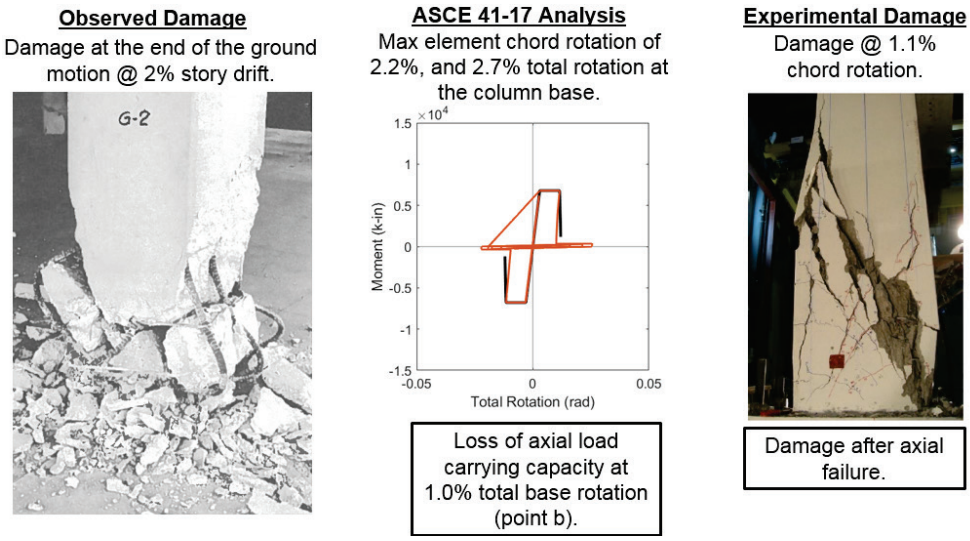


Figure 6-16 Comparison of observed and experimental damage for column G2 in the first story.

Overall, the model seems to reasonably agree with the observed damage and test data. However, in this case, the models and the experiments predict that the recorded

This publication is available free of charge from: https://doi.org/10.6028/NIST.GCR.22-917-50

response is well past failure, so it is difficult to verify agreement of the prediction of the onset of failure.

6.4 Nonlinear Dynamic Procedure with Vertical Ground Motion

6.4.1 Modeling Approach

ASCE 41-17 procedures instruct that the effect of vertical motions be considered for this building due to the cantilevered beams. Accordingly, the vertical component of the recorded motion was added, and the model described in Section 6.3.1 was reassessed. ASCE 41-17 does not require the effect of vertical motions to be considered concurrently with horizontal motions; however, by running the analysis concurrently allows for investigation of whether the vertical motion affects the response and damage assessment, and, if so, assessment of the effect concurrently on the simulation results. Masses were assigned in the vertical direction at ends of cantilever beams, as well as other critical locations.

6.4.2 Results and Comparison to Observed Performance

In terms of story drifts and accelerations, the response of the building was very similar to that reported in Section 6.3. In general, these results indicate that the vertical ground motion does not substantially alter the assessment of performance, which is unsurprising given the relatively low intensity of the recorded vertical motion (Figure 6-6). The model also does not capture axial-flexure or axial-shear interaction, limiting the possible influence of this change on the models. None of the damage surveys and reconnaissance reports attribute any damage to the vertical component of shaking.

6.5 Nonlinear Dynamic Procedure with Soil-Structure Interaction

6.5.1 Modeling Approach

ASCE 41-17 provisions instruct engineers to consider soil-structure interaction (SSI) when "fixed or pinned boundary elements cannot be justified" (ASCE 41-17 Section 10.12.2) or when "an increase in fundamental period caused by SSI effects results in an increase in spectra accelerations" (ASCE 41-17 Section 7.2.7). NIST GCR 12-917-21, *Soil-Structure Interaction for Building Structures* (NIST, 2012), provides further guidance: The structure-to-soil stiffness ratio check is used to determine if the effects of soil-foundation-structure interaction should be considered, where the structure-to-soil stiffness ratio is the ratio of the height of the structure to the product of the fundamental period and the shear wave velocity, $h/(V_s T)$. If the structure-to-soil stiffness ratio is greater than 0.1 it is suggested that SSI effects be considered. For this building, the structure-to-soil stiffness ratio is 0.45 in the north-south direction. Accordingly, this section includes SSI considerations in the nonlinear model. Pile foundations are represented by translational, rotational, and axial springs

This publication is available free of charge from: https://doi.org/10.6028/NIST.GCR.22-917-50

at the pile cap location. The properties of the axial and rotational springs were determined by ASCE 41-17 Equations 8-13 and 8-14, respectively. The properties of the translational springs were determined from P-Y analysis of individual piles using OpenSees. The base of the first-story walls are supported by grade beams framing into the pile caps as well as axial springs intended to represent soil bearing resistance. For this model, the free-field acceleration recording, rather than the foundation recording, was used for excitation (Figure 6-6b).

6.5.2 Global Performance: Model vs. Observation

Including the foundation flexibility effects of soil-structure-interaction improved the estimation of global response in the north-south and east-west directions, as illustrated in Figure 6-17. In particular, the torsional period increased from 0.23 sec. to 0.31 sec., and the amplitude of the torsional response in the north-south direction provides a closer match to the response observed (maximum errors in torsional amplitude reduced from about a 67% to about 50%). An exception is the north-south roof accelerations. Responses shown in Figure 6-17 are recorded at the east side of the building to illustrate the effects of torsion. Therefore, the fixed-based responses differ from those presented in Figure 6-9, which are recorded at the center of the building.

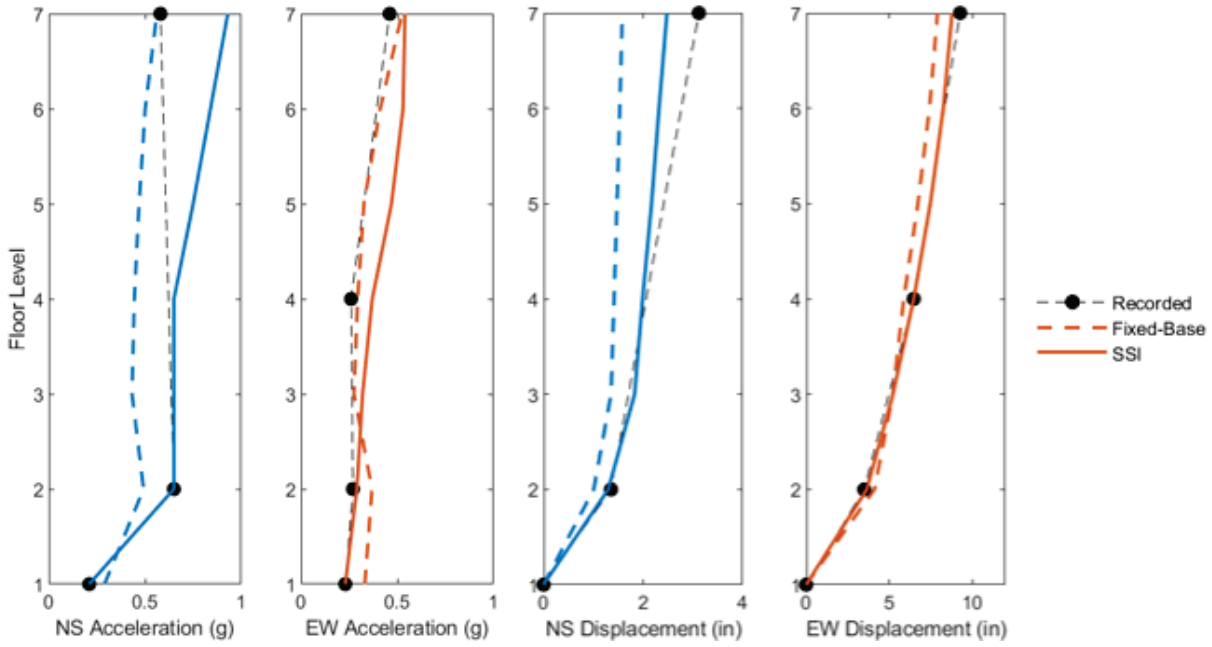


Figure 6-17 NDP with SSI: Comparison of recorded and simulated peak displacement profiles for the model with soil-structure-interaction. In the north-south direction, both the recorded and model displacements are at the east side of the building (so they account for building torsion). The SSI model is assessed using the free-field motion, while the fixed-base model is assessed using the motion recorded at the ground floor of the building.

This publication is available free of charge from: https://doi.org/10.6028/NIST.GCR.22-917-50

Figure 6-18 shows that the effects of the soil-structure interaction and foundation flexibility also provide more realistic representation of the building frequency content (as interpreted from spectra computed from roof accelerations).

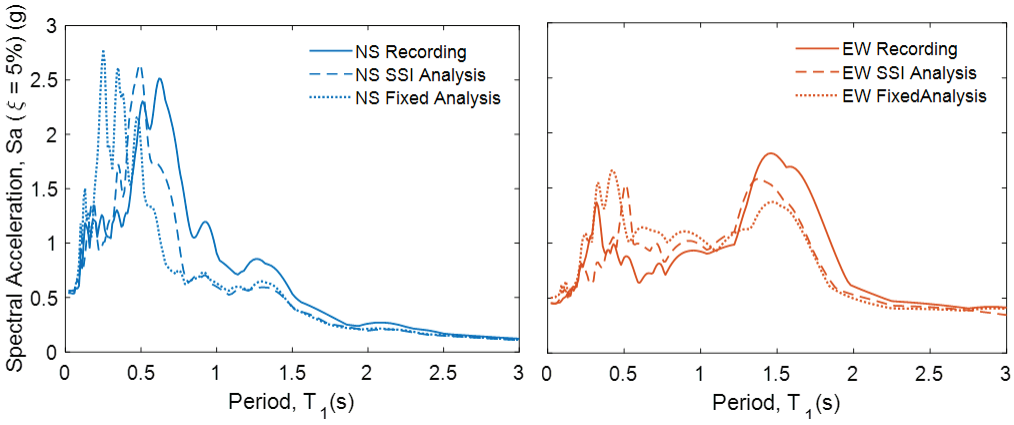


Figure 6-18 NDP with SSI: Comparison of roof acceleration spectra from models with and without soil-structure-interaction. These spectra are computed from the accelerations recorded at the center of the roof in each direction.

6.5.3 Component Performance: Model vs. Observation

Most of the trends of the response are similar to those observed in Section 6.3. However, adding pile springs reduced the in-plane shear forces in the north-south walls in the first story by around 30%.

6.6 Linear Dynamic Procedure

6.6.1 Modeling Approach

A three-dimensional numerical model of the structure was created in OpenSees and evaluated using linear response history analysis as described in ASCE 41-17 Section 7.4.2. Stiffness for beams, columns, walls and joints are based on ASCE 41-17. Walls, beams, and columns all use line elements. The effect of wall length is captured by adding a rigid "beam" to the top of the wall line element. The diaphragms were modeled as rigid and the foundation modeled as fixed. Joint stiffnesses were modeled implicitly based on the procedure described in ASCE 41-17 Section 10.4.2.2. The linear model was assigned 5% damping in modes 1 and 3, applied with Rayleigh damping.

As modeled, the structure has a period of 1.17 seconds in the east-west frame direction, and 0.28 seconds in the north-south wall-frame direction. In the east-west direction, the model is substantially more flexible than indicated by the ambient periods (Section 6.2) due to ASCE 41-17 stiffness modeling assumptions.

This publication is available free of charge from: https://doi.org/10.6028/NIST.GCR.22-917-50

6.6.2 *Global Performance: Model vs. Observation*

Figure 6-19 compares the acceleration and displacement profiles between the recordings and the simulation in both the east-west and north-south directions. The linear model generally underestimates the displacement demands on the structure, even after the linear modification factors of C_1, C_2, and torsional factors are applied; these factors only make a difference in the north-south response. This underestimation is likely due to the substantial damage and nonlinear response incurred in this structure that cannot be captured by the linear model even with the adjustment factors. Accordingly, accelerations are also overestimated by the model.

Examining the response in more detail, the roof displacement response from the linear model in Figure 6-20 in the east-west direction shows relatively good agreement with the instrumentation until about 8 seconds into the motion. At this time, the nonlinear model response indicates significant damage in the building; the linear model is not able to capture period elongation and the related effects on displacement demand. In the north-south direction, displacement response prediction is impaired by the lack of consideration of soil-structure-interaction (see Section 6.5). The linear model underpredicts torsional effects in part because nonlinear response of columns is amplifying torsion, as shown in Figure 6-21.

Despite the significant differences between simulated and recorded structural demand parameters, the model predicts that the structure will fail the Collapse Prevention acceptance criteria, which is consistent with the observed damage to the structure.

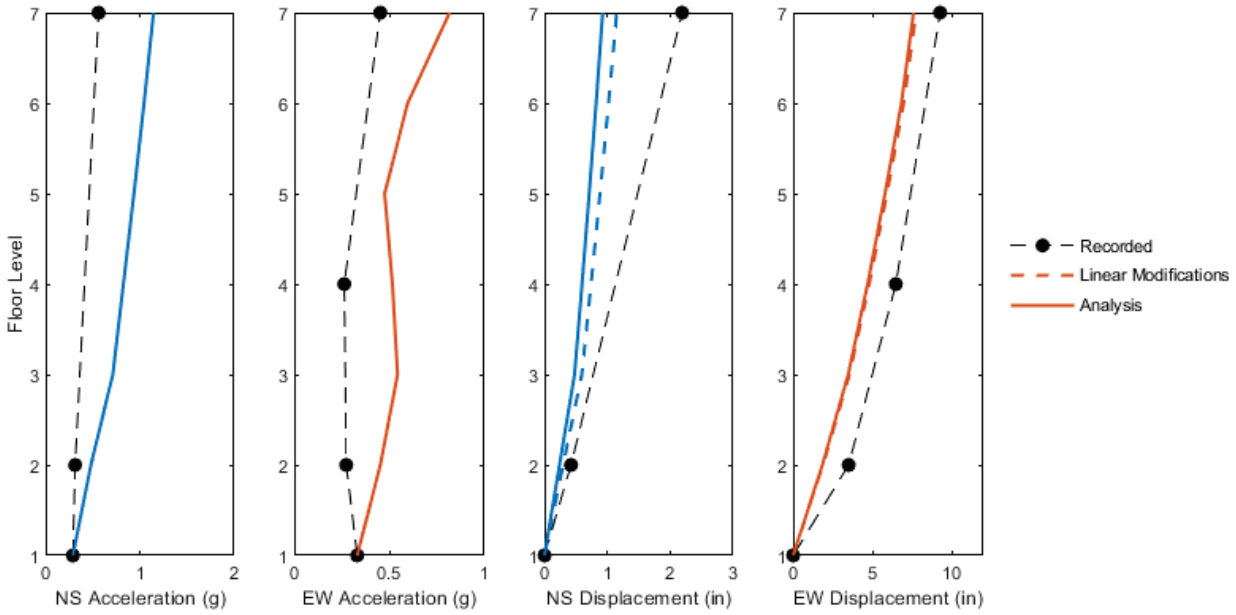


Figure 6-19 LDP: Comparison of recorded and simulated peak acceleration and displacement profiles. These displacements are measured at the center of building in plan in each direction.

This publication is available free of charge from: https://doi.org/10.6028/NIST.GCR.22-917-50

This publication is available free of charge from: https://doi.org/10.6028/NIST.GCR.22-917-50

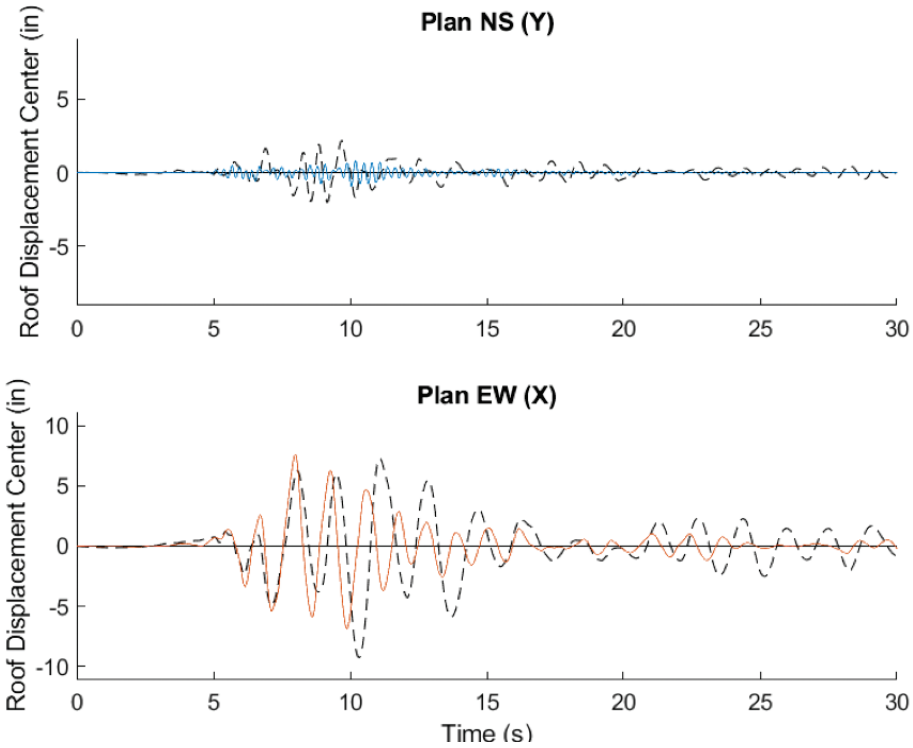


Figure 6-20 LDP: Comparison of recorded and simulated acceleration time histories at the roof.

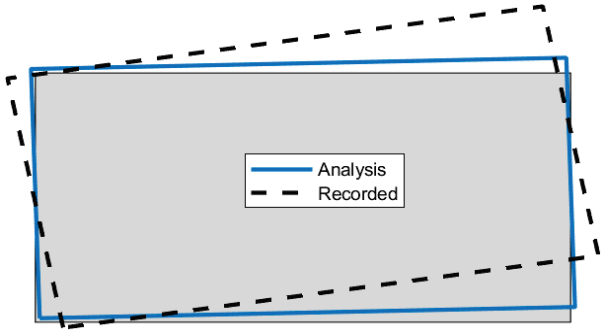


Figure 6-21 LDP: Comparison of recorded and simulated peak torsion response (exaggerated by a factor of 100).

6.6.3 Component Performance: Model vs. Observation

The outcome of the linear model in terms of component acceptance criteria at the first story is shown in Figure 6-22. These results show that all of the columns exceed the linear Collapse Prevention acceptance criteria for both flexure and shear demands at their bases, as indicated by demand-capacity-ratios (DCRs) that have been modified by Collapse Prevention *m*-factors; DCR/*m* values greater than 1 indicate failure to meet Collapse Prevention criteria. The tops of the first-story columns, which have a much tighter transverse reinforcement spacing, also fail to meet Collapse Prevention criteria, but to a lesser extent than the column bases. The model

predicts the largest column axial loads to occur on the eastern-most column line in the corner columns, as observed in the damage patterns. The first-story demands in the north-south direction are smaller in the linear analysis response than in the nonlinear analysis, and therefore predicts less column deformation in that direction, and the bi-directional shear behavior may have contributed to their failure in the actual building. Columns were modeled without considering bi-directional shear effects as ASCE 41-17 does not explicitly provide guidelines on modeling such columns.

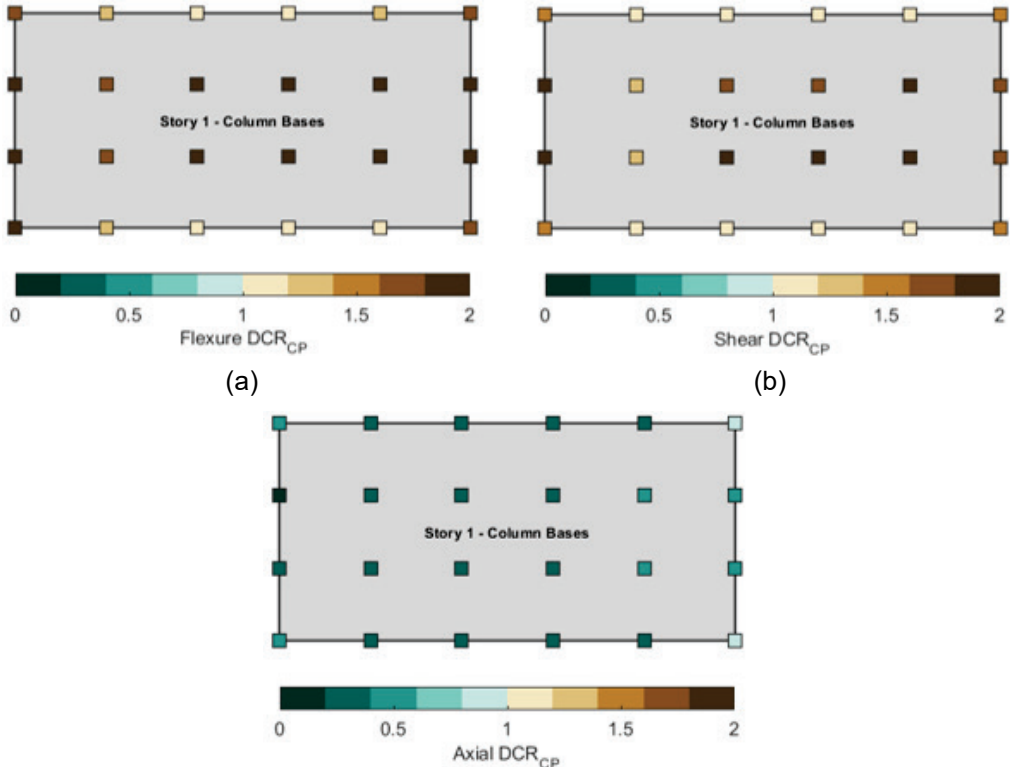


Figure 6-22 Linear Collapse Prevention Demand-Capacity Ratios modified by m-factors (DCR/*m*) at base of first-story columns for: (a) flexure; (b) shear; and (c) axial.

Acceptance criteria for the frame lines in the rest of the building are shown in Figure 6-23. The analysis predicts that some columns and beams at upper stories fail Life Safety acceptance criteria, and many of the interior joints fail to meet Collapse Prevention and Life Safety acceptance criteria, despite the limited observed damage. The analysis also predicts the first-story walls and the upper story wall on the east side will fail to meet the Collapse Prevention criteria. This result is inconsistent with observations of damage, which report only diagonal cracking on the first-story walls and minor cracking on the upper story walls. In the nonlinear assessment, the first-story columns undergo significant strength deterioration, forming a first-story column mechanism which protects the upper stories from extensive drifts and damage. The

This publication is available free of charge from: https://doi.org/10.6028/NIST.GCR.22-917-50

linear assessment is not able to represent this type of behavior leading to more significant damage predictions in the upper stories. As expected, for severely damaged buildings, linear methods cannot capture effects of damage concentration that may lead to conservative assessments of damage.

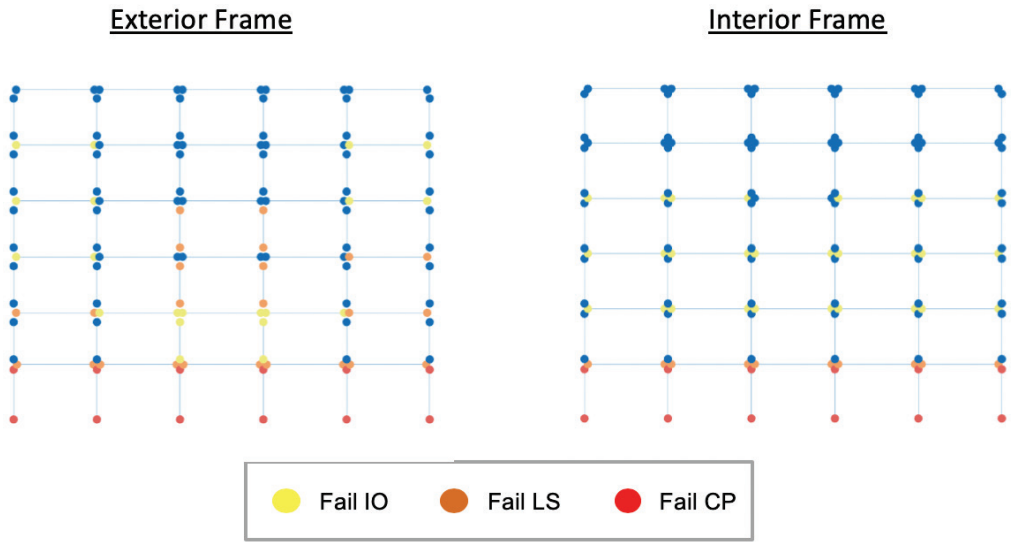


Figure 6-23 Assessment of column and beam response relative to ASCE 41-17 acceptance criteria. Immediate Occupancy (IO), Life Safety (LS), and Collapse Prevention (CP).

6.7 FEMA P-58 Damage Assessment

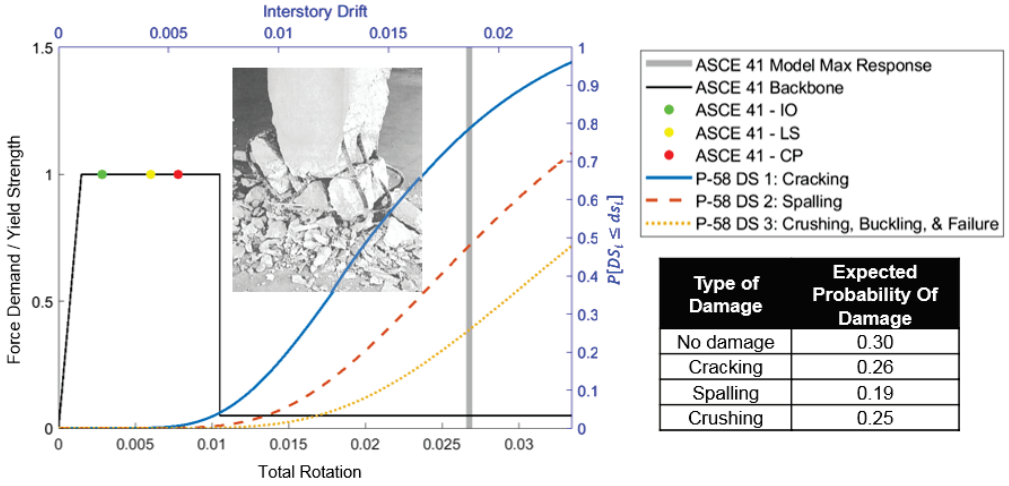
The assessment methodology described in FEMA P-58 (FEMA, 2018c) is implemented using the nonlinear dynamic model developed for this study building and the damage predicted from the assessment are compared with the damage observed in the Imperial Valley Earthquake. This comparison takes advantage of the FEMA P-58 fragility database to map the simulated responses to damage.

The assessment focuses first on Columns G1 and G2 in the first story. Column G2 corresponds to a FEMA P-58 fragility defined as a non-conforming moment frame with shear-controlled columns. Note that the FEMA P-58 fragilities are based on subassembly response (i.e., drifts), but ASCE 41 models are based on element response. These values are converted as described in Section 2.2.4. Figures 6-24 and 6-25 report the outcome of the FEMA P-58 assessment and present descriptions of each of the damage states and the probabilities of being in the damage states based on the simulations.

At the base of Column G2, ASCE 41-17 analysis predicts that the column collapses axially, as it is well beyond the *b* value given by ASCE 41-17. From FEMA P-58, these drift assessments indicate an almost equal likelihood that the column is in any of the three damage states or undamaged. The observed damage to the column seems

This publication is available free of charge from: https://doi.org/10.6028/NIST.GCR.22-917-50

to correspond to crushing. However, the ASCE 41 backbone seems to predict more damaged response than the FEMA P-58 fragilities.



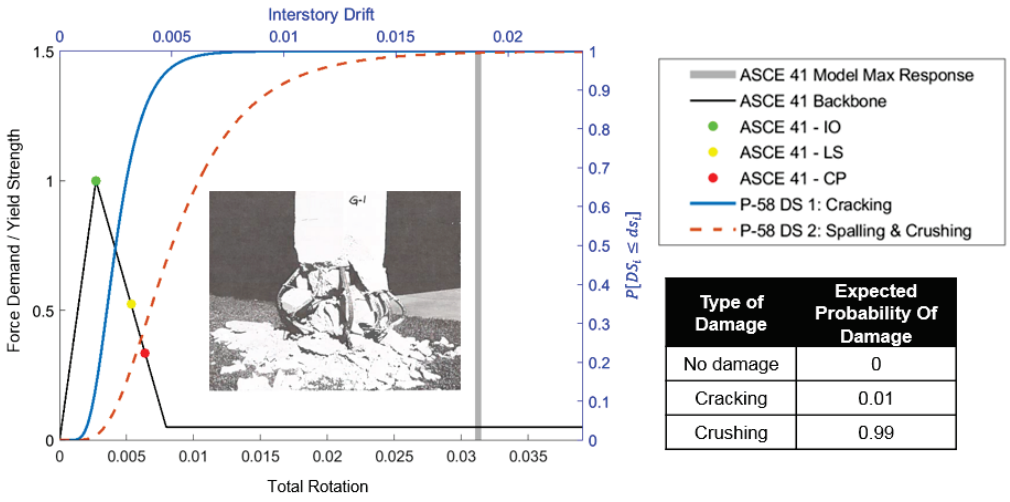
Type of Damage	Expected Probability Of Damage
No damage	0.30
Cracking	0.26
Spalling	0.19
Crushing	0.25

Figure 6-24 FEMA P-58 assessment of damage to base of Column G2, comparing ASCE 41-17 backbone (black axes) to FEMA P-58 fragilities (blue axes). Total rotation is defined as the sum of half of the elastic rotation of the element and the plastic rotation of the hinge. The vertical FEMA P-58 axes (blue) shows the probability of exceeding the i^{th} damage state (DS_i).

The base of first-story Column G1 is assigned the FEMA P-58 fragility for a non-conforming moment frame with shear-controlled columns and high axial load. This assignment was determined by the comparison of the axial load from the dynamic analysis to the capacity, using axial capacities based on lower-bound material properties. For Column G1, the demand-to-capacity ratio, $P/A_g f'_{cL}$, was greater than 0.6, indicating the column had high axial loads. Results are provided in Figure 6-25, showing good agreement between the ASCE 41 model, the observed damage, and FEMA P-58 assessment of crushing. Because of the assignment of the high axial load fragility to the corner columns on the east side of the building, the FEMA P-58 assessment consistently predicts the worst damage to those columns.

The response of the first-story walls is also compared to a FEMA P-58 damage assessment. Reconnaissance reports indicated some (shear) cracking of these walls, but not significant damage. For the western-most wall, the FEMA P-58 assessment produces a 96% chance of no damage and a 4% chance of cracking at the demands simulated in the model. For the eastern-most wall, the FEMA P-58 assessment produces a 73% chance of no damage and a 27% chance of cracking at the demands simulated in the model. The demands are higher in these eastern-most walls due to torsion. The ASCE 41 model for these walls expects the walls to undergo minor stiffness degradation, but not reaching their capacity.

This publication is available free of charge from: https://doi.org/10.6028/NIST.GCR.22-917-50



Type of Damage	Expected Probability Of Damage
No damage	0
Cracking	0.01
Crushing	0.99

Figure 6-25 FEMA P-58 assessment at base of Column G1, comparing ASCE 41 backbone (black axes) to FEMA P-58 fragilities (blue axes). Total rotation is defined as the sum of the elastic rotation of half of the element and the plastic rotation of the hinge. The vertical FEMA P-58 axes (blue) shows the probability of exceeding the i^{th} damage state (DS_i).

Damage assessment for beams and columns at upper stories from FEMA P-58 is also consistent with the observed damage. FEMA P-58 predicted, in most cases, only small probabilities of damage, and very limited damage was reported during reconnaissance. Response from the model typically reaches just past the yield point of the ASCE 41 backbone.

6.8 Fragility Assessment

Collapse fragility curves developed for the building are provided in Figure 6-26. Collapse is defined for two mechanisms, sidesway (lateral instability) and gravity collapse. Sidesway collapse is triggered when interstory drifts exceed 6% drift, and gravity collapse is triggered when the static expected gravity loads exceed the residual axial capacity of the first-story columns. Nonconvergence was not an issue, as the simulation model consistently converged numerically beyond 6% drift. The study defined unacceptable response as the exceedance of 1.5 times the modeling rotation limit (*b* value) of any one component, after which there may be significant uncertainty in component response and modeling parameters. Figure 6-26 shows that unacceptable response may occur prior to gravity collapse for several ground motions, but generally occurs after gravity collapse and before sidesway collapse.

This publication is available free of charge from: https://doi.org/10.6028/NIST.GCR.22-917-50

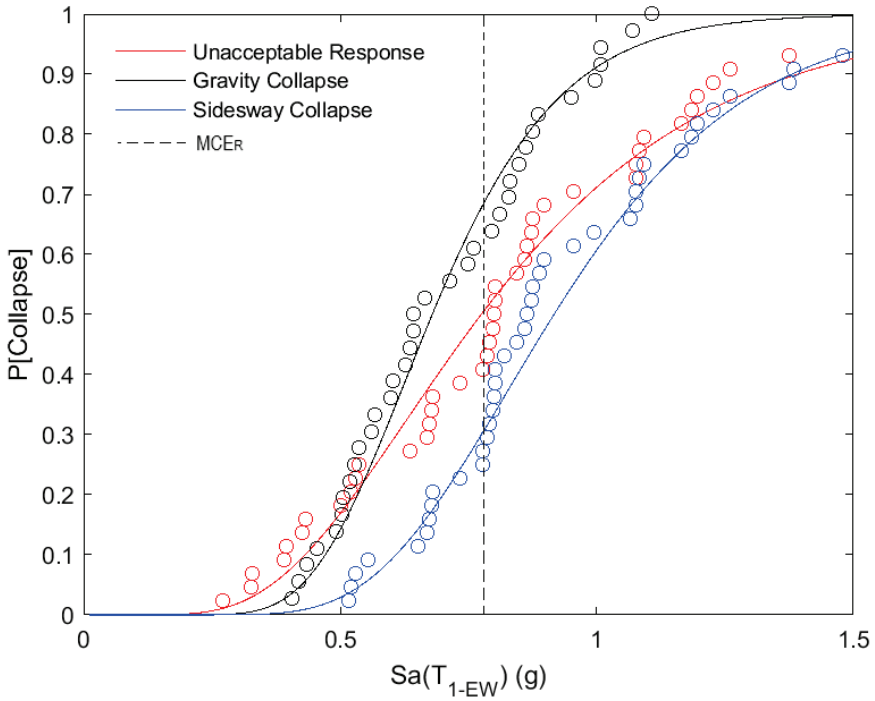


Figure 6-26 Collapse fragility and unacceptable response limit-state curves with respect to spectral accelerations at the fundamental period of the building in the east-west direction.

Collapse of the model occurs in the north-south direction induced from torsion for about 75% of the ground motions and in the east-west direction for about 25% of ground motions. The east-west collapse mechanism initiates with the failure of the base of the first-story columns (*b* values of 0.005 to 0.025) due to the wide spacing of transverse reinforcement, essentially creating a pinned base response. This behavior is followed by the top of the first-story columns failing at much larger drifts (*b* values as large as 0.08, as shown in Figure 6-27) which causes instability. Column-to-beam strength ratios at the top of the first story range from 1.0 to 1.2. This characteristic of the building delays the creation of a first-story mechanism well beyond the loss of lateral capacity at the base column hinges.

Collapse fragility curves can be compared to the benchmark value of 10% probability of collapse at the MCE_R intensity for modern buildings, as defined in FEMA P-695 (FEMA, 2009). To do so, the simulated fragility curves are adjusted based on FEMA P-695. At the MCE_R value defined for the building site in USGS (2014), the adjusted curve produces a 20% probability of sidesway collapse, a 30% probability of gravity collapse, and a 27% probability of unacceptable response (see also Table 6-2). The "true" probability of failure is likely between these three numbers, indicating that this building is likely to perform worse than a modern code designed building.

This publication is available free of charge from: https://doi.org/10.6028/NIST.GCR.22-917-50

This publication is available free of charge from: https://doi.org/10.6028/NIST.GCR.22-917-50

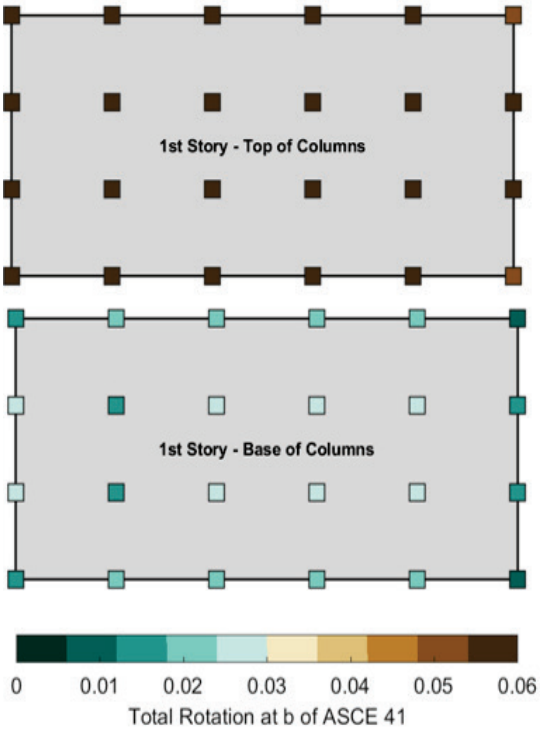


Figure 6-27 Comparison of *b* values (rotation limits) at bottom and top of first-story columns.

Table 6-2 FEMA P-695 Assessment of the Fixed Base Model

Case	Median S_a (g)	CMR[1]	SSF[2]	3D Factor[3]	ACMR[4]	Adjusted P["C"|MCE$_R$]
Collapse - Sidesway	0.92	1.16	1.3	1.1	1.66	20%
Collapse - Gravity	0.68	0.86			1.23	30%
Unacceptable Response	0.77	0.98			1.4	27%

[1] "CMR" is ratio of the median S_a to the MCE_R value.

[2] *SSF* is spectral shape factor as defined in FEMA P-695 and Chapter 2.

[3] A 3D factor of 1.1 was employed here, based on comparison of 2D and 3D analysis of this building.

[4] *ACMR* is the adjusted collapse margin ratio.

The collapse fragility curves can also be compared with fragility curves of component-based acceptance criteria. Figure 6-28 shows several fragility curves that define the probability of failing Collapse Prevention acceptance criteria based on different definitions of the number of components required to trigger global Collapse Prevention failure. Each curve represents the probability of exceeding component-based Collapse Prevention for a given number of components in the collapse mechanism, expressed as percentage of the components in the collapse mechanism.

The story mechanism percentages are based in the east-west direction on the number of column hinges failing (nonlinear) Collapse Prevention out of 48 total column hinges in 24 columns; in the north-south direction, these percentages area based on the number of walls failing Collapse Prevention out of 4 total walls. (For this purpose, no FEMA P-695 adjustments are applied to the curves.)

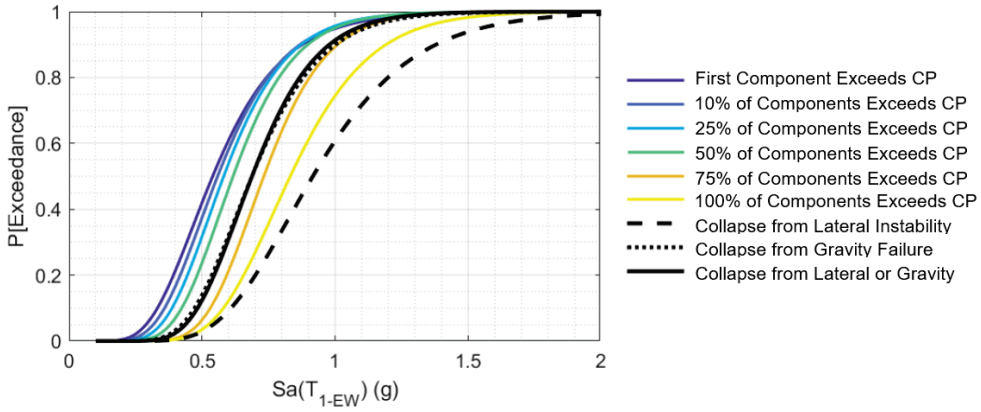


Figure 6-28 Fragility curves showing probability of percent of components in collapse mechanism exceeding the Collapse Prevention acceptance criteria (all curves without FEMA P-695 adjustments).

Results show a significant difference between the ASCE 41-17 Collapse Prevention acceptance criteria (any one component exceeding the Collapse Prevention criteria), which occurs at a median intensity of $S_a(T_1 = 1.1\text{s})$ of 0.53g, and the sidesway collapse fragility at 0.92g or the gravity collapse fragility at 0.68g. Component-based Collapse Prevention fragility curves do not approach the collapse fragilities until around 50% or more of the components exceed Collapse Prevention acceptance criteria. These results indicate that using the failure of a single poor performing component as an indicator of collapse prevention acceptance criteria may lead to a conservative assessment.

Alternatively, system-level metrics for collapse prevention can be developed instead of component-based metrics. For example, a peak story drift ratio threshold, such as 2%, could be used as a Collapse Prevention acceptance criterion. Figure 6-29 shows the probability of achieving a "near-collapse" collapse margin for both CP and drift-based limit states, where collapse margin is defined as the ratio of S_a at collapse to the S_a at which the alternative metric provides an indicator of collapse (Maison et al., 2009); here, a "near-collapse" collapse margin is defined as less than 1.1. In other words, a high probability of the "near-collapse" collapse margin indicates that the metric is consistent with the simulated sidesway or gravity collapse mechanism.

For this building, peak story drifts greater than 2% have a high probability (greater than 90%) of indicating "near-collapse" conditions (Collapse Margin <1.1) for gravity failure, and peak story drifts greater than 4% for sidesway collapse; the

This publication is available free of charge from: https://doi.org/10.6028/NIST.GCR.22-917-50

average rotational capacity (*b* value) of the base of the first story columns is 0.017. On the other hand, component-based CP limit states do not tend to achieve "near-collapse" conditions until more than 50% of the components in the collapse mechanism exceed CP.

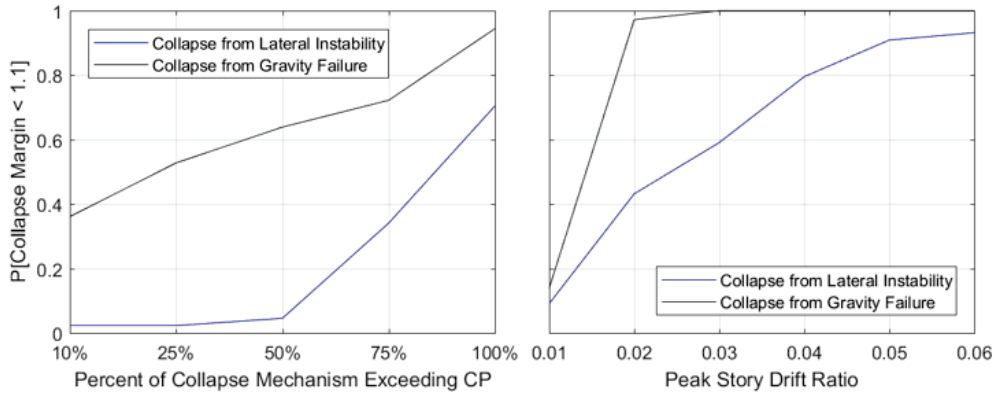


Figure 6-29 Probability of resulting in a "near-collapse" Collapse Margin (less than 1.1) for (a) component-based CP limit states, and for (b) drift-based limit states.

The fragility assessment of the ASCE 41-17 model shows that component-based acceptance criteria for Collapse Prevention occur well before any global indicators of collapse (sidesway or gravity). This indicates significant residual capacity in the building after the failure of the first component-based trigger. Results show that the structure can trigger up to 50% of the component-based Collapse Prevention acceptance criteria in the first-story columns and walls before approaching global collapse consequences. While the model does not explicitly capture the failure and redistribution of axial loads, the results point to conservatism in the component-based procedure, and also the importance of continuing to refine models at higher demands (i.e., pushing the limits of what is meant by unacceptable response).

6.9 Eurocode Evaluation

This building was evaluated using acceptance criteria of Eurocode 8 (2005) for columns for the Near Collapse limit state (Section 2.4.2), with results shown in Figure 6-30. The figure shows that Eurocode assessment results in a lower probability of Near Collapse limit state than ASCE 41 Collapse Prevention based on the column base response. For these column hinges, which have relatively high axial loads and low transverse reinforcement ratios, the Eurocode Near Collapse acceptance criteria are associated with a larger rotation than ASCE 41. However, in the Eurocode assessment, the tops of the columns exceed the Near Collapse limit state sooner than ASCE 41 exceeds the Collapse Prevention limit state. Therefore, as more columns exceed the collapse acceptance criteria, the difference between the ASCE 41 and Eurocode component-based fragilities tends to become smaller.

This publication is available free of charge from: https://doi.org/10.6028/NIST.GCR.22-917-50

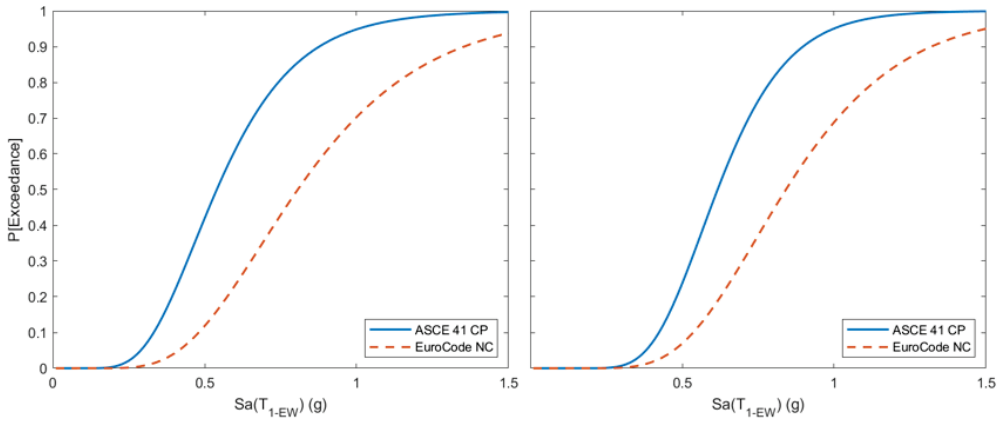


Figure 6-30 Fragility curves obtained from Eurocode Near Collapse (NC) limit state, as compared to ASCE 41-17 Collapse Prevention (CP) limit state, showing probability the limit state is exceeded in (a) one column hinge, and (b) 50% of the column hinges. This assessment is based the first-story column hinges in the east-west direction.

The Eurocode assessment of Near Collapse is associated with somewhat larger ground shaking intensities than the ASCE 41 Collapse Prevention limit state for the study building. These differences can be attributed to differences in column acceptance criteria in the two documents; although they are similar on average, Eurocode Near Collapse acceptance criteria are generally less sensitive to column axial load and transverse reinforcement.

6.10 Summary

6.10.1 Global Performance

ASCE 41-17 procedures successfully identified the first-story deficiency of study building. This first-story deficiency, associated with the large (non-ductile) stirrup spacing at the base of the columns and discontinuous walls, is readily apparent. Both the linear and nonlinear evaluations identified the first-story deficiency, but also overpredicted damage in other components. The response of the nonlinear dynamic evaluation reflected the high drifts in the first story, torsion amplifying response of the east side, and high axial loads on the east corner columns of the observed model. However, torsion was significantly underpredicted, and roof drifts in the north-south direction also somewhat underpredicted.

6.10.2 Component Performance

ASCE 41-17 nonlinear evaluation procedures correctly identified the vulnerability of the eastern-most column line. The assessment indicates shear failure of these columns, followed by loss of gravity load carrying capacity. However, the assessment also identified more damage to other components than was observed.

This publication is available free of charge from: https://doi.org/10.6028/NIST.GCR.22-917-50

Nearly all first-story column bases were well beyond modeling parameter *b* in the assessment, indicating the loss of the ability to resist axial load. In the actual building, only four east-side columns showed loss of axial capacity, with shear cracking and some light spalling noted on the rest of the columns. The point of loss of gravity load carrying capacity defined by the ASCE 41 backbone (i.e., modeling parameter *b*) seems to be conservative compared with observed behavior, experimental testing of similar columns, and FEMA P-58 damage fragilities for these columns. The conservative value of *b* in the ASCE 41 assessment may indicate to the assessor that more columns need to be retrofit than would truly be required to achieve collapse prevention.

6.10.3 Analytical Study Takeaways

The results show that, as the modeling of the structure becomes more complex, estimates of response and damage generally become less conservative and closer to observed performance; for example, the nonlinear results are less conservative than the linear results, and the model with soil structure interaction gives better match with the observed response than the fixed base model. However, even though the simplest approach overestimates damage to the upper stories, they correctly identify the critical first story and vulnerability of the eastern columns.

For this building, the analysis also indicates important needs to improve modeling capabilities. These include modeling strategies to capture bi-directional shear interaction, as well as axial-shear interaction, and axial collapse. These effects have an important influence on the response.

6.10.4 Study Limitations

These conclusions must be considered in the context of several limitations:

- Nominal material properties from the construction documents were used and modified to calculate expected material properties based on ASCE 41-17 Table 10-1. Some experimental material data exists for select members, but this information was not comprehensive enough for use in the assessment. A few sample material strength tests taken after the earthquake indicated that the four east-side first-story columns may have concrete strengths lower than what was used in this study, but this may also be attributed to microcracking associated with earthquake damage (Selna and Boyens, 1980).
- Four boring logs are used to develop a soil profile for the analysis of the model with foundation flexibility. Soil properties that are not provided by the boring logs are assumed based on engineering judgment.
- Displacement recordings are calculated through double integration of the 13 accelerometer recordings. Therefore, potential residual drifts are not captured by

This publication is available free of charge from: https://doi.org/10.6028/NIST.GCR.22-917-50

the recordings. However, damage observations indicated that the building exhibited no significant residual drifts after the earthquake (Wosser et al., 1980). Accelerometers were placed at the ground floor, second-level, fourth-level, and roof; therefore, recordings of acceleration and displacement were not available at every story.

- The most detailed damage observations pertain to the four east-side first-story columns, which exhibited axial failure. Damage observations for the rest of the building were typically more general and do not necessarily exist for every building component.

This publication is available free of charge from: https://doi.org/10.6028/NIST.GCR.22-917-50

Chapter 7

Seven-story Frame Building in California

This publication is available free of charge from: https://doi.org/10.6028/NIST.GCR.22-917-50

7.1 Overview

This chapter presents benchmarking studies for a 7-story reinforced concrete moment frame building located in Van Nuys, California, shown in Figure 7-1. The building was designed in 1965 and built in 1966; it is a representative example of nonductile reinforced concrete construction in California in accordance with the seismic codes prior to the 1971 San Fernando Earthquake. The building has perimeter frames with interior slab-column frames and provides the opportunity to evaluate the modeling parameters and acceptance criteria of beams, columns, and slab-column connections. The building was instrumented with 16 accelerometers and calculated performance metrics are compared with observed damage for strong motion records from the 1994 Northridge Earthquake.



Figure 7-1 Photograph of reinforced concrete moment frame building in Van Nuys.

The building was evaluated in accordance with the linear and nonlinear dynamic procedures of ASCE 41-17 using OpenSees and ETABS software, respectively. The models were constructed per details presented in Appendix A, unless otherwise noted

This chapter also provides results of a fragility analysis showing the collapse potential of the as-modeled building, as compared to the likelihood of exceeding ASCE 41-17 acceptance criteria.

7.2 Building Description and Observed Performance

7.2.1 Building Description

The building is rectangular in plan with eight bays in the east-west direction (total dimension of 150'-0") and three bays in the north-south direction (total dimension of 62'-0"), as shown in Figures 7-2 through 7-4. The structural system of the building consists of perimeter (exterior) spandrel beam-column frames and interior slab-column frames. Exterior walls in the north and south ends consisted of plaster on metal studs (Blume and Associates, 1973). The interior flat slabs are 10 in. thick on the second floor, 8.5 in. thick on the third through seventh floors and 8 in. thick at the roof. Typical exterior columns dimensions are 14 in. by 20 in., and interior square columns have dimensions of 20 in. by 20 in. in the first story and 18 in. by 18 in. for the remaining stories. The strong axis of the columns is oriented in the east-west direction.

Normal weight concrete was used throughout the building, with design strengths ranging from 3,000 to 5,000 psi. Grade 40 reinforcing steel was used in the beams and slabs and grade 60 steel was used in the columns.

The foundation system of the building consists of 38 in. deep pile caps supported by groups of two to four 24 in. diameter cast-in-place reinforced concrete friction piles. The piles are 40 ft. long (Todorovska and Trifunac, 2008). The building was located over silty fine sand with a dry density ranging between 96 and 105 lbs per cubic feet up to a depth of 45 ft. (Todorovska and Trifunac, 2008).

This publication is available free of charge from: https://doi.org/10.6028/NIST.GCR.22-917-50

This publication is available free of charge from: https://doi.org/10.6028/NIST.GCR.22-917-50



Figure 7-2 Photograph of south-west elevation (Trifunac et al., 1999).

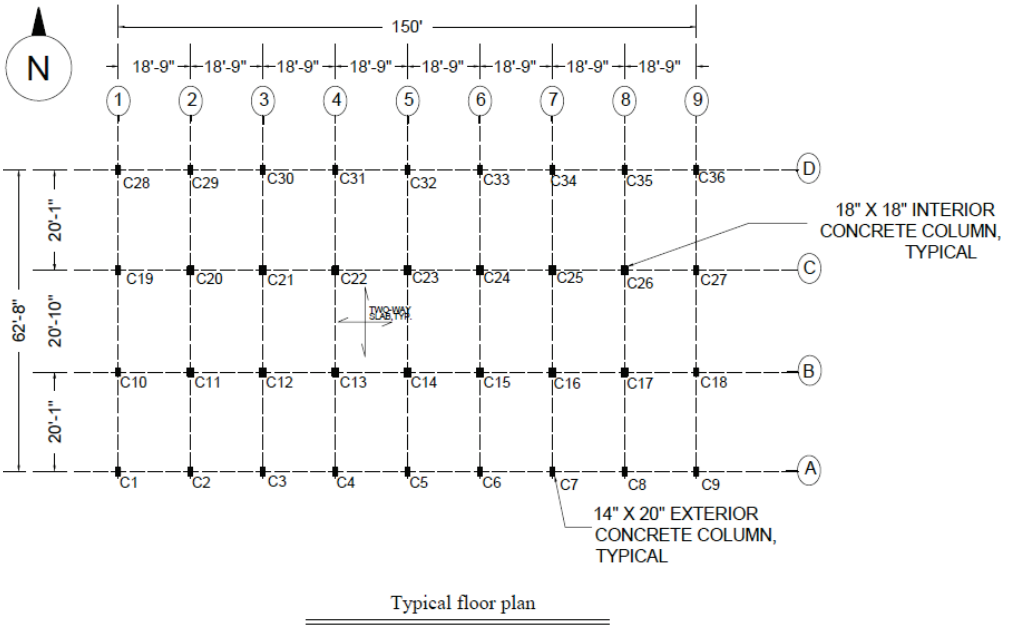


Figure 7-3 Typical floor plan (source: original drawings by Rissman and Rissman Associates).

This publication is available free of charge from: https://doi.org/10.6028/NIST.GCR.22-917-50

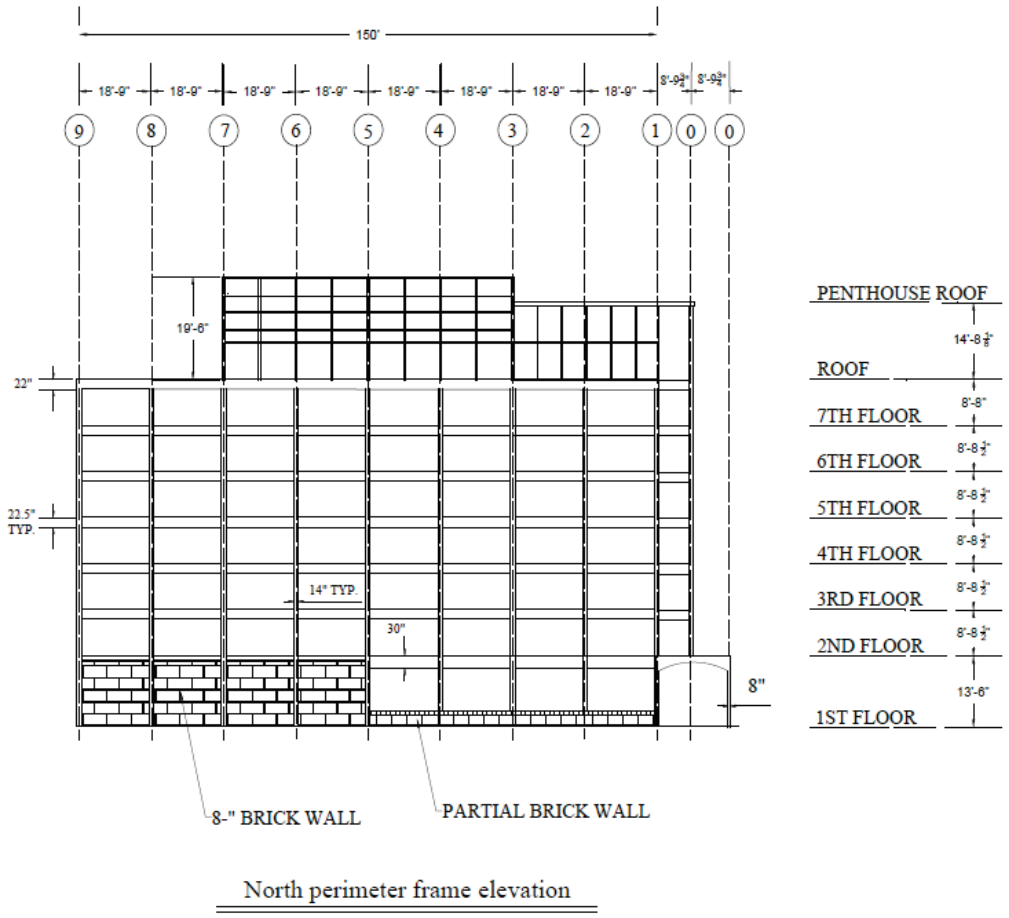


Figure 7-4 Elevation of study building (source: original drawings by Rissman and Rissman Associates).

Material Properties

The building structure had normal weight aggregate concrete with specified concrete compressive strength values shown in Table 7-1. Specified compressive strength was higher at lower floors both for beams and columns. Reinforcing steel strengths were different for beams and columns, with higher grade reinforcement used in building columns. Specified strengths were taken to be the lower bound strengths in accordance with ASCE 41-17 Section 10.2.2.1.2. Mean expected strength values were calculated using material factors in ASCE 41-17 of 1.5 for concrete and 1.25 for reinforcing steel.

Table 7-1 Average Material Properties

Component	Property	Based on Specified Values, ksi	
		Lower-Bound (Specified)	*Mean (Expected)*
Column reinforcement	Yield Stress, f_y	60	75
Beam and slab reinforcement	Yield Stress, f_y	40	50
Column concrete, ground to 2nd floor	Peak Strength, f_c'	5	7.5
Column concrete, 2nd to 3rd floor	Peak Strength, f_c'	4	6
Beam and slab concrete, 2nd floor	Peak Strength, f_c'	4	6
All other concrete, 3rd to roof	Peak Strength, f_c'	3	4.5

Building Weight

The weight of the building was calculated including the weight of the slab, electrical and mechanical equipment, partitions, flooring, ceiling, beams, and columns. A partition load of 10 psf was added to all stories with exception of the roof. Calculated unit gravity loads were 150 psf for the roof, 166 psf between the third and seventh floors, and 193 psf for the second floor (first elevated slab). Calculated story weights and the total weight of the building are presented in Table 7-2.

Table 7-2 Building Weight by Floor Level

Floor Level	Story Weight kips
Roof	1,372
7th	1,521
6th	1,521
5th	1,521
4th	1,521
3rd	1,521
2nd	1,766
Total	10,744

7.2.2 Building Instrumentation

The building has been instrumented by the California Strong Motion Instrumentation Program since the early 1970s with an array of strong motion accelerometers. During the 1971 San Fernando Earthquake, the building was instrumented with 9 accelerometers located at the roof, fourth, and ground floors. In 1980, the instrument array was increased by adding 7 channels for a total of 16. The strongest earthquakes for which digitized records are available are 1971 San Fernando, 1987 Whittier

This publication is available free of charge from: https://doi.org/10.6028/NIST.GCR.22-917-50

Narrows, and 1994 Northridge earthquakes. The instrumentation plan of the building during the 1994 Northridge Earthquake is presented in Figure 7-5.

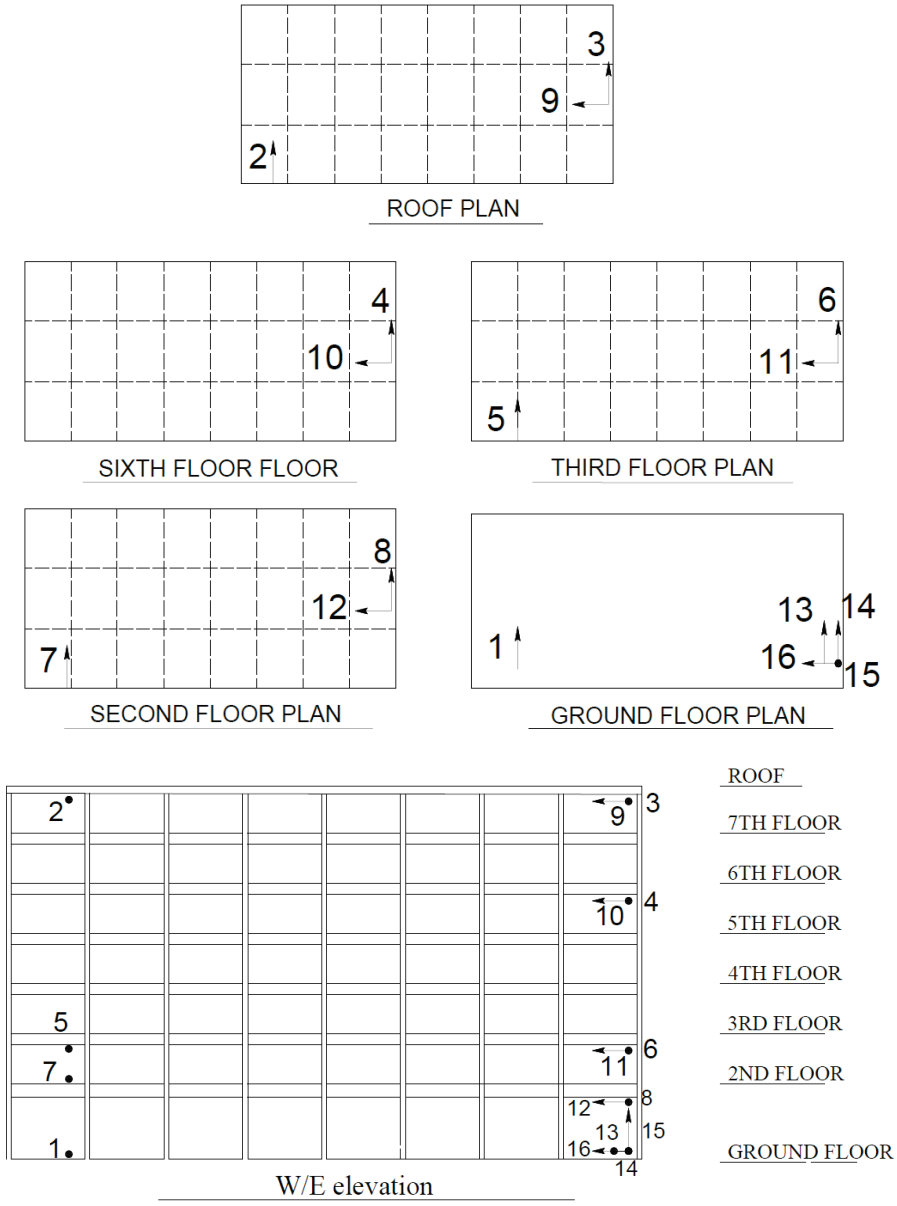


Figure 7-5 Building instrumentation plan.

7.2.3 Ground Motion

Strong motion records recorded at the site during the 1994 Northridge Earthquake are used for this study. At the time of the Northridge Earthquake, the building had 10 accelerometers recording motion in the north-south direction and 6 accelerometers recording motion in the east-west direction. Nonlinear analyses performed in this study were performed with the building subjected to horizontal acceleration records available from instruments designated 1 (north-south component) and 16 (east-west

This publication is available free of charge from: https://doi.org/10.6028/NIST.GCR.22-917-50

component) in Figure 7-5. Acceleration histories from these two records are shown in Figures 7-6 and 7-7, and acceleration spectra are shown in Figure 7-8. Peak ground accelerations recorded during the 1994 Northridge Earthquake were 0.39g and 0.45g for the north-south and east-west components, respectively, and 0.27g for the vertical direction. Effective periods of the building calculated using ASCE 41-17 provisions for effective stiffness including the effect of the masonry infills at the base floor were 1.88 sec. in the north-south direction and 1.83 sec. in the east-west direction. Previous work has studied two-dimensional analyses of the building in the east-west direction, which sustained the most damage during the Northridge Earthquake, and reported periods ranging between 0.86 sec. (Blume and Associates, 1973) and 1.93 sec. (Paspuleti, 2002). The former corresponded to adjusted gross section properties and the latter to the effective period of a nonlinear model.

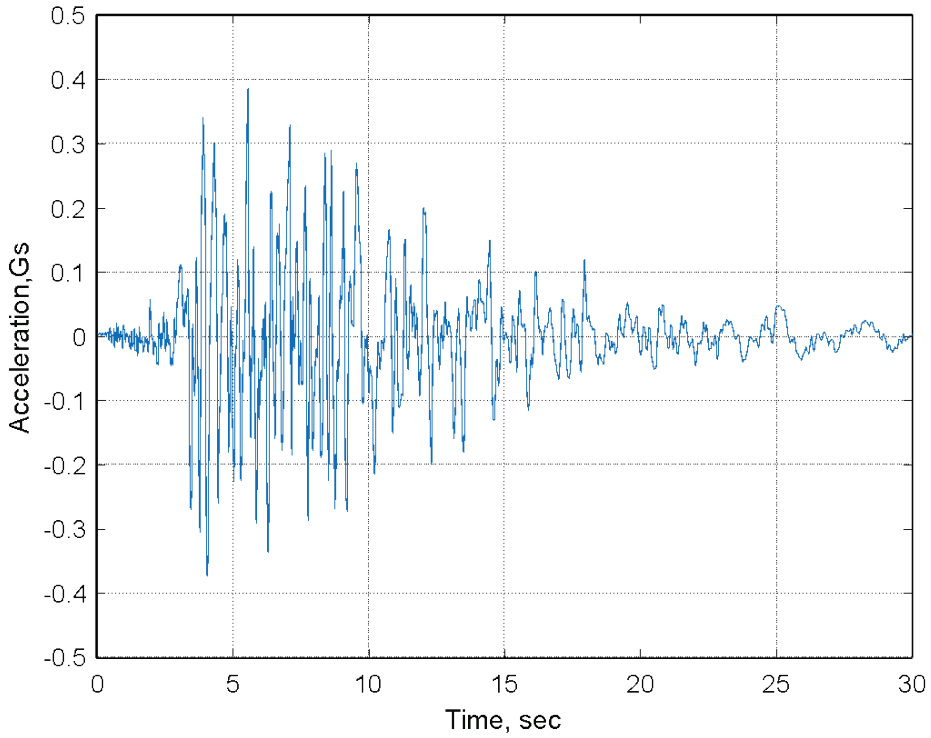


Figure 7-6 Acceleration record for 1994 Northridge Earthquake at the ground level, north-south component.

This publication is available free of charge from: https://doi.org/10.6028/NIST.GCR.22-917-50

This publication is available free of charge from: https://doi.org/10.6028/NIST.GCR.22-917-50

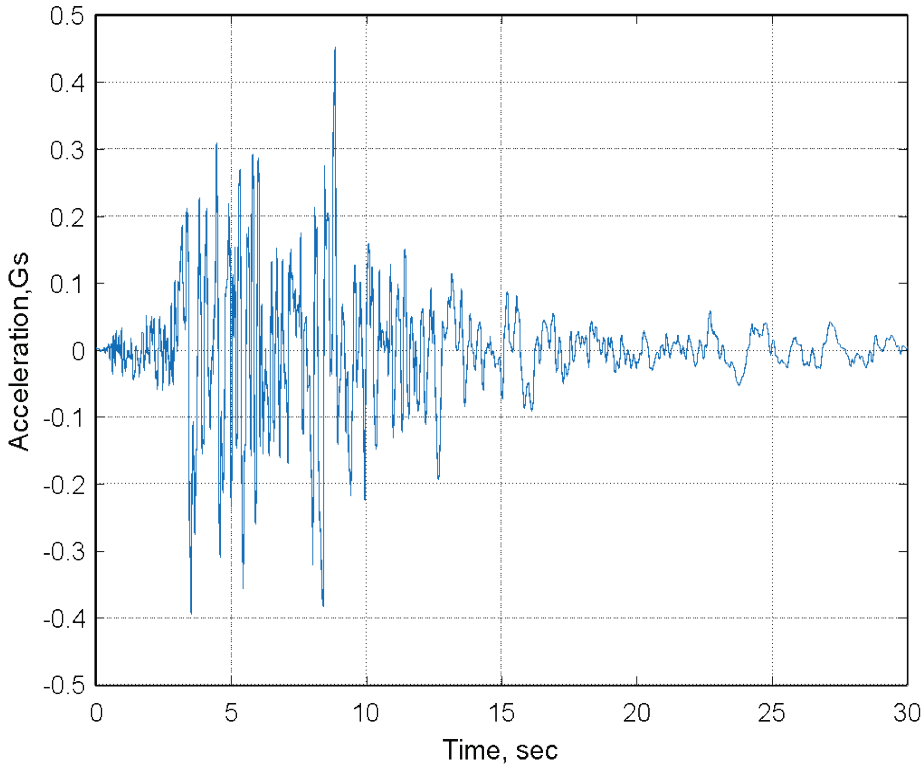


Figure 7-7 Acceleration record for 1994 Northridge Earthquake at the ground level, east-west component.

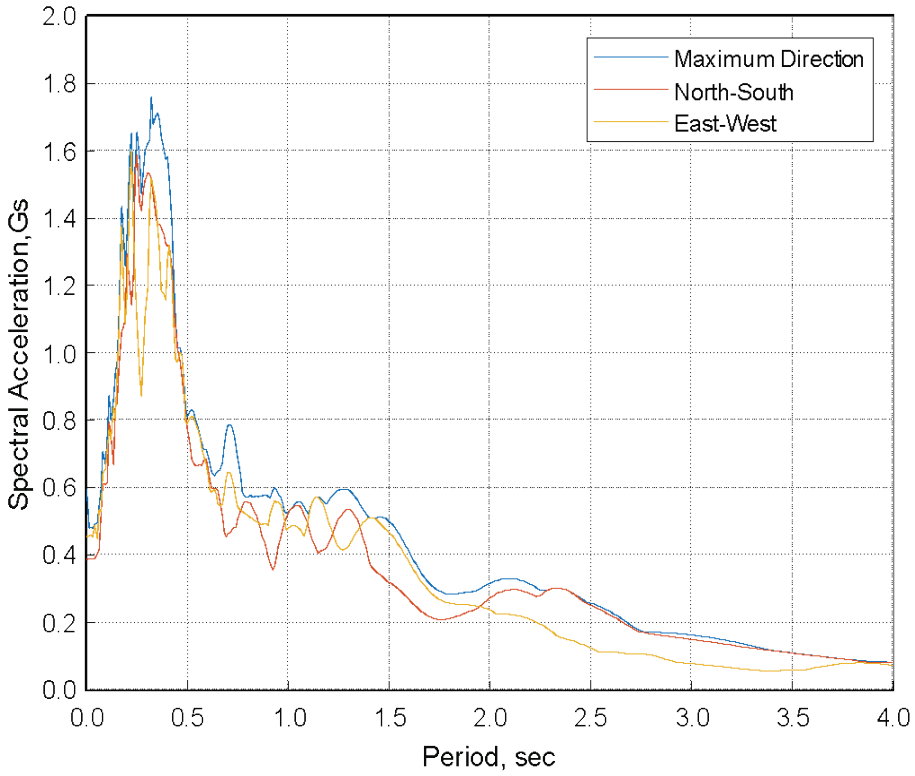


Figure 7-8 1994 Northridge earthquake acceleration spectra for 5% damping.

The acceleration spectra show that energy was highest in the range between 0.05 sec. and 1.5 sec. The displacement spectra (Figure 7-9) show significantly different behavior between the north-south and east-west components. While the east-west component reached the nearly constant displacement region at a period of approximately 1.5 sec., the north-south component showed an increase in displacement from 6 in. to 16 in. between periods of 1.75 sec. and 2.4 sec. Even though the north-south component had a smaller peak ground acceleration, it had greater displacements for periods exceeding 1.94 sec. For reference, Paspuleti (2002) calculated effective periods for the east-west direction of approximately 2.3 sec. at 10 seconds into the earthquake, increasing to approximately 2.7 sec. at 20 seconds into the earthquake. Islam (1996) calculated effective periods in the north-south direction of approximately 2.2 sec. at 10 seconds into the earthquake, and 2.2 sec. at 20 seconds into the earthquake. The first three calculated periods were 1.83 sec., 1.83 sec., and 1.68 sec. for the nonlinear model without infills, and 1.83 sec., 1.72 sec., and 1.46 sec. for the nonlinear model with infills.

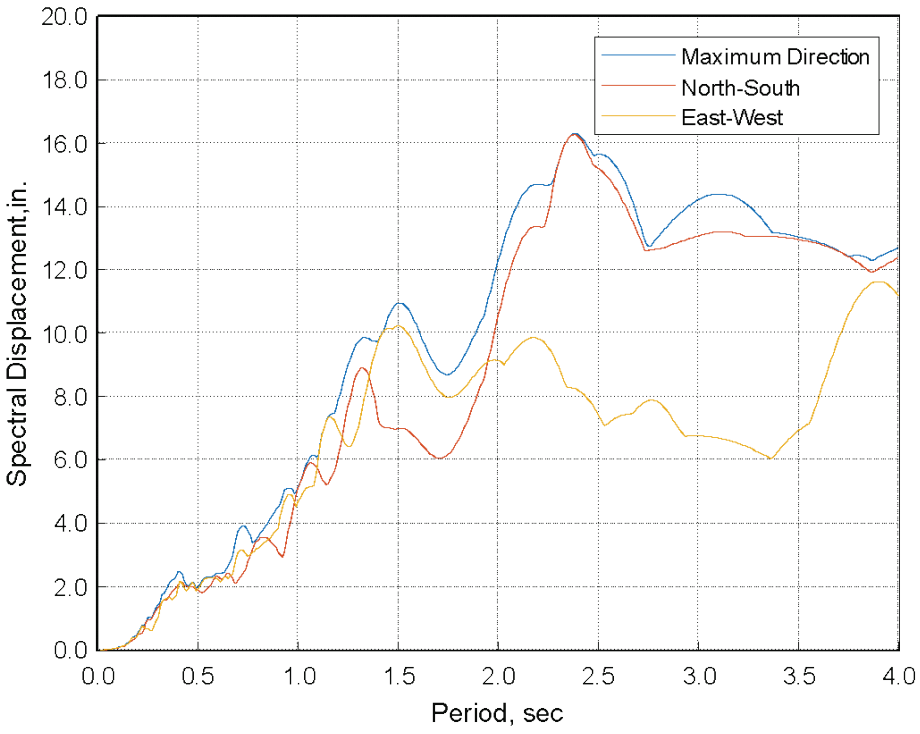


Figure 7-9 1994 Northridge earthquake displacement spectra for 5% damping.

7.2.4 Observed Performance

The 1994 Northridge Earthquake caused severe structural damage concentrated in the fourth and fifth levels of the east-west perimeter frames, where several columns sustained shear failure (Figures 7-10 through 7-13). Trifunac et al. (1999) and Trifunac and Hao (2001) present the results of damage surveys conducted on

This publication is available free of charge from: https://doi.org/10.6028/NIST.GCR.22-917-50

February 4, 1994 and April 19, 1994 following the earthquake. They report structural damage in the form of shear failure of columns and beam-column joints in the exterior frames. Reported damage includes spalling of the concrete cover, buckling of the longitudinal reinforcement, and through cracks that were several inches wide in the columns. Damage to the south exterior frame occurred at six locations on the fifth floor (column lines A-3, 4, 5, 7, 8, and 9) and one at the third floor (column line A-9). Damage to the north frame occurred in the full-height infill masonry walls at the ground floor and at the base of the captive columns at the ground floor in column lines D-2, D-3, and D-4. Damage was also reported at 12 different locations at beam-column joints at the second through fifth floors.

The building sustained minor structural damage and severe nonstructural damage during the 1971 San Fernando Earthquake (Blume and Associates, 1973). Structural damage consisted of a flexural crack in a single beam, located on the north side of the east end of the building, at the ground floor (Blume and Associates, 1973). Cracks were also observed at some column cold joints, near exterior beam soffits. Nonstructural damage was extensive throughout the building, affecting drywall partitions, bathtubs, bathroom tiles, and plumbing fixtures.

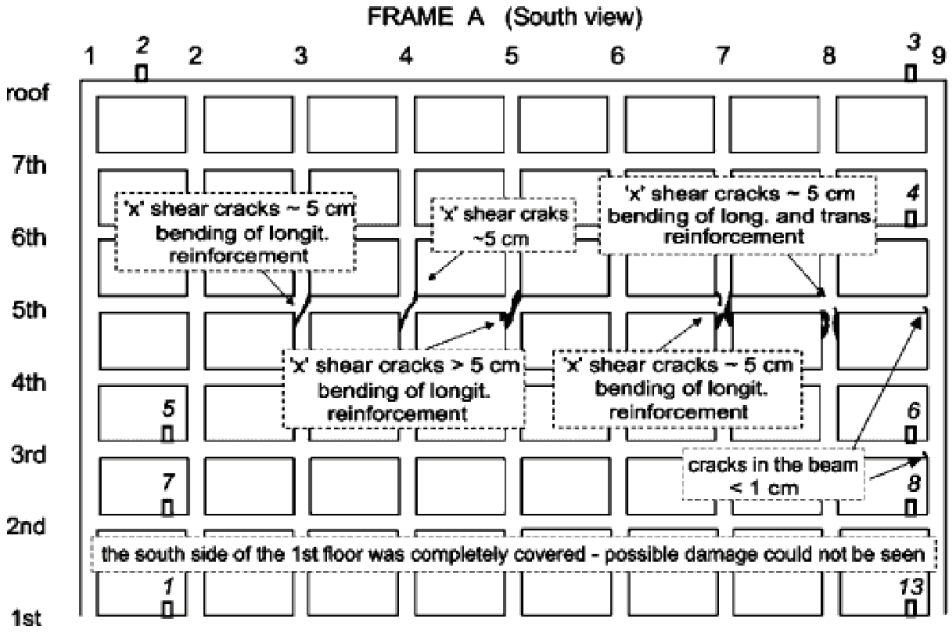


Figure 7-10 Structural damage to south perimeter frame after 1994 Northridge Earthquake (Trifunac et al., 1999).

This publication is available free of charge from: https://doi.org/10.6028/NIST.GCR.22-917-50

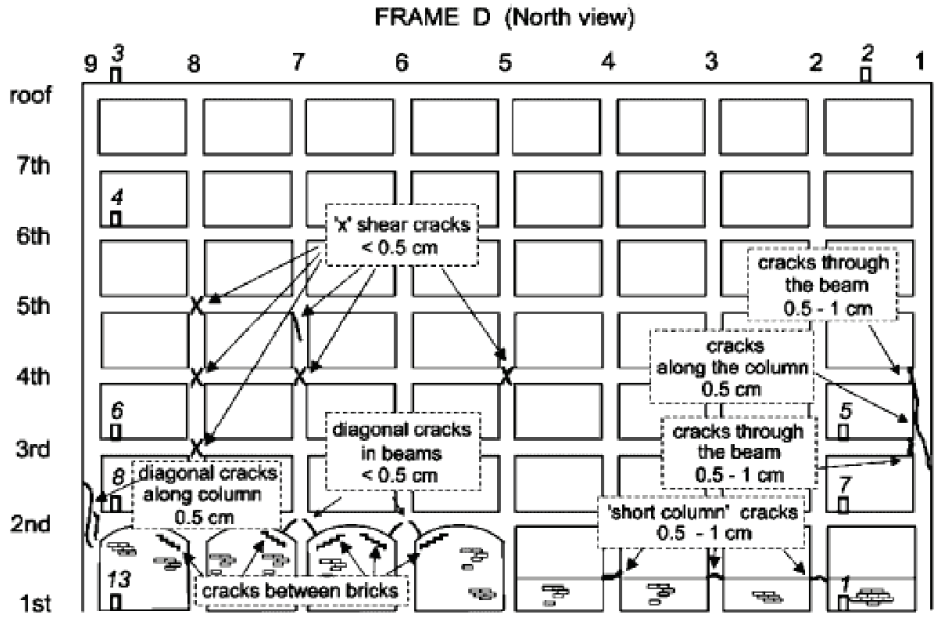


Figure 7-11 Structural damage to north perimeter frame after 1994 Northridge Earthquake (Trifunac et al., 1999).



Figure 7-12 Structural damage to columns of south exterior frame after 1994 Northridge Earthquake (Concrete Coalition, 2019). Braced frames added after the earthquake as temporary lateral support.

This publication is available free of charge from: https://doi.org/10.6028/NIST.GCR.22-917-50



Figure 7-13 Structural damage to fifth floor columns of south exterior frame after 1994 Northridge Earthquake (Naeim et al., 2005). Braced frames added after the earthquake as temporary lateral support.

7.3 Nonlinear Dynamic Procedure

7.3.1 Modeling Approach

A three-dimensional numerical model of the structure was created in OpenSees. The structure was modeled with fixed base and rigid diaphragms at each story. The total mass of each story was divided into 36 small masses, and each small mass was assigned to a master node located at each of the 36 beam-column and slab-column intersections.

Perimeter beams and columns were modeled as elastic beam-column elements with zero-length inelastic rotational springs at both ends, as shown in Figure 7-14. Beam and column elements spanned between joint faces with zero-length rotational springs located at the joint face. Translational degrees of freedom were constrained so the rotational springs and the elastic beam-column elements would have the same displacements. In the elastic range, flexibility of the elastic beam-column element was defined as 10 times the flexibility of the rotational springs, with the combined stiffness of the elastic beam-column element and the spring being equal to the effective stiffness of the corresponding beam or column. In the inelastic range, the flexibility of the inelastic rotational spring was adjusted so the combined stiffness of the elastic beam-column element and the inelastic rotational spring would produce the stiffness of the corresponding beam or column in the inelastic range.

This publication is available free of charge from: https://doi.org/10.6028/NIST.GCR.22-917-50

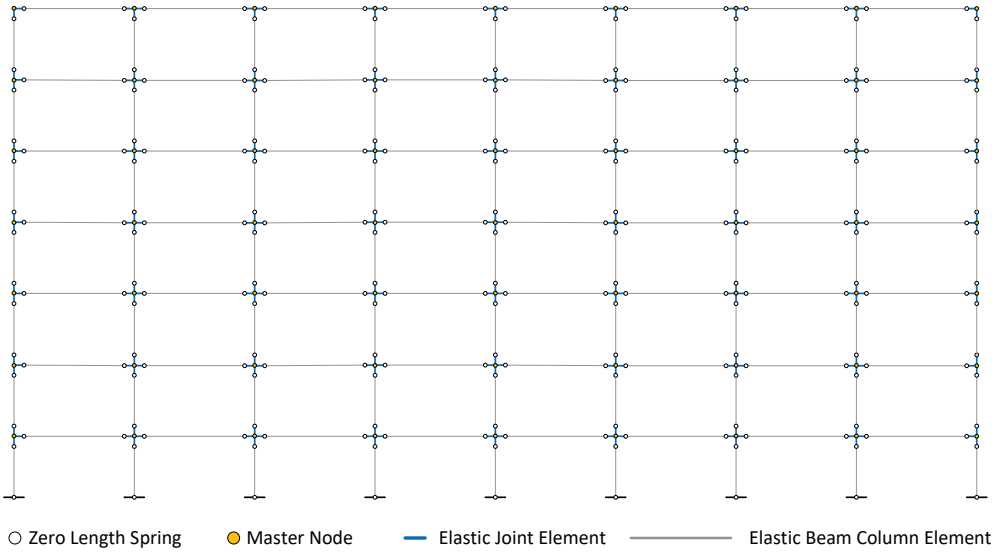


Figure 7-14 Representative east-west frame of OpenSees lumped-plasticity model with nonlinear zero-length rotational springs.

The moment-rotation relationship for the nonlinear rotational springs was defined using the envelope curve and hysteresis rules in the peak-oriented modified Ibarra-Medina-Krawinkler (IMK) material model. The parameters that define the moment-rotation curve are: initial stiffness, K_e, yield moment, M_y, capping moment, M_u, capping deformation, θ_p, post-capping deformation, θ_{pc}, residual moment, M_r, and ultimate deformation, θ_u (Figure 7-15).

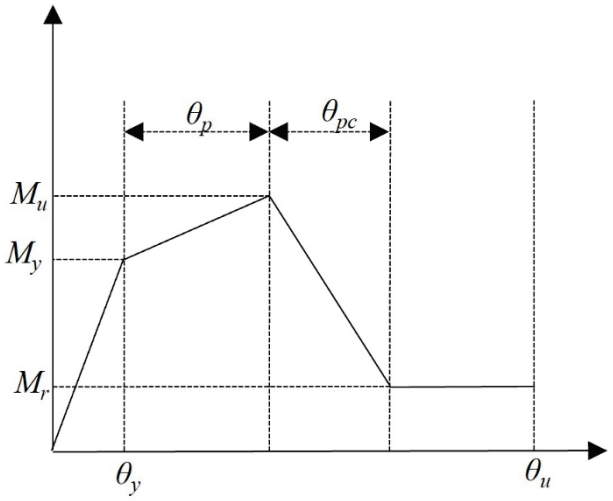


Figure 7-15 Modeling parameters of Ibarra-Krawinkler-Medina model.

Moment capacities of beams and columns were determined based on expected material properties. Columns had symmetric reinforcement, and different beam capacities were specified in the model for the positive and negative moment directions. Computed stiffness and strength values of beam elements included the effect of the slab in the interior side of perimeters beams, with effective flange widths

This publication is available free of charge from: https://doi.org/10.6028/NIST.GCR.22-917-50

computed in accordance with the provisions of ACI 318. Rotation limits for the moment-rotation relationship of beams and columns were defined using modeling parameters *a* and *b* in ASCE 41-17.

Axial load ratios for gravity loads ranged between 1% and 6% of $f_c'A_g$ for corner columns, 2% and 12% for exterior columns, and 4% and 22% for interior columns. All perimeter frame columns were expected to reach flexural yielding with computed V_p to V_n ratios (V_{yE} to V_{ColOE} according to ASCE 41 notation) ranging between 0.60 and 0.98. According to the decision tree in ASCE 41-13, columns with ratios between 0.6 to 1.0 would be expected to fail in shear after yielding of the longitudinal reinforcement (flexure-shear critical), although columns with ratios close to 1.0 have a high likelihood of failing in shear prior to flexural yielding. Interior columns had higher axial loads and higher amounts of longitudinal reinforcement, with V_p to V_n ratios ranging between 0.73 and 1.07. In columns controlled by shear (V_p to V_n ratio greater than or equal to 1.0) the flexural capacity of the rotational springs was reduced to the moment corresponding to the nominal shear capacity, with parameter *a* and *b* values calculated following the provisions of ASCE 41-17.

Provisions for slab-column frames in ASCE 41-17 Section 10.4.4.1 indicate that analytical models of slab-column frames may be created using the effective beam-width model, the equivalent frame model, or a finite element model. In this study, the flexibility of interior frames was calculated based on the effective beam width model where slabs are represented by line elements, and the slab width included in the model is adjusted to account for the flexibility of the slab-column connection. Flexural stiffness of interior frame slab line elements was computed using effective slab width and stiffness factors proposed by Hwang and Moehle (2000). Strength of the line elements of interior frames was calculated using the reinforcement in the column strip, both in the negative and positive directions. The modeling of line elements was similar to that of beam elements, and elastic beam-column elements with zero-length rotational springs were placed at each end. Similar to the case of beam elements, zero-length springs were defined using the peak oriented modified Ibarra-Medina-Krawinkler material model.

Deformation limits of the moment-rotation relationship of the zero-length springs were defined using modeling parameters for slab-column connections in ASCE 41-17. Slab column connections had ratios of gravity load demand to punching shear capacity (V_g/V_o) ranging between 0.22 and 0.32. Development length of the bottom slab reinforcement in the column strip specified in the plans was not clearly visible, but it appears that half the bottom slab reinforcement was extended 9 in. or approximately 14 bar diameters beyond the center of the column. Analyses in which this reinforcement was included in strength calculations resulted in more accurate estimates of displacement than models in which the contribution of the bottom slab reinforcement was neglected (Suwal, 2018). This assumption also affected the

This publication is available free of charge from: https://doi.org/10.6028/NIST.GCR.22-917-50

classification of the slab-column connections, making the connections conforming or non-conforming depending on whether the reinforcement was assumed to be fully anchored or not. For this study, it was assumed that the reinforcement was fully anchored in the interest of obtaining more accurate estimates of slab strength and higher demands on interior columns, although that might have caused deformation capacities of slab column connections to be unconservative.

Masonry infill walls were only present in the first four bays of the first floor in the north perimeter frame (Figure 7-12). They were modeled as compression-only truss elements following the provisions in ASCE 41-17 Sections 10.6 and 11.4. Because masonry properties were not specified in the plans, representative values for clay masonry listed in TMS 402 of f'_{me} = 1000 psi and E_m = 700 f'_{me} were adopted. Masonry walls were classified as relatively flexible panels and the surrounding frames as ductile according to the provisions of ASCE 41. Shear strength was calculated according to ASCE 41-17 Equation 11-33 using a cohesion value calculated with the provisions in TMS 402 for panels with no axial stress. The deformation limits of the panels were defined based on ASCE 41-17 Tables 11.10 and 11.11.

Beam-column joints were modeled using linear elastic elements. The presence of reinforcement in the joints is not legible in the copy of the plans available, so it was not possible to determine with certainty if there was any reinforcement in the joints. A typical column detail in the report by Blume and Associates (1973) shows a reinforcing bar at the center of the joint, which would be sufficient to classify the joint as conforming according to the provisions in ASCE 41. Interior joint shear demands in perimeter frames were calculated for representative joints in all stories and found to range between approximately $7\sqrt{f'_{cE}}$ and $15\sqrt{f'_{cE}}$, which exceeds the capacity of non-compliant joints ($12\sqrt{f'_{cE}}$) but is below the capacity of compliant joints ($20\sqrt{f'_{cE}}$). Although damage surveys show that there were shear cracks in the joints (Figure 7-16), the width of the observed shear cracks in the joints was small, and distress in the columns was severe (Figure 7-17). Columns had observed crack widths on the order of inches (Trifunac et al., 1999). Based on the information available, joints were modeled as compliant elements with a capacity of $20\sqrt{f'_{cE}}$ using elastic elements to include joint flexibility. This assumption was made to reduce computational cost, which was very significant for the model, particularly for the fragility analysis presented in Section 7.4. It was found to provide a more accurate building response for the 1994 Northridge Earthquake than the models shown in ASCE 41-17 Figure 10-2c, 10-2d, and 10-2e (Suwal, 2018).

This publication is available free of charge from: https://doi.org/10.6028/NIST.GCR.22-917-50



Figure 7-16 Shear distress in beam-column joint (Trifunac et al., 1999).



Figure 7-17 Shear distress in Column A5, fifth floor (Trifunac et al., 1999).

This publication is available free of charge from: https://doi.org/10.6028/NIST.GCR.22-917-50

Nonlinear analyses were performed using 2% and 5% Rayleigh damping anchored at the fundamental first and fourth mode periods of the building, with different combinations of mass-proportional and stiffness-proportional damping (Suwal, 2018). Of all combinations, models with 5% Rayleigh damping with mass- and stiffness-proportional damping provided the best estimates of displacement, although the difference in the response history was not very significant. This approach, intended to improve accuracy, is consistent with ASCE 41-17 Section 7.2.3.6 that stipulates that for nonlinear dynamic analyses 3% viscous damping should be used, and that higher damping ratios shall be permitted if substantiated through analyses. The analysis accounted for large deformation effects by using the P-delta transformation for all column elements.

7.3.2 Global Performance: Model vs. Observation

The simulated and recorded performance of the building are compared in this section. All response quantities presented correspond to the nonlinear model that included the brick masonry walls.

Figures 7-18 and 19 show the maximum calculated acceleration at each floor level and maximum recorded accelerations with the instrument array. The instrument locations shown in Figure 7-5 were chosen because they correspond to direct measurements and do not require interpolation and extrapolation based on measurements from multiple instruments.

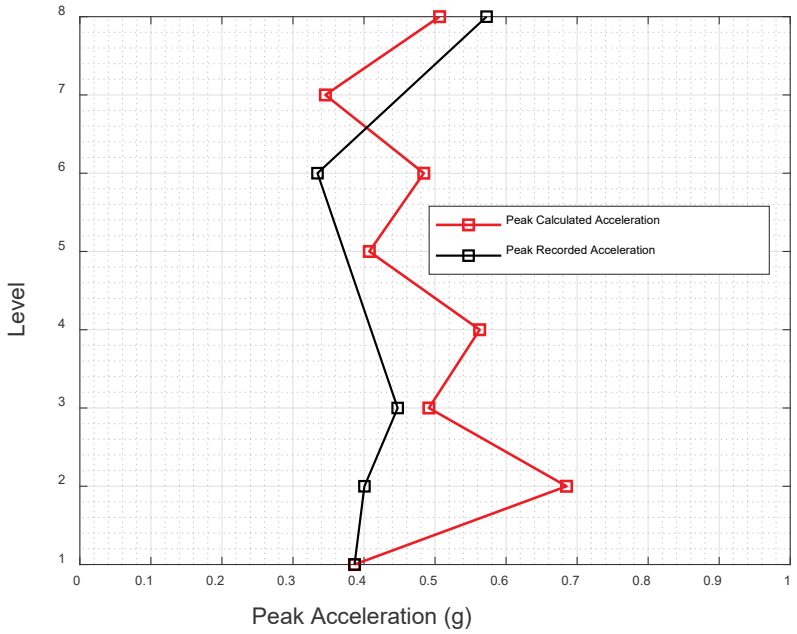


Figure 7-18 NDP: Maximum accelerations at each floor level in the north-south direction.

This publication is available free of charge from: https://doi.org/10.6028/NIST.GCR.22-917-50

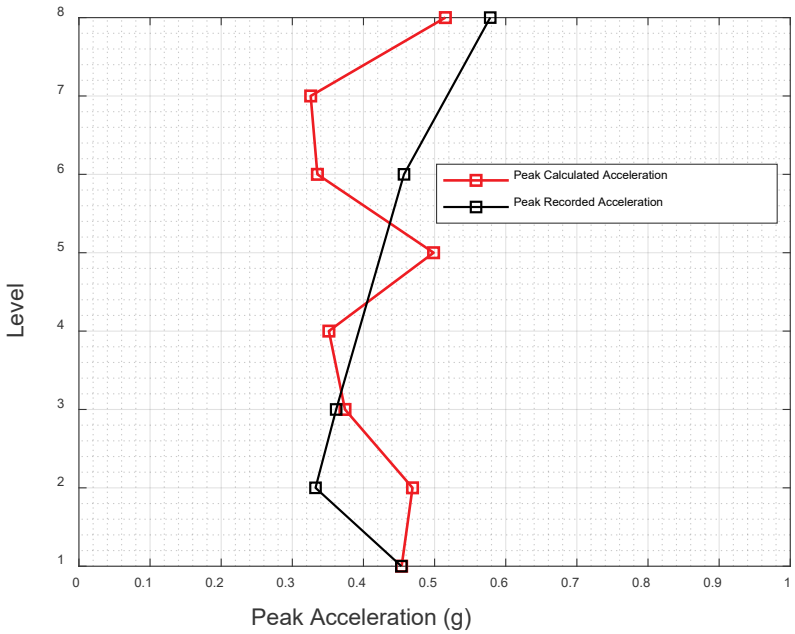


Figure 7-19 NDP: Maximum accelerations at each floor level in the east-west direction.

Accelerations in the north-south direction correspond approximately to the location of instruments 1, 2, 5, and 7. Accelerations in the east-west direction correspond to instruments 9, 10, 11, 12, and 16. Figures 7-20 through 7-24 show acceleration time histories at selected instrument locations. In both directions, calculated peak accelerations (Figures 7-18 and 7-19) were most accurate at the roof and third floor levels, and least accurate at the second floor (Figure 7-24). The comparison shows that the model provided accurate estimates of acceleration at the upper stories with the exception of the sixth floor, where peak values were off by approximately 35%, and the lower two stories of the building that were affected by the assumption of a fixed foundation. Furthermore, the analysis was performed using the acceleration record from a single instrument instead of multiple support excitation, which affected the torsional response of the building. Like the assumption of a fixed foundation, this source of error is expected to have a greater effect on the second story response of the model.

This publication is available free of charge from: https://doi.org/10.6028/NIST.GCR.22-917-50

This publication is available free of charge from: https://doi.org/10.6028/NIST.GCR.22-917-50

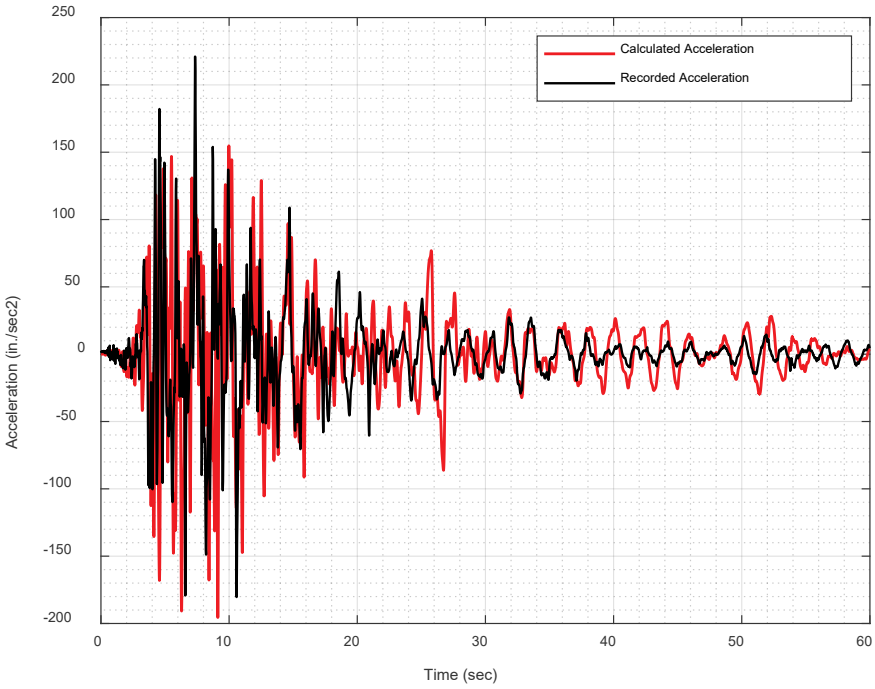


Figure 7-20 NDP: Acceleration time history for instrument 3, north-south direction at the roof.

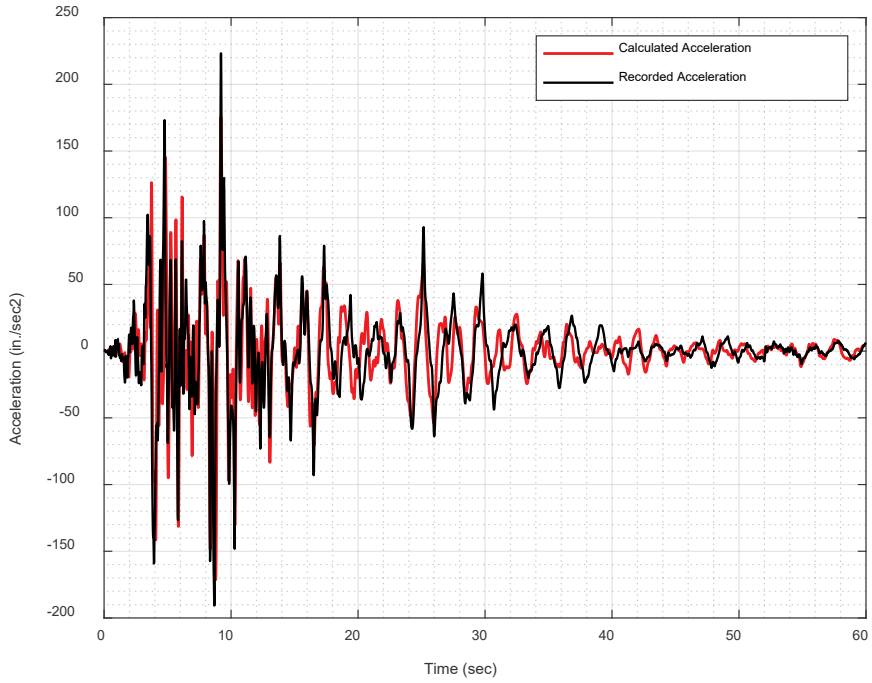


Figure 7-21 NDP: Acceleration time history for instrument 9, east-west direction at the roof.

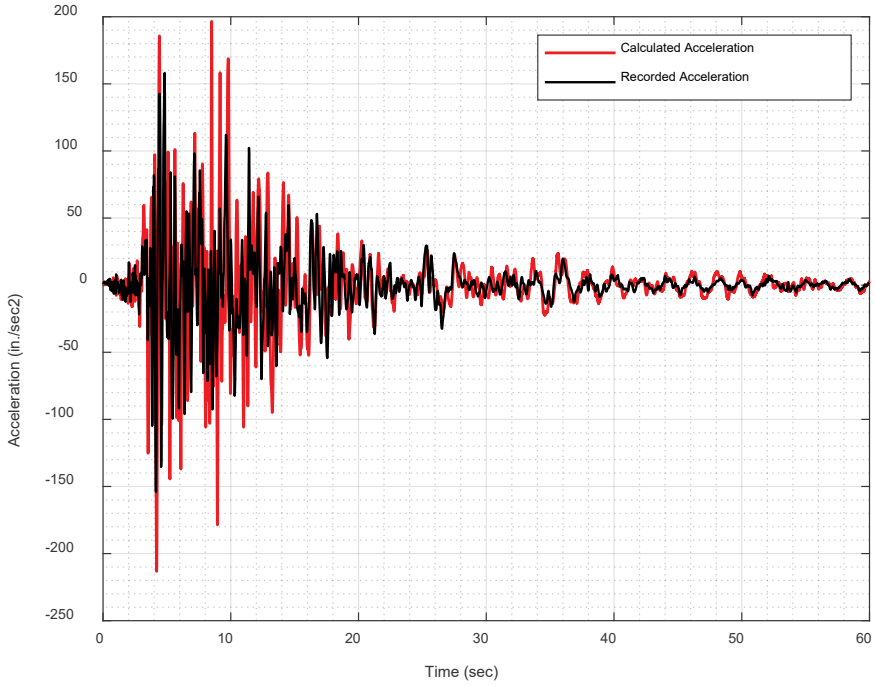


Figure 7-22 NDP: Acceleration time history for instrument 5, north-south direction at the third floor.

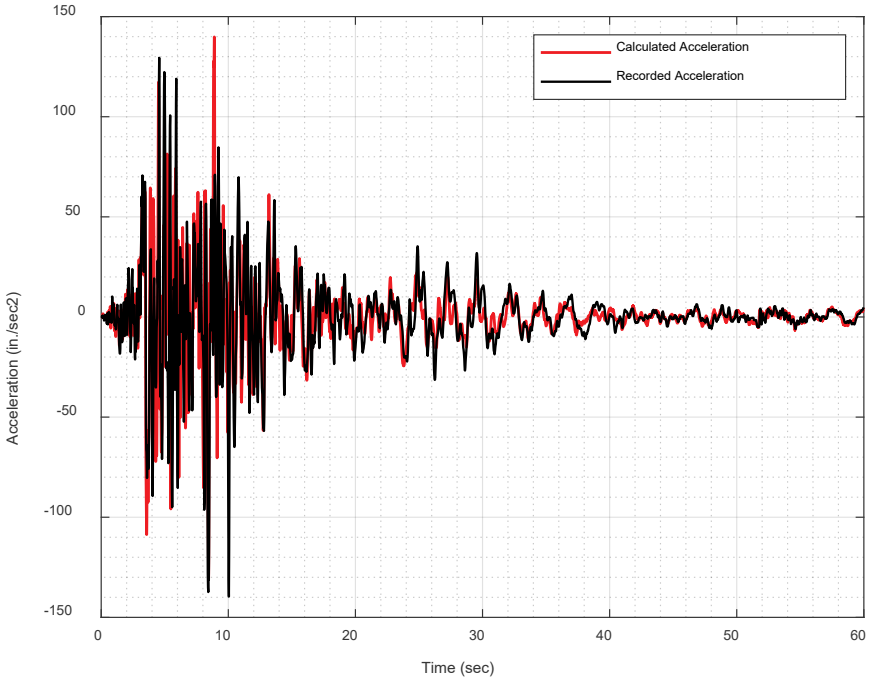


Figure 7-23 NDP: Acceleration time history for instrument 11, east-west direction at the third floor.

This publication is available free of charge from: https://doi.org/10.6028/NIST.GCR.22-917-50

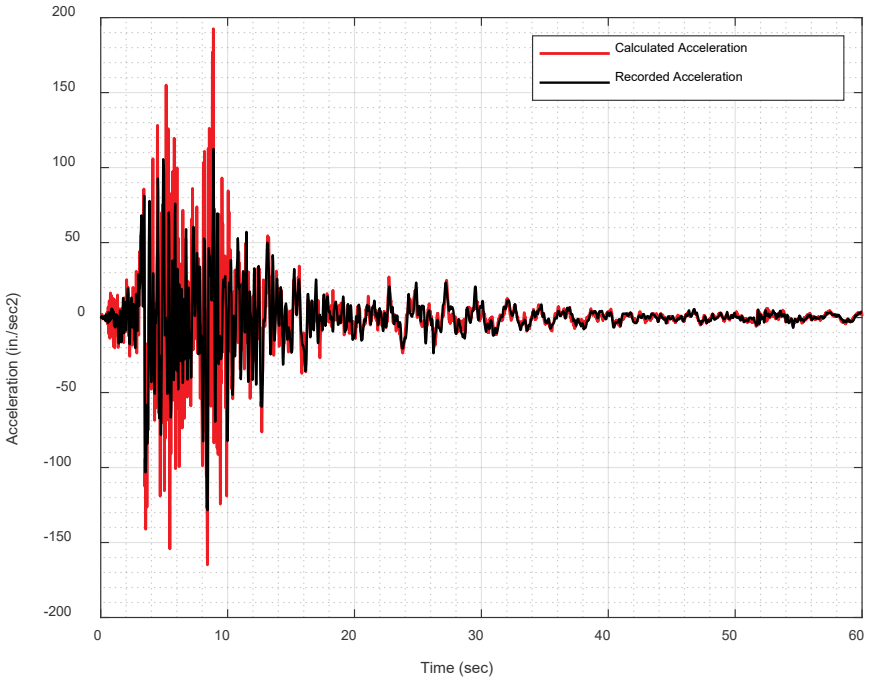


Figure 7-24 NDP: Acceleration time history for instrument 12, east-west direction at the second floor.

Calculated and measured roof displacement time histories are presented in Figures 7-25 and 7-26. The instrumentation array did not include any sensors for direct measurement of displacement, so recorded values in the figures correspond to those reported by the California Strong Motion Instrumentation Program for instruments 9 and 2 that were obtained by integrating and filtering the acceleration records. Calculated values correspond to the three-dimensional model of the building including compression-only truss elements in the first floor at bays with masonry infills. The figures show good agreement between measured and calculated values, both in terms of period and amplitude.

Calculated maximum drift ratio over the height of the building is shown in Figures 7-27 and 7-28 for models with and without masonry infills, for nodes at the northwest corner of the building. Measured values in the figures were inferred from processed displacement records at the only two locations instrumented at consecutive floors. In the north-south direction (Figure 7-27) drift ratios are slightly higher for the model with masonry infills, which is attributed to torsional effects, but the difference was not significant. Both models with and without masonry walls had measured-to-calculated ratios of 0.80 and 0.86, at the first and second floors, respectively. In the east-west direction (Figure 7-28), the effect of the stiffness of the infill masonry walls on the maximum drift ratio was most noticeable in the first and second stories, and not very significant at higher levels. Measured-to-calculated ratios for the model with infills were 2.22 and 1.23 at the first and second floors, respectively. For the

This publication is available free of charge from: https://doi.org/10.6028/NIST.GCR.22-917-50

model without infills, measured-to-calculated ratios were 0.67 and 1.02, at the first and second floors, respectively. Those results show that model without walls had more accurate estimates of drift ratio in the lower two stories of the building.

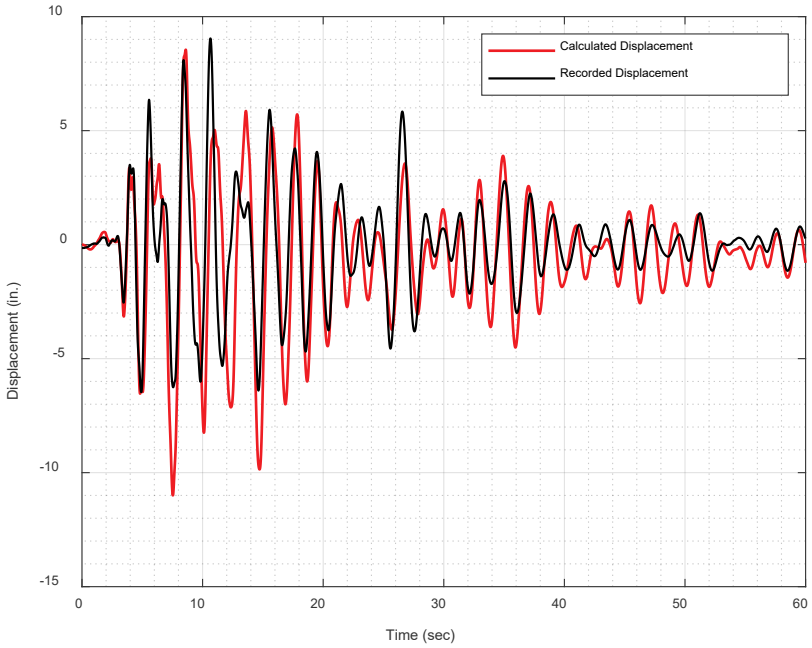


Figure 7-25 NDP: Displacement time history for instrument 2, north-south direction at the roof.

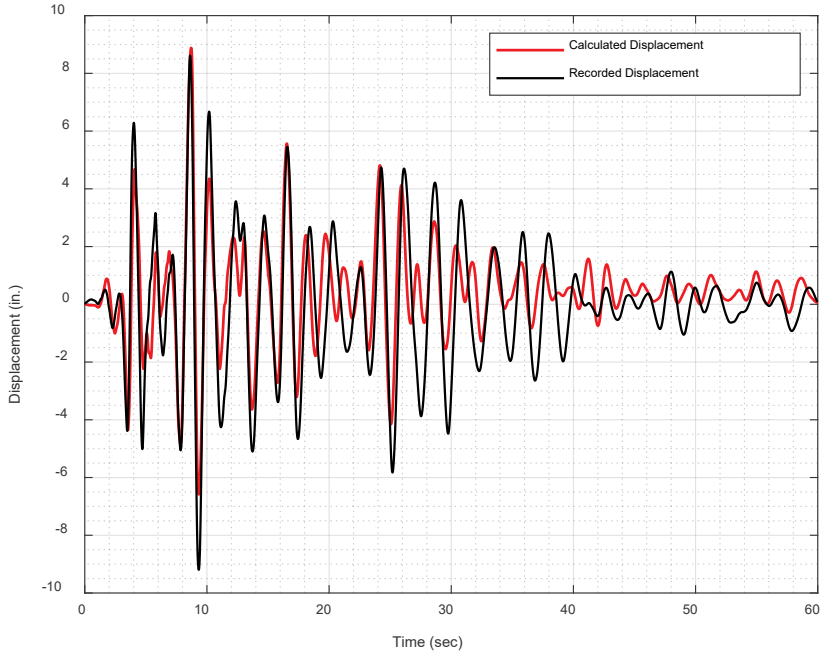


Figure 7-26 NDP: Displacement time history for instrument 2, north-south direction at the roof.

This publication is available free of charge from: https://doi.org/10.6028/NIST.GCR.22-917-50

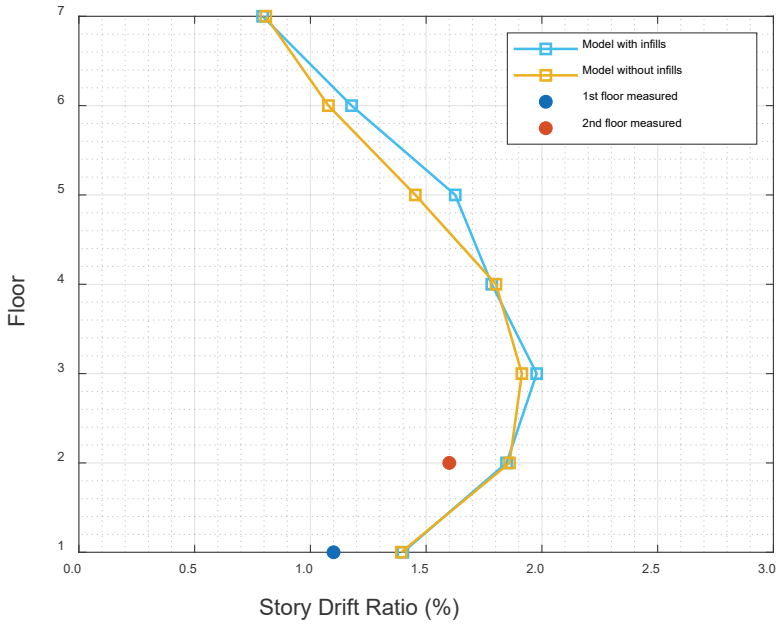


Figure 7-27 NDP: Maximum drift ratio at each story, north-south direction.

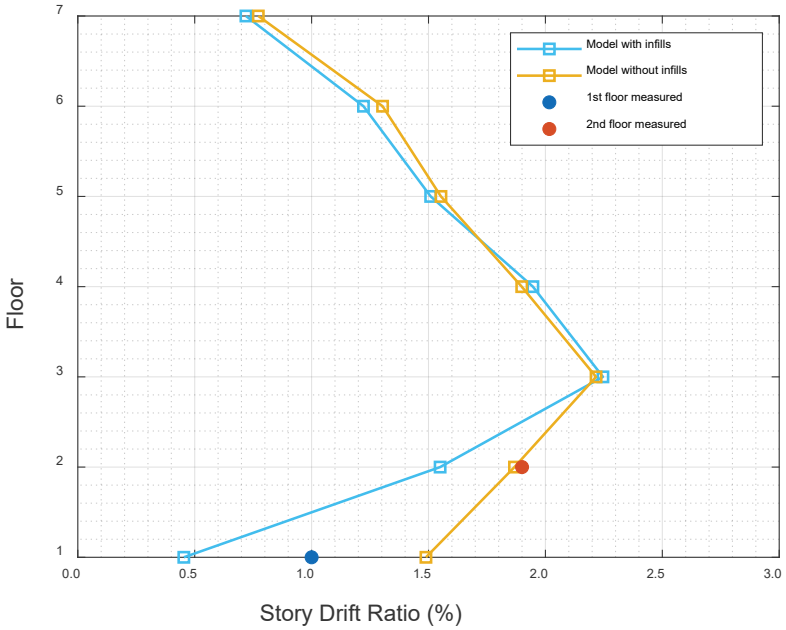


Figure 7-28 NDP: Maximum drift ratio at each story, east-west direction.

Calculated base shear histories are presented in Figures 7-29 and 7-30. Maximum base shear demand in the north-south direction was 1,677 kips, which corresponds to 15.6% of the building weight. In the east-west direction, the maximum calculated base shear was 1,900 kips, which corresponded to 17.7% of the building weight. Base shear coefficients were similar to those calculated by Suwal (2018) using pushover analyses of two-dimensional models. Several researchers have published studies with two-dimensional models of the frames in the east-west direction, where

This publication is available free of charge from: https://doi.org/10.6028/NIST.GCR.22-917-50

the heaviest damage occurred. Paspuleti (2002) reported values of base shears in the east-west direction of 12%, 10%, and 10% of the building weight for uniform, linear, and FEMA 356 (FEMA, 2000) load distributions. Krawinkler (2005) reported base shear strengths of 10% and 15% of the weight for two different models using the FEMA 356 load distribution. Barin and Pincheira (2002) reported a base shear strength of 15% of the building weight using a triangular load distribution.

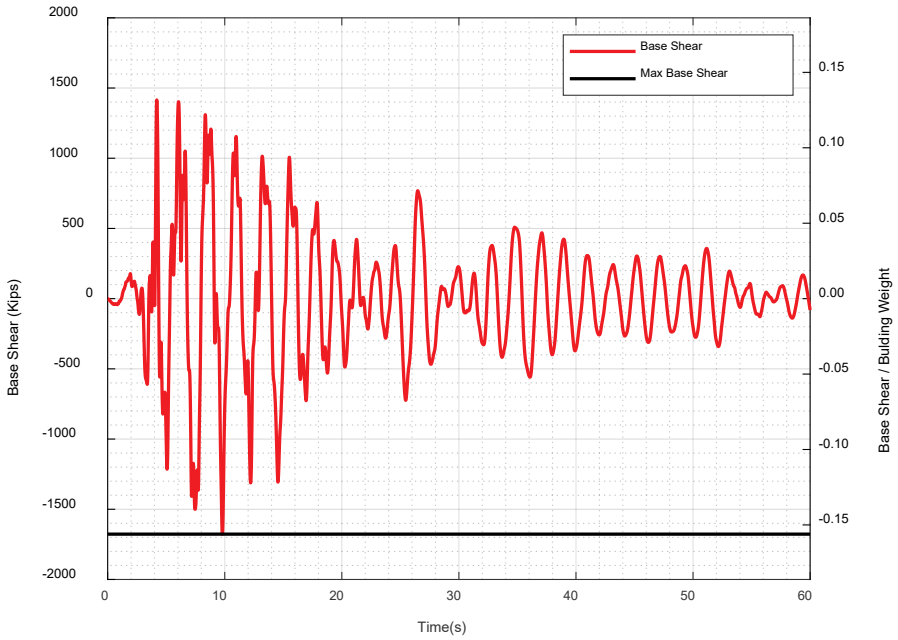


Figure 7-29 NDP: Base shear history in the north-south direction.

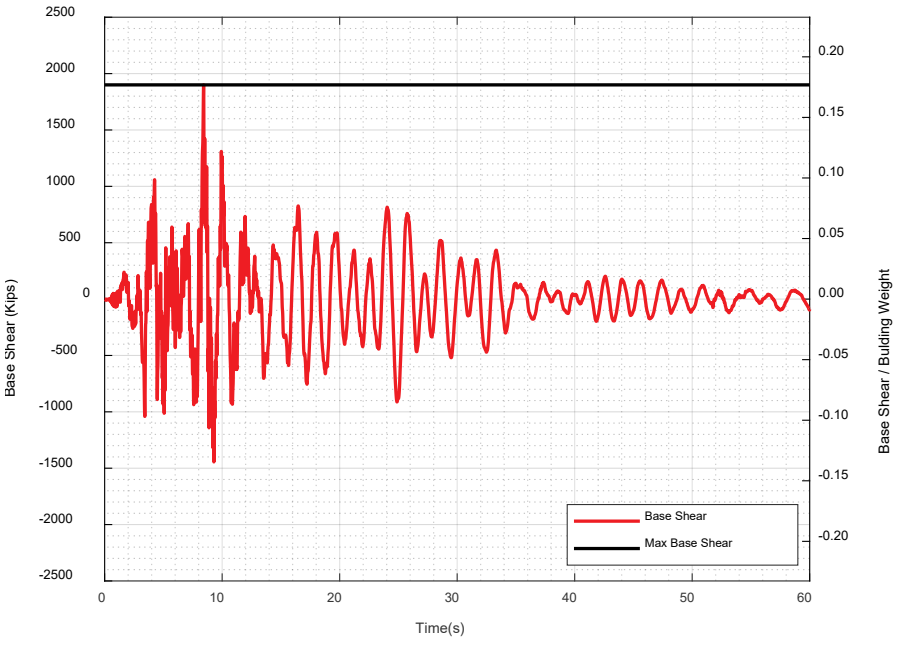


Figure 7-30 NDP: Base shear history in the east-west direction.

This publication is available free of charge from: https://doi.org/10.6028/NIST.GCR.22-917-50

The higher base shear strengths calculated with the models in this study are attributed to the inclusion of continuity reinforcement in the strength of the slab-column frames and differences in the effective width of the slabs with respect to other studies.

Calculated accelerations and displacements in Figures 7-18 to 26 show that the numerical model of the building reproduced measured and inferred values accurately at levels above the first two stories.

Calculated drift ratios using the nonlinear model were highest between the third and fourth floors, both for the east-west and north-south directions. In the east-west direction, calculated maximum drift ratios between the second and third, third and fourth, and fourth and fifth floors ranged approximately between 1.8 and 2.0%. In the north-south direction, maximum calculated drift ratios between the second and third floor and between the fourth and fifth floor were approximately 1.9%. The calculated drift ratio in the north-south direction was largest between the third and fourth floors where it reached a maximum of 2.2%.

Several researchers that have studied this building have relied on direct comparisons between interstory drift ratios and estimates of deformation capacity of the columns. For exterior frame columns between the second and fifth floors, chord rotations at initiation of loss of lateral load capacity ($\theta_y + a$) calculated with the ASCE 41-17 provisions ranged between 2.5 and 2.8%, exceeding drift ratios calculated with the nonlinear model. For interior frame columns between the second and fifth floors, chord rotations at initiation of loss of lateral load capacity calculated with the ASCE 41-17 provisions were approximately 1.9%, lower than maximum drift ratios calculated with the nonlinear model.

The observed damage pattern in the building showed severe shear distress in columns of exterior frames (Figures 7-11, 7-12 and 7-17). Damage reports from the 1994 Northridge Earthquake (Trifunac et al., 1999; Trifunac and Hao, 2001) do not make any reference to damage to interior columns or slab-column connections, and they describe limited damage to beams.

Observed damage was most severe in the fourth and fifth stories of the east-west frame, which corresponded to stories where calculated drift ratios were highest. If drift ratio were used as a global damage indicator in the east-west direction, it would correctly identify the exterior columns as likely to experience shear failure, but the same criterion would incorrectly identify interior columns as likely to experience shear failure as well. The main difference between the two is that exterior columns frame into stronger and stiffer spandrel beams while interior columns frame into more flexible slab strips, so rotation demands are significantly different.

Calculated maximum drift ratios were higher for the north-south direction than the east-west direction, although there was no damage reported in columns of the north-

This publication is available free of charge from: https://doi.org/10.6028/NIST.GCR.22-917-50

south exterior frames (Trifunac et al., 1999; Trifunac and Hao, 2001). Damage surveys after the 1971 San Fernando (Blume and Associates, 1973) and 1994 Northridge (Trifunac et al., 1999; Trifunac and Hao, 2001) earthquakes documented substantial nonstructural damage in the interior of the building. Because there was a greater number of partition walls oriented in the north-south direction, it is likely nonstructural elements helped dissipate energy and lower deformation demands in the columns, protecting them from structural damage. The models evaluated in this study did not include internal partitions, so they cannot capture this effect.

The observed damage pattern indicates that the building was near collapse due to axial failure of exterior frame columns. Calculated drift ratios indicate that this was a plausible failure mechanism, although interior columns and slab-column connections could have been also under severe distress. A more detailed analysis of estimates of damage in all building components is presented in the next section.

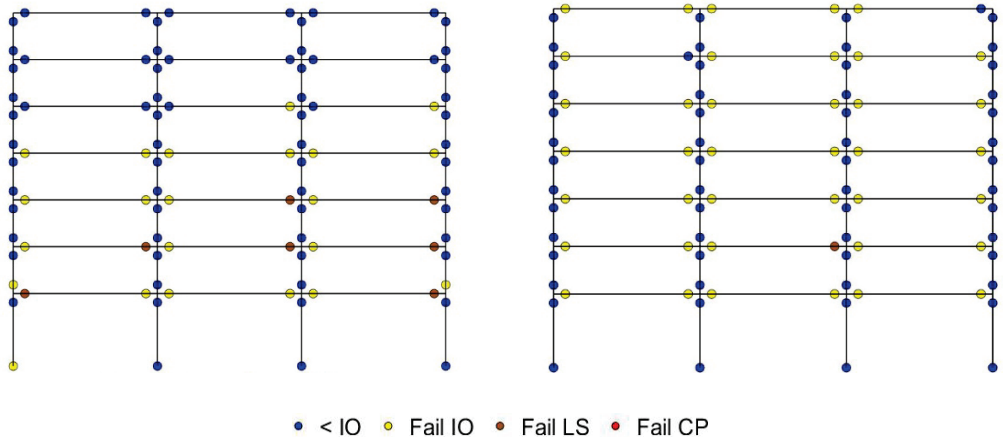
7.3.3 Component Performance: Model vs. Observation

This building had several types of structural components susceptible to severe damage during strong earthquakes due to its structural configuration and detailing. This section describes the calculated distribution of nonlinear deformations among building components for the model including brick walls and the implications of modeling provisions in ASCE 41-17 on that distribution. Inelastic deformations in structural components depend on modeling parameters, and although numerical models may be capable of simulating global response accurately, in this building the distribution of inelastic deformations between elements is heavily influenced by parameters such as post-yield slope and rotation at initiation of loss of lateral load capacity ($\theta_y + a$).

Calculated demands in beam-column joints and infill panels showed that these members remained in the linear range, so the results in this section focus on beam, column, and slab-column connections, all of which were modeled using nonlinear rotational springs. Rotational spring performance levels in the north and west perimeter frames and their adjacent interior frames are shown in Figures 7-31 and 7-32, where blue dots represent calculated rotations below Immediate Occupancy (IO) performance level, yellow dots represent calculated rotations between IO and Life Safety (LS) performance levels, orange dots represent calculated rotations between LS and Collapse Prevention (CP) performance levels, and red dots represent rotations exceeding CP performance level. None of the springs in these frames exceed the Collapse Prevention (CP) performance level. Figures 7-31 and 7-32 show that calculated column deformations were low, and that inelastic rotations concentrated in beam elements. This deformation pattern is consistent with a structure with strong columns and weak beams, which is in fact the case for the study building (in lower stories column-to-beam flexural capacity ratios were as high as

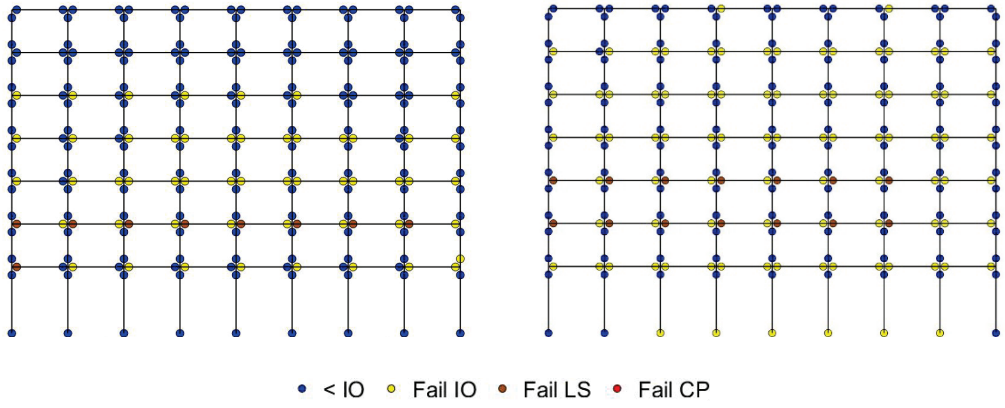
This publication is available free of charge from: https://doi.org/10.6028/NIST.GCR.22-917-50

1.2). The damage pattern in the model based on calculated deformations was significantly different from the damage that was observed in the building, where significant damage to the columns occurred between the fourth and fifth stories (Figures 7-10 to 7-13, and Figure 7-17). A possible explanation for the difference is that beam axial forces, neglected in the analyses, could have increased beam flexural strength significantly, reducing column-to-beam flexural capacity ratios and increasing inelastic rotation demands in columns.



(a) Exterior Frame (b) Interior Frame

Figure 7-31 NDP: Calculated performance level for rotational springs in north-south frames (West exterior frame on the left and adjacent interior frame on the right) for Northridge Earthquake.



(a) Exterior Frame (b) Interior Frame

Figure 7-32 NDP: Calculated performance level for rotational springs in east-west frames (exterior north frame on the left and adjacent interior frame on the right) for Northridge Earthquake.

The level of damage from analysis was also established by comparing inelastic rotations at hinge locations, $\theta_{inelastic}$, with the corresponding modeling parameter *a* in ASCE 41-17 that is indicative of the beginning of lateral strength loss. Members in which the inelastic rotation exceeded parameter *a* were considered to have sustained severe damage according to the nonlinear analysis, while members in which the

This publication is available free of charge from: https://doi.org/10.6028/NIST.GCR.22-917-50

inelastic rotation was lower than parameter *a* were considered to have sustained moderate damage.

Inelastic rotations presented in Figures 7-33 to 7-36 were extracted from rotational springs. Circle diameters at hinge locations are proportional to the ratio of $\theta_{inelastic}$ to modeling parameter *a*. Circle color is also an indicative of the ratio of $\theta_{inelastic}$ to modeling parameter *a*, with red circles indicating locations where $\theta_{inelastic}$ exceeded modeling parameter *a*. Ratios of calculated inelastic rotations to modeling parameter *a* presented in Figures 7-33 through 7-36 are consistent with the calculated damage patterns in Figures 7-31 and 32, which showed that computed column deformations were small, with most of the column elements not exceeding yield. Calculated inelastic rotations exceeded parameter *a* for a few beams in the lower stories of the exterior north-south frame (Figure 7-33) and the interior east-west frame (Figure 7-36), where no severe damage was reported.

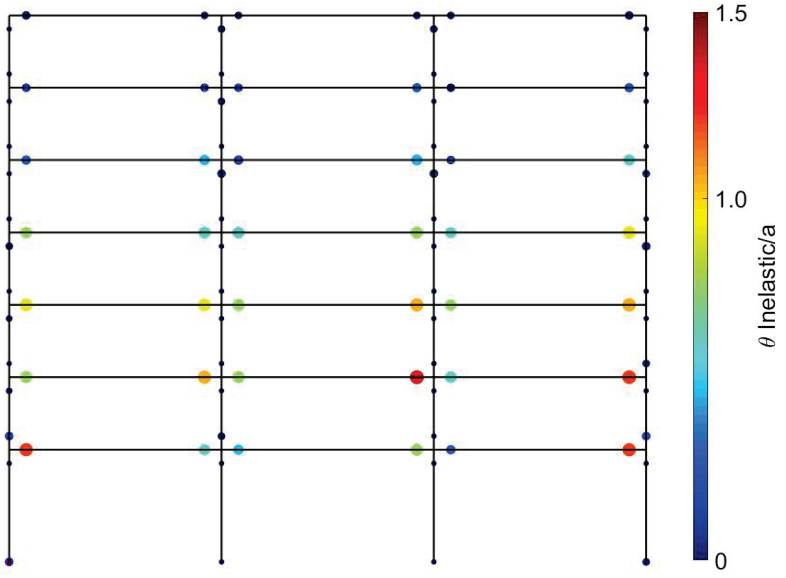


Figure 7-33 NDP: Ratio of maximum beam and column rotation to ASCE 41 parameter *a* for exterior frame oriented in the north-south direction.

This publication is available free of charge from: https://doi.org/10.6028/NIST.GCR.22-917-50

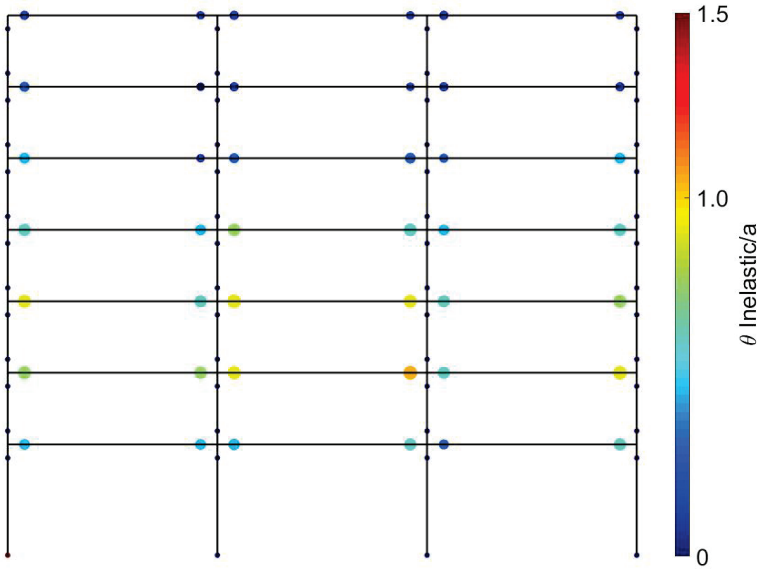


Figure 7-34 NDP: Ratio of maximum beam and column rotation to ASCE 41 parameter *a* for the interior frame oriented in the north-south direction.

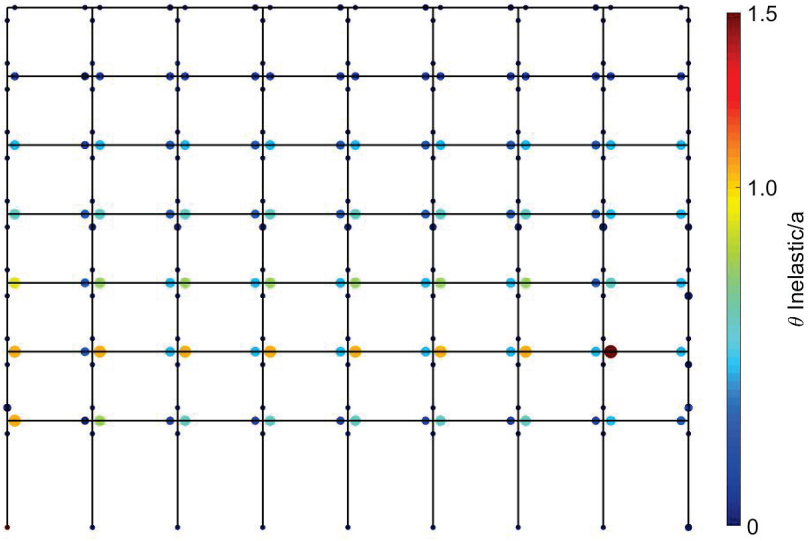


Figure 7-35 NDP: Ratio of maximum beam and column rotation to ASCE 41 parameter *a* for the exterior frame oriented in the east-west direction.

This publication is available free of charge from: https://doi.org/10.6028/NIST.GCR.22-917-50

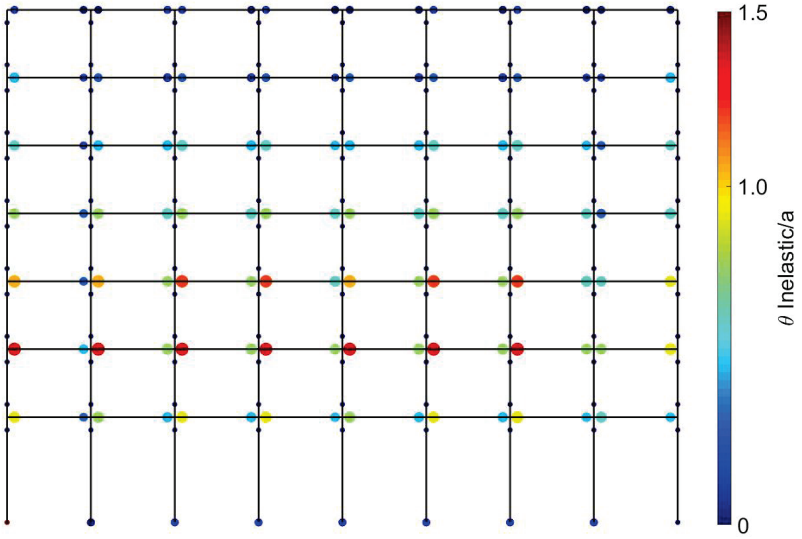


Figure 7-36 NDP: Ratio of maximum beam and column rotation to ASCE 41 parameter *a* for the interior frame oriented in the east-west direction.

Damage characterization in terms of modeling parameter *a* was consistent with the damage characterization in terms of acceptance criteria and show that for the level of intensity of the 1994 Northridge Earthquake records the numerical model of the building using modeling parameters in ASCE 41-17 resulted in large inelastic deformation in beam elements and slab-column connections and relatively low deformation demands in column elements.

Calculated rotations in exterior beam elements, as large as ASCE 41-17 rotations associated with loss of lateral load capacity, were not consistent with documented damage in the exterior frames. This shows that there were differences in the manner in which inelastic deformations were distributed between beams and columns between the nonlinear model and the building system. The difference is also caused by the fact that modeling parameters and acceptance criteria for beams and slab-column connections are the same adopted in FEMA 356, and correspond to safe lower bound values based on engineering judgement. In the case of columns, modeling parameters and acceptance criteria have been modified two times since the publication of FEMA 356, and current values were calibrated to be representative of the mean response of column subassemblies tested in the laboratory.

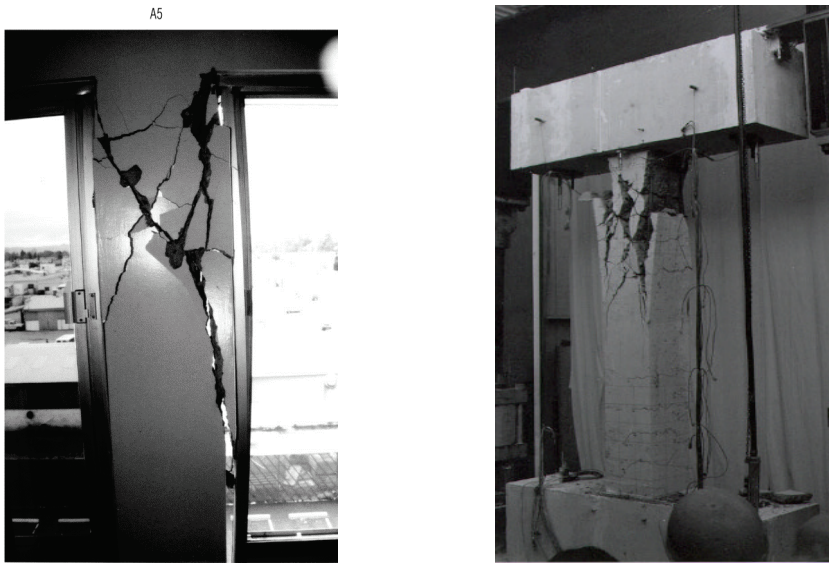
In the case of slab-column connections of the east-west frame, calculated inelastic rotations were on the order of 50% higher than ASCE 41 parameter *a* (Figure 7-36), which is indicative of severe distress. Although there is no documented damage at interior slab-column connections, this type of damage is difficult to inspect because connections are covered by floor finishes and ceilings. Also, as in the case of beams, modeling parameters and acceptance criteria for slab-column connections have not been updated since FEMA 356.

This publication is available free of charge from: https://doi.org/10.6028/NIST.GCR.22-917-50

7.3.3.1 Column Performance: Model vs. Observation vs. Test Data

The calculated response from the ASCE 41 numerical model is compared with test data for a heavily damaged column in the fifth story: Column A5 of the south frame in the fifth floor (Figure 7-11).

A comparison between Column A5 and a similarly configured column (Specimen 3CLH18) tested in the laboratory by Lynn (1999) is presented in Figure 7-37. Properties for the two columns are presented in Table 7-3, and the calculated response of the OpenSees model is presented in Figure 7-38.



(a) (b)

Figure 7-37 Columns (a) A5 at the fifth floor of the south frame (Trifunac et al., 1999), and (b) Specimen 3CLH18 tested by Lynn (1999).

Table 7-3 Properties for Column A5 and Test Specimen

Column Property	Column A5	Specimen 3CLH18
ρ_L	1.3%	3.0%
ρ_t	0.07%	0.07%
Shear span-to-depth ratio	4	3.7
$N_{UD} / A_g f'_{cE}$	0.10	0.07
Maximum drift ratio	1.75% from OpenSees model Figure 7-38	1.5 to 2% corresponding to photograph Figure 7-37b

This publication is available free of charge from: https://doi.org/10.6028/NIST.GCR.22-917-50

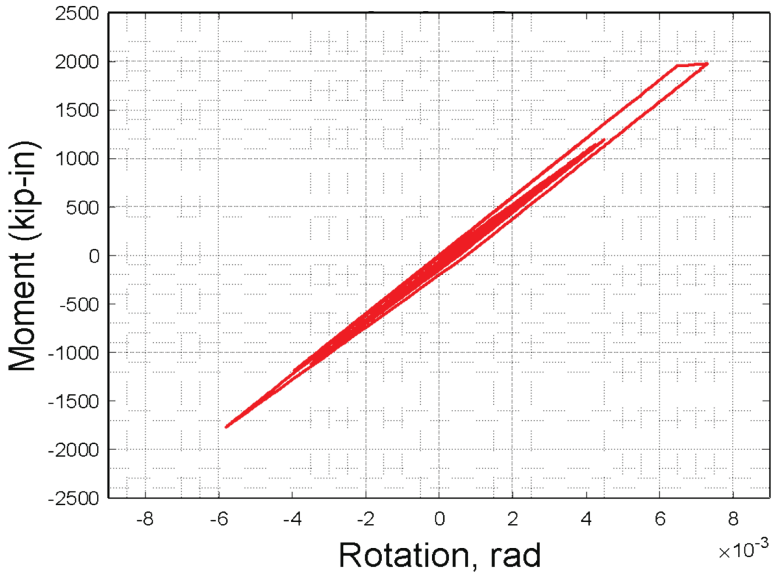


Figure 7-38 NDP: Calculated moment-rotation relationship for rotational spring at the top of Column A5.

Specimen 3CLH18 was a square 18 in. by 18 in. column with No. 3 hoops spaced at a distance equal to the column dimension. Column A5 had a rectangular section of 14 in. by 20 in. with 4 legs of No. 2 bars spaced at 12 in. Both Column A5 and Specimen 3CLH18 showed a damage pattern consistent with shear failure. Specimen 3CLH18 was shear critical due to the larger longitudinal reinforcement ratio, while Column A5 with a much lower longitudinal reinforcement ratio was flexure-shear critical with a ratio of shear corresponding to yielding of the longitudinal reinforcement to calculated shear strength of approximately 0.85 and a capping rotation of approximately 2%.

Figure 7-37 shows that the two columns, subjected to the similar drift ratios, experienced similar levels of damage. The main difference between Specimen 3CLH18 and Column A5 is that the former had rigid beams so the lateral deformation at the level of the top girder was equal to the lateral deformation of the column.

Columns in the study building framed into beams with lower flexural stiffness and strengths, so a significant fraction of the lateral deformation of the building was transformed into inelastic deformations in the beams. Figure 7-38 shows that calculated chord rotations in the column exceeded the yield rotation but were far below the capping rotation of approximately 2%.

7.4 Linear Dynamic Procedure

A three-dimensional numerical model of the building was created in ETABS to evaluate assessment outcomes using the Response Spectrum Method for linear dynamic procedure (LDP). Analyses were performed using the horizontal spectra

This publication is available free of charge from: https://doi.org/10.6028/NIST.GCR.22-917-50

components of the ground motion. Two versions of the model were studied in order to evaluate the effects of the masonry infill on the north side of the building: one without any infill and one with the full height masonry infill. The model without the infill panels is considered to be the baseline model. Results are presented in the following sections.

7.4.1 Modeling Approach

The elastic model was created in ETABS, as shown in Figure 7-39, to conduct a three-dimensional modal response-spectrum analysis. The modal response spectrum analysis was performed following the provisions in ASCE 41-17 Section 7.4.2.

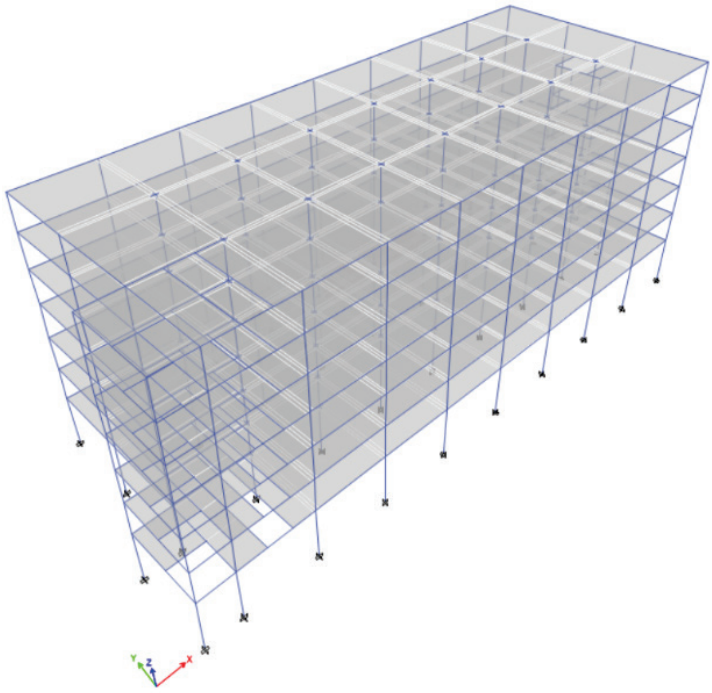


Figure 7-39 ETABS Linear 3D Model.

For this analysis, the east-west direction of the building was designated as X or longitudinal direction. The north-south direction of the building was designated as Y or transverse direction. These designations are used interchangeably throughout this chapter.

All structural elements were modeled as linear elastic with effective stiffnesses adjusted per ASCE 41-17 Table 10-5. Perimeter moment frames as well as interior gravity slab-column frames were considered primary elements per ASCE 41-17 Section 7.2.3.3. Beams and columns were modeled using line elements and slabs were modeled using shell elements.

The modeling approach for noncontact masonry infill panels are not covered by ASCE 41-17. Since in-plane damage was observed in the panels, they are thought to

This publication is available free of charge from: https://doi.org/10.6028/NIST.GCR.22-917-50

have participated in the seismic event nonetheless. Therefore, an upper-bound elastic study was performed to evaluate their impact on global behavior. In one model the panels were completely excluded and in the other model, only the full height panels were modeled using elastic shell elements with an in-plane stiffness modification factor of 0.5. The effects of the 1 in. gap around the infill panel were not explicitly considered in this study.

7.4.2 Global Performance: Model vs. Observation

Results show that gravity columns contribute significantly to the lateral strength and stiffness of the structure. The slab-column moment frame created by the gravity system resisted 66% of the base shear in the longitudinal direction and 77% of the base shear in the transverse direction. The predicted gravity system contribution from the model is similar to the Krawinkler (2005) study. A more detailed comparison can be found in Section 7.6.1.

The period corresponding to the first fundamental mode of the structure was calculated as 1.5 seconds in the transverse direction (north-south, Y in Figure 7-39), and the period corresponding to the second fundamental mode was 1.48 seconds in the longitudinal direction (east-west, X in Figure 7-39). When the infill panels are included in the model, the second fundamental mode decreases to 1.32 sec. in the longitudinal direction with the addition of torsional participation. These periods are lower than those calculated with the nonlinear model that included infills (1.83 sec. for the north-south and east-west directions, and 1.68 sec. for the torsional direction).

Spectral accelerations at the fundamental periods from the response spectra calculated with records from the ground floor of the building during the 1994 Northridge Earthquake were 0.32g for the transverse direction and 0.48g for the longitudinal direction. The infill panel model has a spectral acceleration of 0.45g for the longitudinal direction.

Seismic story drift demands calculated at the center of mass of each story are shown in Figure 7-40. Similar to the results from the nonlinear model, the infill walls had a negligible effect on the calculated response in the transverse direction. In the longitudinal direction, seismic drifts are reduced significantly.

This publication is available free of charge from: https://doi.org/10.6028/NIST.GCR.22-917-50

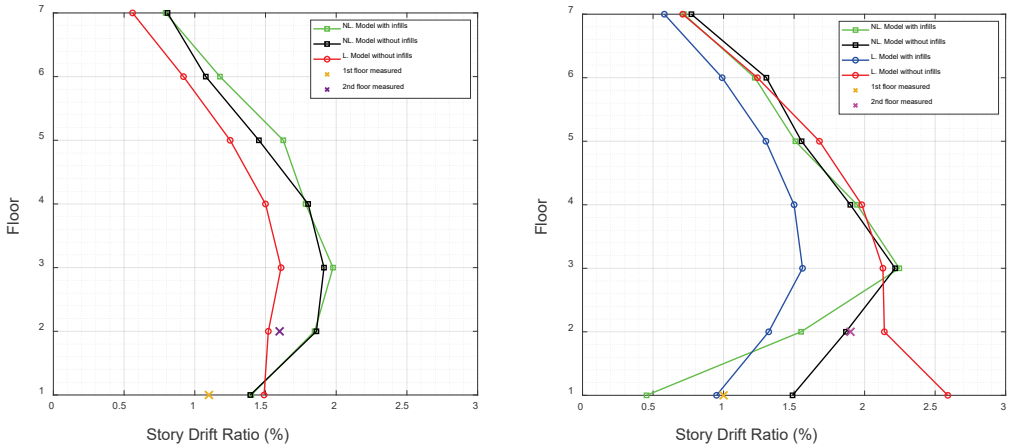


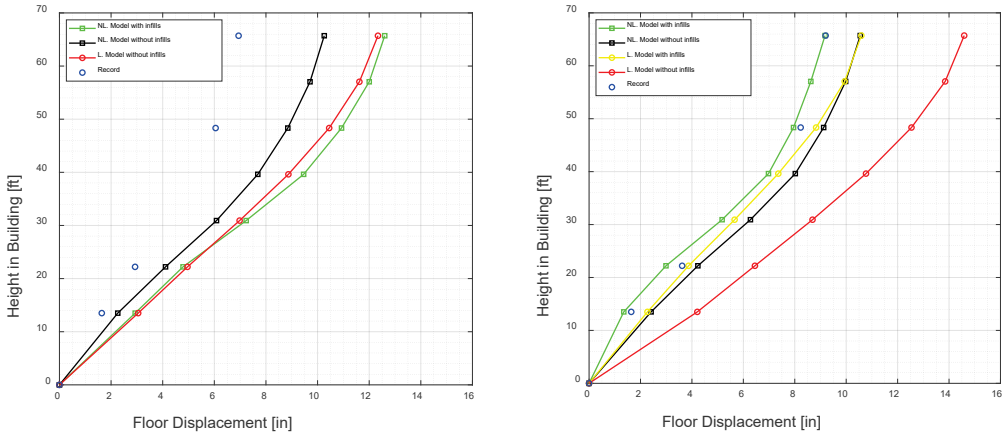
Figure 7-40 LDP: Seismic drift at center of mass (a) north-south direction, and (b) east-west direction.

The largest drift ratio of 2.6% occurs in the model without infill in the longitudinal (east-west) direction at the first story; however, the first story drift ratio is less than 1% when the infill panels are included. Calculated drift ratios in the third and fourth stories were approximately 1.5% in both directions when infill panels are included and 2% for the east-west direction without infill. In both the north-south and east-west directions of linear models with infills, drift ratios at the third and fourth floors are significantly lower than those calculated with the nonlinear dynamic analysis procedure. The difference between calculated displacements with the linear and nonlinear analysis procedures at the roof level is on the order of 40%. Drift ratios at the third and fourth floors in the east-west direction of the linear model without infills were similar to those calculated with the nonlinear dynamic procedure, in both models with and without infills.

The observed damage was most severe in the fourth story. This is somewhat consistent with the calculated drift profiles that show that the peak drifts occur in the third and fourth stories in the north-south direction and the east-west direction (when infill is considered). The model without infills significantly overestimated first story drift despite being modeled with a fixed base.

Seismic floor displacements from the linear analysis are shown in Figure 7-41 and compared with peak displacements from processed acceleration records. Figure 7-41 shows that for the model without infills the linear analysis procedure overestimated measured displacements at all levels, but the model with infill panels closely approximated the peak displacements in the east-west direction (X in Figure 7-41).

This publication is available free of charge from: https://doi.org/10.6028/NIST.GCR.22-917-50



(a) (b)

Figure 7-41 LDP: Seismic floor displacement at the southeast corner of the building in the (a) north-south direction and (b) east-west direction.

The results are taken from the southeast corner of the building. Due to the asymmetry in infill panel location, the southern edge of the building displaced more than the northern edge. This is in agreement with the observation that the most severe damage occurred in the south longitudinal frame. Similar to the nonlinear simulations, the linear model overestimates displacements in the north-south direction. This may be due to contribution of the nonstructural partitions which have not been included in the simulation. In the east-west direction, the most accurate estimates of floor displacements were obtained using the linear model with infills, which provided similar estimates of displacement as the nonlinear models.

7.4.3 Component Performance: Model vs. Observation

The linear analysis beam and column component results for all stories are shown in Figure 7-42 for the model without infill. The shear and flexure demand-capacity-ratios (DCRs) modified by the Collapse Prevention (CP) *m*-factors are presented in the results. Components with DCR/*m* values greater than 1.0 indicate failure to meet the CP acceptance criteria.

Results show that all first story columns exceed the CP criteria for shear and flexural demands, and that DCR/*m* values were larger for shear than flexure. Most DCR/*m* values for beams were below 0.5 for shear and flexure. A few beams in the north-south direction had DCR/*m* values in flexure between 0.5 and 1.0, and a beam in the second floor was the only element that exceeded DCR/*m* of 1.0 (Figure 7-42).

This publication is available free of charge from: https://doi.org/10.6028/NIST.GCR.22-917-50

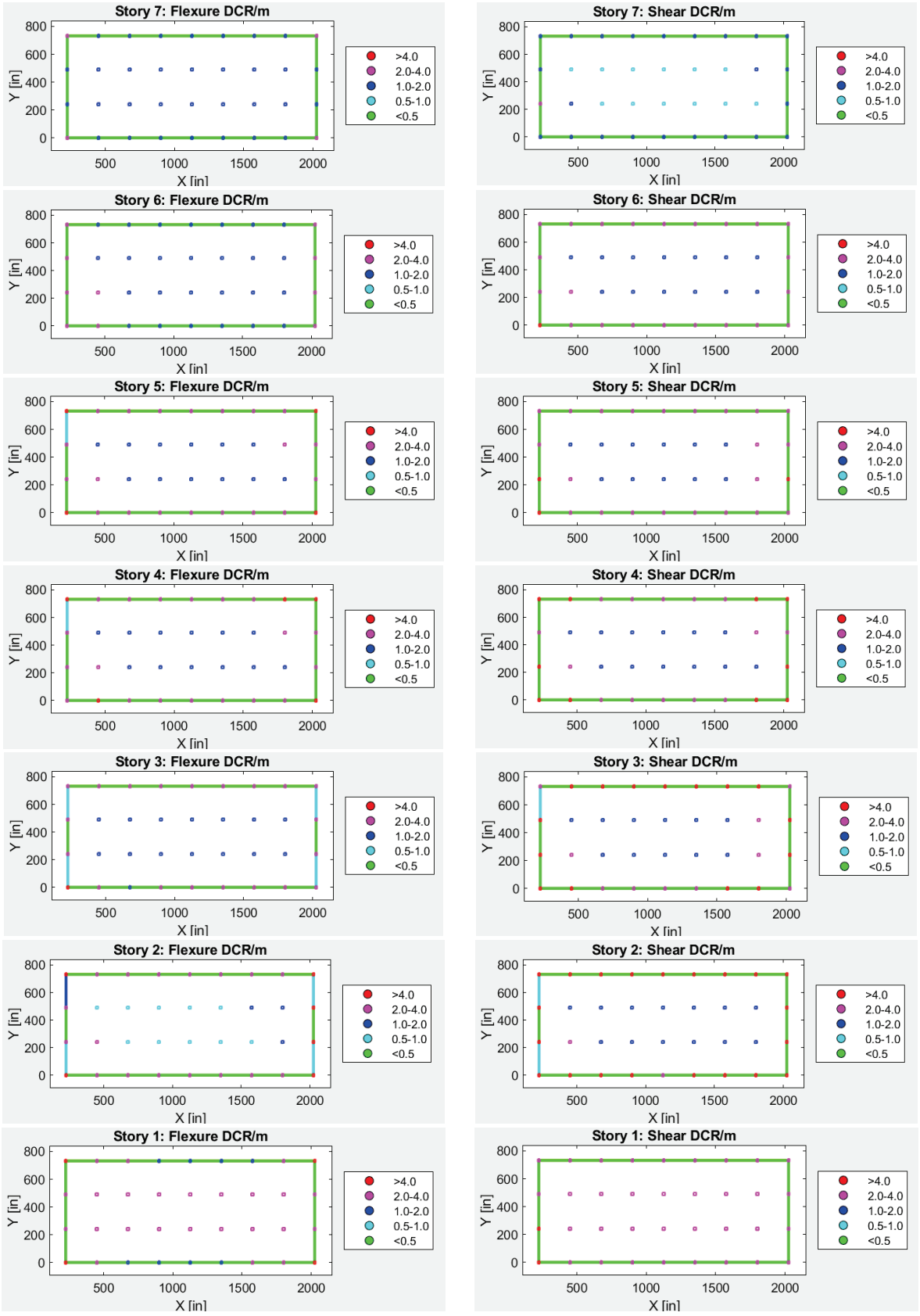


Figure 7-42 Collapse prevention demand capacity ratio for each story.

This publication is available free of charge from: https://doi.org/10.6028/NIST.GCR.22-917-50

The results from the non-infill model show the first story to be the critical story for the gravity columns; however, the perimeter seismic system is most heavily taxed in the third (DCRs for shear higher than 4) and fourth stories (DCRs for shear higher than 2), which is consist with the location of the highest observed damage in the exterior E-W frames.

Nearly all moment frame joints at all stories fail the CP limit with the exception of roof level L-shaped joints, located at the ends of moment frames (commonly referred to as roof exterior, roof corner, or as knee joints in ASCE 41 Figure 10-3c), and lower level T-shaped joints, located at the ends of the moment frames (exterior joints in ASCE 41 Figure 10-3c or 10-3d). DCRs peak at the third and fourth stories by as much as 2.5 times the CP limit. This is consistent with the frequency and concentration of joint damage observed across the building.

DCR for the slab components of the slab-column moment frames meet (within 10%) the CP limit state for both shear and flexure across all floors and in both plan directions. However, the roof is flexurally controlled, while all other floors are shear controlled. It is unknown whether damage of the slab-column moment frames occurred.

7.5 Fragility Assessment

Fragility curves for ASCE 41-17 backbone modeling parameters, acceptance criteria, and building collapse developed for the building are shown in Figures 7-43 and 7-44. The curves are based on incremental dynamic analysis (IDA) using the 22 earthquake records in the FEMA P-695 (FEMA, 2009) far-field set. Consistent with ASCE 41 requirements, all analyses were performed with the two components of the earthquake record applied in both directions of the building. Collapse was defined as the intensity measure in which an interstory drift ratio of 6% was exceeded at any of the floors, or at the highest intensity measure in which the model reached convergence. For most earthquake records, the building model did achieve convergence at an interstory drift ratio exceeding 6%. A second metric used as indicative of collapse was the intensity measure corresponding to the first element to reach an inelastic rotation of 1.5 times modeling parameter *b* as illustrated in Figure 2-1.

This publication is available free of charge from: https://doi.org/10.6028/NIST.GCR.22-917-50

This publication is available free of charge from: https://doi.org/10.6028/NIST.GCR.22-917-50

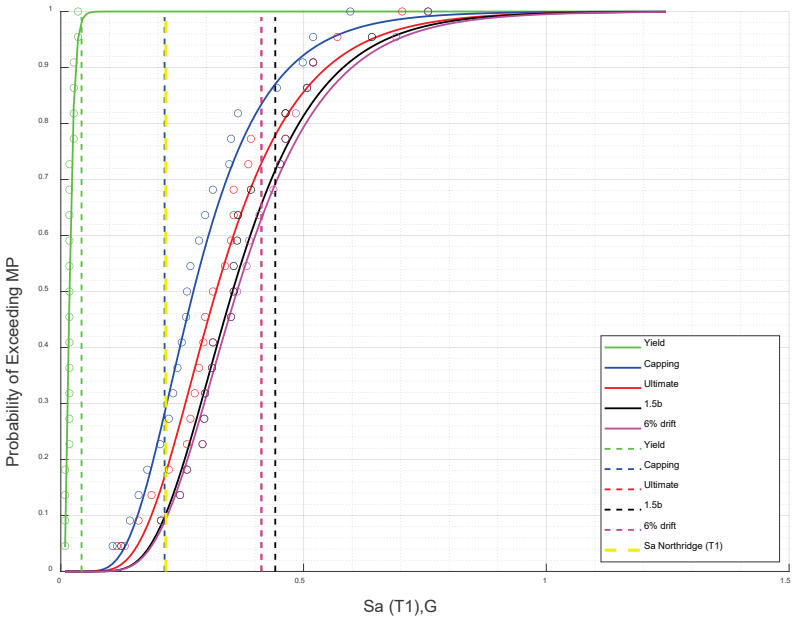


Figure 7-43 Fragility curve for ASCE 41-17 modeling parameters.

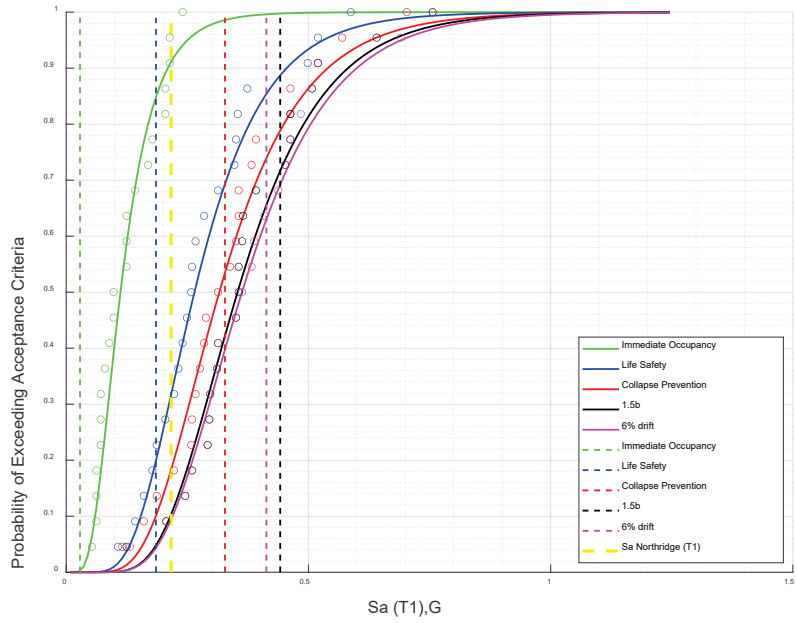


Figure 7-44 Fragility curve for ASCE 41-17 acceptance criteria.

Figures 7-43 and 7-44 show that the response of the building was very brittle in nature, meaning that fragility curves for limit states like capping (inelastic rotation equal to *a*) and ultimate (inelastic rotation equal to *b*) associated with severe element damage, were well below the fragility curve for 6% drift ratio, associated with dynamic instability of the frame.

Vertical lines in Figures 7-43 and 7-44 show spectral accelerations at which the first element in the building exceeded the corresponding modeling parameter or acceptance criterion for the IDA with the 1994 Northridge Earthquake record at the building site. Spectral accelerations corresponding to the vertical lines in Figures 7-43 and 7-44 were calculated as the product of the scale factor extracted from the IDA and the acceleration at the fundamental effective period of the building obtained from the response spectrum of the 1994 Northridge Earthquake.

Figure 7-43 shows the probability of exceedance of modeling parameters and Figure 7-44 shows the probability of exceedance of acceptance criteria. Figure 7-43 shows that the acceleration at which the first element yielded for the Northridge Earthquake IDA corresponded approximately to a 98% probability of exceedance in the yield modeling parameter fragility obtained with the FEMA P-695 far-field set. The fact that the Northridge Earthquake IDA curve for the yield modeling parameter had approximately a 100% probability of in the FEMA P-695 fragility curve for yield is indicative of a close match between the two. The yellow dashed line corresponding to the S_a for the Northridge Earthquake shows that the FEMA P-695 fragility curve for yield estimated that the 1994 Northridge Earthquake would be expected to induce inelastic rotations in many elements throughout the building, as it actually happened.

The Northridge Earthquake IDA acceleration at which the first element lost flexural strength (chord rotation exceeded the capping point, or inelastic rotation exceeding modeling parameter *a*) corresponded to a much lower probability of exceedance (approximately 28%) in the FEMA P-695 fragility curve for loss of lateral load capacity (designated as capping in Figure 7-43). If the IDA results and the fragility relationship were a perfect match, the probability of exceedance in the FEMA P-695 fragility curve corresponding to the S_a at which the first element exceeded the capping modeling parameter in the IDA would be 100%. The low probability of exceedance, 28%, of the FEMA P-695 fragility curve for the first element experiencing loss of lateral load capacity in the IDA indicates that the FEMA P-695 fragility is significantly less conservative than the results of the IDA for the capping modeling parameter.

Given the conservative nature of a single element exceedance criterion, the FEMA P-695 fragility relationship estimated that few, if any, elements were expected to exceed the capping point, which contradicts observed column damage in the building. To that effect, the FEMA P-695 fragility relationships were unconservative predictors of column capping modeling parameter in the building. Because fragility relationships are derived using the nonlinear model of the building, they are affected by limitations and inaccuracies of the model, which did a poor job of capturing the relative distribution of inelastic rotations in beams and columns, and underestimated column rotations.

This publication is available free of charge from: https://doi.org/10.6028/NIST.GCR.22-917-50

The vertical line corresponding to the spectral acceleration at which the first element exceeded the capping modeling parameter was very close, and a little smaller, than the spectral acceleration at the fundamental effective period for the 1994 Northridge Earthquake (yellow dashed line). The proximity between these two lines shows that according to the IDA, the 1994 Northridge Earthquake was strong enough to almost cause the first element in the building to deform beyond the capping point, while the FEMA P-695 curves showed low probabilities of exceeding the capping and ultimate (inelastic rotation exceeding loss of gravity load capacity) modeling parameters.

Because element inelastic rotations corresponding to a drift ratio of 6% were lower than 1.5*b*, the vertical line corresponding to loss of gravity load capacity modeling parameter (labeled as ultimate in Figure 7-43) coincides with the vertical line for 6% drift ratio. The spectral acceleration corresponding to the first element losing gravity load capacity (ultimate, or inelastic rotation exceeding modeling parameter *b*) for the Northridge Earthquake IDA corresponded to approximately 74% probability of exceedance for loss of gravity load capacity the FEMA P-695 data set fragility. According to this comparison, ground shaking that is strong enough to cause loss of gravity load capacity in at least one element according to the Northridge Earthquake IDA would have a high probability of exceedance of the same limit state in the corresponding FEMA P-695 fragility curve, but less than 100%. The high probability of exceedance indicates that the FEMA P-695 fragility curve for loss of gravity load capacity was also less conservative than the Northridge Earthquake IDA for the ultimate modeling parameter (inelastic rotation equal to *b*), although the difference between the two was much smaller than for the capping modeling parameter (26% for ultimate versus 72% for capping modeling parameter). In the context of observed damage, there were zero elements that experienced loss of lateral load capacity. The IDA correctly estimated that it would take a ground motion stronger than the 1994 Northridge Earthquake to cause loss of gravity load capacity in at least one element, although observed column damage indicates that at least one element was near the ultimate modeling parameter while the IDA estimates that it would take a ground motion nearly twice as strong as the Northridge record to cause loss of gravity load capacity in at least one element. Based on that observation, the IDA appeared to be an unconservative estimate of modeling parameter *b*. The same can be said about the FEMA P-695 fragility curves because the S_a for the Northridge Earthquake corresponded approximately to an 18% probability of exceedance of modeling parameter *b*, which is low in the context of the observed damage.

Accelerations at the fundamental effective period from the Northridge Earthquake IDA for IO, LS, and CP acceptance criteria (Figure 7-44) correspond to probabilities of exceedance of approximately < 1%, 20%, and 55% for the FEMA P-695 fragilities, respectively. These numbers suggest that the Northridge IDA was much more conservative than the FEMA P-695 fragility curves for acceptance criteria than

This publication is available free of charge from: https://doi.org/10.6028/NIST.GCR.22-917-50

they were for modeling parameters, and that the difference in degree of conservatism between the Northridge Earthquake IDA and FEMA P-695 fragility curves decreased from IO to LS and from LS to CP.

In this case the yellow dashed line indicates that for the Northridge Earthquake IDA, the spectral acceleration at the fundamental period was slightly higher than the spectral acceleration corresponding to the first element exceeding LS acceptance criteria, which is consistent with the observed damage in the building. Based on this observation, the Northridge IDA provided a more accurate representation of observed damage than the FEMA P-695 fragility curves.

A more detailed fragility analysis was performed to investigate the effect of multiple elements with inelastic deformations exceeding the inelastic rotation corresponding to different modeling parameters and acceptance criteria in ASCE 41-17. The first step of the analysis consisted of identifying a collapse mechanism for each of the 22 earthquakes in the FEMA P-695 far-field data set using the results from the incremental dynamic analysis. Because the fragility analysis was performed with a three-dimensional building model, collapse could be triggered by localized deformations in frames oriented in the east-west or north-south directions, extending over one or several stories. Owing to the different dynamic characteristics of each earthquake in the FEMA P-695 far-field set, there were significant differences in the configuration of the collapse mechanism obtained with each ground motion pair.

The first step of the detailed fragility analysis was to identify the primary direction and critical story of the collapse mechanism for each earthquake in the set. Collapse was defined as a deformed configuration where the story drift ratio exceeded 6% in one story. For each record, at the ground motion intensity associated with collapse, critical stories were identified as those where the largest number of beam, slab-column connection, and column inelastic springs had rotations exceeding CP performance level, and the corresponding number springs where rotations exceeded CP performance level was recorded. In this analysis, beams and slab-column connections were lumped together. This information is summarized in Tables 7-4 and 7-5 for beam and slab-column connection springs and column springs, respectively.

This publication is available free of charge from: https://doi.org/10.6028/NIST.GCR.22-917-50

Table 7-4 Location of Collapse Mechanism and Percentage of Beam and Slab-Column Connection Spring Elements Exceeding Collapse Prevention Performance Level

	Primary Direction			Secondary Direction	
FEMA P-695 Earthquake Number	*Critical Frame Orientation*	*Critical Story(ies)*	*% Springs Exceeding CP at Critical Story*	*Critical Story(ies)*	*% Springs Exceeding CP at Critical Story*
1	S-N	2,3	69	2,4	0
2	S-N	2	81	2	0
3	S-N	3,4	76	3,4	25
4	E-W	3,4	25	2	0
5	S-N	2,3	78	3	11
6	E-W	2,3,4	53	5	13
7	E-W	3,4	34	3,4	44
8	E-W	4	28	-	-
	S-N	1	31	-	-
9	S-N	1,2	63	2,3	45
10	E-W	4	72	6,7	22
11	E-W	4	25	1	39
12	S-N	1,2,3	100	3	0
13	S-N	1,2,3,4	100	5	25
14	S-N	6,7	28	3	48
15	E-W	3,4	34	3	0
16	E-W	3,4,5	100	-	-
	S-N	4,5	78	-	-
17	E-W	4	25	4	0
18	S-N	1,2	94	3	0
19	S-N	1	57	3	
20	S-N	3	22	3	8
21	E-W	3,4	52	-	-
	S-N	2,3,4	89	-	-
22	E-W	3,4	28	-	-
	S-N	1	22	-	-

This publication is available free of charge from: https://doi.org/10.6028/NIST.GCR.22-917-50

Table 7-5 Location of Collapse Mechanism and Percentage of Column Springs Exceeding Collapse Prevention Performance Level

	Primary Direction			Secondary Direction	
FEMA P-695 Earthquake Number	*Critical Frame Orientation*	*Critical Story(ies)*	*% Springs Exceeding CP at Critical Story*	*Critical Story(ies)*	*% Springs Exceeding CP at Critical Story*
1	S-N	5	6	2	0
2	S-N	5	6	2,3	0
3	E-W	5	31	5	19
4	E-W	3	15	1	1
5	S-N	1,2	11	4	3
6	E-W	5	83	5	13
7	E-W	5	89	5	8
8	E-W	5	69	5	6
9	E-W	3	14	2	10
10	E-W	5	61	5	7
11	E-W	5	63	1	13
12	S-N	1	22	2	0
13	S-N	3	92	6	54
14	E-W	5	40	5	15
15	E-W	5	69	1	1
16	E-W	5	100	5	13
17	E-W	5	39	5	8
18	S-N	1	15	2	0
19	S-N	1	15	6	3
20	S-N	5	3	4	1
21	E-W	5	69	5	25

The collapse mechanism analysis showed that there was no dominant direction for the collapse mechanisms of the building. This is attributed to the fact that this is a moment frame building and response is highly nonlinear near collapse, so torsion affects element deformation significantly. Table 7-4 shows that there were more instances where the number of beam and slab-column connection springs that exceeded CP performance level were located in frames oriented in the north-south direction. In the vast majority of cases, the critical story was located in the lower part of the building, between stories 1 and 4.

Table 7-5 shows that for column springs there were more instances where the largest number of springs exceeding CP performance level were located in frames oriented in the EW direction. In the majority of frames, the critical story was the fifth, which

This publication is available free of charge from: https://doi.org/10.6028/NIST.GCR.22-917-50

is consistent with the observed damage in the building in the 1994 Northridge Earthquake (Figures 7-10 to 7-13, and 7-17).

The number of springs where rotations exceeded CP performance level at the critical story of the collapse mechanism, referred to as the critical number of springs, were used to compute fragility relationships corresponding to different percentages of springs participating in the collapse mechanism exceeding modeling parameters and acceptance criteria in ASCE 41-17. Fragility relationships were computed based on the number of beam and slab-column connection spring elements because the analysis described in Section 7.3.3 showed that for the Northridge ground motion the computer model had low rotation demands in columns, and much higher rotation demands in beams and slab-column connections (Figures 7-31 to 7-36).

Figures 7-45 to 7-50 show fragility relationships corresponding to the first spring, 10%, 25%, 50%, 75%, and 100% of the springs exceeding different modeling parameters and acceptance criteria defined in ASCE 41-17. In all figures, fragility relationships corresponding to the drift ratio exceeding 6% in at least one story and the first spring exceeding an inelastic rotation of 1.5 × modeling parameter *b* are presented for reference. These two parameters are indicative of global and localized collapse. Also, a dashed vertical line shows the spectral acceleration corresponding to the fundamental effective period of the structure, T_1, extracted from the response spectrum for the 1994 Northridge Earthquake ground motion.

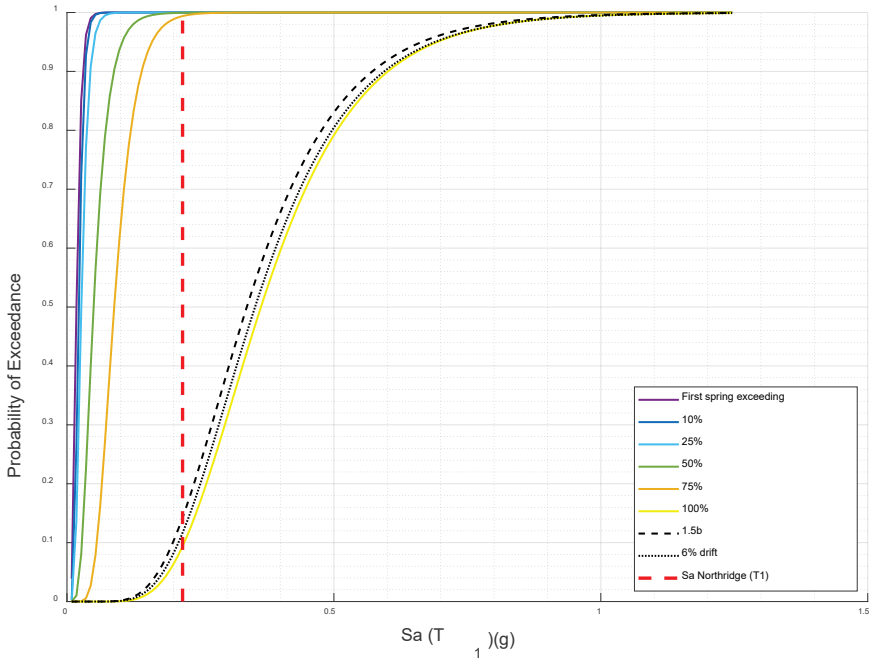


Figure 7-45 Fragility curve for different percentages of critical springs exceeding the yield rotation.

This publication is available free of charge from: https://doi.org/10.6028/NIST.GCR.22-917-50

This publication is available free of charge from: https://doi.org/10.6028/NIST.GCR.22-917-50

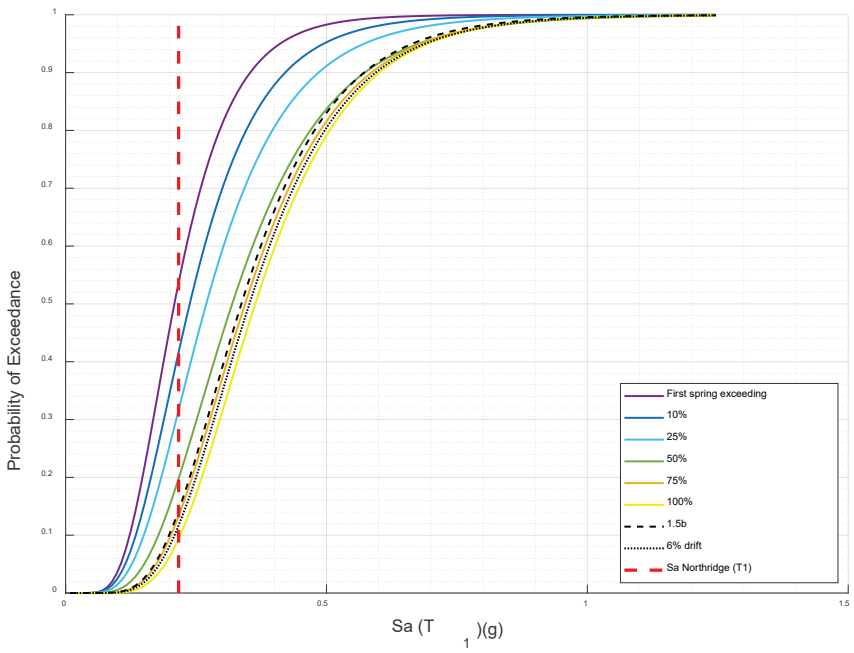


Figure 7-46 Fragility curve for different percentages of critical springs exceeding the rotation corresponding to loss of flexural strength.

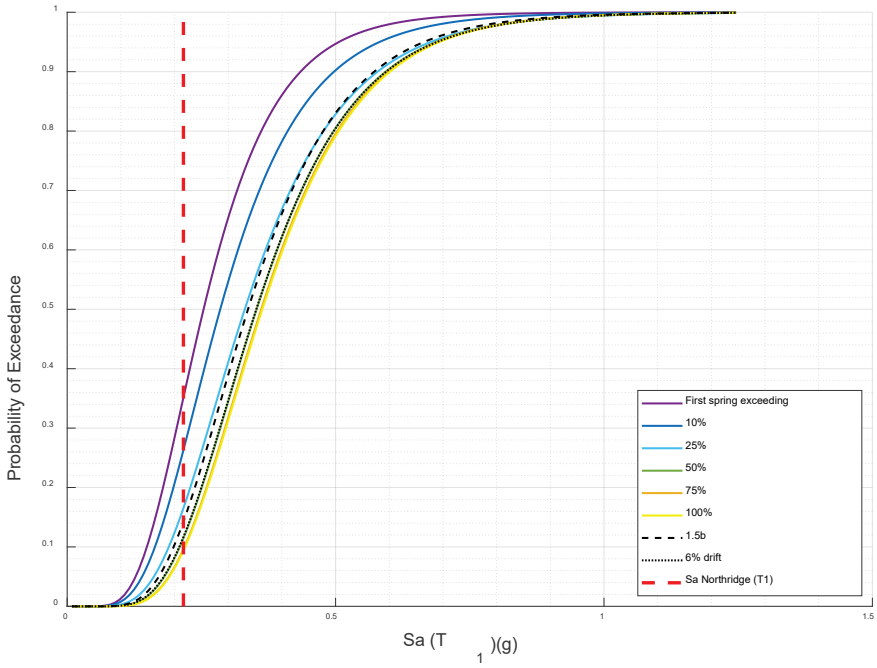


Figure 7-47 Fragility curve for different percentages of critical springs exceeding the rotation corresponding to loss of gravity load carrying capacity.

This publication is available free of charge from: https://doi.org/10.6028/NIST.GCR.22-917-50

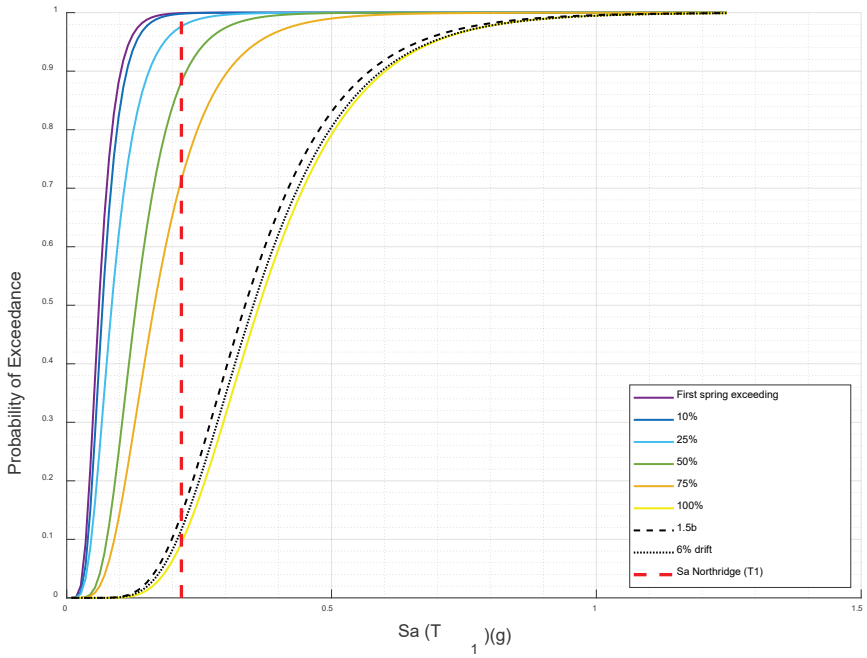


Figure 7-48 Fragility curve for different percentages of critical springs exceeding the IO performance level.

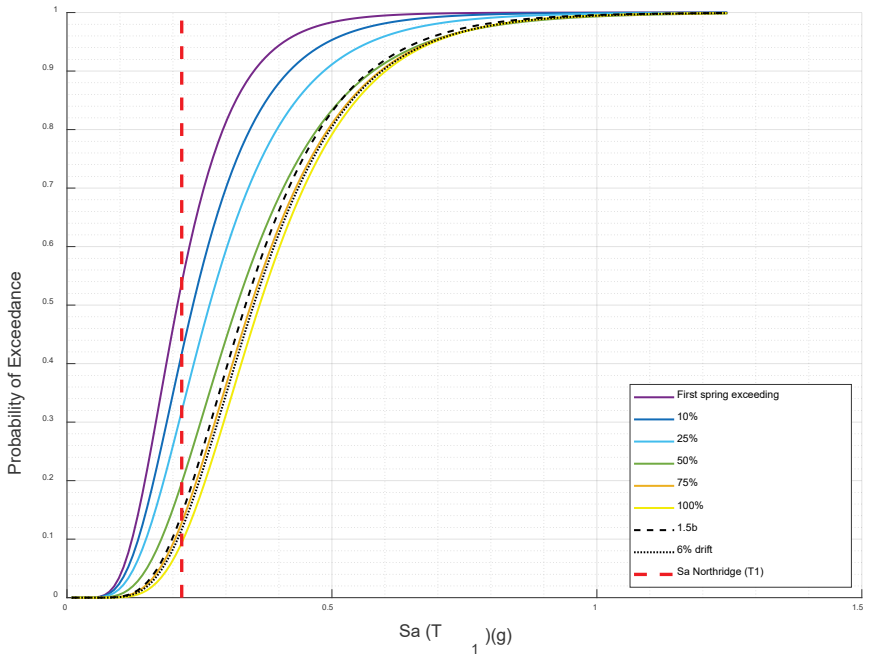


Figure 7-49 Fragility curve for different percentages of critical springs exceeding LS performance level.

This publication is available free of charge from: https://doi.org/10.6028/NIST.GCR.22-917-50

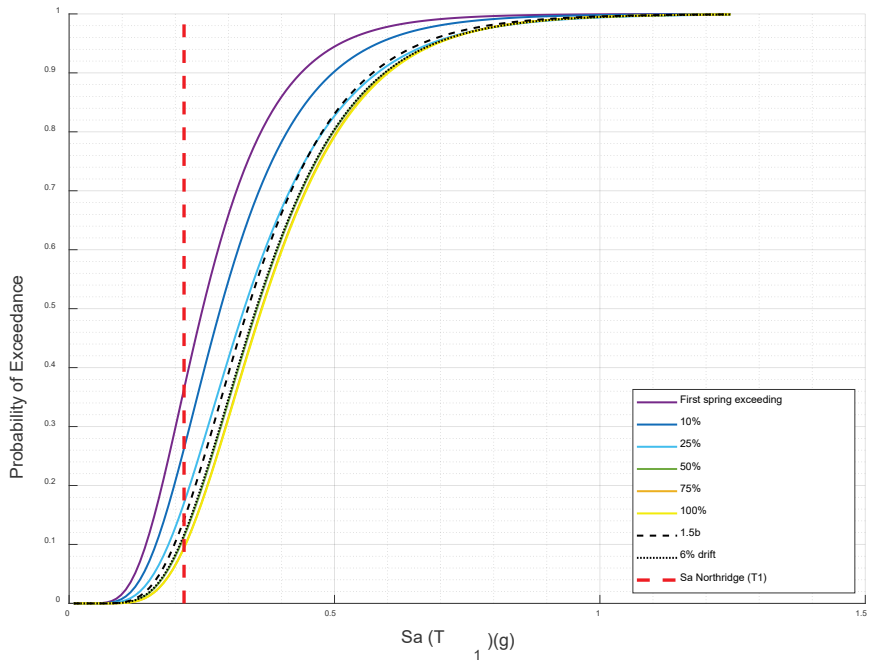


Figure 7-50 Fragility curve for different percentages of critical springs exceeding CP performance level.

Figure 7-45 shows fragility relationships for different percentages of critical springs where calculated rotations exceeded the rotation at yield. The fragility curves in Figure 7-45 show that at levels of shaking comparable to that of the 1994 Northridge Earthquake, there was a 99% probability of exceeding the yield rotation in as many as 75% of the critical springs, and a 10% probability of exceeding the yield rotation in 100% of the critical springs. Fragility curves corresponding to the first critical spring exceeding yield, 10%, 25%, 50%, and 75% of critical springs exceeding yield were close together. These results indicate that a large percentage of critical springs, on the order of 75%, is likely to reach yield with low and moderate levels of shaking, and that it takes significantly stronger ground motions to cause 100% of critical springs to reach yield causing the collapse of the building due to the formation of a sidesway mechanism.

Figures 7-46 and 7-47 show similar fragility curves for rotations corresponding to loss of flexural strength (inelastic rotation equal to modeling parameter *a* or capping point), and loss of gravity load carrying capacity (inelastic rotation equal to modeling parameter *b*). Figure 7-46 shows that the loss of strength modeling parameter had the largest difference between spectral acceleration corresponding to 10% and 50% of critical springs exceeding. For a 50% probability of exceedance, the spectral acceleration for 10% of the critical springs exceeding the modeling parameter was approximately 0.22g, and the spectral acceleration for 50% of the critical springs exceeding the modeling parameter was approximately 0.33g. Fragility curves corresponding to 50%, 75%, and 100% of the critical springs exceeding the modeling

parameter were very close to each other and to the collapse indicators. These results indicate that for this building, when 50% of the critical springs exceed the loss of strength modeling parameter (inelastic deformation exceeding modeling parameter *a*) the building is very close to collapse. For the spectral acceleration corresponding to the fundamental effective period extracted from the 1994 Northridge Earthquake response spectrum, fragility curves ranged between 10% probability that 100% of the critical springs exceed the capping point, and a 52% probability that at least one spring exceeds the capping point.

The damage survey presented in Figures 7-10 and 7-11 did not record significant damage to beam or slab-column elements, but showed that approximately 30% of column plastic hinge regions in the critical story of the building were near or exceeded the capping point. Even though the fragility relationships in Figures 7-45 to 7-50 were derived based on damage to critical beam and slab-column springs because that is where inelastic rotations were higher in the ASCE-41-17 model, all comparisons in this section are framed on the assumption that the fragility curves in Figures 7-45 to 7-50 are representative of the entire set of elements. This approach is conservative for this building because if similar fragility curves were derived solely based on critical column springs, spectral accelerations would be higher.

Figure 7-46 shows that the probability that 25% of the critical springs exceeded the capping point was approximately 30%, while the probability that 50% of the critical springs exceeded the capping point was approximately 20%, both of which are well below 100% probability corresponding to the damage observed in the building. This shows again that the fragility curves derived using this procedure were unconservative, likely due to limitations of the nonlinear model.

Figure 7-47 shows that fragility curves corresponding to loss of gravity load carrying capacity (inelastic deformation exceeding modeling parameter *b* or ultimate) were close to those corresponding to the collapse indicators. For a 50% probability of exceedance, the curve corresponding to the first spring, 10%, and 25% of the critical springs exceeding the modeling parameter had spectral accelerations of approximately 0.25g, 0.28g, and 0.33g, respectively. The curve corresponding to 25% of the critical springs exceeding the modeling parameter was very close to curves with 50%, 75%, and 100% of the critical springs exceeding the modeling parameter, and very close to the fragility curves for the collapse indicators. For the spectral acceleration corresponding to the fundamental effective period extracted from the 1994 Northridge Earthquake response spectrum, fragility curves ranged between 10% probability that 100% of the critical springs exceed loss of gravity load capacity and a 34% probability that at least one spring exceeds loss of gravity load capacity, which shows that the 1994 Northridge Earthquake had a low probability of causing building collapse. Damage surveys show that at most one column location was near loss of gravity load capacity, without any damage indicative of gravity load

This publication is available free of charge from: https://doi.org/10.6028/NIST.GCR.22-917-50

redistribution in the beams. If the observed damage is interpreted as having zero instances of loss of gravity load, the methodology was conservative for this particular modeling parameter because it produced probabilities of 34% that at least one element would lose gravity load, which although low, are significant. To that effect, the best predictor of loss of gravity load capacity based on the model was the fragility curve corresponding to 100% of the critical springs exceeding loss of gravity load capacity, which had a probability of exceedance of 10% for the Northridge Earthquake S_a at the fundamental period of the building.

Figures 7-48, 7-49, and 7-50 show fragility curves for different percentages of critical springs exceeding IO, LS, and CP performance levels, respectively. Fragility curves for the IO performance level (Figure 7-48) were similar to fragility curves corresponding to yield (Figure 7-45). Fragility curves corresponding to the first spring, 10%, 25%, 50%, and 75% of critical springs exceeding the IO performance level were close together, while the fragility curve for 100% of the critical springs exceeding the IO performance level was very close to the fragility curves for the collapse indicators. For ground motions with intensity similar to the 1994 Northridge Earthquake, there is approximately a 72% probability that the IO performance level would be exceeded in 75% of the critical springs.

The LS performance level (Figure 7-49) had the most evenly spaced set of fragility curves. For a 50% probability of exceedance, fragility curves corresponding to the first spring, 10%, 25%, 50%, 75%, and 100% of the critical springs exceeding the LS performance level had spectral accelerations of approximately 0.20g, 0.24g, 0.27g, 0.32g, 0.49g, and 0.50g, respectively. This was the only set of fragility curves where this level of separation was observed.

Fragility curves for the CP performance level, shown in Figure 7-50, had a similar distribution to those for loss of gravity load carrying capacity (inelastic deformation exceeding modeling parameter *b*), shown in Figure 7-47.

Fragility curves in Figure 7-50 indicate that the model was near collapse when 25% of the springs exceeded CP performance level. Aside from comparisons between probability of collapse and observed damage already addressed, the close grouping of fragility curves corresponding to 25% to 100% of critical springs exceeding the CP performance level is indicative of the brittle nature of the building model given the rapid progression to collapse after 25% of the critical springs exceed CP performance level.

A comparison among Figures 7-48, 7-49, and 7-50 show that there is a progression in the grouping of the fragility curves as damage increases. For IO performance level (Figure 7-48), fragility curves corresponding to one critical spring to 75% of critical springs exceeding IO are close together and far from the curves corresponding to

This publication is available free of charge from: https://doi.org/10.6028/NIST.GCR.22-917-50

100% critical springs exceeding and building collapse. For the LS performance level (Figure 7-49), fragility curves for 50 to 100% exceeding are close to the building collapse fragility curve, and separated from fragility curves corresponding to 1 critical spring and up to 25% of critical springs exceeding LS. For the CP performance level (Figure 7-50), fragility curves for 25 to 100% exceeding are close to the building collapse fragility curve, and separated from fragility curves corresponding to 1 critical spring and 10% of critical springs exceeding CP. For the study building, this progression indicates that if performance assessments were to be based on this type of fragilities and ASCE 41-17 modeling parameters and acceptance criteria, it would be appropriate to reduce the percentage of critical springs to assess a performance level with increasing damage. For example, for this particular building, criteria could be established so that the building is considered to meet IO if less than 50% of critical springs exceeds IO, 25% of critical springs exceed LS, and 10% of the critical springs exceed CP.

For the nonlinear building model, the probability of exceeding loss of strength parameter (Figure 7-46), loss of gravity load carrying capacity (Figure 7-47), LS and CP performance levels (Figures 7-49 and 7-50) in 100% of the critical springs in ground motions with intensity similar to the 1994 Northridge Earthquake was very low (below 10%). These probabilities of exceedance indicate that fragility curves calculated using the ASCE 41-17 nonlinear model and associated with heavy damage show a low probability of collapse, even if 100% of the critical springs exceeding the modeling parameter or acceptance criteria are used as a threshold for collapse.

7.6 Summary

7.6.1 Global Performance

Overall, the ASCE 41-17 nonlinear dynamic evaluation procedures were able to identify an important source of potential distress in the building associated with slab-column connections. For the 1994 Northridge Earthquake records obtained at the building site, roof drifts, story accelerations, and base shears calculated with the OpenSees nonlinear numerical model were accurate. Although calculated accelerations in the sixth story were off by approximately 40%, calculated accelerations in the roof and third stories were accurate and so were the calculated roof displacements. The type of mechanisms that developed in the OpenSees model caused nonlinear deformations to concentrate in beams. The distribution of calculated element nonlinear deformations throughout the building is attributed to weak-beam strong-column configuration causing a structure-type mechanism instead of a story-type mechanism. The nonlinear dynamic procedure did not provide accurate distributions of damage between various components in the frames and severely underestimated deformation demands on columns.

This publication is available free of charge from: https://doi.org/10.6028/NIST.GCR.22-917-50

Comparisons between simulation results and observed damage patterns show that although the overall estimate of drift ratio was accurate, the distribution of nonlinear deformations throughout the structure was skewed, with nonlinear deformations in columns being underestimated and nonlinear deformations in beams being overestimated. In that respect, this study highlights the effects of having modeling parameters with varying degrees of conservatism, or conversely accuracy, in ASCE 41-17.

The linear dynamic analysis procedure provided a very conservative estimation of damage in building components, in particular, estimates of column flexure and shear and beam-column joints. Estimates of damage in spandrel beams indicated few concerns (Figure 7-42). To that effect, the damage pattern estimated with the linear model was in direct contradiction with the results of the nonlinear model. Calculated forces showed that slab-column frame action was one of the major sources for lateral force resistance. Calculated displacements in the lower stories were very sensitive to the presence of infill walls in the model, and the model with infill walls provided estimates of story displacements close to those obtained by processing acceleration records.

Global performance parameters calculated in this study and other previous work are summarized in Table 7-6 below.

Table 7-6 Summary of Calculated Building Response Parameters

	Direction	Linear Analysis (No infill)	SEAONC (Nabih Youssef)	Krawinkler (2005)	Record
Weight (kip)	-	9,386	9,999	9,715	9,375
Fundamental Periods (sec.)	Trans Dir.	1.50	-	1.27s	1.5s
	Long. Dir.	1.48	1.45s	1.20s	
	Torsional	1.26	-	1.03s	
Max. Roof Drift Roof Displ. / Building Height	Trans Dir.	1.1%			1.15%
	Long. Dir.	1.7%			1.17%
Max. Story Drift (in any story)	Trans Dir.	1.47%			1.6%
	Long. Dir.	2.36%			1.9%
Max Base Shear	Trans Dir.	0.42g			
	Long. Dir.	0.43g			
Max Roof Acceleration	Trans Dir.	0.61g	-		0.56g
	Long. Dir.	0.74g	0.79g		0.58g
Gravity Frame Stiffness	Trans Dir.	77%	-	84%	
	Long. Dir.	66%	33% (assumed)	60%	

This publication is available free of charge from: https://doi.org/10.6028/NIST.GCR.22-917-50

7.6.2 Component Performance

Calculated nonlinear deformations were significantly higher in beams than columns, so ASCE 41-17 acceptance criteria indicated damage primarily to beams and slab-column connections, and light or no damage to columns. This contradicts the observed damage pattern. The inconsistency between calculated column deformations and observed damage was caused most likely by a systemic underestimation of beam strength or post-yield stiffness. The underestimation of beam strength can be attributed to several possible causes not currently addressed in ASCE 41, including:

- Neglecting strength of the reinforcement outside the effective slab width.
- Neglecting axial forces induced in the beams due to collector loads and by the axial constraint imposed by the diaphragm as beams lengthen due to inelastic rotations.
- Large inelastic rotations in beams bring about large strain demands in the reinforcement. Test data has shown that at 5% strain, the overstrength factor for reinforcing steel is on the order of 1.7, significantly higher than the material factor specified in ASCE 41-17 which provides the same material factor regardless of expected strain demand. For comparison, ASCE 41 has a material factor of 1.25 for all types of reinforcing steel, regardless of strain demand.
- The difference between overstrength factors for concrete (1.5) and steel (1.25) may have led to larger column-to-beam strength ratios than calculated by previous researchers because concrete compressive strength has a greater effect on flexural strength of columns than flexural strength of beams. This difference affects post-yield stiffnesses as well if ASCE 41-17 Section 10.3.1.2 allowing the use of a post yield slope between 0 and 10% of the initial slope is implemented.

Column modeling parameters were updated twice since FEMA 356 (Elwood et al. 2007; Ghannoum and Matamoros, 2014; and Ghannoum 2017), and in the process were increased substantially to reach mean estimates of experimental data. Moreover, the beam modeling parameters and acceptance criteria remained unchanged since FEMA 356 and are substantially lower than column values given similar detailing. These differences in conservatism in modeling parameters generated skewed damage outcomes per ASCE 41-17, whereby more severe damage was predicted in beams than the columns. This is inconsistent with observed damage that was moderate to limited in the beams. Updates for the beam modeling parameters and acceptance criteria are recommended for ASCE 41.

In the LDP, flexural DCRs were not reasonable in large part due to the effects of tension. Tensile demands on the columns in the LDP were larger than those in the columns of the real structure because columns were assumed to be fully restrained at

This publication is available free of charge from: https://doi.org/10.6028/NIST.GCR.22-917-50

the base and the upper limit on tensile demand caused by component yielding was not reflected in the model. When the column forces are in tension, the flexural capacity approaches zero, leading to unreasonable flexural DCR values. Also, bi-directional interaction in corner columns, where beams frame in two orthogonal directions, should be considered based on observed damage.

7.6.3 Analytical Study Takeaways

This building is challenging to model because the lateral force-resisting system has slab-column and beam-column moment frames. The nonlinear model was able to reproduce accurately global response parameters such as interstory drift ratios and story accelerations. Estimates were least accurate in the first two stories, which was expected because interaction between the foundation and surrounding soil was not accounted in the model.

The distribution of nonlinear deformation among components was not accurate. The model assigned the largest inelastic deformations to beams and slab column connections, while inelastic deformations in the columns were very small. This pattern contradicts the observed damage in the building during the 1994 Northridge Earthquake, and is likely caused by difference in the level of conservatism of modeling parameters and acceptance criteria for different components in ASCE 41-17.

The LDP provided a very conservative estimation of damage in building components. Calculated forces showed that slab-column frame action was one of the major sources for lateral force resistance. Calculated displacements in the lower stories were very sensitive to the presence of infill walls in the model, and the model with infill walls provided estimates of story displacements close to those obtained by processing acceleration records. Although estimates of damage obtained with the linear procedure were very conservative, results were inconsistent because drifts calculated with the linear procedure were lower than those calculated with the nonlinear dynamic analysis procedure.

7.6.4 Fragility Analysis

Fragility relationships created using the FEMA P-695 far-field set showed that analyses with the 1994 Northridge Earthquake records and the ASCE 41-17 nonlinear model had a high probability that spring rotation would exceed the yield modeling parameter and the IO acceptance criteria, which is consistent with the observed damage. For other modeling parameters and acceptance criteria probabilities of exceedance were moderate to low. The detailed fragility analysis showed that at IO and CP performance level fragilities corresponding to different percentages of critical springs were close together. For IO performance level fragilities, a small intensity of shaking was sufficient to cause 75% of the critical springs to exceed the acceptance

This publication is available free of charge from: https://doi.org/10.6028/NIST.GCR.22-917-50

criteria. For the CP performance level, there was very small increase in spectral acceleration between 25% and 100% of the critical springs exceeding the performance level, which indicates that collapse is likely to occur rapidly after a small number of elements of the critical mechanism exceed collapse prevention.

The spectral acceleration at the fundamental effective period of the building for the 1994 Northridge Earthquake was approximately 0.22g. The results from the IDA with the 1994 Northridge Earthquake ground motion showed that for scale factor of 1.0 the performance level was approximately Collapse Prevention given that several beams and slab-column connections in both directions failed LS (Figures 7-31 and 7-32). This is consistent with the observed damage although for the wrong reasons because the model allocated the damage to beams and slab-column connections while the observed damage occurred in columns. The calculated damage distribution in Figures 7-31 and 7-32 shows that most columns satisfied IO performance level, and the few columns that failed IO were on the first floor of the building. Fragility analysis shows that for a spectral acceleration at the fundamental effective period of 0.22g (same intensity as the 1994 Northridge Earthquake), there was a 50% probability of exceeding LS performance level in at least 1 critical spring and a 10% probability of exceeding LS performance level in 100% of the critical springs. The level of conservatism decreased with increasing percentage of critical elements exceeding the performance limit, but in this particular case the better estimate of global performance was obtained by the fragility relationship corresponding to a single element exceeding the limit state.

7.6.5 Study Limitations

The results of this investigation are contextualized within the following limitations:

- Measured material properties were not available. Expected material properties for concrete and reinforcing bars were defined by adopting specified strengths as lower bound material properties and using material factors in ASCE 41-17. Material properties for masonry walls were not available and had no specified values, so suggested values were adopted from TMS 402.
- Drawings were illegible in many locations, including reinforcement schedules, thus the reinforcement layout is based on the best interpretation of the numbers stated in the drawings.
- The instrumentation array in the building only had accelerometers. Displacements were calculated based on digitized and processed records which included filtering of the ground motion.
- Foundation flexibility and soil flexibility were not modeled.

This publication is available free of charge from: https://doi.org/10.6028/NIST.GCR.22-917-50

- Masonry walls at the base had a gap to avoid contact with the frame elements. In models that included the masonry wall panels the presence of the gap was neglected. Partial depth brick walls in the first level were not included.
- The building model included only the reinforced concrete structure. The light gage steel roof structure was not included in the model.
- Damage surveys gathered after the 1994 Northridge Earthquake provided substantial information about structural elements of the exterior moment frames, located at the façades of the building. No damage was documented in slab-column connections of interior frames, although damage reports do not indicate if slab-column connections were subjected to detailed inspection.

This publication is available free of charge from: https://doi.org/10.6028/NIST.GCR.22-917-50

Chapter 8

Five-story Wall Building in New Zealand

This publication is available free of charge from: https://doi.org/10.6028/NIST.GCR.22-917-50

8.1 Overview

This chapter presents benchmarking studies for a 5-story reinforced concrete wall building in Christchurch, New Zealand, shown in Figure 8-1. The building was constructed circa 1966 and was occupied by the Pyne Gould Corporation at the time of the earthquake. The building sustained damage in the September 4, 2010 Darfield Earthquake and collapsed in the February 22, 2011 Christchurch Earthquake. The building had reinforced concrete gravity and lateral systems. A detailed investigation of the collapse was published (Beca, 2011) and serves as the basis of the information in this study.



Figure 8-1 Photograph of Pyne Gould Corporation Building prior to collapse (from Jury and Sharpe, 2011, North arrow added).

The building was evaluated in accordance with the nonlinear and linear dynamic procedures of ASCE 41-17 using OpenSees and ETABS software, respectively. The models were constructed per details presented in Appendix A, unless otherwise noted.

This chapter also provides results from a FEMA P-2018, *Seismic Evaluation of Older Concrete Buildings for Collapse Potential*, (FEMA, 2018b) evaluation of the building, as well as a brief summary of an evaluation with New Zealand Guidelines, *The Seismic Assessment of Existing Buildings* (NZSEE et al., 2017).

8.2 Building Description and Seismic Performance

8.2.1 Building Description

The study building was a five-story reinforced concrete shear wall structure located in the Central Business District in Christchurch, New Zealand. The building was designed in 1963 based on NZSS 95:1955 (New Zealand Standard Institute, 1955) and constructed circa 1966 with a primary use of office space.

The building was purchased by Pyne Gould Corporation in 1997, at which it was evaluated and retrofit. However, drawings of the retrofit were not available for this study. The retrofit included changes to wall and floor openings and the addition of steel "prop" columns placed adjacent to the existing reinforced concrete columns on the perimeter. Changes to wall and floor openings were considered in the study presented here. However, the "prop" columns were not included in the study as the connection details of these elements to the existing frame was assumed to be inadequate to enable columns to contribute significant lateral resistance.

Gravity and lateral force-resisting systems were discontinuous at the second floor (i.e., the interface of the first and second stories). Within the gravity system, which consisted of two-way slabs supported by beams, columns, and walls, perimeter gravity columns were inset at the first story as shown in Figure 8-2. Gravity forces were transferred between the first- and second-story perimeter columns using transfer beams. The first-story columns were circular, steel-jacketed members, whereas the columns above were rectangular, as shown in Figure 8-3. On the building perimeter, these rectangular columns were small (10 in. by 10 in.) with light transverse reinforcement, including in the beam-column joint region; this likely motivated the retrofit using the steel "prop" columns, which were rectangular HSS members bolted to beams above and below using end plates. Table 8-1 shows axial load ratio, reinforcement ratio, and splice length for these smaller columns at the second story.

This publication is available free of charge from: https://doi.org/10.6028/NIST.GCR.22-917-50

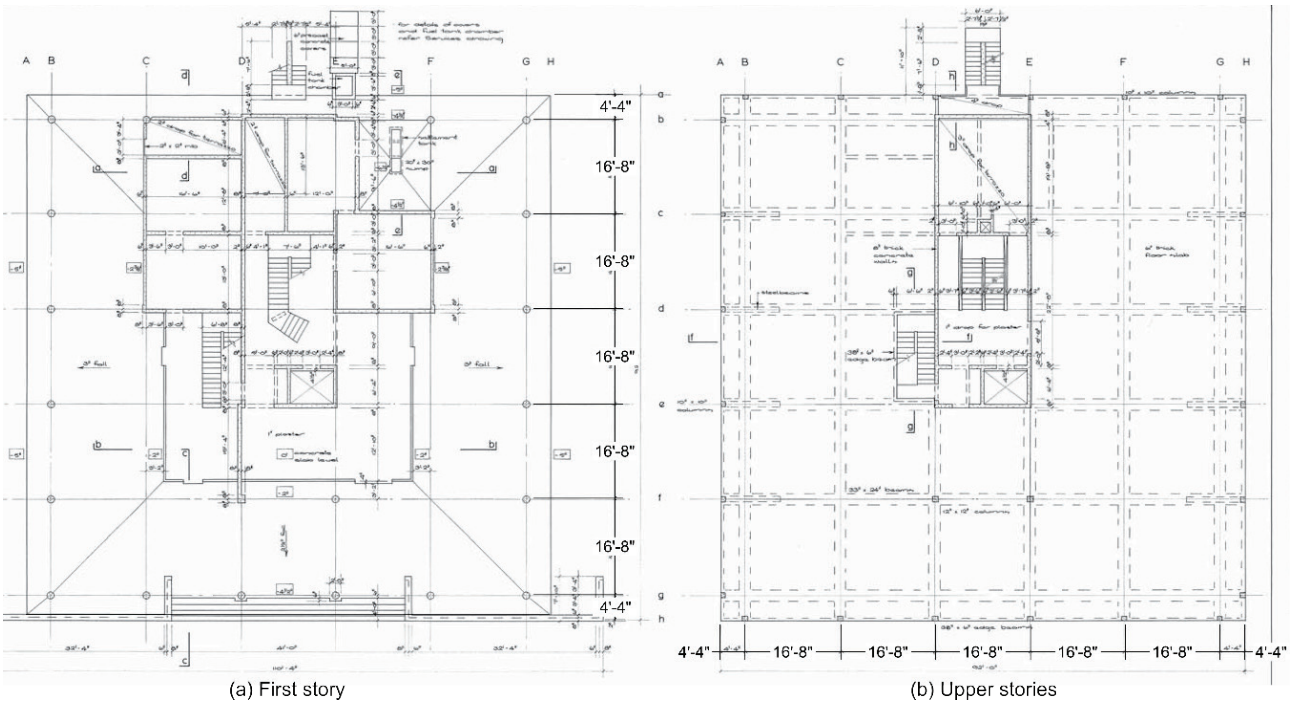


Figure 8-2 Building plan showing (a) first story and (b) upper stories (adapted from Beca, 2011).

This publication is available free of charge from: https://doi.org/10.6028/NIST.GCR.22-917-50

This publication is available free of charge from: https://doi.org/10.6028/NIST.GCR.22-917-50

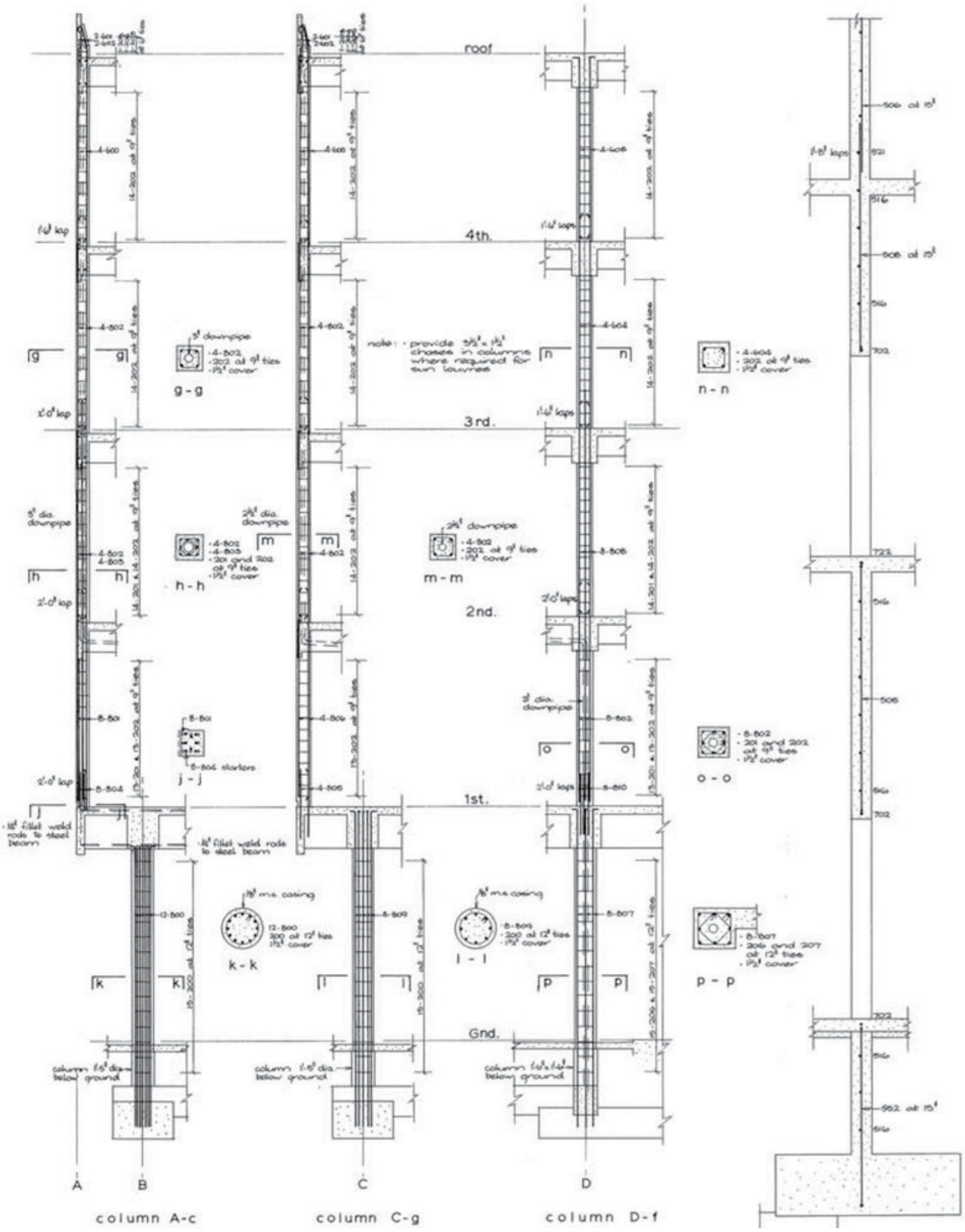


Figure 8-3 Building drawing showing column and wall dimensions and reinforcement details (Beca, 2011).

Table 8-1 Overview of Column and Wall Properties at Second Story

Member	Axial Load Ratio (Gravity Only), $N_{UG}/A_g f'_c$	Longitudinal Reinforcement Ratio, ρ_l	Transverse Reinforcement Ratio, ρ_t	Splice length, l_b/d_b
Column Type A-c	0.24	0.063	0.0019	24
Column Type C-g	0.17	0.031	0.0011	24
Column Type D-f	0.28	0.044	0.0015	24
Wall	0.11-0.34	0.0026	0.0026	29

The lateral force-resisting system consisted of thin (8 in. thick), lightly reinforced shear walls at the building core; this reinforcement consisted of #5 reinforcing steel spaced at 15 in. vertically and horizontally in a single layer in each direction (see Table 8-1 for properties at second story). The core was offset in plan toward the north of the building, but most of the wall area was still concentrated toward the center. The walls had regular openings to permit doors and windows.

8.2.2 Building Instrumentation

The building was not instrumented at the time of the earthquakes.

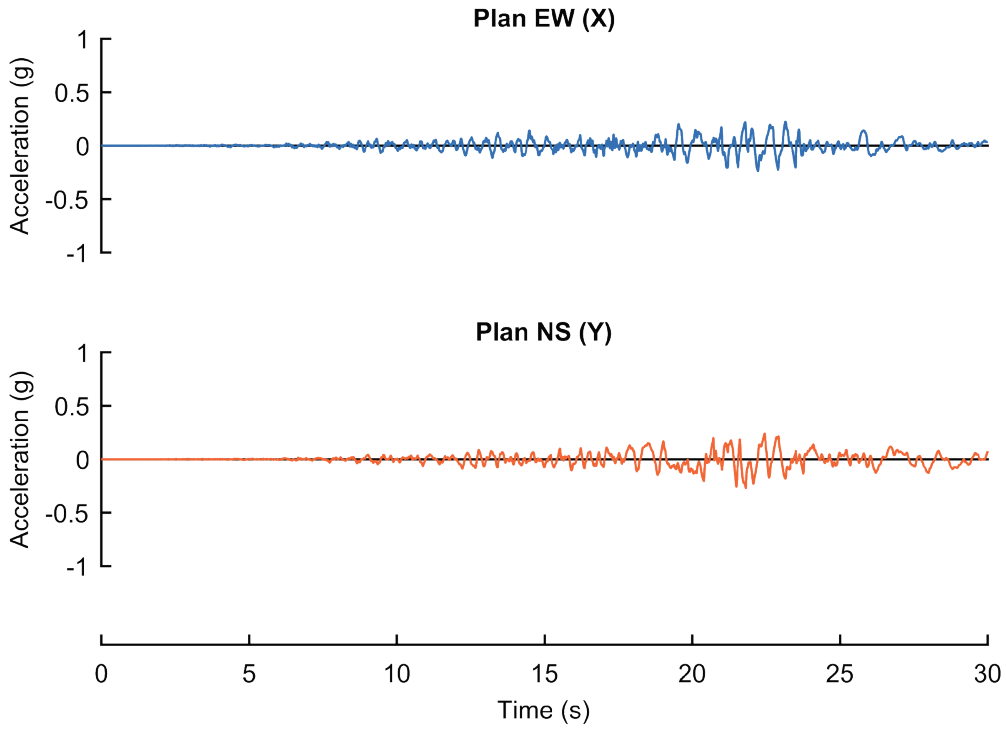
8.2.3 Ground Motion

The building was affected by two major earthquakes which were part of the 2010 -2011 Canterbury Earthquake Sequence: the September 4, 2010 Darfield Earthquake (M_w7.1) and the February 22, 2011 Christchurch Earthquake (M_w6.2). These large magnitude events were most significant, but the building was also subjected to many lower magnitude events that were not considered in this evaluation.

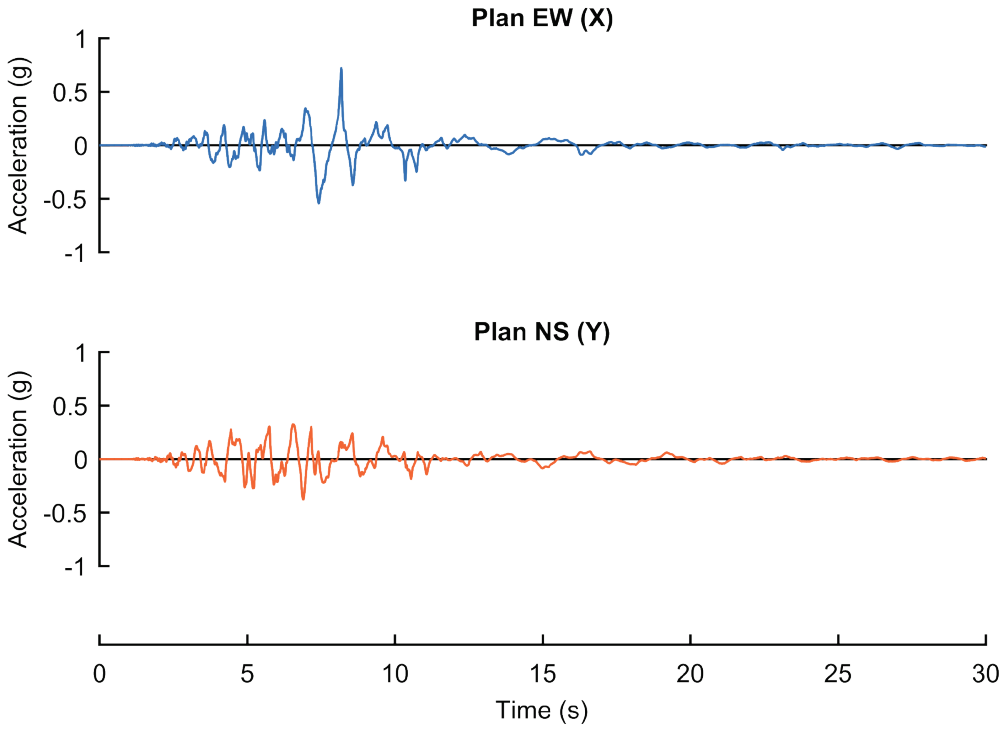
The best estimate recordings for the building site are from the Resthaven Station (REHS) site, located 0.42 miles (670 m) from the building (Beca, 2011). Figures 8-4 and 8-5 show the acceleration time history and 3%-damped acceleration response spectra in the east-west and north-south directions. Note that 3% damping was used to compute these spectra, since this is consistent with the assumed damping ratio used in the nonlinear analyses presented later. In the 2010 Darfield Earthquake, the peak ground accelerations were 0.24g and 0.27g in the east-west and north-south directions, respectively. In the 2011 Christchurch Earthquake, the peak ground accelerations were 0.72g and 0.38g in the east-west and north-south directions, respectively. The 3%-damped velocity and displacement response spectra, including annotated peak ground velocities (PGV) and displacements (PGD), are provided in Figures 8-6 and 8-7, respectively.

This publication is available free of charge from: https://doi.org/10.6028/NIST.GCR.22-917-50

This publication is available free of charge from: https://doi.org/10.6028/NIST.GCR.22-917-50

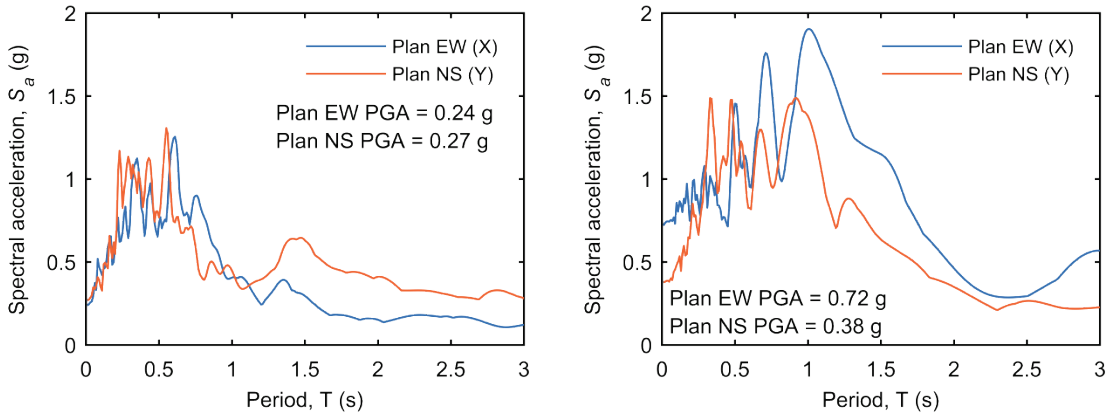


(a) 2010 Darfield Earthquake



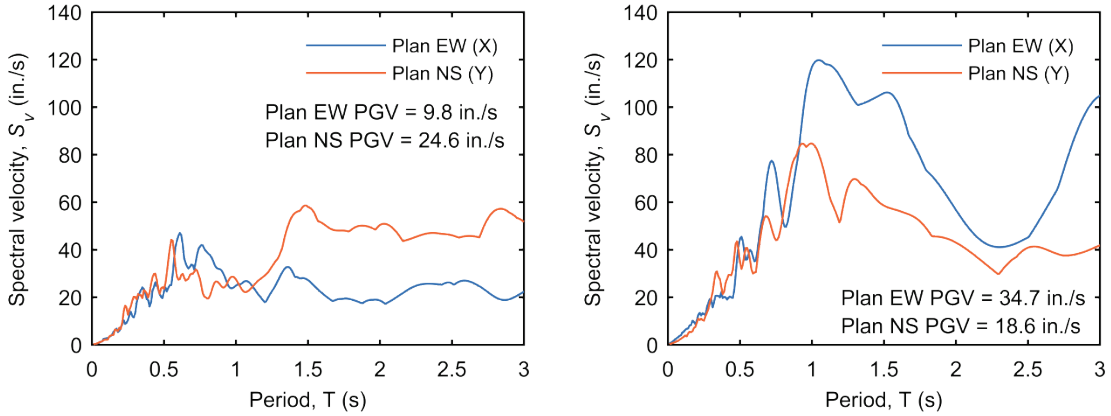
(b) 2011 Christchurch Earthquake

Figure 8-4 Acceleration time history at REHS site for two earthquakes.



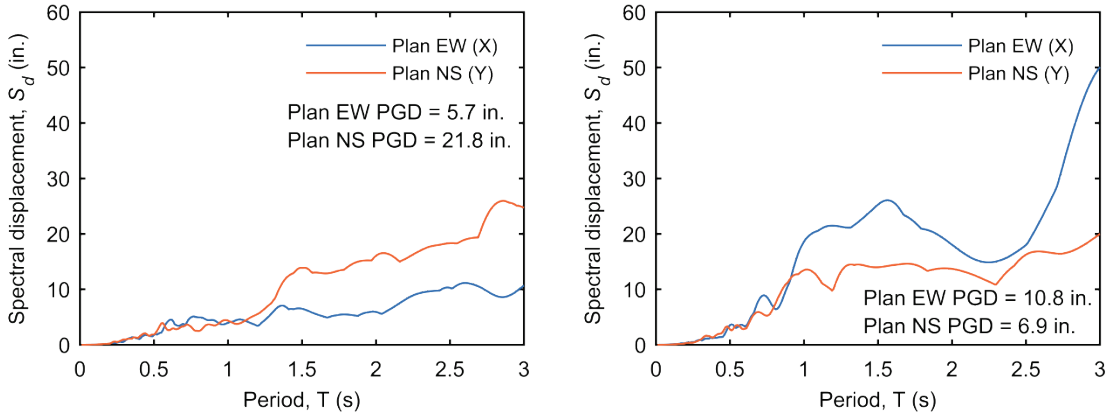
(a) 2010 Darfield Earthquake (b) 2011 Christchurch Earthquake

Figure 8-5 Horizontal acceleration response spectra with 3% damping at REHS site for two earthquakes.



(a) 2010 Darfield Earthquake (b) 2011 Christchurch Earthquake

Figure 8-6 Horizontal velocity response spectra with 3% damping at REHS site for two earthquakes.



(a) 2010 Darfield Earthquake (b) 2011 Christchurch Earthquake

Figure 8-7 Horizontal displacement response spectra with 3% damping at REHS site for two earthquakes.

This publication is available free of charge from: https://doi.org/10.6028/NIST.GCR.22-917-50

The analyses were conducted with the 2010 Darfield and 2011 Christchurch Earthquakes recorded at the REHS site in sequence with a period of free vibration between motions.

8.2.4 Observed Performance

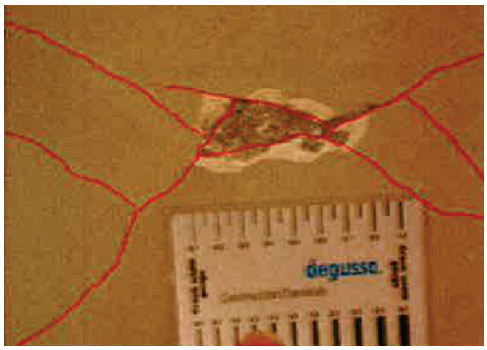
Simulated results are compared to observed residual damage from the 2010 Darfield Earthquake and collapse damage from the 2011 Christchurch Earthquake.

2010 Darfield Earthquake

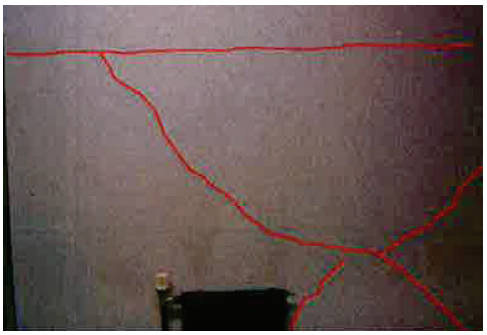
The 2010 Darfield Earthquake caused significant nonstructural damage to the building, as shown in Figure 8-8a. This nonstructural damage was immediately concerning for the occupants. In addition, there was cracking and minor spalling recorded, as shown in Figures 8-8b through 8-8d. The damage was judged to be minor, and the building was ultimately green tagged (i.e., INSPECTED) and reoccupancy was allowed. In lower magnitude events between the 2010 Darfield and 2011 Christchurch Earthquakes, building occupants reported that the structure was "more responsive" (Beca, 2011), perhaps indicating increased flexibility due to the sustained wall damage.



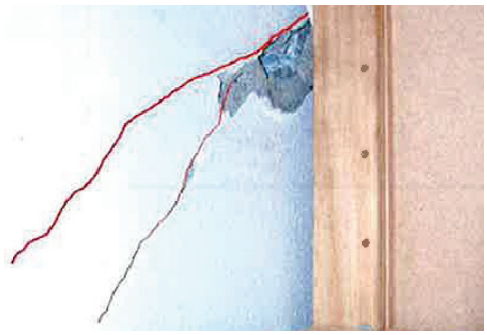
(a) Nonstructural damage



(b) Cracking (≤ 0.2 mm) and minor spalling near middle of east wall



(c) Cracking (≤ 0.2 mm)



(d) Cracking (0.2 mm – 0.6 mm) steel on east side of south wall

Figure 8-8 Damage observed after 2010 Darfield Earthquake (Department of Building and Housing, 2010).

This publication is available free of charge from: https://doi.org/10.6028/NIST.GCR.22-917-50

2011 Christchurch Earthquake

The building collapsed in the 2011 Christchurch Earthquake, resulting in 18 deaths. Figure 8-9 shows the collapsed state of the building viewed from the south, where the following can be observed:

- The first floor was essentially undamaged, as reported by Beca (2011) but all floors above collapsed due to failure of the gravity and lateral systems.
- Based on the residual configuration of the core, the building collapsed towards the east.
- The core was largely intact above the second story, indicating hinging of the wall at this location followed by large rigid body rotation that enforced deformation compatibility (and hence large displacement demands) on the upper stories.

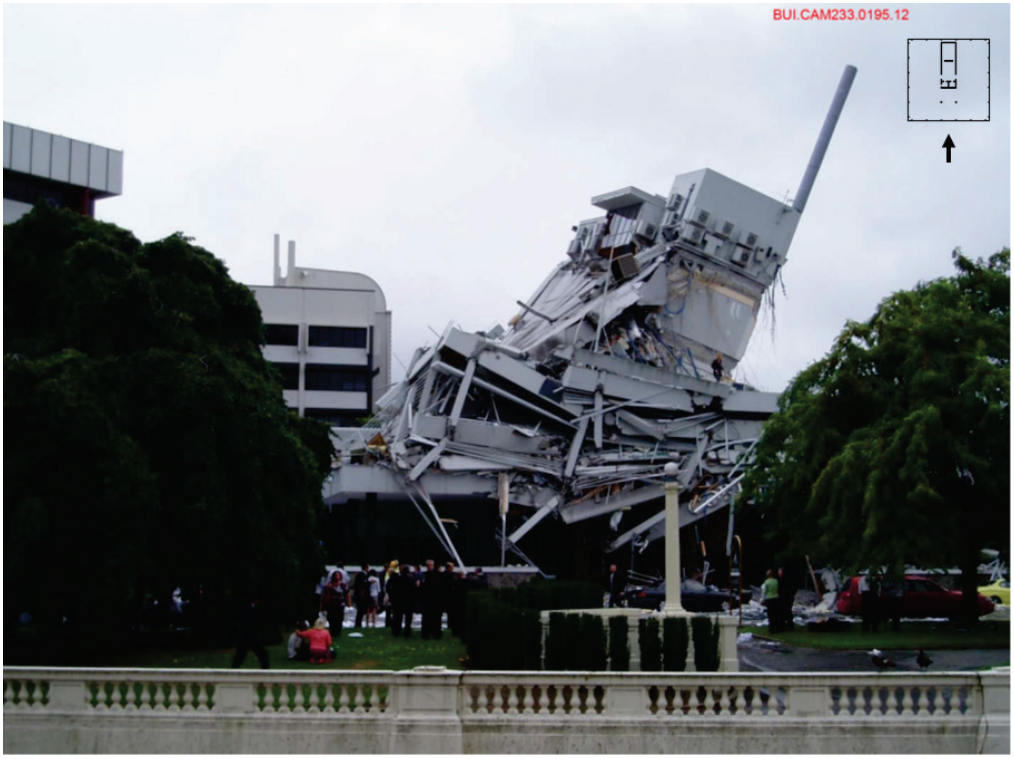


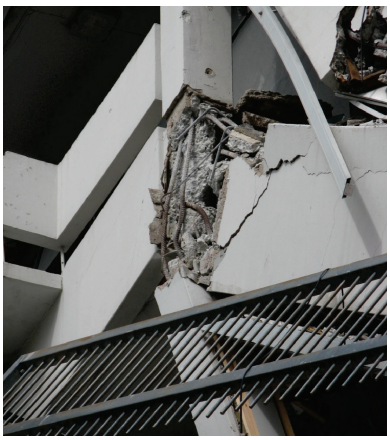
Figure 8-9 Photo showing collapsed building viewed from south (across the Avon River; adapted from Jury and Sharpe [2011]).

The perimeter beam-column joints sustained significant damage as shown in Figure 8-10. The observed failures were a function of lack of confinement in the joint region and relatively short longitudinal-reinforcement splices ($24d_b$) directly above the joint region. There was no evidence suggesting obvious flexural or shear failure of the columns.

Figure 8-11 shows the wall failure mode in greater detail. As indicated by the circled area of the photograph, the east flange of the wall failed axially at the second story,

This publication is available free of charge from: https://doi.org/10.6028/NIST.GCR.22-917-50

resulting in rotation of the core above. This rotation was large and precipitated failure of the gravity system due to the deficient beam-column joints, column splice details, and fracture of the slab reinforcement at the wall interface (see Figure 8-12). Figure 8-11 also shows that the steel "prop" columns added in the late 1990s were ineffective, as the end-plate connections were not able to sustain the large rotations imposed following the wall failure.



(a) Typical beam-column joint damage



(b) Beam-column joint damage with pullout of spliced reinforcing steel

Figure 8-10 Photo of damaged beam-column joints (Jury and Sharpe, 2011).



Figure 8-11 Photo showing overview of collapsed building from north; circle indicates location of axial failure of east wall (obscured; adapted from Jury and Sharpe [2011]).

This publication is available free of charge from: https://doi.org/10.6028/NIST.GCR.22-917-50



Figure 8-12 Photo of fractured slab reinforcement at slab-wall interface (Jury and Sharpe, 2011).

8.3 Nonlinear Dynamic Procedure

8.3.1 Modeling Approach

A three-dimensional numerical model of the structure was created in OpenSees using assemblage of line and zero-length elements. Gravity loading was applied at the center of gravity of each column, wall segment, and beam intersection. A rigid diaphragm constraint was used to tie these nodes together. Seismic mass was similarly distributed and applied in both lateral degrees of freedom; note that this mass distribution results in inherent torsional excitation. All line elements were modeled with geometric nonlinearity using the corotational coordinate transformation.

The shear walls at the core of the building were modeled using displacement-based beam-column elements with distributed plasticity to simulate nonlinear flexural response and zero-length spring elements at the base of each story to simulate shear response. Displacement-based beam-column elements with distributed plasticity were selected to minimize convergence issues at sudden loss of strength or stiffness. The walls were divided in plan into 9 segments on the first story and 7 segments on the upper stories based on the actual openings (doorways and windows) and the effective flange widths were computed based on Chapter 18 of ACI 318, as required by ASCE 41-17 (see Figure 8-13). The first- and second-story wall element

This publication is available free of charge from: https://doi.org/10.6028/NIST.GCR.22-917-50

centerlines do not align in plan due to this segmentation and were connected with rigid beam-column elements to transfer load between these stories. The wall segments were coupled using elastic beam-column elements with shear deformation. Each wall segment had a distinct fiber section that was distributed over 6 elements per story with 5 integration points per element. The coupling action and effective flange widths resulted in three wall groups: (1) box section; (2) I-shaped section; and (3) C-shaped section. The concrete constitutive model used was regularized after Marafi et al. (2019), and the steel constitutive model was "wrapped" such that its strength and stiffness reduced to essentially zero upon spalling of the surrounding concrete or fracture (based on the usable strain limit in ASCE 41-17). Note that the steel tensile strain was limited by fracture because the wall reinforcement was spliced over an 18 in. length ($29d_b$) at each story, which is adequate for development based on Chapter 25 of ACI 318.

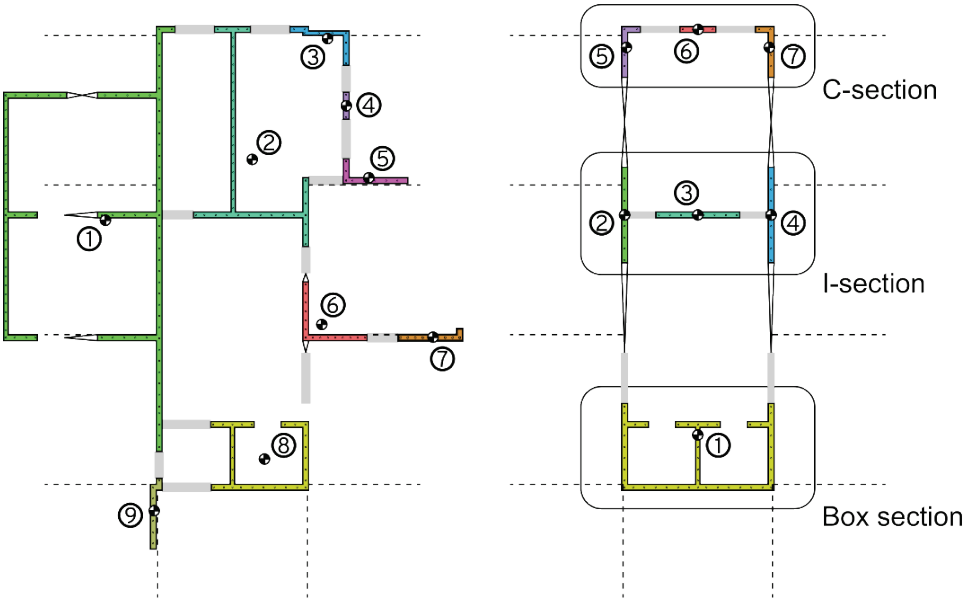


Figure 8-13 Wall segments in nonlinear analysis model.

Shear springs were included between wall elements at each story. Two approaches for modeling wall shear were investigated with two separate building models: (1) linear-elastic shear response and (2) nonlinear shear response using the strength and modeling parameters of ASCE 41-17. It is noted that the former approach is not compliant with ASCE 41-17 but was evaluated to attempt to simulate the observed wall failure mechanism and building collapse mode. In both cases, the shear springs had elastic stiffness consistent with the corresponding cracked section. The wall segments were fixed at the bases of the first story shear springs.

Column, beam, and beam-column joints were modeled based on their respective ASCE 41-17 modeling parameters. The columns were modeled using nonlinear

This publication is available free of charge from: https://doi.org/10.6028/NIST.GCR.22-917-50

fiber-based hinges in series with limit-state moment-rotation springs, as described in Appendix A. These limit-state moment-rotation springs accounted for nonlinear response due to both shear/flexure-shear and splice failure mechanisms. The columns were fixed at their bases and were modeled as elastic beam-column elements with cracked section properties between hinge regions. Beams were modeled as T-sections and also utilized fiber-based hinges at their ends. Beam-column joints were modeled explicitly using nonlinear rotational springs.

Figure 8-14 depicts the first mode shape computed for the nonlinear models (the modes are identical between the two model variations, since the elastic shear response of the walls is the same). The periods and descriptions of shapes of the first three modes are provided in Table 8-2. Modal damping was applied for the first 5 mode shapes with supplemental initial-stiffness-proportional Rayleigh damping. The total damping ratio from modal and Rayleigh damping was 3% of critical; ASCE 41-17 specifies a damping ratio of up to 3% for most buildings.

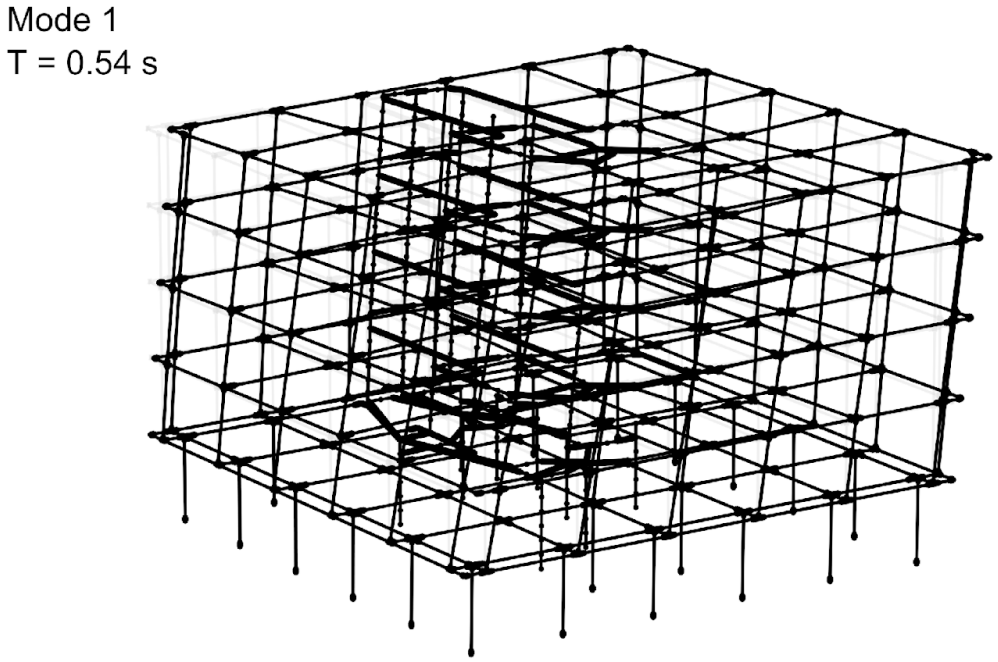


Figure 8-14 First mode shape.

Table 8-2 Mode Shapes

	Period (s)		
Mode	*Linear*	*Nonlinear*	Shape or direction
1	0.52	0.54	East-west translation
2	0.31	0.41	Torsion
3	0.25	0.26	North-south translation

This publication is available free of charge from: https://doi.org/10.6028/NIST.GCR.22-917-50

The building had h/T of 24.6 m/s, which implies soil-structure interaction (SSI) would not be expected to significantly contribute to the response for V_s greater than 246 m/s. This V_s was judged to be sufficiently low to neglect SSI.

8.3.2 Global Performance: Model vs. Observation

Figures 8-15 and 8-16 present the story drift response history results in the east-west and north-south directions, respectively, for both nonlinear and linear-elastic wall shear response models (note that both results are based on nonlinear building models; the linear building model is discussed in Section 8.4) with the 2010 Darfield and 2011 Christchurch Earthquake records applied between 0-35 seconds and 45-80 seconds of the time history, respectively. When the wall was modeled with nonlinear response in shear, the second story drift exceeded 10% in the east-west direction (see Figure 8-15b) at about 55 seconds; this led to numerical nonconvergence but at deformations well beyond the valid range of modeling.

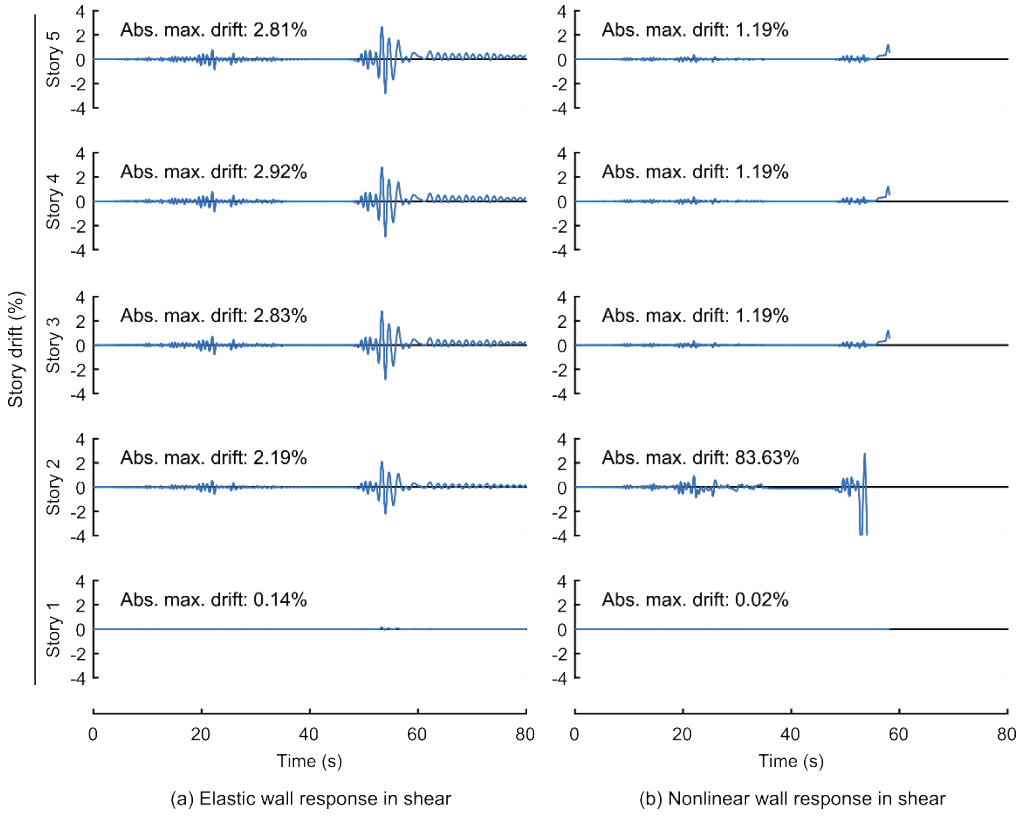


Figure 8-15 NDP: Comparison of story drift response histories in east-west direction. Note that drift histories show response to the 2010 Darfield Earthquake in the time period 0-35 seconds followed by response to the 2011 Canterbury Earthquake in the time period 45-80 seconds.

This publication is available free of charge from: https://doi.org/10.6028/NIST.GCR.22-917-50

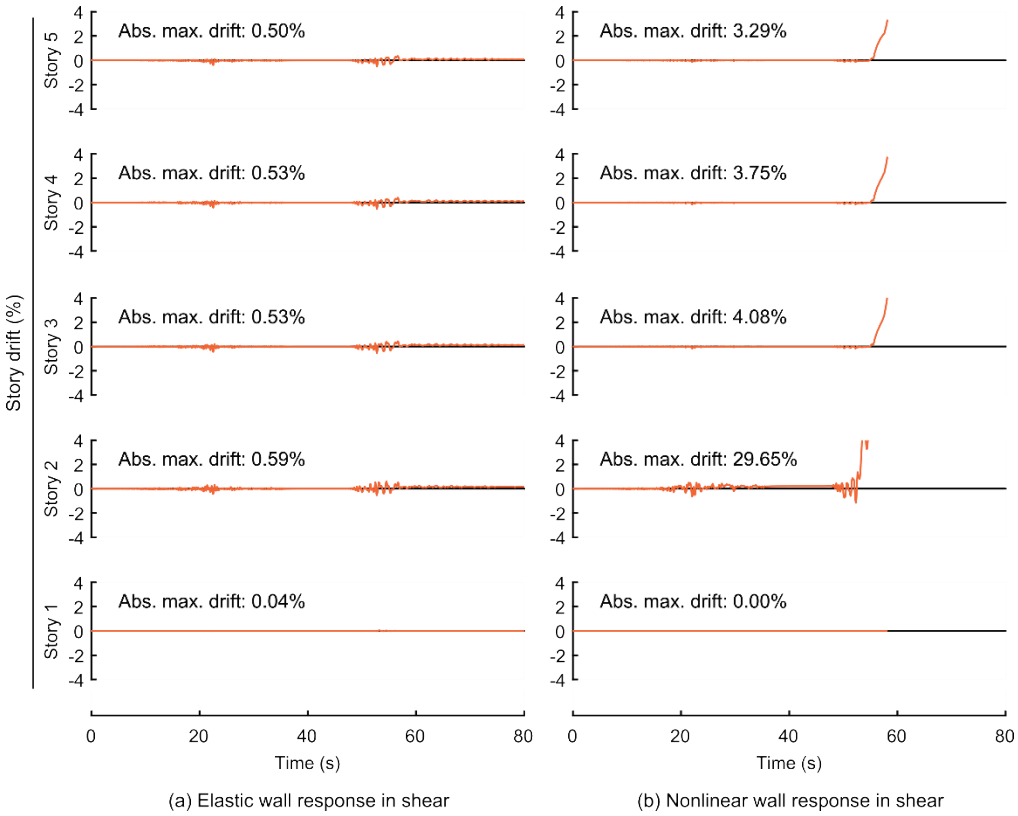


Figure 8-16 NDP: Comparison of story drift response histories in north-south direction. Note that drift histories show response to the 2010 Darfield Earthquake in the time period 0-35 seconds followed by response to the 2011 Canterbury Earthquake in the time period 45-80 seconds.

Story drifts were measured from the center of mass of the effective southern core (closest to the building center) and hence the torsional influence was limited. While the building is classified as Extremely Torsionally Irregular based on ASCE 7, the overall torsional response was not significant due to strength and stiffness degradation of the walls at low deformation demands (less than 0.5% drift).

Neither model predicted collapse in the 2010 Darfield Earthquake, but the demand exceeded the yield deformation limit for multiple wall elements at the second story for both models.

The deformation demands reached levels associated with collapse in the 2011 Christchurch Earthquake. Similar extreme demands were observed when the models were analyzed using the 2011 Christchurch Earthquake only. In the model with elastic wall response in shear (i.e., an elastic shear spring), the response was flexural, and the fibers sustained damage to the concrete in compression and fracture of the longitudinal reinforcement. The response of these damaged wall segments in the model was essentially that of a rocking wall, with the interior of the wall resisting minimal flexural demands but still capable of resisting shear (this behavior has been

This publication is available free of charge from: https://doi.org/10.6028/NIST.GCR.22-917-50

seen in tests before, see Lehman et al., 2013). As such, the severely damaged walls rocked about the base of the second story.

In addition, the damage to the core wall section was less than the other two wall segments and acted to constrain the displacement distribution over the height of the building, resulting in a more or less even distribution of story drift demands.

This response is consistent with the observed failure of the gravity system in the upper stories of the building. Specifically, strong beams could be expected to result in column and joint damage and the development of a soft-story mechanism; however, the stiffness and strength of the wall could also be expected to constrain the drift distribution, resulting in severe damage to the gravity system at every story level.

In the model with nonlinear shear response (i.e., nonlinear shear springs), the shear springs at the base of the second story reached the drift corresponding to the residual strength; this resulted in a soft-story effect, which was not the observed damaged mode. This unrealistic concentration of drift in one story has been observed in other studies using nonlinear springs to represent wall shear response [e.g., Kolozvari and Wallace (2016)]. Using this modeling approach, stories above the second story were predicted to have significantly less damage although the model predicted collapse.

Story drift was substantially lower in the north-south direction with elastic shear response, but these drifts increased without bound with nonlinear wall response in shear, due to the unstable response in the east-west direction. The predicted torsional response was low and generally consistent with the observed collapse mechanism.

Table 8-3 summarizes the accuracy of the global response based on the apparent collapse mechanism of the actual building. Maximum story drift was predicted to occur in the east-west direction in both cases, but collapse was predicted when the nonlinear shear spring was used to bound the wall response (see second story response in Figure 8-16b). Note that the first story, which had stronger columns and significantly more wall area, had virtually no predicted damage.

This publication is available free of charge from: https://doi.org/10.6028/NIST.GCR.22-917-50

Table 8-3 Comparison of Simulated Response to Observed Damage

Attribute	Elastic wall response in shear	Nonlinear wall response in shear
Story drift vertical distribution	Match	No match
Story drift severity at critical story	Match*	Match[a]
Story drift severity everywhere else	Match	Below
Direction of maximum drift	Match	Match
Torsion	Match	Match

*Simulated collapse (inferred from story drift exceeding 10% where nonlinear shear response in the wall is considered, and implicitly predicted due to nearly all gravity columns above the first story being pushed beyond CP when only elastic shear response of the wall is considered.)

8.3.3 Component Response: Model vs. Observation

It is difficult to classify the component failure mechanisms that led to collapse of the structure, but several observations can be made from the available photographic evidence:

- The walls sustained compressive failure at the second story that suggests the wall flanges resisted significant flexural and axial demands resulting from coupling action.
- There was significant spalling of concrete and buckling of the reinforcement in the joint region.
- There was significant spalling and, in most cases, complete failure of the column splice region above the joint.
- The slab reinforcement fractured at the slab-to-wall interface.

Table 8-4 summarizes the accuracy of the predicted response of the columns, walls, and joints. In general, failure mechanisms were not well predicted with the ASCE 41-17 nonlinear procedure. When the walls were modeled with elastic shear response (i.e., shear failure is neglected), wall failure was successfully predicted due to flexure. However, such a model is not compliant with ASCE 41-17. With both shear models for the wall elements, the column failure mechanism was predicted as a shear failure only, with no predicted failure due to inadequate development or splicing. Further, while the beam-column joints were predicted to sustain damage, this was limited to a small number of columns, and none were predicted to reach the point of axial failure (modeling parameter *b* on the ASCE 41 backbone curve definition).

This publication is available free of charge from: https://doi.org/10.6028/NIST.GCR.22-917-50

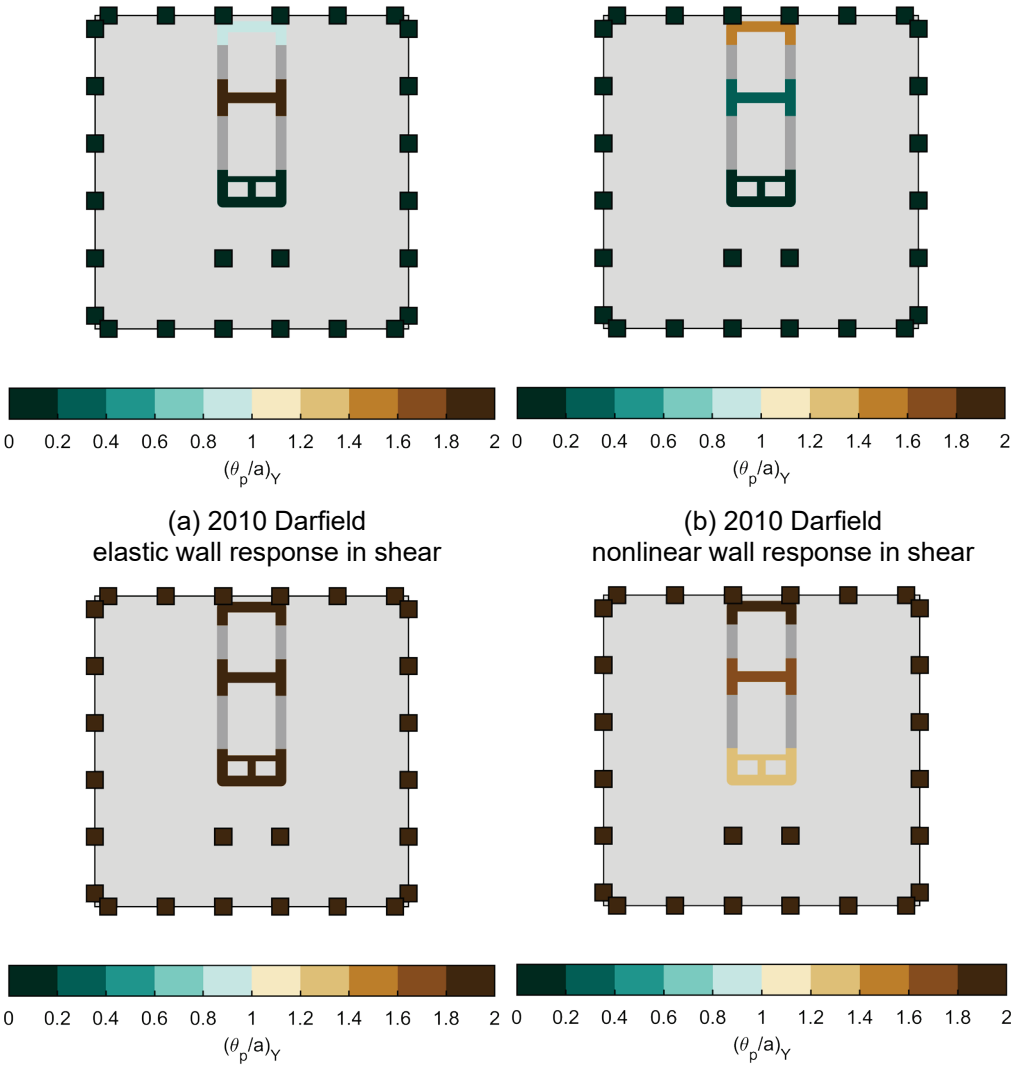
Table 8-4 Comparison of Predicted Local Response to Observed Damage

	Elastic Wall Response in Shear		Nonlinear Wall Response in Shear	
Component	*Failure Mechanism*	*Level of Damage*	*Failure Mechanism*	*Level of Damage*
Walls	Match	Match	No match	Match
Columns	No match	Above	No match	Above
Joints	No match	Below	No match	Below

Figures 8-17 through 8-19 provide a spatial distribution of the severity of predicted column and wall damage on the basis of plastic hinge rotations relative to the ASCE 41-17 modeling parameters *a* and *b* in Figure 2-1 and the acceptance criteria at the second story. These distributions are shown for the 2010 Darfield Earthquake ground motion and 2010-2011 Canterbury Sequence (the 2010 Darfield and 2011 Christchurch ground motions in series). It is noted that no column damage was observed after the 2010 Darfield Earthquake, but some concrete spalling was identified in the box section of the core wall. For the 2010 Darfield Earthquake only, both models overpredict the level of damage to the walls but predict the lack of column damage well. In addition, it is noted that the acceptance criteria suggest collapse due to failure of the walls and columns in the 2011 Christchurch Earthquake for both models.

This publication is available free of charge from: https://doi.org/10.6028/NIST.GCR.22-917-50

This publication is available free of charge from: https://doi.org/10.6028/NIST.GCR.22-917-50



(a) 2010 Darfield
elastic wall response in shear

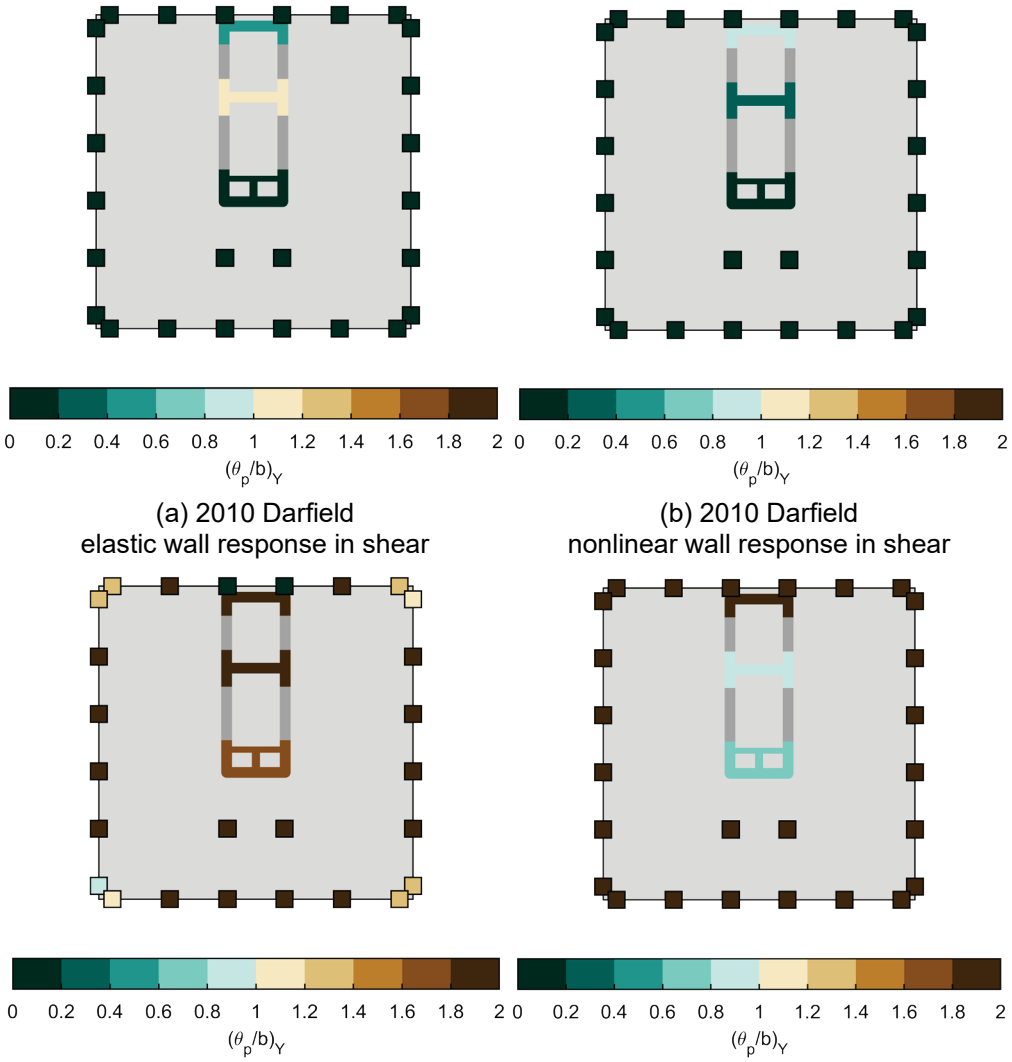
(b) 2010 Darfield
nonlinear wall response in shear

(c) 2010 Darfield and 2011 Christchurch
elastic wall response in shear

(d) 2010 Darfield and 2011 Christchurch
nonlinear wall response in shear

Figure 8-17 NDP: Heatmap of second-story column and wall plastic rotation DCRs relative to modeling parameter *a* in the east-west direction.

This publication is available free of charge from: https://doi.org/10.6028/NIST.GCR.22-917-50



(a) 2010 Darfield elastic wall response in shear

(b) 2010 Darfield nonlinear wall response in shear

(c) 2010 Darfield and 2011 Christchurch elastic wall response in shear

(d) 2010 Darfield and 2011 Christchurch nonlinear wall response in shear

Figure 8-18 NDP: Heatmap of second-story column and wall plastic rotation DCRs relative to modeling parameter *b* in east-west direction.

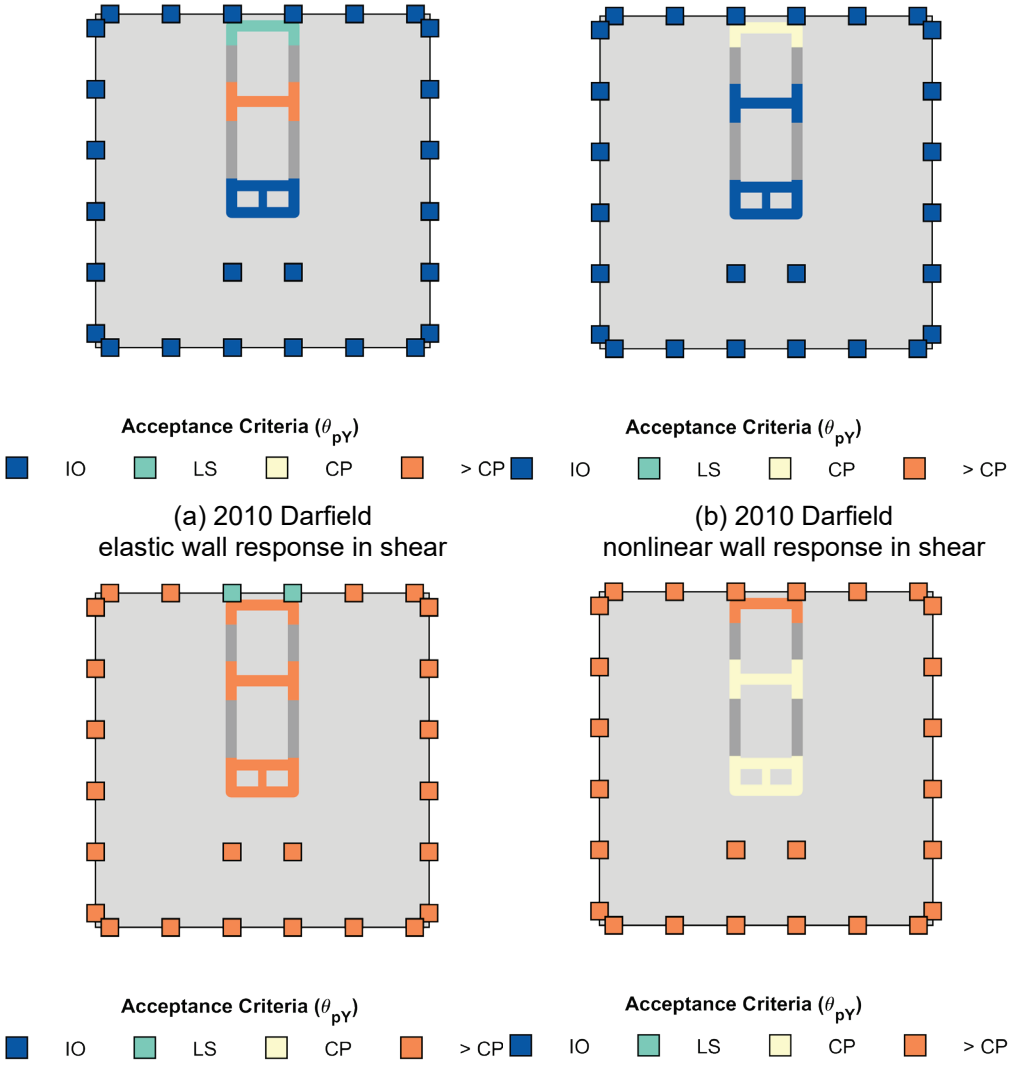


Figure 8-19 NDP: Heatmap of second-story column and wall plastic rotation acceptance criteria in east-west direction. Shown relative to ASCE 41-17 nonlinear acceptance criteria Immediate Occupancy (IO), Life Safety (LS), and Collapse Prevention (CP).

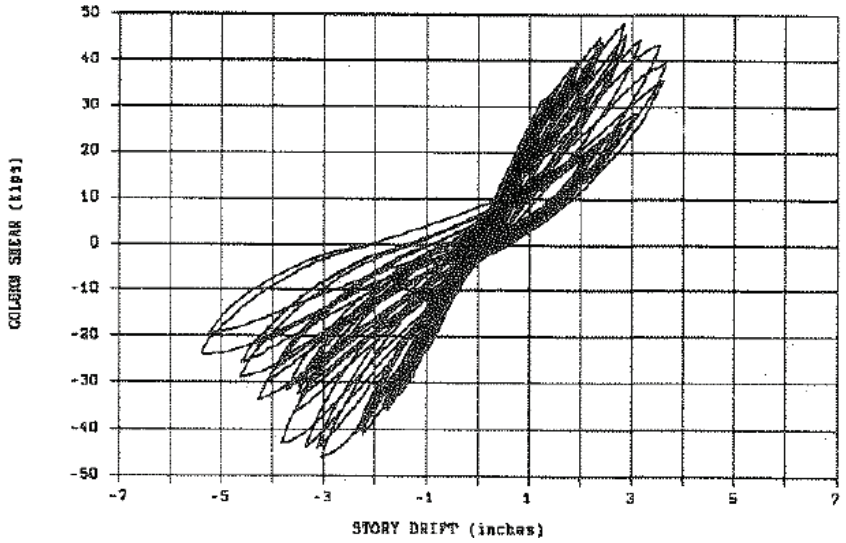
8.3.3.1 Frame Response: Comparison to Similar Experimental Specimens

The observed response of the gravity framing was assumed to be nonductile and driven by bond failure in the joint region and the adjacent column splice region (see photographs in Figure 8-10). The beams were strong and deep relative to the columns and appeared largely undamaged in the collapsed state of the building. This assumed failure mechanism in the joint region is complex and not addressed by ASCE 41-17, in which the impact of splices in the vicinity of the joint is not considered. Consequently, this failure mechanism was not simulated in the nonlinear analyses; instead, the analyses predicted gravity framing failure due to a flexural-

This publication is available free of charge from: https://doi.org/10.6028/NIST.GCR.22-917-50

shear response in the columns, which is not substantiated by the photographic evidence.

There are limited experimental data for beam-column joint subassemblages with these design characteristics. Specimen 2 of Pessiki et al. (1990) was a cruciform beam-column specimen with similar characteristics to the gravity framing of the study building and provides some insight. The test specimen had weak columns relative to the beams with widely spaced transverse joint reinforcement, no joint ties, and a splice above the joint. Figure 8-20a shows measured hysteretic response of the experimental specimen, and Figure 8-20b shows a diagram of cracking and spalling in the specimen at the end of the test. Flexural cracking in the column and inclined cracking in the joint occurred prior to flexural yielding [approximately 0.84 inches (0.67%) story drift in Figure 8-20a]. After yielding, vertical splitting cracks developed on the column faces perpendicular to the plane of loading, leading to spalling, exposure of the longitudinal reinforcement of the column, and significant deterioration of lateral resistance. The peak resistance was obtained at a story drift of 2.84 inches (2.3%). The drift capacity prior to deterioration is larger than predicted by the ASCE 41 parameters for the second story columns in the study building (where deterioration occurs at 0.7-1.5% story drift, depending on column location), but the damage illustrated in Figure 8-20b is similar to that of Figure 8-10, suggesting that this mechanism is likely to have occurred. Further work is needed to incorporate these effects in ASCE 41.



(a) Column shear v. drift response

(b) Beam-column joint damage at end of test

Figure 8-20 Measured hysteretic response and damage for Specimen 2 (Pessiki et al., 1990).

This publication is available free of charge from: https://doi.org/10.6028/NIST.GCR.22-917-50

This publication is available free of charge from: https://doi.org/10.6028/NIST.GCR.22-917-50

8.3.3.2 Wall Response: Comparison to Similar Experimental Specimens

The responses of each of the three main wall sections are evaluated in more detail here and compared to tests of lightly reinforced shear walls. There are limited data for walls of this type, especially with complex section geometry (flanged and asymmetric sections) and coupling. Lu et al. (2017) conducted tests of planar walls with low reinforcement ratios. These specimens had no boundary elements; vertical and horizontal reinforcement ratios of 0.53% and 0.25%, respectively; axial load ratios of 3.5%; and varying shear span ratios. Note that the building walls had vertical and horizontal reinforcement ratios of 0.26% and larger axial load ratios.

Figure 8-21 shows the moment-rotation response from response-history analysis for the box, I- ,and C-sections at the base of the second story of the building in the elastic wall shear response model. The ASCE 41-17 backbone curves in the east-west direction of loading are superimposed on the plots (shaded region) to indicate the magnitude of the deformation demand; each of the walls sustained deformations well beyond the level of axial load failure according to the ASCE 41-17 modeling parameters. Although the deformation capacity exceeds the modeling criteria, the acceptance criteria were used to determine level of damage and collapse potential. Instead of the prescribed moment-rotation envelope, the usable strain limits defined by Section 10.3.3.1 of ASCE 41-17 were used to determine degradation of the wall response, which is an acceptable modeling approach. As mentioned in Section 8.3.1, the concrete constitutive model was regularized in this work, and it is recommended that regularization techniques for fiber-based modeling of softening systems be addressed by ASCE 41.

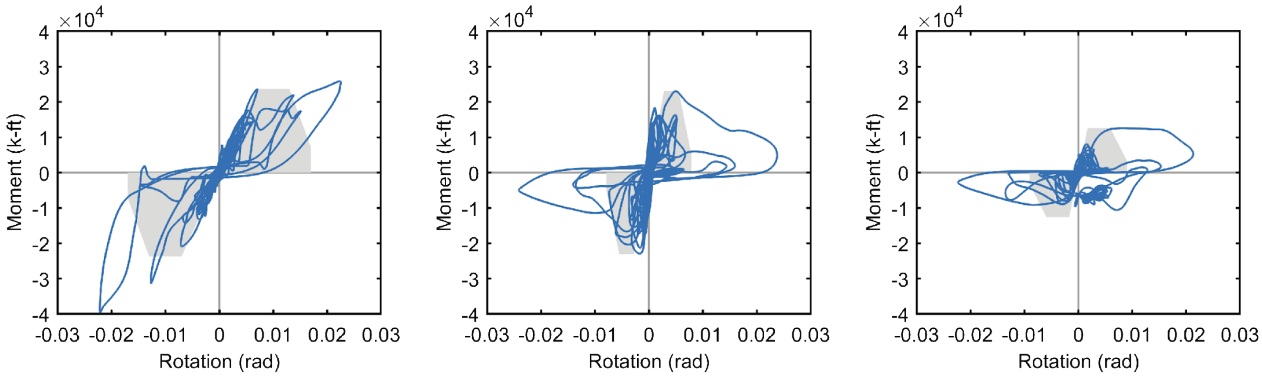
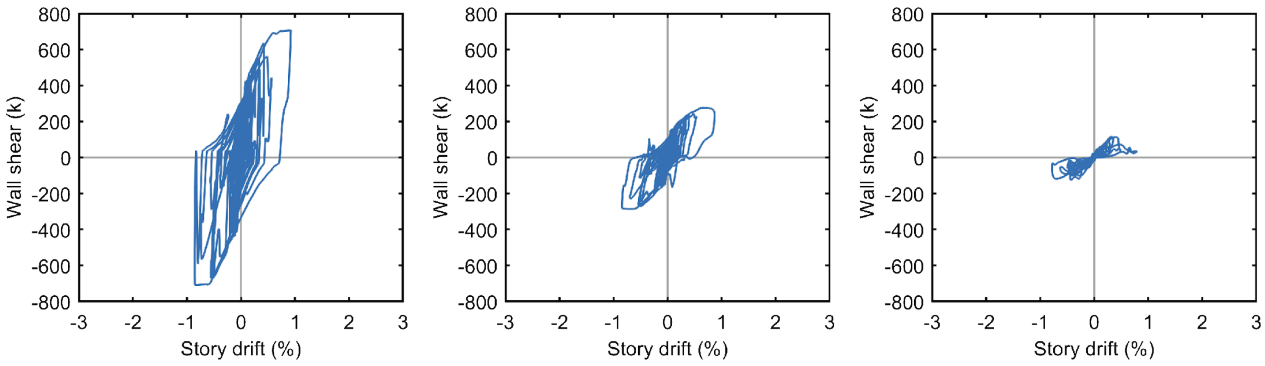


Figure 8-21 Wall moment-rotation response at base of second story in elastic wall shear response model; shaded region indicates ASCE 41-17 backbone curve.

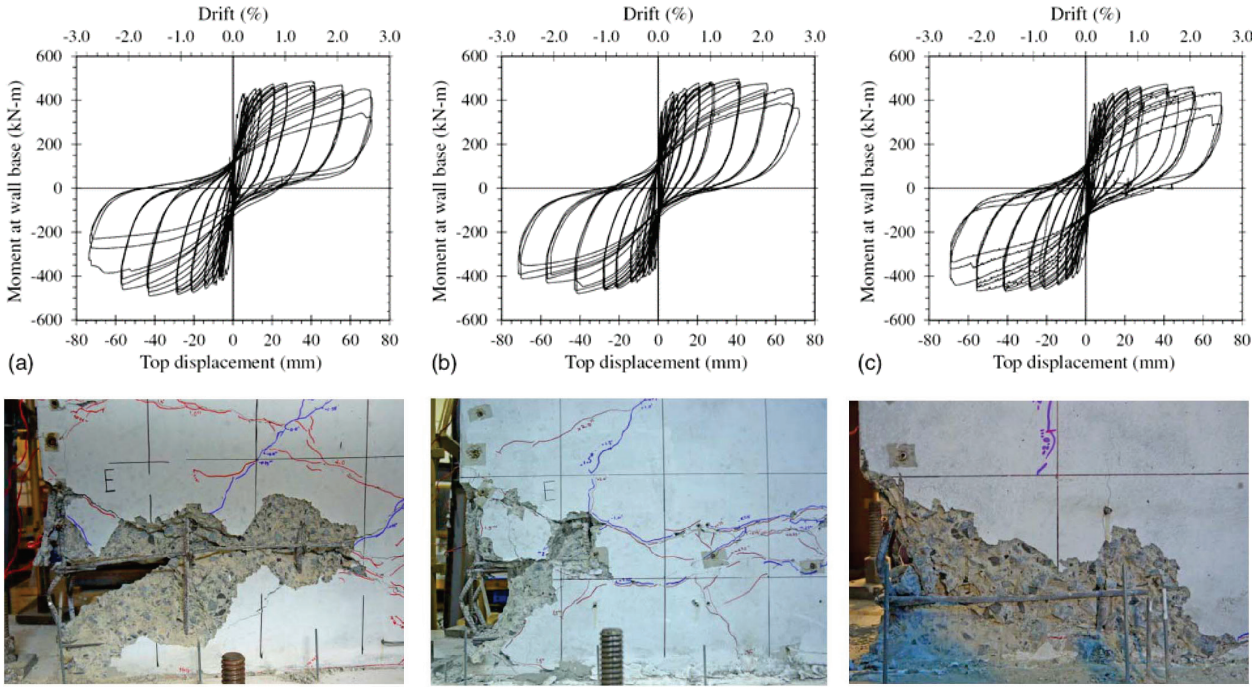
Figure 8-22 shows the shear-drift response for the box, I-, and C-sections at the base of the second story in the nonlinear wall shear response model (moment-rotation response is not shown since the shear springs are in series with the wall beam-column elements).



(a) Box section (b) I-section (c) C-section

Figure 8-22 Wall shear-story drift response at base of second story in nonlinear wall shear response model.

The responses of Specimens C1 through C3 from Lu et al. (2017) are shown in Figure 8-23. In comparison to both the flexure- and shear-controlled predicted responses of the walls of the study, these specimens were more ductile but had similar heavily pinched hysteresis. The lower ductility of the building walls is attributed to their lower reinforcement ratios and higher axial load ratios.



(a) Specimen C1 (b) Specimen C2 (c) Specimen C3

Figure 8-23 Measured hysteretic response and toe damage at end of each test for Specimens C1, C2, and C3 (from Lu et al., 2017).

This publication is available free of charge from: https://doi.org/10.6028/NIST.GCR.22-917-50

8.4 Linear Dynamic Procedure

8.4.1 Modeling Approach

A two-dimensional numerical model of the structure was created in ETABS v18 and evaluated using the response spectrum method for linear dynamic procedure (ASCE 41-17 Section 7.4.2.2.3) and the linear response history method (ASCE 41-17 Section 7.4.2.2.4).

The ETABS analysis model is shown in Figure 8-24 with gridlines for reference. All elements are modeled as linear elastic with effective stiffnesses per ASCE 41-17 Table 10-5. The walls are considered primary elements and the frames are considered secondary elements per ASCE 41-17 Section 7.2.3.3. The beams and columns are modeled as line elements while the slabs and walls are modeled as shell elements. Due to the poor development of the beam reinforcing into the walls, the ends of the beams are released for moment where supported by walls. The ends of the north-south beams on Gridlines B and G at the first floor are also released for moment because their connections are poor due to the interference with the embedded steel beams found at Gridlines C, D, E, and F where the perimeter columns discontinue and their load is transferred to the inset first story columns.

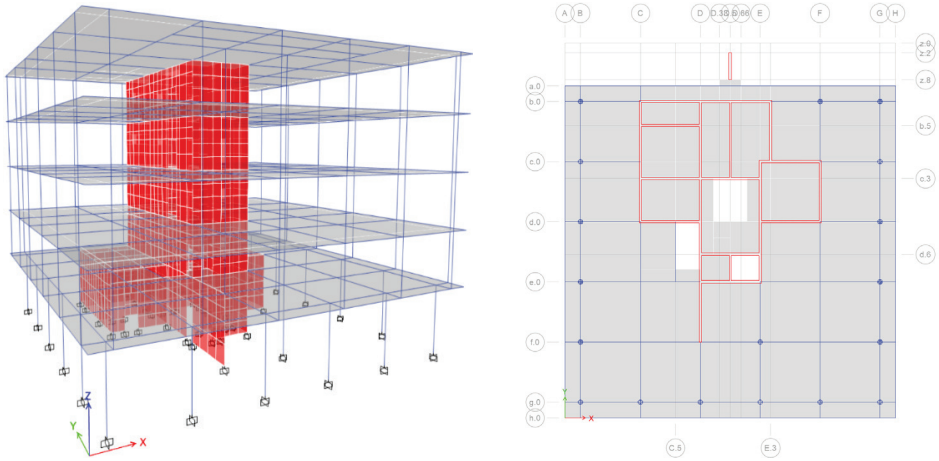


Figure 8-24 Linear: 3D model developed with ETABS.

8.4.2 Global Performance: Model vs. Observation

The first mode period of the structure as obtained from the analysis is 0.52 sec. primarily translational in the transverse (EW, X) direction, while the second mode period is 0.31 sec. with a primarily torsional response. The third mode period is 0.25 sec. primarily translational in the longitudinal (NS, Y) direction. These periods are compared to the nonlinear model periods in Table 8-2. The response types of the first three modes match between model types. The torsional (second) mode period is notably lower in the linear model, where wall torsional stiffness is better approximated using shell elements.

This publication is available free of charge from: https://doi.org/10.6028/NIST.GCR.22-917-50

The structure is characterized as Extremely Torsionally Irregular per ASCE 7 (ASCE, 2017a). The analysis considers inherent torsion and accidental torsion from 5% mass displacement. However, the accidental torsion was not amplified further.

The spectral accelerations associated with the periods in the primary orthogonal directions are 1.1g in the transverse direction and 0.64g in the longitudinal direction according to the recorded response spectra from the REHS site.

The maximum seismic story drifts results are reported in the transverse (EW, X) and longitudinal (NS, Y) directions. Figure 8-25a presents the drifts at the center of mass. The torsional response of the building in the transverse direction amplifies drifts on the southern edge of the building as can be seen in Figure 8-25b. The relatively low first story seismic drift is due to the large amount of first story shear walls. The largest drift can be seen in the transverse direction at the second story, which is where the walls failed. This is in agreement with the building response.

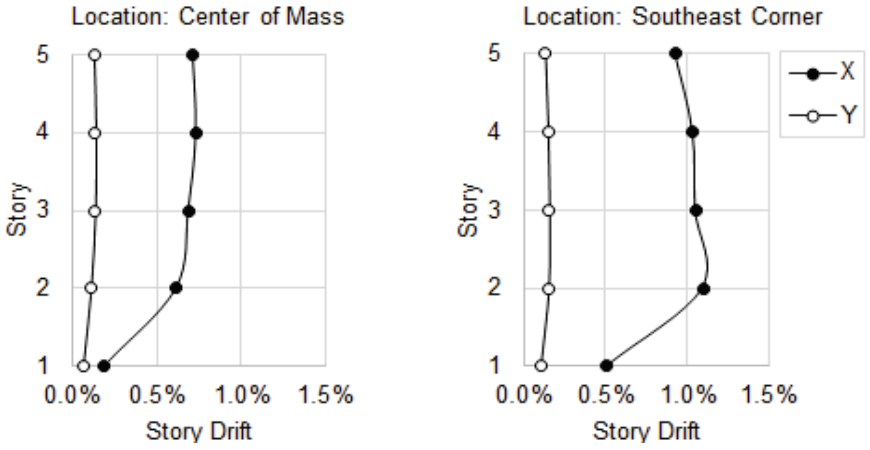


Figure 8-25 Linear: Maximum story drift at two different locations.

8.4.3 Component Performance: Model vs. Observation

Linear analysis results for the first and second story are shown in Figure 8-26 for ground motions applied in both directions simultaneously. The shear and flexure demand-capacity-ratios (DCRs) modified by the Collapse Prevention (CP) *m*-factors are presented in the results. Those components with DCR/*m* values greater than 1.0 indicate failure to meet the CP acceptance criteria. The results show that nearly all of the frame elements meet the CP criteria while nearly all of the wall elements fail to meet the CP criteria. DCR/*m* for walls are largest in the second story in the transverse direction making these the most critical elements. This is in agreement with the most common building mechanism failure theory. Beams with poor detailing or anchorage were assigned moment releases in the model as they would be unable to contribute to the strength and post-yield stiffness of the structure. As such, results for these beams are not displayed in the following plots. Solid line type between shear wall elements indicates coupling beams.

This publication is available free of charge from: https://doi.org/10.6028/NIST.GCR.22-917-50

This publication is available free of charge from: https://doi.org/10.6028/NIST.GCR.22-917-50

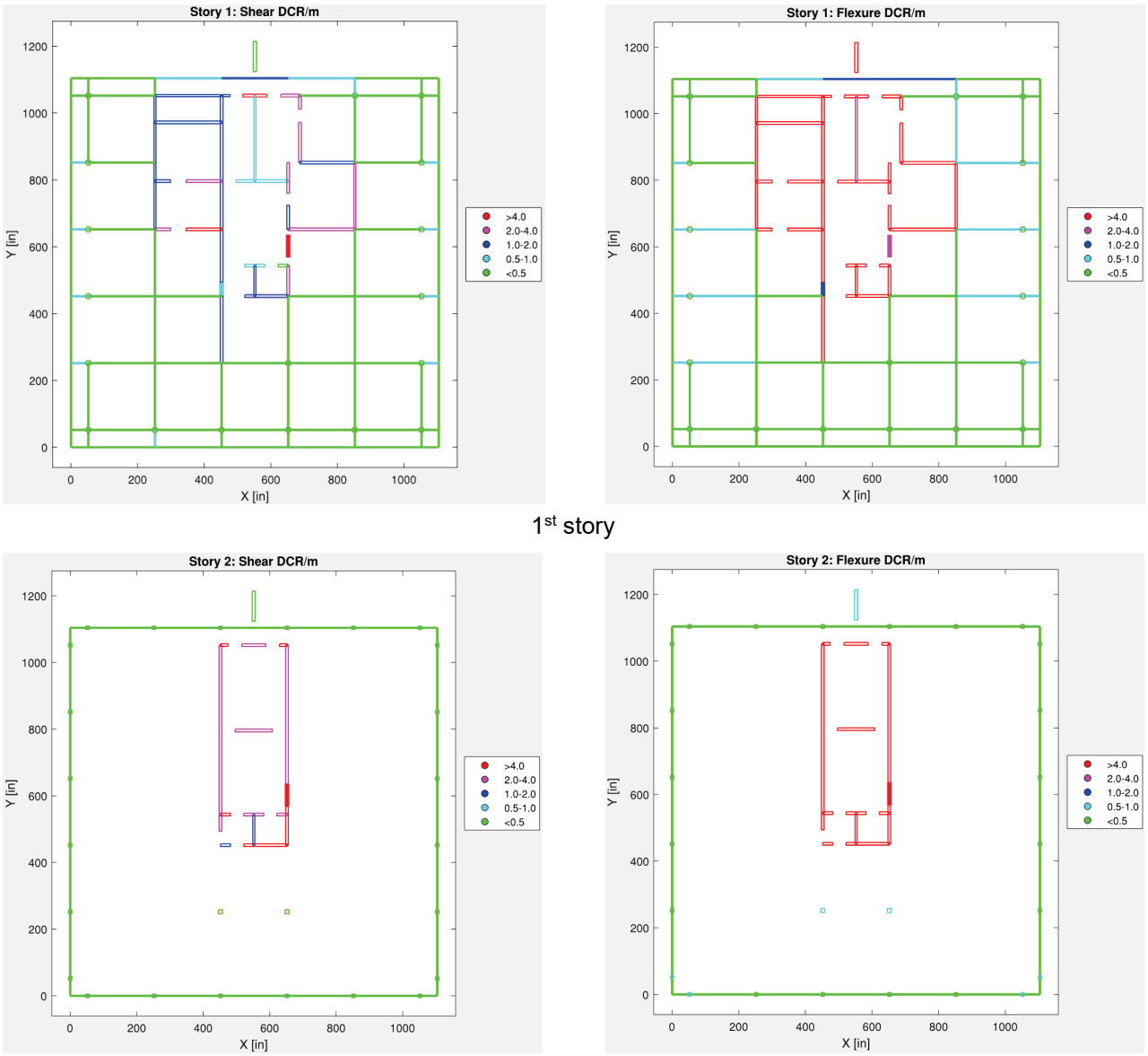


Figure 8-26 Linear: Demand-capacity ratios for Collapse Prevention.

8.4.4 Comparison to Linear Response History Method

The structure was also analyzed using linear response history procedures in order to evaluate the differences in linear analysis methods. The response history analysis was conducted using both modal analysis and direct integration. The expectation was for the modal history to be similar to the response spectrum and for the direct integration history to predict the highest story drifts.

Figure 8-27 shows global response comparison using peak (max) drift and story shear results. The peak story drift is taken at any location on the floor plate for a given direction due to seismic excitation in the same direction.

This publication is available free of charge from: https://doi.org/10.6028/NIST.GCR.22-917-50

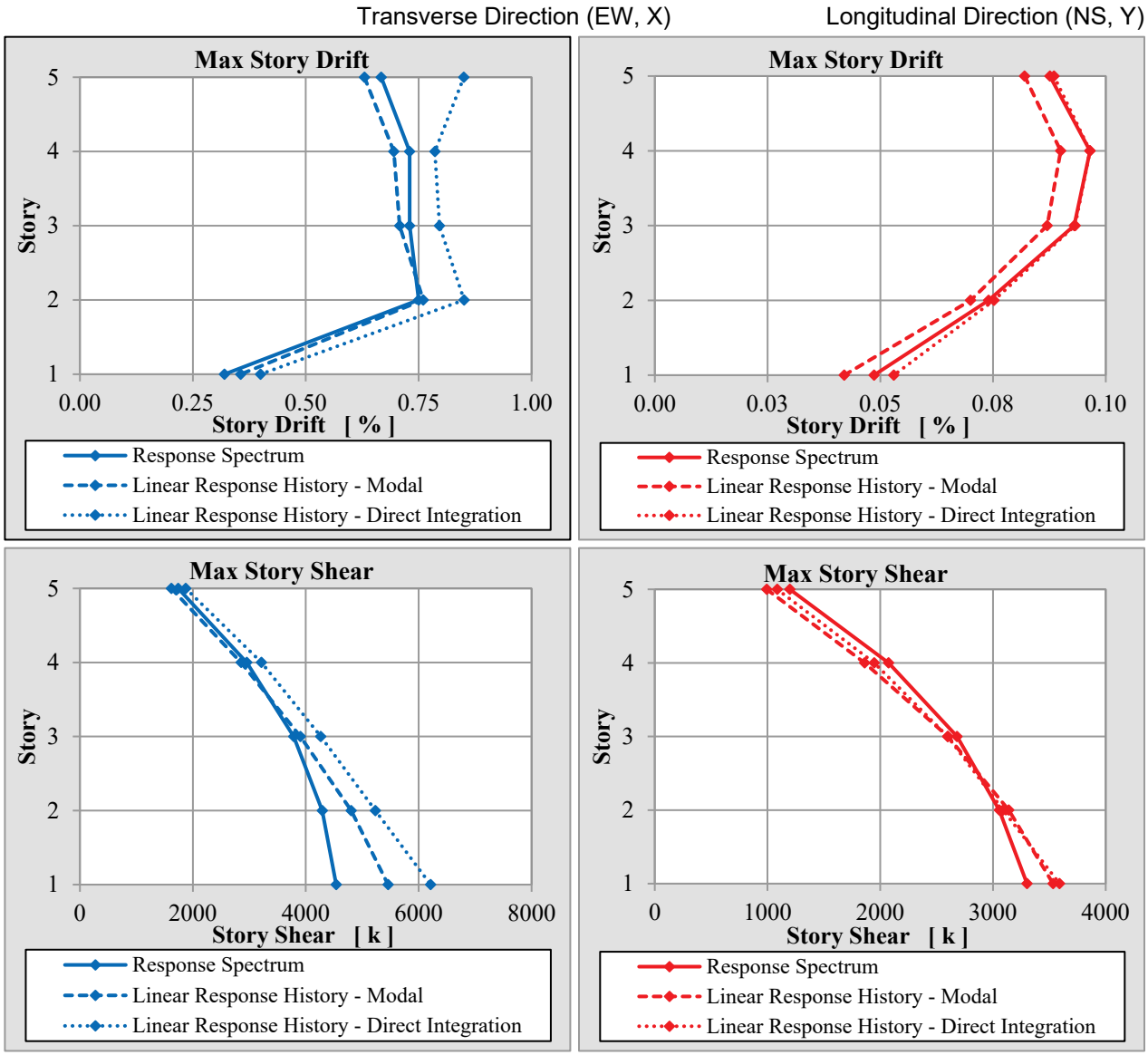


Figure 8-27 Linear: Comparison of modal and direct integration methods for linear response history method.

As shown in Figure 8-27, the direct integration method results in the highest story drifts. They are on average 20% higher than the response spectrum results in the transverse direction. The modal history method results do not track as closely to the response spectrum method results, but it is not considered significant. The story and base shear forces from the direct integration response history analysis are larger than those from the modal response history analysis. The difference is larger in the shear force results than in the drift results since the displacement response is less sensitive to the spikes of the response spectra of the measured ground motion near the fundamental periods than the force response. In linear analysis, the component DCR increase would be linearly proportional to the increase of the force demands from the response history analysis.

8.5 FEMA P-2018 Evaluation

8.5.1 Evaluation Approach

The building was evaluated using the procedure outlined in FEMA P-2018, *Seismic Evaluation of Older Concrete Buildings for Collapse Potential* (FEMA, 2018b). The building was classified as a "frame-wall system" in both orthogonal directions and accordingly evaluated per Chapter 7 of FEMA P-2018. The spectral acceleration utilized in the evaluation were extracted from response spectra that were generated from the recorded ground motions.

8.5.2 Global Performance: Evaluation Procedure vs. Observation

Table 8-5 provides a summary of the key evaluation parameters and results in the transverse (EW, X) direction and longitudinal (NS, Y) direction. Table 8-6 provides a summary of the corresponding story ratings calculated in each direction.

Table 8-5 Summary of Key Evaluation Parameters and Results

Parameter	EW(X)-Direction	NS(Y)-Direction	Units	Description
W	6,574	6,574	kips	Total building weight
T_e	0.77	0.36	sec	Effective fundamental period
S_a @ T_e	1.23	0.96	g	Spectral acceleration at T_e
V_y	282	1,139	kips	Base shear yield strength
Mechanism	4	2	-	Governing plastic mechanism
Critical Story	2	1	-	Critical story
$\mu_{strength}$	23.0	4.4	-	Global DCR
δ_{eff}	11.6	2.0	in	Global equivalent SDOF drift
$\delta_{eff,roof}$	16.2	2.7	in	Global roof drift
$\delta_{eff,roof}$ / h_{roof}	2.1%	0.3%	-	Global roof drift ratio

Table 8-6 Story Ratings

Story	EW(X)-Direction	NS(Y)-Direction
1	0.25	0.10*
2	0.90*	0.71
3	0.59	0.10
4	0.59	0.10
5	0.60	0.10

* Indicates critical story

In the transverse (EW, X) direction, the critical story was the second story. The limited lateral strength at this critical story resulted in a large global demand-capacity

This publication is available free of charge from: https://doi.org/10.6028/NIST.GCR.22-917-50

ratio, $\mu_{strength}$, of 23.0, and global roof drift ratio, $\delta_{eff,roof} / h_{roof}$, of 2.1%. The story rating for this story was calculated to be 0.90.

In the longitudinal (NS, Y) direction, the critical story was the first story. The building was found to have a significantly higher base shear yield strength in the NS direction than in the EW direction. Accordingly, the building's global demand-capacity ratio and roof drift were significantly lower in the NS direction. Although the story rating for the critical (first) story was found to be 0.10, the story rating for the second story was calculated to be 0.71 due to the discontinuous columns located at this story.

The final FEMA P-2018 building rating was selected as the larger of the critical story ratings in the EW and NS directions. Since the EW direction governed, the building rating was accordingly found to be 0.90, the highest possible building rating per FEMA P-2018. In accordance with FEMA P-2018 Section 10.3.1, the building was deemed an "exceptionally high seismic risk building," because the building rating exceeded 0.7.

The results of this FEMA P-2018 evaluation generally appear to be consistent with the observed response of the building. Collapse of this structure has been largely attributed to inadequate wall strength in the EW (X) direction, which correlates well with the findings of the FEMA P-2018 evaluation. The relationship between the rating and the spectral acceleration is shown in Figure 8-28.

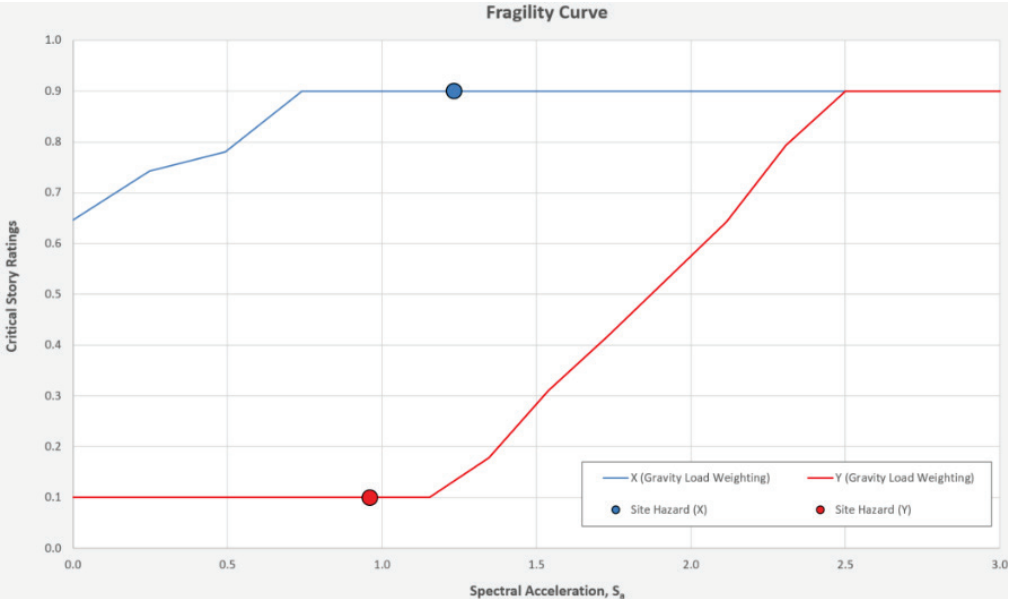


Figure 8-28 Relationship of FEMA P-2018 rating and spectral acceleration.

This publication is available free of charge from: https://doi.org/10.6028/NIST.GCR.22-917-50

8.6 New Zealand Assessment Guidelines

This building was evaluated in prior work by Beca (2011) using the NZSEE *Guidelines*, including capacity spectrum evaluation. A separate analysis was not performed in this study, but the results from ASCE 41-17 evaluations were found to be consistent with their findings. Using the NZS1170.5 spectrum, the building is rated between 36% and 50% of the New Building Standard. Using 5%-damped response spectra from the 2010 Darfield and 2011 Christchurch Earthquakes, the demands were 1.5 and 5.8 times the estimated capacity from pushover analysis (Beca, 2011). The damage sustained in the 2010 Darfield Earthquake is uncertain, but the observed collapse in the 2011 Christchurch Earthquake was identified by the large demand-capacity ratios from the NZSEE assessment, large DCR/*m* values for Collapse Prevention using the ASCE 41-17 linear analysis procedures, and simulated collapse using the ASCE 41-17 nonlinear analysis procedures.

8.7 Summary

The 5-story wall building was damaged to the point of collapse in the 2010-2011 Canterbury Earthquake Sequence. Cracking and minor spalling of the reinforced concrete shear wall was noted in the 2010 Darfield Earthquake, and collapse occurred in the 2011 Christchurch Earthquake due to successive failure of the shear walls and gravity framing. The building was evaluated using best-estimate ground motions from both earthquakes under the ASCE 41-17 Tier 3 linear- and nonlinear response-history analysis procedures. A FEMA P-2018 study was also conducted. This section summarizes findings from these evaluations, including two shear wall model variations investigated in the nonlinear procedure, where the nonlinear models were as follows:

- A model in which nonlinear shear response in the wall is neglected (noncompliant with ASCE 41-17)
- A model in which nonlinear shear response is modeled using the prescribed ASCE 41-17 backbone curve

8.7.1 Global Performance

Overall, the global building response is well predicted using the ASCE 41-17 evaluation procedures and the best estimate ground motions, which were recorded at a station 0.67 km from the building site. Both the linear and nonlinear analysis procedures predict performance at or in exceedance of the collapse-prevention state for the primary lateral-load-resisting system (i.e., high probability of collapse) in the 2011 Christchurch Earthquake; however, the performance state is overpredicted in the 2010 Darfield Earthquake. The following conclusions are made based on the analysis results and observed damage from both events:

This publication is available free of charge from: https://doi.org/10.6028/NIST.GCR.22-917-50

- The maximum story drift in both the linear and nonlinear analyses is in the EW direction, which is consistent with the direction of collapse. Although the linear model indicates extreme torsional irregularity, rapid strength and stiffness deterioration of the north wall segments limited the torsional response in the nonlinear analyses; this limited torsional response is consistent with the observed damage.
- Two linear procedures, linear response spectrum and response history analyses were used in the linear evaluation. The response history analysis yields larger deformation and force demand.
- In the linear analyses, the second story is identified as the critical story, which had the highest collapse vulnerability and collapse prevention DCRs. The analysis results are consistent with the collapse behavior of the building during the 2011 Christchurch Earthquake. However, as reported in the evaluation for the 2010 Darfield Earthquake, the wall flexural DCRs exceed the CP acceptance criteria by a factor of fourwhich overpredicts the damage as it compares with the actual damage.
- When nonlinear shear response in the wall is considered, collapse is explicitly predicted (maximum story drift well above 10%). The collapse mechanism is not predicted well with this approach, because damage concentrates on the second story due to the large shear demand-to-capacity ratio at this location and rapid post-peak strength degradation.
- When only elastic shear response in the wall is considered, collapse is implicitly predicted based on the performance of the gravity columns. In this case, nearly all columns above the first story exceed the collapse-prevention acceptance criteria due to the axial-flexural failure of the wall at the second story; this matches the observed damage better.
- Using the FEMA P-2018 procedure, the building was classified as an "exceptionally high seismic risk building," which is consistent with the actual poor performance in the 2011 Christchurch Earthquake. The critical story was also correctly identified as the second story, where failure of the shear wall precipitated collapse.

8.7.2 Component Performance

Although collapse is predicted in the ASCE 41-17 response history analysis procedures, the components or component failure mechanisms that lead to collapse are not always correctly identified.

- In the linear analyses with the 2010 Darfield and 2011 Christchurch seismic loads, the walls are identified as the most vulnerable components and exceed the

This publication is available free of charge from: https://doi.org/10.6028/NIST.GCR.22-917-50

Collapse Prevention acceptance criteria. However, the beams and columns satisfied the criteria in general in the two earthquakes.

- Regardless of the approach for modeling shear response in the wall, at least one of the wall segments is predicted to exceed the Life Safety or Collapse Prevention acceptance criteria in the 2010 Darfield Earthquake, whereas limited cracking and spalling was observed. Where nonlinear wall shear response is modeled, this discrepancy can be partially attributed to the underestimated shear strength for slender, flanged walls in ACI 318. On the other hand, the walls were nonductile and may not have exhibited significant damage preceding collapse.
- Observations suggest that the shear walls sustained axial-flexural failure in the 2011 Christchurch Earthquake, but this is not simulated when the shear response of the wall is modeled following the ASCE 41-17 modeling recommendations. In this approach, the walls fail laterally in shear at the second story, resulting in a localized collapse of the second story. When the shear response is modeled as elastic (i.e., with unbounded shear capacity), a flexural response is induced in the walls, leading to the correct global collapse mechanism, as noted above.
- The observed gravity-frame failure mechanism is most likely a combination of bond failure in the beam-column joint region and column splice failure immediately above the joint. The analyses do not predict these failure modes; rather, the columns fail in shear or flexure-shear modes using the fiber-based limit-state element approach. The beams are correctly predicted to remain elastic.

8.7.3 Analytical Study Takeaways

Key outcomes from the linear and nonlinear analysis procedures are as follows:

- In the linear analyses, the mechanism and the most vulnerable components were identified. However, the linear procedures would likely overestimate the expected damage and do not have the resolution to estimate the damage levels when significant damage is expected. The linear procedures may be improved with an updated set of the *m*-factors. However, the fundamental limitation of the linear analysis, in which the seismic load is distributed based on the stiffness but not strength, cannot be overcome, and the redistribution or concentration of the load is not likely identified.
- It should be emphasized that the linear analysis procedures should be used for a conservative measure of the seismic performance evaluation but for estimating behavior or damage. It is recommended to implement a nonlinear analysis for the retrofit once the overall building performance is identified to avoid an inefficient or ineffective retrofit. The implementation of a relatively simple plastic mechanism analysis, such as FEMA 2018 methodology, might provide a

This publication is available free of charge from: https://doi.org/10.6028/NIST.GCR.22-917-50

better estimation of the building behavior without implementing a full nonlinear analysis.

- Global response mechanisms are generally well predicted, but the collapse mechanism in the 2011 Christchurch Earthquake is only matched when the shear response of the wall is elastic, which is not compliant with ASCE 41-17. Further work is needed to improve shear wall modeling recommendations, which were largely developed from research on planar walls. Specifically, research of flanged or other complex wall configurations require further investigation to improve prediction of shear capacity and to develop appropriate modeling parameters and acceptance criteria. The nonlinear analyses presented here show that fiber-based beam-column elements with distributed plasticity may be used to simulate the flexural response of lightly reinforced, flanged shear walls, but limited experimental data exist to validate this finding.
- Bond failure in the beam-column joint region and adjacent column splice region likely contributed to collapse of the gravity framing, but this is not addressed by ASCE 41-17. As such, the analyses do not predict joint failure. Provisions for evaluation of this bond failure mode in the joint should be developed from relevant experimental data (e.g., Pessiki et al. [1990]), though this is a significant modeling challenge. First, the vulnerability of the column splice must be characterized. It is noted that column splice generally did not control the strength or deformation capacity of the building columns per ASCE 41-17. Second, the joint capacity must be reduced after column yielding in the splice region. This could be accomplished using a limit-state model in the joint that monitors the column rotation demand in real time. Further work is needed to investigate this failure mode and potential modeling strategies to correctly identify vulnerabilities in buildings with similar characteristics.

8.7.4 Study Limitations

The results of this investigation are contextualized within the following limitations:

- Material testing was performed for a limited number of components. The compressive strength of concrete and yield stress of steel in components that did not undergo material testing were inferred based on specified properties. No material testing data are available for the walls. An average of the material properties of the beams and columns was used for the wall properties.
- The building was not instrumented. Observed response was based on photographic evidence. Due to collapse of the study building and the associated emergency response, almost no information on the state of the internal building components, including the wall, is available.

This publication is available free of charge from: https://doi.org/10.6028/NIST.GCR.22-917-50

- Drawings of the retrofit conducted in the late 1990s were not available. The steel "prop" columns added in the retrofit were not considered in the analyses as connection detailing was assumed to be inadequate to enable columns to contribute significant lateral resistance.
- Embedded drainage pipes in the columns and steel transfer beams over the cantilevered spans were not considered in the analyses.
- Corrosion of some reinforcement in the building was noted, but this was not considered in the analyses.
- The best-estimate ground motions were recorded at a site 0.42 mi from the building site. Ground-motion recordings at the site were not available.
- The foundation and soil flexibility were not modeled.
- The linear procedure was performed even though it is not applicable per Section 7.3.1 ASCE 41-17 since the building has torsional strength irregularity and the demand to capacity ratio larger than 3.
- Torsional amplification was not considered.

This publication is available free of charge from: https://doi.org/10.6028/NIST.GCR.22-917-50

Chapter 9
Three-story Frame with Masonry Infill Building in Taiwan

This publication is available free of charge from: https://doi.org/10.6028/NIST.GCR.22-917-50

9.1 Overview

This chapter presents benchmarking studies for a 3-story frame building with masonry infill in Taiwan, shown in Figure 9-1. The structure was one of three district office buildings that were damaged in the Meinong (Tainan) Earthquake in 2016 (Sumearll et al., 2018). The building had a regular configuration and sustained damage that was readily observable and typical of nonductile concrete frame buildings. This building was subsequently demolished and replaced.



Figure 9-1 Photograph of building from the south (Pujol et al. 2017).

The building was evaluated in accordance with the nonlinear and linear dynamic procedures of ASCE 41-17 using OpenSees and SAP200 software, respectively. The models were constructed per details presented in Appendix A, unless otherwise noted.

This chapter also provides results of a fragility analysis showing the collapse potential of the as-modeled building, as compared to the likelihood of exceeding ASCE 41-17 acceptance criteria. Results from a FEMA P-2018, *Seismic Evaluation of Older Concrete Buildings for Collapse Potential*, (FEMA, 2018b) evaluation are also presented.

9.2 Building Description and Observed Performance

9.2.1 Building Description

The building was located in the Nanhua District of Tainan City, Taiwan. The structure was designed and built in the late 1960s (available drawings are dated 1967), and it housed municipal office and community gathering spaces resulting in a mixture of open and partitioned floor plans. An addition was constructed northwest of the main building at an unknown date; this addition was not considered to be integral with the primary building because the connections between the structures were sparse (see locations in Figure 9-2) with no obvious transfer mechanism for diaphragm forces.

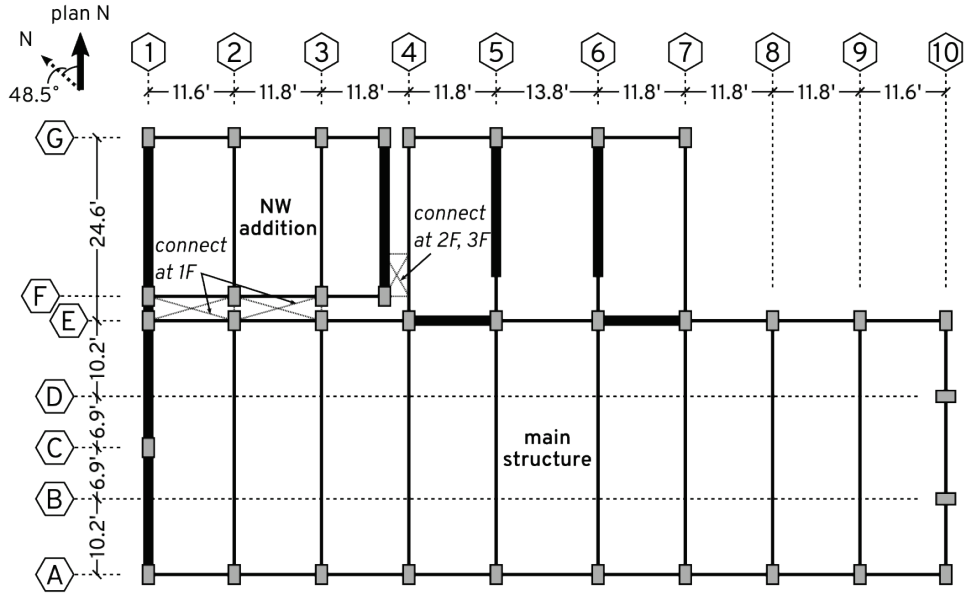


Figure 9-2 Plan dimensions of building. Thickened lines indicate full-height masonry-infill walls.

In plan, the primary building was rectangular with a section missing between Columns 7 and 10 and E and F, as shown in Figure 9-2. The primary axes are oriented 48.5 degrees clockwise relative to cardinal directions. The long direction of the building is designated as the east-west direction and the short direction is designated as north-south direction. The original building extended from Gridline A to G in the north-south direction, but it only extended the full length in the east-west direction from Gridlines A to E and, instead, extended from Gridlines 4 to 7. The addition extended from Gridlines 1 to 3 and F to G and was approximately 32.0 ft by 21.3 ft in plan (747 sf per floor). This resulted in a total floor area of approximately 4,600 sf per floor. Each story height was approximately 11.8 ft, resulting in a total building height of approximately 35.4 ft. The primary building and addition were estimated to weigh 2,261 k and 451 k, respectively. Table 9-1 details the distribution of this weight at each floor.

This publication is available free of charge from: https://doi.org/10.6028/NIST.GCR.21-917-50

Table 9-1 Vertical Distribution of Building Weight

	Weight (kips)	
Floor	*Main Structure*	*NW Addition*
Roof	573	121
3	798	158
2	890	173
Total	2261	451

The primary building and addition are assumed to have the same structural systems. Gravity loads were transferred to columns by two-way slabs (4.72 in. thick) on the second and third stories and open-web steel joists on the roof. Lateral loads were resisted by exterior moment frames in the east-west direction and full-height masonry-infill walls in the central interior and west exterior end in the north-south direction (see thickened lines in Figure 9-2). Two full-height masonry-infill walls were also located in the east-west direction in the building interior on Gridline E. The interior infill walls are considered secondary components in this study; these walls were thinner and, in some cases, were not bounded by columns, had openings for doorways, or were discontinuous along the height.

Frame lines run in the east-west direction along Gridlines A, E, and G. Figure 9-3 shows the structural framing including the partial-height masonry infill (detailed with a brick pattern) that creates a captive-column effect, which was considered in the analysis. This infill extends 39.4 in. (100 cm) from the top of the slab. In the analysis this was simulated as a short, captured-column effect.

Material testing was not performed; thus, all material properties were based on the construction documents and the concrete strength increase based on building age and ASCE 41-17 recommendations. Table 9-2 reports the lower-bound and expected strengths used in this evaluation. These values are consistent with those used for evaluation of other district offices of similar vintage in the Tainan region which were also damaged in the Meinong Earthquake (Lai et al., 2018). Additional information about the building can be found in Sumearll (2019).

This publication is available free of charge from: https://doi.org/10.6028/NIST.GCR.22-917-50

This publication is available free of charge from: https://doi.org/10.6028/NIST.GCR.21-917-50

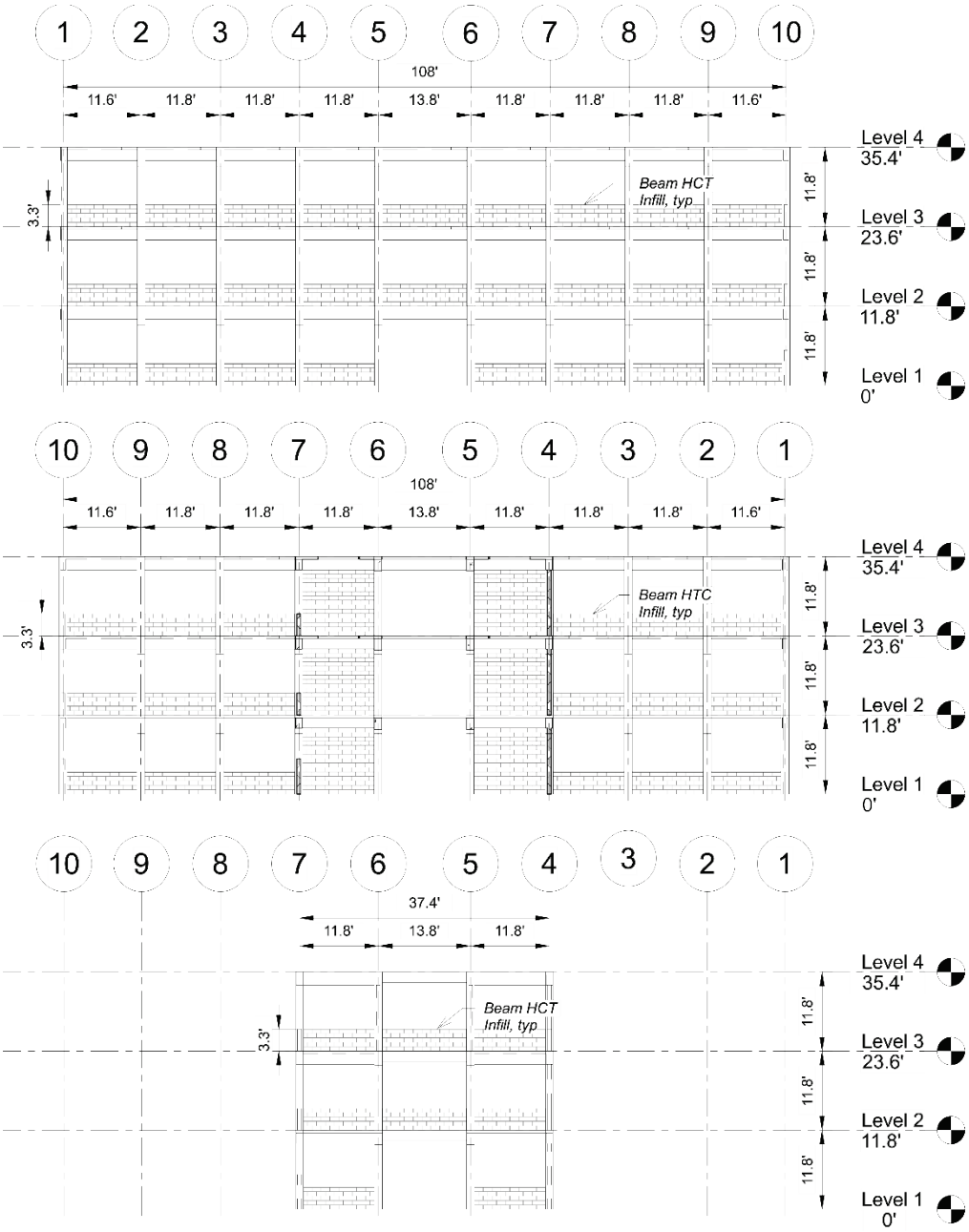


Figure 9-3 Elevations: (a) frame at Gridline A, (b) frame at Gridline E, (c) frame at Gridline G (units in cm).

Table 9-2 Salient Material Properties

Material	Property	Lower Bound	Expected
Concrete	Compressive strength	3.0 ksi	4.5 ksi
Reinforcing steel	Yield stress	40 ksi	50 ksi
	Hardening ratio	1.5%	
Masonry	Compressive strength	1.2 ksi	1.6 ksi

9.2.2 Ground Motion

On February 6, 2016, Southern Taiwan experienced significant ground shaking as a result of the M_w6.4 Meinong Earthquake. Building damage was concentrated in the Tainan City region.

Ground acceleration records were collected from local recording sites tracked by the Taiwan Central Weather Bureau (CWB). Figure 9-4 shows to the building site, the fault epicenter, and various ground motion recording stations within close proximity of the building. Site-specific information, such as ground motion and soil profile, were not available for the building.



Figure 9-4 Ground motion recording stations (numbered), site, and epicenter (adapted from Google, 2022).

Figures 9-5 and 9-6 are two visualizations of the intensity of the event as produced by the US Geological Survey (USGS). Research relating intensity to measured damage for this earthquake showed that of all the scalar ground intensity measures, the value of the peak ground velocity (PGV) best correlated with the intensity of damage (Lee et al., 2017). The building was located outside the areas of highest PGV but close to the epicenter (see Figure 9-5). In contrast, spectral acceleration, S_a, did not correlate to regional structural damage. This suggests that other factors such as forward directivity effects or substantial structural deficiencies may have led to the observed severe damage to the building.

This publication is available free of charge from: https://doi.org/10.6028/NIST.GCR.22-917-50

This publication is available free of charge from: https://doi.org/10.6028/NIST.GCR.21-917-50

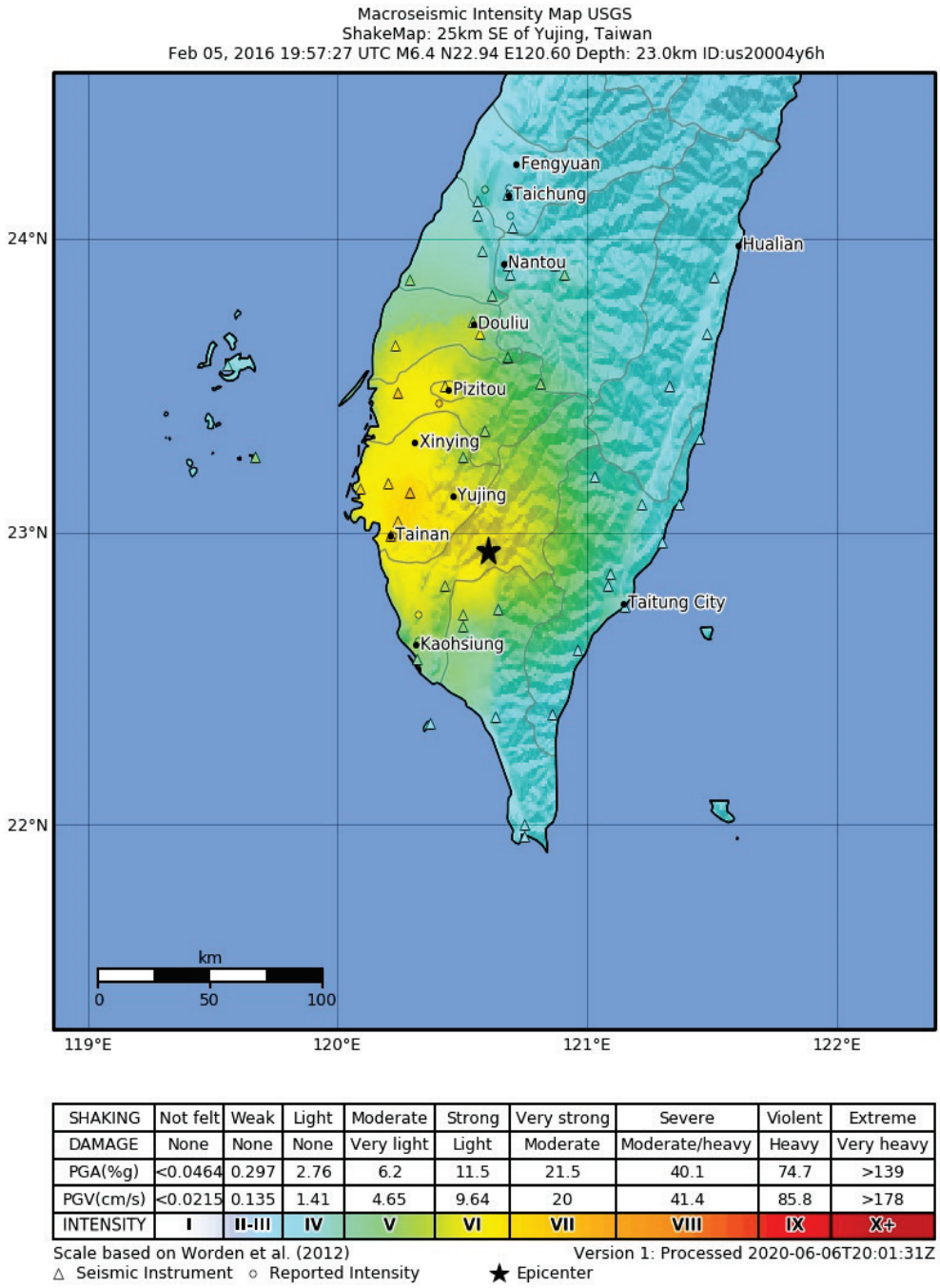


Figure 9-5 USGS intensity map for 2016 Meinong Earthquake (USGS, 2020).

This publication is available free of charge from: https://doi.org/10.6028/NIST.GCR.22-917-50

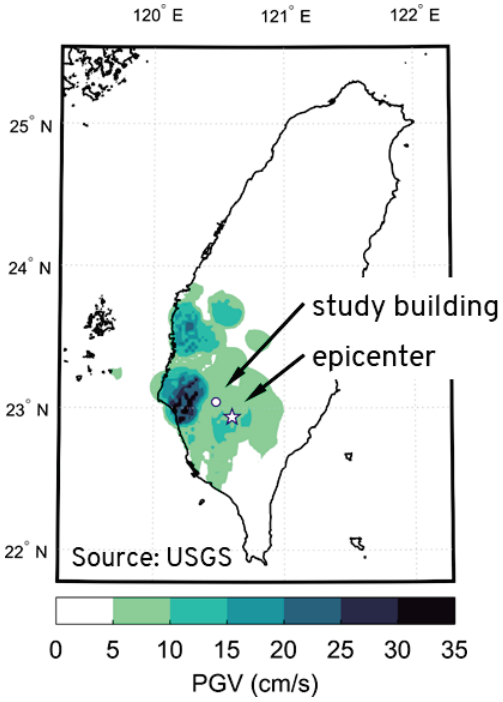


Figure 9-6 PGV intensity map with location of study building relative to epicenter.

Figure 9-7 plots of the tri-directional acceleration records closest to the building location, which are from Station A730 (Site No. 6 shown in Figure 9-4).

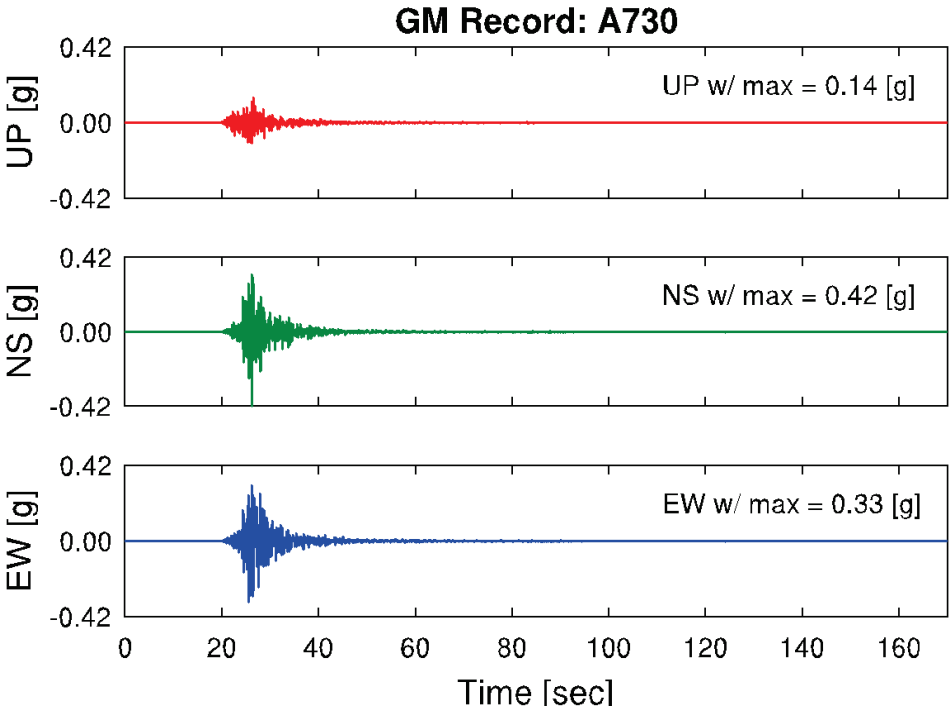


Figure 9-7 Measured records for recording Station A730.

This record was selected by the geotechnical engineer based on being the closest record to the site, being at a similar azimuth from the epicenter as the building, and the record exhibiting some extent of forward directivity that was likely experienced at the building site. A Newmark constant-acceleration time integration was performed to develop individual, 3%-damped response spectra. These spectra are shown with respect to the building east-west and north-south directions in Figure 9-8b. The bidirectional nature of the ground shaking is evident in Figure 9-8a.

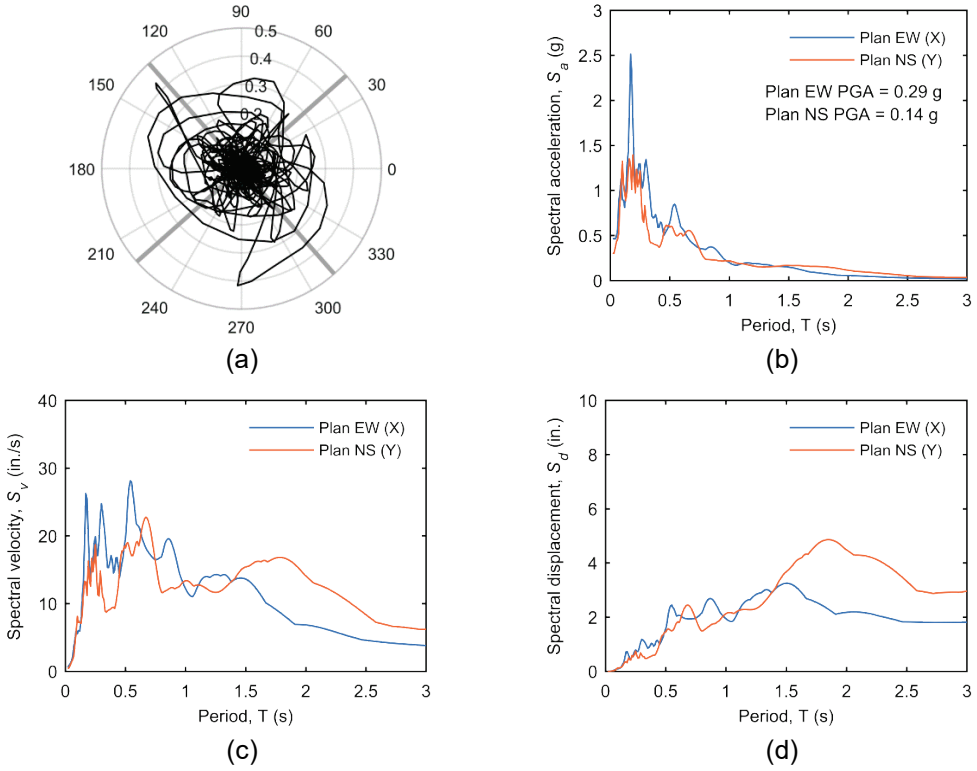


Figure 9-8 Station A730 (a) acceleration orbital with building axes in gray, (b) building-oriented acceleration response spectra, (c) building-oriented velocity response spectra, and (d) building-oriented displacement spectra.

9.2.3 Observed Performance

This building was not instrumented. The predicted results are compared to observed residual damage from post-earthquake reconnaissance.

Damage to the building included the following:

- Inclined (diagonal) cracking in lower story columns (Figure 9-9a and 9-9b)
- Spalling at the top of some of the first-story columns. (Figure 9-9a)
- Spalling along the column length (Figure 9-9c)
- Damage to full-height masonry infill in the east-west direction of loading (Figure 9-9d)

This publication is available free of charge from: https://doi.org/10.6028/NIST.GCR.21-917-50



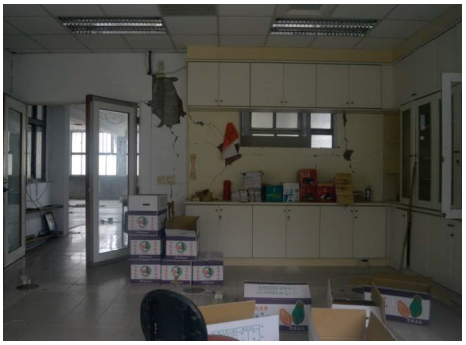
(a) Column damage in Frame A



(b) Column damage (typical)



(c) Extensive damage to Column E8



(d) Damage to interior wall of addition

Figure 9-9 Damage to column and interior walls (Pujol et al., 2017).

The observed damage was primarily concentrated in the first story and distributed as shown in Figure 9-10. Based on the damage patterns, it is postulated that the columns sustained flexural damage in the form of spalling at the top of the column but lost strength due to shear demands that exceeded their shear capacity. Research indicates that spalling follows flexural yielding in columns with low axial stresses, which is the case for these columns. In addition, some columns were constructed with piping placed within their cross section, which likely decreased their shear strength. None of the columns were observed to have lost vertical load-carrying capacity and the building did not collapse. The performance of the columns is judged to be between Life Safety and Collapse Prevention based on the performance state descriptions of ASCE 41-17 Section C10.4.2.2.2 that specifically describe minor spalling (Life Safety) and limited cracking (Collapse Prevention) for nonductile columns.

Additional damage is noted within the walls of the building and there is damage in the form of horizontal and diagonal cracking in the second story columns. Permanent lateral residual displacement of the building was not reported.

This publication is available free of charge from: https://doi.org/10.6028/NIST.GCR.22-917-50

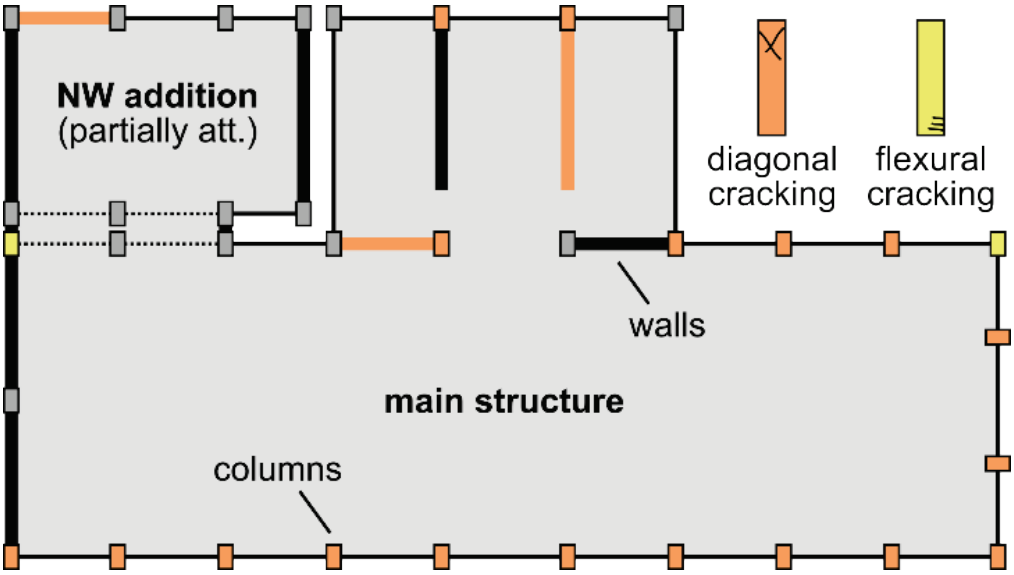


Figure 9-10 Illustration of column and full-height masonry wall damage at first story. (Damage was not observed in the walls colored black).

9.3 Nonlinear Dynamic Procedure

9.3.1 Modeling Approach

A three-dimensional model of the structure was created in OpenSees. A rigid diaphragm constraint was employed to constrain column lateral displacement at each floor to each other and to the mass node. Gravity loading was applied to each column based on tributary area and the total mass of each story was placed at the story center of mass. Mass was applied in both lateral degrees of freedom, the vertical degree of freedom (where vertical ground motion was studied), and the torsional degree of freedom. All line elements were modeled with geometric nonlinearity using corotational coordinate transformation.

Two column modeling approaches were utilized due to significant column damage observed in the earthquake: (1) a conventional moment-rotation hinge; and (2) nonlinear fiber-based hinges in series with "Limit State" moment-rotation springs, as described in the expanded zero-length segments in Figure 9-11. The latter modeling approach is based on Elwood (2004) and enables updating of column modeling parameters *a* and *b* at each time step of the analysis. The limit state spring controls the column strength degradation properties while the fiber section controls the nonlinear axial-flexural hysteretic behavior prior to onset of degradation. In both cases, the columns were fixed at their bases and were modeled as elastic beam-column elements with cracked section properties between nonlinear hinges.

This publication is available free of charge from: https://doi.org/10.6028/NIST.GCR.21-917-50

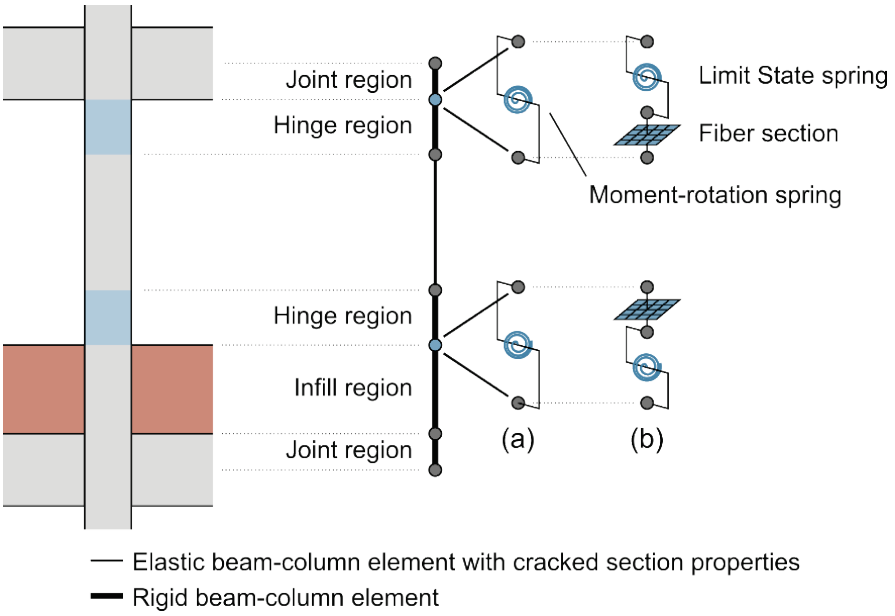


Figure 9-11 Column modeling approaches with lumped plasticity using (a) conventional moment-rotation springs and (b) fiber-limit state hinge.

Column strength was controlled by shear throughout the building and therefore the flexural strength of the modeled hinge was capped at $V_{ColOE}L/2$ to ensure the shear strength could not be exceeded. For the fiber limit state hinge depicted in Figure 9-11b, the strength of the limit state spring is capped when shear controls; calibration of the fiber material models is not required because the limit state spring and fiber section are in series. Note that strength degradation of the concrete fibers is also not modeled because this response is controlled entirely by the limit state spring. Since softening of compressive strength in the concrete is not modeled, regularization of the concrete material is also not required.

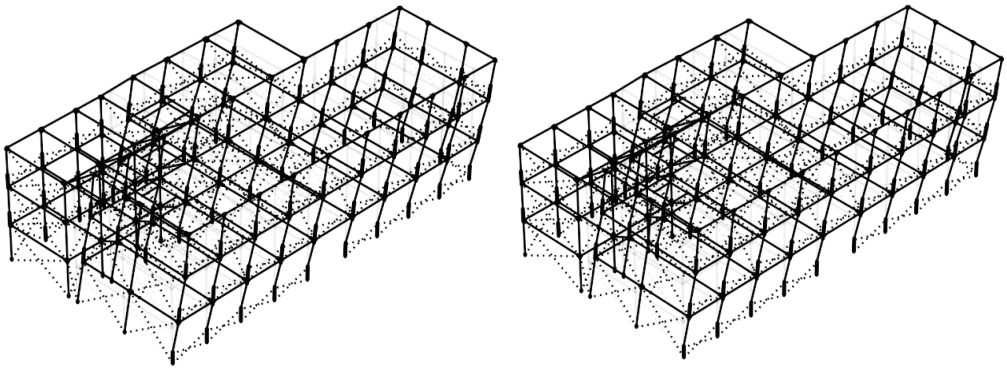
Beams were modeled as T-beams using the same modeling approach as was used for columns (i.e., using spring or fiber hinges at the element ends). Transverse interior roof beams between Gridlines A and E were not modeled to simulate the lack of rotational restraint which would be provided by the open-web steel joists at this location.

Beam-column joints were modeled implicitly with stiff offset elements. ASCE 41 requires modeling nonlinear joint response; however joint forces, computed using demands imposed on the joint by the beams and columns framing into the joint, did not exceed expected joint strengths; thus, using nonlinear joint models was not required by ASCE 41. Note that there was no observed joint damage in the building and, further, the beams and infill are hypothesized to have significantly restrained the joint region to prevent this damage mode. All masonry infill, including permanent interior partitions, was modeled using nonlinear compression-only truss elements with properties based on ASCE 41-17 Chapter 11.

This publication is available free of charge from: https://doi.org/10.6028/NIST.GCR.22-917-50

The building addition in the north-west corner was included in the nonlinear model. Because the exact section properties of the addition components were not known, they were modeled similarly to adjacent columns in the original structure. The addition was attached to the original structure with compression-only contact elements (translational springs) with a 2in. thick initial gap. As such, the modes of vibration of the addition are independent.

Figure 9-12 depicts the first mode shape computed for the two model variations. The first three periods for each are also tabulated in Table 9-3. Note that the mode shapes and periods are similar for the two models. In both cases, these periods are shorter than those of the linear models discussed later; this can be attributed to use of the rigid diaphragm constraint (elastic shell elements are used to model the diaphragm in the linear analysis), higher initial stiffness (i.e., uncracked stiffness) for the fiber sections at the ends of the columns, different approach to modeling the masonry infill, and different software. Modal damping was applied for the first seven modes with supplemental initial-stiffness-proportional Rayleigh damping. The total damping ratio from modal and Rayleigh damping was 3% of critical.



(a) Moment-rotation spring hinges (b) Fiber-based limit-state hinges

Figure 9-12 First mode shapes; diagonal struts for masonry infill shown as dotted lines.

Table 9-3 Modes of Vibration for Nonlinear Models

	M-θ Hinge		Fiber-limit State Hinge	
Mode	*Period (s)*	*Shape or Direction*	*Period (s)*	*Shape or Direction*
1	0.49	east-west	0.46	east-west
2	0.40	north-south	0.39	north-south
3	0.39	north-south+	0.39	north-south*

* Mode associated with north-west addition.

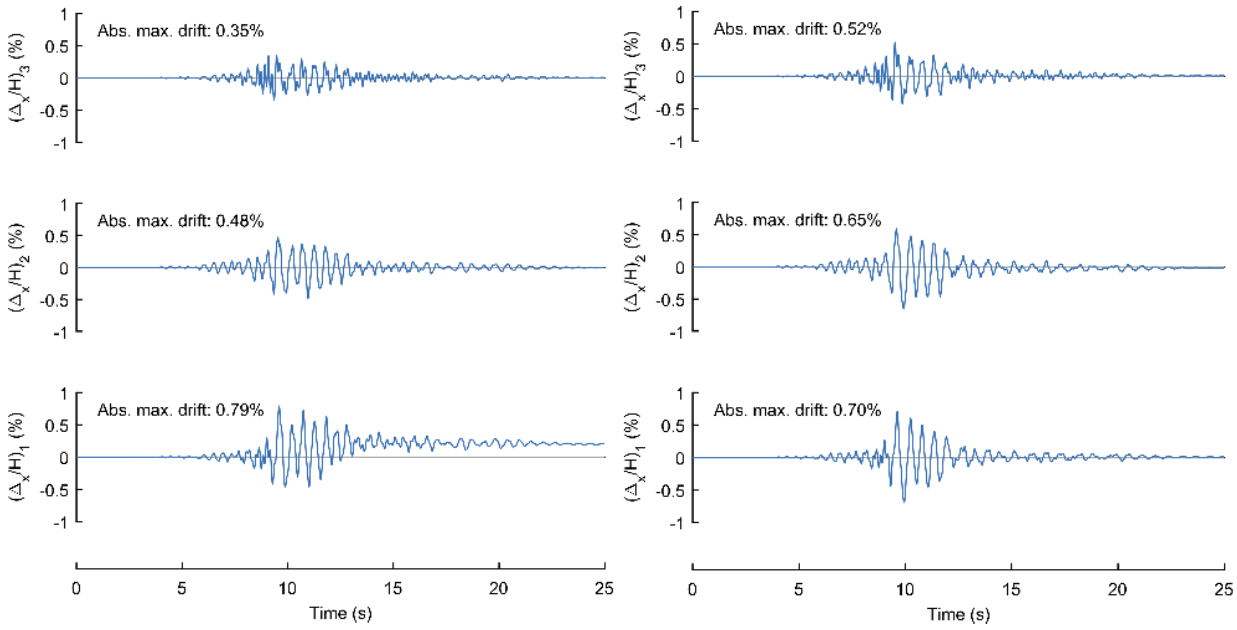
9.3.2 Global Performance: Model vs. Observation

To facilitate comparison of the building models with moment-rotation spring and fiber-based limit-state hinge approaches, results from each are presented together in

This publication is available free of charge from: https://doi.org/10.6028/NIST.GCR.21-917-50

this section. In both models, the maximum response occurred in the east-west direction. Figures 9-13 and 9-14 show the story drift response of each model taken from the centers of mass in each direction, and Table 9-4 compares the predicted and observed global response. The response was primarily in the east-west direction, which is consistent with observed damage, but relatively low in magnitude (< 0.8%); the observed damage would have likely occurred under large drift demands, and this evaluation of damage severity is addressed in more detail in the proceeding section.

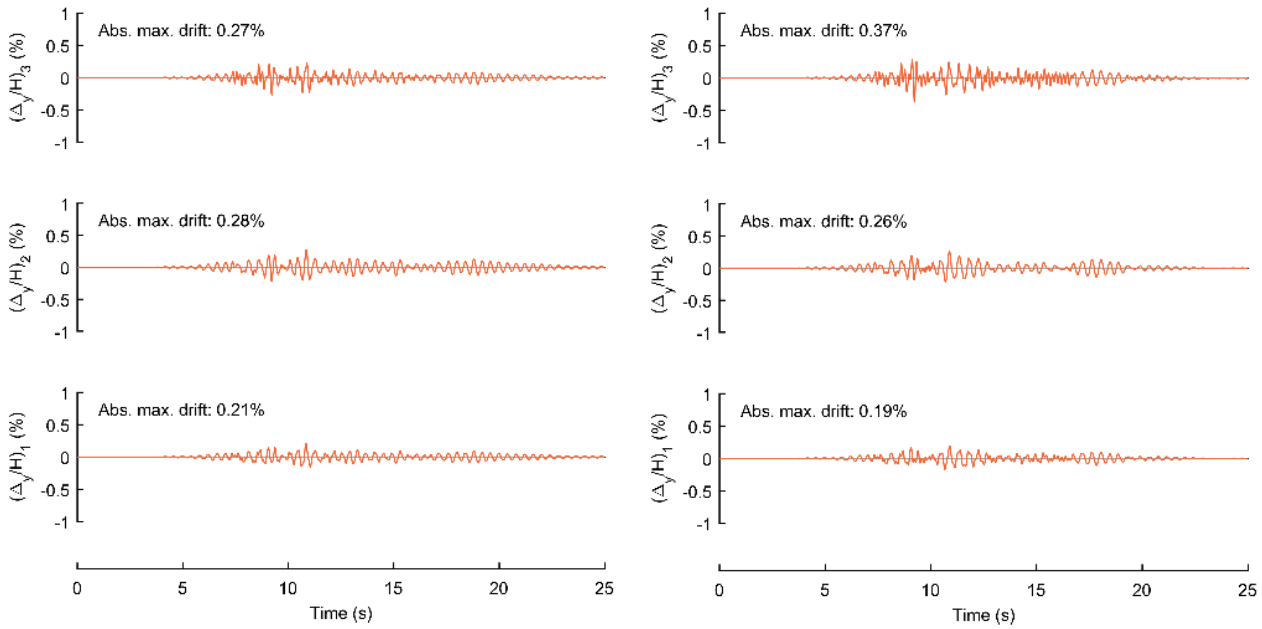
The vertical distribution of story drift in this direction is not the same for the results of each modeling approach. At the instant of maximum first story drift, the moment-rotation spring hinge model concentrates drift in the first story while the fiber-based limit-state hinge model distributes damage over the two lower stories, as shown in Figure 9-15. The soft first story mechanism predicted by the moment-rotation spring hinge model better correlates with the observed building damage.



(a) Moment-rotation spring hinges (b) Fiber-based limit-state hinges

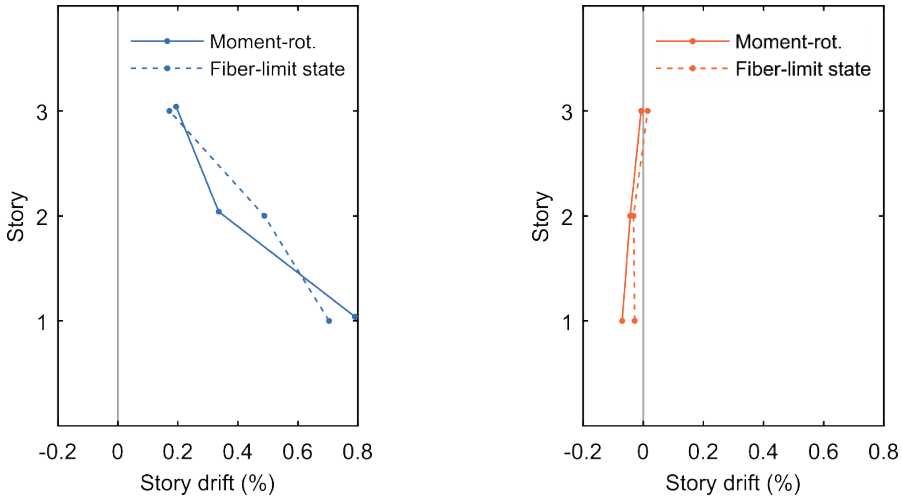
Figure 9-13 NDP: Story drift response histories in east-west direction.

This publication is available free of charge from: https://doi.org/10.6028/NIST.GCR.22-917-50



(a) Moment-rotation spring hinges (b) Fiber-based limit-state hinges

Figure 9-14 NDP: Story drift response histories in north-south direction.



(a) EW direction (b) NS direction

Figure 9-15 NDP: Story drift vertical distribution at maximum first-story drift (approximately t = 9.6 sec. in both models).

Table 9-4 Comparison of Predicted Global Response to Observed Damage

Attribute	Moment-Rotation Spring Model	Fiber-Limit State Model
Story-drift distribution along building height	Match	No match
Damage severity at critical story	Below	Below
Damage severity at other stories	Match	Above
Direction of maximum drift	Match	Match
Torsion	Match	Match

This publication is available free of charge from: https://doi.org/10.6028/NIST.GCR.21-917-50

In the north-south direction, the magnitude of story drift was also lower, in this case smaller than 0.4%. When comparing the two models, the vertical distribution of the demand was similar. The maximum story drift in the north-south direction occurred on the third story, likely due to the flexibility of the roof joists. This magnitude of drift is consistent with the limited flexural cracking observed in the bases of the third-story columns.

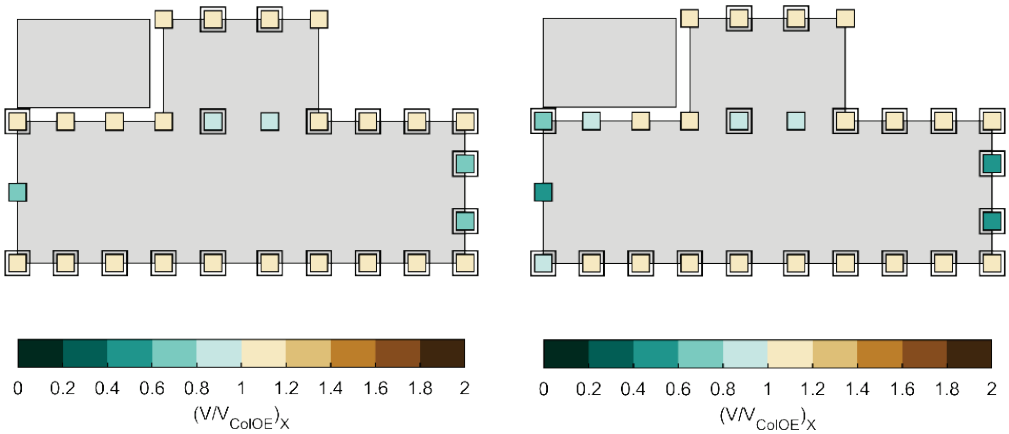
Significant torsion was not evident from the observed damage in this building, and the model also predicted this limited torsional response.

9.3.3 Component Performance: Model vs. Observation

Table 9-5 summarizes the accuracy of the general column and masonry response in each model. While the predicted story drifts were somewhat lower than expected from experimental results on flexure-shear critical columns for both models, Figure 9-16 shows that most first-story columns developed their expected shear capacities, as determined using ASCE 41, under loading in the east-west direction. As shown previously, some of the observed column damage suggests flexural yielding preceded diagonal cracking due to shear, and this sequence of flexural yielding and shear failure is not simulated using the current ASCE 41 modeling provisions.

Table 9-5 Comparison of Predicted to Observed Damage at Critical Story

	Moment-Rotation Spring Model		Fiber-Limit State Model	
Component	*Failure Mechanism*	*Level of Damage*	*Failure Mechanism*	*Level of Damage*
Columns	Match	Below	Match	Below
Full-height masonry	Match	Below	Match	Below
Partial-height masonry	Match	Match	Match	Match

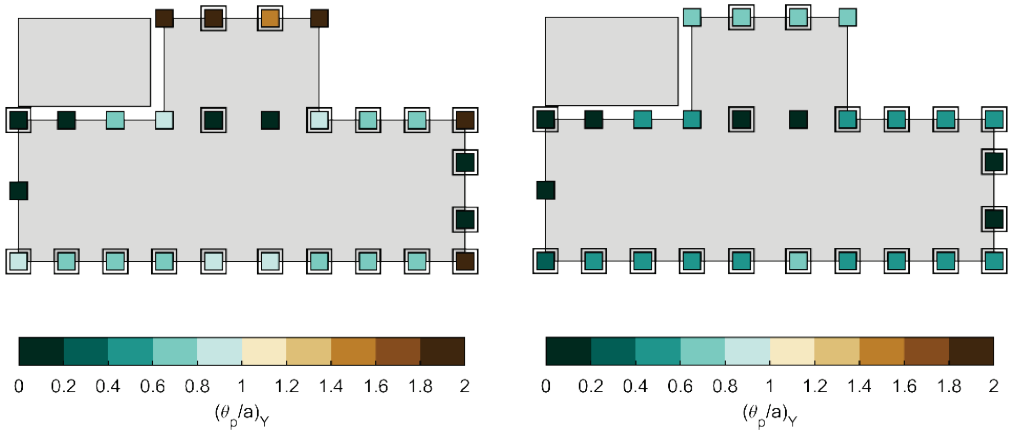


(a) Moment-rotation spring hinges (b) Fiber-based limit-state hinges

Figure 9-16 NDP: Heatmap of first-story column shear DCR in east-west direction; boxed columns indicate locations of observed damage.

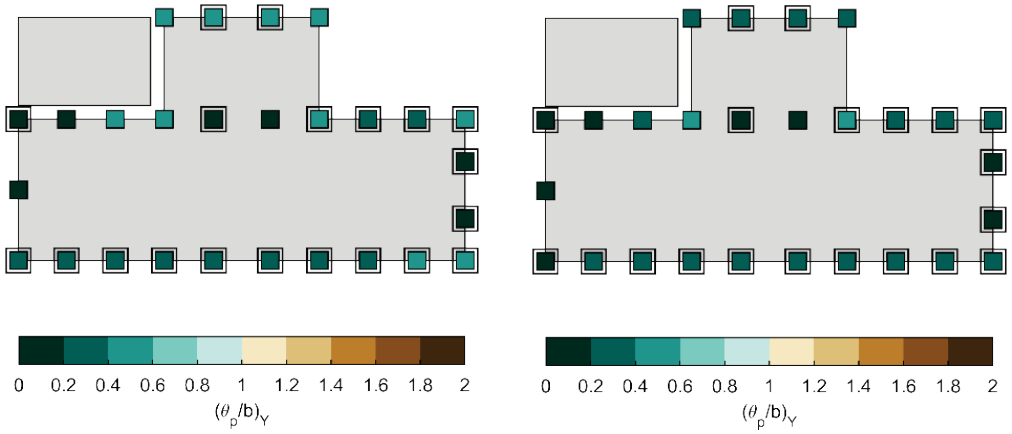
This publication is available free of charge from: https://doi.org/10.6028/NIST.GCR.22-917-50

As shown in Figure 9-17, most first-story columns did not sustain rotations large enough to trigger strength degradation defined by the ASCE 41-17 modeling parameters (i.e., plastic rotation beyond *a*). In the moment-rotation spring model, 6 of 27 columns sustained strength degradation for loading in the east-west direction, although damage was only reported in 4 of these 6 columns. Significantly more columns had diagonal cracking but no predicted strength degradation from the analysis. None of the columns had rotations which exceeded *a* in the fiber-based limit-state hinge model. While the moment-rotation spring model predicts more column damage on this basis, both models underpredict the overall level of damage and do not predict the distribution of damage. Figure 9-20 shows plastic rotation demand-capacity ratios relative to parameter *b*, where it can be seen that neither model predicts axial-load failure; this is consistent with the observed building damage as axial-load failure was not experienced by the columns.



(a) Moment-rotation spring hinges (b) Fiber-based limit-state hinges

Figure 9-17 NDP: Heatmap of first-story column plastic rotation DCR relative to parameter *a* in east-west direction; boxed columns indicate locations of observed damage.



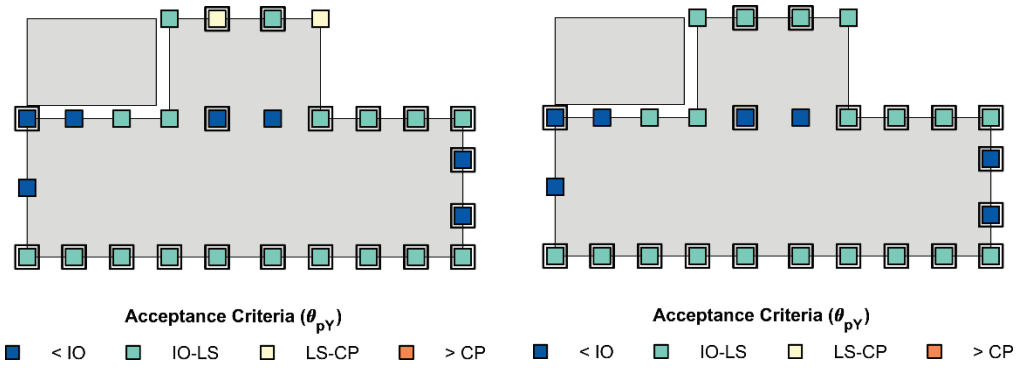
(a) Moment-rotation spring hinges (b) Fiber-based limit-state hinges

Figure 9-18 NDP: Heatmap of first-story column plastic rotation DCR relative to parameter *b* in east-west direction; boxed columns indicate locations of observed damage.

This publication is available free of charge from: https://doi.org/10.6028/NIST.GCR.21-917-50

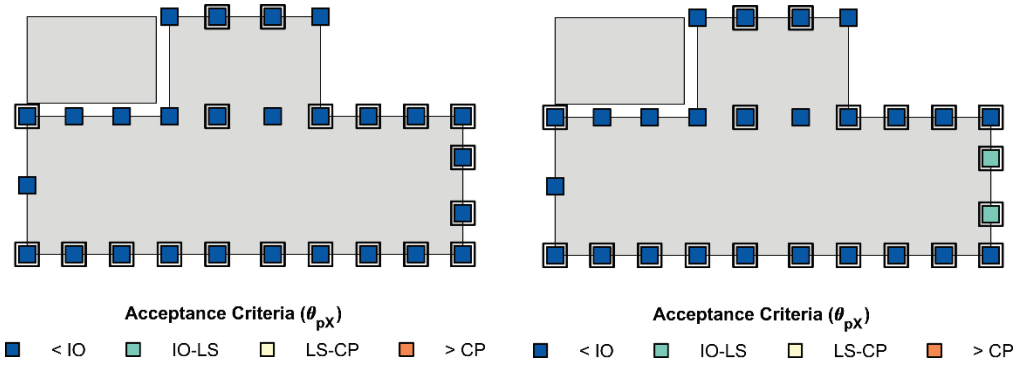
Figures 9-19 and 9-20 summarize predicted column performance using ASCE 41 acceptance criteria. It is difficult to classify the observed damage using these criteria; nonetheless, it is clear that columns that sustained significant diagonal cracking (i.e., most first-story columns) would not meet Immediate Occupancy criteria. The simulation results indicate also that most columns would sustain damage beyond the Immediate Occupancy level. Thus, performance is well predicted on the low end, with both observation and simulation indicating most first story columns have damage exceeding that associated with Immediate Occupancy. However, limitations in the collected damage data do not support conclusions about the accuracy with which damage states beyond Immediate Occupancy are simulated.

It is noted that the demands on Columns B10 and D10 exceed the Immediate Occupancy level but in the north-south direction only (transverse direction from critical direction of other columns). This is indicative of a small torsional response and consistent with the observed direction of diagonal cracking in these columns.



(a) Moment-rotation spring hinges (b) Fiber-based limit-state hinges

Figure 9-19 NDP: Heatmap of first-story column acceptance criteria in east-west direction; boxed columns indicate locations of observed damage.



(a) Moment-rotation spring hinges (b) Fiber-based limit-state hinges

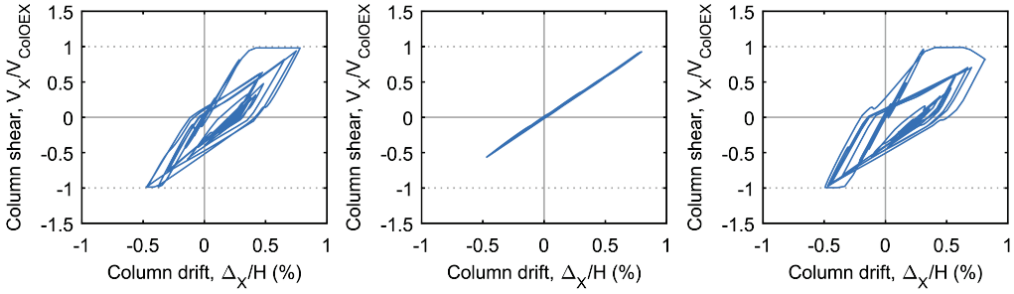
Figure 9-20 ND: Heatmap of first-story column acceptance criteria in north-south direction; boxed columns indicate locations of observed damage.

This publication is available free of charge from: https://doi.org/10.6028/NIST.GCR.22-917-50

Masonry was modeled using compression-only diagonal truss elements, and none of these struts developed forces in excess of their computed capacities. Some diagonal cracking and crushing at column-wall interfaces was noted in full-height masonry infill walls in the building, but severe damage to these walls was not observed. Thus, the severity of predicted full-height masonry infill damage was slightly below that which was observed.

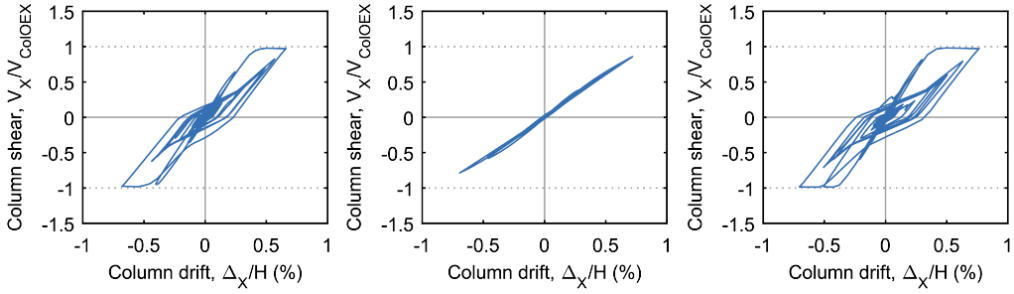
9.3.3.1 Column Response: Comparisons to Similar Experimental Specimens

The three first-story columns in Gridline 5 were evaluated in more detail to compare their observed damage and predicted response to experimental damage and response. The predicted hysteretic responses of these columns (A5, E5, and G5) in the east-west direction are shown in Figure 9-21 for the moment-rotation spring hinge model and Figure 9-22 for the fiber-based limit-state hinge model. Table 9-6 details these column properties and those of two similar experiments in the literature: Specimen SC3 from Aboutaha (1994) and Specimen 40.033 from Wight and Sozen (1973).



(a) Column A5 (b) Column E5 (c) Column G5

Figure 9-21 NDP: Moment-rotation spring model column hysteretic response in east-west direction.



(a) Column A5 (b) Column E5 (c) Column G5

Figure 9-22 NDP: Fiber-based limit-state hinge model column hysteretic response.

This publication is available free of charge from: https://doi.org/10.6028/NIST.GCR.21-917-50

Table 9-6 Building and Similar Experimental Column Properties

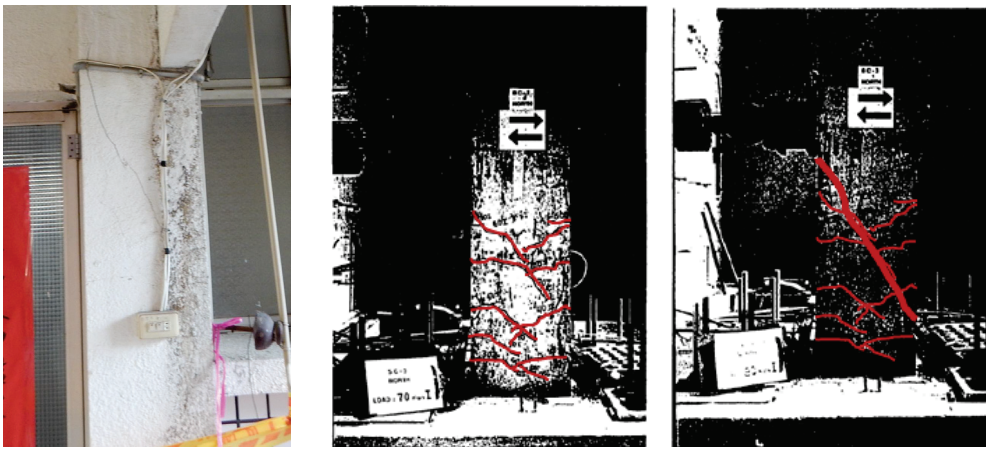
Properties	Nanhua District Office *Columns A5/E5/G5*	Aboutaha (1994) *Specimen SC3*	Wight and Sozen (1973) *Specimen 40.033*
ρ_l	1.8%	1.9%	2.4%
ρ_t	0.1%	0.1%	0.3%
a/d	3.2	3.1	3.5
s/d	0.88	1.0	0.50
$\frac{N_{UG}}{A_g f'_{cE}}$	0.09/0.15/0.06	0.00	0.11
$\frac{N_{UG}}{A_g f'_{cE}}$ *	0.11/0.19/0.12		

* Values shown are maxima from moment-rotation spring hinge model; values from fiber-based limit-state hinge model are similar.

The building columns are nominally identical but are subjected to different axial loads under gravity and under dynamic loading. Using the nonlinear analysis, the predicted maximum axial load ratios ($N_{UD}/A_g f'_c$) of Columns A5 and G5 were approximately 10%, and approximately 20% for Column E5. The test columns have similar reinforcement ratios, aspect ratios, and transverse reinforcement spacing to the building columns, but were tested without axial load (Specimen SC3) or constant axial load ratio of 11% (Specimen 40.033). Since Column G5 has a lower axial load ratio, it is compared here to Specimen SC3, while Columns A5 and E5 are compared to Specimen 40.033.

Figure 9-23 compares photographs of observed damage in Column G5 and Specimen SC3 at similar drift levels. Column G5 had residual diagonal cracking as shown in Figure 9-23a, though this was less severe than that observed in Columns A5 and E5. At 0.5-1.0% story drift, Specimen SC3 exhibited cracking (Figure 9-23b) that was more extensive than that observed in Column G5. However, it must be noted that the photograph of Column G5 was taken at a residual (i.e., unloaded) state in the building, while the specimen photograph was taken under load at an imposed drift in the experiment. Thus, the cracks in Figure 9-23b would be expected to be wider and more easily distinguishable at comparable maximum drift levels. The hysteretic response of Specimen SC3 is plotted in Figure 9-24a, which suggests that damage at these drift levels would not be associated with strength degradation. This is generally consistent with both the moment-rotation spring and fiber-based limit-state hinge model results, as well as the observed damage in Column G5.

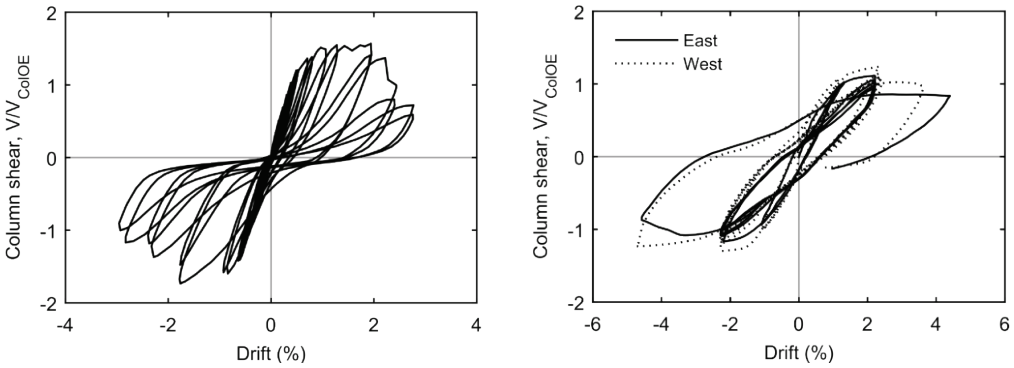
This publication is available free of charge from: https://doi.org/10.6028/NIST.GCR.22-917-50



(a) Column G5 residual damage; predicted maximum story drift of 0.7-0.8%

(b) Specimen SC3—cracks highlighted in red at story drifts of 0.5% (left) 0.5-1.0% (right)

Figure 9-23 Comparison of observed column damage in building to Specimen SC3 (Aboutaha, 1994).



(a) Specimen SC3 (Aboutaha 1994)

(b) Specimen 40.033 (Wight and Sozen 1973)

Figure 9-24 Hysteretic response of similar experimental specimens.

Figure 9-25 compares observed residual damage from Columns A5 and E5 to that of Specimen 40.033. Column A5 sustained diagonal cracking with wide residual crack openings (Figure 9-25a). Column E5 had more extensive concrete spalling at its base after undergoing approximately the same drift demands (maximum story drift demands of 0.7%-0.8%). The increased damage severity versus that observed in Column E5 is attributed in part to the higher axial load demands on these columns. Despite the greater damage to Column E5, essentially elastic behavior was predicted in the nonlinear analyses (see Figures 9-21b and 9-22b). Note that Column A5 had partial-height masonry infill that created a captive-column condition, while Column E5 was adjacent to full-height masonry infill on one side. The response of Column E5 may be affected by the adjacent masonry infill, which is visibly damaged in Figure 9-25a. Specimen 40.033 had similar column properties, but the only photographic evidence of damage available is after loading to approximately 4.0% drift, which is well over the predicted drift demands on the building. Thus, it is

This publication is available free of charge from: https://doi.org/10.6028/NIST.GCR.21-917-50

difficult to draw comparisons between Columns A5, E5, and Specimen 40.033 based on reported damage alone. The hysteretic response of Specimen 40.033 is shown in Figure 9-24b. These plots show that strength degradation in this specimen did not occur until approximately 4.0% drift, which is well above the predicted drift demands from the analysis. Although the observed damage does not indicate significant strength degradation, the level of residual cracking and spalling does indicate more inelastic action than implied by the simulated response (Figures 9-21 and 9-22) and the experimental response at the same drift level (Figure 9-24b). This comparison suggests the maximum drift is under predicted in the analysis, which may be due to the inconsistency between the site ground motion and best estimate ground motion used in the simulation.



(a) Column A5 residual damage; predicted maximum story drift of 0.7-0.8%

(b) Column E5 residual damage; predicted maximum story drift of 0.7-0.8%

(c) Specimen 40.033 residual damage on west (left) and east (right) ends; maximum story drift of approximately 4.0%

Figure 9-25 Comparison of observed column damage in building to Specimen 40.033 (Wight and Sozen, 1973).

9.4 Linear Dynamic Procedure

A three-dimensional model of the Nanhua District Office building was assembled using SAP2000 software and the modeling recommendations in ASCE 41-17. The building addition on the north-west corner was not included in the model.

9.4.1 Modeling Approach

Four linear models were developed with the following objectives:

1. Evaluate the accuracy of the linear model to predict damage mechanism and the performance state of the components.
2. Evaluate the impact of the masonry infill on the component demands
3. Evaluate the impact of different modeling approaches for the full- and partial-height infill, specifically comparing four different types of approaches: (1) no

This publication is available free of charge from: https://doi.org/10.6028/NIST.GCR.22-917-50

infill, also referred to as bare frame; (2) ASCE 41-17 minimally compliant model using rigid end zones to account for the restraint provided by the partial-height infill; (3) shell elements; or (4) compression-only struts.

The baseline model of the bare frame (BF model) was generated as follows:

- Nodes were defined at column centerlines with beam connectivity matching measurements from the construction documents.
- Mass was assigned to all story nodes in the translational degrees of freedom based on tributary floor area including the masonry. The total seismic weight equaled 2,261 kips.
- All base nodes (bottom of columns) of the model were fully restrained against translation and rotation without consideration of foundation or soil flexibility. While the site *Vs* was not known, the building has h/T between 8.3 and 12.9 m/s (varies depending on modeling approach), which implies SSI is not expected to significantly contribute to the response for *Vs* greater than 129 m/s.
- Columns and beams were modeled as two-dimensional line ("frame") elements. Effective stiffness values in flexure, shear, and axial were $0.3E_{cE}I_g$, $0.4E_{cE}A_w$ and $E_{cE}A_g$ respectively (see ASCE 41-17 Table 10-5). Floor slabs were modeled with shell elements assigned a thin-plate formulation and out-of-plane effective stiffness values that were the same as the beams, i.e., $0.3E_{cE}I_g$, $0.4E_{cE}A_w$ and $E_{cE}A$.
- Joint offsets were assigned at the tops of columns and at both ends of the beams to meet the requirements of ASCE 41-17 Figure 10-2.
- Dead and live loads are presented in Table 9-7.

Table 9-7 Dead and Live Loads

Variable	Value - unit		Comments
DL	25	psf	Estimated
LL	40	psf	Office space (ASCE 7-16)
Partition DL	10	psf	Partition load incl in seismic weight (ASCE 7-16)
Slab DL	59.1	psf	Self-weight (area equivalent)
Beam DL	52.3	psf	Self-weight (area equivalent)
Column DL	varied	lb	Self-weight (concentrated)
Infill DL	varied	plf	Self-weight (distributed)

Three models shown in Figure 9-26 were developed in addition to the bare frame model presented above. ASCE 41-17 does not provide a specific modeling approach for simulating the effects of partial-height masonry infill, so both partial-height and

This publication is available free of charge from: https://doi.org/10.6028/NIST.GCR.21-917-50

full-height masonry infill were modeled consistently in one of the three ways as described for each of the following models:

- RO model using rigid offsets to simulate the partial-height masonry infill (minimum required by ASCE 41, columns stiffened at full-height masonry locations)
- SH model which uses elastic shell elements to model both the full-height and partial-height masonry infill. Effective stiffness values for flexural, axial, and shear response were $0.15E_mI_g$, $1.0E_mA_g$, and $0.29G_mA_g$, respectively where E_m and G_m were based on f'_{mL} = 1200 psi with $E_m = 700f'_{mL}$ as defined by TMS-402 Section 1.8.2.2.1 (MSJC, 2011). Effective stiffness modifiers were adopted from NIST GCR 17-917-45 (NIST, 2017).
- DS model where the infill is modeled using compression-only diagonal struts, where the struts were connected to the end nodes of the columns bounding the full-height masonry and a node at the top of the height of the partial-height masonry infill. The effective width of the strut, a, was calculated using the recommendations from FEMA 356 (FEMA, 2000) Section 7.5.2.1 as provided below where λ_1 is used to determine a, the effective width based on the geometry and material properties of the infill (*inf*) and concrete columns. As defined in the equation, h_{col} is the height between centerlines of beams, h_{inf} is the height of infill, t_{inf} is the thickness of infill (24 cm); r_{inf} is the diagonal length of the infill and I_{col} is the moment of inertia of adjacent columns. The material properties are based on the elastic modulus of the infill, E_m and framing elements $E_{c,fe}$, respectively.

$$\lambda_1 = \left[\frac{E_{me}t_{inf}\sin(2\theta)}{4E_{fe}I_{col}h_{inf}}\right]^{\frac{1}{4}}$$

$$a = 0.175\left(\lambda_1 h_{col}\right)^{-0.4} \times r_{inf}$$

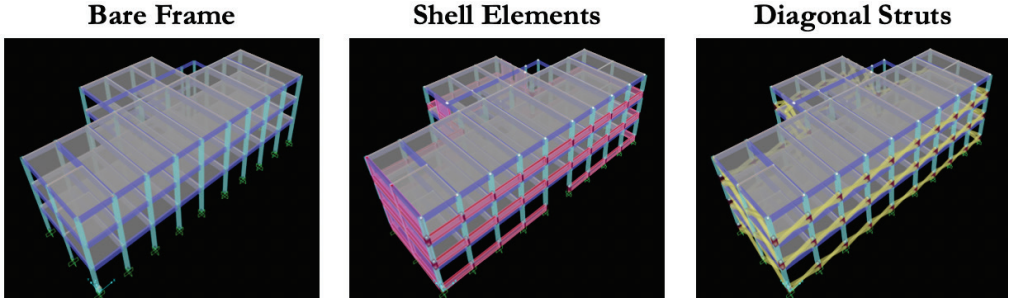


Figure 9-26 Linear model variations.

Table 9-8 provides the first three periods of each of the models. The RO model provides the lowest period and therefore highest stiffness.

This publication is available free of charge from: https://doi.org/10.6028/NIST.GCR.22-917-50

Table 9-8 Modes of Vibration for Linear Models

Model	Mode	Period (sec.)	Shape description
BF	1	0.92	Lateral east-west
	2	0.73	Lateral north-south
	3	0.70	Torsion
RO	1	0.59	Lateral east-west
	2	0.49	Lateral north-south
	3	0.47	Torsion
SH	1	0.65	Lateral east-west
	2	0.47	Lateral north-south
	3	0.23	Torsion
DS	1	0.70	Lateral east-west
	2	0.42	Lateral north-south
	3	0.31	Torsion

More information about the linear model can be found in Sumearll (2019).

9.4.2 Global Performance: Model vs. Observation

The linear response models were analyzed using the A730 ground motion. For the first-story columns, moment and shear force demand-capacity ratios were computed and compared with appropriate *m* factors. The following provides a summary of the predicted global and local responses predicted from the models in comparison with the observed response for the first story. The focus is on the first story because there was essentially no structural damage observed elsewhere. Further, a linear dynamic analysis would not simulate the observed plastic mechanism (hence overpredicting demand at the upper stories.

Table 9-9 provides a summary of the global response predicted by the models. In all cases, the drift demands were largest in the east-west (long) direction of the building, which corresponded to the observed damage direction. Overall, the observed damage state is estimated to have been between life safety and collapse prevention, therefore an accurate prediction would be a DCR_m approaching 1.0 for shear and flexure, where DCR_m is defined as the demand-to-capacity ratio where the capacity is determined using the *m*-factor for the Collapse Prevention acceptance criteria. This is predicted by the models with stiffness of the masonry infill modeled, including rigid offset, shell element and diagonal strut modeling approaches, but not the bare frame model (see Table 9-9).

This publication is available free of charge from: https://doi.org/10.6028/NIST.GCR.21-917-50

Table 9-9 Comparison of Predicted Global Response to Observed Damage

	ASCE 41 Noncompliant	ASCE 41 Compliant		
Attribute	*Bare Frame Model*	*Rigid Offset Model*	*Shell Element Model*	*Diagonal Strut Model*
Direction of maximum drift	Match	Match	Match	Match
Torsion	Match	Match	Match	Match

9.4.3 Component Performance: Model vs. Observation

Figure 9-27 shows the results for the four models in terms of predicted damage and observed damage, where the column was predicted to be damaged if the flexural or shear demand capacity ratio (expressed in terms of *m* for Collapse Prevention for the flexural capacity) exceeds 1. Note that axial-flexural interaction was considered to compute the flexural capacity, but biaxial bending was not evaluated; neglecting biaxial bending was deemed appropriate as it was only expected to increase the DCR for flexure, which exceeded 1 (see second and third bullet). The following statements can be made:

- None of the models predict DCR_m values exceeding 1 in the Y-direction. This is consistent with the observed damage.
- In the bare frame (BF) model, the predicted flexural DCR_m is approximately or slightly larger than 1.0 in some of the damaged columns but less than 1 for most. The predicted shear DCR_m is less than 1 for all of the columns (both damaged and undamaged).
- For all of the models that include the masonry infill, the predicted flexural DCR_m exceeds 1 in the overwhelming majority of the damaged columns. This type of damage is consistent with photographs that show spalling (indicative of flexural damage) in many of the photographs of the first-story columns, as shown in Figure 9-10a indicating the flexural strength was developed. However, the severity of damage (i.e., beyond Collapse Prevention performance) is over-predicted by the simulation.
- A similar observation is made for the predicted shear DCR_m, where the majority of the columns that sustained damage in the form of diagonal cracking had shear DCR_m values that exceeded 1. This suggests shear failure controlled or followed flexural yielding, the latter being more consistent with the observed damage type (Figure 9-10). The analysis predicts more severe damage than observed.
- Figure 9-28 shows the accuracy of the prediction of exceeding the allowable strength, which are indicative of damage and failure mode. The results show that the BF model does not predict the failure model correctly of any of the columns.

This publication is available free of charge from: https://doi.org/10.6028/NIST.GCR.22-917-50

- The models that include masonry infill all predict similar distributions of damage that are more accurate than that of the bare frame model. Figure 9-28 visualizes the accuracy in terms of the gross damage observed or not observed of the SH and DS models, which have the same damage distribution.
- Table 9-10 summarizes the overall findings relative to the predicted failure mode of the components. The results indicate that the models with the effect of the stiffness of the masonry infill modeled or the masonry infill modeled directly predicts the correct failure mode of the columns (flexure-shear response).

Table 9-10 Comparison of Predicted Local Response to Observed Damage

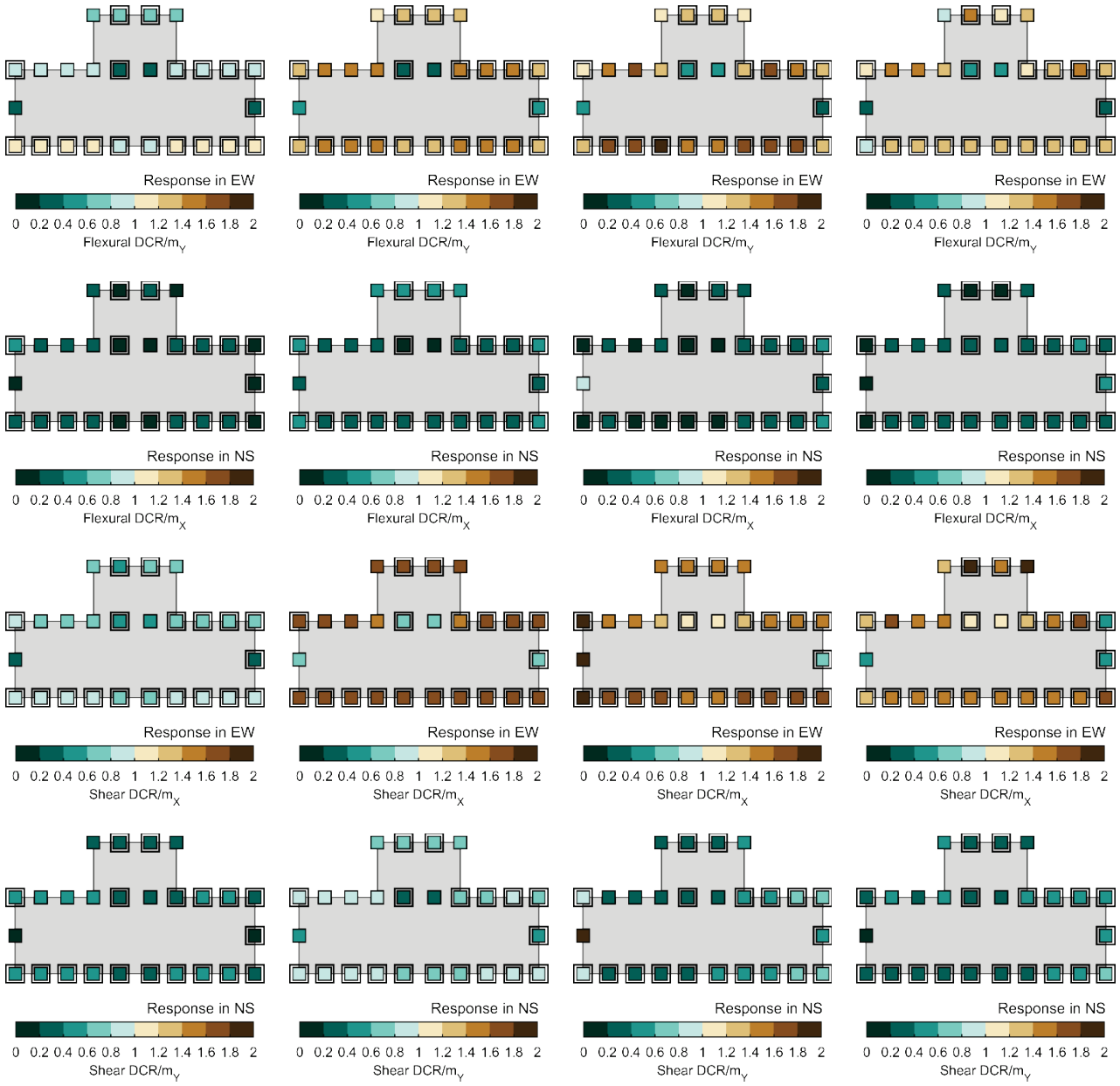
	ASCE 41 Non-compliant		ASCE 41 Compliant					
	Bare Frame Model		*Rigid Offset Model*		*Shell Element Model*		*Diagonal Strut Model*	
Component	*Failure Mechanism*	*Level of Damage*	*Failure Mechanism*	*Level of Damage*	*Failure Mechanism*	*Level of Damage*	*Failure Mechanism*	*Level of Damage*
Columns	No match	No match	Match	Match	Match	Match	Match	Match

Comparison of linear dynamic analysis results and observed damage supports the following observations and conclusions:

- More accurate simulation of building response requires simulation of masonry infill. For this evaluation, multiple methods for simulating infill were considered (i.e., all models except BF model). Comparison of simulated response and observed damage does not lead to identification of any one modeling approach as preferable, since the overall results were the same.
- Expected material properties are used to determine column flexural strength to calculate the flexural DCR in ASCE 41. However, the material properties used to determine column shear strength are not clearly defined and, in this study, lower-bound material properties were used. Since column DCRs were larger than anticipated based on the observed damage, it is suggested to clarify ASCE 41 to recommend consistent strengths for both flexure and shear.
- Consideration of the ASCE 41 evaluation process leads to the conclusion that it would be helpful if ASCE 41 included default values for k_{nl} in ASCE 41-17 Equation 10-3 for cases in which a pushover analysis or iterative linear response-history analysis had not been conducted. Currently, this coefficient depends on the displacement ductility demand. In addition, it would be helpful to clarify that k_{nl} can be less than 1 even in the flexural DCR is less than 1.

This publication is available free of charge from: https://doi.org/10.6028/NIST.GCR.21-917-50

This publication is available free of charge from: https://doi.org/10.6028/NIST.GCR.22-917-50



(a) BF (b) RO (c) SH (d) DS

Figure 9-27 LDP: Heatmap of first-story flexural and shear DCR/*m* values; boxed columns indicate locations of observed damage.

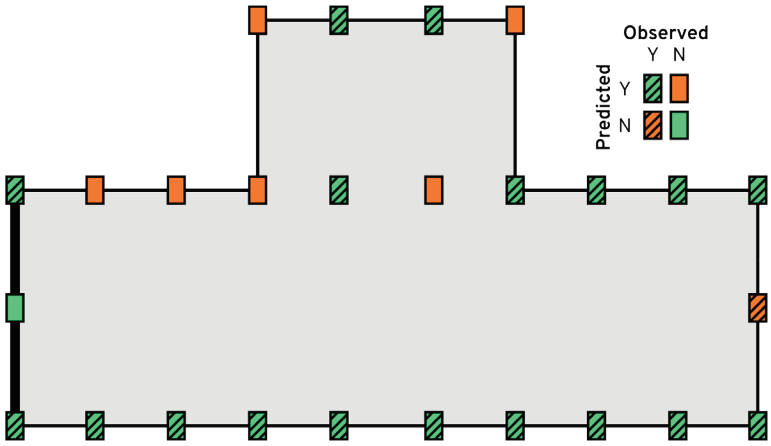


Figure 9-28 LDP: Spatial comparison of predicted versus observed damage based on flexure and shear limit states (data are consistent for all ASCE 41-compliant models).

9.5 FEMA P-58 Damage Assessment

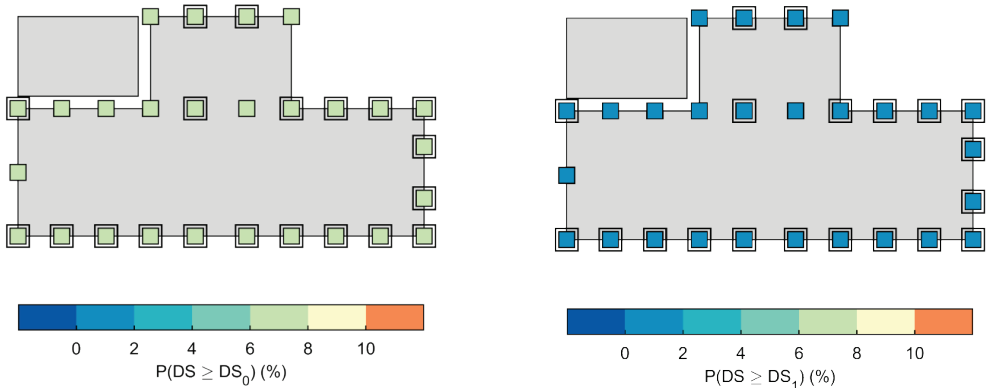
The assessment methodology described in FEMA P-58 (FEMA, 2018c) is implemented using the nonlinear dynamic model developed for this study building and the damage predicted from the assessment are compared with the damage observed in the Meinong Earthquake. This comparison takes advantage of the FEMA P-58 fragility database to map the simulated responses to damage.

The assessment focuses on the first-story columns of the study building. Specifically, the assessment considers the plastic rotations in the east-west direction of loading predicted using the moment-rotation spring model (this model predicted slightly larger rotations than the fiber-based limit-state hinge model). The FEMA P-58 fragility curve B1041.111a," which corresponds to weak columns subjected to low to moderate axial loads in non-conforming moment-frames, was used to compute damage state probabilities for each column; this fragility curve is appropriate for non-conforming moment frames, which do not meet code requirements, with weak columns and with beams on one side of the frame, which do not meet building code requirements. The probabilities of exceedance for Damage States 0 and 1 are shown in Figure 9-29.

These results indicate low probabilities of damage in the columns, which is not consistent with the observed damage. Notably, the assessment procedure suggests that the columns would have less than a 2% probability of exceedance of Damage State 1, which is characterized by residual crack widths greater than 0.06 in., no significant spalling, and no fracture or buckling of reinforcing steel. This discrepancy between observed and predicted damage from the FEMA P-58 may be due to the limited test data used to derive the B1041.111a fragility (in particular, the fragility curve is not specifically for use with columns that are captive due to partial-

This publication is available free of charge from: https://doi.org/10.6028/NIST.GCR.21-917-50

height infill) or underprediction of column plastic rotation demands in the nonlinear analysis using the best-estimate ground motion.



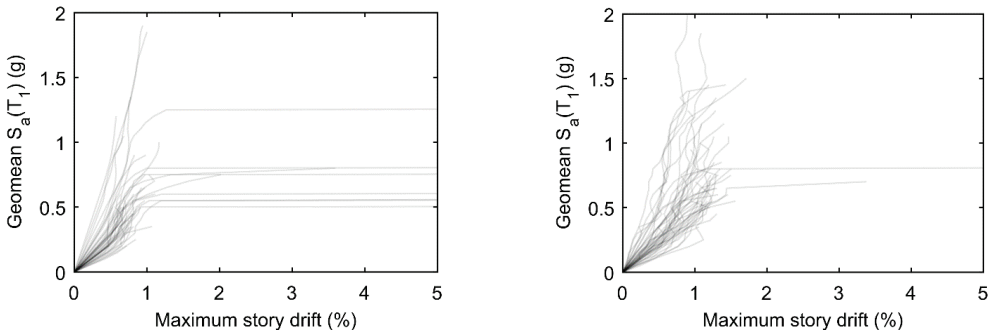
(a) Damage State 0 (b) Damage State 1

Figure 9-29 Heatmap of first-story column probabilities of exceedance of damage states in east-west direction based on FEMA P-58 evaluation.

9.6 Fragility Assessment

Incremental dynamic analyses (IDA) were performed on both model variations using the FEMA P-695 far-field ground motion set to evaluate collapse probability on the basis of exceedance of the Collapse Prevention limit state, sidesway collapse (story drift beyond 5%), and numerical nonconvergence. Collapse margin ratios were not computed for this structure because the spectral acceleration corresponding to MCE_R-level shaking is not available for this site outside the US.

Figure 9-30 shows IDA curves (spectral acceleration of the ground-motion "cloud" versus maximum story drift recorded in the corresponding analysis) for the moment-rotation spring and fiber-based limit-state hinge models. In this figure, all curves that are incomplete (no "flat-lining" to collapse) represent analyses that have not converged to a solution. Most instances of collapse or nonconvergence begin between approximately 1.0 and 1.5% story drift, regardless of spectral acceleration. This suggests that the building would be near collapse even at the relatively low story drifts predicted from the best-estimate ground motions.



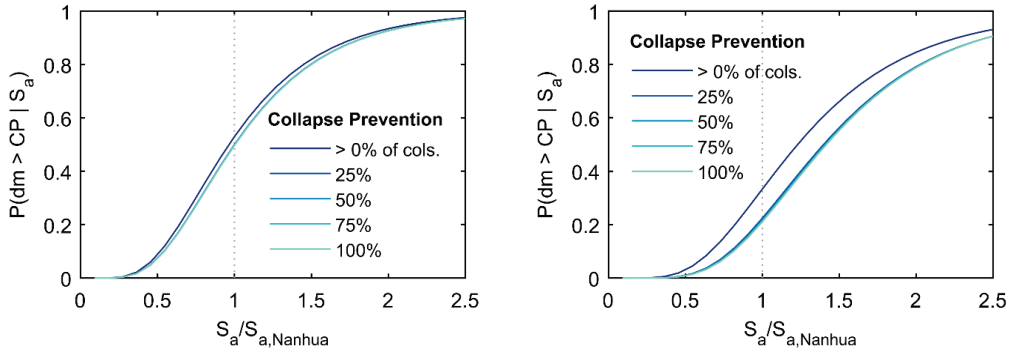
(a) Moment-rotation spring (b) Fiber-based limit-state hinge

Figure 9-30 Incremental dynamic analysis curves.

This publication is available free of charge from: https://doi.org/10.6028/NIST.GCR.22-917-50

Using the best-estimate ground motion, the fiber-based limit-state hinge model exhibited a more even distribution of damage between the first and second stories, which does not match the observed damage pattern consistent with a soft first-story response. However, the IDA collapse mechanisms in both the moment-rotation spring and fiber-based limit state hinge models match the observed damage distribution. This may suggest that the best-estimate ground motion is not appropriate for the building, although this is unclear because such inconsistencies were not observed in the moment-rotation spring model results.

Figure 9-31 provides fragility curves for the Collapse Prevention acceptance criteria for the critical (first-story) columns in the building. These fragility curves were produced for various percentages of columns at this performance level to provide estimated probabilities of exceedance with respect to spectral acceleration. Note that the sidesway collapse fragility curve is identical to the 100% curve in Figure 9-31. Spectral acceleration is normalized here by that of the best-estimate ground motion for the building. There are two key observations from this figure. First, there is relatively little difference in the fragilities based on the percentage of columns that reach collapse prevention. This indicates that the response of the building is brittle, and failure of several columns quickly leads to failure of the others on that story. Second, the fiber-based limit-state hinge model predicts a lower probability of exceeding the collapse-prevention acceptance criteria. At the spectral acceleration of the best estimate ground motion, the moment-rotation spring model results in an approximately 50% collapse probability versus 20% for the fiber-based limit-state model. This makes sense because the column strength, stiffness, and degradation parameters are dynamically updated in this model, while the moment-rotation spring parameters are based on the expected maximum axial demand.



(a) Moment-rotation spring (b) Fiber-based limit-state hinge

Figure 9-31 Fragility curves for column collapse prevention acceptance criteria.

9.7 FEMA P-2018 Evaluation

The building was evaluated using the procedure outlined in FEMA P-2018, *Seismic Evaluation of Older Concrete Buildings for Collapse Potential* (FEMA, 2018b). The

This publication is available free of charge from: https://doi.org/10.6028/NIST.GCR.21-917-50

building is classified as a "frame system" in both orthogonal directions despite the presence of masonry infill and evaluated per Chapter 6 of FEMA P-2018.

Evaluations were performed considering the SRSS response spectrum for the best-estimate ground motion and the 5%/50-year uniform hazard spectrum (UHS). The 5%/50-year UHS was considered because (1) there is uncertainty in the best-estimate ground motion's accuracy at the building site and (2) this hazard level is that recommended for use in FEMA P-2018 for standard evaluations. In this study, the 5%/50-year UHS was estimated using linear interpolation in logarithmic space between the 10%/50-year and 2%/50-year UHS computed for Tainan by Lee et al. (2017) and shown in Figure 9-32. The starred dashed lines in the figure indicate the spectral accelerations at the effective period in the east-west direction (0.88 sec.), effective period in the north-south direction (0.58 sec.), approximate period per ASCE 7-10 (0.42 sec.), and period per ASCE 41-17 Chapter 4 (0.47 sec.). Note that only the FEMA P-2018 effective periods are used in the evaluation and that the effective periods are based on a building weight of 2,463 kips.

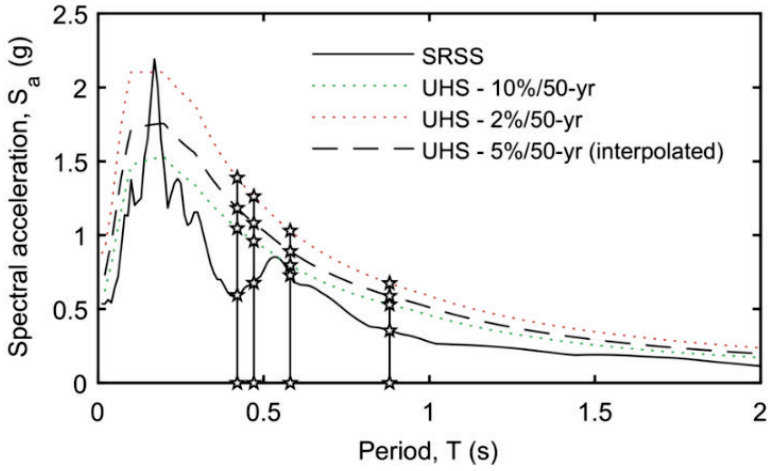


Figure 9-32 SRSS 5%-damped acceleration response spectrum for best-estimate ground motion (A730) and UHS for Tainan.

Tables 9-11 and 9-12 show the key evaluation parameters and results based on the SRSS response spectrum and 5%/50-year UHS, respectively. The EW-direction corresponds to east-west in plan and the NS-direction corresponds to north-south in plan. Table 9-13 shows the story ratings calculated for each story in each direction using both spectra.

The controlling plastic mechanism was "Plastic Mechanism 2" (full frame mechanism) in the east-west direction and "Plastic Mechanism 1" in the north-south direction (soft first-story mechanism). The first story was the critical story in both cases. Based on the observed damage, the actual mechanism was a soft first-story mechanism in the east-west direction. Thus, the procedure did not correctly identify the east-west plastic mechanism. This is likely attributed to the lack of consideration

This publication is available free of charge from: https://doi.org/10.6028/NIST.GCR.22-917-50

Table 9-11 Summary of Key Evaluation Parameters and Results Using SRSS Response Spectrum

Parameter	EW-Direction	NS-Direction	Units	Description
S_a @ T_e	0.35	0.73	g	Spectral Acceleration at T_e
V_y	588	1319	kips	Base Shear Yield Strength
Mechanism	2	1	-	Governing Plastic Mechanism
Critical Story	1	1	-	Critical Story
$\mu_{strength}$	1.34	1.22	-	Global DCR
δ_{eff}	2.68	2.47	in	Global Equivalent SDOF Drift
$\delta_{eff,roof}$	7.43	6.64	in	Global Roof Drift
$\delta_{eff,roof} / h_{roof}$	1.7%	1.5%	-	Global Roof Drift Ratio

Table 9-12 Summary of Key Evaluation Parameters and Results Using 5%/50-Year UHS

Parameter	EW-Direction	NS-Direction	Units	Description
S_a @ T_e	0.59	0.89	g	Spectral Acceleration at T_e
V_y	588	1319	kips	Base Shear Yield Strength
Mechanism	2	1	-	Governing Plastic Mechanism
Critical Story	1	1	-	Critical Story
$\mu_{strength}$	2.22	1.50	-	Global DCR
δ_{eff}	4.55	3.06	in	Global Equivalent SDOF Drift
$\delta_{eff,roof}$	12.6	8.24	in	Global Roof Drift
$\delta_{eff,roof} / h_{roof}$	2.8%	1.8%	-	Global Roof Drift Ratio

Table 9-13 Story Ratings

	SRSS Response Spectrum		5%/50-Year UHS	
Story	*EW-Direction*	*NS-Direction*	*EW-Direction*	*NS-Direction*
1	0.11*	0.27*	0.38*	0.40*
2	0.10	0.13	0.37	0.25
3	0.10	0.10	0.37	0.10

* Indicates critical story

of masonry infill. In particular, the partial-height masonry infill in the east-west direction of the actual building effectively shortened the column height and increased the flexural resistance of the beams in this direction to help induce a soft-story response mechanism.

This publication is available free of charge from: https://doi.org/10.6028/NIST.GCR.21-917-50

Using the SRSS response spectrum, the FEMA P-2018 building rating was 0.27 and controlled by the north-south story rating. This classifies the building as a "Lower Seismic Risk." Although the actual ground motion was used here, the incorrect mechanism controlled the evaluation, and the resulting rating is inconsistent with the observed substantial diagonal cracking in the columns in the east-west direction.

Using the interpolated 5%/50-year spectrum, the FEMA P-2018 building rating was 0.40, which was also controlled by the north-south story rating. However, the east-west story rating was similar (0.38). This classifies the building as a "Higher Seismic Risk" and demonstrates that, if the FEMA P-2018 procedure is used for this building without knowledge of the actual ground motion, the overall vulnerability of the building would be identified.

9.8 Summary

The study building was damaged in the 2016 Meinong Earthquake and evaluated using ASCE 41-17 linear and nonlinear dynamic procedures. The building had reinforced concrete moment-resisting frames in which columns sustained severe diagonal cracking at the first story due to the presence of partial-height masonry infill. Limited damage occurred in the north-south direction, primarily in the columns on the east side of the building. This section summarizes findings from analyses using different modeling approaches for infill (linear procedure) and columns (nonlinear procedure).

Infill modeling approaches used in the linear procedure included a:

- baseline, noncompliant model in which infill was neglected,
- compliant model in which infill was implicitly considered using column offsets,
- compliant model in which infill was explicitly modeled with shell elements, and
- compliant model in which infill was explicitly modeled with compression-only diagonal struts.

Two column-modeling approaches were investigated for the nonlinear procedure. Each approach used concentrated hinges at the top and bottom of each column with behavior defined by either:

- moment-rotation springs with backbone curves per ASCE 41-17 based on axial load determined from iterative nonlinear response-history analysis or
- fiber-based limit-state hinges with updated response based on axial load (i.e., axial-flexural interaction using current axial load and deformation limits using maximum axial load). In this model, reinforced concrete columns exhibited onset of strength loss at the rotation demand levels specified in ASCE 41-17.

This publication is available free of charge from: https://doi.org/10.6028/NIST.GCR.22-917-50

9.8.1 Global Response

The ASCE 41-17 linear and nonlinear evaluation procedures provide a reasonable estimate of global building response using the site's best-estimate ground motion. The best-estimate ground motion was recorded 1.55 miles (2.5 km) from the site at a location with similar distance and azimuth from the epicenter. Flexibility of the soil and the foundations were not included in the model, although there was no indication of soil movement or foundation rocking after the event. The following conclusions are made based on analysis results and the damage patterns observed after the earthquake:

- The direction of maximum story drift in both the linear and nonlinear models was in the east-west direction; this is consistent with observed column damage in the building.
- The magnitude of the maximum first-story drift was small (less than 1%) and approximately the same using each of the two nonlinear modeling approaches. Building damage suggests a concentration of drift in the first story, and this distribution was more accurately predicted using the moment-rotation spring model than the fiber-based limit-state hinge model. In the fiber-based limit-state hinge model, the upper-story columns had smaller cracked stiffness, resulting in a more uniform distribution of maximum story drift over the building height.
- Incremental dynamic analysis (IDA) of the building was performed using the best-estimate ground motion and both modeling approaches. The results of these IDAs indicate a brittle collapse response, with onset of collapse being very sensitive to ground motion scale factor. Results show also that the distribution of story drift predicted using the fiber-based limit-state hinge model corresponds to the observed damage pattern. This suggests that the best-estimate ground motion may have been incorrect and that the fiber-based limit-state hinge model results in global response that is similar to that simulated using the moment-rotation spring model under more intense ground shaking. In addition, the IDA predicts a lower probability of collapse at the spectral acceleration of the best-estimate ground motion using the fiber-based limit-state hinge versus the moment-rotation spring model (approximately 20% versus 50%). Although the magnitude of response using the best-estimate ground motion did not differ significantly based on modeling approach, the IDA results show that these modeling decisions have a greater impact at larger deformations. This finding is expected as the modeling approaches primarily impact nonlinear response.

9.8.2 Component Response

The impacts of modeling decisions were more evident in predicted component response than in predicted global response. The observed column damage pattern of

This publication is available free of charge from: https://doi.org/10.6028/NIST.GCR.21-917-50

concrete spalling at the column ends and diagonal cracking along the length of the column in the first-story columns indicates a flexure-shear failure mode.

The column damage mode was predicted to be both shear and flexure using the linear procedures with models that included the stiffening effects of partial-height masonry infill. Note that three approaches were used to model the partial-height masonry infill (column offsets, shell elements, and compression-only diagonal struts) and there was minimal difference in the predictions (approximately 70% columns with correct level of damage). However, the column failure mechanism and level of damage were not well predicted when the masonry infill was ignored (approximately 30% columns with correct level of damage).

In both nonlinear modeling approaches, shear strength limited the capacity of the columns. Consequently, the flexural strength in the ASCE 41-17 simplified backbone response was adjusted to simulate this column shear capacity until the specified plastic rotation at onset of strength degradation was exceeded. Approximately 62% of the columns in the building were predicted to develop maximum shear strength and although this might indicate shear damage, it does not indicate shear failure. Instead, degree of damage is determined by the rotation (or drift) demands. Using the drift demands predicted from the nonlinear analyses, the column damage determined using the ASCE 41-17 values and results from both models was less than that observed for experimental specimens with similar reinforcement detailing, geometry, and deformation demand. However, there are a limited number of experiments that closely resemble the column properties and strong comparisons between crack widths in the same loading state (residual versus peak deformation) could not be made. The findings suggest that the rotation capacities in ASCE 41-17 may be higher than appropriate for these columns (leading to less degradation than sustained by the actual columns) and/or the input, best-estimate ground motion in the analysis did not adequately represent ground shaking at the building site .

The response of the masonry infill, which was modeled using compression-only diagonal struts, was consistent with the observed limited damage (i.e., some diagonal cracking but no crushing).

9.8.3 Analytical Study Takeaways

Key outcomes from the linear and nonlinear dynamic analysis procedures are as follows:

- Global and local response mechanisms were predicted reasonably well, but the magnitude of the first-story drift response was underestimated using the nonlinear analysis procedures (predicted column performance lower than expected based on observed damage) and overestimated using the linear analysis

This publication is available free of charge from: https://doi.org/10.6028/NIST.GCR.22-917-50

procedures (many columns beyond Collapse Prevention performance, suggesting collapse).

- Results from the linear procedures clearly demonstrate that modeling of partial-height masonry infill is required to adequately predict response and identify vulnerabilities.
- The linear procedure results do not provide sufficient information to design a retrofit strategy because damage mechanisms are not necessarily distinctly identified (e.g., type of column response) and inelastic damage concentration is not identified. As such, utilizing other simplified procedures based on mechanism analysis (e.g., FEMA P-2018) as an alternative or supplement may be beneficial.

Nonlinear analysis is expected to provide greater retrofit guidance, but the ASCE 41-17 column modeling approach did not predict the damage mode. The approach used to model column changed significantly in this edition, where a unified flexure/flexure-shear/shear model was introduced to capture all failure modes, including flexure, flexure-shear, and shear, in a single approach. However, analysis of this approach using the building damage and selected columns shows that the modeling approach may not be accurate for flexure-shear and shear damage. In particular, the modeling approach does not simulate the sequence of flexural yielding and shear degradation suggested by the observed damage. The general underestimation of column performance state (i.e., most columns at Life Safety rather than Collapse Prevention) also suggests that the modeling parameter *a* may underestimate plastic rotation at onset of strength degradation for these columns. However, there is still significant uncertainty in the ground motion for the site, so these results should be interpreted with caution.

9.8.4 Study Limitations

These conclusions must be considered in the context of several limitations:

- Measured material properties of the building components were not available. Expected properties were inferred based on building age.
- Drawings of the northwest building addition, including information on attachment to the main structure, were not available.
- Construction quality, including pipes running through columns and improperly placed reinforcing steel, were ignored.
- The building was not instrumented. Observed response was based on photographic evidence.
- Site properties and ground motion recordings at the site were not available.
- Basement, foundation, and soil flexibility were not modeled.

This publication is available free of charge from: https://doi.org/10.6028/NIST.GCR.21-917-50

Chapter 10

Seven-Story Moment Frame and Wall Building in Mexico City

This publication is available free of charge from: https://doi.org/10.6028/NIST.GCR.22-917-50

10.1 Overview

This chapter presents benchmarking studies for a 7-story reinforced concrete building located in Mexico City, shown in Figure 10-1. The building was designed in 1979 and according to its occupation plaque, construction started in October 1980; it is a representative example of nonductile reinforced concrete construction in Mexico City designed in accordance with the 1976 Mexico City building Code, which had detailing requirements similar to ACI 318-71. The building sustained damage in the 2017 Puebla Earthquake and was strengthened subsequently with reinforced concrete walls. The building was not instrumented during the 2017 Puebla Earthquake, and the nearest strong motion record available is from a station located at the Jardín de Niños Luz Garcia Campillo, 1.4 miles away.



Figure 10-1 Photograph of west façade of reinforced concrete moment frame and structural wall building in Canal de Miramontes, Colonia Girasoles, Mexico City following the 2017 Puebla Earthquake.

The building was evaluated in accordance with the nonlinear dynamic procedures of ASCE 41-17 using OpenSees software. The models were constructed per details presented in Appendix A, unless otherwise noted. Calculated performance metrics of the original building are compared with detailed damage surveys conducted after the 2017 Puebla Earthquake.

10.2 Building Description and Observed Performance

Building information in the form of original drawings was made available to the project team for use during the study via original drawings by Dirac Ingenieros Consultores (2019a). A selection of the drawings utilized are presented throughout this Chapter. Dimensions on the drawings were provided in metric units.

10.2.1 Building Description

The west façade of the building faced the street (shown in Figure 10-1). At the south boundary, the building was separated from a three-story commercial building by approximately 8 inches. Damage due to pounding between in the two structures was observed after the 2017 Puebla Earthquake, in the second and fifth stories. At the north and east boundaries, the building was separated from adjacent structures by a distance of approximately 25 ft (Figure 10-2). The 6-story masonry building adjacent to the north collapsed during the 2017 Puebla Earthquake.

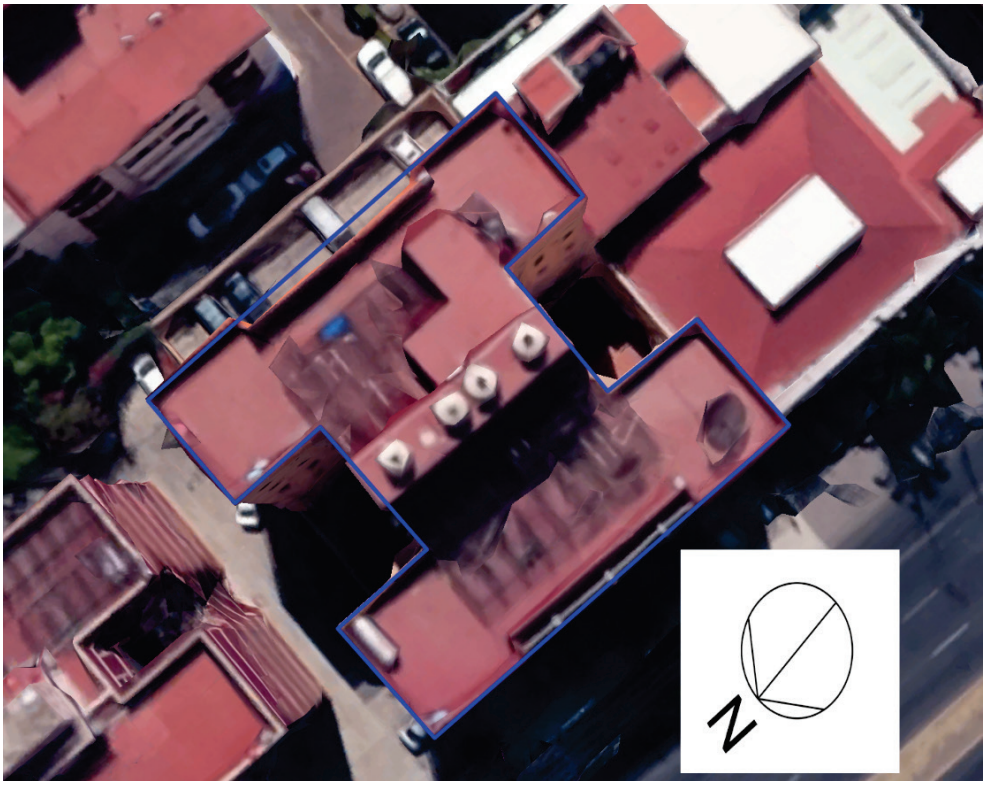


Figure 10-2 Photo showing building plan view from the top (Source: Google Earth).

This publication is available free of charge from: https://doi.org/10.6028/NIST.GCR.22-917-50

The first story or ground floor has parking spaces and two commercial units; the remaining 6 floors had 24 apartment units with a total area of approximately 36,700 ft^2.

The building has an H-shaped configuration in which the east and west wings are joined monolithically with a central wing housing the elevator and stairs (Figure 10-2). This configuration allows illumination to would provide natural light to the apartment units in the east and west wings of the building. East and west wings were symmetric with respect to the center of the building and had moment-resisting frames. The center wing has four uncoupled reinforced concrete walls oriented in the north-south direction. Exterior frames in the east and west wings have concrete masonry unit (CMU) infills. Figures 10-3 and 10-4 present a typical floor plan (original and simplified, respectively). There are also CMU partition walls inside the apartment units and CMU walls with openings in the east and west façades of the building (Figure 10-1). The structural configuration of this building provides the opportunity to evaluate modeling parameters and acceptance criteria of beams, columns, walls, and masonry-infilled frames.

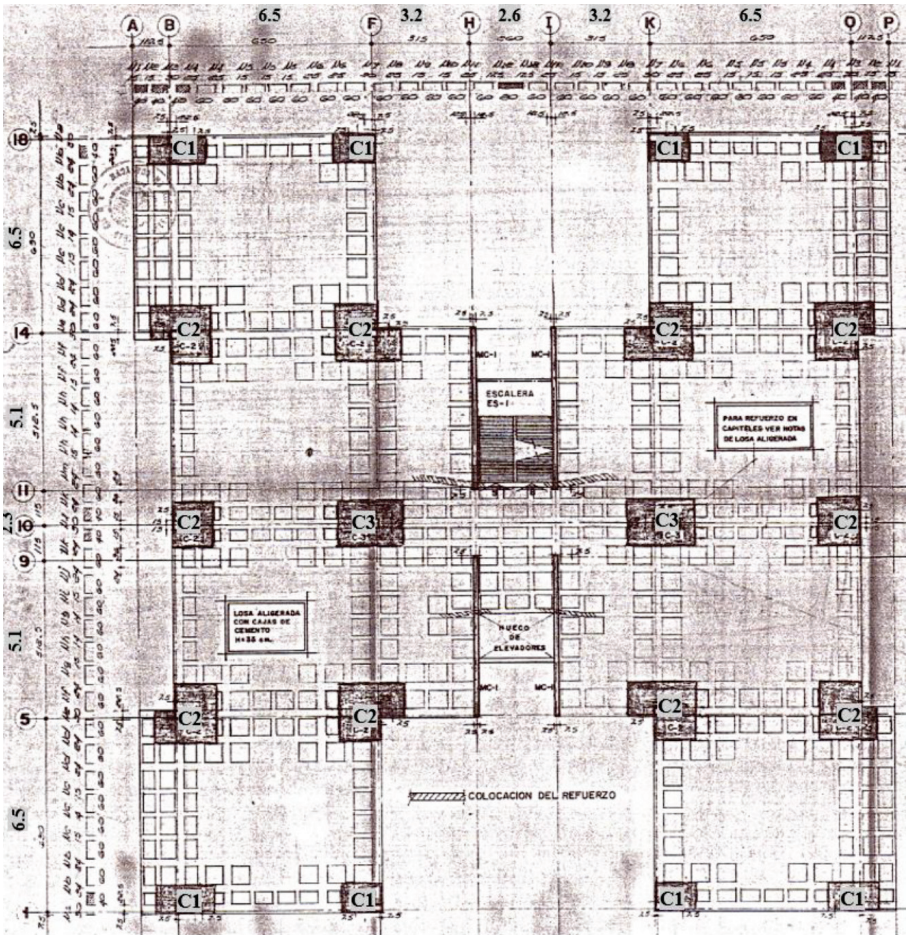


Figure 10-3 Original structural drawing showing typical floor plan.

This publication is available free of charge from: https://doi.org/10.6028/NIST.GCR.22-917-50

This publication is available free of charge from: https://doi.org/10.6028/NIST.GCR.22-917-50

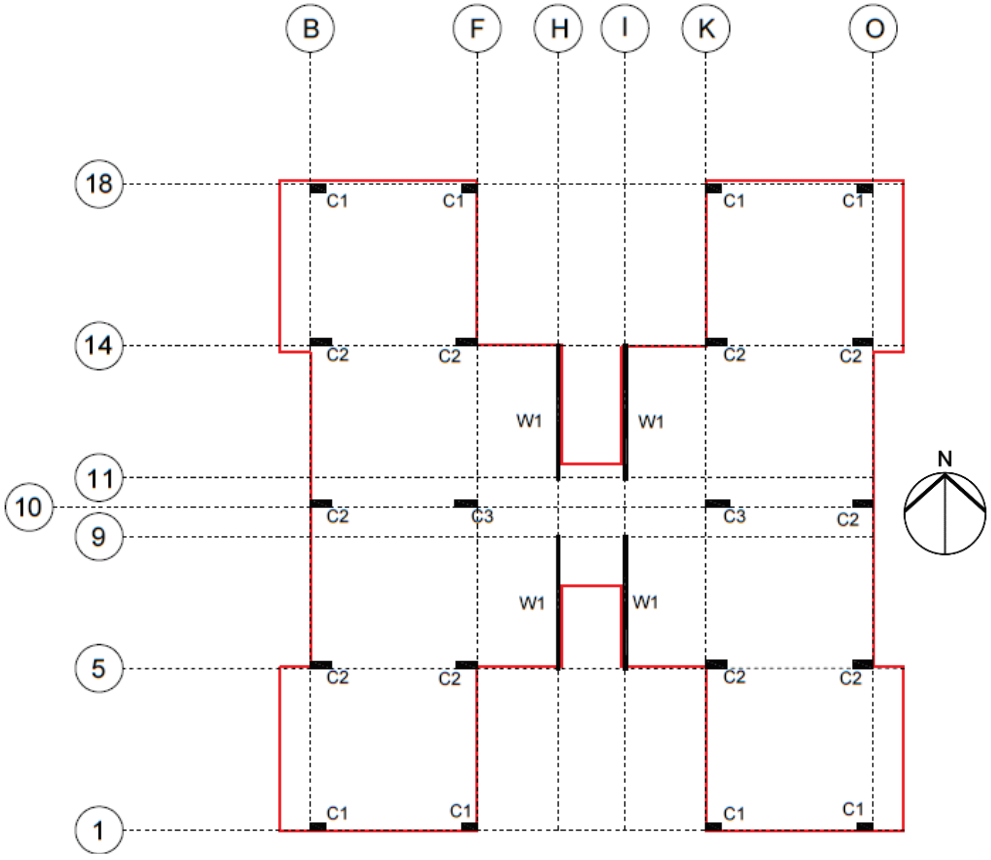


Figure 10-4 Simplified typical floor plan used in this study.

The east and west wings of the H-Shaped building plan have a single bay in the east-west direction and four bays in the north-south direction. The center wing has three bays in the east-west direction, column-to-wall, wall-to-wall, and wall-to-column. In the north-south direction the center wing also has three bays, two occupied by walls and the center bay occupied by the ribbed slab, which provides minimal coupling between walls. Total building length in the east-west direction is 24.25 m (79'-6.7"), and in the north-south direction, parallel to the street, it is 25.30 m (83'-1") . The building had a total height of 18.53 m (60'-10"), with a story height of 2.63 m (8'-7.5") in the first floor and 2.65 m (8'-8") in the remaining floors, as shown in Figure 10-5. The moment frame layout is presented in Figure 10-24, and masonry wall locations are shown in Figures 10-29, 10-30, and 10-33, in Section 10.3.1 where the modeling approach is discussed.

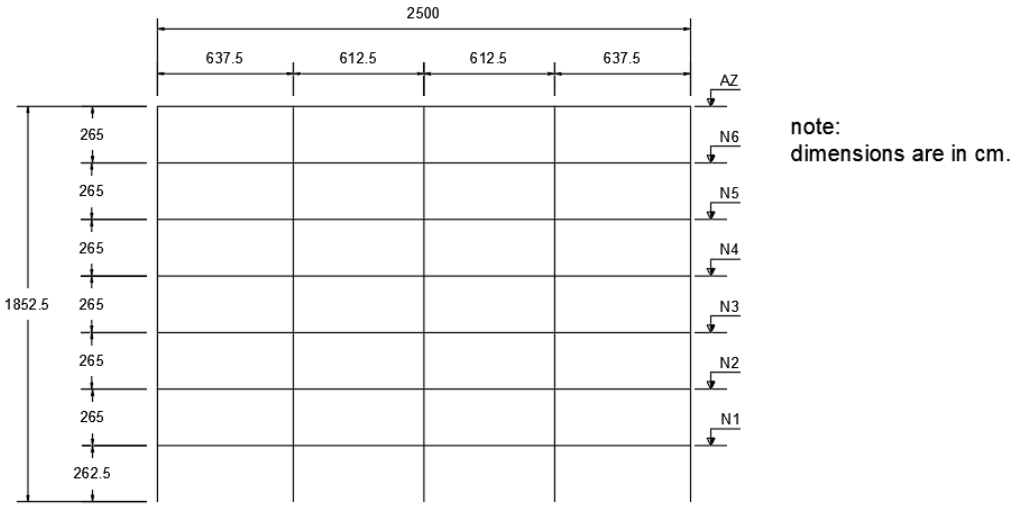


Figure 10-5 Elevation in the north-south direction. Dimensions are presented in centimeters.

The structural system of the building consists of moment-resisting frames in the east and west wings and reinforced concrete walls oriented in the north-south direction in the center wing (Figures 10-3 through 10-5, and Figure 10-24). North and south perimeter bays in the east and west wings had unreinforced concrete masonry unit infills. There are also unreinforced CMU partition walls inside the apartment units and CMU walls with openings in the east and west façades (Figure 10-1). The connection between the CMU walls and the frames was not detailed for transmission of seismic forces, and the CMU walls located away from moment frames did not have confining elements. East and west wings have exterior masonry cladding in the east and west façades, and masonry infilled frames in the north and south façades.

In this report, the term masonry infill is used in reference to exterior walls where the masonry occupied the entire bay with small or no openings. The term partition walls is used to refer to interior walls that did not extend over the entire length of the bay or had large openings. Masonry cladding refers to façade elements not aligned with the moment frames. All masonry elements in the building were not designed to be part of the lateral load resisting system.

The floor system (Figure 10-3) consists of ribbed slabs framing into columns and walls, with drop panels at column locations. Slab depth between the ribs is 5 cm (2 in.), total rib depth from top of the slab to bottom of the rib is 35 cm (14 in.) (Figures 10-5 and 10-26). Rib width varies between 30 cm (12 in.) for ribs along column lines and 15 cm (6 in.) for ribs away from column lines in the central region of spans. Rib openings are 60 cm by 60 cm (24 in. by 24 in.) in the central region of spans, and 40 cm by 40 cm (16 in. by 16 in.) near columns, so the center-to-center spacing of ribs is closer near columns than at midspan. In most columns drop panels extend over two

This publication is available free of charge from: https://doi.org/10.6028/NIST.GCR.22-917-50

rib openings (Figure 10-3), although there are instances where they extend over only one opening.

The strong axes of the columns were aligned in the east-west direction. Column section sizes and reinforcing details for columns identified in Figure 10-4 are provided in Table 10-1.

Table 10-1 Column Dimensions

Column Designation	Detail	Foundation to N3	Level N3 to N5	Level N5 to Roof
C1	Dimensions (mm)	600 x 300	500 x 300	500 x 300
	Longitudinal Reinforcement	8 no. 8 + 2 no. 4	4 no. 8 + 4 no. 6 + 2 no. 4	4 no. 8 + 4 no. 6 + 2 no. 4
	Transverse Reinforcement	no. 3 @ 300	no. 3 @ 300	no. 3 @ 300
C2	Dimensions (mm)	800 x 300	700 x 300	600 x 300
	Longitudinal Reinforcement	8 no. 8 + 4 no. 6	4 no. 8 + 4 no. 6 + 4 no. 4	4 no. 8 + 2 no. 4
	Transverse Reinforcement	no. 3 @ 300 + no. 2.5 @ 300	no. 3 @ 300	no. 2.5 @ 300
C3	Dimensions (mm)	900 x 300	800 x 300	700 x 300
	Longitudinal Reinforcement	8 no. 8 + 4 no. 4	4 no. 8 + 4 no. 6 + 4 no. 4	4 no. 8 + 4 no. 6 + 2 no. 4
	Transverse Reinforcement	no. 3 @ 300	no. 3 @ 300	no. 3 @ 300

The building has a buoyancy raft or hollow box foundation system (Figure 10-6) with a depth of 4.6 m (15 ft). This type of foundation is used in locations with soft or very weak soils like Mexico City to reduce load intensity from the weight of the building by replacing the volume of soil occupied by the foundation with empty space. The foundation has reinforced concrete slabs at the top and bottom, joined by perimeter and interior walls to form the hollow boxes.

This publication is available free of charge from: https://doi.org/10.6028/NIST.GCR.22-917-50

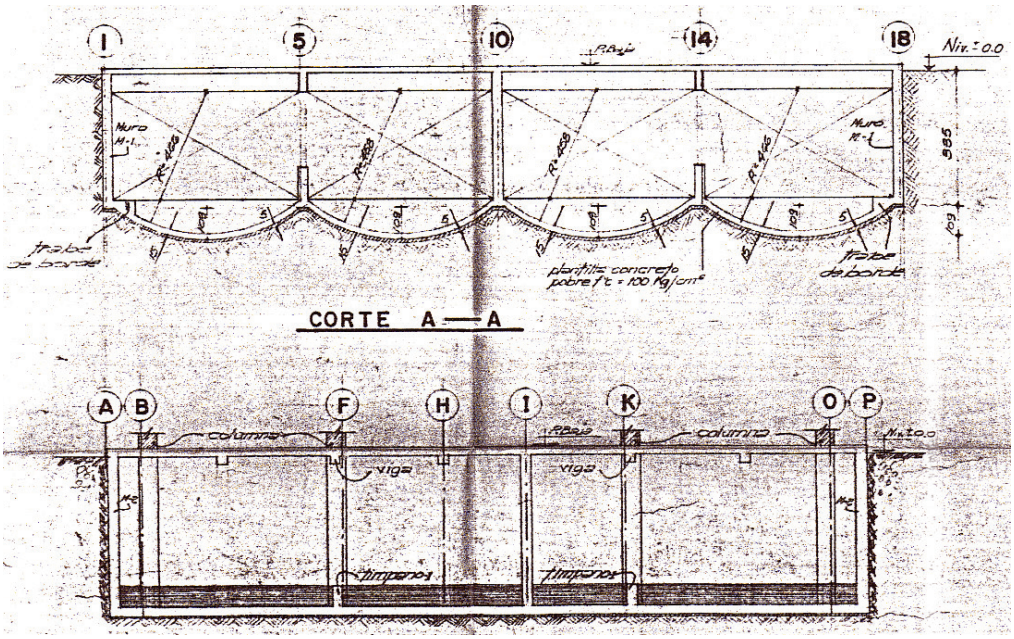


Figure 10-6 Schematic of raft foundation shown in original drawings.

Material Properties

The building structure had normal weight aggregate concrete with specified concrete compressive strength values shown in Table 10-2. Normal weight concrete was used throughout the building, with design strengths of 24.5 MPa (5,300 psi). Grade 42 (kg/cm^2) reinforcing steel was used for all elements of the building, with a nominal yield strength of 392 MPa (57,000 psi). Properties of reinforcing steel bars were provided by the engineering firm that performed the retrofit of the building, based on statistical studies of bars produced by three different manufacturers in Mexico City between 1967 and 1971. Grade 42 bars used in the building have the properties presented in Table 10-2. Material properties for masonry walls were not specified in the plans and test data was not available. Strength values were adopted from default values in ASCE 41-17 and TMS 402 (MSJC, 2011). Strength calculations for masonry walls were performed using lower bound properties. Allowable tensile stresses in masonry were adopted using Table 8.2.4.2 of the TMS-402 standard as a reference, and the lower bound value was adopted based on engineering judgment.

Specified strengths were taken to be the lower bound strengths in accordance with ASCE 41-17 Section 10.2.2.1.2. Mean expected strength values were calculated using material factors in ASCE/SEI 41 of 1.5 for concrete, 1.25 for reinforcing steel, and 1.3 for masonry.

This publication is available free of charge from: https://doi.org/10.6028/NIST.GCR.22-917-50

Table 10-2 Average Material Properties

Component	Property	Based on Specified Values, MPa (ksi)	
		Lower-Bound (Specified)	Mean (Expected)
Reinforcement	Yield Stress (f_y)	392 (57)	490 (71)
Concrete	Peak Strength $\left(f'_c\right)$	24.5 (3.5)	36.75 (5.3)
Masonry	Peak Strength $\left(f'_{me}\right)$	3.1 (0.45)	4.15 (0.6)
Masonry	Tensile Strength $\left(f'_{me}\right)$	0.04 (0.006)	0.06 (0.008)

Building Weight

The weight of the building was calculated including the weight of the slab, electrical and mechanical equipment, partitions, flooring, ceiling, beams, columns, and walls. Roof loads included weight due to waterproofing and Tezontle gravel filling. Additional loads were added to account for masonry partitions, parapets, and the glass enclosure at their respective locations. Masses were assigned to all column nodes in the translational degrees of freedom based on tributary floor area. Average unit gravity loads for typical floors were approximately 7.7 kN/m^2 (160 psf) and 9.1 kN/m^2 190 psf for the roof. Consistent with the provisions in ASCE 41, live loads were not considered in mass calculations. Additional weight was placed on roof elements assuming that an additional floor and corresponding walls existed in the area shown in Figure 10-7.

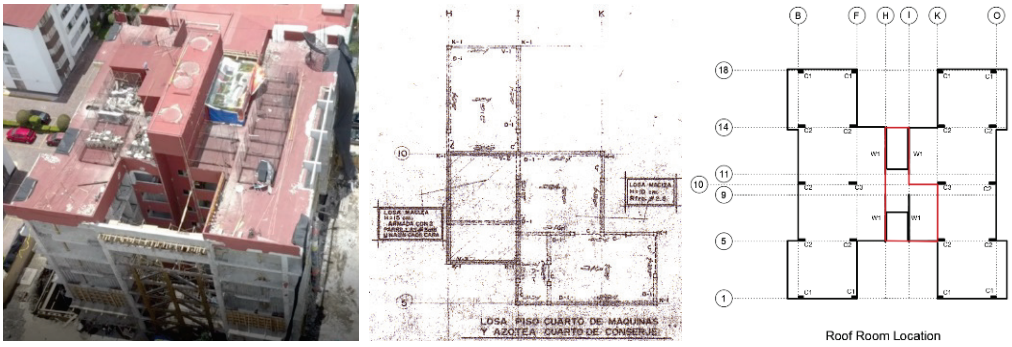


Figure 10-7 Roof area housing mechanical systems.

Calculated story weights and the total weight of the building are presented in Table 10-3.

This publication is available free of charge from: https://doi.org/10.6028/NIST.GCR.22-917-50

Table 10-3 Building Weight by Floor Level

Floor Level	Story Weight kN (kips)
7th	4131 (929)
6th	3508 (789)
5th	3512 (789)
4th	3512 (789)
3rd	3551 (798)
2nd	3551 (798)
1st	3551 (798)
Total	25313 (5,691)

10.2.2 Building Instrumentation

The building was not instrumented at the time of the 2017 Puebla Earthquake.

10.2.3 Ground Motion

Analyses were performed using strong motion records from a nearby station obtained during the September 19, 2017 Puebla Earthquake. The epicenter of the 2017 Puebla Earthquake (Lat 18.568 N, Long 98.481 W) was located approximately 55 km (34 mi) south-southwest of the city of Puebla and 120 km (75 mi) from Mexico City. The Jardín de Niños Luz García Campillo (Lat 19.3161 N, Long 99.1059 W) strong motion station was located 106 km (66 mi) from the earthquake epicenter, and 2.3 km (1.4 mi) away from the building.

Acceleration histories from the 2017 Puebla Earthquake recorded at Jardín de Niños station in the north-south and east-west directions are shown in Figures 10-8 and 10-9 Peak ground acceleration recorded during the 2017 Puebla Earthquake was approximately 0.13g for both horizontal components.

Acceleration spectra are shown in Figure 10-10, where the line designated 2D spectrum corresponds to the resultant of north-south and east-west components. MCE uniform hazard and MCE elastic spectra shown in Figure 10-11 correspond to the Mexico City Construction Code (SMIE, 2020). The acceleration spectra show that energy was highest in the range between 1.1 sec. and 2.1 sec.

Displacement spectra for the north-south and east-west components (Figure 10-11) had a similar shape, with a peak displacement of approximately 47 cm (18.5 in.) at a period of approximately 1.75 sec., followed by a nearly constant displacement of approximately 15 cm (6 in.) at longer periods. The spectral shape indicates that this ground motion is most harmful to structures with a period of approximately 1 to 1.2

This publication is available free of charge from: https://doi.org/10.6028/NIST.GCR.22-917-50

seconds, because damage-induced softening may increase displacement demand by a factor upto 5.

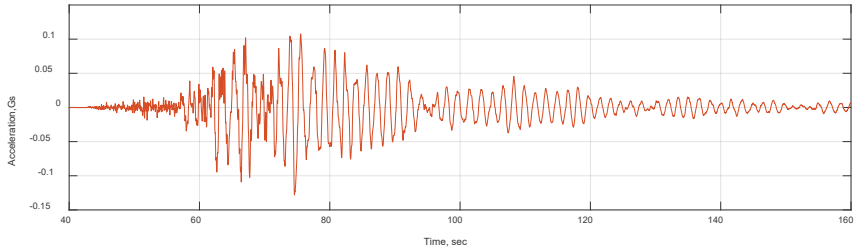


Figure 10-8 Acceleration record for 2017 Puebla Earthquake at Jardín de Niños Luz García Campillo station, in the north-south (wall) direction.

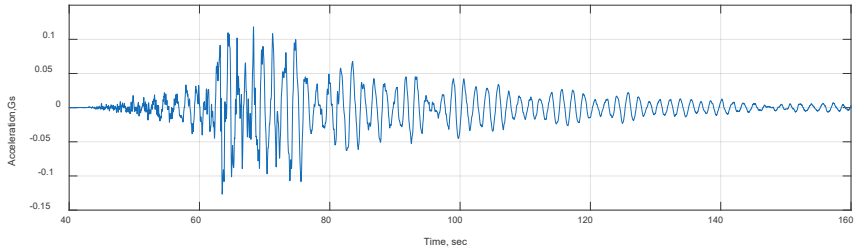


Figure 10-9 Acceleration record for 2017 Puebla Earthquake at Jardín de Niños Luz García Campillo station, in the east-west (frame) direction.

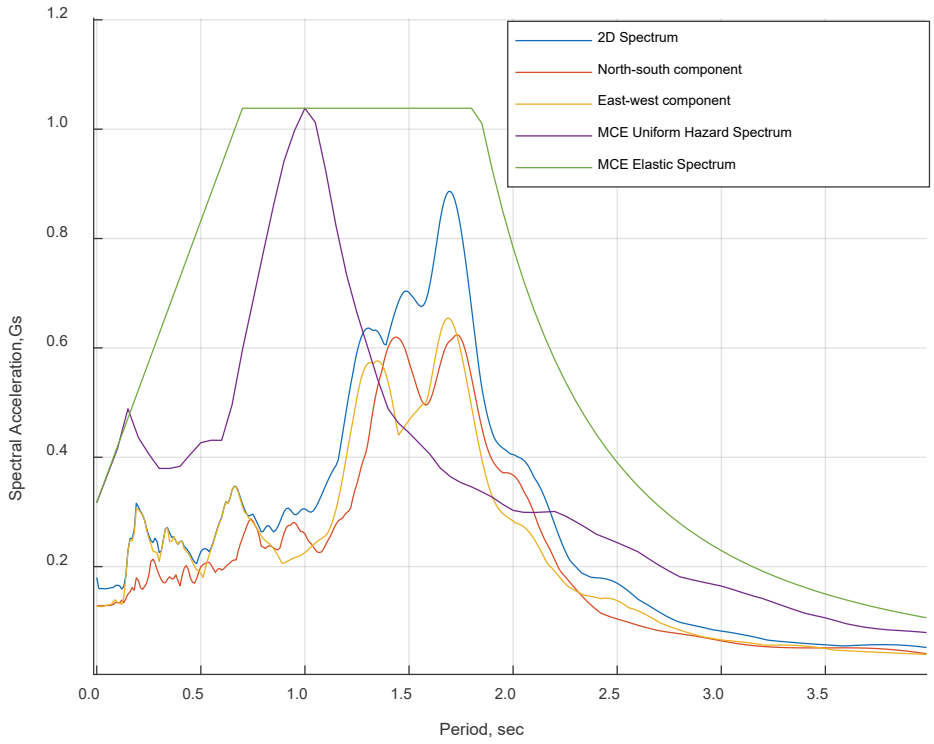


Figure 10-10 Acceleration spectra for 2017 Puebla Earthquake at Jardín de Niños Luz García Campillo station, 5% damping ratio.

This publication is available free of charge from: https://doi.org/10.6028/NIST.GCR.22-917-50

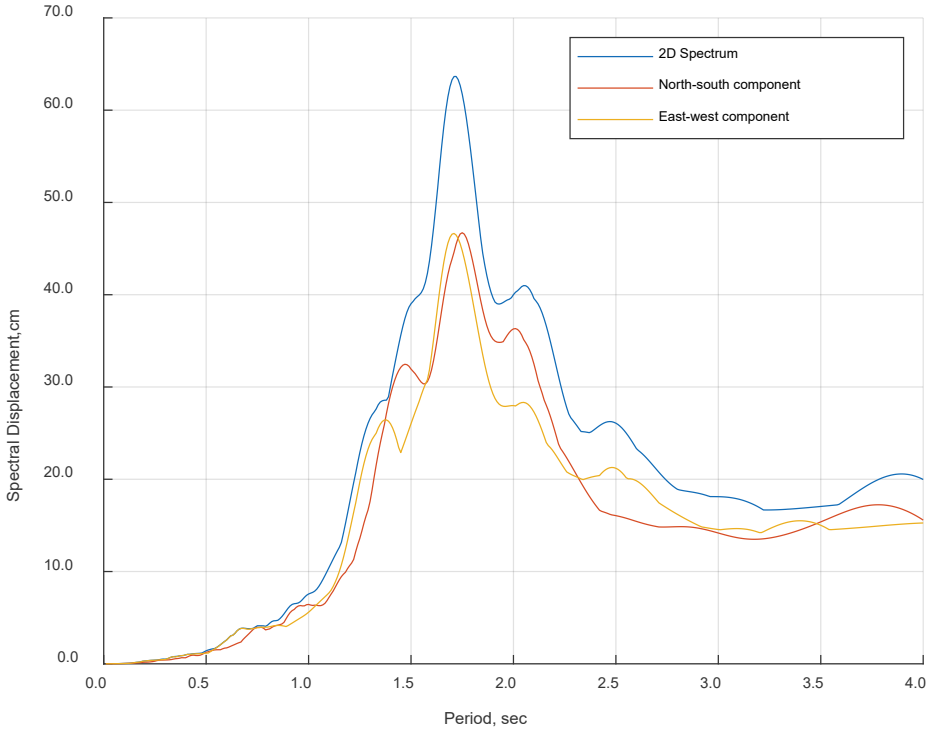


Figure 10-11 Displacement spectra for 2017 Puebla Earthquake at Jardín de Niños Luz García Campillo station, 5% damping ratio.

A second hazard scenario was studied to evaluate damage in structural elements for a ground motion level that would severely damage most masonry walls and likely cause building collapse. The goal of evaluating this scenario was to obtain an indication of the progression of damage that would lead to building collapse, as well as the type of collapse mechanism expected in the building. For this scenario, the ground motion from the 2017 Puebla Earthquake shown in Figures 10-8 and 10-9 was scaled to the MCE uniform hazard spectrum for the site, obtained from the Instituto para la Seguridad de las Construcciones in la Ciudad de Mexico (Figure 10-10). The 2017 Puebla record was scaled by the ratio of the spectral acceleration for the MCE spectrum and the 2017 Puebla Earthquake records (Figure 10-10) corresponding to the effective fundamental period of the building (1.08 sec.). This procedure resulted in a scale factor of approximately 4.

10.2.4 Observed Performance

The 2017 Puebla Earthquake caused some structural and significant nonstructural damage to the building. According to the local damage evaluation standard (CENAPRED, 2001), the damage level was classified as "severe." Damage was documented during post-earthquake evaluations by Dirac Ingenieros Consultores (2019b), an excerpt is shown in Figure 10-12.

This publication is available free of charge from: https://doi.org/10.6028/NIST.GCR.22-917-50

This publication is available free of charge from: https://doi.org/10.6028/NIST.GCR.22-917-50

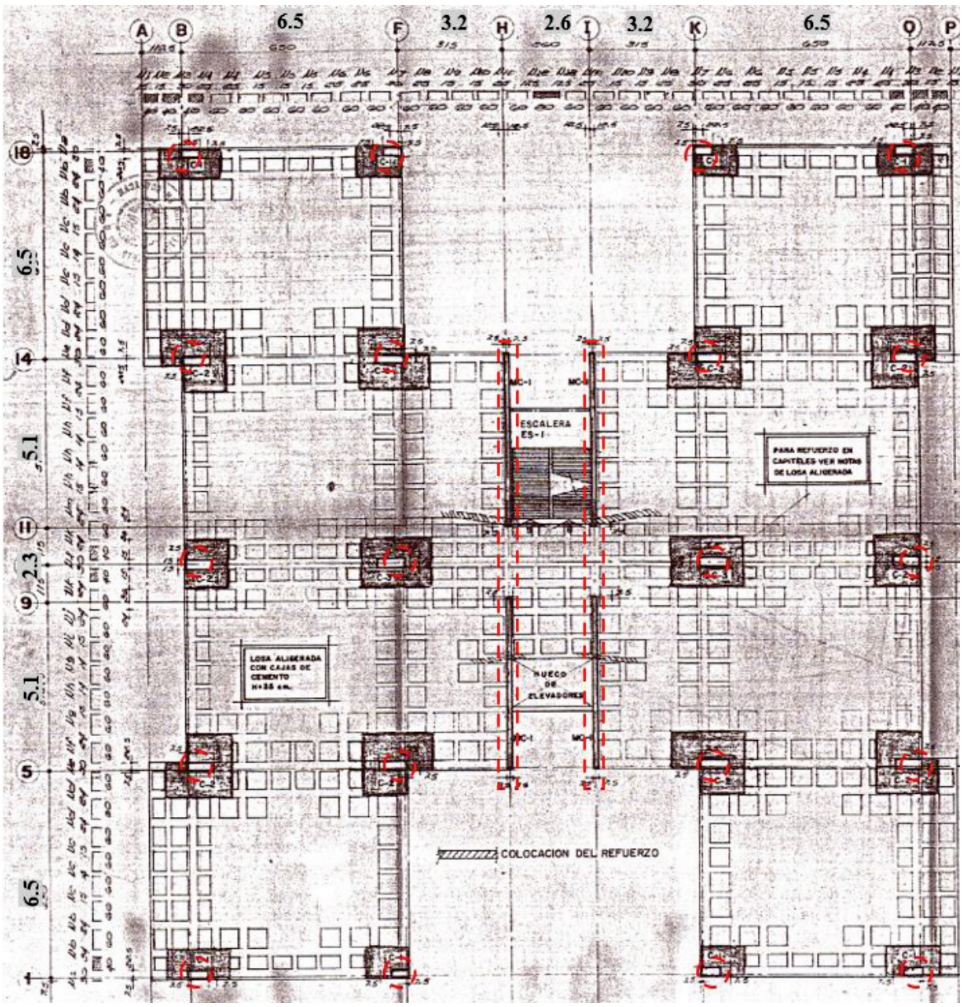


Figure 10-12 Structural damage observed in the building after the 2017 Puebla Earthquake (Dirac Ingenieros Consultores, 2019b).

Structural damage reported after the 2017 Puebla Earthquake included narrow inclined cracks in columns observed at multiple locations throughout the building (Figure 10-13). Damage reports (Dirac Ingenieros Consultores, 2019b) state that the largest crack widths measured in columns were on the order of 2 mm (0.08 in.). There were also documented observations of loss of concrete cover in columns causing the reinforcement to be exposed. As discussed in Chapter 2 of this report and in ASCE 41-17 Table C2-4, the Immediate Occupancy (IO) performance level of primary concrete frame elements is defined as minor cracking, limited yielding at a few locations, and minor spalling of concrete cover. The Life Safety (LS) performance level of concrete frames is defined as extensive damage to beams, spalling of the cover and shear cracking in ductile columns. Based on these criteria the performance level of the moment frames was between IO and LS, considering that narrow shear cracks were observed in nonductile columns.

This publication is available free of charge from: https://doi.org/10.6028/NIST.GCR.22-917-50



Figure 10-13 Inclined cracks observed in first story column (Dirac Ingenieros Consultores, 2019b).

Damage to reinforced concrete walls consisted of inclined cracks, loss of cover concrete, and reinforcement buckling (Figure 10-14) at the elevator wall boundary in the first floor. Although it is not documented in the damage reports, Figure 10-14 appears to show some corrosion damage to wall reinforcement, which could have been a contributing factor to the damage induced by the earthquake.



Figure 10-14 Damage at the edge of first story structural wall (Dirac Ingenieros Consultores, 2019b).

In Table C2-4 of ASCE 41-17 the IO performance level of concrete wall primary elements is described minor diagonal cracking in walls and beams, and the LS performance level is described as cracking and spalling in some boundary elements, limited buckling of reinforcement, and damage around openings. Considering that some limited buckling of the reinforcement and loss of cover were observed in one of the first floor walls, damage caused by the 2017 Puebla Earthquake corresponds to a performance level between IO and LS.

The most severe damage in the building occurred in masonry walls (Figures 10-15 through 10-20). Reports indicate cracks widths as large as 10 cm (4 in.) (Figure 10-19), with instances of partial detachment and falling wall pieces (Figure 10-19). Masonry wall damage was reported to be heaviest in the 4th and 5th floors. ASCE 41-17 Table C2-4 indicates that for unreinforced masonry infill walls Collapse Prevention (CP) performance level corresponds to extensive cracking and crushing, with some infill walls on the verge of falling out, which is the type of damage observed in Figures 10-15 to 10-20. Damage surveys show the building collided with a three-story structure adjacent to the south, and that the interaction between the two buildings likely affected the damage pattern. Interaction between the two structures was not included in the study.

Although masonry walls were not intended to resist lateral loads in the original design, their unintended participation strongly influenced the performance of the building. Masonry walls served as sacrificial elements that carried a significant fraction of the lateral load, which protected the columns in the east-west direction from experiencing shear failure. Participation of the masonry walls was most important in the first floor in the frame direction, where they likely prevented collapse due to a soft story mechanism. Further damage to first story the walls would have likely caused lengthening of the period, causing it to shift to a more harmful region of the displacement spectrum (Figure 10-11). In the north-south direction, participation of the walls in the lateral load resisting system was less critical due to the presence of the structural walls, although they helped reduce wall demands.

Based on the building performance levels described in ASCE 41-17 Table C2-3, observed damage to structural components matches the description of IO (no permanent drift and the structure substantially retains original strength and stiffness) while the nonstructural components match the description of CP (extensive damage with infills failed or at incipient failure).

This publication is available free of charge from: https://doi.org/10.6028/NIST.GCR.22-917-50

This publication is available free of charge from: https://doi.org/10.6028/NIST.GCR.22-917-50



Figure 10-15 Damage to west façade masonry walls (Dirac Ingenieros Consultores, 2019b).



Figure 10-16 Damage to façade masonry walls in north illumination shaft (Dirac Ingenieros Consultores, 2019b).



Figure 10-17 Damage to first story masonry walls in north building boundary (Dirac Ingenieros Consultores, 2019b).



Figure 10-18 Photograph showing damage to first story masonry walls and close proximity of adjacent building in south boundary (Dirac Ingenieros Consultores, 2019b).

This publication is available free of charge from: https://doi.org/10.6028/NIST.GCR.22-917-50



Figure 10-19 Damage to interior masonry walls in apartment unit (Dirac Ingenieros Consultores, 2019b).



Figure 10-20 Damage to interior masonry walls in apartment unit (Dirac Ingenieros Consultores, 2019b).

10.3 Nonlinear Dynamic Procedure

10.3.1 Modeling Approach

A three-dimensional numerical model of the structure was created using OpenSees. The computer model of the building only included the building itself and did not consider interaction with the three-story structure located 8 inches south of the building (Figure 10-2). This is a limitation of the study because the damage report

This publication is available free of charge from: https://doi.org/10.6028/NIST.GCR.22-917-50

(Dirac Ingenieros, 2019b) documented collision between the two structures and stated that it affected the spatial distribution of damage.

ASCE 41-17 provisions instruct engineers to consider soil-structure interaction (SSI) when "fixed or pinned boundary elements cannot be justified" (ASCE 41-17 Section 10.12.2) or when "an increase in fundamental period caused by SSI effects results in an increase in spectra accelerations" (ASCE 41-17 Section 7.2.7). NIST GCR 12-917-21, *Soil-Structure Interaction for Building Structures* (NIST, 2012), provides further guidance: The structure-to-soil stiffness ratio check is used to determine if the effects of soil-foundation-structure interaction should be considered, where the structure-to-soil stiffness ratio is the ratio of the height of the structure to the product of the fundamental period and the shear wave velocity, $h/(V_s T)$. If the structure-to-soil stiffness ratio is greater than 0.1 it is suggested that SSI effects be considered. For this building, this assessment is based on building properties and shear wave velocities in the lake region and across the transition zone in Mexico City reported by Gurler et al. (2000), who indicated that the expected range is between 51 m/s and 134 m/s. Given the limited geotechnical information available, interaction between the foundation and surrounding soil was not considered and the building was modeled with a fixed base.

A sensitivity analysis was performed because according to the Mexico City code provisions, the floor layout is considered to be irregular in plan due to the size of the openings. The study showed that modeling the floor system as a rigid or flexible diaphragm did not have significant effect on calculated displacements and forces in the model elements, so a rigid diaphragm approach was adopted for simplicity. Masses were assigned to all column nodes in the translational degrees of freedom based on tributary floor area as shown in Figure 10-21. Solid lines in Figure 10-21 show the location of masonry infills and exterior cladding.

Beams and columns were modeled as elastic beam-column elements with zero-length inelastic rotational springs at both ends. Translational degrees of freedom were constrained so that rotational springs and elastic beam-column elements connected to them would have the same displacements. In the elastic range, effective stiffness of the beam-column elements was calculated based on ASCE 41-17 Table 10-5. Flexibility of the elastic beam-column element was defined as 10 times the flexibility of the rotational springs, so the combined stiffness of the elastic beam-column element and the spring were equal to the effective stiffness of the corresponding beam or column. In the inelastic range, the flexibility of the inelastic rotational spring was adjusted so the combined stiffness of the elastic beam-column element and the inelastic rotational spring would produce the stiffness of the corresponding beam or column in the inelastic range.

This publication is available free of charge from: https://doi.org/10.6028/NIST.GCR.22-917-50

This publication is available free of charge from: https://doi.org/10.6028/NIST.GCR.22-917-50

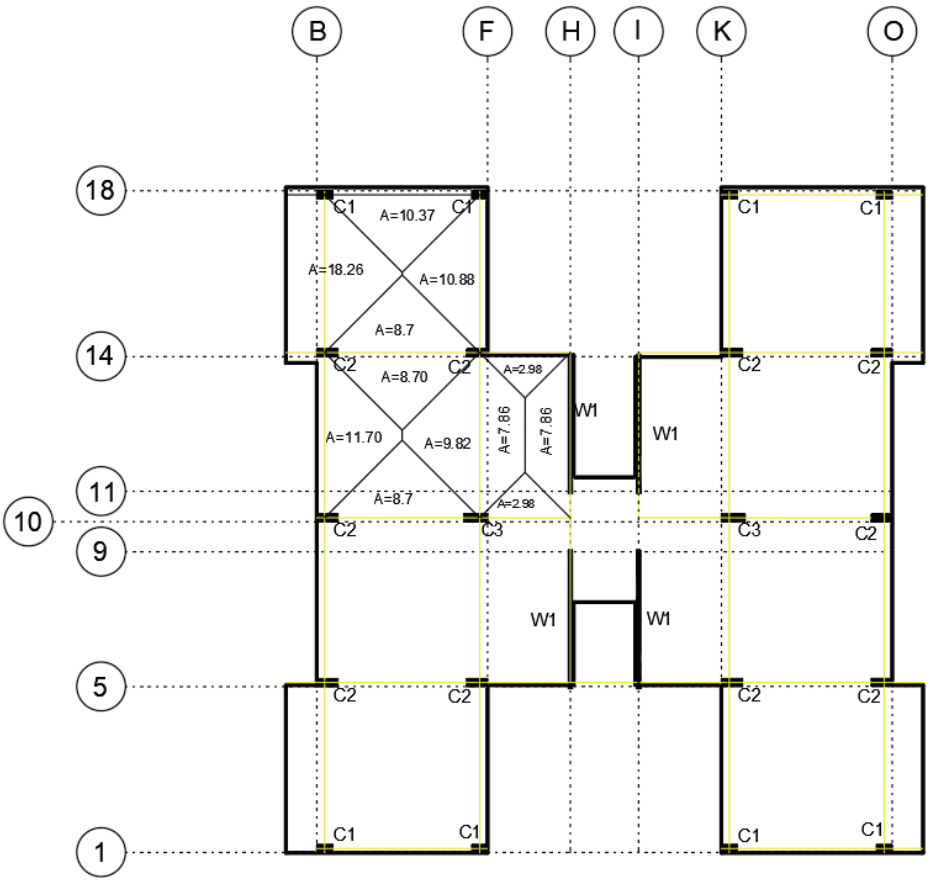


Figure 10-21 Column tributary areas shown for the northwest corner of the symmetric plan.

Beam and column elements span between drop panel faces and connected to the drop panels by zero-length rotational springs. Drop panel dimensions were extracted from the original building drawings, which did not include reinforcement details. Drop panel reinforcement details considered in the study (Figure 10-22) were obtained from the firm that designed the building and correspond to typical reinforcement details used in other projects designed during the same time frame. In the OpenSees model, drop panels were modeled as elastic beam column elements. Schematics showing beam and column elements, as well as inelastic spring locations, are shown in Figures 10-23, 10-29, and 10-32. Green dots in Figure 10-23 show nonlinear spring locations for beam elements.

The floor layout was such that three ribs typically framed into column drop panels, so beam properties were calculated using a T-beam configuration with three ribs. The effective flange length and reinforcing details of a typical floor beam element are shown in Figure 10-24.

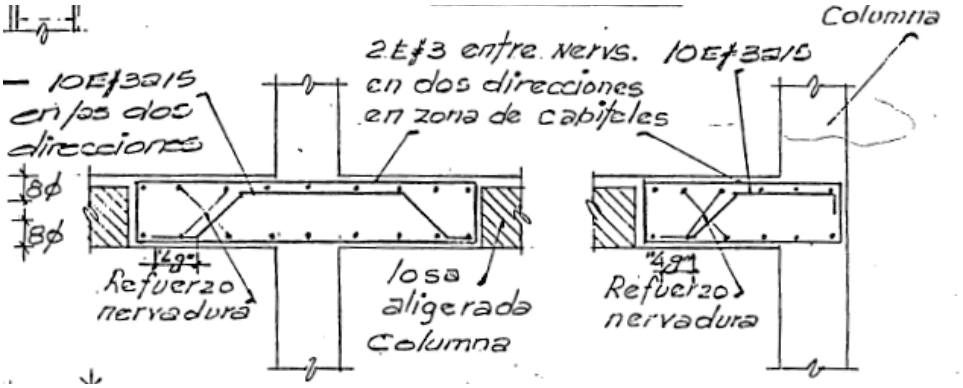


Figure 10-22 Drop panel reinforcement details.

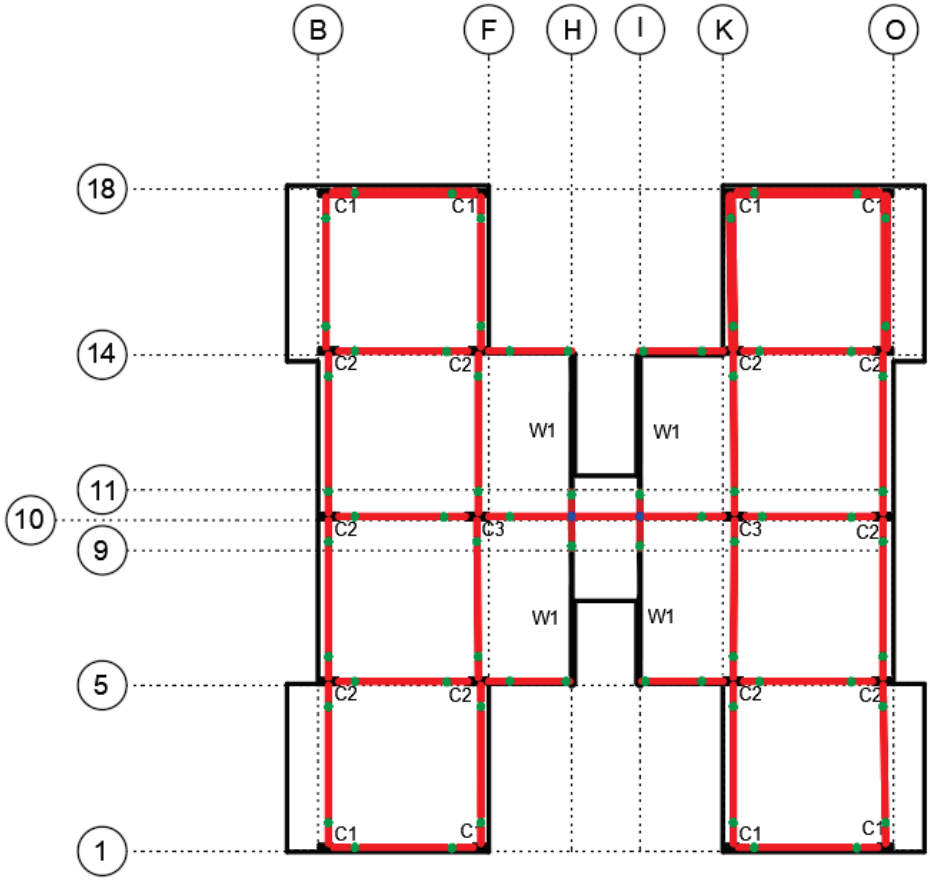


Figure 10-23 Schematic of OpenSees lumped-plasticity model with nonlinear zero-length rotational springs shown as green dots.

This publication is available free of charge from: https://doi.org/10.6028/NIST.GCR.22-917-50

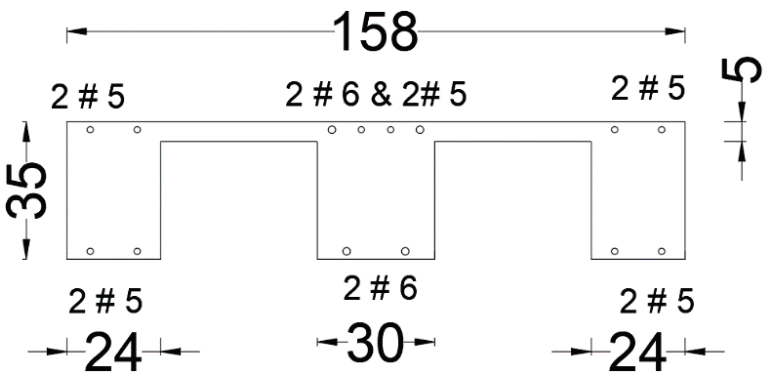


Figure 10-24 Dimensions (in units of cm) and reinforcement configuration of a typical beam element.

The moment-rotation relationship for the nonlinear rotational springs was defined using the envelope curve and hysteresis rules in the peak-oriented modified Ibarra-Medina-Krawinkler (IMK) material model. The parameters that define the moment-rotation curve are: initial stiffness, K_e, yield moment, M_u, capping moment, M_c, capping deformation, θ_p, post-capping deformation, θ_{pc}, residual moment, M_r, and ultimate deformation, θ_u (Figure 10-25).

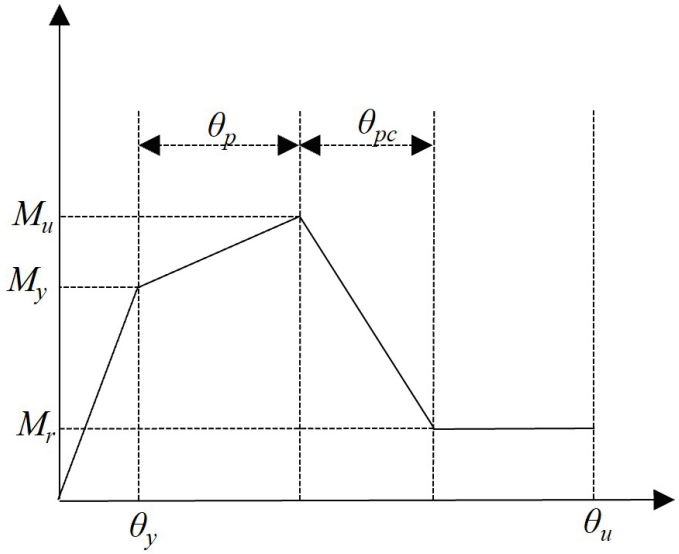


Figure 10-25 Modeling parameters of Ibarra-Krawinkler-Medina model.

Yield moments of beams and columns were determined using the equivalent rectangular stress block as defined in ACI 318-19 (ACI, 2019) with expected material properties. Peak or ultimate flexural capacities were calculated in the same manner using 1.15 f_{yE} instead of the expected yield strength of the reinforcement. Beam capacities in the positive and negative directions were defined based on the different reinforcement present, while columns had symmetric reinforcement. Computed

This publication is available free of charge from: https://doi.org/10.6028/NIST.GCR.22-917-50

stiffness and strength values of beam elements included the effect of the slab as shown in Figure 10-25. Rotation limits for the moment-rotation relationships of beams and columns were defined using modeling parameters *a* and *b* in ASCE 41-17.

Column axial loads used in the calculation of modeling parameters were computed using ASCE 41-17 Equations 7-3 and 7-34. In ASCE 41-17 Equation 7-3, live load action Q_L was calculated using 25% of the unreduced live load specified in ASCE 7, but not less than the actual live load. Axial load due to earthquake was calculated based on the plastic shear of the beams framing into the connections.

Equation 10-3 of ASCE 41 was used to calculate the shear capacity of columns. The nominal shear capacity of the columns was compared with the plastic shear demand to determine if columns were controlled by flexure or controlled by shear. Most columns were found to be controlled by shear in both strong and weak directions. In columns that were controlled by shear, the yield and maximum moments of the flexural spring were reduced in proportion to the ratio of shear strength to shear at yielding of the longitudinal reinforcement. Column-to-beam flexural strength ratios in the frame direction (largest column strength) indicated strong column-weak beam behavior with a few exceptions in the last two stories. In the wall direction (smallest column strength) most cases had weak column-strong beam behavior due to the controlling shear strength of the columns.

The plans did not include details for column laps splices. Splice lengths were calculated using the provisions of ACI 318-71, the prevailing code at the time the building was designed and evaluated with ASCE 41-17 Equation 10-1a. According to the provisions in ACI 318-71, tension lap splices in columns are classified as Class B or Class C splices, depending on the number of bars being spliced. Class B splices require a development length of 1.3 l_d, while Class C splices require a development length of 1.7 l_d. For both cases, the existing development length would have been sufficient to develop a stress of f_{ye}. If Class A splices were provided instead, with a development length of 1.0 l_d, the maximum steel stress developed would be approximately equal to the lower bound yield stress. This would not have affected the modeling parameters of shear critical columns, because shear strength was a greater limiting factor, but it would reduce the strength and deformation capacity of columns in the wall direction. Based on the calculations, all analyses were performed assuming that column modeling parameters would not be controlled by development length.

The hysteretic behavior of the shear critical columns was modeled in OpenSees using rotational springs with the modified Peak-Oriented Ibarra-Medina-Krawinkler material model, with the shape of the moment-rotation envelope defined using modeling parameters *a* and *b* in ASCE 41-17. Because modeling parameters *a* and *b* of ASCE 41 refer to plastic rotation, and not plastic shear deformations, this was the

This publication is available free of charge from: https://doi.org/10.6028/NIST.GCR.22-917-50

only alternative available to model shear critical members with flexural springs. A typical hysteretic response for the nonlinear spring of a shear critical column is shown in Figure 10-26.

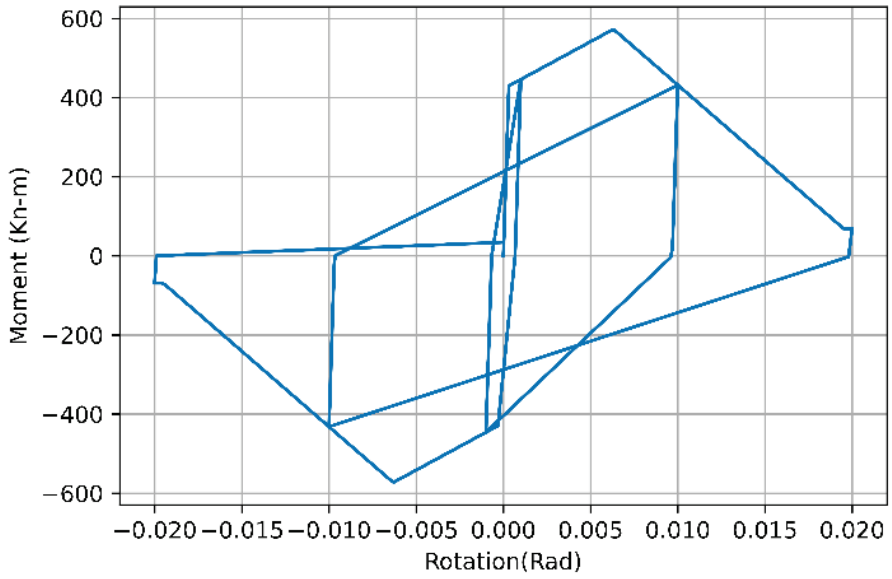


Figure 10-26 Moment-rotation relationship for rotational spring of column element controlled by shear.

Shear capacity of the walls was calculated using ACI 318-19 Equation 18.10.4.1. Inelastic behavior of walls was found to be controlled by flexure based on ASCE 41-17 Section 10.7.2. Based on these findings, structural walls were simulated using rotational springs, with ASCE 41 modeling parameters corresponding to walls in which boundary elements are not confined. A moment-rotation envelope curve for a wall spring is shown in Figure 10-27.

Masonry infill walls were modeled as compression-only truss elements following the provisions in ASCE 41-17 Sections 10.6 and 11.4. Masonry partitions were modeled using a framing system with shear springs in the columns and elastic beam elements. Strength of masonry struts and zero length shear springs in columns were calculated according to the provisions in ASCE 41 Chapter 11. The placement of masonry infill and partitions is shown in Figure 10-28. Because the building is symmetric, masonry walls for only one quarter of the building are shown in Figure 10-28.

Designation and location of each of the masonry wall element use to simulate the wall layout are shown in Figure 10-29. Masonry truss elements in the frame and wall directions were designated WN_m, while masonry partition frame members are designated CN_m and EBN_m, where N corresponds to the element number. The designation CN_m was used for masonry column elements and EBN_m for elastic masonry beam elements.

This publication is available free of charge from: https://doi.org/10.6028/NIST.GCR.22-917-50

This publication is available free of charge from: https://doi.org/10.6028/NIST.GCR.22-917-50

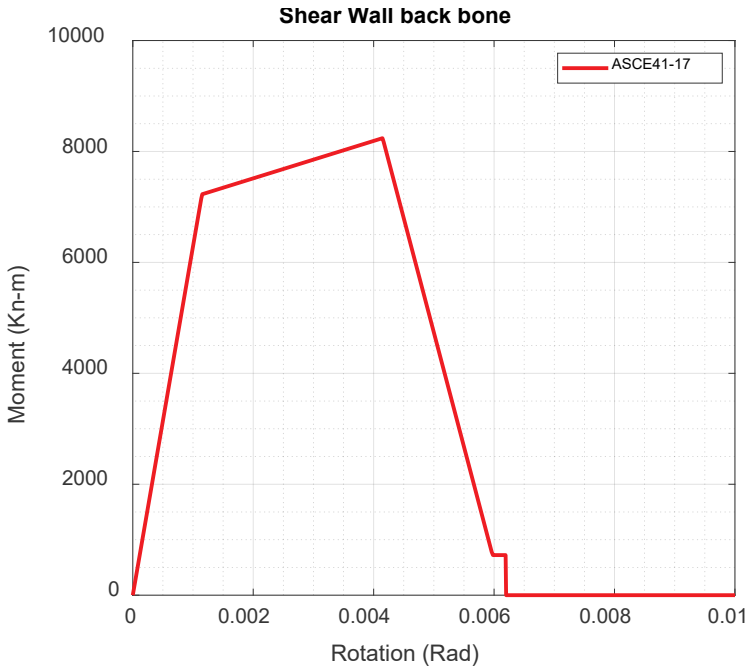


Figure 10-27 Moment-rotation relationship for rotational spring of wall element.

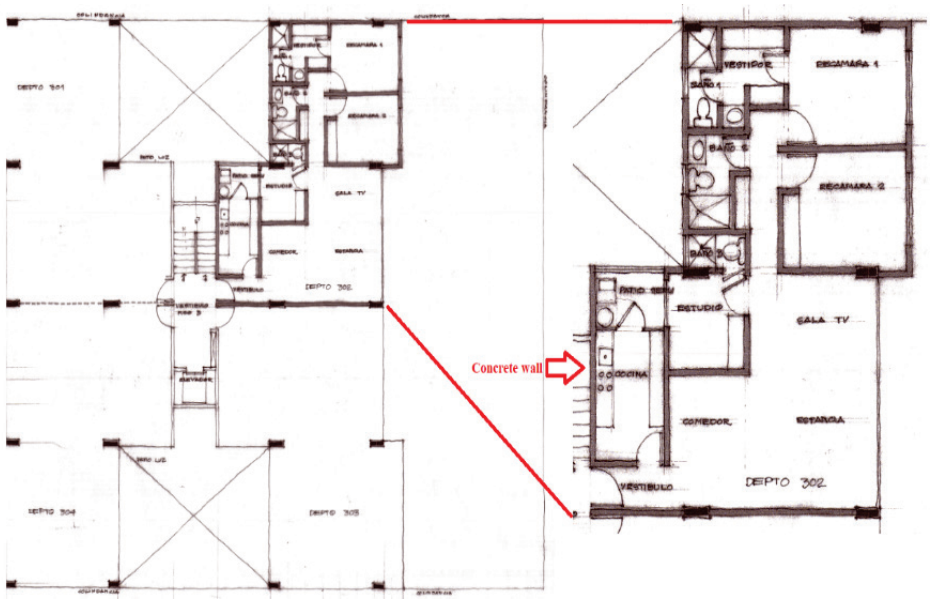


Figure 10-28 Masonry wall and infill wall locations for an apartment unit of a typical floor.

This publication is available free of charge from: https://doi.org/10.6028/NIST.GCR.22-917-50

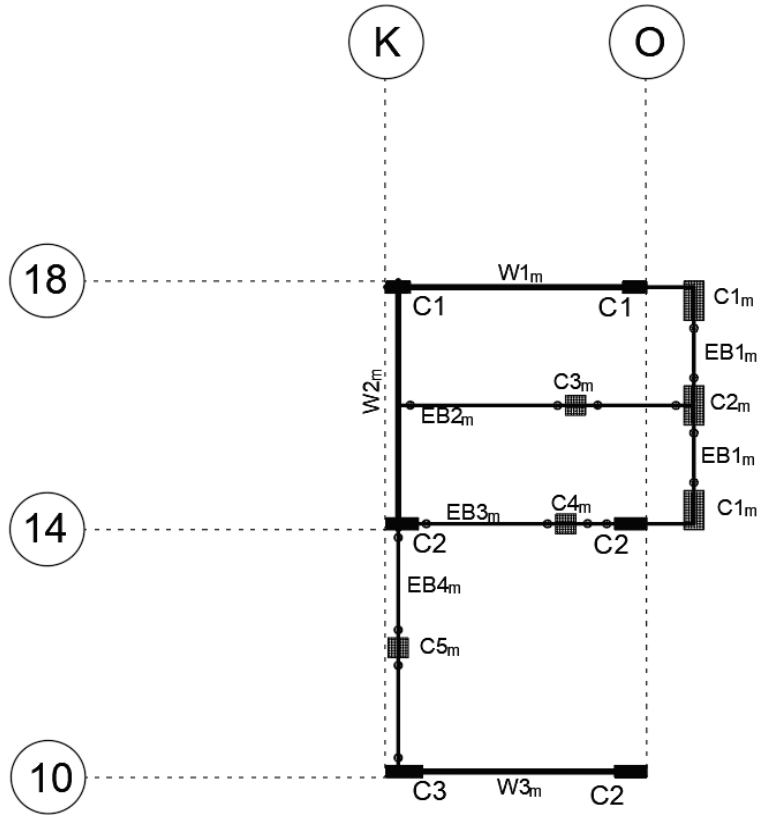


Figure 10-29 Masonry wall, infill wall, and elastic masonry beam element location and designation for an apartment unit of a typical floor.

Masonry infill walls acting in the frame and wall directions were classified as relatively flexible panels and the surrounding frames as nonductile according to the provisions of ASCE 41. Shear strength was calculated according to ASCE 41-17 Equation 11-33 using a cohesion value calculated with the provisions in TMS 402 for panels with no axial stress. Deformation limits of the panels were defined based on ASCE 41-17 Tables 11-10 and 11-11. The hysteretic behavior of the masonry infill truss elements WN_m is shown in Figure 10-30, and the hysteretic behavior of the shear spring of a typical masonry partition element CN_m is shown in Figure 10-31.

The placement and designation of masonry infills implemented in the numerical model and the location of the shear springs are shown in Figures 10-32 through 10-34. Where masonry beams intersected with main floor beams, the beams were split at the intersection point in order to make the vertical displacement of the beams compatible (Figure 10-32).

A masonry frame system was used to model the elements of the masonry façade. Columns were considered rigid between masonry beams, and shear springs were placed at the top elevation of masonry beams (bottom of the openings), as shown in Figures 10-33 and 10-34. Where main floor beams or masonry beams intersected the

masonry columns, shear springs were placed at the elevation corresponding to the top of beams, as shown in Figures 10-33 and 10-34.

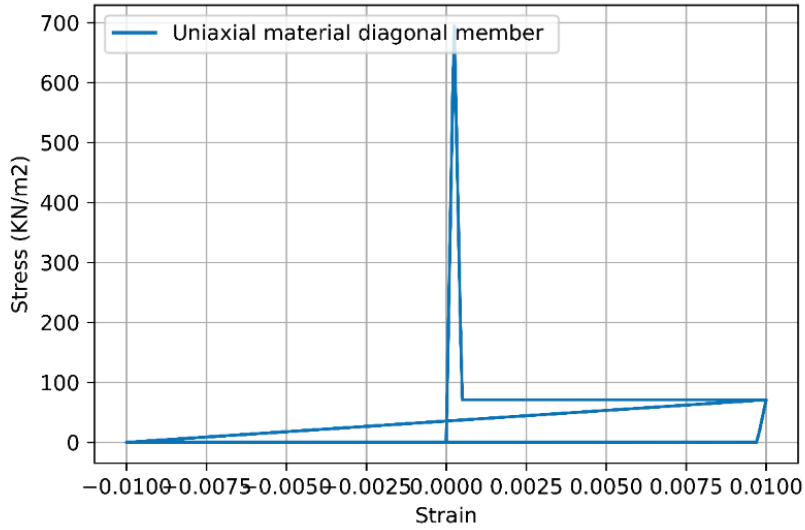


Figure 10-30 Hysteretic behavior of masonry infill strut element.

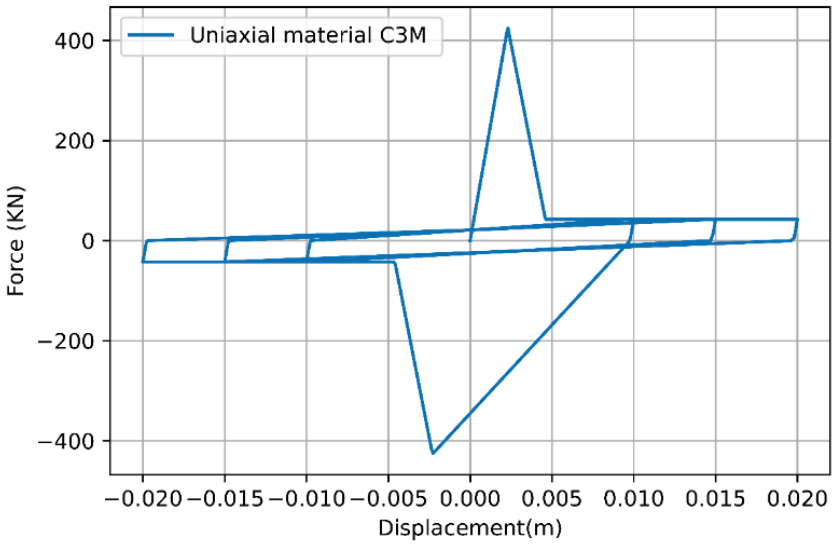


Figure 10-31 Hysteretic behavior for masonry partition frame element *C3m*.

This publication is available free of charge from: https://doi.org/10.6028/NIST.GCR.22-917-50

This publication is available free of charge from: https://doi.org/10.6028/NIST.GCR.22-917-50

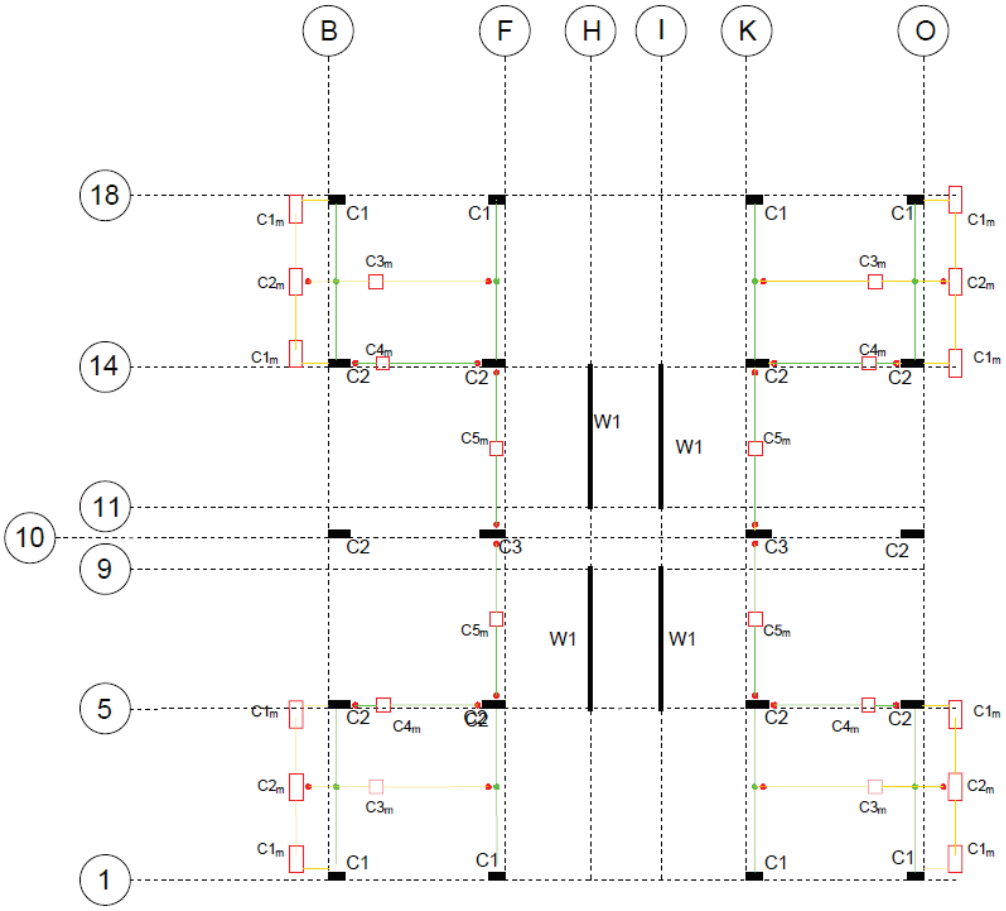


Figure 10-32 Masonry spring designation and location.

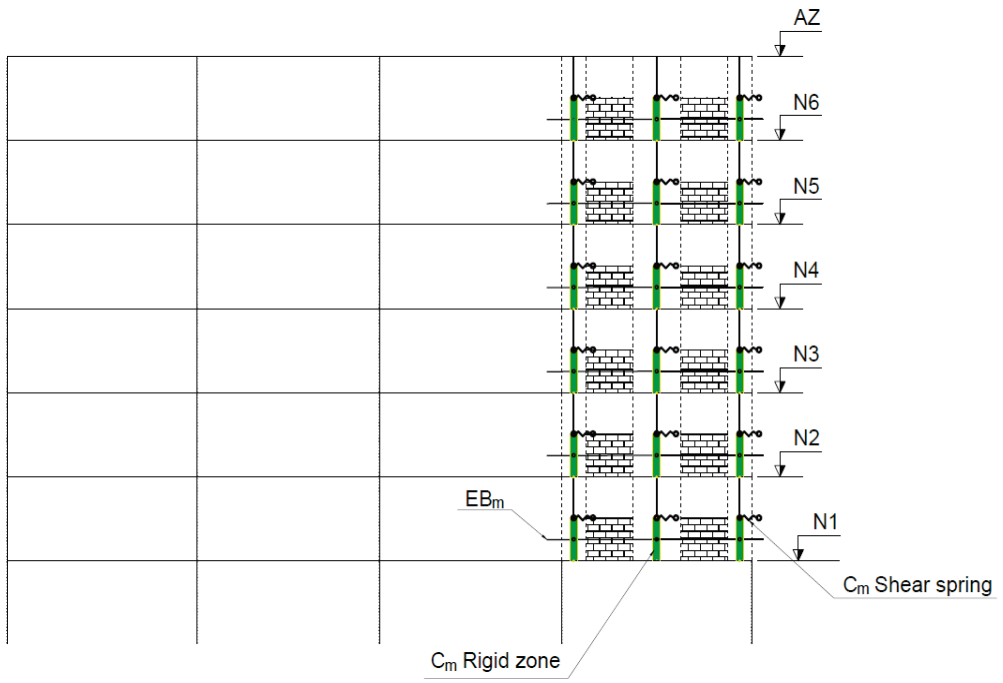


Figure 10-33 Masonry frame system used to model the façade.

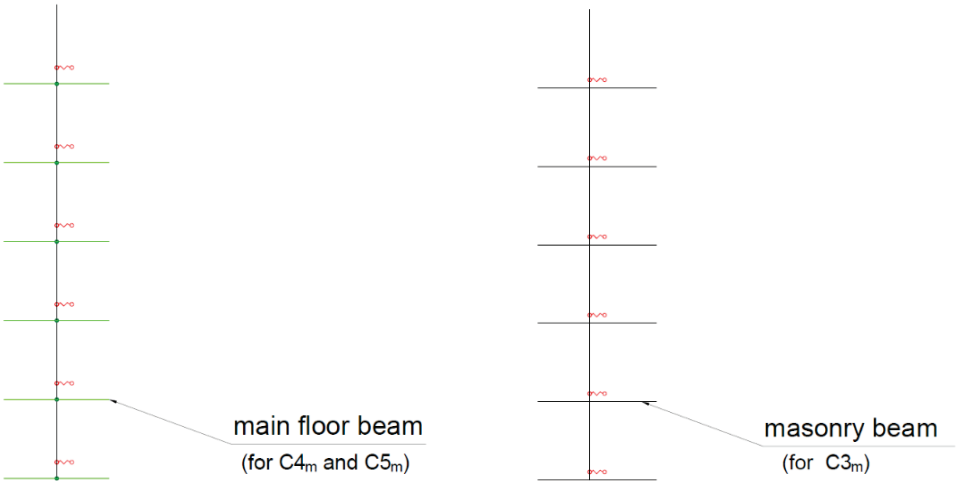


Figure 10-34 Masonry frame system used to model partition walls.

Nonlinear analyses were performed using 2% Rayleigh damping anchored at the fundamental first and fourth mode periods of the building, with mass-proportional and stiffness-proportional damping. The analysis accounted for large deformation effects by implementing the P-delta transformation in all column elements. Analyses were performed for two different models including and neglecting the effect of the masonry walls and infills.

10.3.2 Global Performance: Model vs. Observation

Fundamental periods of the building calculated using ASCE 41-17 effective stiffness provisions are presented in Table 10-4. For the model that included the effect of the masonry infills the fundamental periods were 1.05 sec. in the torsional direction, 0.98 sec. in the frame (east-west) direction and 0.52 sec. in the wall (north-south) direction. For the model in which the effect of masonry infills was neglected, effective periods were 1.39 sec. in the torsional direction, 1.39 sec. in the frame (east-west) direction and 0.65 sec. in the wall (north-south) direction. Calculated periods indicate that masonry infills helped the building significantly by lowering the period in the torsional and frame (east-west) directions below the range of periods with the most destructive effect in the displacement spectra (Figure 10-11). Damage to the masonry infills would increase the period in the frame (east-west) direction, moving it to the range of periods in the ground motion that was most destructive in Figure 10-11. This effect would be more significant in a model that includes the flexibility of the soil.

This publication is available free of charge from: https://doi.org/10.6028/NIST.GCR.22-917-50

Table 10-4 Calculated Periods for Models with and without Masonry Elements

	Period Direction (sec.)		
	Torsional	*Frame*	*Wall*
Model with masonry elements before the earthquake	1.05	0.98	0.52
Model with masonry elements after the earthquake	1.11	1.04	0.63
Model without masonry elements before the earthquake	1.39	1.39	0.65
Model without masonry elements after the earthquake	2.08	1.60	0.65

Eigenvalue analyses before and after the 2017 Puebla Earthquake for the models with and without infills confirm that the effect of the infills was most significant in the frame direction. Damage to infills caused the period in the frame direction to increase from 0.98 sec. to 1.04 sec., compared with a period of 1.39 sec. for the model without infills before the earthquake. Even though infill walls in the frame direction were damaged, masonry partition walls remained mostly undamaged and continued to provide significant stiffness. Damage to the partition walls in the model would have increased the period and caused it to move further into the most harmful region of the displacement spectrum.

In the wall direction, analyses before and after the earthquake show that masonry infill damage caused the period to increase almost to the period of the model without masonry walls. Although the masonry infills in the wall direction dissipated energy from the earthquake, their contribution was not as critical because the reinforced concrete walls protected the building by effectively decoupling the fundamental period in the north-south direction from the fundamental period of the soil below.

Pushover Analyses

Pushover analyses were performed for models with and without masonry elements, in both the frame and the wall directions, to evaluate the effect of the masonry on strength and deformation capacity of the frames (Figure 10-35). As expected, the stiffness and base shear capacity of the building were higher for the model with masonry infills. In the frame direction, both models experienced a sudden loss of lateral load capacity at a mean drift ratio of approximately 2%. The similarity in the shape of the pushover curve is a result of the nonductile behavior of both columns and masonry walls. The main difference between the two is that the model with masonry walls had approximately 35% higher base shear capacity than the model where the effect of the masonry walls was neglected.

This publication is available free of charge from: https://doi.org/10.6028/NIST.GCR.22-917-50

In the concrete wall direction behavior was much more ductile as a result of the dominant behavior of the concrete walls, and the strength of the two models was very similar. Columns were modeled so they would retain axial capacity with zero stiffness when exceeding the plastic rotation corresponding to modeling parameter *b* so the pushover curves shown in Figure 10-35b do not capture column axial failure.

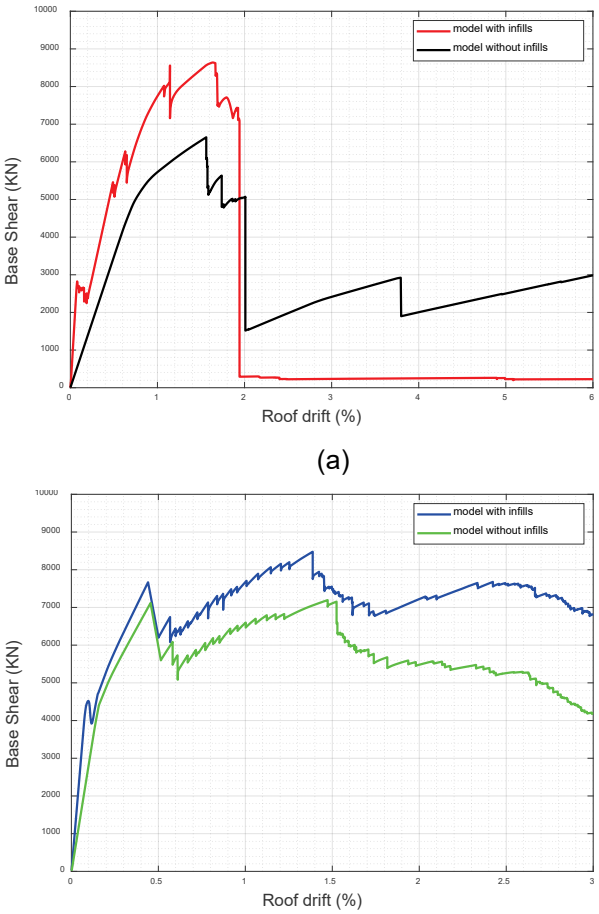
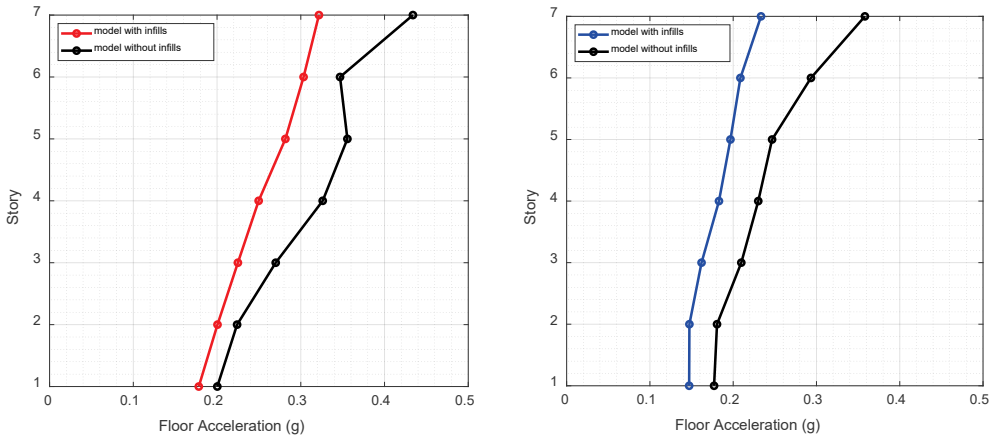


Figure 10-35 Pushover analysis results in (a) frame direction and (b) wall direction.

Nonlinear Dynamic Analyses

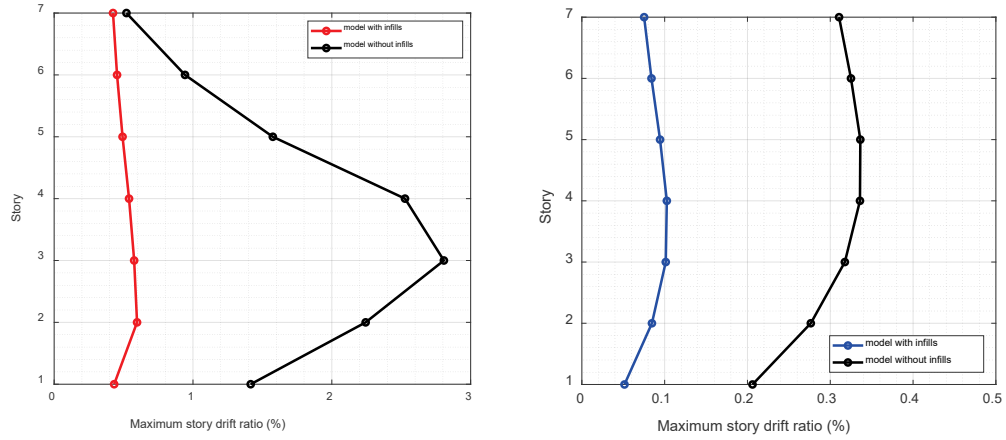
The simulated and observed performance of the building are compared in this section. Performance metrics for the 2017 Puebla Earthquake record at Jardín de Niños station are plotted for the model with and without masonry infills in Figures 10-36 and 10-37. Figure 10-37 shows that drift ratios were low in both directions, but significantly lower in the wall direction (north-south). Peak drift ratio in the frame direction of the model with masonry elements was approximately 0.50%, compared with almost 3% for the model without masonry elements. The large difference between the two shows that masonry walls and partitions contributed significantly to reduce drift demands in the frame direction.

This publication is available free of charge from: https://doi.org/10.6028/NIST.GCR.22-917-50



(a) (b)

Figure 10-36 Acceleration profiles calculated with nonlinear model including masonry walls and infills for the 2017 Puebla Earthquake (a) frame direction, and (b) wall direction.



(a) (b)

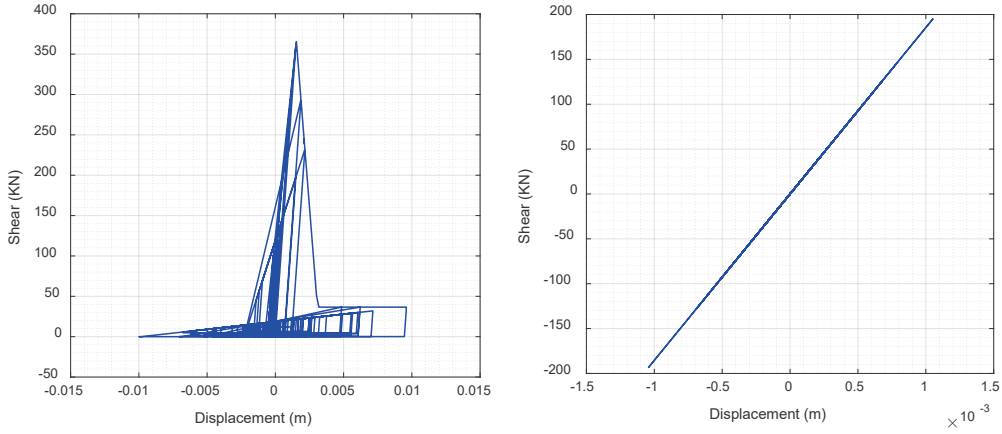
Figure 10-37 Drift ratio profiles calculated with nonlinear model including masonry walls and infills for the 2017 Puebla Earthquake (a) frame direction, and (b) wall direction.

All members, except masonry infill struts (Figure 10-38a) in the frame and wall directions, remained in the linear range of response. Façade masonry elements (Figure 10-38b) remained in the linear elastic range even though significant damage was observed in the building.

Calculated base shear histories for the 2017 Puebla Earthquake are shown in Figures 10-39 and 10-40, where black horizontal lines show the base shear strength calculated with the pushover analyses (Figure 10-35). In both the frame and wall directions, calculated base shear demands were significantly lower than the calculated base shear strength, which confirms that calculated demands were not high enough to cause significant damage.

This publication is available free of charge from: https://doi.org/10.6028/NIST.GCR.22-917-50

The calculated global response for the 2017 Puebla Earthquake ground motion indicates that masonry walls would be expected to contribute significantly to resist lateral loads, sparing reinforced concrete beam and column elements from any damage.



(a) (b)

Figure 10-38 Hysteretic response of (a) first story masonry infill and (b) façade masonry element for the 2017 Puebla Earthquake.

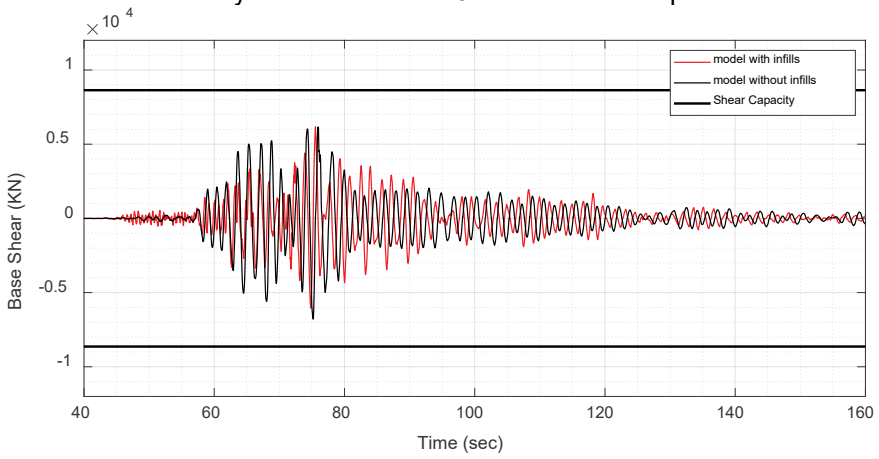


Figure 10-39 Base shear history in the frame direction.

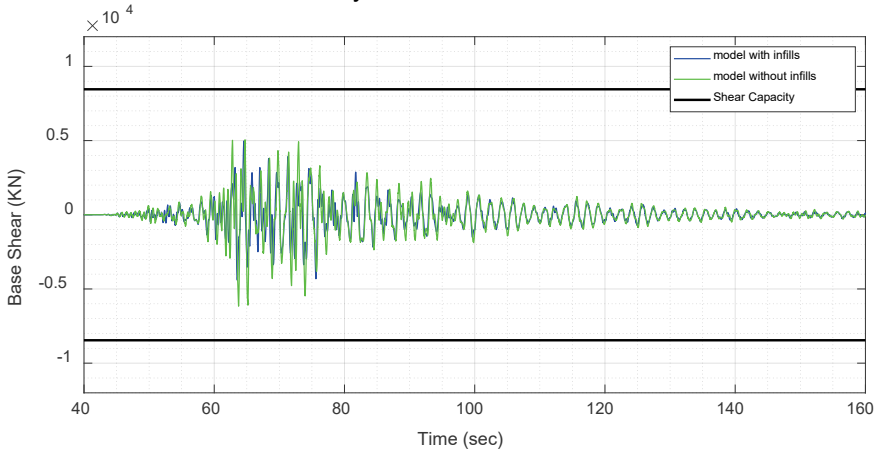


Figure 10-40 Base shear history in the wall direction.

This publication is available free of charge from: https://doi.org/10.6028/NIST.GCR.22-917-50

Observed damage included significant damage to masonry walls (Figures 10-15 to 10-20) in multiple stories and locations, both in the interior and exterior of the building. This is in direct contrast to the calculated response, which was accurate only in estimating severe damage (Figure 10-38a) to the infill struts (Figures 10-16 through 10-18). Because the model estimated damage to masonry walls in far fewer locations than was observed, the model was unconservative estimating the spatial distribution of damage to masonry infill and partitions.

The model did accurately estimate the level of damage to beam and column elements. Narrow inclined cracks observed in the columns (Figure 10-13) indicate that transverse reinforcement remained in the elastic range and that columns were not under severe distress. Estimated damage to columns was closely related to the effect of the walls in the overall response, which significantly reduced drift demand on the building. The stiffness afforded by the masonry walls protected the columns from reaching their proportional limit, which in most cases was dictated by shear strength. Structural walls sustained some damage at the boundaries in the first floor of the building (Figure 10-14), although the model indicates that no damage other than flexural cracking was expected. The maximum flexural demand on the walls was approximately 6000 kN-m (4425 kip-ft) (Figure 10-41b), higher than the flexural cracking load of 2550 kN-m (1880 kip-ft), and close the flexural yielding moment of approximately 7000 kN-m (5160 kip-ft) (Figure 10-27).

Nonlinear Dynamic Analyses for MCE

Defining the observed performance level of this building is complicated because of the drastic difference between the performance of structural and nonstructural elements. Beam and column elements experienced small amounts of damage consistent with IO performance level. The structural walls experienced some damage in the first floor, at the elevator wall boundary (Figure 10-14), but the amount of damage observed at this location was well within the LS performance level. The most severe damage was observed in the masonry walls, which were not intended to be part of the lateral load-resisting system, but did attract a significant portion of the lateral forces. Although not a part of the lateral load resisting system, damage to masonry walls did pose two major sources of risk to building occupants. The first is associated with unstable wall pieces falling inside apartment units or exterior wall pieces falling to the ground and injuring people outside the building. The second source of risk was that in the case of a large aftershock or another strong earthquake, the damaged masonry walls would not be able to resist lateral forces, leaving shear-critical column elements exposed to shear failure and loss of gravity load carrying capacity.

Due to the dominant role that masonry walls played in the global response, a second hazard scenario was explored evaluating the performance of the building under the

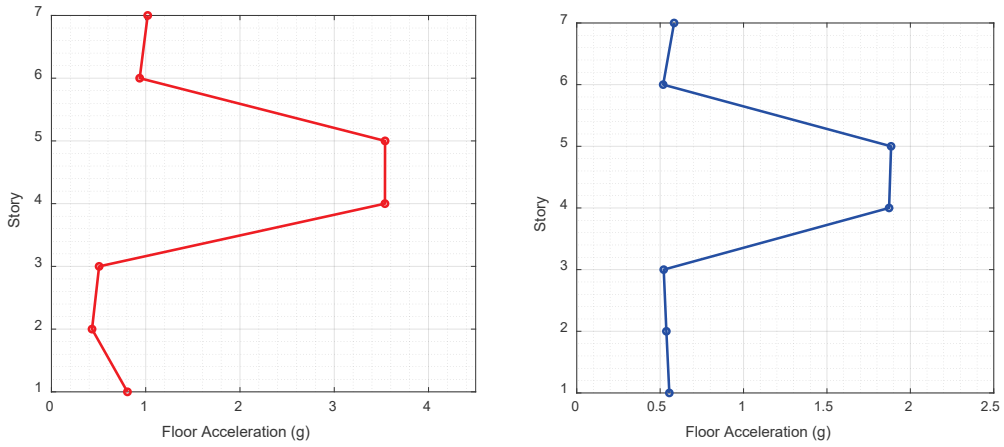
This publication is available free of charge from: https://doi.org/10.6028/NIST.GCR.22-917-50

MCE level earthquake. Because the intensity of the MCE level earthquake was sufficient to severely damage masonry walls and infills and cause building collapse, this scenario was intended to show the progression of damage and provide an indication of the type of collapse mechanism that would develop after masonry are no longer able to limit deformation demands.

In the MCE scenario, ground motions from the 2017 Puebla Earthquake record at Jardín de Niños station were amplified by a factor of approximately 4, which corresponds to the ratio of spectral acceleration ordinates at the fundamental effective period of the building for the MCE and the 2017 Puebla Earthquake (Section 10.2.3). The distribution of accelerations and drift ratios over the height of the building for the MCE-scaled ground motion are presented in in Figures 10-41 and 10-42, which show that these global response metrics were significantly higher than those calculated with the unscaled 2017 Puebla Earthquake. Figure 10-42 shows that drift ratios in both directions were indicative of collapse, with the largest deformations occurring in the ground level. Peak drift ratio in the frame direction exceeded 6% in the first floor, which suggests that in MCE hazard simulations, masonry infills and walls were damaged beyond the point where they could contribute to reduce drift demands, indicating a story mechanism in the first floor of the building.

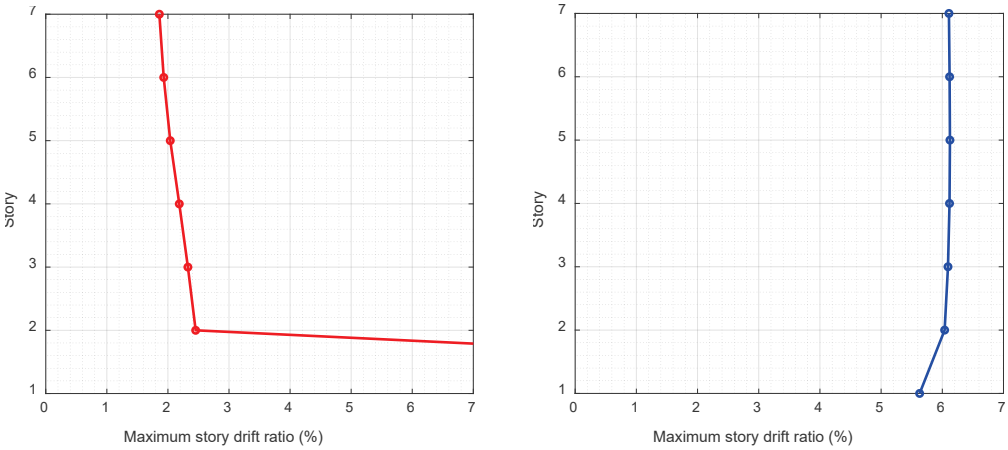
Figure 10-43 shows drift ratio histories in the frame (Figure 10-43a) and wall directions (Figure 10-43b), respectively, at the onset of building collapse. Drift ratio histories shown in this figure provide a clear indication of the global behavior that led to the collapse of the building. Masonry walls at the first floor in the frame direction lost lateral load capacity at or before a time of 62.9 sec., increasing building flexibility and placing a significant demand on the columns. The columns, which were shear critical in the frame direction, were severely damaged due to the deformation demand, precipitating the collapse of the building. Figure 10-43b shows that between 62 sec. and 64 sec., the maximum drift ratio in the wall direction was approximately 4%, which the pushover analysis in Figure 10-35b shows would have been sufficient to heavily damage the wall, pushing it into unstable behavior. The simulation indicates that excessively large deformations of the building in the frame direction would have likely triggered collapse in the wall direction.

This publication is available free of charge from: https://doi.org/10.6028/NIST.GCR.22-917-50



(a) (b)

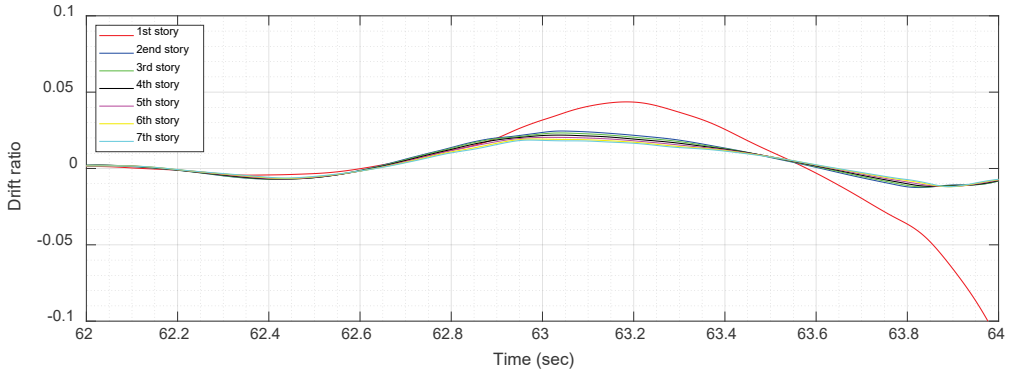
Figure 10-41 Acceleration profiles for (a) frame and (b) wall direction calculated with nonlinear model including masonry walls and infills for the 2017 Puebla Earthquake scaled to the MCE uniform hazard spectrum.



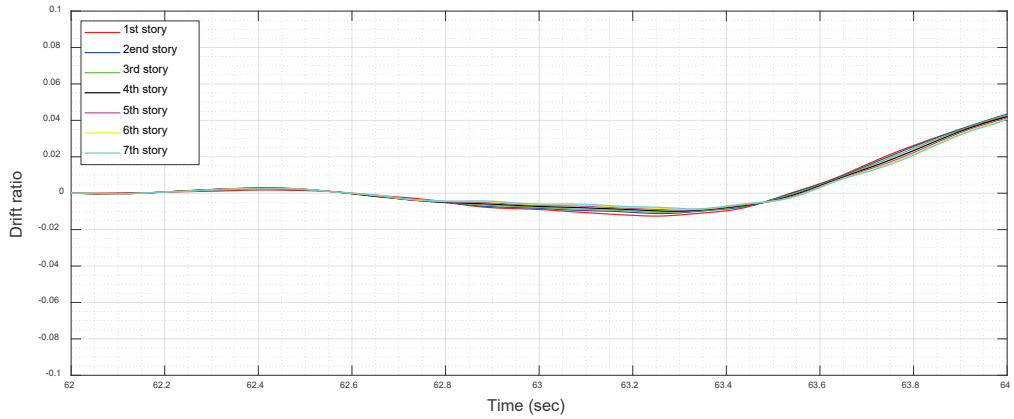
(a) (b)

Figure 10-42 Drift ratio profiles for (a) frame and (b) wall direction calculated with nonlinear model including masonry walls and infills for the 2017 Puebla Earthquake scaled to the MCE uniform hazard spectrum.

This publication is available free of charge from: https://doi.org/10.6028/NIST.GCR.22-917-50



(a)



(b)

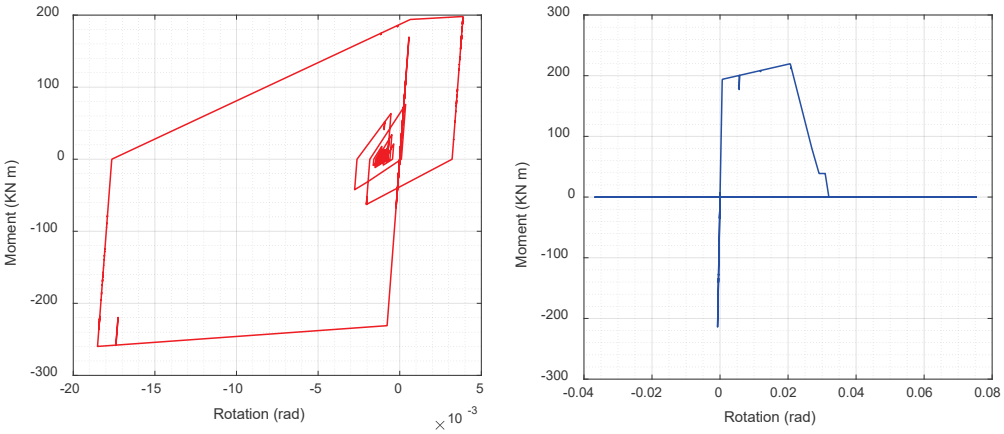
Figure 10-43 Drift ratio histories for (a) frame and (b) wall direction calculated with nonlinear model including masonry walls and infills for the 2017 Puebla Earthquake scaled to the MCE uniform hazard spectrum.

The progression of damage observed in the OpenSees model suggests that although columns in the building did not exhibit severe damage after the 2017 Puebla Earthquake, the building may have been very close to collapse. Damage surveys conducted after the 2017 Puebla Earthquake documented severe damage in the first story masonry walls (Figures 10-17 and 10-18), which was the collapse trigger in the MCE hazard simulation.

Although the OpenSees simulation achieved convergence beyond 64 seconds, results after this time are not meaningful given the magnitude of the lateral deformations both in the frame and wall directions. The response of first story nonlinear springs simulating beam, column, and wall elements is shown in Figures 10-44 to 10-46 for the entire duration of the ground motion. Beam (Figure 10-44) and column (10-45) elements had plastic deformations greater than modeling parameter *b* in the frame and wall directions. Figure 10-46 shows that for the MCE level hazard wall springs oriented in the frame and wall directions had inelastic rotations exceeding modeling parameter *b*. For the lumped plasticity approach used in the simulations, the OpenSees model had springs in the two principal directions of walls and columns that

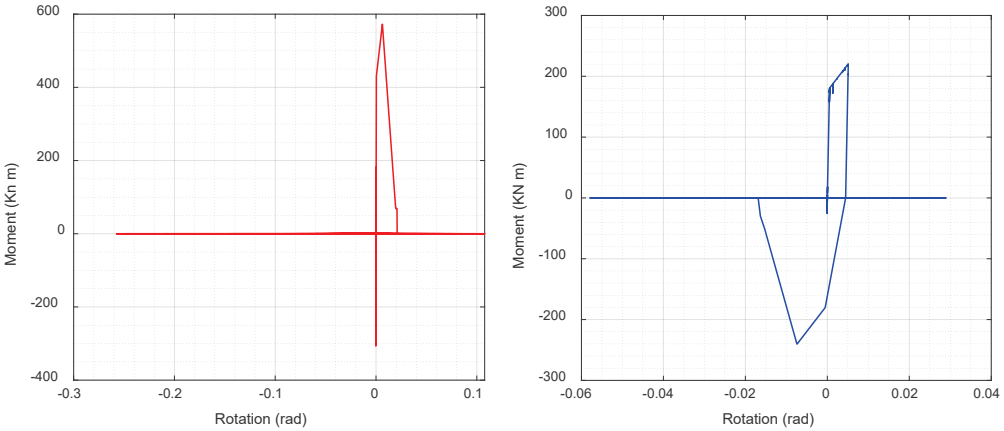
This publication is available free of charge from: https://doi.org/10.6028/NIST.GCR.22-917-50

were completely uncoupled, so damage in the weak direction of the wall did not affect its behavior in the strong direction. Figure 10-42b shows that the intensity of shaking for the MCE level event would have been sufficient to cause severe damage to the wall due to excessive rotations in the weak direction.



(a) (b)

Figure 10-44 Hysteretic response of first story beam springs in the (a) frame and (b) wall directions for the 2017 Puebla Earthquake scaled to the MCE uniform hazard spectrum.



(a) (b)

Figure 10-45 Hysteretic response of first story column springs in the (a) frame and (b) wall directions for the 2017 Puebla Earthquake scaled to the MCE uniform hazard spectrum.

This publication is available free of charge from: https://doi.org/10.6028/NIST.GCR.22-917-50

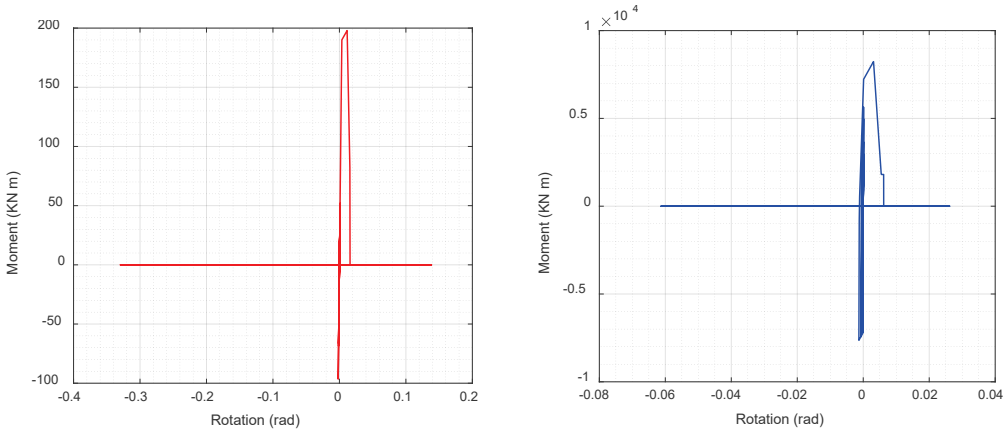


Figure 10-46 Hysteretic response of first story wall springs in the (a) frame and (b) wall directions for the 2017 Puebla Earthquake scaled to the MCE uniform hazard spectrum.

Calculated base shear histories for the MCE level hazard are shown in Figures 10-47 and 10-48, where black horizontal black lines correspond to the base shear strength calculated using a pushover analysis. In both the frame and wall directions, calculated base shears exceeded the base shear strength, which shows that calculated demands were high enough to inflict significant damage. According to the Figure 10-44, collapse initiated at approximately 63 seconds, when the drift ratio in the first story started to become significantly larger than in all others. Base shear histories show that this time coincides with peak base shear demands in the frame (Figure 10-47) and wall (Figure 10-48) directions. Base shear histories calculated after 64 seconds are not meaningful because it is likely the model would have collapsed already.

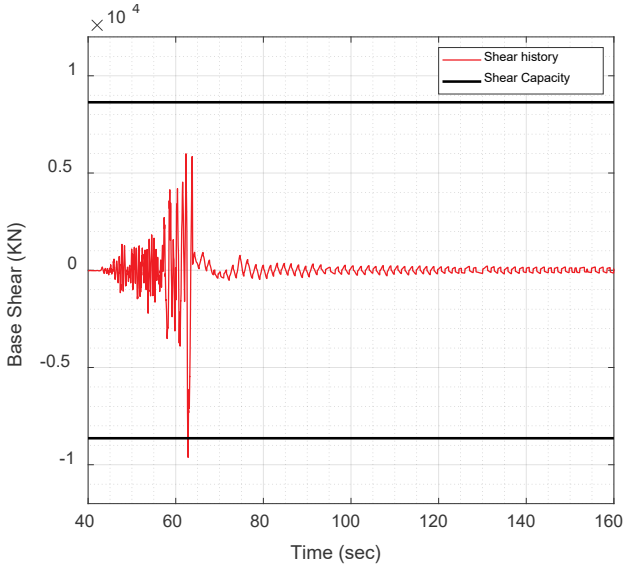


Figure 10-47 Base shear in the frame direction for the 2017 Puebla Earthquake scaled to the MCE uniform hazard spectrum.

This publication is available free of charge from: https://doi.org/10.6028/NIST.GCR.22-917-50

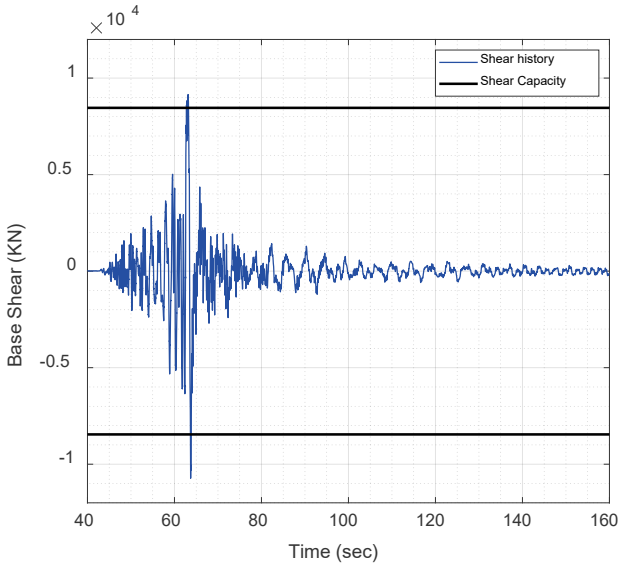


Figure 10-48 Base shear in the wall direction for the 2017 Puebla Earthquake scaled to the MCE uniform hazard spectrum.

A more detailed analysis of estimates of damage in all building components is presented in the Section 10.3.3.

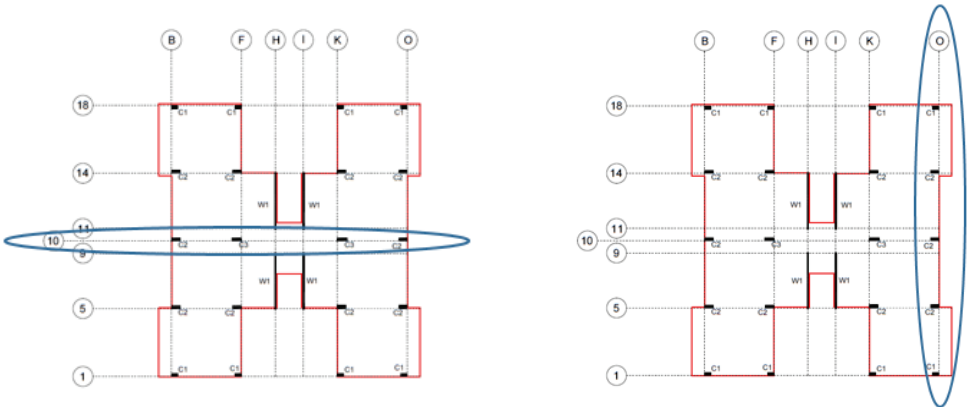
10.3.3 Component Performance: Model vs. Observation

Structural components in this building included beams, columns, reinforced concrete walls, masonry walls, and masonry infill in reinforced concrete frames. This section describes the calculated distribution of nonlinear deformations among building components and the implications of modeling provisions in ASCE 41-17 on that distribution.

As described in Section 10.3.1, beams, columns, and reinforced concrete walls were modeled using nonlinear rotational springs. Rotational spring performance levels in the frame and wall directions are discussed in this section for the two frames shown in Figure 10-49. Performance levels are presented for two different hazards, the 2017 Puebla Earthquake record obtained near the building, and the MCE level hazard calculated as described in Section 10.2.3 to illustrate the damage distribution caused by the earthquake and near collapse.

Estimated performance levels are presented using two different metrics. The first is a direct comparison between calculated element rotation and deformation limits established in ASCE 41-17 for each performance level. In this metric, elements are classified according to the worst performance level for which the limit was exceeded. In figures showing performance levels, blue dots represent calculated rotations below IO performance level, yellow dots represent calculated rotations between IO and LS performance levels, orange dots represent calculated rotations between LS and CP performance levels, and red dots represent rotations exceeding CP performance level.

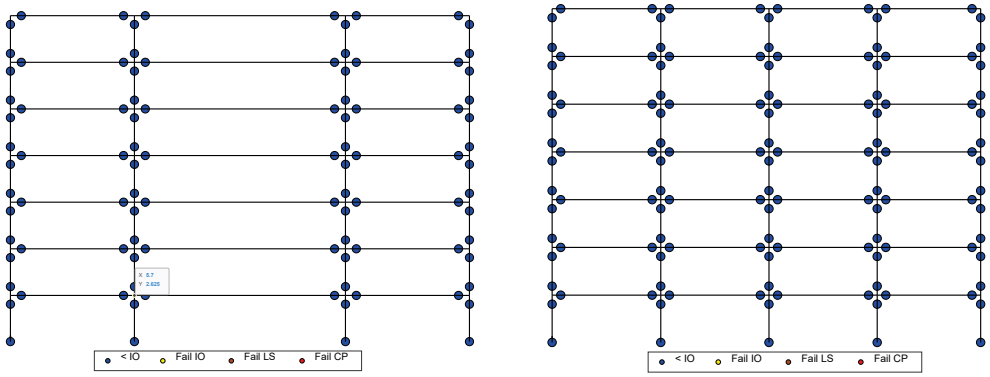
This publication is available free of charge from: https://doi.org/10.6028/NIST.GCR.22-917-50



(a) (b)

Figure 10-49 Sketch showing frames for which element performance is presented: (a) Gridline 10 in the frame direction (east-west), and (b) Gridline O in the wall direction (north-south).

Performance levels for the 2017 Puebla Earthquake are shown in Figure 10-50a for the frame in Gridline 10 (frame direction) and in Figure 10-50b for Gridline O (wall direction). All beam and column elements in the two frames had a performance level of IO, in large part due to the lateral loads carried by the masonry walls and infill.



(a) (b)

Figure 10-50 Element performance levels for the 2017 Puebla Earthquake: (a) Gridline 10 in the frame direction (east-west), and (b) Gridline O in the wall direction (north-south). Shown relative to ASCE 41-17 nonlinear acceptance criteria Immediate Occupancy (IO), Life Safety (LS), and Collapse Prevention (CP).

Performance levels for the 2017 Puebla Earthquake scaled to the MCE hazard level are shown in Figure 10-51a for the frame in Gridline 10 (frame direction) and in Figure 10-51b for Gridline O (wall direction). As expected, all beam and column elements in frame and wall directions showed substantially greater damage than for the unscaled record. The most useful observation from Figure 10-51a is that damage was largest in first story columns, clearly showing the formation of a collapse mechanism.

This publication is available free of charge from: https://doi.org/10.6028/NIST.GCR.22-917-50

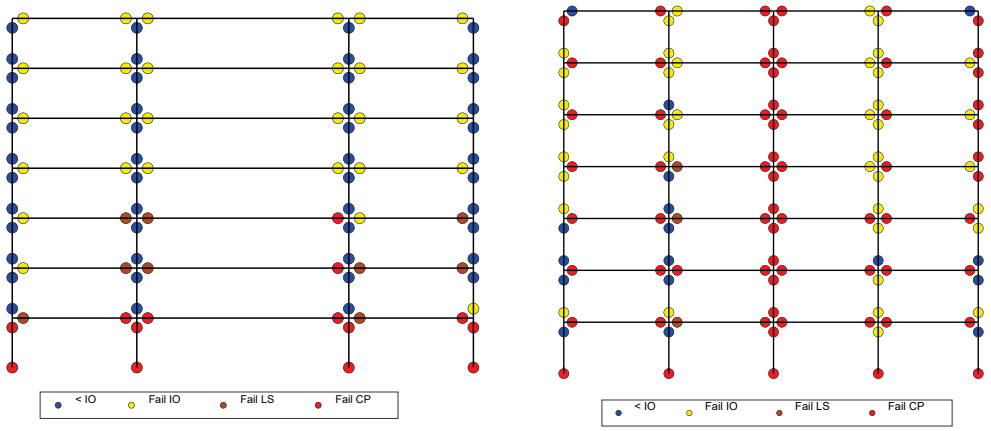


Figure 10-51 Element performance levels for the 2017 Puebla Earthquake scaled to the MCE hazard level: (a) Gridline 10 in the frame direction (east-west), and (b) Gridline O in the wall direction (north-south). Shown relative to ASCE 41-17 nonlinear acceptance criteria Immediate Occupancy (IO), Life Safety (LS), and Collapse Prevention (CP).

Damage distribution in the wall direction is more difficult to interpret, but shows the most severe damage concentrated in the center column, which was the least protected by masonry beams and columns.

The second metric used to evaluate damage is the ratio of inelastic rotation at hinge locations ($\theta_{inelastic}$) to the corresponding modeling parameter *a* in ASCE 41-17, which is indicative of the beginning of lateral strength loss. Members in which the inelastic rotation exceeded modeling parameter *a* are considered to have sustained severe damage according to the nonlinear analysis, while members in which the inelastic rotation is lower than parameter *a* are considered to have sustained moderate damage. In figures showing this damage indicator, circle diameters at hinge locations are proportional to the ratio of $\theta_{inelastic}$ to modeling parameter *a*. Circle color is also an indicative of the ratio of $\theta_{inelastic}$ to modeling parameter *a*, with red circles indicating locations where $\theta_{inelastic}$ exceeded modeling parameter *a*. A minimum diameter was used in the figures to ensure visibility of elements in which inelastic rotations were very small.

This second damage indicator (ratio of $\theta_{inelastic}$ to modeling parameter *a*) is shown in Figures 10-52 through 10-55 for the two frames shown in Figure 10-49. Results for this second metric are consistent with performance levels shown in Figures 10-50 and 10-51. For the 2017 Puebla Earthquake, inelastic rotations in beams and columns are zero or very small. As shown in Figure 10-41, although they exceeded their flexural cracking moment, reinforced concrete walls remained below yield, so their plastic rotation was zero. Damage estimates to beams and columns inferred from Figures 10-50 and 10-51 are in good agreement with observed damage after the 2017 Puebla Earthquake described in Section 10.2.4, which shows damage consisting of narrow

This publication is available free of charge from: https://doi.org/10.6028/NIST.GCR.22-917-50

shear cracks in columns (Figure 10-13) and loss of shell and some buckling in one of the reinforced concrete walls (Figure 10-14). For the MCE level hazard, significant damage was found in multiple beams and columns of the model throughout the building. Figure 10-54 shows that in the frame direction a story mechanism formed in the first story of the model, which is consistent with the damage pattern in Figure 10-51a and the drift ratios shown in Figure 10-43. Figure 10-55 shows that inelastic demands were largest in the center column, which is consistent with the damage pattern in Figure 10-51b.

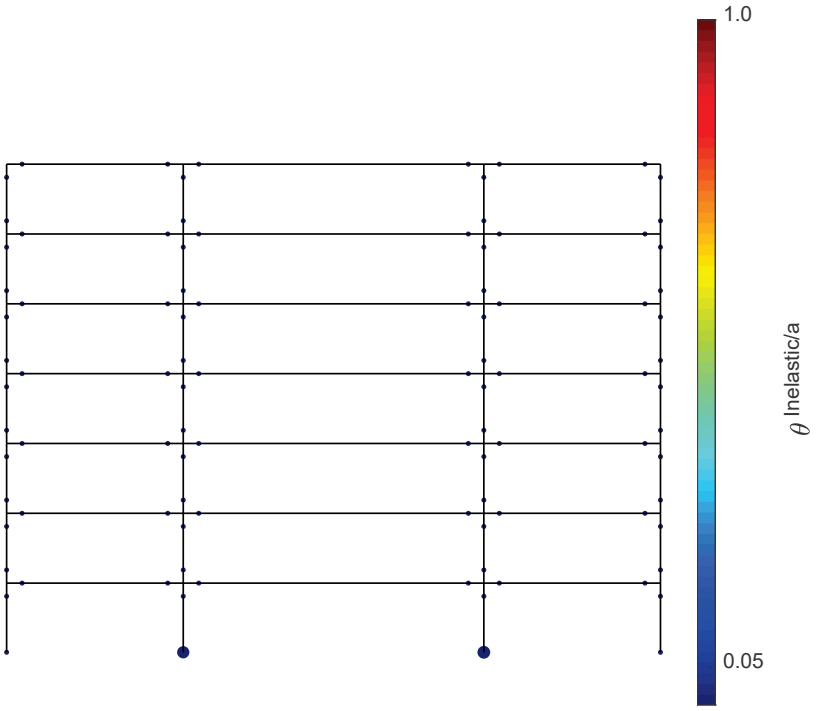


Figure 10-52 Ratio of inelastic rotation to modeling parameter *a* for the 2017 Puebla Earthquake, Gridline 10 in the frame direction (east-west).

This publication is available free of charge from: https://doi.org/10.6028/NIST.GCR.22-917-50

This publication is available free of charge from: https://doi.org/10.6028/NIST.GCR.22-917-50

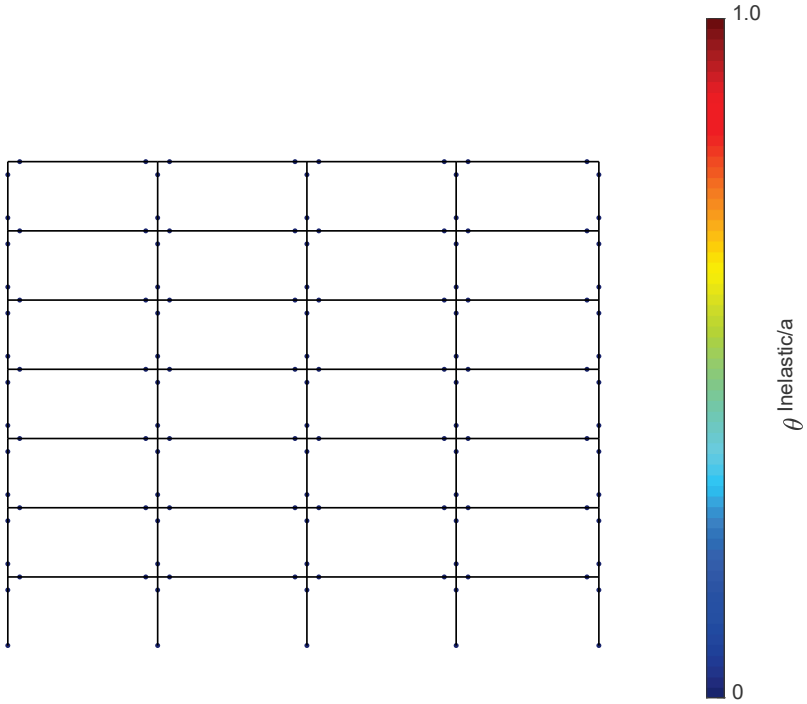


Figure 10-53 Ratio of inelastic rotation to modeling parameter *a* for the 2017 Puebla Earthquake, Gridline O in the wall direction (north-south).

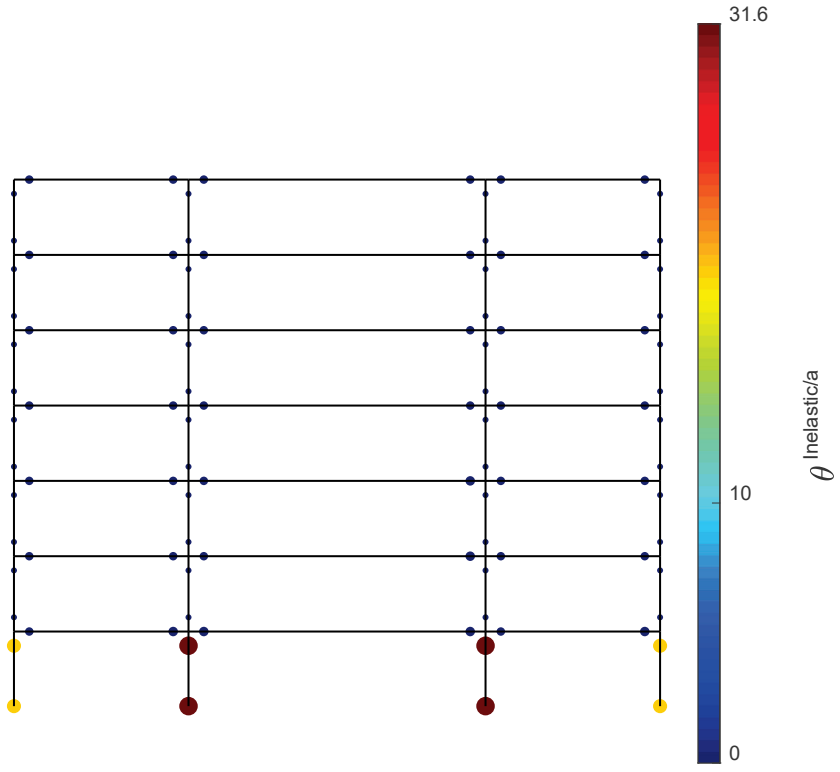


Figure 10-54 Ratio of inelastic rotation to modeling parameter *a* for the 2017 Puebla Earthquake scaled to the MCE hazard level, Gridline 10 in the frame direction (east-west).

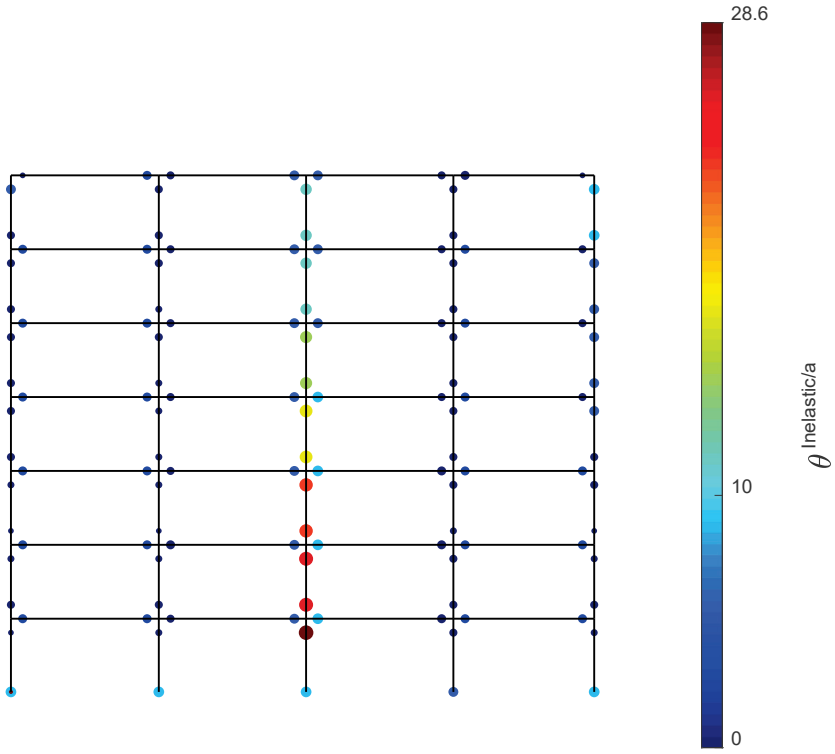


Figure 10-55 Ratio of inelastic rotation to modeling parameter *a* for the 2017 Puebla Earthquake scaled to the MCE hazard level, Gridline O in the wall direction (north-south).

A comparison between observed damage and the hysteretic response of the masonry façade elements is shown in Figure 10-56. Each row in Figure 10-56 shows the calculated shear-displacement relationship of masonry façade element C_{1m} (Figure 10-29) in a different story of the building for the unscaled and scaled ground motions. The image on the left of Figure 10-56 shows that there was no façade element in the bottom story, so hysteretic curves correspond to the remaining six stories. As described in Section 10.3.1, in the computer model façade columns are considered rigid between masonry beams, and shear springs are placed at the top elevation of masonry beams (bottom of the openings), as shown in Figure 10-31. In the actual building, damage to the masonry façade could be the result of excessive shear or flexural demands on the masonry beams, which are modeled as elastic elements, or excessive demands in the column shear springs. Hysteresis curves for column element C_{1m} shown in Figure 10-56 for the unscaled 2017 Puebla Earthquake ground motion indicate that masonry façade elements in the model remained in the linear range during the 2017 Puebla earthquake and that as a result the model indicated that little damage was expected. A comparison between the hysteresis curves and the image on the left of the figure shows that actual damage was more severe than estimated with the computer model.

This publication is available free of charge from: https://doi.org/10.6028/NIST.GCR.22-917-50

The image on the left of Figure 10-56 shows vertical racks at the edges of masonry beams. If columns are ruled out as the cause of damage as implied by the computer model, the remaining possible cause of damage would be flexural or shear cracking of masonry beam elements, which were modeled as linear elastic (Figure 10-29 and 10-32). Calculations show that maximum shear demands in masonry beam elements are well below their capacity, on the order of 20% of capacity for the MCE level hazard and below 10% of capacity for the unscaled 2017 Puebla Earthquake ground motion. Given that shear demands are too low to cause damage to the beam façade elements, the other plausible explanation is that the cracks shown in Figure 10-56 are caused by masonry beams in the model exceeding their capacity in flexure. To that effect, calculations were performed to estimate tensile stresses in the masonry beams based on maximum moment demands and gross section properties. Calculated tensile stresses for the unscaled 2017 Puebla Earthquake ground motion are on the order of 115 kN/m^2 (approximately 17 psi), which is sufficiently high to cause the cracking observed in the beam based on the expected tensile strength in Table 10-2.

Figure 10-57 shows a similar comparison between observed damage and the hysteretic response of the masonry infill elements in the frame direction. As described in Section 10.3.1, masonry infills are modeled as compression-only struts. Hysteresis curves in Figure 10-57 show the calculated response of compression-only strut element $W1_m$ (Figure 10-29) at each story of the building. Hysteresis curves for column element $W1_m$ shown in Figure 10-57 for the unscaled 2017 Puebla Earthquake ground motion indicate that masonry strut elements are expected to sustain very severe damage, much worse than the level of damage observed. Calculated displacements exceeded the limit in ASCE 41 Table 11-13 for CP performance level.

This publication is available free of charge from: https://doi.org/10.6028/NIST.GCR.22-917-50

This publication is available free of charge from: https://doi.org/10.6028/NIST.GCR.22-917-50

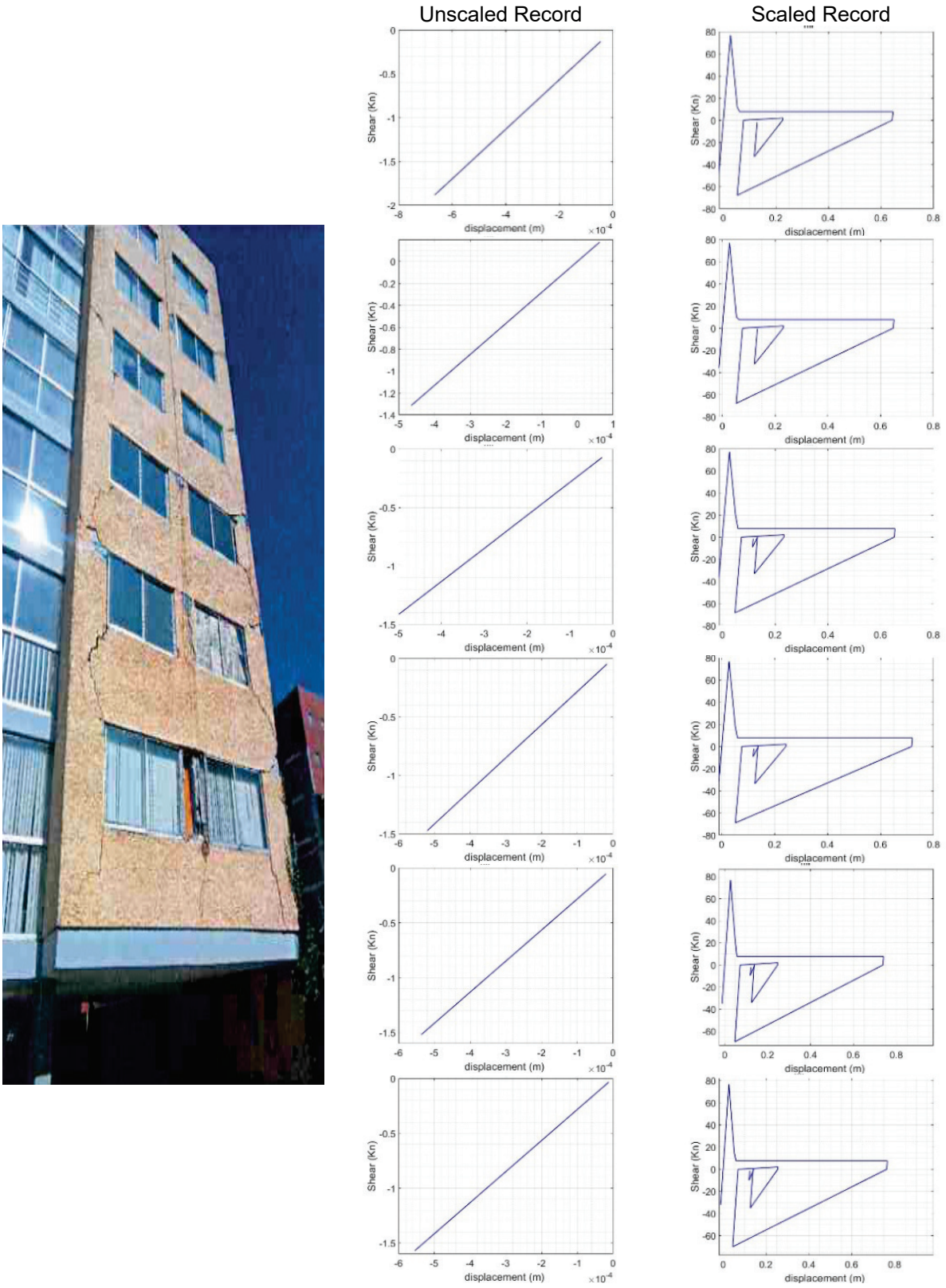


Figure 10-56 Comparison of observed damage (left) and hysteretic response (right) for masonry elements in building façade for unscaled and scaled ground motion. Each row on the right represents one story of the building starting from the ground floor at the bottom.

This publication is available free of charge from: https://doi.org/10.6028/NIST.GCR.22-917-50

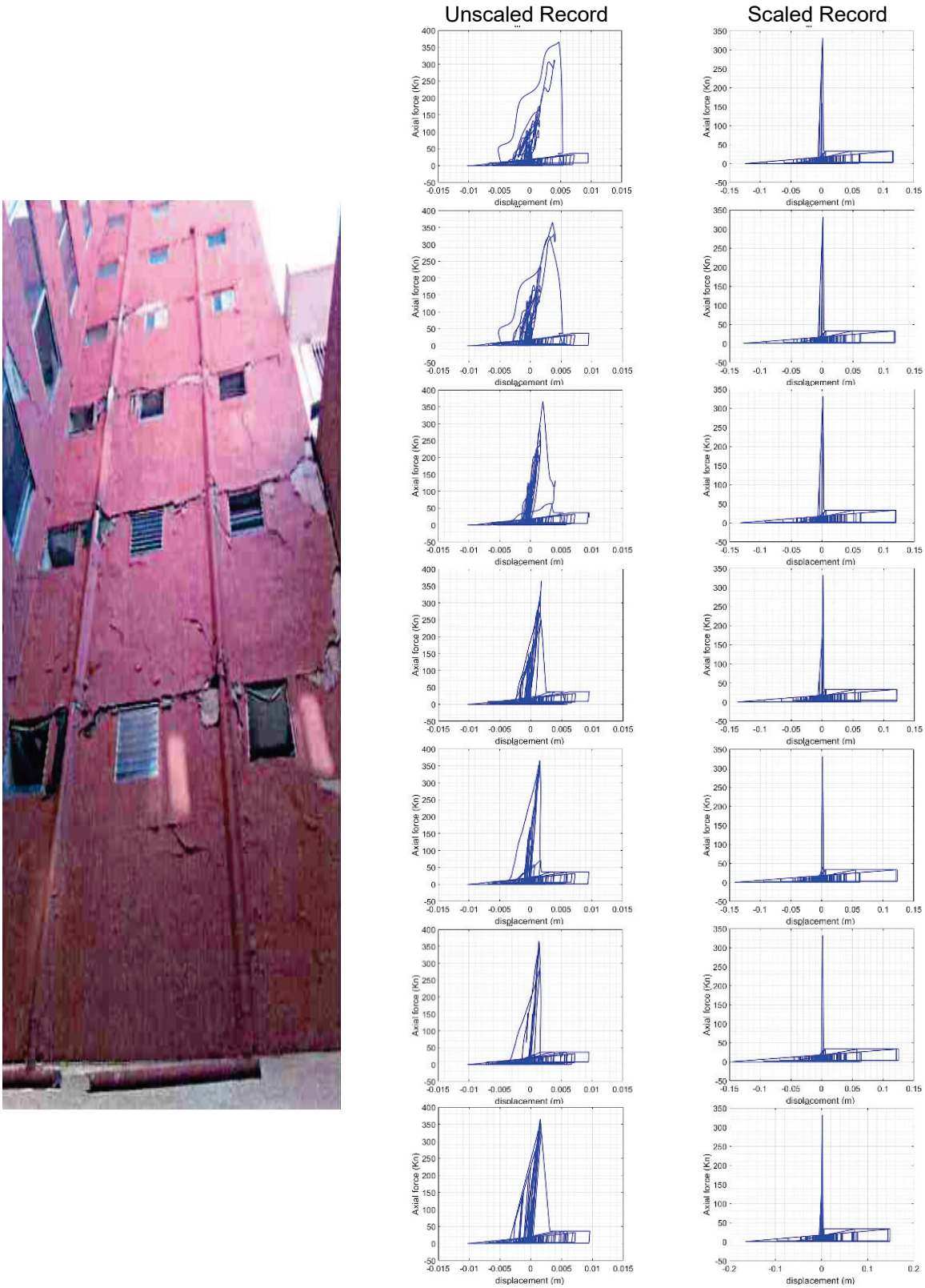


Figure 10-57 Comparison of observed damage (left) and hysteretic response (right) for masonry infills in the frame direction for unscaled and scaled ground motion. Each row on the right represents one story of the building starting from the ground floor at the bottom.

10.4 Summary

10.4.1 Global Performance

Overall, the ASCE 41-17 nonlinear dynamic evaluation procedures were able to identify an important source of potential distress in the building associated with the columns. Shear cracks in columns can develop before flexural reinforcement yields. This appears to be the case in this building given the narrow width of shear cracks observed after the 2017 Puebla Earthquake, and the lack of damage indicative of flexural hinge formation (Figure 10-13). Observed shear crack widths also indicate that shear demands were not high enough to cause column shear reinforcement to yield. In members with sufficient transverse reinforcement, developing narrow shear cracks before the proportional limit is exceeded is not a concern. The problem with this building is that the low amount of column transverse reinforcement provided makes these elements shear critical, lacking any significant deformation capacity beyond the proportional limit. Although the damage pattern observed in the columns is consistent with calculated demands that remained below the proportional limit and in the IO performance level, a ground motion strong enough to severely damage the first story masonry walls would have likely caused the formation of a story mechanism due to the limited deformation capacity of first story columns and the effect of the less damaged masonry elements on the distribution of stiffness over the height of the building.

The model correctly showed that masonry elements would effectively protect the lateral load-resisting system of the building by de-coupling the fundamental period of the reinforced concrete structure from the range of periods where the ground motion was most destructive, keeping drift demands sufficiently low to prevent brittle reinforced concrete columns from reaching their proportional limit. According to the criteria in ASCE 41-17, structural components in the model had IO performance level for the 2017 Puebla Earthquake ground motion because they remained within their elastic limits. Observed damage in beams and columns is consistent with the description in ASCE 41-17 Table C2-4 for IO performance level, while reinforced concrete walls did sustain small damage consistent with LS performance level. Based on the images included in the damage report (Figure 10-14), deterioration due to exposure to the elements could have been a contributing factor to the wall damage. Masonry infill elements in the model, which were not intended to be part of the lateral load-resisting system in the original design, exceeded the CP performance level for nonstructural components in ASCE 41-17. Masonry partition elements in the model had IO performance level because they remained in the linear elastic range, while observed damage is indicative of exceeding CP performance level. Calculated tensile stresses in the masonry façade elements, modeled as linear elastic beam column elements, exceeded expected tensile strength for the type of masonry in the building façade. Because the elements were modeled as linear elastic it is not

This publication is available free of charge from: https://doi.org/10.6028/NIST.GCR.22-917-50

possible to establish a performance level based on calculated deformations, but the magnitude of the computed stresses indicates that the IO performance level was exceeded and the observed damage is consistent with the description of LS performance level in ASCE 41.

Based on building performance levels described in ASCE 41-17 Table C2-3, damage to structural elements of the model would be classified as IO, and damage to nonstructural components of the model would be classified as exceeding CP. These two characterizations are in close agreement with the damage observed in the building.

Analyses for MCE level hazard showed that if subjected to stronger shaking, the building could be in serious risk of collapse because severe damage to the masonry would leave the columns exposed to shear and axial failure. The type of damage observed after the 2017 Puebla Earthquake is deceptive because even though performance level of the lateral load-resisting system was well below LS, damage to masonry was very severe, reducing its capacity to protect the lateral load-resisting system. Analysis for the MCE level hazard showed that after the lateral load resisted by the masonry walls becomes negligible, it is likely that the moment frame would not have been able to sustain deformation demands forming a collapse mechanism in the first story of the building. Damage observed in first story masonry walls of the building after the 2017 Puebla Earthquake is consistent with the progression of damage in the model for the MCE hazard, which suggests it is likely that a first story mechanism was likely to form under stronger or longer shaking.

10.4.2 Component Performance

Calculated nonlinear deformations for the 2017 Puebla Earthquake concentrated primarily in masonry elements. To that effect, the model was able to estimate accurately damage to masonry infills, where estimated and observed performance levels were CP. The same is true for façade elements, where calculated flexural stresses in masonry beam elements exceeded expected tensile strengths, matching the observed damage. However, this was not the case for shear springs simulating interior masonry partition walls. The model estimated small amounts of damage to these elements, even though they were severely damaged during the earthquake. It is important to note that provisions for modeling masonry walls are difficult to implement because modeling parameters in ASCE 41-17 are provided in terms of drift ratios. Models with shear springs like those implemented in the analysis of this building require assumptions to define spring stiffness, which likely was a contributing factor in the discrepancy between observed and calculated damage. Furthermore, deformation modeling parameters for masonry in ASCE 41-17 are defined based on few input variables that cover a wide range of wall configurations, which also makes modeling load-deformation response of masonry elements

This publication is available free of charge from: https://doi.org/10.6028/NIST.GCR.22-917-50

challenging. Designers can approach modeling of masonry elements in many different ways, which increases uncertainty in model results.

The model with masonry walls provided accurate estimates of observed performance levels in beam, column, and wall elements. The difficulty with establishing a performance level for this building o is that according to ASCE 41-17 Table C2-3, the performance level of structural components would be classified as IO while the performance level of the masonry elements would exceed CP. The progression of damage observed in the MCE hazard analysis suggests that a ground motion capable of causing more severe damage to the first story masonry walls would have led to the formation of a first story collapse mechanism. Concerns about the performance of the building under stronger ground motions than the 2017 Puebla Earthquake were significant enough to bring about the retrofit of the structure with reinforced concrete walls. Analyses performed did not provide a rational basis to determine if ASCE 41 modeling parameters or acceptance criteria are too conservative because elements were not placed in significant distress under the 2017 Puebla Earthquake and damage under the MCE level event was too severe.

10.4.3 Analytical Study Takeaways

The most significant modeling challenge for this building was to represent accurately the contribution of masonry components to the lateral force-resisting system. Analyses showed that the masonry walls served as a vibration protection system that is highly brittle and drastically changed the probability of collapse for ground motions with moderate intensity. The compression-only strut elements used to model masonry infill were successful in establishing that the 2017 Puebla Earthquake ground motion was sufficiently strong to cause substantial damage to these elements, although it was not successful in estimating the spatial distribution of the damage. Modeling of other masonry components had mixed results. Shear spring elements used to model partition walls were not successful in detecting the heavy damage observed following the 2017 Puebla Earthquake, so this is an area where closer inspection could lead to improvements in ASCE 41 provisions. For example, ASCE 41-17 Tables 11-10 and 10-11 of provide few categories for drift at peak strength and drift at the onset of residual strength of infilled frames, corresponding to relatively stiff and relatively flexible panels, and do not provide guidance on how to calculate the stiffness of shear spring elements.

Although it is not possible to confirm the collapse mechanism empirically, observed damage to the first story masonry walls in the frame direction is consistent with the progression of damage in the MCE hazard analysis, in which the simulations showed collapse due to a first story mechanism.

This publication is available free of charge from: https://doi.org/10.6028/NIST.GCR.22-917-50

10.4.4 Study Limitations

The results of this investigation are contextualized within the following limitations:

- Measured material properties were not available. Expected material properties for concrete and reinforcing bars were defined by adopting specified strengths as lower bound material properties and using material factors in ASCE 41-17. Material properties for masonry walls were not available and had no specified values, so default values were adopted from ASCE 41-17 and TMS 402.
- Original drawings obtained were illegible in some locations, thus the reinforcement layout is based on the best interpretation of the numbers stated in the drawings.
- The building was not instrumented. Acceleration records used in the study were recorded at a strong motion station located in the proximity of the building.
- Foundation flexibility and soil flexibility were not modeled.
- Some masonry walls at the base had a gap to avoid contact with the frame elements. In models that included the masonry wall panels the presence of the gap was neglected.
- Damage surveys show the building collided with a three-story structure adjacent to the south, and that the interaction between the two buildings likely affected the damage pattern. Interaction between the two structures was not included in the study.
- The building model included only the reinforced concrete structure. The roof structure was not included in the model.
- The best-estimate ground motions were recorded at a site 1.4 mi from the building site. Ground-motion recordings at the site were not available.

This publication is available free of charge from: https://doi.org/10.6028/NIST.GCR.22-917-50

Chapter 11

Summary of Results

11.1 Overview

This section presents summary results for benchmarking studies of ASCE 41-17 evaluation procedures where analytical results for eight structures are compared to observed performance through review of component and global response. Table 11-1 summarizes the structural system, earthquake event, data availability, and observed performance for eight reinforced concrete structures studied.

Table 11-1 Summary of Study Structures

Chapter No.	Structural System, Name, Location	Earthquake Event	Data Availability	Observed Performance
3	3-story test frame UC Berkeley 2008	Shaketable: 4.06 × Llolleo recording of 1985 Valparaiso (Chile)	Measured	Column diagonal (shear) and axial failure
4	4-story test frame and wall E-Defense 2010	Shaketable: 100% of JMA recording of 1995 Kobe (Japan)	Measured	Beam-column joint failure and wall boundary element failure
5	10-story test frame and wall E-Defense 2015	Shaketable: 100% of JMA recording of 1995 Kobe (Japan)	Measured	Damage to joints, minor spalling of wall boundary zones and minor cracking and spalling at base of columns
6	6-story frame and wall building Imperial County Services Building, California	1979 Imperial County	Accelerometer	Column diagonal (shear) and axial failure, amplified by torsion
7	7-story frame building Hotel in Van Nuys, California	1994 Northridge	Accelerometer	Column diagonal (shear) failure
8	5-story wall building Pyne Gould Corporation Building, New Zealand	2010-2011 Canterbury Sequence (New Zealand)	Photographs and observations	Collapse
9	3-story frame with masonry infill building Nanhua District Office Building, Taiwan	2016 Meinong (Taiwan)	Photographs and observations	Column diagonal cracking
10	7-story frame and wall with masonry infill building Residential building in Mexico	2017 Puebla (Mexico)	Photographs and observations	Damage to masonry infill panels and perimeter masonry spandrel frames

All structures were analyzed with a selection of software tools using the nonlinear dynamic procedures described in ASCE 41-17, and six of the structures were also analyzed using linear dynamic procedures described in ASCE 41-17. In order to examine collapse sensitivity of study buildings, the models were pushed beyond the

This publication is available free of charge from: https://doi.org/10.6028/NIST.GCR.22-917-50

intensity or record of shaking experienced in the damaging earthquake to create limit state fragilities.

In addition, evaluation and assessment methods documented in FEMA P-2018, *Seismic Evaluation of Older Concrete Buildings for Collapse Potential* (FEMA, 2018c), *Eurocode 8* (European Committee for Standardisation, 2005), and *The Seismic Assessment of Existing Buildings* (NZSEE et al., 2017), were implemented on selected buildings to better understand the requirements and capabilities of these methodologies and bring forward any relevant recommendations for improving ASCE 41. Component fragilities in FEMA P-58 (FEMA, 2018b) were used to map model component response to damage for selected buildings.

11.2 Results from ASCE 41 Studies

Chapters 3 through 10 present detailed information about the structure geometry, seismic demand, observed performance, analytical models, and evaluation results, as well as a summary documenting relative comparison of analytical results to observed performance at global and component levels.

Chapter 2 provides an overview of the project approach for comparing analytical results obtained from models developed in accordance with ASCE 41-17 provisions to observed performance of buildings. In this project, multiple models were created for all buildings in order to study the implications of various modeling approaches for element behavior on the simulated building response. The simulated building response could then be compared to the response of observed structures to assess which approach led to better estimates of observed building response. In practice, engineers may not create multiple models with varying modeling approaches as they do not know how the structure will actually behave in a major seismic event.

This section presents a summary of results, compared both quantitatively and qualitatively, in order to draw broader conclusions. The comparisons examine both component and global response and damage. For structures with either measured data (shaketable testing) or accelerometer data (instrumented buildings) , responses from the model and the actual building can be directly compared. For non-measured buildings where the performance is documented in photographs and observations, the comparison is based on qualitative observations of the type and distribution of damage and drift demands from comparable test specimens, as described in Section 2.3.1.

Studies documented in Chapters 3 through 10 include both direct implementation of ASCE 41-17 procedures with simple evaluation objectives and selected investigations for potential methods for improving evaluation results by implementation of changes to the modeling assumptions. The results presented in this section present comparison of results from models that are considered to reflect a

This publication is available free of charge from: https://doi.org/10.6028/NIST.GCR.22-917-50

typical application of ASCE 41-17 provisions by practicing engineers. The creation of the models began by following the provisions and recommendations of ASCE 41-17 as closely as possible. Further iterations of the models were based on decisions made where ASCE 41-17 provisions were unclear or provided latitude to the modeling approach. Examples of these modifications include modeling of masonry infill, considerations of joint nonlinearity, consideration of biaxial column loading, and member stiffness values. Studies also included use of different analysis software; it is noted that results from application of different analytical tools vary due to modeling decisions by the authors. Further, the results of this study are not sufficient to make conclusions about software selection. Also note that linear models were only developed for six buildings; 10-story test frame and wall structure (2015 E-Defense) and 7-story frame and wall with masonry infill building in Mexico are not included in tables for linear results.

11.2.1 Global Response

At the global level, the comparison examines the following questions, introduced in Chapter 2:

- **Did the model predict the correct story mechanism and location within the building?** This comparison applies to all study buildings.
- **Did the model accurately predict the value of the drift at critical story?** Computed drifts are compared to the observed or measured drifts at the expected critical story. Accuracy of drifts is judged to be a match if the difference between the modeled and measured value is within 20%. For non-measured buildings, the comparison is based on deformations in comparable test specimens as described in Section 2.3.1.
- **Did the model predict the value of the drift at stories other than critical?** Computed drifts are compared to the observed or measured drifts elsewhere within the structure. Accuracy of drifts is judged to be a match if the difference between the modeled and measured value is within 20%. For non-measured buildings, the comparison is based on deformations in comparable test specimens as described in Section 2.3.1.
- **Did the model predict the floor and roof accelerations?** This comparison only applies to measured buildings. Accuracy of peak floor accelerations is judged to be a match if the difference between the modeled and measured value is within 20%.
- **Did the model predict the value of residual drift at roof?** This comparison only applies to measured buildings. Accuracy of residual drift is judged to be a match if the difference between the modeled and measured value is within 20%.

This publication is available free of charge from: https://doi.org/10.6028/NIST.GCR.22-917-50

Tables 11-2 and 11-3 summarize the comparison results for nonlinear and linear models, respectively. (M) indicates match; (O) indicates overprediction; (U) indicates underprediction in accordance with the comparison metrics discussed above. No Match indicates that the results were not consistent; N/A indicates that this comparison cannot be conducted.

Table 11-2 Global Response for Nonlinear Models

Structure	Model(1)	Story Mechanism	Drift at Critical Location	Drift Elsewhere	Acceleration	Residual Drift
3-story test frame	Perform3D Frame	M	M	U	O	O
4-story test frame and wall	OpenSees Frame LP NJ	No Match	U	M	O	M
	OpenSees Wall LP NJ	M	M	O	U	O
	Perform3D Frame LP NJ	M	M	M	M	M
	Perform3D Wall LP NJ at Frames and Fiber Wall Elements	M	M	O	U	O
10-story test frame and wall	OpenSees Frame – Fiber NJ Option 2	M	M	M	O	M
	OpenSees Wall Fiber NJ Option 2	M	U	O/U(3)	O	M
	Perform3D Frame LP NJ at Frames	No Match	U	U	U	M
	Perform3D Wall LP NJ at Frames and Fiber Wall Elements	No Match	U	M	M	O
6-story frame and wall	OpenSees without SSI	M	M	U	M	M(2)
7-story frame	OpenSees without SSI	No Match	M	M	M	M(2)
5-story wall (New Zealand)	Linear Shear Spring for Wall	M	M	M	N/A	N/A
	Nonlinear Shear Spring for Wall	No Match	M	U	N/A	N/A
3-story frame with masonry infill (Taiwan)	Moment Rotation for Column	M	U	M	N/A	M(2)
	Fiber for Column	No Match	U	O	N/A	M(2)
7-story frame and wall with masonry infill (Mexico)	Frame Direction	M	M	M	N/A	M(2)
	Wall Direction	M	M	M	N/A	M(2)

(1) Refer to Chapters 3 to 10 for model details: Lumped plasticity (LP), nonlinear joint modeling (NJ), soil-structure interaction (SSI).

(2) Simulated results and observed buildings showed no signs of residual drift, and the results are therefore considered a match.

(3) O/U indicates that while some results were overpredicted(O), some were underpredicted (U).

This publication is available free of charge from: https://doi.org/10.6028/NIST.GCR.22-917-50

Table 11-3 Global Response for Linear Models

Structure	Story Mechanism	Drift at Critical Location	Drift Elsewhere	Acceleration
3-story test frame	M	U	O	O
4-story test frame and wall – Frame model	M	M	M	N/A
	M	U	U	N/A
4-story test frame and wall – Wall model	M	U	U	N/A
6-story frame and wall	M	U	U	O
7-story frame	No Match	O	O	N/A
5-story wall	M	N/A	N/A	N/A
3-story frame with masonry infill	M	U	N/A	N/A

The ability of the nonlinear and linear analysis models to predict the global response of the structural behavior is evaluated by comparing the observed and modeled story mechanism location for all structures. In structures that did not collapse, the story mechanism location is taken as the story with the highest concentration of damage. Proper identification of the story mechanism is judged based on whether the model was able to predict the story location with the highest levels of damage as compared to the observed behavior, as defined by subjective engineering judgement.

Where available, Tables 11-2 and 11-3 include comparison of drift, acceleration, and residual drift. Although these response parameters are generally not used as performance measures in ASCE 41 evaluation procedures or when estimating the collapse probability of a structure, they are used when estimating seismic damage and losses. Over or underprediction of these parameters can have significant impact on loss estimation results and the validity of the results should be carefully assessed. Further, interstory drifts are strongly correlated with plastic hinge rotations and chord rotations that are the basis for ASCE 41 evaluations.

The following bullets in **bold** present general conclusions observed from summary results; discussion in *italics* presents additional information and exceptions, where present.

- **Linear and nonlinear models predict the story with the most damage.**
- **Nonlinear models generally match drifts at the critical location, defined as drifts at the story with the highest level of damage.**
    - *Nonlinear analysis models accurately captured drifts at the critical story location with the exception of the 4-story test frame and wall (2010 E-*

This publication is available free of charge from: https://doi.org/10.6028/NIST.GCR.22-917-50

Defense) OpenSees model in the frame direction, 10-story test frame and wall (2015 E-Defense) OpenSees model in the wall direction, and the 3-story frame with masonry infill building in Taiwan.

- **Linear models generally underpredict drifts at the critical location, defined as the drifts at the story with the highest level of damage.**
    - *Drifts calculated by linear models at the critical location do not accurately match the measured behavior, with most of models underpredicting and the remaining model overpredicting. These results suggests that linear models may produce unconservative estimations of drift at critical locations. However, the level of damage was overpredicted at the critical location based on the acceptance criteria.*
- **Neither linear nor nonlinear models accurately predict the drifts at other, non-critical locations.**
    - *No consistent trends were observed in the results to explain why some models overpredict and some underpredict the drift.*
- **Nonlinear models overpredict residual drifts in the buildings with the highest levels of observed damage.**
    - *This is likely due to the shape of nonlinear hysteretic curves used in the nonlinear models: the pinched nature of true hysteric behavior is generally not captured accurately by nonlinear models, the absence of which tends to increase residual displacements.*
- **Nonlinear models generally match or overpredict measured accelerations.**
    - *Floor accelerations predicted by nonlinear models match or overpredict measured values by as much as 60%. Accelerations at the roof level generally match measured values better than accelerations at lower levels.*
- **Linear methods greatly overpredict measured accelerations.**
    - *Accelerations from linear dynamic response history and response spectrum models overpredict floor accelerations significantly because yielding of the structure is not modeled directly.*

11.2.2 Component-Based Response

The ability of analysis models to predict the response of structural elements (components) is evaluated by comparing the observed component failure mechanism to that predicted by the model for each component, as well as the level of damage throughout the structure for each component. Table 11-4 summarizes the generalized result for nonlinear models for each structure.

This publication is available free of charge from: https://doi.org/10.6028/NIST.GCR.22-917-50

Table 11-4 Component-Based Response for Nonlinear Models

Structure	Component*	Observed Failure Mechanism	Level of Damage at Critical Location	Level of Damage Everywhere Else
3-story test frame	Columns	M	O	M
	Beams	M	M	M
	Joints	M	M	M
	Walls	N/A	N/A	N/A
4-story test frame and wall	Columns	M	M	M
	Beams	M	O	O
	Joints	M	M	O
	Walls	No Match	M	M
10-story test frame and wall OpenSees NJ Option 2	Columns	M	M	M
	Beams	M	M	M
	Joints	M	U	M
	Walls	M	M	M
6-story frame and wall	Columns	M	O	M
	Beams	M	M	M
	Joints	M	M	M
	Walls	M	M	M
7-story frame	Columns	No Match	U	U
	Beams	No Match	O	O
	Joints*	No Match	U	M
	Walls	N/A	N/A	N/A
5-story wall Linear Shear Spring for Wall	Columns	No Match	O	N/A
	Beams	M	M	N/A
	Joints	No Match	U	N/A
	Walls	M	M	N/A
3-story frame with masonry infill	Columns	M	U	M
	Beams	M	M	M
	Joints	M	M	M
	Walls	No Match	U	M
7-story frame and wall with masonry infill	Columns	M	M	M
	Beams	M	M	M
	Joints	M	M	M
	Walls	M	M	M

* Joints were modeled as elastic elements and demand-to-capacity ratios from the simulation were less than 1.0.

This publication is available free of charge from: https://doi.org/10.6028/NIST.GCR.22-917-50

The following bullets in **bold** present general conclusions observed from summary results; discussion in *italics* presents additional information and exceptions, where present.

- **Analytical results generally match observed component failure mechanism with a few exceptions**

  For the 4-story test frame and wall structure (2010 E-Defense) and 7-story frame building in California, nonlinear analysis models overpredict flexural damage in the beam elements compared to the response observed in the actual structures. This is because the beam element modeling parameters currently specified by ASCE 41-17 used in the analytical models underpredict the deformation capacity of the beams, which causes the beams to yield and limits the demands imposed on the columns and joints. For the 7-story frame model, the joints were modeled as elastic, based on the results of a mechanism analysis which showed that they have sufficient capacity to develop the beams. However, the joints were observed to have shear damage that was not predicted by the model. For the 7-story frame model, the demands on the columns were capped by the yielding beams, leading to low flexural demands on the columns. The columns in the actual structure showed high levels of shear damage, which was not captured by the analysis model.

  - *For the 10-story test structure (2015 E-Defense), a mechanism analysis per ACI would suggest that the joints should remain elastic. However, the observed behavior and the models with joint nonlinearity included showed damage to the joints. This suggests that a mechanism evaluation may not reliably predict the relative distribution of demands in the beam and joint, but might still capture the global story drift demands.*
  - *Nonlinear results for wall component behavior for the 4-story test structure (2010 E-Defense) and 5-story wall building in New Zealand did not match the observed failure model. For the 4-story test structure, the observed performance of the walls showed sliding behavior at the base after the failure of the boundary elements. ASCE 41-17 does not currently provide modeling or acceptance criteria for wall sliding behavior, and therefore, this behavior was not captured by the models. For the 5-story wall building, the analysis model predicted shear failure of the walls that is not believed to have occurred in the actual structure. The current ASCE 41-17 modeling requirements for shear in walls show that this mode would be the controlling mechanism. When wall shear behavior was modeled using elastic elements, the model correctly captured the compression failure of the walls.*

This publication is available free of charge from: https://doi.org/10.6028/NIST.GCR.22-917-50

- **Analytical results generally match or overpredict the observed level of damage at the critical location**
    - *Nonlinear analysis models, with the exception of the 7-story frame and wall building in California, overpredict the level of damage in column and beam elements where columns in the building were capacity-protected by the beams. In addition, the model for the 3-story frame with masonry infill building in Taiwan also predicted less damage to column elements than observed in the actual building.*

11.2.3 Component-Based Acceptance Criteria Assessment

The ability of the analysis models to predict the state of components related to the ASCE 41-17 acceptance criteria is evaluated by comparing simulated performance levels and the qualitative damage descriptions provided in ASCE 41-17 Table C2-4 to the observed damage in critical components. Tables 11-5 and 11-6 summarize the results for nonlinear and linear models, respectively.

The tables summarize acceptance criteria at critical location in terms of the range of Structural Performance Levels as defined in ASCE 41-17 and discussed in Section 2.2 with reference to Figure 2-1 as follows:

- "Limited" damage occurs if the damage description is less than Immediate Occupancy (IO). Damage in this range is denoted as < IO.
- "Moderate" damage occurs if the damage description is more than Immediate Occupancy (IO) but less than Collapse Prevention (CP). Damage in this range is denoted IO – CP.
- "Severe" damage occuris if the damage description exceeds Collapse Prevention (CP). Damage in this range is denoted as > CP.

The following bullets in **bold** present general conclusions observed from summary results; discussion in *italics* presents additional information and exceptions, where present.

- **Both linear and nonlinear methods generally match the observed performance level damage range, but overpredict how far beyond the Collapse Prevention performance level the elements have been pushed.**
    - *Both linear and nonlinear analysis models generally predict exceedance of the Collapse Prevention acceptance criteria correctly. However, in many cases, analysis models predict demands several times higher than the acceptance criteria and thus overpredict the level of damage.*

This publication is available free of charge from: https://doi.org/10.6028/NIST.GCR.22-917-50

Table 11-5 Component-Based Acceptance Criteria at Critical Location for Nonlinear Models

Structure	Component	Observed damage	Model Prediction	Observed v. Model
3-story test frame	Columns	>CP	>CP	M
	Beams	IO-CP	IO-CP	M
	Joints	IO-CP	IO-CP	M
	Walls	N/A	N/A	N/A
4-story test frame and wall	Columns	IO-CP	IO-CP	M
	Beams	IO-CP	>CP	O
	Joints	>CP	>CP	M
	Walls	>CP	>CP	M
10-story test frame and wall	Columns	IO-CP	IO-CP	M
	Beams	IO-CP	IO-CP	M
	Joints	IO-CP	IO-CP	M
	Walls	IO-CP	IO-CP	U
6-story frame and wall	Columns	>CP	>CP	M
	Beams	IO-CP	IO-CP	M
	Joints	<IO	<IO	M
	Walls	IO-CP	IO-CP	M
7-story frame	Columns	>CP	IO-CP	U
	Beams	IO-CP	IO-CP	M
	Joints	IO-CP	Not Modeled	Not modeled
	Walls	N/A	N/A	N/A
5-story wall	Columns	IO-CP	>CP	O
	Beams	IO-CP	<IO	M
	Joints	>CP	<IO	U
	Walls	>CP	>CP	M
3-story frame with masonry infill	Columns	LS-CP	IO-LS	U
	Beams	<IO	<IO	M
	Joints	<IO	<IO	M
	Walls	N/A	N/A	N/A
7-story frame and wall with masonry infill	Columns	IO-CP	<IO	U
	Beams	IO-CP	<IO	U
	Joints	IO-CP	<IO BD	U
	Walls	IO-CP (conc), >CP (masonry)	<IO (conc), > CP (masonry)	U (conc) M (masonry)

Note: CP = Collapse Prevention; IO = Immediate Occupancy; IO-CP = Range between Immediate Occupancy and Collapse Prevention

This publication is available free of charge from: https://doi.org/10.6028/NIST.GCR.22-917-50

Table 11-6 Component-Based Acceptance Criteria at Critical Location for Linear Models

Structure	Component	Observed Damage	Model Prediction	Observed v. Model
3-story test frame	Columns	>CP	>CP	M
	Beams	IO-CP	IO-CP	M
	Joints	IO-CP	IO-CP	M
	Walls	N/A	N/A	N/A
4-story test frame and wall	Columns	IO-CP	>CP	O
	Beams	IO-CP	>CP	O
	Joints	>CP	>CP	M
	Walls	>CP	>CP	M
6-story frame and wall	Columns	>CP	>CP	M
	Beams	IO-CP	>LS	O
	Joints	<IO	>CP	O
	Walls	IO-CP	>CP	O
7-story frame	Columns	>CP	>CP	O
	Beams	IO-CP	IO-CP	M
	Joints	>CP	>CP	M
	Walls	N/A	N/A	N/A
5-story wall	Columns	unknown	IO-CP	unknown
	Beams	unknown	IO-CP	unknown
	Joints	>CP	>CP	M
	Walls	>CP	>CP	M
3-story frame with masonry infill	Columns	IO-CP	>CP	M
	Beams	<IO	<IO	M
	Joints	<IO	<IO	M
	Walls	N/A	<IO	M

Note: CP = Collapse Prevention; IO = Immediate Occupancy

- *Further, analysis models predict several components to exceed Collapse Prevention acceptance criteria while the observed level of damage suggest better performance than Collapse Prevention in some of these components.*

- **Linear analysis models predict damage in elements that would be capacity-protected by failure or yielding of other components in the load path.**
  - *Linear models show that the Collapse Prevention acceptance criteria are exceeded in many components that otherwise would have been capacity-protected by other yielding elements in the structure. This could lead to the conclusion that elements that are capacity-protected by other*

This publication is available free of charge from: https://doi.org/10.6028/NIST.GCR.22-917-50

elements are deficient or require retrofit. This could incorrectly identify vulnerabilities that do not exist in the actual structure.

11.2.4 Global Acceptance Criteria Assessment

The ability of analysis models to predict the expected state of the structure regarding the Structural Performance Level per ASCE 41-17 Tables C2-3 and C2-4 and to identify the most vulnerable components for retrofit is evaluated by considering the overall global behavior of the analysis models versus the observed performance. Tables 11-7 and 11-8 summarize the results for nonlinear and linear models, respectively.

Table 11-7 Nonlinear Global Acceptance Criteria

Structure	Model	Performance Level	Most Vulnerable Components for Retrofit
3-story test frame		M	M
4-story test frame and wall	OpenSees	M	M
	Perform3D	M	M
10-story test frame and wall	OpenSees	M	M
	Perform3D	M	M
6-story frame and wall		M	M
7-story frame		U	No Match
5-story wall		M	No Match
3-story frame with masonry		M	M
7-story frame and wall with masonry infill		M	M

Table 11-8 Linear Global Acceptance Criteria

Structure	Performance Level	Most Vulnerable Components for Retrofit
3-story test frame	M	M
4-story test frame and wall	M	No Match
6-story frame and wall	M	M
7-story frame	M	M
5-story wall	M	M
3-story frame with masonry	M	M

In general, the following are observed:

This publication is available free of charge from: https://doi.org/10.6028/NIST.GCR.22-917-50

- **Both linear and nonlinear methods accurately predict the overall Performance Level of the observed structure.**
    - *Most of the structural model simulations identified a number of elements exceeding the Collapse Prevention criteria to an extent much higher than the observed structures' global state would suggest.One exception is the 7-story frame building in California (Chapter 7) where the simulation did not identify the high level of observed damage to the concrete columns. It is noted that the buildings studied for this project were subjected to shaking intensities that led to significant levels of structural damage. Therefore, meaningful comparisons of performance at lower levels of shaking are not possible.*
- **Both linear and nonlinear methods predict the most vulnerable components; however, the failure mechanism in those elements is not always correct.**
    - *Both linear and nonlinear analysis evaluation methods correctly predict the most vulnerable components that would likely have required retrofit for most of the simulations. The exceptions include the 4-story test frame and wall structure (2010 E-Defense) and 7-story frame building in California, where higher levels of damage at beam elements were predicted by the simulations compared to the low level of damage observed. This discrepancy is likely related to the beam modeling parameters and acceptance criteria in ASCE 41-17 that underpredict the beam flexural deformation capacities and acceptable deformations, which produce beam flexural failure that was not observed. Additionally, underestimation of flexural capacities of beams due to potential axial loads could lead to incorrect mechanism hierarchy.*
    - *Nonlinear models for 4-story test frame and wall (2010 E-Defense) and 5-story wall building in New Zealand did not capture the correct wall failure mode. In the case of the 4-story test, the actual test structure showed both sliding and flexural failure at the base. Sliding was not modeled in the simulation model as ASCE 41-17 does not provide guidance for this failure mode. For 5-story wall building, the models predicted shear failure in the walls that is not believed to have occurred in the actual structure. However, even though the models did not predict the observed failure mode, the overall expected global performance of the structure matched the Performance Level indicated by observation.*

11.3 Comparison of Global Fragility Curves

All buildings were evaluated to develop global fragility curves representing probability of collapse and other limit states, including ASCE 41 acceptance criteria and modeling paramters as a function of ground motion intensity. The results can be

This publication is available free of charge from: https://doi.org/10.6028/NIST.GCR.22-917-50

useful to compare the component-based acceptance criteria that define acceptance in ASCE 41-17 versus global-based acceptance criteria.

Some of the buildings exhibited large differences between the component acceptance criteria and global acceptance criteria. For example, in the 3-story test frame, on average, collapse (defined as when interstory drifts exceed 6%) is reached at a shaking intensity of 1.4 times the shaking intensity at which the first component reaches the Collapse Prevention limit state. A similar ratio of collapse to first component reaching Collapse Prevention is observed for the 4-story test frame and wall (2010 E-Defense). For the 6-story frame and wall building in California, this ratio is 1.7. In these buildings, when the global response is defined by an "unacceptable response" limit state (i.e., before the element deformation exceeds $1.5 \times b$), there is significant reserve capacity between the first component reaching Collapse Prevention and a global limit state. These buildings have some brittle columns and some ductile columns, so the more ductile columns "support" the system and delay collapse. In particular, in the 3-story test frame, two of the columns are ductile and the other two are brittle due to how the experimental specimen was designed; in the 6-story frame and wall building, the tops of all columns are much more ductile than the bases. In contrast, results for the 3-story frame building with masonry infill in Taiwan show component-based fragility curves that are similar to the global fragility curve. The columns in the first (critical) story of the building are all brittle and fail nearly simultaneously.

These results indicate that structures that fail the current component-based ASCE 41-17 Collapse Prevention criteria may have very different reserve capacities. On one extreme, the 3-story frame building in Taiwan is expected to be very close to collapse. On the other extreme, other buildings, such as the 6-story frame and wall building in California may have significant reserve capacity. These findings indicate a need for a more consistent definition of ASCE 41 global acceptance criteria.

11.4 Results from Additional Studies

11.4.1 FEMA P-2018 Evaluations

Four structures (3-story test frame, 4-story test frame and wall (2010 E-defense), 5-story wall building in New Zealand, and 3-story wall with masonry infill building Taiwan) were evaluated using the procedure outlined in FEMA P-2018, *Seismic Evaluation of Older Concrete Buildings for Collapse Potential*. The methodology provided a reasonable performance evaluation and correctly estimated the critical direction and critical story for three of the structures (3-story Test, 4-story Test, and 5-story New Zealand).

The 3-stoy Taiwan building was evaluated prior to update of FEMA P-2018 to address masonry infill, and the results were not consistent with the observed damage.

This publication is available free of charge from: https://doi.org/10.6028/NIST.GCR.22-917-50

The observed story mechanism was not identified and the building vulnerability was underestimated. Although the captive-column effect of the partial-height masonry infill was included in the evaluation, full consideration of masonry infill effects in compliance with FEMA P-2018 may help resolve these inconsistencies.

The FEMA P-2018 methodology provides an alternative perspective of evaluating building seismic performance to that of the ASCE 41 Tier 3 methodology by providing a single rating representing the seismic performance of a building. Since ASCE 41 is a component-based evaluation approach, the global performance is not as easily quantified. As such, the FEMA P-2018 rating complements the limitations of ASCE 41. The deformation capacities implemented in FEMA P-2018 are generally based on the nonlinear acceptance criteria in ASCE 41-17. Therefore, the FEMA P-2018 methodology may provide a valuable single rating both complementary and consistent with the ASCE 41 approach for both linear and nonliear evaluations. The FEMA P-2018 approach, which utilizes a weighted average of the component ratings in a critical story, can be implemented in a future version of ASCE 41 if a parameter representing the overall seismic performance of a structure is required.

The FEMA P-2018 procedure, which is based on the plastic mechanism analysis, may provide supplemental information in the cases where the ASCE/SEI 41 linear analysis is implemented. In the ASCE 41 linear static and dynamic procedures, the seismic loads are distributed to a structure based only on stiffness and not based on strength. Therefore, the redistribution and concentration of the seismic demand is not always captured adequately in a linear analysis. The FEMA P-2018 methodology provides engineering parameters such as drift distribution and mechanism development that would be used to understand the nonlinear behavior of a structure without implementing full nonlinear analysis. The level of effort to perform FEMA P-2018 evaluation is similar to that of a comprehensive ASCE 41 Tier 3 linear analysis utilizing a three-dimensional computer model. However, once the component capacities are calculated for the linear evaluation, the FEMA P-2018 evaluation can be performed without a significant additional effort.

11.4.2 Eurocode Evaluations

Two structures, 6-story frame and wall building in California and 4-story test frame and wall (E-Defense 2010) were assessed using the acceptance criteria in Eurocode 8 (2005). For this study, fragility curves were developed for the Eurocode Near Collapse acceptance criteria as described in Sections 2.3 and 2.4.2 and were compared with the acceptance criteria fragility curves from ASCE 41. The same ASCE 41 model was used for both the ASCE 41 and Eurocode acceptance criteria fragility curves.

This publication is available free of charge from: https://doi.org/10.6028/NIST.GCR.22-917-50

In general, this study found that the Eurocode Near Collapse acceptance criteria for columns are less sensitive to column axial loads and transverse reinforcement detailing. Therefore, depending on column properties, Eurocode performance evaluation may be more or less conservative in relation to ASCE 41. However, when global performance is based on the performance of multiple components, ASCE 41 and Eurocode provide similar results because the differences in the component acceptance criteria are essentially averaged. This observation indicates that acceptance criteria based on global behavior, rather than component behavior, are less sensitive to individual component acceptance criteria that may differ from standard to standard.

11.4.3 NZSEE Assessments

The 4-story test frame and wall structure (2010 E-Defense) was evaluated in accordance with NZSEE *Guidelines.* The lateral base shear capacity calculated from the pushover analysis for the frame direction was much lower than the capacity predicted from the ASCE 41-17 Nonlinear Dynamic Procedure and the measured experimental value. In the wall direction, both ASCE 41-17 nonlinear dynamic and NZSEE pushover analysis underestimated the measured experimental base shear capacity. The hierarchy method in NZSEE *Guidelines* is meant to identify the first element to suffer damage. In its application to this building, the result was similar to that of the ASCE 41 Nonlinear Dynamic Procedure and the experiment in that all three showed damage in the joints and beams. The difference was that both the experiment and ASCE 41 Nonlinear Dynamic Procedure results showed that the building had significant deformation and base shear capacity beyond that point where joint damage was initiated, and the hierarchy method in the NZSEE *Guidelines* is not suited to determine capacities beyond element failure.

The 5-story wall building in New Zealand was previously evaluated using the NZSEE *Guidelines* in work by Beca (2011). This work reported that the demands from the 2011 Christchurch Earthquake were 5.8 times the estimated capacity from pushover analysis. This is consistent with the ASCE 41-17 findings where the results showed large DCR/*m* for Collapse Prevention using the ASCE 41-17 linear analysis procedures, and simulated collapse using the ASCE 41-17 nonlinear analysis procedures.

11.4.4 FEMA P-58 Damage Assessments

One part of the FEMA P-58 assessment methodology was used to map simulation results to damage descriptors that can be used to compare model output to observed damage for two non-measured buildings, 6-story frame and wall building in California and 3-story wall building with masonry infill in Taiwan. This

This publication is available free of charge from: https://doi.org/10.6028/NIST.GCR.22-917-50

methodology links engineering demand parameters from nonlinear simulation models to damage in components. The approach is described in Section 2.3.2.

The 6-story frame and wall building in California contained some first-story columns classified as low axial load and others classified as high axial load, due to variation in axial demands over the plan of the building. For the shear-controlled columns with high axial loads, both the FEMA P-58 damage assessment and ASCE 41 backbones showed good agreement with the observed damage. For most shear-controlled columns with low axial loads, the FEMA P-58 matched observed damage well, while the ASCE 41 backbones overpredicted damage; this observation may indicate that ASCE 41 backbones may be overly conservative for shear-controlled columns with low axial loads. However, for the two corner shear critical columns on the east side of the building (with relatively low axial loads), ASCE 41 backbones matched the observed shear and axial failure well, while the FEMA P-58 damage assessment was inconsistent with the severity of the observed damage. This discrepancy may indicate either a lack of granularity in axial load classification for the FEMA P-58 fragilities (meaning two axial load categories cannot fully capture the range of response), or indicate damage from bi-axial column response that is not captured in FEMA P-58 in which components are assessed separately in the two building directions. For other components throughout the building (beams, joints, walls, and upper story columns) both the FEMA P-58 damage assessment and ASCE 41 backbones matched the observed damage, or lack-there-of, well.

The first-story columns of the 3-story building in Taiwan had relatively low axial loads, and the FEMA P-58 component damage fragilities were assigned accordingly. Both the ASCE 41 backbones and FEMA P-58 damage assessment underpredicted damage to the first-story columns, but this underprediction was more significant in the FEMA P-58 damage assessment. Although this result may be partially due to the underprediction of column plastic rotation demands in the ASCE 41 model, the underprediction from FEMA P-58 may be due to a lack of granularity in the axial load definition for shear controlled columns in the FEMA P-58 component fragility database. In addition, the first-story columns in the building are captive due to partial-height infill, which was reflected in the model, but FEMA P-58 does not include short-column fragilities that would be appropriate here.

Overall, these findings show that ASCE 41 backbones provide similar estimations of damage to the FEMA P-58 component fragilities. However, some discrepancies exist between ASCE 41 backbones and FEMA P-58 component fragilities for non-conforming shear-controlled columns with low axial loads. These discrepancies may be due to conservatisms in ASCE 41 backbones for shear critical columns, the discrete nature and lack of granularity in the FEMA P-58 component classifications for shear-controlled columns with low axial loads and captive columns, and lack of consideration of bi-axial response in the FEMA P-58 damage assessment procedures.

This publication is available free of charge from: https://doi.org/10.6028/NIST.GCR.22-917-50

Chapter 12
Findings and Recommendations

12.1 Overview

ASCE 41 is intended to serve as a tool used for the purpose of undertaking seismic evaluation or retrofit of existing buildings based on a selected Performance Objective. Therefore, one of the main goals of the procedures and requirements of ASCE 41 is to accurately estimate demands and damage levels to a wide range of building types to varying levels of seismic hazards. The focus of this project is to benchmark the performance of computer simulation models developed following the requirements of ASCE 41 to the performance of reinforced concrete buildings subjected to earthquake shaking. This chapter presents findings and recommendations based on the key trends arising from the studies summarized in the previous chapters. The findings are used to develop recommendations for consideration by the ASCE/SEI Seismic Rehabilitation of Existing Buildings Standards and ACI 369 Seismic Repair and Rehabilitation Committees in future editions of the standards.

The assessment comparisons rely on only one ground motion to evaluate the response of the structure while ASCE 41 aims to provide performance estimates to a wide range of ground motions with varying characteristics for each hazard level considered. Therefore, the results of this study do not pertain to the hazard and ground motion selection criteria of the standard. Additionally, while not required by ASCE 41, the impact of modeling and material uncertainties is not considered in this study. Future studies could expand this work to explicitly consider material and modeling decisions that result in variations among ASCE 41 compliant models to provide additional insights into how the standard could be improved. Further, most of the structures studied were subject to ground shaking levels that produced significant damage such that meaningful comparisons of performance could be made between simulated and observed response. Therefore, no attempt was made to assess the performance of buildings to low-to-moderate levels of shaking.

It is recognized that other seismic performance methodologies rely on analysis models and performance evaluations developed using the ASCE 41 Standard. Where applicable, findings and recommendations relating to these types of assessments are also provided.

This publication is available free of charge from: https://doi.org/10.6028/NIST.GCR.22-917-50

12.2 Key Takeaways from the ASCE 41 Studies

The results of this project show that ASCE 41 generally does an acceptable job at capturing the expected response and identifying the location of critical components for reinforced concrete structures subjected to strong ground motions.

12.2.1 Simulated Performance Estimates with Good Correlation to Observed Performance

- **Identification of Critical Damage Location.** Both linear and nonlinear models accurately predict the story levels with the highest levels of damage.
- **Drifts at Critical Locations.** Nonlinear models generally matched the observed level of drifts at the stories with the highest levels of damage. Linear models tended to underpredict the drifts at critical stories, but this did not lead to underestimation of damage at those locations.
- **Overall Performance Level.** Both linear and nonlinear models produce an overall structural performance level comparable to that of the observed structures. Most of the structures were shown to be beyond the Collapse Prevention acceptance criteria, and observed performance showed damage that would objectively be judged to be beyond Collapse Prevention. For the Mexico City building (Chapter 10), damage inferred from the simulated response generally matched the moderate levels of observed damage.

12.2.2 Simulated Performance Estimates with Mixed or Poor Correlation to Observed Performance

- **Mechanism Prediction.** The simulations provided mixed results when predicting the observed failure mechanisms. In some cases, the simulation predicted damage to beam elements, while the observed damage was in column elements. For concrete shear walls, the simulations were not able to capture sliding, and in some cases shear mechanisms were predicted that were not present in the observed condition. The simulated response of beam-column joints did not always match the observed behavior. In some cases, joints were observed to be damaged where a mechanism analysis would suggest that they would have adequate capacity to develop the elements framing into the joint.
- **Drifts at Noncritical Locations.** Drifts at non-critical locations over the height of the structure predicted by the simulated response did not provide a good match to the observed drifts at those locations. It is understood that these non-critical drifts are not a focus of attention for ASCE 41 when evaluating the response of structures near collapse. However, other assessment methodologies that rely on these drift profiles may be affected by these inaccuracies.
- **Floor Accelerations.** Nonlinear simulation models tended to overestimate the floor accelerations compared to the measured response. The linear simulation

This publication is available free of charge from: https://doi.org/10.6028/NIST.GCR.22-917-50

models greatly overpredict accelerations since yielding of the structure is not considered. Similar to drifts, while accelerations are not typically directly used for structural response evaluation, they are sometimes to determine the demands on select structural and nonstructural elements. Additionally, other assessment methodologies that rely on these acceleration profiles may be affected by these inaccuracies.

- **Residual Drifts.** The simulated response generally overpredicts residual drift in the buildings with the highest levels of observed damage.
- **Element-Level Acceptance Criteria.** The element-level damage based on the acceptance criteria for the simulated response tends to overestimate the damage compared to that of the observed structures. In many cases, the simulations produce element deformation demands that were several times beyond the ASCE 41 acceptance criteria, while the observed damage would generally not be judged to have reached that level of damage.

12.3 Recommendations for Improving ASCE 41

12.3.1 Consideration of Uncertainty of Element Strength and Deformation Capacities Related to Hierarchy of Mechanism Formation

ASCE 41-17 currently considers uncertainty in deformation capacities related to acceptance criteria. However, the provisions only require that elements be modeled with a single strength-deformation relationship. Accordingly, the use of a single representation of element capacities for analysis may not capture conditions where the relative capacities of the elements vary from the assumed conditions. This could lead to identifying the incorrect failure mechanism, and over or underestimation of building response. For example, where the relative strengths of beam and columns control which element contributes to the mechanism formation and distribution of deformations between elements, consideration of a single strength capacity for each element may incorrectly identify the vulnerable component. An underestimation of beam flexural capacity could suggest that the beams would yield and protect the columns from damage. If the actual beam flexural capacity was higher than the value used in the analysis, the actual damage may be concentrated in the columns rather than the beams. It is recommended that modeling of elements consider uncertainty in the strengths and modeling parameters to account for possible differences in the relative capacities of elements of the as-built elements. The impact on building performance and mechanism formation of these assumptions and different modeling strategies should be studied and quantified to better understand the range of potential structural response.

This publication is available free of charge from: https://doi.org/10.6028/NIST.GCR.22-917-50

12.3.2 General Element Modeling

The modeling and acceptance criteria for deformation-controlled elements are typically dependent on the level of axial and shear load present in the element. It is often unclear how these axial loads and shear loads are to be determined. It is recommended that where these parameters are required, clear, consistent guidance be provided to the user for methods to determine the appropriate demands.

Additional element-specific recommendations include:

Shear Wall Elements

- Wall shear behavior modeling parameters need further research and improved recommendations. This includes the overall shape of the backbone curves for shear response, in addition to consideration of the shear strength provided by walls loaded out-of-plane.
- Wall shear sliding modeling parameters need to be addressed by the standard. It is understood that at the time of this publication this topic is being considered by the ACI 369 Committee.

Beam Elements

- Beam linear and nonlinear modeling and acceptance criteria need further research and improved recommendations. This includes both the deformation limits and the strength of these elements. It is possible that the presence of axial loads in concrete beam elements could have substantial impact on the flexural strength of these members. Where the strengths of the beams compared to the columns and joints are relatively close, underestimation of beam strength could lead to the prediction of damage in the beams rather than the columns or joints. This could lead to underestimation of the hazard posed by potential column failure.

Columns

- Currently, the application of the modeling parameters and acceptance criteria is unclear for columns controlled by shear. The ASCE 41-17 modeling parameters and acceptance criteria should clearly distinguish the different requirements for shear-controlled vs. flexure-controlled columns and how the modeling parameters should be applied for each condition.

Beam-Column Joint Elements

- The strength and nonlinear response of beam-column joints currently specified in the ASCE/SEI 41 document does not correctly capture the observed performance of the joints for the buildings in this project. Further research is needed to improve the prediction of strength and nonlinear deformation behavior of these elements.

This publication is available free of charge from: https://doi.org/10.6028/NIST.GCR.22-917-50

Masonry Infill

- The current modeling requirements for masonry infill elements could be improved. The current version of ASCE/SEI 41 does not provide the user with clear direction as to how to include the effect of infill.

12.3.3 Acceptance Criteria for Collapse Prevention

It is suggested that ASCE 41 transition to the use of acceptance criteria based on global building performance rather than worst-case component performance. Basing Collapse Prevention performance acceptance on the behavior of individual deformation-controlled elements may lead to an overly conservative estimate of the global collapse potential of a building, and lead to inconsistent levels of conservatism across different buildings. Collapse assessment based on the impact of element damage on overall building stability are recommended.

12.3.4 Use of Limit-State and Mechanism Analysis to Augment Linear Evaluation Methods

Linear evaluation methods of buildings subject to intense ground motions have no direct means of assessing the impact of local yielding or global mechanism development on individual elements. Thus, if local limit-state evaluation is not considered, elements may be found to be deficient that would otherwise be capacity-protected by other yielding elements. Similarly, without identification of global mechanisms, elements in stories that would have limited demands due to yielding elsewhere in the structure may incorrectly be identified as deficient. It is recommended that linear evaluation methods include recommendations for limit-state evaluation of local mechanisms and consideration of global mechanism development such as those used by FEMA P-2018.

12.4 Opportunities for Future Work

Improved guidance for the following topics should be developed with basis on detailed studies:

- Modeling and performance evaluation of columns or joints subject to bidirectional shear loading.
- Modeling fiber-based elements. Currently, the modeling of fiber elements is typically based on the nonlinear stress-strain relation of the concrete and rebar elements. Although this has some advantages in that P-M-M interaction and cracking could potentially be captured directly, the cyclic behavior of elements with strength loss is not accurately represented with these fiber elements. Guidance on calibration of fiber elements such that the overall element behavior better matches cyclic testing of components is required.
- Modeling masonry infill.

This publication is available free of charge from: https://doi.org/10.6028/NIST.GCR.22-917-50

- Modeling of hysteretic behavior of nonlinear elements. This guidance should acknowledge the limitations of currently available commercial software.
- Estimation of relative story displacements and local mechanism development for linear procedures.

In addition, future studies can provide recommendations for:

- The impact of applying different modeling strategies
- Consideration of variability of element strength and deformation behavior as well as representation of the element response in the numerical model. This study may take the form of applying element properties in a random fashion within specified bounds.
- The impact of applying different combinations of local and global mechanisms for linear evaluations.

This publication is available free of charge from: https://doi.org/10.6028/NIST.GCR.22-917-50

Appendix A
Modeling of Elements per ASCE 41

This publication is available free of charge from: https://doi.org/10.6028/NIST.GCR.22-917-50

All study buildings were modeled in accordance with ASCE 41-17 Standard. In general, the modeling parameters for concrete elements were used directly from tables in ASCE 41-17 Chapter 10. In some cases, the modeling parameters were adjusted based on judgement or taken from testing of similar elements. This appendix describes the element modeling approaches used in accordance with ASCE 41-17, and it is best used with ASCE 41-17 as reference. Where identical provisions apply to different elements, the discussion is repeated for ease of reference. Refer to the individual chapter discussions for description of modeling parameters and acceptance criteria for masonry walls or masonry infill elements.

A.1 Material Properties and Component Strengths

Where evaluating the behavior of deformation-controlled actions, the expected strength, Q_{CE}, is used. Q_{CE} is defined as the mean value of resistance of a component at the deformation level anticipated for a population of similar components, including consideration of the variability in material strength, strain hardening, and plastic section development. Where evaluating the behavior of force-controlled actions, a lower-bound estimate of the component strength, Q_{CL}, is used. Q_{CL} is defined as the mean minus one standard deviation of the yield strengths, Q_Y, for a population of similar components.

Per ASCE 41-17 Section 10.3.2.2 and 10.3.2.3, the procedures specified in ACI 318 to calculate strengths may be used for both expected and lower-bound values, with the appropriate material strengths used (expected or lower-bound) with $\phi = 1$.

Mechanical properties of materials are obtained from available drawings, specifications, material testing, and utilizing material standards from the age of construction of the buildings.

A.1.1 Expected Material Properties

A.1.1.1 Material Properties Based on Testing

Expected material properties are based on mean values of tested material properties.

A.1.1.2 Material Properties Based on Drawing Information

Nominal material properties are taken as lower-bound material properties. Corresponding expected material properties are calculated by multiplying lower-

bound values by a factor taken from ASCE 41-17 Table 10-1 to translate from lower-bound to expected values.

A.1.2 Lower Bound Material Properties

A.1.2.1 Material Properties Based on Testing

Lower-bound material properties are based on mean values of tested material minus one standard deviation. Nominal material properties, or properties specified in construction documents, are taken as lower-bound material properties.

A.1.2.2 Material Properties Based on Drawing Information

Nominal material properties are taken as lower-bound material properties.

A.1.3 Concrete Material Nonlinear Properties

Unless otherwise noted in the chapters, where fiber elements are used to model flexure or axial behavior, unconfined concrete is modeled using the Hogestad model. Confined concrete is modeled using the Mander model when using Perform3D, and Concrete02 with modified Mander when using OpenSees.

When lumped plasticity models are used, behavior is defined by the backbone parameters provided in ASCE 41-17.

Fiber-type plastic-hinge models utilize one-dimensional material response models to predict the flexural response of a reinforced concrete (beam, column or wall) cross section. Numerous models exist in the literature for simulating the one-dimensional cyclic response of concrete and reinforcing steel. Figures A-1 and A-2 show examples of commonly used (a) concrete and (b) steel models available in OpenSees.

Fundamental characteristics of the concrete constitutive model are typically: (1) monotonic compressive strength expressed using a parabolic expression up to the peak strength $\left(f'_{ce}\right)$ and a linear descending post-peak response; (2) multi-linear unload-reload curve where reloading is bounded by the monotonic curve; and (3) damage-type response in tension. For confined concrete, compressive strength is increased using a confined concrete strength model. Models such as that proposed by Mander et al. (1988) and Saatcioglu and Razvi (1992) are used commonly; modification for elements with widely spaced ties or rectangular sections without support of every longitudinal bar is provided by Welt et al. (2017). A critical aspect of modeling reinforced concrete components that exhibit softening response is material regularization. Description of material regularization approaches is available elsewhere (NIST, 2017; Coleman and Spacone, 2012; Pugh et al., 2015; Almeida et al., 2016).

This publication is available free of charge from: https://doi.org/10.6028/NIST.GCR.22-917-50

This publication is available free of charge from: https://doi.org/10.6028/NIST.GCR.22-917-50

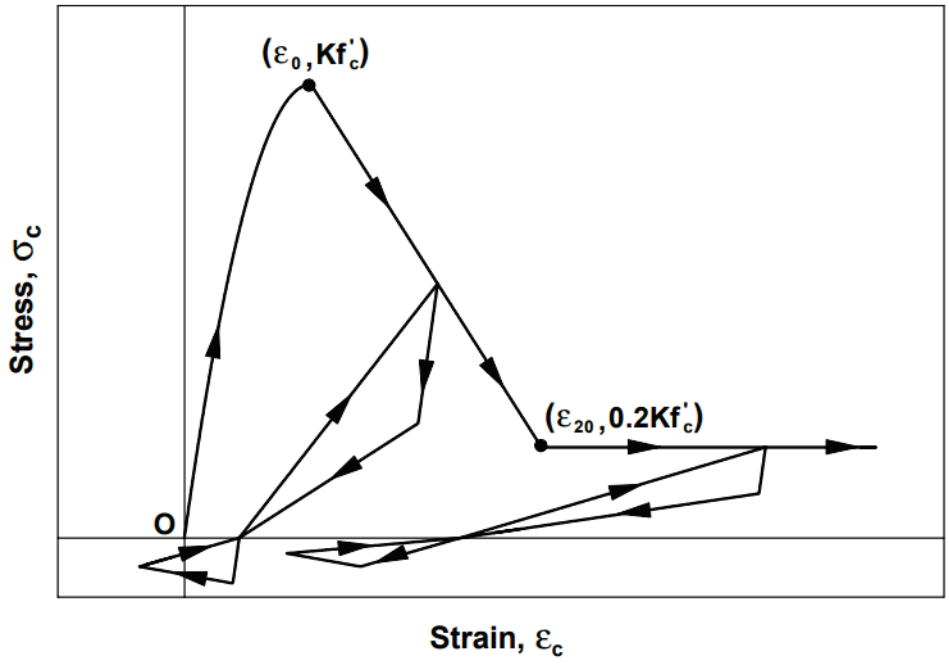


Figure A-1 Nonlinear cyclic concrete model, which employs the monotonic Modified Kent-Park model (Yassin, 1994; Scott et al., 1982) as presented by Orakcal et al. (2006). Note that compressive stress-strain is positive.

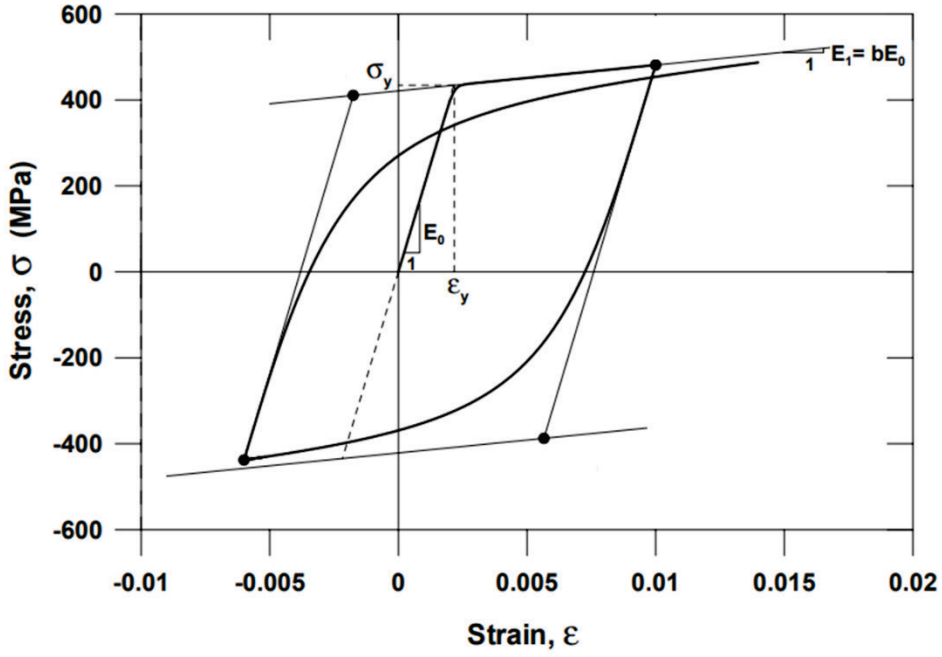


Figure A-2 Example of nonlinear reinforcing steel model for 60 ksi steel. Menegotto-Pinto-Filippou reinforcing steel model (1983) as presented by Orakcal et al. (2006). Note that tension stress-strain is positive.

A.1.4 Reinforcement Material Nonlinear Properties

Explicit modeling of the reinforcing steel properties may be required. In some cases (e.g., for the PF3D model in Perform3D), the reinforcement fiber definition is adjusted to ensure that overall member behavior matches the backbone parameters provided in ASCE 41-17. This is the exception. In most cases, the response of the longitudinal reinforcing steel model is modeled explicitly, preferably using a curvilinear unload-reload curve that simulates the Bauschinger effect (Figure A-2). Other response models that predict similar cyclic response histories may also appropriate for use.

A.2 Modeling of Beam Elements

A.2.1 Linear Analysis

A.2.1.1 Stiffness

Where design actions are determined using linear procedures, component effective stiffness correspond to the secant value to the yield point of the component. Alternatively, effective stiffness values per ASCE 41-17 Table 10-5 are used.

Gravity-load effects considered for effective stiffness of components are determined using ASCE 41-17 Equation 7-3.

$$Q_G = Q_D + Q_L + Q_S \qquad \text{(ASCE 41-17 Eq. 7-3)}$$

The-strength of beam elements are calculated considering a width of effective flange on each side of the web equal to the smallest of the following: the provided flange width; eight times the flange thickness; half the distance to the next web; or one-fifth of the beam span length.

Where the flange is in compression, the concrete and reinforcement within the effective width is considered effective in resisting flexure and axial load. Where the flange is in tension, longitudinal reinforcement within the effective width of the flange and developed beyond the critical section is considered fully effective for resisting flexure and axial loads. The portion of the flange extending beyond the width of the web is assumed to be ineffective in resisting shear.

The stiffness of the beam with flange is calculated based on the above effective flange width or twice of the value of I_g of the web alone.

Where longitudinal spacing of transverse reinforcement exceeds half the component effective depth, transverse reinforcement is assumed to have reduced effectiveness in resisting shear by a factor of $2(1 - s/d)$. Where longitudinal spacing of transverse reinforcement exceeds the component effective depth, transverse reinforcement is assumed ineffective in resisting shear.

This publication is available free of charge from: https://doi.org/10.6028/NIST.GCR.22-917-50

Development of splices of reinforcement is evaluated per ASCE 41-17 Section 10.3.5.

A.2.1.2 Strength

Flexural strength of beam elements is calculated using expected material properties. Shear strength of beam elements is calculated using lower-bound material properties. Development of splices of reinforcement are evaluated per ASCE 41-17 Section 10.3.5.

A.2.1.3 Demands

Deformation-controlled actions, Q_{UD}, are calculated in accordance with ASCE 41-17 Equation 7-34:

$$Q_{UD} = Q_G + Q_E \qquad \text{(ASCE 41-17 Eq. 7-34)}$$

where Q_G is determined per ASCE 41-17 Equations 7-1 and 7-2:

$$Q_G = 1.1(Q_D + Q_L + Q_S) \qquad \text{(ASCE 41-17 Eq. 7-1)}$$

$$Q_G = 0.9Q_D \qquad \text{(ASCE 41-17 Eq. 7-2)}$$

Force-controlled actions, Q_{UF}, are calculated in accordance with ASCE 41-17 Equation 7-35:

$$Q_{UF} = Q_G \pm \frac{\chi Q_E}{C_1 C_2 J} \qquad \text{(ASCE 41-17 Eq. 7-35)}$$

where χ is taken as 1.0 assuming Collapse Prevention and J is taken as 2.0 for High Seismicity.

A.2.1.4 Demand-to-Capacity Checks

Elements are checked using acceptance criteria. Deformation-controlled actions are evaluated using ASCE 41-17 Equation 7-36:

$$m\kappa Q_{CE} > Q_{UD} \qquad \text{(ASCE 41-17 Eq. 7-36)}$$

where m-factors are taken from ASCE 41-17 Table 10-13 and κ is assumed to be 1.0.

Force-controlled actions are evaluated using ASCE 41-17 Equation 7-37:

$$\kappa Q_{CL} > Q_{UF} \qquad \text{(ASCE 41-17 Eq. 7-37)}$$

where κ is assumed to be 1.0.

A.2.2 Nonlinear Analysis

The nonlinear load-deformation relationships are based on experimental evidence or taken from quantities specified in ASCE 41-17 Sections 10.4 through 10.12. For the nonlinear dynamic procedure (NDP), load-deformation relations define behavior

This publication is available free of charge from: https://doi.org/10.6028/NIST.GCR.22-917-50

under monotonically increasing lateral deformation and under multiple reversed deformation cycles.

Per ASCE 41-17 Section 10.3.1.2.2, the generalized load-deformation relation shown in ASCE 41-17 Figure 10-1 are described by linear response from A to an effective yield B, then a linear response at reduced stiffness from B to C, then sudden reduction in force resistance to point D, response at reduced resistance to E, then loss of strength beyond E. The slope from A to B is based on effective stiffness in the linear analysis. The slope from B to C, ignoring the effects of gravity loads acting through lateral displacements, are taken as between zero and 10% of the initial slope.

For this project, the basic backbone shape definition from ASCE 41-17 Figure 10-1 is adjusted as shown in Figure A-3. Beyond point C, a straight line to point E is used, and a reduced residual strength beyond point E is assumed to continue without total loss of strength.

Modeling parameters and numerical acceptance criteria are taken from ASCE 41-17 Table 10-7. Acceptance criteria are based on the plastic deformation in the nonlinear element.

ASCE 41-17 notes that the shear used to determine the modeling parameters is to be taken as "the design shear force from [nonlinear static procedure] NSP or [nonlinear dynamic procedure] NDP." This definition is somewhat vague. For this project, V is taken as the shear associated with development of the expected flexural strength of the beam added to the gravity shear demand.

Nonlinear force-deformation relationships were simulated using either lumped plasticity (concentrated hinge) or distributed plasticity (fiber) models. When fiber models were used, their stress-strain relationships were modified to simulate the shapes of ASCE 41-17 backbone curves based on the distribution of the fibers and assumed plastic hinge length.

The force or deformation reversal including post-elastic pinching was modeled based on the hysteresis shapes observed from the experimental results of the similar members.

This publication is available free of charge from: https://doi.org/10.6028/NIST.GCR.22-917-50

This publication is available free of charge from: https://doi.org/10.6028/NIST.GCR.22-917-50

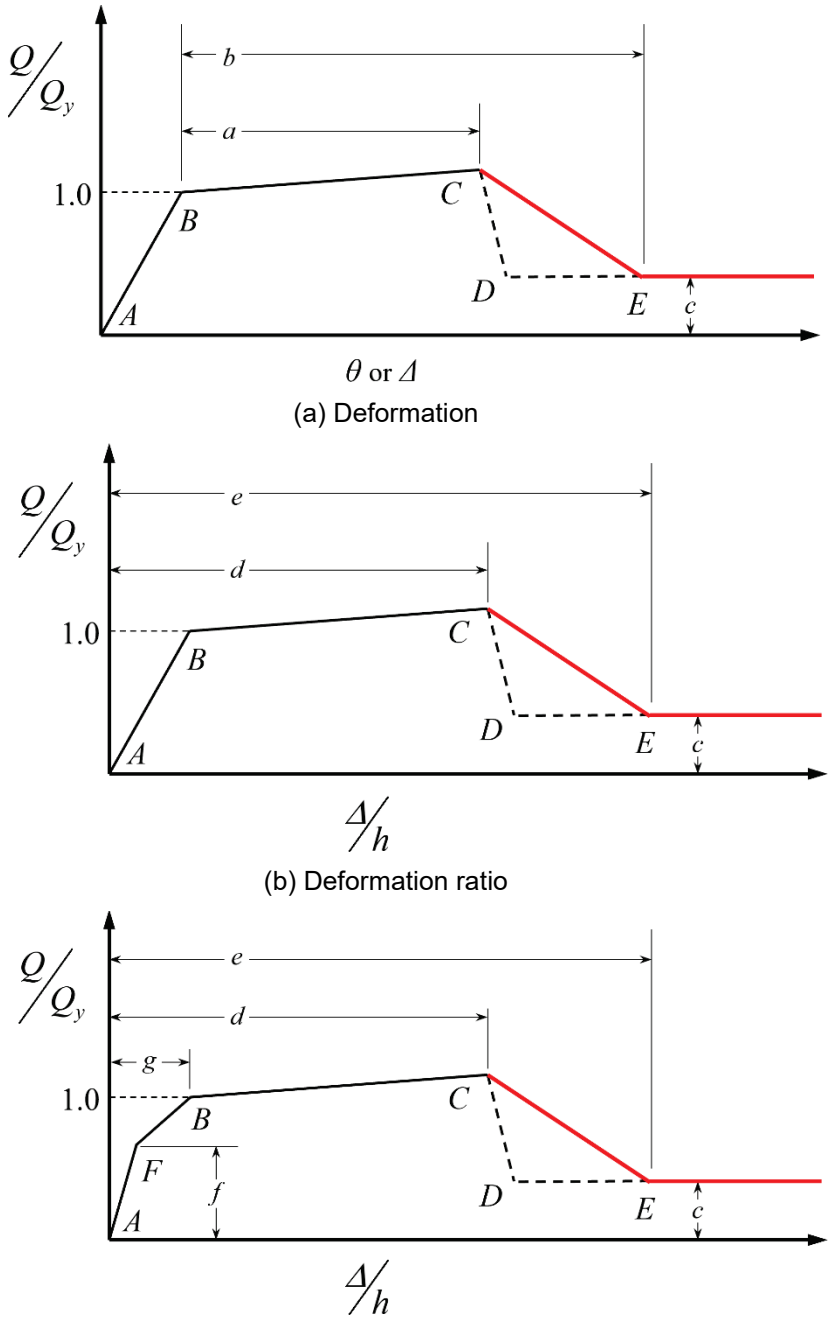


Figure A-3 Generalized force-deformation relation for concrete elements or components used in this project (black and red). Dashed line shows the relationship according to ASCE 41-17 Figure 10-1. Adapted from ASCE.

A.2.2.1 Lumped Plasticity Concentrated Hinge Models

Flexural hinges are determined directly from ASCE 41-17 Table 10-7. Strength, Q_Y, is taken as the expected component strength. The yield chord rotation is taken as $(M_{CE}\, L_{clear}) / (6EI_{eff})$. This is used to determine the initial elastic slope of the

backbone curve. Note that some programs use hinges that have some elastic flexibility included prior to yield, while other programs assume rigid behavior up to yield. For programs where the hinges behave in a rigid response until yield, the elastic line element between the hinges is modeled similar to the linear elastic methods (see Section A.2.1.1 above.) Where the hinge has some flexibility before yield, the elastic line element between hinges needs to be stiffer than specified in Section A.2.1.1 such that the total stiffness is consistent with the targeted stiffness values.

The maximum strength at the capping point is taken as the lower of the following:

- The strength of the element calculated using material properties equal to 1.15 times the expected strength properties.
- The strength associated with the "*a*" point assuming a post-elastic slope of 10% of the initial elastic slope.

Where beams are controlled by shear, flexural hinges are used with adjusted flexural strengths that limit the shear in the element to its shear strength. The flexural strength of the hinges is determined using the limit-state analysis based on capacity design concept. The slope of the backbone from B to C is taken as zero.

Cyclic degradation is accounted for differently depending on which program is used. See the specific building example problems for further discussion.

A.2.2.2 Fiber-Section Modeling

The nonlinear response of flexure in beams, columns, or walls can be modeled using fiber sections. Figure A-4 shows idealizations of the most commonly used modeling approaches. As noted in the figure, there are five approaches to modeling reinforced concrete components, divided by concentrating the plasticity in a spring or distributing the plasticity along a finite length or along the full component length. In this project, the approaches shown in Figures A-4b, A-4c, and A-4d are used, with this section focusing on the finite-length, fiber-discretized modeling approach.

Fiber modeling offers accurate, computationally efficient, and numerically robust simulation of the cyclic response of flexure-controlled reinforced concrete components. Using these models, nonlinear flexural response (i.e., moment and axial load) is simulated at the section level using a fiber-type discretization of the cross-section in which one-dimensional, cyclic stress-strain models are used to define concrete and steel fiber response. Use of a fiber-type section model enables simulation of impact of axial load on flexural response (i.e., P-M interaction). Accurate assessment of local demands (i.e., strains and rotation) and accurate simulation of strength loss require regularization of concrete and steel material response using a mesh-dependent characteristic length and a measure of energy

This publication is available free of charge from: https://doi.org/10.6028/NIST.GCR.22-917-50

dissipated in the post-yield or post-peak regime. For distributed plasticity element formulations, such as those shown in Figures A-4d and A-4e, the section response is integrated along the length of the element to define element response using either a force- or displacement-based beam-column element formulation. These elements are not used in this project and therefore are not addressed.

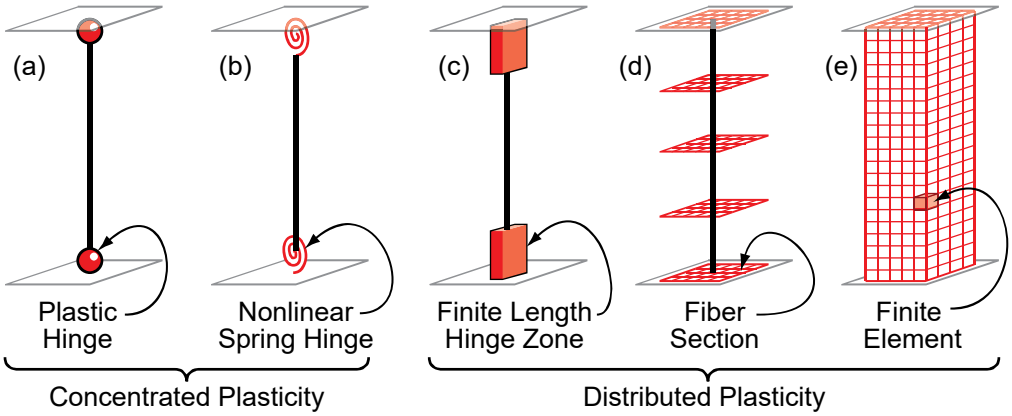


Figure A-4 Idealizations of models used for simulating the nonlinear response of reinforced concrete components using concentrated plasticity or distributed plasticity approaches (from NIST, 2010).

The typical fiber-type beam-column element formulation uses a fiber-type discretization of the reinforced-concrete cross section and nonlinear one-dimensional cyclic material response models. Sufficient discretization is needed in the unconfined and confined regions of the cross sections. Typically, a minimum of 2 layers are used along the depth of the cover (unconfined) section and a minimum of 15 layers are used along the depth of the core confined section for rectangular sections. For circular sections, the uniform radial discretization scheme is to divide the section into 20 core transverse subdivisions, 10 core radial subdivisions, 20 cover transverse subdivisions, and 1 cover radial subdivision (recommendations by Berry and Eberhard (2007)). Shear deformations on the section are assumed to be negligible such that plane sections remain plane and perpendicular to the neutral axis; thus, the strain demand in an individual fiber is defined by the curvature and axial strain demand. Nonlinear one-dimensional material response models define fiber stress-strain relations. Section moment and axial load are computed by integrating fiber stresses along the length of the cross section.

Nonlinear zero-length hinge models are used to simulate nonlinear response mechanisms as part of an earthquake performance assessment. Using a zero-length fiber-type hinge model requires the use of an appropriate plastic hinge length. A length equal to half the depth of the section is typically employed. The length

This publication is available free of charge from: https://doi.org/10.6028/NIST.GCR.22-917-50

associated with the fiber section, L_{IP}, should be taken equal to the plastic hinge length,

A.3 Modeling of Column Elements

A.3.1 Linear Analysis

A.3.1.1 Stiffness

Where design actions are determined using linear procedures, component effective stiffness corresponds to the secant value to the yield point of the component. Alternatively, effective stiffness values per ASCE 41-17 Table 10-5 is used.

Gravity-load effects considered for effective stiffness of components is determined using ASCE 41-17 Equation 7-3:

$$Q_G = Q_D + Q_L + Q_S \qquad \text{(ASCE 41-17 Eq. 7-3)}$$

A3.1.2 Strength

Axial-Flexural Strength

The combined strength is evaluated considering biaxial bending as illustrated in Figure A-5.

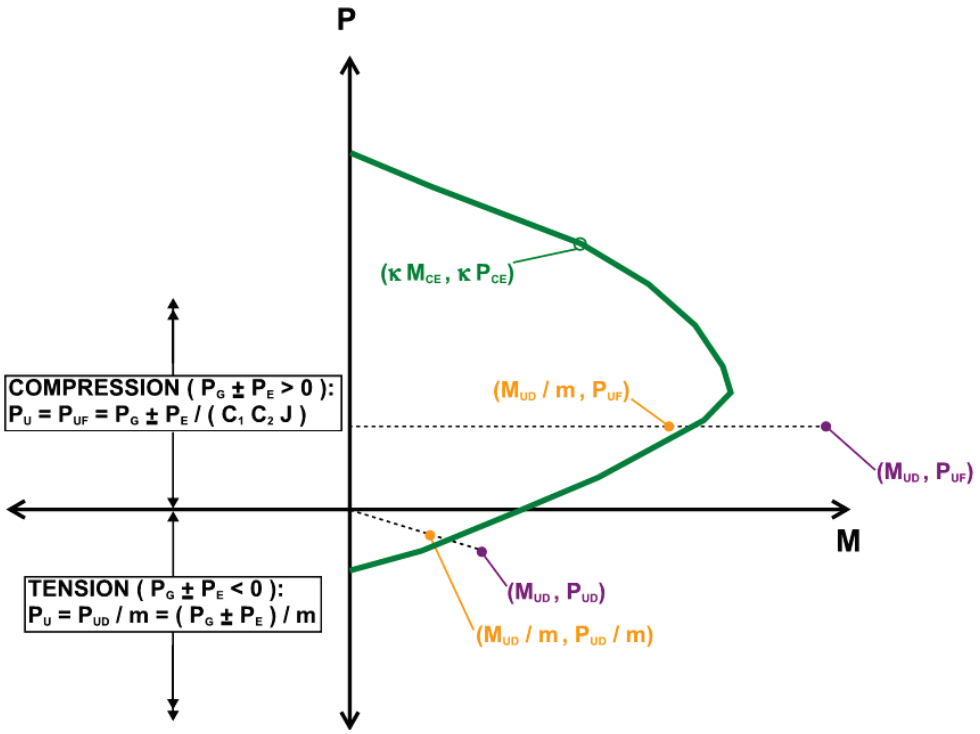


Figure A-5 Illustration of ASCE 41-17 Section 10.3.3 P-M interaction requirements.

This publication is available free of charge from: https://doi.org/10.6028/NIST.GCR.22-917-50

Axial loads used for cases where the column is in tension, P_{UD}, are based on deformation-controlled demands, while axial loads used for cases where the column is in compression, P_{UF}, are based on force-controlled demands. The axial load P_{UF} or P_{UD} is be calculated as a force-controlled action or deformation-controlled action per ASCE 41-17 Section 7.5.2. Applied bending moments are calculated as M_{UD}/m. Acceptance is based on the applied bending moments lying within the expected strength envelope calculated at an axial load level of P_{UF} if the member is in compression or P_{UD}/m if the member is in tension. Development of splices of reinforcement is evaluated per ASCE 41-17 Section 10.3.5.

Shear Strength

For columns, the shear strength, V_{Col}, is calculated using ASCE 41-17 Equation 10-3. Column shear strength is calculated using lower-bound material properties:

$$V_{Col} = k_{nl} V_{col0} = k_{nl} \left[\alpha_{Col} \left(\frac{A_v f_{ytL/E} d}{s} \right) + \lambda \left(\frac{6\sqrt{f'_{cL/E}}}{M_{UD} / V_{UD} d} \sqrt{1 + \frac{N_{UG}}{6A_g \sqrt{f'_{cL/E}}}} \right) 0.8 A_g \right] \text{ (lb/in}^2\text{)}$$

(ASCE 41-17 Eq. 10-3)

where:

- k_{nl} is 1.0 in regions where displacement ductility demand is less than or equal to 2, 0.7 in regions where displacement is greater than or equal to 6, and varies linearly for displacement ductility between 2 and 6. For this project, the k_{nl} value is taken as 1.0.
- λ is 0.75 for lightweight aggregate concrete and 1.0 for normal-weight aggregate concrete.
- N_{UG} is the axial compression force calculated using ASCE 41-17 Equation 7-3 (set to zero for tension force).
- $M_{UD}/V_{UD}d$ is the largest ration of moment to shear time effective depth for the column under design loadings evaluated using ASCE 41-17 Equation 7-34 but is not be taken as greater than 4 or less than 2.
- αCol = 1.0 for $s/d \leq 0.75$, 0.0 for $s/d \geq 1.0$, and varies linearly for s/d between 0.75 and 1.0.

A.3.1.3 Demands

Deformation-controlled actions, Q_{UD}, are calculated in accordance with ASCE 41-17 Equation 7-34.

$$Q_{UD} = Q_G + Q_E \qquad \text{(ASCE 41-17 Eq. 7-34)}$$

where Q_G is determined per Equations 7-1 and 7-2:

This publication is available free of charge from: https://doi.org/10.6028/NIST.GCR.22-917-50

$$Q_G = 1.1(Q_D + Q_L + Q_S) \quad \text{(ASCE 41-17 Eq. 7-1)}$$

$$Q_G = 0.9(Q_D) \quad \text{(ASCE 41-17 Eq. 7-2)}$$

Force-controlled actions, Q_{UF}, are calculated in accordance with ASCE 41-17 Equation 7-35:

$$Q_{UF} = Q_G \pm \frac{\chi Q_E}{C_1 C_2 J} \quad \text{(ASCE 41-17 Eq. 7-35)}$$

where χ is taken as 1.0 assuming Collapse Prevention and J is taken as 2.0 for High Seismicity.

A.3.1.4 Demand-to-Capacity Checks

Elements are checked using acceptance criteria for Collapse Prevention. Deformation-controlled actions are evaluated using ASCE 41-17 Equation 7-36:

$$m\kappa Q_{CE} > Q_{UD} \quad \text{(ASCE 41-17 Eq. 7-36)}$$

where m-factors are taken from ASCE 41-17 Table 10-13 and κ is assumed to be 1.0.

Force-controlled actions are evaluated using ASCE 41-17 Equation 7-37:

$$\kappa Q_{CL} > Q_{UF} \quad \text{(ASCE 41-17 Eq. 7-37)}$$

where κ is assumed to be 1.0.

A.3.2 Nonlinear Analysis

The nonlinear load-deformation relationships are based on experimental evidence or taken from quantities specified in ASCE 41-17 Section 10.4. For the nonlinear dynamic procedure (NDP), load-deformation relations are defined by behavior under monotonically increasing lateral deformation and under multiple reversed deformation cycles.

Per ASCE 41-17 Section 10.3.1.2.2, the generalized load-deformation relation shown in ASCE 41-17 Figure 10-1 is described by linear response from A to an effective yield B, then a linear response at reduced stiffness from B to C, then sudden reduction in force resistance to point D, response at reduced resistance to E, then loss of strength beyond E.

The slope from A to B is based on effective stiffness in the linear analysis. The slope from B to C, ignoring the effects of gravity loads acting through lateral displacements, is taken as between zero and 10% of the initial slope.

For this project, the basic backbone shape definition from ASCE 41-17 Figure 10-1 is adjusted as shown in Figure A-3. Beyond point C, a straight line to point E is used,

This publication is available free of charge from: https://doi.org/10.6028/NIST.GCR.22-917-50

and a reduced residual strength beyond point E is assumed to continue without total loss of strength.

Load-deformation relations follow the generalized load-deformation relation shown in Figure A-3. The generalized deformation in Figure A-3 is plastic hinge rotation.

Modeling parameters and numerical acceptance criteria are taken from ASCE 41-17 Tables 10-8 and 10-9.

N_{UD} (P_{UD} for column axial loads) is taken as the maximum compressive axial load accounting for the effects of lateral forces as described in ASCE 41-17 Equation 7-34, or alternatively, from a limit-state analysis. This project considered several approaches for determining the axial loads including maximum forces from pushover analysis, maximum forces from nonlinear response history analysis, or from a limit-state analysis. The maximum force is used to determine the backbone modeling parameters and the acceptance criteria.

$$Q_{UD} = Q_G + Q_E \qquad \text{(ASCE 41-17 Eq. 7-34)}$$

V_{yE} is calculated based on the expected flexural strength of the column element calculated at an axial load taken as N_{UD}.

The nonlinear force-deformation relationships are simulated using either lumped plasticity (concentrated hinge) or distributed plasticity (fiber) models. When fiber models are used, their stress-strain relationships are modified to simulate the shapes of ASCE 41-17 backbone curves based on distribution of the fibers and assumed plastic hinge length.

The force or deformation reversal including post-elastic pinching is modeled based on the hysteresis shapes observed from the experimental results of the similar members.

A.3.2.1 Lumped Plasticity Concentrated Hinge Models

Flexural hinges are defined directly by the parameters in ASCE 41-17 Tables10-8 and 10-9.

The strength, Q_Y, is taken as the expected component strength.

The yield chord rotation is taken as $(M_{CE}\, L_{clear}) / (6EI_{eff})$. This is used to determine the initial elastic slope of the backbone curve. Note that some programs use hinges that have some elastic flexibility included prior to yield, while other programs assume rigid behavior up to yield. For programs where the hinges behave in a rigid response until yield, the elastic line element between the hinges is modeled similar to the linear elastic methods (see Section 1.3.1.1 above.) Where the hinge has some

This publication is available free of charge from: https://doi.org/10.6028/NIST.GCR.22-917-50

flexibility before yield, the elastic line element between hinges needs to be stiffer than specified in Section A.3.1.1.

The maximum strength at the capping point is taken as the lower of the following:

- The strength of the element calculated using material properties equal to 1.15 times the expected strength properties.
- The strength associated with the "a" point assuming a post-elastic slope of 10% of the initial elastic slope.

Where columns are controlled by shear, flexural hinges are used with adjusted strengths. The flexural strength of the hinges is determined using the limit-state analysis based on capacity design concept. The slope of the backbone from B to C is taken as zero.

Cyclic degradation is accounted for differently depending on which program is used. See the specific building example problems for further discussion.

For models assessed using Perform3D with lumped plasticity (concentrated hinge) to simulate the nonlinear behavior of a column, the interaction of axial force and moment in each orthogonal direction was modeled using a P-M2-M3 hinge. While the interaction of the axial force and moments can be numerically simulated, the vertical deformation and rotation in each orthogonal direction were considered independently without considering interaction. However, when the deformation demand to capacity ratio (DCR) is evaluated, the DCR in each direction is combined at each time step using square root of the sum of the squares (SRSS) to determine the largest DCR considering the multi-directional effect. The modeling parameters to generate a backbone curve for the inelastic hinge were selected based on the maximum assumed axial compression including gravity and earthquake load effect to conservatively estimate deformation capacity and energy dissipation capacity in the inelastic behavior.

A.4 Modeling of Joint Elements

A.4.1 Linear Analysis

A.4.1.1 Stiffness

Where joint stiffness is not explicitly modeled, the moment frame centerline model is adjusted per ASCE 41-17 Figure 10-2, shown in Figure A-6.

M_{ColE} is calculated considering axial force from the gravity loads specified in ASCE 41-17 Section 7.2.2:

$$Q_G = 1.1(Q_D + Q_L + Q_S) \qquad \text{(ASCE 41-17 Eq. 7-1)}$$

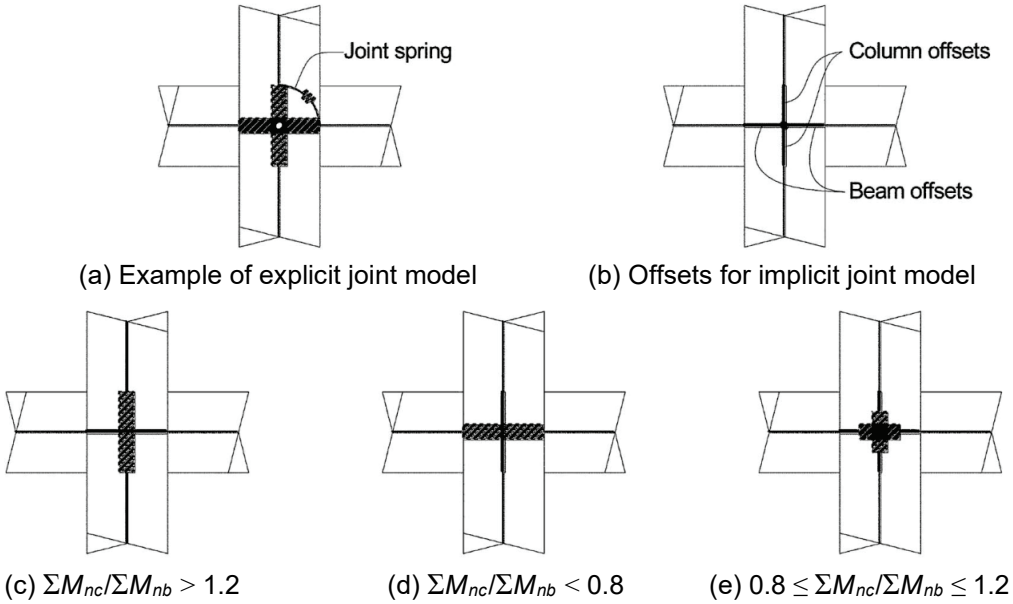
This publication is available free of charge from: https://doi.org/10.6028/NIST.GCR.22-917-50

where:

Q_D = Action caused by dead loads;

Q_L = Action caused by live load, equal to 25% of the unreduced live load obtained in accordance with ASCE 7 but not less than the actual live load; and

Q_S = Action caused by effective.



(a) Example of explicit joint model (b) Offsets for implicit joint model

(c) $\Sigma M_{nc}/\Sigma M_{nb} > 1.2$ (d) $\Sigma M_{nc}/\Sigma M_{nb} < 0.8$ (e) $0.8 \leq \Sigma M_{nc}/\Sigma M_{nb} \leq 1.2$

1. For $\Sigma M_{ColE}/\Sigma M_{BE} > 1.2$, column offsets are rigid and beam offsets are not;
2. For $\Sigma M_{ColE}/\Sigma M_{BE} < 0.8$, beam offsets are rigid and column offsets are not; and
3. For $0.8 \leq \Sigma M_{ColE}/\Sigma M_{BE} \leq 1.2$, half of the beam and column offsets are considered rigid.

Figure A-6 Beam-column joint modeling (hatched portions indicate rigid element) (ASCE, 2017). Printed with permission from ASCE

A.4.1.2 Strength

The joint shear strength, V_J is calculated using the general procedures of ACI 318, as modified by ASCE 41-17 Equation 10-4:

$$V_J = \lambda\gamma\sqrt{f'_{cL} / E}\,A_j \text{ (lb/in.}^2\text{ units)} \qquad \text{(ASCE 41-17 Eq. 10-4)}$$

Expected material properties are used to determine the joint shear strength.

A.4.1.3 Strength Demands

Design forces are calculated based on development of flexural plastic hinges in adjacent framing members, including effective slab width, but need not exceed values calculated from design gravity and earthquake-load combinations.

This publication is available free of charge from: https://doi.org/10.6028/NIST.GCR.22-917-50

A.4.1.4 Demand-to-Capacity Checks

Elements are checked using acceptance criteria for Collapse Prevention. Deformation-controlled actions are evaluated using ASCE 41-17 Equation 7-36:

$$m\kappa Q_{CE} > Q_{UD} \qquad \text{(ASCE 41-17 Eq. 7-36)}$$

where *m*-factors are taken from ASCE 41-17 Table 10-14 and κ is assumed to be 1.0.

A.4.2 Nonlinear Analysis

Load-deformation relations follow the generalized load-deformation relation shown in Figure A-3. The generalized deformation in Figure A-3 is shear strain.

ASCE 41-17 joint modeling parameters are dependent on the ratio V/V_j per ASCE 41-17 Table 10-11. V is defined as design shear force from NSP or NDP. For this study, V is taken as the maximum shear force from the analysis, considering potential inelastic action of adjacent elements. ASCE 41-17 uses V_J in ASCE 41-17 Table 10-11, however the footnotes refer to V_n. The use of the term V_n is ambiguous in this case since the joint shear strength in ASCE 41-17 Equation 10-4 uses both lower-bound and expected strength options. For this study, the V_J term is determined using expected material properties.

The parameters are also dependent on P, taken as the axial force above the joint calculated either using a limit-state analysis or directly as the maximum force from analysis.

A.5 Modeling of Wall Elements

A.5.1 Wall Elements

Effective flange widths are computed using ACI 318 Chapter 18.

Slender structural walls and wall segments are modeled as either equivalent beam-column elements that include both flexure and shear deformation or using a layered fiber element.

A.5.1.1 Beam-Column Element Modeling

The flexural strength of the beam-column element includes the interaction of axial load and bending.

The rigid connection zone at beam connections to the equivalent beam-column element is represented as the distance from the wall centroid to the edge of the wall.

A beam element that incorporates both bending and shear deformations is used to model coupling beams.

This publication is available free of charge from: https://doi.org/10.6028/NIST.GCR.22-917-50

Effective stiffness of elements between hinges are taken from ASCE 41-17 Table 10-5.

A.5.1.2 Layered Fiber Element Modeling

The stress-strain relationship of the fiber elements was calibrated to simulate the nonlinear moment-rotation relationships required by ASCE 41-17 Tables 10-19 and 10-20 as shown in Figure A-7. This modification was specific to the assumed mesh size and fiber distribution used in the model. Absence of this modification typically results in the overestimation of deformation and energy dissipation capacities of the member modeled with fiber elements.

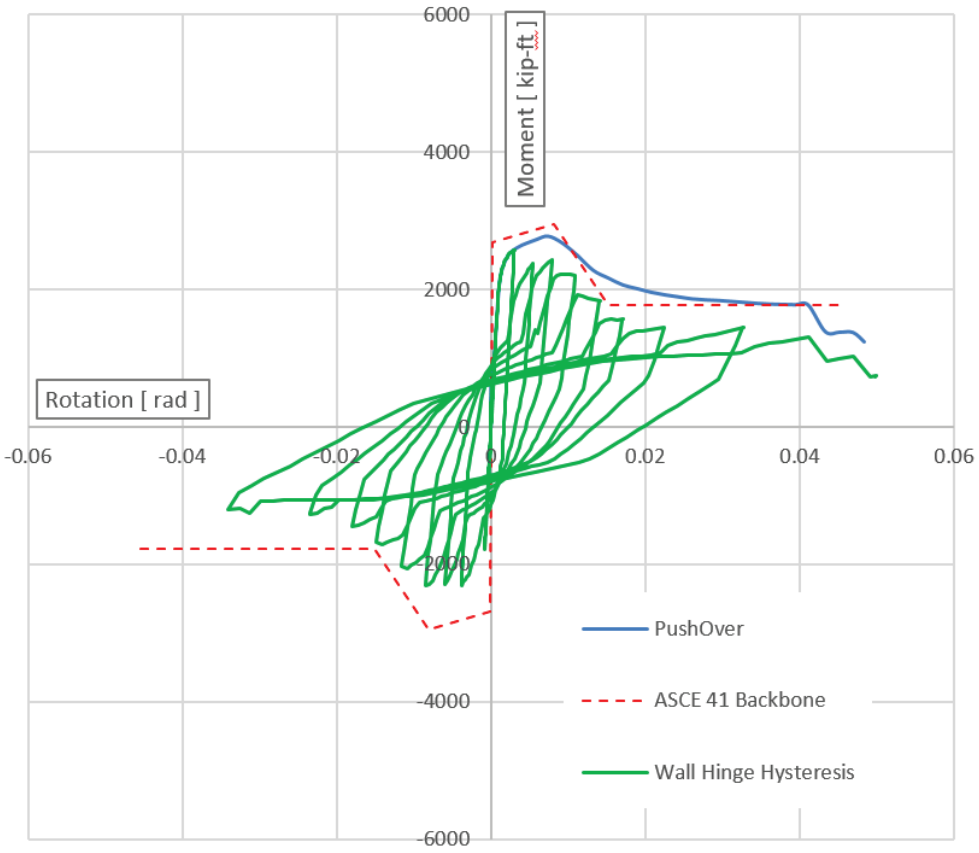


Figure A-7 Calibration of stress-strain relationship of the fiber elements to simulate the nonlinear moment-rotation relationships.

The shear behavior of the wall element is developed in accordance with ASCE 41-17 Table 10-20. The shear layer is placed on the layered fiber element and the analysis force demands determine if flexure or shear governs the response.

A.5.1.3 General ASCE 41 Backbone Definition

Load-deformation relationships for walls and wall elements follow the general requirements of Figure A-3.

This publication is available free of charge from: https://doi.org/10.6028/NIST.GCR.22-917-50

A.5.1.4 Flexure vs. Shear Behavior Determination for Walls

Critical behavior of walls is determined by comparing the wall aspect ratio (height/length) with the guidelines given in the appendix of Chapter 10 of ASCE 41-17:

- If the aspect ratio (height/length) of the wall is > 3.0, then the wall is considered to be slender and flexure controlled; if the aspect ratio is < 1.5, then the wall is considered to be squat and shear controlled.
- If the aspect ratio falls in-between these two boundaries, then the shear span ratio is checked (Pugh et al., 2015) where shear span ratio is defined as ratio of maximum moment demand or maximum shear demand to length of the wall. If the shear span ratio is greater than 2, the wall is considered to be flexure-controlled, otherwise the wall is shear-controlled.

For linear analysis, the check of shear vs. flexure-controlled walls is determined using ASCE 41-17 Section 10.7.2.4.1 where a uniform shear distribution is assumed.

A.5.1.5 Hinge Definition for Flexure-Controlled Response

The load-deformation relationship shown in Figure A-3 is used with rotation over the plastic hinging region at the end of the member as shown in ASCE 41-17 Figure 10-4 (Figure A-8 below).

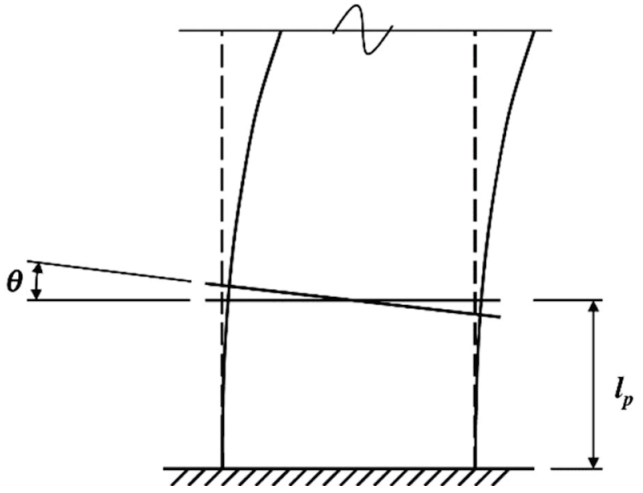


Figure A-8 Plastic hinge rotation in shear wall where flexure dominates inelastic response (Figure 10-4; ASCE, 2017). Printed with permission from ASCE.

Hinge rotation at point B (in Figure A-3) is taken as the yield point, θ_y, per ASCE 41-17 Equation 10-5:

$$\theta_{yE} = \left(\frac{M_{yE}}{(EI)_{eff}} \right) l_p \qquad \text{(ASCE 41-17 Eq. 10-5)}$$

This publication is available free of charge from: https://doi.org/10.6028/NIST.GCR.22-917-50

where l_p is assumed plastic hinge length. For analytical models of structural walls and wall segments, the value of l_p is set equal to 0.5 times the flexural depth of the element but less than one story height for structural walls and less than 50% of the element length for wall segments.

Modeling parameters are taken from ASCE 41-17 Table 10-19.

Flexural strength at point B, M_{yE}, is calculated using expected material properties at an axial load as defined in ASCE 41-17 Section 7.2.2

Flexural strength at point C, M_{pr}, is taken as the flexural strength calculated using $1.25f_{ylE}$ for the reinforcement at an axial load as defined in ASCE 41-17 Section 7.2.2.

The *P* term from ASCE 41-17 Table 10-19 is determined as the maximum load from the analysis including earthquake and gravity load contributions.

The *V* term from ASCE 41-17 Table 10-19 is determined as the maximum load from the analysis including earthquake and gravity load contributions but is limited to the shear from a limit-state analysis.

A.5.1.6 Hinge Definition for Shear-Controlled Response

Structural walls and wall segments governed by shear are represented by the load-deformation relationship in Figure A-3c, with deformation taken as the lateral drift ratio.

For walls, the lateral drift ratio is taken as the story drift. For wall segments, member drift is taken from ASCE 41-17 Figure 10-5 (Figure A-9 below). For coupling beams use Figure A-3b or A-3c with deformation taken as chord rotation as shown in ASCE 41-17 Figure 10-6 (Figure A-10 below).

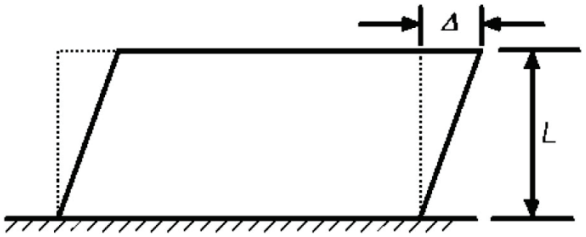


Figure A-9 Story drift in structural wall where shear dominates inelastic response (Figure 10-5, ASCE, 2017). Printed with permission from ASCE.

Shear strength of structural wall, wall segments, and coupling beams are determined per ACI 318 Chapter 18.

The shear strength at point B is calculated using expected material properties.

This publication is available free of charge from: https://doi.org/10.6028/NIST.GCR.22-917-50

The shear strength at point C is taken as the same as strength at point B.

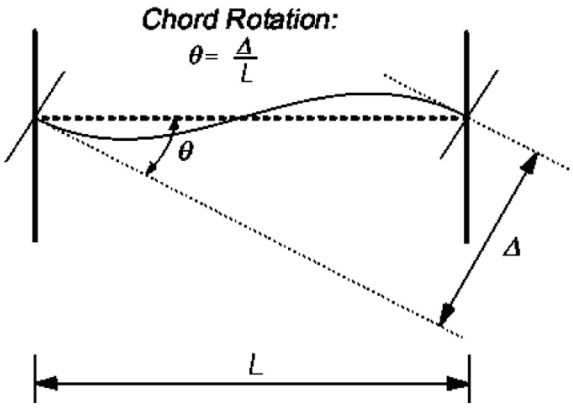


Figure A-10 Chord rotation for structural wall coupling beams (Figure 10-6, ASCE, 2017). Printed with permission from ASCE.

Where a wall is modeled using fiber elements, the stress-strain relationship of the shear layer of the element is similar to shear force-drift relationship identified in ASCE 41-17 Table 10-20 and Figure A-3c. In NDP, the classification of a wall may change from flexural or shear controlled depending on the axial load level at the time step. In that case, an appropriate shear layer is overlaid to the flexural fiber elements to consider the both behaviors which is the similar approach to use of lumped flexural hinges in combination with a shear hinge in a frame element.

This publication is available free of charge from: https://doi.org/10.6028/NIST.GCR.22-917-50

References

Aboutaha, R.S., 1994, *Seismic Retrofit of non-Ductile Reinforced Concrete Columns Using Rectangular Steel Jackets*, PhD dissertation, University of Texas at Austin.

ACI, 2002, *Recommendations for Design of Beam-Column Connections in Monolithic Reinforced Concrete Structures*, ACI PRC-352-02, American Concrete Institute, Farmington Hills, Michigan.

ACI, 2014, *Building Code Requirements for Structural Concrete and Commentary*, ACI CODE 318-14, American Concrete Institute, Farmington Hills, Michigan.

ACI, 2017, *Standard Requirements for Seismic Evaluation and Retrofit of Existing Concrete Buildings and Commentary*, ACI CODE-369.1-17, American Concrete Institute, Farmington Hills, Michigan.

ACI, 2019, *Building Code Requirements for Structural Concrete and Commentary*, ACI CODE 318-19, American Concrete Institute, Farmington Hills, Michigan.

AIJ, 1999, *Design Guidelines for Earthquake Resistant Reinforced Concrete*, Architectural Institute of Japan.

Almeida, J.P., Targuini, D., and Beyer, K., 2016, "Modelling approaches for inelastic behaviour of RC walls: multi-level assessment and dependability of results," *Archives of Computational Methods in Engineering*, Vol. 23, No. 1 pp. 69-100.

ASCE, 2003, *Seismic Evaluation of Existing Buildings*, ASCE/SEI 31-03, Structural Engineering Institute of American Society of Civil Engineers, Reston, Virginia.

ASCE, 2007, *Seismic Rehabilitation of Existing Buildings (including Supplement 1)*, ASCE/SEI 41-06, Structural Engineering Institute of American Society of Civil Engineers, Reston, Virginia.

ASCE, 2014, *Seismic Evaluation and Retrofit of Existing Buildings*, ASCE/SEI 41-13, Structural Engineering Institute of American Society of Civil Engineers, Reston, Virginia.

This publication is available free of charge from: https://doi.org/10.6028/NIST.GCR.22-917-50

This publication is available free of charge from: https://doi.org/10.6028/NIST.GCR.22-917-50

ASCE, 2017, *Minimum Design Loads and Associated Criteria for Buildings and Other Structures*, ASCE/SEI 7-16, Structural Engineering Institute of American Society of Civil Engineers, Reston, Virginia.

ASCE, 2017, *Seismic Evaluation and Retrofit of Existing Buildings*, ASCE/SEI 41-17, Structural Engineering Institute of American Society of Civil Engineers, Reston, Virginia.

ATC, 1984, *An Evaluation of the Imperial County Services Building Earthquake Response and Associated Damage*, ATC-09, Applied Technology Council, Redwood City, California.

ATC, 1987, *Evaluating the Seismic Resistance of Existing Buildings*, ATC-14 Report, Applied Technology Council, Redwood City, California.

Barin, B., and Pincheira, J.A., 2002, *Influence of Modeling Parameters and Assumptions on the Seismic Response of an Existing RC Building*, Department of Civil and Environmental Engineering University of Wisconsin-Madison.

Beca Carter Hollings & Ferner Ltd., 2011, *Investigation into the Collapse of the Pyne Gould Corporation Building on 22 February 2011*, prepared for the Department of Building and Housing. Available at: https://www.mbie.govt.nz/dmsdocument/89-quake-pyne-gould-corp-investigation-report-pdf, last accessed March 2, 2022.

Belarbi A., and Hsu, T.C., 1994, "Constitutive laws of concrete in tension and reinforcing bars stiffened by concrete," *ACI Structural Journal*, Vol. 91, No. 4, pp. 465-474.

Berry, M.P., and Eberhard, M.O., 2007, *Performance Modeling Strategies for Modern Reinforced Concrete Columns*, Pacific Earthquake Engineering Research Center Report, PEER 2007/7, University of California, Berkeley.

Berry M.P., Parrish M., and Eberhard M.O., 2004, *PEER Structural Performance Database User's Manual*, Pacific Earthquake Engineering Research Institute, University of California Berkeley. Available at https://nisee.berkeley.edu/spd/, last accessed March 20, 2022.

Blume, J.A.a.A., Engineers, 1973, *Holiday Inn (29), San Fernando, California, Earthquake of February 9, 1971*, V1. Part a. U.S. Department of Commerce, National Oceanic and Atmospheric Administration (NOAA), Washington, D.C., pp. 359-393.

BSSC, 1992, *NEHRP Handbook for the Seismic Evaluation of Existing Buildings*, developed by the Building Seismic Safety Council for the for the Federal Emergency Management Agency, Washington, D.C.

This publication is available free of charge from: https://doi.org/10.6028/NIST.GCR.22-917-50

Buniya, M., Barbosa, A., and Sattar, S., 2020, "Assessment of a 12-story code-compliant reinforced concrete special moment frame using performance-based seismic engineering standards and guidelines: ASCE 41, TBI, and LATBSDC," *ACI SP-339*, American Concrete Institute, Farmington Hills, Michigan.

Celik, O.C., and Ellingwood, B.R., 2008, "Modeling beam-column joints in fragility assessment of gravity load designed reinforced concrete frames," *Journal of Earthquake Engineering*, Vol. 12, No. 3, pp. 357-381.

CENAPRED, 2001, *Norma para la Evaluación del Nivel del Daño por Sismo en Estructuras y Guía Tecnica de Rehabilitación*, Centro Nacional de Prevencion de Desastres, Secretaria de Gobernación, Mexico, D.F.

Coleman, J., and Spacone, E., 2001, "Localization issues in forced-based frame elements," Journal of Structural Engineering, Vol. 127, No. 11, pp. 1257-1265.

Concrete Coalition, 2019, *Concrete Buildings Damaged in Earthquake, A Collection of Case Studies*. Available at http://db.concretecoalition.org/building/147, last accessed December 2019.

Department of Building and Housing, 2010, *Photographic Summary of Primary Damage Observed*, Exhibit of the Royal Commission of Inquiry into Building Failure Caused by the Canterbury Earthquakes, New Zealand Department of Internal Affairs. Available at: https://canterbury.royalcommission.govt.nz/documents-by-key/2011-09-2316, last accessed March 2, 2022.

Dirac Ingenieros Consultores, 2019a, *Memoria de Cálculo del Proyecto de Rehabilitación Sísmica del Edificio, Miramontes 3020*, Revisión 0, personal communication to ATC-134 project team.

Dirac Ingenieros Consultores, 2019b. *Informe del Levantamiento de Daños del Edificio, Miramontes 3020*, personal communication to ATC-134 project team.

Elwood K.J., and Eberhard M.O., "Effective stiffness of reinforced concrete columns," *ACI Structural Journal*, Vol. 106, No. 4, pp. 476-84.

Elwood, K.J., Matamoros, A.B., Wallace, J.W., Lehman, D.E., Heintz, J.A., Mitchell, A.D., and Comartin, C.D., 2007, "Update to ASCE/SEI 41 concrete provisions," *Earthquake Spectra*, Vol. 23, No. 3, pp. 493-523.

European Committee for Standardisation, 2005, *Eurocode 8: Design of Structures for Earthquake Resistance, Part 3: Assessment and Retrofitting of Buildings*, EN 1998-3.

Faison, H., Comartin, C.D., and Elwood, K.J., n.d., *Housing Report: Reinforced Concrete Moment Frame Building without Seismic Details*.

FEMA, 1997a, *NEHRP Guidelines for the Seismic Rehabilitation of Buildings*, FEMA 273, prepared by the Applied Technology Council for the Building Seismic Safety Council and the Federal Emergency Management Agency, Washington, D.C.

FEMA, 1997b, *NEHRP Commentary on the Guidelines for the Seismic Rehabilitation of Buildings*, FEMA 274, prepared by the Applied Technology Council for the Building Seismic Safety Council and the Federal Emergency Management Agency, Washington, D.C.

FEMA, 1998, *Handbook for the Seismic Evaluation of Buildings—A Prestandard*, FEMA 310, prepared by the American Society of Civil Engineers for the Federal Emergency Management Agency, Washington, D.C.

FEMA, 2000, *Prestandard and Commentary for the Seismic Rehabilitation of Buildings,* FEMA 356, prepared by the American Society of Civil Engineers for the Federal Emergency Management Agency, Washington, D.C.

FEMA, 2009, Quantification of Building Seismic Performance Factors, FEMA P-695, prepared by the Applied Technology Council for the Federal Emergency Management Agency, Washington, D.C.

FEMA, 2009, *Quantification of Building Seismic Performance Factors*, FEMA P-695, prepared by Applied Technology Council for the Federal Emergency Management Agency, Washington, D.C.

FEMA, 2018a, *Example Application Guide for ASCE/SEI 41-13 Seismic Evaluation and Retrofit of Existing Buildings with Additional Commentary for ASCE/SEI 41-17*, FEMA P-2006, prepared by the Applied Technology Council for the Federal Emergency Management Agency, Washington, D.C.

FEMA, 2018b, *Seismic Evaluation of Older Concrete Buildings for Collapse Potential*, FEMA P-2018, prepared by the Applied Technology Council for the Federal Emergency Management Agency, Washington, D.C.

FEMA, 2018c, *Seismic Performance Assessment of Buildings, Volume 1 – Methodology*, FEMA P-58-1 Second Edition, prepared by the Applied Technology Council for the Federal Emergency Management Agency, Washington, D.C.

Garcia Gomez, C.A., 2020, *Nonlinear Dynamic Analysis of a Ten-Story Reinforced Concrete Building*, MS Thesis, University of California, Los Angeles, Department of Civil and Environmental Engineering.

This publication is available free of charge from: https://doi.org/10.6028/NIST.GCR.22-917-50

Ghannoum W. M., and Moehle J. P., 2012, "Shake-table tests of a concrete frame sustaining column axial failures," *ACI Structural Journal*, Vol. 109, No. 3, pp. 393-402.

Ghannoum W.M., 2007, *Experimental and Analytical Dynamic Collapse Study of a Reinforced Concrete Frame with Light Transverse Reinforcements*, PhD Thesis, University of California, Berkeley.

Ghannoum, W., 2017, "Updates to modeling parameters and acceptance criteria for non-ductile and splice-deficient concrete columns," *16th World Conference on Earthquake Engineering*, Santiago, Chile, paper No 1010.

Ghannoum, W., and Matamoros, A., 2014, "Nonlinear modeling parameters and acceptance criteria for concrete columns," *ACI SP-297: Seismic Assessment of Existing Reinforced Concrete Buildings*, American Concrete Institute, Farmington Hills, Michigan.

Gurler, E.D., Nakamura, Y., Saita, J., and Sato, T., 2000, "Local site effect of Mexico City based on microtremor measurement," *6th International Conference on Seismic Zonation*, Palm Spring Riviera Resort, California, pp. 65.

Hakuto, S., Park, R., and Tanaka, H., 1999, "Effect of deterioration of bond of beam bars passing through interior beam-column joints on flexural strength and ductility," *ACI Structural Journal*, Vol. 96, No. 5, pp. 858-864.

Hakuto, S., Park, R., and Tanaka, H., 2000, "Seismic load tests on interior and exterior beam-column joints with substandard reinforcing details," *ACI Structural Journal*, Vol. 97, No. 1, pp. 11-25.

Huang, Y-N., Whittaker, A.S., and Luco, N., 2008, "Maximum spectral demands in the near-fault region," *Earthquake Spectra*, Vol. 24, No. 1, pp. 319-341.

Hwang, S.-J., and Moehle, J.P., 2000,"Models for laterally loaded slab-column frames," *ACI Structural Journal*, Vol. 97, No. 2, pp. 345-352.

Ibarra, L.F., Medina, R.A., and Krawinkler, H., 2005, "Hysteretic models that incorporate strength and stiffness deterioration," *Earthquake Engineering & Structural Dynamics*, Vol. 34, No. 12, pp. 1489-1511.

Vamvatsikos, D., and Cornell, C., 2002, "Incremental dynamic analysis," *Earthquake Engineering and Structural Dynamics*, Vol., 31, No. 3, pp. 491-514.

Islam, M.S., 1996, "Analysis of the Northridge earthquake response of a damaged non-ductile concrete frame building," *Structural Design of Tall Buildings*, Vol. 5, pp. 151-182.

Jury, R., and Sharpe, R., 2011, *Investigation into the collapse of the Pyne Gould Corporation Building*, Hearing of the Royal Commission of Inquiry into Building Failure Caused by the Canterbury Earthquakes, New Zealand

This publication is available free of charge from: https://doi.org/10.6028/NIST.GCR.22-917-50

Department of Internal Affairs. Available at: https://canterbury.royalcommission.govt.nz/documents-by-key/20111130.1381, last accessed March 2, 2022.

Kajiwara, K., Tosauchi, Y., and Sato, E., 2017, "2015 Three-dimensional shaking table test of a 10-story reinforced concrete building on the E-Defense, Part1: Overview and specimen design of the base slip and base fixed tests," *16th World Conference on Earthquake Engineering*, Santiago, Chile.

Kolozvari, K., Anaraki, K., Orakcal, K., and Wallace, J.W., 2021, "Three-dimensional model for nonlinear analysis of slender flanged reinforced concrete walls," *Engineering Structures*, Vol. 236, pp 1-17. Available at https://doi.org/10.1016/j.engstruct.2021.112105, last accessed March 17, 2022.

Kolozvari, K., and Wallace, J. W., 2016, "Practical nonlinear modeling of reinforced concrete structural walls," *ASCE Journal of Structural Engineering*, Vol. 142, No. 12.

Krawinkler, H., 2005, *Van Nuys Hotel Building Testbed Report: Exercising Seismic Performance Assessment*, Pacific Earthquake Engineering Research Center Report 2005/11, Department of Civil and Environmental Engineering, Stanford University.

Kreger, M.E., and Sozen, M.A., 1983, *A Study of the Causes of Column Failures in the Imperial County Services Building during the 15 October 1979 Imperial Valley Earthquake*, Civil Engineering Studies SRS-509, University of Illinois Engineering Experiment Station. College of Engineering. University of Illinois at Urbana-Champaign.

Kreger, M.E., and Sozen, M.A., 1990, "Seismic response of Imperial County Services Building in 1979," *Journal of Structural Engineering*, Vol. 115, No. 12.

Kwon J., 2016, *Strength, Stiffness, and Damage of Reinforced Concrete Buildings Subjected to Seismic Motions*, PhD Thesis, University of Texas at Austin.

Kwon J., Ghannoum W.M., 2016, "Assessment of international standard provisions on stiffness of reinforced concrete moment frame and shear wall buildings," *Engineering Structures*, Vol. 128, pp. 149-60.

Lai, J.W., Kim, I., Hagen, G., Johnston, K., Zepeda, D., and Hwang, S.J., 2018, "Seismic evaluation of three district office buildings damaged during 2016 Meinong, Taiwan Earthquake using ASCE 41," *Proceedings of the 11th National Conference on Earthquake Engineering*, Los Angeles, California.

This publication is available free of charge from: https://doi.org/10.6028/NIST.GCR.22-917-50

Lee, Y.T., Wang, Y.J., Chan, C.H., and Ma, K.F., 2017, "The 2016 Meinong earthquake to TEM PSHA2015," *Terrestrial, Atmospheric and Oceanic Sciences*, Vol. 28, No. 5, pp. 703-713.

Lehman, D., Lowes, L., Turgeon, J., Birely A., Kuchma D., Marley, K., and Hart C., 2013, "Seismic behavior of modern coupled walls", *ASCE Journal of Structural Engineering*, Vol. 139, Special Issue: NEES 2: Advances in Earthquake Engineering, pp. 1371-1381.

Lu, Y., Henry, R.S., Gultom, R., and Ma, Q.T., 2017, "Cyclic testing of reinforced concrete walls with distributed minimum vertical reinforcement," *Journal of Structural Engineering*, Vol. 143, No. 5.

Lynn, A., 1999, *Seismic Evaluation of Existing Reinforced Concrete Building Colums*, Ph.D. Thesis, University of California at Berkeley, Berkeley, California, 1999, 284 pages.

Maison, B. F., Kasai, K., and Deierlein, G., 2009, "ASCE-41 and FEMA-351 evaluation of E-Defense collapse test," *Earthquake Spectra*, Vol. 25, No. 4, pp. 927-953.

Mander, T.J., Matamoros, A.B., 2019, "Constitutive modeling and overstrength factors for reinforcing steel," *ACI Structural Journal*, Vol. 116, Vo. 3, pp. 219-232.

Mander, J.B., Priestley, M.J., and Park, R., 1988a, "Theoretical stress-strain model for confined concrete," *Journal of Structural Engineering*, Vol. 114, No. 8, pp. 1804-1826.

Mander, J., Priestley, M., and Park, R., 1988b, "Observed stress-strain behavior of confined concrete," Journal of Structural Engineering, Vol. 114, No. 8, pp. 1827-1849.

Marafi, N.A., Ahmed, K.A., Lehman, D.E., and Lowes, L.N., 2019, "Variability in seismic collapse probabilities of solid- and coupled-wall buildings," *Journal of Structural Engineering*, Vol. 145, No. 6.

McKenna, F., Fenves, G.L., Scott, M.H., Jeremic, B., 2000, *Open System for Earthquake Engineering Simulation (OpenSees)*, Pacific Earthquake Engineering Research Center, College of Engineering, University of California, Berkeley.

Moehle, J.P., 2014, *Seismic Design of Reinforced Concrete Buildings*, McGraw-Hill, New York, 760 pp.

MSJC, 2011, *Building Code Requirements and Specification for Masonry Structures*, TMS-402, developed by the Masonry Standards Joint Committee (MSJC), TMS 402/602-11 edition.

This publication is available free of charge from: https://doi.org/10.6028/NIST.GCR.22-917-50

MSJC, 2011, *Building Code Requirements and Specification for Masonry Structures*, TMS-402, developed by the Masonry Standards Joint Committee (MSJC), TMS 402/602-11 edition.

Naeim, F., Hagie, S., Alimoradi, A., and Miranda, E., 2005, *Automated Post-Earthquake Damage Assessment and Safety Evaluation Of Instrumented Buildings*, JAMA Report number: 10639.

Nagae, T., Ghannoum, W.M., Kwon, J., Tahara, K., Fukuyama, K., Matsumori, T., Shiohara, H., Kabeyasawa, T., Kono, S., and Nishiyama, M., 2015, "Design implications of large-scale shake-table test on four-story reinforced concrete building," *ACI Structural Journal*, Vol. 112, No. 2.

New Zealand Standard Institute,1955, *NZ Standard - Model Building By-Laws*, Part IV and V, NZSS 95: 1955, Wellington, New Zealand.

NIST, 2009, *Research Required to Support Full Implementation of Performance-Based Seismic Design*, NIST GCR 09-917-02, prepared by the Building Seismic Safety Council of the National Institute of Building Sciences for the National Institute of Standards and Technology, Gaithersburg, Maryland.

NIST, 2012, *Soil-Structure Interaction for Building Structures*, NIST GCR 12-917-21, prepared by the NEHRP Consultants Joint Venture, a partnership of the Applied Technology Council and the Consortium of Universities for Research in Earthquake Engineering, for the National Institute of Standards and Technology, Gaithersburg, Maryland.

NIST, 2012, *Soil-Structure Interaction for Building Structures*, NIST GCR 12-917-21, prepared by the NEHRP Consultants Joint Venture, a partnership of the Applied Technology Council and the Consortium of Universities for Research in Earthquake Engineering, for the National Institute of Standards and Technology, Gaithersburg, Maryland.

NIST, 2016, *Seismic Design of Reinforced Concrete Special Moment Frames: A Guide for Practicing* Engineers, *Second Edition,* NIST GCR 16-917-40, prepared by the NEHRP Consultants Joint Venture, a partnership of the Applied Technology Council and the Consortium of Universities for Research in Earthquake Engineering, for the National Institute of Standards and Technology, Gaithersburg, Maryland.

NIST, 2017, *Recommended Modeling Parameters and Acceptance Criteria for Nonlinear Analysis in Support of Seismic Evaluation, Retrofit, and Design*, GCR 17-917-45, prepared by the Applied Technology Council for the National Institute of Standards and Technology, Gaithersburg, Maryland.

This publication is available free of charge from: https://doi.org/10.6028/NIST.GCR.22-917-50

NZSEE, SESOC, New Zealand Geotechnical Society, Inc, Ministry of Business, Innovation a& Employment, and Earthquake Commission, 2017, *The Seismic Assessment of Existing Buildings*, published July 2017. Available at: http://www.eq-assess.org.nz/assets/2017-07/Overview_of_the_Seismic_Assessment_Guidelines_20170703.pdf, last accessed December 31, 2021.

Orakcal, K., Massone, L., and Wallace, J., 2006, *Analytical Modeling of Reinforced Concrete Walls for Predicting Flexural and Coupled-Shear-Flexural Responses*, PEER Report 2006/08, Pacific Earthquake Engineering Research Center, College of Engineering, University of California, Berkeley.

Pampanin, S., Calvi, G.M., and Moratti, M., 2002, "Seismic behaviour of RC beam-column joints designed for gravity loads," *Proceedings of 12th European Conference on Earthquake Engineering*, London, United Kingdom. Paper 726.

Pampanin, S., Magenes, G., and Carr, A., 2003, "Modelling of shear hinge mechanism in poorly detailed RC beam-column joints," *Proceedings of the Concrete Structures in Seismic Regions: fib 2003 Symposium*, Federation International du Beton, Athens, Greece, Paper No. 171.

Pardoen, G.C., and Shepherd, R., n.d., *Experimental and Analytical Studies of the Imperial County Services Building*.

Pardoen, G.C., Carr, A.J., and Moss, P.J., 1979, Imperial County Services Building - *Elastic and Inelastic Analysis Results*, Christchurch, New Zealand.

Paspuleti, C., 2002, *Seismic Analysis of an Older Reinforced Concrete Frame Structure*, University of Washington.

Pauschke, J.M., 1981, *Dynamic Response of the Imperial County Services Building*, PhD Dissertation, Stanford University, Stanford, California.

PEER, 2011, *Design and Instrumentation of the 2010 E-Defense Four-Story Reinforced Concrete and Post-Tensioned Concrete Buildings*, PEER Report 2011/104, Pacific Earthquake Engineering Research Center, University of California, Berkeley.

Pessiki, S. P., Conley, C. H., Gergely, P., and White, R. N., 1990, *Seismic Behavior of Lightly-Reinforced Concrete Column and Beam-Column Joint Details*, Technical Report NCEER-90-0014, National Center for Earthquake Engineering Research, Buffalo, New York.

Petersen, M. D., Moschetti, M. P., Powers, P. M., Mueller, C. S., Haller, K. M., Frankel, A. D., Zeng, Y., Rezaeian, S., Harmsen, S. C., Boyd, O. S., Field, Chen, E. H. R., Rukstales, K. S., Luco, N., Wheeler, R. L., Williams, R. A.,

This publication is available free of charge from: https://doi.org/10.6028/NIST.GCR.22-917-50

and Olsen, A. H., 2014, *Documentation for the 2014 Update of the United States National Seismic Hazard Maps*, Open-File Report 2014-1091. United States Geological Survey. Available at https://doi.org/10.3133/ofr20141091, last accessed March 2, 2022.

Pugh, J.S., Lowes, L.N., and Lehman, D.E., 2015, "Nonlinear line-element modeling of flexural reinforced concrete walls," *Engineering Structures*, Vol. 104, pp. 174-192.

Pujol S., 2002, *Drift Capacity of Reinforced Concrete Columns Subjected to Displacement Reversals*, PhD Dissertation, Purdue University, Indiana.

Pujol, S., Irfanoglu, A., Jahanshahi, M., Laughery, L. A., Puranam, A., Cheng, L., Hesam, P., Lund, A., Wu, R., Hwang, S., Chiou, T., Chung, L., Wu, C., Shen, W., Li, Y., Weng, P., Hsiao, F., Tsai, T., Lam, W., Lin, C., Li, C., 2017, *Performance of Reinforced Concrete Buildings in the 2016 Taiwan (Meinong) Earthquake*, Purdue University Research Repository. doi:10.4231/R7M32SZ3A.

Razvi, S., and Saatcioglu, M., 1999, "Confinement model for high strength concrete," *Journal of Structural Engineering*, Vol. 125, No. 3, pp. 281-289.

Saatcioglu, M., and Razvi, S.R., 1992, "Strength and ductility of confined concrete," *Journal of Structural Engineering*, Vol. 118, No. 6, pp. 1590-1607.

Sato, E., Tosauchi, Y., and Fukuyama, K., 2017, "2015 three-dimensional shaking table test of a 10-story reinforced concrete building on the E-Defense, Part2: Specimen fabrication and construction, test procedure, and instrumentation program," *16th World Conference on Earthquake Engineering*.

Sattar, S., 2018, "Evaluating the consistency between prescriptive and performance-based seismic design approaches for reinforced concrete moment frame buildings," *Engineering Structures*, Vol. 174, pp. 919-931.

Selna, L.G., and R.D. Boyens, 1980, "Performance of the Imperial County Services Building, El Centro," *Proceedings*, Structural Engineers Association of California, Annual Convention, Monterey, California.

Sezen H., Moehle J.P., 2006, "Seismic tests of concrete columns with light transverse reinforcement," *ACI Structural Journal*, Vol. 103, No. 6, pp. 842-849.

Sezen, H., 2002, *Seismic Behavior and Modeling of Reinforced Concrete Building Columns*, PhD Dissertation, University of California, Berkeley.

Shiohara, H., Sho, H., and Kusuhara, F., 2013, "Behavior at large deformation of R/C interior beam-column joints of joint yielding," *Summaries of Technical Papers of Annual Meeting*, Architectural Institute of Japan, pp. 723-724. (In Japanese).

This publication is available free of charge from: https://doi.org/10.6028/NIST.GCR.22-917-50

SMIE, 2020, *Normas Técnicas Complementarias para Diseño por Sismo de la Ciudad de México*, Sociedad Mexicana de Ingenieria Estructural, Mexico, D.F. Available at: https://sasid.unam.mx/webNormasCDMX/default.aspx, last accessed on November 2021.

Sumearll, J., 2019, *Evaluation of Seismic Assessment Procedures for Existing Reinforced Concrete Buildings using Damage Data from the 2016 Meinong Earthquake*, MS Thesis, University of Washington.

Sumearll, J., Galeotti, F., and Lehman, D., 2018, "Evaluation of buildings RC frame buildings damaged in Meinong earthquake," *Proceedings of the 11th National Conference on Earthquake Engineering*, Los Angeles, California.

Suwal, A., 2018, *Performance Evaluation of a Non-ductile Reinforced Concrete Moment Frame Building*, PhD Dissertation, Department of Civil and Environmental Engineering, University of Texas at San Antonio, 313 pp.

Tanaka H., 1990, *Effect of Lateral Confining Reinforcement on the Ductile Behaviour of Reinforced Concrete Columns*, PhD Dissertation, University of Canterbury, Auckland, New Zealand.

Todorovska, M.I., and Trifunac, M.D., 2007, "Earthquake damage detection in the Imperial County Services Building I: The data and time-frequency analysis," *Soil Dynamics and Earthquake Engineering*, Vol. 27, No. 6.

Todorovska, M.I., and Trifunac, M.D., 2008, "Impulse response analysis of the Van Nuys 7-storey hotel during 11 earthquakes and earthquake damage detection," *Structural Control and Health Monitoring*, Vol. 15, pp. 90-116.

Tosauchi, Y., Sato, E., and Fukuyama, K., 2017, "2015 Three-dimensional shaking table test of a 10-story reinforced concrete building on the E-Defense, Part3: Base slip and base fixed test results," *16th World Conference on Earthquake Engineering*, Santiago, Chile.

Trifunac, M.D., and Hao, T-Y., 2001, *7-Storey Reinforced Concrete Building in Van Nuys, California: Photographs of the Damage from the 1994 Northridge Earthquake*, Report CE 01-05, Department of Civil Engineering, University of Southern California.

Trifunac, M.D., Ivanovic, S.S., and Todorovska, M.I., 1999, *Instrumented 7-Storey Reinforced Concrete Building in Van Nuys, California: Description of Damage from the 1994 Northridge Earthquake and Strong Motion Data*, Report CE 99-02, Department of Civil Engineering, University of Southern California.

Unal, M.E., Kolozvari, K., Wallace, J.W., Kajiwara, K., Kang, J-D., Tosauchi, Y., Sata, E., Kabeyasawa, T., Shiohara, H., Nagae, T., and Kabeyasawa, T.,

This publication is available free of charge from: https://doi.org/10.6028/NIST.GCR.22-917-50

2020, *Assessment of the 2015 and 2018 E-Defense 10-Story Reinforced Concrete Buildings Based on ACI 318-19 and ASCE 7-16*, Draft Final Report, UCLA Structural/Earthquake Engineering Research Laboratory Report SEERL 2020/2, Los Angeles California.

USGS, 2020, "M 6.4 - 25km SE of Yujing, Taiwan," *Earthquake Hazards Program*, United States Geological Survey. Available at: https://earthquake.usgs.gov/earthquakes/eventpage/us20004y6h/shakemap/intensity, last accessed July 14, 2020.

Welt, T., Massone, L., LaFave, J., Lehman, D., McCabe, S. and Polanco, P., 2017, "Confinement behavior of rectangular reinforced concrete prisms simulating wall boundary elements," *Journal of Structural Engineering*, Vol. 143, No. 4.

Wight, J.K., and Sozen, M.A., 1973, "Shear strength decay in reinforced concrete columns subjected to large deflection reversals," *Structural Research Series No. 403*, University of Illinois Experiment Research Station, Urbana, Illinois.

Woods, C., and Matamoros, A.B., 2008, "Effect of longitudinal reinforcement ratio on the failure mechanism of R/C columns most vulnerable to collapse," *Proceedings of the 9th U.S. National and 10th Canadian Conference on Earthquake Engineering, Toronto, Ontario, Canada,* Paper No. 1636.

Wosser, T., Campi, D., Fovinci, M., and Smith. W.H., 1980, "On the earthquake induced failure of the Imperial County Service Building," in *EERI Reconnaissance Report*, Earthquake Engineering Research Institute, pp. 159-172.

Yassin, M., 1994, *Nonlinear Analysis of Prestressed Concrete Structures under Monotonic and Cyclic Loads*, Ph.D. thesis, Department of Civil and Environmental Engineering, University of California, Berkeley.

This publication is available free of charge from: https://doi.org/10.6028/NIST.GCR.22-917-50

Project Participants

This publication is available free of charge from: https://doi.org/10.6028/NIST.GCR.22-917-50

National Institute of Standards and Technology

Siamak Sattar
Engineering Laboratory (MS8662)
National Institute of Standards and Technology
100 Bureau Drive
Gaithersburg, Maryland 20899

Steven L. McCabe
Engineering Laboratory (MS8604)
National Institute of Standards and Technology
100 Bureau Drive
Gaithersburg, Maryland 20899

Dustin Cook
Engineering Laboratory (MS8662)
National Institute of Standards and Technology
100 Bureau Drive
Gaithersburg, Maryland 20899

Applied Technology Council

Jon A. Heintz (Program Manager)
Applied Technology Council
201 Redwood Shores Parkway, Suite 240
Redwood City, California 94065

Ayse Hortacsu (Associate Program Manager)
Applied Technology Council
201 Redwood Shores Parkway, Suite 240
Redwood City, California 94065

Program Committee on Seismic Engineering

Jon A. Heintz (Chair)
Applied Technology Council
201 Redwood Shores Parkway, Suite 240
Redwood City, California 94065

Michael Cochran
Thornton Tomasetti
4551 Glencoe Avenue, Suite 350
Marina del Rey, California 90292

James R. Harris
J.R. Harris & Company
1775 Sherman Street, Suite 1525
Denver, Colorado 80203

James Jirsa
Dept. of Civil, Architectural and Environmental Engineering
University of Texas at Austin
301 E. Dean Keeton Street, Stop C1700
Austin, Texas 78712

Roberto Leon
Dept. of Civil and Environmental Engineering
Virginia Tech
102-D Patton Hall
Blacksburg, Virginia 24061

James O. Malley
Degenkolb Engineers
375 Beale Street, Suite 500
San Francisco, California 94105

Donald Scott
PCS Structural Solutions
811 First Avenue, Suite 620
Seattle, Washington 98104

Andrew Whittaker
Dept. of Civil, Structural and Environmental Engineering
University at Buffalo
230 Ketter Hall
Buffalo, New York 14260

This publication is available free of charge from: https://doi.org/10.6028/NIST.GCR.22-917-50

Project Technical Committee

Russel Berkowitz (Project Director)
Forell/Elsesser Engineers, Inc.
160 Pine Street, 6th Floor
San Francisco, California 94111

Wassim Ghannoum
Dept. of Civil and Environmental Engineering
The University of Texas at San Antonio
Building: BSE Room 1.328
One UTSA Circle
San Antonio, Texas 78249

Insung Kim
Degenkolb Engineers
375 Beale Street
Suite 500
San Francisco, California 94105

Dawn Lehman
University of Washington
214B Moore Hall, Box 352700
Seattle, Washington 98195

Abbie Liel
University of Colorado at Boulder
1793 Yellow Pine Avenue
Boulder, Colorado 80304

Laura Lowes
University of Washington
233C More Hall, Box 352700
Seattle, Washington 98195

Adolfo Matamoros
Dept. of Civil and Environmental Engineering
The University of Texas at San Antonio
One UTSA Circle
San Antonio, Texas 78249

Farzad Naeim
Farzad Naeim, Inc.
100 Spectrum Center Drive, Suite 900
Irvine, California 92618

Rob Smith
555 12th Street #1700
Oakland, California 94607

John Wallace
5731C Boelter Hall
Department of Civil and Environmental Engineering
University of California
Los Angeles, California 90095

Project Review Panel

Brian Kehoe
Wiss, Janney, Elstner Associates, Inc.
2000 Powell Street, Suite 1650
Emeryville, California 94608

Santiago Pujol
University of Canterbury
5 Kruger Road
Halswell
Christchurch, 8025
New Zealand

Peter Somers
Magnusson Klemencic Associates
1301 Fifth Avenue, Suite 3200
Seattle, Washington 98101

Daniel Zepeda
300 South Grand Avenue
Suite 3850
Los Angeles, California 90071

Working Group Members

Saman A. Abdullah
Dept. of Civil and Environmental Engineering
University of California
Los Angeles, California 90095

Tarbin Basnet
Dept. of Civil and Environmental Engineering
The University of Texas at San Antonio
One UTSA Circle
San Antonio, Texas 78249

Travis Chrupalo
Degenkolb Engineers
375 Beale Street
Suite 500
San Francisco, California 94105

Alex Chu
Degenkolb Engineers
375 Beale Street
Suite 500
San Francisco, California 94105

Dustin Cook
Engineering Laboratory (MS8662)
National Institute of Standards and Technology
100 Bureau Drive
Gaithersburg, Maryland 20899

Ariel Creagh
Degenkolb Engineers
375 Beale Street
Suite 500
San Francisco, California 94105

John A. Egan
766 Brookside Drive
Danville, California 94526

Hamid Khodadadi
Dept. of Civil and Environmental Engineering
The University of Texas at San Antonio
One UTSA Circle
San Antonio, Texas 78249

Kristijan Kolozvari
Dept. of Civil and Environmental Engineering
College of Engineering and Computer Science
California State University, Fullerton
800 N. State College Blvd.
Fullerton, California 92834

Ali Roufegarinejad
Forell/Elsesser Engineers, Inc.
160 Pine Street, 6th Floor
San Francisco, California 94111

Andrew Sen
Engineering Hall, 209
Marquette University
P.O. Box 1881
Milwaukee, Wisconsin 53201

This publication is available free of charge from: https://doi.org/10.6028/NIST.GCR.22-917-50